Quasielastic Neutron Scattering

Principles and Applications in Solid State Chemistry, Biology and Materials Science

M Bée

Laboratoire de Dynamique des Cristaux Moléculaires,
Université des Sciences et des Techniques de Lille Flandres Artois, France

Adam Hilger, Bristol and Philadelphia

British Library Cataloguing in Publication Data

Bée M. (Marc)
Quasielastic neutron scattering.
1. Neutron. Quasielastic scattering
I. Title
539.7'213

ISBN 0-85274-371-8

Library of Congress Cataloging-in-Publication Data

Bée M. (Marc)
Quasielastic neutror scattering: principles and applications in solid state chemistry, biology, and materials science/M. Bée.
437p. 23.4cm.
Bibliography: p.
Includes index.
1. Neutrons–Scattering. 2. Solid state chemistry. 3. Biology. 4. Materials.
QC793.5.N4628B44 1988 88-1916
539.7'213–dc19 CIP

ISBN 0-85274-371-8

Consultant Editor: **D J Millen**

Published under the Adam Hilger imprint by IOP Publishing Ltd
Techno House, Redcliffe Way, Bristol BS1 6NX, England
242 Cherry Street, Philadelphia, PA 19106, USA

Printed in Great Britain by J W Arrowsmith Ltd, Bristol

To my wife
and to my children

Contents

Preface

The idea for this book arose during my appointment at the Institut Laue–Langevin, Grenoble, France. The basic purpose of this research institute is to make the experimental facilities of its high-flux nuclear reactor accessible to the international scientific community. I am aware that the composition of this volume has been largely influenced by the particular atmosphere which is present there, one where there is much discussion and exchange of ideas, which has made this experience unique.

Quasielastic neutron scattering has gradually developed into a powerful analytical technique for the motions of atoms, molecules and chemical moieties. It can be applied to problems dealing with physics and chemistry as well as biology and materials science. Unfortunately this method still remains unfamiliar, mainly because of the rather small number of spectrometers with a sufficiently high resolution which exist at present. With respect to the development of new kinds of instruments, with higher performances and higher fluxes, quasielastic neutron scattering is likely to become an increasingly useful tool for many fields of research; for example, nuclear magnetic resonance and light spectroscopy. Therefore it seemed relevant to bring together in one volume the principles of this method and to describe selected recent applications, in order to present to future users the powerful possibilities that they may expect for their own studies.

I am grateful to all my friends and colleagues at the Institut Laue–Langevin for the many fruitful discussions we have had. I shall mention in particular Dr A J Dianoux and Dr F Volino, who have contributed a lot to the development of the quasielastic scattering technique by calculating numerous mathematical models for various physical situations. I express my gratitude to Dr D Middendorf for the kind and friendly way in which he made me more familiar with biology.

Special thanks are due to Dr C Poinsignon for her help in writing this book. She instigated this volume and was also responsible for a considerable extension of its original scope by drawing my attention to numerous elegant experiments, and making many useful comments about the manuscript. Finally I acknowledge the ladies of the physicist's secretarial office at the Institut Laue–Langevin who typed successive versions of the manuscript, and also to Mrs Stadler and Mr Claisse for drawing the figures.

M Bée
Lille, December 1987

Chapter 1 Survey of the Book

Low-energy neutrons have two remarkable properties which make them a unique probe for the investigation of molecular dynamics in condensed phases, and especially for the study of the rotations of the molecules and of the translation of their centres of mass. The neutron energy is comparable to the molecular rotational energy levels, and the wavelength associated with the neutron is of the order of the interatomic distances in the condensed phases. It is an essential feature of the neutron scattering technique to provide information about both the dynamical and the geometrical aspects of the system under test.

'Quasielastic' scattering is mainly interested in the region of the energy-distribution spectrum of the scattered neutrons, corresponding to small energy transfers with the atoms of the sample, typically ± 2 meV ($\pm 16\,\mathrm{cm}^{-1}$). These originate from interactions of the neutrons with particles diffusing or reorienting over a time-scale *ca* 10^{-10}–10^{-12} s. Such phenomena produce a broadening of the elastic line associated with neutrons scattered without energy transfer. The earliest experiments were carried out with low instrument resolutions and the analyses were often restricted to simple measurements of the overall broadening of the quasielastic peak. The availability of large fluxes of low-energy neutrons from nuclear reactors permitted the design of spectrometers with much better resolution and it became possible to investigate more accurately the exact lineshapes. Their description stimulated numerous theoretical models, which produced a considerable quantity of information about the dynamics of atoms and molecules in solids and liquids. This flourishing development was favoured by the wide variety of subjects of studies encountered in chemical physics, chemistry, biology, etc.

Now, quasielastic neutron scattering has become a technique complementary to light-spectroscopy measurements, NMR, dielectric relaxation and x-ray crystallography. Actually, it turns out that it is not yet a very commonly used method, in spite of the value of the information that it provides.

Neutron scattering measurements need to be performed at nuclear research centres. So they can appear to be a very sophisticated method, restricted to well-defined applications. Besides, they provide a large amount of data, with which it may seem very difficult to deal. This book aims to help future users to overcome these difficulties. An explanation of the basic principles of quasielastic neutron scattering, and a description of the usual types of spectrometers, is intended to make them more familiar with the technique. As a help in data handling, most of the mathematical models elaborated over the last twelve years, are developed. They are illustrated by numerous examples of experiments where they were successfully applied. Thus this book is addressed to those who work with neutrons as a tool in molecular research as well as those who may be interested in the results that this technique can provide, whether they be postgraduates, teachers or research workers. Wherever possible, the neutron results have been related to the conclusions of other techniques, which are extensively referenced.

Readers who are not aware of the neutron scattering technique, can find in chapter 2 an introduction to the basic aspects of this spectroscopy, starting from the elementary level of the neutron properties and of the neutron–matter interaction. The two different features, coherent and incoherent, of the neutron scattering are evidenced and the scattering function is separated into its coherent and incoherent parts. Both are formulated in terms of the classical pair-correlation and self-correlation functions of the scatterers, respectively. The scattering function, or scattering law, appears as the relevant expression to be evaluated for a microscopic interpretation of the experimental data. The linear response theory sometimes provides a convenient framework for this derivation.
Because of the huge incoherent cross section of hydrogen, as compared to the other chemical elements, neutron scattering from hydrogenous compounds is essentially incoherent. This yields a powerful way of investigating the motions of one individual proton, and, therefrom, those of chemical groups or whole molecules. The incoherent scattering law is analysed in terms of single particle motions. Assuming that interactions between the various degrees of freedom can be ignored, the overall scattering is expressed as a convolution of individual effects due to vibration, translation and rotation. Each term is considered successively and its effects on the observed spectra are discussed. Vibrations originating from either inner molecule deformations or collective lattice modes give rise to inelastic scattering. Although these lines are located

outside the energy-transfer range of interest, they can provide some information about the height of the energy barriers against molecule or chemical group reorientations. The translational and the rotational terms are the relevant quantities which are analysed in detail in the following chapters, on the basis of numerous dynamical models. When dealing with orientational disorder in solids, one is mainly concerned with the rotational term. Conversely, long-range diffusion of atoms in solids or monoatomic liquids are analysed from the broadening of the translational term. Molecular liquids are more complex, because of the existence of simultaneous rotations and translations whose mixed effects have to be studied via the convolution product of the two terms. In every case, a basic quantity, the 'elastic incoherent structure factor' (EISF), turns out to be of fundamental importance. It is defined as the relative amount of purely elastically scattered intensity and yields direct information about the geometry of the motions.

Chapter 3 deals with the techniques commonly used in quasielastic neutron scattering. Most of the experiments on which we report in this book were carried out at the Institut Laue-Langevin, in Grenoble (France). The High Flux Reactor and the hot and cold neutron sources are briefly described. Then the various spectrometers working by time-of-flight, backscattering or spin–echo techniques are presented. The basic principles on which they are built, are outlined. Their very different characteristics, either from the point of view of the energy-scale of analysis, or of the Q range accessible in reciprocal space, or of the resolution (minimum measurable energy-exchange) are complementary. Neutron scattering studies often require the use of several instruments, each of them being best adapted to reveal some particular aspects of the problem. Other instruments installed on steady reactors, for example the Orphée reactor in Saclay (France), are also presented. Neutrons are also available from quite different sources using the spallation technique. The Spallation Neutron Source at the Rutherford Appleton Laboratory (UK) is briefly described. Built there is the high-resolution inelastic spectrometer IRIS, which takes advantage of the pulsed character of the neutron beam.

The expression of the scattering law given in chapter 2 assumes that once scattered, the neutron goes out of the sample without being absorbed or further scattered. Actually, in slow neutron scattering the neutron mean free path in the material is often comparable with the macroscopic dimensions of the sample. So the experimental spectra may have to be corrected for the contribution from neutrons which have been scattered several times and for the attenuation in single scattering due to absorption and self-shielding. The aim of chapter 4 is to present the methods usually used to correct for multiple scattering. Results of exact calculation according to a method indicated by Sears are compared

with the results of a Monte Carlo simulation technique. Then an approximation is developed in the case of quasielastic scattering, which allows a further analytical treatment. Examples of applications are given.

Long-range diffusion of particles in solids and liquids has been investigated for many years using the neutron scattering techniques. These studies have stimulated several types of descriptions which we review in chapter 5. The most simple is the continuous diffusion model according to Fick's law. It corresponds on a microscopic scale to the Brownian motion of particles and yields a lorentzian-shaped scattering function. The broadening varies as DQ^2 as a function of the momentum transfer Q and thus enables a determination of the diffusion constant, D. Liquid argon provides a good example of this model. Hydrogen diffusion in solids rather occurs through a jump-diffusion mechanism, amongst a set of well-defined sites. The original model of Chudley and Elliott, later extended to the general case of non-equivalent sites on a non-Bravais lattice shows a strong departure of the broadening variation from the DQ^2 law, at large Q values, where the smallest jump-lengths are revealed. The Singwi–Sjölander model takes into account successive oscillatory and diffusive states. This model was elaborated to interpret the mechanism of diffusion of molecules in water.

Chapter 6 is devoted to the calculation of the rotational incoherent scattering law for different cases of molecular motions. Octaphenylcyclotetrasiloxane and norbornane provide good examples of isotropic rotational diffusion, i.e. the molecules have no preferred orientation in space and reorient themselves continuously by small angular steps. Conversely, the reorientational jump model assumes a set of preferential orientations around which the molecules oscillate. From thermal activation, jumps, assumed to be instantaneous, occur between these orientations. One does not seek to describe the motion of the molecule when it is passing from one orientation to another. The discrete orientational distribution function is obtained by solving a set of stochastic differential equations involving the jump-probabilities per unit time. In spite of the fact that the jumps are not actually instantaneous and that the orientational probability is a continuous function, the number of molecules performing a reorientation is much fewer than the number of molecules in the equilibrium orientations. Consequently, accepting that, in most cases studied so far, the real motion is much more complicated, it has been possible to give an adequate description of the motions on the basis of jump-models with a set of discrete orientations located on the minima of the continuous orientational distribution function.

There exist numerous neutron quasielastic scattering studies of organic compounds in which a chemical group undergoes reorientational jumps about one axis among a set of N orientations. The corresponding scattering laws are derived and illustrated for several values of N:

proton exchange mechanism ($N = 2$), CH_3 rotating group ($N = 3.6$), cyclopentadienyl rings of ferrocene and nickelocene ($N = 5$) or aromatic rings ($N = 6$) in arene metal carbonyls.

When reorientational jumps can occur about more than one axis, as for example about different lattice directions, the use of group theory greatly simplifies the calculation of the scattering law. The formalisms both of Rigny and of Thibaudier and Volino are presented, and compared to each other. The latter is then applied to the case of reorientations about the cube axes (adamantane) and then to more complicated physical situations when reorientations about both fixed (crystalline) and mobile (molecular) axes simultaneously occur. This is illustrated by several investigations of methyl group dynamics in various tertiary butyl compounds. Other examples, with nearly spherical molecules are also reported: the adamantane derivatives (1-halide-adamantane, 1-cyanoadamantane, 2-adamantanone) and the three related molecules bicyclo-octane, triethylenediamine and quinuclidine. Last, we present a generalisation of the method.

In chapter 7 we shall be concerned with special features of quasielastic neutron scattering. Neither the rotational diffusion model nor the jump model are fully satisfactory. The former totally ignores the existence of preferred orientations of the molecule. The second restricts the angular displacement to a set of rotations corresponding to well-defined trajectories for each atom of the molecule (just allowing small librations around the equilibrium orientations). It becomes certainly less valid at high temperature. In fact, over a sufficiently large time-scale, each orientation in space can be accessed. But some orientations are much more probable than others. A model based upon an orientational distribution function peaked at one point was developed in connection with molecular motions in liquid crystals. It was successfully applied to describe the motions of a large molecule, octaphenylcyclotetrasiloxane, and also of dimeric units in the plastic phase of pivalic acid, where it was found consistent with the conclusions of the analysis of the inelastic part of the spectra. Then the following idea arises: to allow any orientation in space but to favour some of them by introducing an angular potential, chosen in a sufficiently realistic way to correctly describe the effective potential experienced by the molecule. For that purpose, we begin to state the stochastic Langevin, Fokker–Planck and Smoluchovski equations, whose basic assumptions are extensively discussed. An application has been given by Dianoux and Volino who have treated the case of a rotation with one degree of freedom in an N-fold cosine potential. They assume that the evolution of the orientational distribution function follows a Fokker–Planck equation involving a phenomenological, frequency-independent diffusion coefficient. According to the height of the potential, they find as limiting cases the free rotational diffusion model or the jump model among equidistant sites.

This model was applied to the study of aligned smectic phases, for both the rotational and the translational case.

The diffusion model of Dianoux and Volino can be generalised to the three-dimensional case. This makes possible the evaluation of the correlation functions of the rotator functions (linear combinations of Wigner functions $D^l_{mn}(\omega)$ of the Euler angles, taking into account both molecular and site symmetries). The incoherent scattering law can then be calculated. By definition, rotator functions possess both the symmetry of the molecule and that of the site. They form an orthogonal basis on which the equilibrium orientational probability and the potential can be expanded. We demonstrate how it is possible to determine the numerical values of the leading coefficients in these expansions from an analysis of x-ray or neutron crystallographic structure measurements and also from the study of the EISF in quasielastic neutron scattering.

The microscopic approach (De Raedt and Michel 1979) also uses the symmetry-adapted functions in the expansion of the neutron scattering law. The Mori–Zwanzig projection-operator technique is used to derive an expression of the correlation functions of these symmetry-adapted functions in terms of their moments. As a concrete example, the case of a dumbbell molecule in an octahedral potential is considered. The most striking feature is that, according to the height of the potential, (or equivalently, according to the value of the temperature), correlation functions are found to have a diffusive or an oscillatory character, corresponding, either to reorientational motions of the molecule or to librations about the potential minima, respectively.

The next section deals with the investigation of orientational disorder by Raman and infrared spectroscopies. Recent studies have evidenced that, from the analysis of the integrated intensity and of the shape of internal modes, it is possible to get information about the numerical values of the coefficients of the expansion of the orientational probability into rotator functions and also about the dynamical aspect of the molecular motion. Examples are given and the results are compared with the conclusions of x-ray and neutron scattering studies.

Incoherent scattering involves the same nucleus at two successive times. So there are no interference effects between the amplitudes scattered by different nuclei. There is no selection rule concerning the momentum transfer vector, $\boldsymbol{Q}$, in contrast to the case of coherent scattering: the total intensity observed results from the simple sum of the different intensities scattered from the individual nuclei. Actually, the momentum transfer vector enters the scattering law. Most of the experiments are performed with polycrystalline samples, and, from the powder average, the dependence on the $\boldsymbol{Q}$-direction is lost. There are, however, some examples of studies with anisotropic samples which we present in chapter 8. The investigation of the reorientations of the NH_4^+

ion in NH_4Cl, or of the adamantane molecule, carried out with single crystals shows how it is possible to take advantage of the dependence of the scattering law on the orientation of Q with respect to lattice axes to discriminate among several dynamical models. Translational diffusion in an anisotropic medium yields the introduction of a diffusion tensor with axial symmetry. An example is given in the bidimensional case with the study of physisorbed species on homogeneous surfaces like CH_4 on graphite. The analysis of the dynamics of water in swelling clays provides an example where two reorientations about perpendicular axes could be evidenced.

Chapter 9 is essentially devoted to the use of the neutron scattering technique in studies of the diffusion of small molecules in restricted geometries. This problem is found in a large variety of physical situations. The simplest case is the problem of diffusion in one dimension between two rigid, impermeable boundaries, solved by Hall and Ross. Later, Volino and Dianoux elaborated a more general formalism to calculate the neutron incoherent scattering law for diffusion in a potential of spherical symmetry. They treated the case of the diffusion of a particle in an impermeable sphere of radius a. This formalism was applied to the study of water mobility in an acid membrane and then generalised to the case of diffusion inside a finite volume with an anisotropic shape. The two scattering laws derived by Hall and Ross, or Volino and Dianoux, evidence a strong departure from the DQ^2 law, in the limit $Q \to 0$ in relation to the presence of the impermeable surface. However, they were evaluated in the framework of the continuous diffusion model and, at large Q values, the variation of the broadening of the spectra follows the usual Fick's law: when motions over short distances only are considered, the influence of the boundaries becomes negligible. Hall and Ross have also considered the case of jump-diffusion which, in addition, shows another departure from the DQ^2 law at large momentum transfer, with a behaviour analogous to the Chudley–Elliott model.

Neutrons have been found to be a powerful probe in the domain of catalysis. Zeolites are porous aluminosilicate crystals presenting in some structural types with nearly spherical cavities distributed over the crystal lattice. These cavities are connected through pores or windows, whose diameters depend on the nature of the zeolite. They have numerous applications in catalysis owing to their structural and chemical properties. They are used, for example, for hydro-dewaxing and isomerisation processes or as hydrocracking catalysts. Owing to the free aperture of the largest pores, they have marked shape selectivity for chemical reactions. Moreover, these materials offer physicists an interesting tool insofar as the cavities may be utilised to isolate one or several molecules, thus constituting a simple physical model. We shall report on

recent neutron studies of various chemical species adsorbed in zeolites: ethylene, benzene, methane, methanol and water.

The availability of very high resolution spectrometers, based on the neutron spin–echo technique permits the analysis of polymers in solutions or in melts. Basic models to describe the local chain motion are reported and the influence of solvent damping or hydrodynamic screening is discussed.

It is impossible to write a book about neutron scattering without reporting on its application to biological systems. Because of the hydrogenous nature of all biomolecules, and because of the importance of water in their function, it is of great interest to be able to probe the degrees of freedom associated with proton motions and to have techniques that can selectively enhance or suppress the signal due to biochemically distinct kinds of protons. The potential of quasielastic neutron scattering for biophysical and biochemical studies is due to three factors, as follows:

(i) The acquisition of data in a large parameter domain not accessible by other biophysical techniques or difficult to interpret otherwise. Spectrally it overlaps with optical, NMR, ESR and Mossbauer work; spatially it extends into the low-Q region of optical methods.

(ii) The wide range of H/D contrast that can be realised with biological samples, both by exchange deuteration of hydrogenous samples and by covalent *in vivo* deuteration (growth of microorganisms in selectively or fully deuterated media) (Crespi 1977).

(iii) Considerable progress has been made in analytical and numerical studies (Brownian dynamics (Dickinson 1985), Monte Carlo (Finney *et al* 1982), quasi-harmonic (Bialek and Goldstein 1985) and *ab initio* simulations (Karplus and McCammon 1981, Levitt 1982, McCammon 1984)) of the intramolecular and intermolecular dynamics of biomolecules. Contacts with experimental work are beginning to be made (Smith *et al* 1986).

Chapter 2 General Aspects of Neutron Scattering

2.1 Properties of the Neutron

The free neutron is an elementary particle liberated for example during the process of fission of a heavy nucleus, with the following properties:

mass:	$m = 1.660 \times 10^{-24}$ g
electric charge:	0
spin:	$\frac{1}{2}$
magnetic moment:	$\mu = -1.913$ nuclear magnetons.

The energy, E, of a free neutron, with velocity $\boldsymbol{v}$, is simply equal to its kinetic energy

$$E = \tfrac{1}{2}mv^2 \tag{2.1}$$

Neutrons can also be considered as plane waves, with wavevector

$$\boldsymbol{k} = \frac{m}{\hbar}\,\boldsymbol{v} \tag{2.2a}$$

and wavelength:

$$\lambda = \frac{2\pi}{|\boldsymbol{k}|} = \frac{h}{mv} \tag{2.2b}$$

so that the (kinetic) energy of a neutron can be written

$$E = \frac{\hbar^2 k^2}{2m} \tag{2.3a}$$

$$= \frac{h^2}{2m\lambda^2}. \tag{2.3b}$$

Neutrons issued from a nuclear reactor core are thermalised when passing through the moderator at the temperature T. The distribution of the velocities of the neutrons follows a Maxwell law about an average value $\bar{v}$ such that

$$\bar{E} = \tfrac{1}{2}m\bar{v}^2 = \tfrac{3}{2}k_B T \tag{2.4}$$

where k_B is the Boltzmann constant. Thermal neutrons, corresponding to $T \simeq 300$ K, have an energy $\bar{E} \simeq 25$ meV and a wavelength $\bar{\lambda} \simeq 1.8$ Å. Therefore the energy of the neutron appears of the same order of magnitude as the intermolecular energies in condensed phases and its wavevector is comparable with the usual molecular dimensions or inter-reticular spacing in solids. These two properties make of (slow) neutrons a very powerful tool for the investigation of dynamical and geometrical properties of matter. Looking for alternative methods, there are photons. X-rays also have wavelengths of the order of 1 Å and therefore, they are widely used for structure analyses. On the other hand, their energy is very large. For instance $E(\text{Cu } K_\alpha) \simeq 8.3$ keV and it will always be found that $E \simeq E_0$. X-ray inelastic scattering might become possible with the high intensity of synchroton radiation sources. Lasers provide an extremely good energy resolution, but their wavelength of 5000 Å only allows excitations to be studied at very low wavevector (Brillouin–Raman scattering). Protons and electrons are charged particles which cannot penetrate deeply into the target because of strong Coulomb interaction. They are therefore restricted to surface studies.

The two basic quantities to be measured in a scattering experiment are: (i) the energy transfer, $\hbar\omega$, between the initial, E_0, and final, E, energies of the neutron

$$\hbar\omega = E - E_0 = \frac{\hbar^2}{2m}(k^2 - k_0^2) \tag{2.5}$$

where $\boldsymbol{k}_0$ and $\boldsymbol{k}$ are the corresponding wavevectors, and (ii) the scattering vector, $\boldsymbol{Q}$, corresponding to the wavevector transfer:

$$\boldsymbol{Q} = \boldsymbol{k} - \boldsymbol{k}_0. \tag{2.6}$$

From considerations concerning the magnitude of the energy of neutrons in materials, it is clear that, for a given scattering angle, ϕ, between $\boldsymbol{k}$ and $\boldsymbol{k}_0$, $\boldsymbol{Q}$ cannot be kept constant while varying the energy transfer (figure 2.1). This point is especially important for time-of-flight experiments (see chapter 3). It will be discussed in detail in §2.10.

So far, we have expressed the energies in millielectronvolts. Other units are frequently used in neutron spectroscopies. Table 2.1 gives a list of conversion factors.

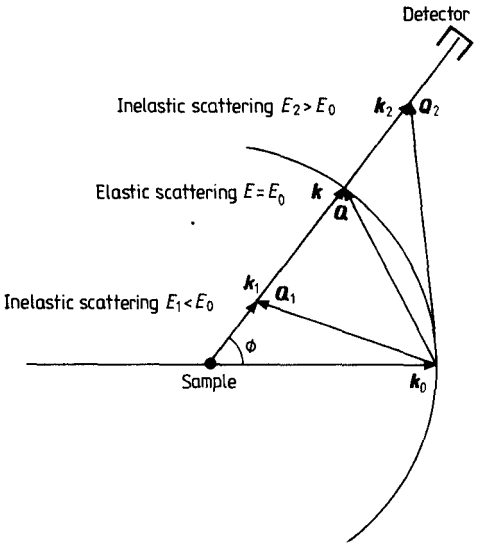

Figure 2.1 Variation of the wavevector transfer $Q = k - k_0$ as a function of the energy transfer $\hbar\omega = E - E_0$ for neutrons detected at constant scattering angle: k_0, incident neutron wavevector; E_0, incident neutron energy; k, k_1, k_2: final neutron wavevectors: E, E_1, E_2: final neutron energies.

2.2 Definition of the Cross Sections

When a neutron passes near a nucleus, there are two possibilities.

(i) The neutron is absorbed, i.e. it is trapped by the nucleus. A compound nucleus in an excited state is formed, which decays into its ground state. In most cases this decay occurs by γ emission. Another possibility, which is used for instance in some neutron detectors, like ^{3}He detectors, is the emission of charged particles like α or tritons. Finally, the compound nucleus can decay by fission, like uranium in a reactor core.

(ii) The neutron is scattered, i.e. its direction as well as its energy are changed. The energy of thermal neutrons is too small to create internal excitations of the nucleus or of the electronic shell. However, the atomic motions that the nucleus experiences and which correspond to much smaller energies can be felt by the neutron and give rise to inelastic scattering.

Assuming a current of I_0 neutrons per second and per square centimetre incident on the specimen, it is possible to define from the

Table 2.1 List of conversion factors. The table is read horizontally, e.g. 1 meV corresponds to 0.0965 kJ mol^{-1} or also to 8.006 cm^{-1}, etc.

	kJ mol^{-1}	kcal mol^{-1}	meV	cm^{-1}	rad s^{-1}	Hz	K	Å	m s^{-1}
kJ mol^{-1}	1	0.2388	10.36	83.58	1.574×10^{13}	2.505×10^{12}	120.3	2.810	1.408×10^{3}
kcal mol^{-1}	4.187	1	43.39	345.0	6.591×10^{13}	1.049×10^{13}	503.3	1.373	2.881×10^{3}
meV	0.0965	0.0230	1	8.006	1.519×10^{12}	2.418×10^{11}	11.605	9.045	437.4
cm^{-1}	1.196×10^{-2}	2.858×10^{-3}	0.1240	1	1.884×10^{11}	2.998×10^{10}	1.439	25.68	154.05
rad s^{-1}	6.351×10^{-14}	1.517×10^{-14}	6.582×10^{-13}	5.309×10^{-12}	1	0.1592	7.640×10^{-12}	1.115×10^{7}	3.547×10^{-4}
Hz	3.991×10^{-13}	9.536×10^{-14}	4.136×10^{-12}	3.336×10^{-11}	6.238	1	4.800×10^{-11}	4.447×10^{6}	8.895×10^{-4}
K	8.314×10^{-3}	1.986×10^{-3}	8.616×10^{-2}	0.6949	1.309×10^{11}	2.083×10^{10}	1	30.81	128.4
Å	7.894	1.885	81.807	659.8	1.243×10^{14}	1.978×10^{13}	949.4	1	3.956×10^{3}
m s^{-1}	5.044×10^{-7}	1.202×10^{-7}	5.227×10^{-6}	4.216×10^{-5}	7.948×10^{6}	1.265×10^{6}	6.066×10^{-5}	3.956×10^{3}	1

Energy	E		: kJ, kcal, meV	$\sim E$
Optical wavevector	$\frac{\nu}{c}$		: cm^{-1}	
Cycles	ω	$E = \hbar\omega$	: rad s^{-1}	
Frequency	ν	$\nu = \frac{\omega}{2\pi}$	: Hz	
Temperature	T	$E = k_B T$	: K	
Wavelength	λ	$E = \frac{h^2}{2m\lambda^2}$	: Å	$\lambda \sim 1/\sqrt{E}$
Velocity	v	$E = \frac{1}{2}mv^2$	: m s^{-1}	$v \sim \sqrt{E}$

$\hbar = h/2\pi$ $\quad h = 6.616\,176 \times 10^{-34}$ J s $\quad m = 1.674\,954 \times 10^{-24}$ g

number I_s or I_a of scattering or absorption events occurring each second, a scattering and an absorption cross section, denoted σ_s and σ_a, respectively, through the relation:

$$I_s = I_0\sigma_s \tag{2.7a}$$

$$I_a = I_0\sigma_a. \tag{2.7b}$$

Both σ_a and σ_s have the dimension of a surface. The usual unit is the barn:

$$1 \text{ barn} = 10^{-24} \text{ cm}^2.$$

At low energies (a few millielectronvolts), σ_a is a smooth function of the neutron energy, proportional to the wavelength of the neutron (hence to the reciprocal of its velocity)

$$\sigma_a \sim \lambda \tag{2.8a}$$

$$\sigma_a \sim \frac{1}{v} \tag{2.8b}$$

Values of σ_a for thermal neutrons, having a velocity $v = 2200 \text{ m s}^{-1}$, i.e. a wavelength $\lambda = 1.8$ Å, are tabulated in table 2.2 (p17).

Together with the cross section σ, two other quantities are commonly used in neutron scattering. The differential cross section in one direction $\mathbf{\Omega}$,

$$\frac{\partial\sigma}{\partial\Omega}$$

gives the probability that a neutron leaves the sample in the solid angle element $d\mathbf{\Omega}$ about the direction $\mathbf{\Omega}$. The double-differential cross section

$$\frac{\partial^2\sigma}{\partial\mathbf{\Omega}\partial E} = \frac{1}{\hbar}\frac{\partial^2\sigma}{\partial\mathbf{\Omega}\partial\omega}$$

gives the probability that a neutron, with incident energy E_0, leaves the sample in the solid angle element $d\mathbf{\Omega}$ about the direction $\mathbf{\Omega}$ and with an energy exchange comprised between $\hbar\omega = E - E_0$ and $\hbar(\omega + d\omega)$. Clearly

$$\sigma = \int d\mathbf{\Omega}\,\frac{\partial\sigma}{\partial\mathbf{\Omega}} = \int d\omega \int d\mathbf{\Omega}\,\frac{\partial^2\sigma}{\partial\mathbf{\Omega}\partial\omega}. \tag{2.9}$$

A neutron interacts with a nucleus via nuclear and magnetic forces. We know from the experimental results that the nuclear part of the interaction has a very short range compared to the (thermal) neutron wavelength and to the nuclear radius. Therefore, it can be shown that the neutron nucleus scattering is isotropic and characterised by a single parameter, b, the scattering length. This parameter is independent of the neutron energy. b can be complex and the real part can be positive

or negative according to the attractive or repulsive nature of the interaction. The imaginary part of b represents absorption.

A neutron interacts with the spin via the dipole–dipole coupling. However, for diamagnetic systems, the magnetic interaction is always negligible compared to the nuclear interaction and will not be considered in this book.

If the nucleus is at the position defined by $\boldsymbol{R}_i$ and the neutron located at $\boldsymbol{r}$, the Fermi pseudopotential is defined as

$$V(\boldsymbol{r}) = \frac{2\pi\hbar^2}{m} b_i \delta(\boldsymbol{r} - \boldsymbol{R}_i) \tag{2.10}$$

In fact, the potential described by (2.10) is simply a formal artifice (Lovesey 1984) accounting for the fact that the neutron–nucleus interaction has a very short range.

In an actual experiment, the specimen is composed of several given atomic species, i, each of them being a mixture of several isotopes possessing a nuclear spin. As can be seen in table 2.2, the scattering lengths, b_i, change not only from one species to another but also for the different isotopes of the same species, because the interaction depends not only on the nature of the nucleus but also on the total spin state of the nucleus–neutron system.

The average $\langle b_i \rangle$ of b_i over all the isotopes and spin states is called the *coherent* scattering length. Simultaneously, the *incoherent* scattering length is defined as the root mean square deviation of b_i from $\langle b_i \rangle$:

$$b_i^{\text{coh}} = \langle b_i \rangle \tag{2.11a}$$

$$b_i^{\text{inc}} = [\langle b_i^2 \rangle - \langle b_i \rangle^2]^{1/2}. \tag{2.11b}$$

Let us consider the case of a single isotope, with nuclear spin, s, interacting with a neutron spin $\frac{1}{2}$. Therefore there are two scattering lengths b^+ and b^-, associated with the two possible spin states, $S^+ = s + \frac{1}{2}$ and $S^- = s - \frac{1}{2}$. Because there are $n^+ = 2S^+ + 1$ and $n^- = 2S^- + 1$ states of spin S^+ and S^-, respectively, if each of them has the same probability,

$$\langle b \rangle = \frac{1}{n^+ + n^-} [n^+ b^+ + n^- b^-] \tag{2.12a}$$

$$b^{\text{inc}} = \frac{1}{2s + 1} [(s + 1)b^+ + sb^-] \tag{2.12b}$$

$$\langle b^2 \rangle = \frac{1}{n^+ + n^-} [n^+ (b^+)^2 + n^- (b^-)^2] \tag{2.13a}$$

$$= \frac{1}{2s + 1} [(s + 1)(b^+)^2 + s(b^-)^2] \tag{2.13b}$$

These expressions of $\langle b \rangle$ and $\langle b^2 \rangle$ permit the evaluation of the so-called bound cross sections, defined as

$$\sigma_{\text{coh}} = 4\pi \langle b \rangle^2 \tag{2.14}$$

for the coherent cross section, and

$$\sigma_{\text{inc}} = 4\pi(\langle b^2 \rangle - \langle b \rangle^2) \tag{2.15a}$$

$$= 4\pi \langle (b - \langle b \rangle)^2 \rangle \tag{2.15b}$$

for the incoherent cross section. The total bound scattering cross section is then

$$\sigma = \sigma_{\text{coh}} + \sigma_{\text{inc}}. \tag{2.16}$$

A very important example for the following of this book is the case of hydrogen. Here the nucleus is simply formed of a single proton with spin $\frac{1}{2}$. The relevant scattering lengths are

$$b^+ = 1.04 \times 10^{-12} \text{ cm}$$

for the triplet total spin state $S^+ = 1$, $n^+ = 3$, and

$$b^- = -4.74 \times 10^{-12} \text{ cm}$$

for the singlet state $S^- = 0$, $n^- = 1$. Therefore, according to (2.12) and (2.13) above

$$\langle b \rangle = \tfrac{1}{4} [3b^+ + b^-] = -0.38 \times 10^{-12} \text{ cm}$$

$$\langle b^2 \rangle = \tfrac{1}{4} [3(b^+)^2 + (b^-)^2] = 6.49 \times 10^{-24} \text{ cm}^2$$

so that the coherent and incoherent cross sections, expressed in barn units (1 barn = 10^{-24} cm^2) are equal to

$$\sigma_{\text{coh}}(\text{H}) = 1.8 \text{ barns}$$

$$\sigma_{\text{inc}}(\text{H}) = 79.9 \text{ barns}.$$

The large difference between $\sigma_{\text{coh}}(\text{H})$ and $\sigma_{\text{inc}}(\text{H})$ arises essentially from the opposite signs of b^+ and b^-. As can be seen in table 2.2, the incoherent cross section for hydrogen is much larger than for any other element. That makes the incoherent neutron scattering a unique tool for the investigation of hydrogenous compounds. Conversely, $\sigma_{\text{coh}}(\text{H})$ is rather small. Considering the case of deuterium, $s = 1$, we obtain for the state $S^+ = \frac{3}{2}$, $n^+ = 4$

$$b^+ = 0.95 \times 10^{-12} \text{ cm}$$

and

$$b^- = 0.10 \times 10^{-12} \text{ cm}$$

for the other state $S^- = \frac{1}{2}$, $n^- = 2$. Hence, the cross sections are

$$\sigma_{coh}(D) = 5.6 \text{ barns}$$

and

$$\sigma_{inc}(D) = 2.0 \text{ barns}.$$

In the study of organic compounds, it turns out that, when we are especially interested in the coherent part of neutron scattering, it is preferable, and even almost necessary, to carry out the experiments with deuterated samples. On the other hand, incoherent neutron scattering studies can take advantage of the deuteration technique to vary the contributions to the scattered intensity originating from different species or chemical groups and to discriminate among them.

It can be seen from the list of values given in table 2.2, that for neutrons, heavy and light elements can have comparable scattering lengths, b. That is the reverse of the situation for x-rays, for which the scattering factors are proportional to the atomic number. It is well known that light elements are almost invisible in x-ray investigations, especially if heavy ions are present. On the contrary, there is *a priori* no obstacle to observing light atoms with neutrons, providing that their scattering length is sufficient.

Generally, the various atomic species present in the specimen are composed of several isotopes. Therefore, the cross sections for each atomic species have to be calculated by taking into account the relative abundance, c_j, of each isotope, j.

$$\langle b \rangle = \sum_j \frac{c_j}{2s_j + 1} [(s_j + 1)b_j^+ + s_j b_j^-] \tag{2.17a}$$

$$\langle b^2 \rangle = \sum_j \frac{c_j}{2s_j + 1} [(s_j + 1)(b_j^+)^2 + s_j (b_j^-)^2] \tag{2.17b}$$

If the neutrons are polarised or the nuclear spins are aligned, the $2s + 2$ spin states of the nucleus–neutron system are not equally probable, and the expressions (2.12) and (2.13) of the averages over spin states are not valid. Some instrumental techniques use neutron polarisation to discriminate between coherent and incoherent scattering. But to avoid the average over isotopes (equation (2.17)) it is necessary to use pure isotopic substances, a condition which is not easily satisfied.

To conclude this section, it is worth noting that, besides hydrogen, two other elements are of particular importance in neutron scattering. Aluminium absorbs very weakly the neutron beams (1% per millimetre thickness). So it will be frequently used to build windows of cryostats, sample-containers, etc. Vanadium is an almost purely incoherent scatterer. ($\sigma_{coh}(V) = 0.03$ barn and $\sigma_{inc}(V) = 5.1$ barns). It is used as standard material for instrument calibrations.

Table 2.2 Summary of bound scattering lengths and cross sections, for low-energy neutron scattering. Only the most common isotopes of each element have been tabulated. The data are obtained from the compilation by Sears (1984). Reproduced by permission of Atomic Energy of Canada Limited). Column 1, chemical symbol of the element; column 2, atomic number; column 3, mass number: column 4, spin parity of the nuclear ground state; column 5, relative abundance (%). For radioisotopes, the half-life is given instead, columns 6, 7, bound coherent and incoherent scattering lengths, respectively. The imaginary part is indicated if existing; columns 8, 9, 10, coherent, incoherent and total scattering cross sections, respectively. As usual they are given in barns (1 barn = 10^{-24} cm^2); column 11, absorption cross section (in barns).

Reference: SEARS, V.F. (1984) 'Thermal-neutron scattering lengths and cross-sections for condensed matter research' Chalk River Nuclear Laboratories, Chalk River, Ontario, Canada.

	Z	A	Spin	Relative abundance	Coherent scattering length (10^{-15} m)		Incoherent scattering length (10^{-15} m)		Cross sections (in barns) Coher.	Incoh.	Scat.	Absorp.
H	1				−3.7409				1.7586	79.90	81.66	0.332 6
		1	1/2	99.985	−3.7423		25.217		1.7599	79.91	81.67	0.332 6
		2	1	0.015	6.674		4.033		5.597	2.04	7.64	0.000 51
		3	1/2	(12.32A)	4.94		0.00		3.07	0.00	3.07	0
He	2				3.26				1.34	0.00	1.34	0.007 47
		3	1/2	0.000 14	5.74	−i × 1.48	−1.8	+i × 2.56	4.42	1.2	5.6	5333.
		4	0	99.999 8	3.26		0		1.34	0	1.34	0
Li	3				−1.90				0.454	0.91	1.36	70.5
		6	1	7.5	2.0	−i × 0.26	−1.79	+i × 0.25	0.51	0.41	0.92	940.
		7	−3/2	92.5	−2.22		−2.49		0.619	0.78	1.40	0.045 4
Be	4	9	−3/2	100	7.79		0.20		7.63	0.005	7.64	0.007 6
B	5				5.30	−i × 0.21			3.54	1.70	5.24	767.
		10	3	20	−0.1	−i × 1.06	−4.7	+i × 1.23	0.14	3.0	3.1	3837
		11	−3/2	80.	6.65		−1.31		5.56	0.22	5.78	0.005 5

Table 2.2 (*cont.*)

	Z	A	Spin	Relative abundance	Coherent scattering length (10^{-15} m)	Incoherent scattering length (10^{-15} m)	Cross sections (in barns) Coher.	Incoh.	Scat.	Absorp.
C	6				6.6484		5.554	0.001	5.555	0.003 50
		12	0	98.9	6.6535	0	5.563	0	5.563	0.003 53
N	7				9.36		11.01	0.49	11.50	1.90
		14	1	99.63	9.37	1.98	11.03	0.49	11.52	1.91
O	8				5.805		4.235	0.000	4.235	0.000 19
		16	0	99.762	5.805	0	4.235	0	4.235	0.000 10
F	9	19	1/2	100	5.654	−0.082	4.017	0.0008	4.018	0.009 6
Ne	10				4.547		2.598	0.008	2.606	0.039
		20	0	90.51	4.610	0	2.671	0	2.671	0.037
Na	11	23	3/2	100	3.63	3.59	1.66	1.62	3.28	0.530
Mg	12				5.375		3.631	0.077	3.708	0.063
		24	0	78.99	5.68	0	4.05	0	4.05	0.051
Al	13	27	5/2	100	3.449	0.26	1.495	0.0085	1.504	0.231
Si	14				4.149		2.163	0.015	2.178	0.171
		28	0	92.23	4.106	0	2.119	0	2.119	0.177
P	15	31	1/2	100	5.13	0.22	3.307	0.006	3.313	0.172
S	16				2.847		1.0186	0.007	1.026	0.53
		32	0	95.02	2.804	0	0.9880	0	0.9880	0.54
Cl	17				9.5792		11.531	5.2	16.7	33.5
		35	3/2	75.77	11.66	6.0	17.08	4.5	21.6	44.1
		37	3/2	24.23	3.08	0.02	1.19	0.0001	1.19	0.433
Ar	18			1.909		0.458	0.22	0.68	0.675	
		40	0	99.600	1.83	0	0.42	0	0.42	0.660

Table 2.2 (*cont.*)

	Z	A	Spin	Relative abundance	Coherent scattering length (10^{-15} m)	Incoherent scattering length (10^{-15} m)	Cross sections (in barns) Coher.	Incoh.	Scat.	Absorp.
K	19				3.71		1.73	0.25	1.98	2.1
		39	3/2	93.258	3.79	1.4	1.81	0.25	2.06	2.1
Ca	20				4.90		3.02	0.03	3.05	0.43
		40	0	96.941	4.99	0	3.13	0	3.13	0.41
Sc	21	45	−7/2	100	12.29	−6.0	19.0	4.5	23.5	27.2
Ti	22				−3.30		1.37	2.67	4.04	6.09
		48	0	73.8	−5.84	0	4.29	0	4.29	7.84
V	23				−0.3824		0.0184	5.187	5.205	5.08
		51	−7/2	99.750	−0.4024	6.419	0.0203	5.178	5.198	4.9
Cr	24				3.635		1.660	1.83	3.49	3.07
		52	0	83.79	4.950	0	3.042	0	3.042	0.76
Mn	25	55	−5/2	100	−3.73	1.79	1.75	0.40	2.15	13.3
Fe	26				9.54		11.44	0.39	11.83	2.56
		56	0	91.7	10.03	0	12.64	0	12.64	2.59
Co	27	59	−7/2	100	2.50	−6.2	0.79	4.8	5.6	37.18
Ni	28				10.3		13.3	5.2	18.5	4.49
		58	0	68.27	14.4	0	26.1	0	26.1	4.6
		60	0	26.10	2.8	0	0.99	0	0.99	2.9
Cu	29				7.718		7.486	0.52	8.01	3.78
		63	−3/2	69.17	6.43	0.22	5.2	0.0061	5.2	4.50
		65	−3/2	30.83	10.61	1.79	14.1	0.40	14.5	2.17

Table 2.2 (*cont.*)

	Z	A	Spin	Relative abundance	Coherent scattering length (10^{-15} m)	Incoherent scattering length (10^{-15} m)	Cross sections (in barns) Coher.	Incoh.	Scat.	Absorp.
Zn	30				5.680		4.054	0.077	4.131	1.11
		64	0	48.6	5.23	0	3.44	0	3.44	0.76
		66	0	27.9	6.01	0	4.54	0	4.54	0.85
		68	0	18.8	6.05	0	4.60	0	4.60	1.1
Ga	31				7.288		6.67	0.0	6.7	2.9
		69	−3/2	60.1						1.68
		71	−3/2	39.9						4.71
Ge	32				8.1939		8.435	0.17	8.60	2.3
		70	0	20.5	9.5	0	11.3	0	11.3	3.43
		72	0	27.4	8.8	0	9.7	0	9.7	0.98
		74	0	36.5	7.9	0	7.8	0	7.8	0.51
As	33	75	−3/2	100	6.58	−0.69	5.44	0.060	5.50	4.5
Se	34				7.970		7.98	0.33	8.31	11.7
		78	0	23.5	8.24	0	8.53	0	8.53	0.43
		80	0	49.6	7.48	0	7.03	0	7.03	0.61
Br	35				6.79		5.79	0.10	5.89	6.9
		79	−3/2	50.69	6.80	−1.07	5.81	0.14	5.95	11.0
		81	−3/2	49.31	6.78	0.58	5.78	0.04	5.82	2.7
Kr	36				7.80		7.65	0.03	7.68	25.
		84	0	57.0		0		0		0.110
		86	0	17.3		0		0		0.003
Rb	37				7.08		6.30	0.3	6.6	0.38
		85	−5/2	72.17	7.01	1.5	6.18	0.3	6.5	0.48
		87	−3/2	27.83	7.27	1.5	6.6	0.3	6.9	0.12

Table 2.2 (*cont.*)

	Z	A	Spin	Relative abundance	Coherent scattering length (10^{-15} m)	Incoherent scattering length (10^{-15} m)	Cross sections (in barns) Coher.	Incoh.	Scat.	Absorp.
Sr	38				7.02		6.19	0.04	6.23	1.28
		88	0	82.58	7.16	0	6.44	0	6.44	0.058
Y	39	89	−1/2	100	7.75	1.09	7.55	0.15	7.70	1.28
Zr	40				7.16		6.44	0.16	6.60	0.185
		90	0	51.45	6.3	0	5.0	0	5.0	0.011
		92	0	17.19	7.5	0	7.1	0	7.1	0.22
		94	0	17.28	8.3	0	8.7	0	8.7	0.0499
Nb	41	93	9/2	100	7.054	−0.139	6.253	0.0024	6.255	1.15
Mo	42				6.95		6.07	0.28	6.35	2.55
		95	5/2	15.92						14.0
		96	0	16.68		0		0		0.5
		98	0	24.13		0		0		0.130
Tc	43									
		99	9/2	(2.13E5A)	6.8		5.8			20.
Ru	44				7.21		6.53	0.07	6.6	2.56
		101	5/2	17.0						3.4
		102	0	31.6		0		0		1.21
		104	0	18.7		0		0		0.32
Rh	45	103	−1/2	100	5.88		4.34			145.
Pd	46				5.91		4.39	0.093	4.48	6.9
		105	5/2	22.33	5.5		3.8			20.
		106	0	27.33	6.4	0	5.1	0	5.1	0.305
		108	0	26.46	4.1	0	2.1	0	2.1	8.5

Table 2.2 (*cont.*)

	Z	A	Spin	Relative abundance	Coherent scattering length (10^{-15} m)		Incoherent scattering length (10^{-15} m)		Cross sections (in barns) Coher.	Incoh.	Scat.	Absorp.
Ag	47				5.992				4.407	0.58	4.99	63.3
		107	−1/2	51.83	7.555		1.00		7.17	0.13	7.30	37.6
		109	−1/2	48.17	4.165		−1.60		2.18	0.32	2.50	91.0
Cd	48				5.1	−i×0.70			3.3	2.4	5.7	2520.
		112	0	24.13	7.4		0		6.9	0	6.9	2.2
						−i×5.73		−i×3.31				
		114	0	28.72	6.4		0		5.1	0	5.1	0.34
In	49				4.065	−i×0.05			2.08	0.54	2.62	193.8
		115	9/2	95.7	4.01		−2.1		2.02	0.55	2.57	202.
Sn	50				6.228				4.874	0.022	4.896	0.626
		118	0	24.3	6.0		0		4.5	0	4.5	0.22
		120	0	32.4	6.6		0		5.5	0	5.5	0.14
Sb	51				5.641				3.999	0.3	4.3	5.1
		121	5/2	57.3								5.9
		123	7/2	42.7								4.2
Te	52				5.43				3.71	0.02	3.73	4.7
		126	0	18.95	5.2		0		3.4	0	3.4	1.04
		128	0	31.69	5.5		0		3.8	0	3.8	0.215
		130	0	33.80	5.6		0		3.9	0	3.9	0.29
I	53	127	5/2	100	5.28		0.0		3.50	0.0	3.50	6.2

Table 2.2 (*cont.*)

	Z	A	Spin	Relative abundance	Coherent scattering length (10^{-15} m)		Incoherent scattering length (10^{-15} m)	Cross sections (in barns) Coher.	Incoh.	Scat.	Absorp.
Xe	54				4.85			2.96			23.9
		129	1/2	26.4							21.
		131	3/2	21.2							85.
		132	0	26.9			0		0		0.45
Cs	55	133	7/2	100	5.42		1.29	3.69	0.21	3.90	29.0
Ba	56				5.25			3.46	0.01	3.47	1.2
		138	0	71.70			0		0		0.360
La	57				8.24			8.53	1.13	9.66	8.97
		139	7/2	99.91	8.243		3.0	8.54	1.13	9.67	8.93
Ce	58				4.84			2.94	0.00	2.94	0.63
		140	0	88.48	4.84			2.94	0	2.94	0.57
Pr	59	141	5/2	100	4.45		−0.36	2.49	0.016	2.51	11.5
Nd	60				7.69			7.43	11.	18.	50.5
		142	0	27.16	7.7		0	7.5	0	7.5	18.7
		144	0	23.8	2.4		0	0.72	0	0.72	3.6
		146	0	17.19	8.7		0	9.5	0	9.5	1.4
Pm	61	147	7/2	(2.62A)	12.6		3.2	20.0	1.3	21.3	168.4
Sm	62				4.2	−i×1.58		2.5	50.	52.	5670.
		147	−7/2	15.1	14.		3.	25.	1.	26.	57.
		152	0	26.6	−5.0		0	3.1	0	3.1	206.
		154	0	22.6	8.		0	8.	0	8.	8.4

Table 2.2 (*cont.*)

	Z	A	Spin	Relative abundance	Coherent scattering length (10^{-15} m)		Incoherent scattering length (10^{-15} m)		Cross sections (in barns) Coher.	Incoh.	Scat.	Absorp.
Eu	63		p		6.68	−i×1.28			5.8	2.2	8.0	4600.
		151	5/2	47.8	5.0	−i×2.56	3.8	−i×2.16	4.0	2.4	6.4	9200.
		153	5/2	52.2	8.22		2.8		8.5	1.0	9.5	322.
Gd	64				9.5	−i×13.5			34.5	158.	192.	48890.
		155	3/2	14.8	13.8	−i×16.9	4.	−i×13.1	60	24.	84.	60900.
		156	0	20.6	6.3		0		5.0	0	5.0	1.5
		157	−3/2	15.7	11.	−i×70.6	26.	−i×54.7	642.	461.	1103.	254000.
		158	0	24.8	8.9		0		10.	0	10.	2.0
		160	0	21.8	9.15		0		10.52	0	10.52	0.77
Tb	65	159	3/2	100	7.38		−0.17		6.84	0.004	6.84	23.4
Dy	66				16.9	−i×0.261			35.9	54.5	90.4	940.
		161	5/2	19.0	10.3		5.1		13.3	3.3	16.6	570.
		162	0	25.5	−1.4		0		0.25	0	0.25	194.
		163	−5/2	24.9	5.0		1.3		3.1	0.21	3.3	130.
		164	0	28.1	49.4	−i×0.74	0	307.0	0		307.	2650.
Ho	67	165	−7/2	100	8.08		−1.7		8.20	0.36	8.56	64.7
Er	68				8.03				8.10	1.2	9.3	159.2
		166	0	33.4	10.4		0		13.6	0	13.6	19.6
		167	7/2	22.9	3.0		2.		1.1	0.5	1.6	659.
		168	0	27.1	8.7		0		9.5	0	0.5	2.74

Table 2.2 (*cont.*)

	Z	A	Spin	Relative abundance	Coherent scattering length (10^{-15} m)	Incoherent scattering length (10^{-15} m)	Cross sections (in barns) Coher.	Incoh.	Scat.	Absorp.
Tm	69	169	1/2	100	7.05	1.8	6.25	0.41	6.66	105.
Yb	70				12.40		19.3	3.0	22.3	35.1
		172	0	21.9	9.43	0	11.2	0	11.2	0.8
		173	−5/2	16.1	9.56	2.	11.5	0.5	12.0	17.1
		174	0	31.8	19.2	0	46.3	0	46.3	67.5
Lu	71				7.3		6.7	0.10	6.8	76.4
		175	7/2	97.39	7.4	0.0	6.9	0.0	6.9	23.1
Hf	72				7.77		7.6	2.6	10.2	104.1
		177	−7/2	18.6	0.7	1.	0.06	0.13	0.2	373.
		178	0	27.1	5.9	0	4.4	0	4.4	84.
		180	0	35.2	13.2	0	21.9	0	21.9	13.04
Ta	73				6.91		6.00	0.020	6.02	20.6
		181	7/2	99.988	6.91	−0.29	6.00	0.011	6.01	20.5
W	74				4.77		2.86	2.00	4.86	18.4
		182	0	26.3	8.21	0	8.5	0	8.5	20.7
		184	0	30.7	7.59	0	7.24	0	7.24	1.7
		186	0	28.6	−1.19	0	0.178	0	0.178	37.9
Re	75				9.2		10.6	0.9	11.5	90.7
		185	5/2	37.40	9.0	2.	10.2	0.5	10.7	112.
		187	5/2	62.60	9.3	2.8	10.9	1.0	11.9	78.0

Table 2.2 (*cont.*)

	Z	A	Spin	Relative abundance	Coherent scattering length (10^{-15} m)		Incoherent scattering length (10^{-15} m)	Cross sections (in barns) Coher.	Incoh.	Scat.	Absorp.
Os	76				11.0			15.2	0.4	15.6	16.0
		189	−3/2	16.1	11.0		2.	15.2	0.5	15.7	25.
		190	0	26.4	11.4		0	16.3	0	16.3	13.1
		192	0	41.0	11.9		0	17.8	0	17.8	2.0
Ir	77				10.6			14.1	0.2	14.3	425.3
		191	3/2	37.3							954.
		193	3/2	62.7							111.
Pt	78				9.63			11.65	0.13	11.78	10.3
		194	0	32.9	10.55		0	14.0	0	14.0	1.2
		195	−1/2	33.8	8.91		−1.0	10.0	0.13	10.1	27.5
		196	0	25.3	9.89		0	12.3	0	12.3	0.72
Au	79	197	3/2	100	7.63		−1.69	7.32	0.36	7.68	98.65
Hg	80				12.66			20.14	6.7	26.8	372.3
		199	−1/2	17.0	16.9	−i×0.60	15.6	35.9	30.5	66.4	2150.
		200	0	23.1			0		0		60.
		202	0	29.6			0		0		4.9
Tl	81				8.785			9.70	0.14	9.84	3.43
		203	1/2	29.524	6.99		0.38	6.1	0.018	6.1	11.4
		205	1/2	70.476	9.54		−0.13	11.4	0.0021	11.4	0.107
Pb	82				9.4003			11.104	0.0030	11.107	0.171
		206	0	24.1	8.8		0	9.7	0	9.7	0.030 6
		207	−1/2	22.1	9.46		0.09	11.25	0.001	11.25	0.712
		208	0	52.4	9.65		0	11.7	0	11.7	0.000 49

Table 2.2 (*cont.*)

	Z	A	Spin	Relative abundance	Coherent scattering length (10^{-15} m)	Incoherent scattering length (10^{-15} m)	Cross sections (in barns) Coher.	Incoh.	Scat.	Absorp.
Bi	83	209	−9/2	100	8.5256	0.239	9.134	0.0072	9.141	0.0338
Po	84									
At	85									
Rn	86									
Fr	87									
Ra	88									
		226	0	(1.60E3A)	10.0	0	12.6	0	12.6	1.8
Ac	89									
Th	90	232	0	100	9.84	0	12.17	0	12.17	7.37
Pa	91									
		231	−3/2	(3.28E4A)	9.1		10.4			200.6
U	92				8.417		8.903	0.004	8.907	7.57
		233	5/2	(1.59E5A)	10.1	0.9	12.8	0.1	12.9	580.3
		238	0	99.275	8.407	0	8.882	0	8.882	2.680
Np	93									
		237	5/2	(2.14E6A)	10.55		14.0			175.9
Pu	94									
		238	0	(87.74A)	14.1	0	25.0	0	25.0	558.
		239	1/2	(2.41E4A)	7.7	1.3	7.5	0.2	7.7	1017.0
		240	0	(6.56E3A)	3.5	0	1.54	0	1.54	289.6
		242	0	(3.76E5A)	8.1	0	8.2	0	8.2	18.5
Am	95									
		243	−5/2	(7.37E3A)	8.3		8.7			75.3
Cm	96									
		244	0	(18.10A)	9.5	0	11.3	0	11.3	16.2

2.3 Neutron Spectroscopy

2.3.1 Principle of a spectroscopic measurement

We shall report the elegant description given by Volino (1978) for the principle of any spectroscopic experiment in terms of a coupling between a probe and a reservoir.

Let us consider a system to be investigated, at thermal equilibrium T. This first system, hereafter designated as the 'reservoir', is composed of N particles, and it is characterised by its hamiltonian, H_R, with eigenvalues $E_{m'}$ and eigenstates $|m'\rangle$. The reservoir can be in any state $|m'\rangle$ with the probability

$$p_{m'} = \frac{1}{Z_R} \exp(-\beta E_{m'}) \tag{2.18a}$$

with $\beta = (k_B T)^{-1}$, k_B being the Boltzmann constant, and

$$Z_R = \sum_m \exp(-\beta E_m). \tag{2.18b}$$

In addition to the reservoir, we consider a second system, the probe, which according to the type of spectroscopic experiment can be either an electromagnetic wave, a neutron, etc. This probe is characterised by its hamiltonian, H_p, with the corresponding eigenvalues and eigenvectors E_m and $|m\rangle$. This probe is able to couple with the reservoir, via a hamiltonian, H_c, and therefore it is used to investigate how the molecular properties of the reservoir vary with time. The principle is the following: the probe is first prepared in a defined state $|m\rangle$. Owing to the interaction with the reservoir, this state will vary with time to another final state $|n\rangle$. In the linear approximation, i.e. if the coupling hamiltonian is small compared to H_R and H_p, the reservoir, initially in the state $|n\rangle$, suffers a subsequent change to another state $|n'\rangle$, according to the Fermi golden rule:

$$W_{nn'mm'} = \frac{2\pi}{\hbar} |\langle n'|\langle n|H_c|m\rangle|m'\rangle|^2 \delta(E_m + E_{m'} - E_n - E_{n'}). \tag{2.19}$$

Here, $W_{nn'mm'}$ is the probability per unit time that the total system composed of the probe and the reservoir changes from the initial state $|m\rangle|m'\rangle$ to the final state $|n\rangle|n'\rangle$. The change of the state of the probe which will be observed is given by the probability per unit time

$$W_{nm} = \sum_{n'} \sum_{m'} W_{nn'mm'} P_{m'} \tag{2.20a}$$

$$= \frac{1}{Z} \sum_{n'} \sum_{m'} W_{nn'mm'} \exp(-\beta E_{m'}). \tag{2.20b}$$

The principle of all the spectroscopic measurements is to measure a quantity which is proportional to W_{nm} as a function of either the final state $|n\rangle$ or the initial state $|m\rangle$ of the probe. In other words, we measure the *response* of the specimen to the *perturbation* caused by the probe. In the limit of weak processes, this response is describable by first order perturbation theory, and, according to the thermal average (2.20b) is determined by the spectrum of the spontaneous fluctuations of the specimen at thermal equilibrium. This result is known as the fluctuation–dissipation theorem (Kubo 1966, Lovesey 1984).

Because a spectroscopy experiment always leads to an analysis of the relevant quantity as a function of the final or initial states $|m\rangle$ and $|n\rangle$ of the probe, it is convenient to omit the dependence on these states in (2.19) by the operator

$$\bar{H}_c = \langle n|H_c|m\rangle \tag{2.21}$$

which acts on the states of the reservoir only. Therefore, (2.20b) above can be rewritten

$$W_{nm} = \frac{2\pi}{\hbar^2} \sum_{n'} \sum_{m'} \frac{1}{Z_R} \exp(-\beta E_{m'}) |\langle n'|\bar{H}_c|m'\rangle|^2 \delta(\omega_{n'm'} - \omega) \tag{2.22}$$

where

$$\hbar\omega = E_n - E_m \tag{2.23a}$$

and

$$\hbar\omega_{n'm'} = E_{m'} - E_{n'}. \tag{2.23b}$$

Thus $\hbar\omega$ is defined as the energy gain of the probe, whilst $\hbar\omega_{n'm'}$ is the energy loss for the reservoir. The Dirac delta function in (2.22) ensures a non-vanishing transition probability when these two quantities are equal.

Using the integral representation for the delta function

$$\delta(\omega_{n'm'} - \omega) = \frac{1}{2\pi} \int_{-\infty}^{\infty} \exp[\mathrm{i}(\omega_{n'm'} - \omega)]\, \mathrm{d}t \tag{2.24}$$

and the expression

$$|\langle n'|\bar{H}_c|m'\rangle|^2 = \sum_{m'} \langle n'|\bar{H}_c|m'\rangle \langle m'|\bar{H}_c^+|n'\rangle \tag{2.25}$$

we obtain, after some straightforward calculations

$$W_{nm} = \frac{1}{\hbar^2} \int_{-\infty}^{\infty} \mathrm{Tr}\{\hat{\rho}_R \bar{H}_c^+(0) \bar{H}_c(t)\} \exp(-\mathrm{i}\omega t)\, \mathrm{d}t \tag{2.26}$$

where the symbol Tr denotes the trace operator in the Hilbert space of the reservoir states. $\hat{\rho}_R$ is the equilibrium density matrix of the reservoir

$$\hat{\rho}_R = \frac{1}{Z_R} \exp(-\beta H_R). \tag{2.27}$$

The notation $\bar{H}_c(t)$ holds for the Heisenberg representation of operator $\bar{H}_c = \bar{H}_c(0)$

$$\bar{H}_c(t) = \exp\left(-\frac{i}{\hbar} H_R t\right) \bar{H}_c \exp\left(\frac{i}{\hbar} H_R t\right). \tag{2.28}$$

So, according to (2.26), the transition probability for the probe W_{nm} from an initial state $|m\rangle$ to final state $|n\rangle$ is given by the time-Fourier transform of the self-correlation function

$$C_{\bar{H}_c \bar{H}_c}(t) = \langle \bar{H}_c^+(0) \bar{H}_c(t) \rangle = \mathrm{Tr}\{\hat{\rho}_R \bar{H}_c^+(0) \bar{H}_c(t)\} \tag{2.29}$$

of the operator $\bar{H}_c = \langle n|H_c|m\rangle$ defined by the matrix element of the coupling hamiltonian H_c between the initial and final states $|m\rangle$ and $|n\rangle$ of the probe. We have

$$W_{nm} = \frac{2\pi}{\hbar^2} C_{\bar{H}_c \bar{H}_c}(\omega) \tag{2.30}$$

with

$$C_{\bar{H}_c \bar{H}}(\omega) = \frac{1}{2\pi} \int_{-\infty}^{\infty} C_{\bar{H}_c \bar{H}_c}(t) \exp(-i\omega t)\, dt. \tag{2.31}$$

The inverse transition probability W_{mn} from the state $|n\rangle$ to the state $|m\rangle$ is easily evaluated by changing ω into $-\omega$. It can be demonstrated (Lovesey 1980, 1984) that it is related to the direct transition W_{nm} through the detailed balance condition:

$$W_{mn} = \exp(-\beta\hbar\omega) W_{nm}. \tag{2.32}$$

2.3.2 *Neutron scattering functions*

In order to apply the general formalism above to the particular case of neutron spectroscopy, we consider a monochromatic beam of neutrons, with energy E_0 and wavevector $\boldsymbol{k}_0$, impinging onto a sample. Scattered neutrons are analysed as a function of both their final energy, $E = E_0 + \hbar\omega$, and the direction, $\boldsymbol{\Omega}$, of their final wavevector, $\boldsymbol{k}$. If I_0 is the number of neutrons per second and per square centimetre incident on the specimen and if I denotes the number of neutrons scattered per second, between $\boldsymbol{k}$ and $\boldsymbol{k} + d\boldsymbol{k}$, we have:

$$I = I_0 \frac{mV}{\hbar k_0} W_{k_0 k} \rho(\boldsymbol{k})\, d\boldsymbol{k}. \tag{2.33}$$

Here, m is the neutron mass, V the sample unit volume and $W_{k_0 k}$ is the

transition probability from the initial state $|\boldsymbol{k}_0\rangle$ of the neutron to its final state $|\boldsymbol{k}\rangle$, such that

$$|\boldsymbol{k}\rangle = \frac{1}{\sqrt{V}} \exp(\mathrm{i}\boldsymbol{k}\cdot\boldsymbol{r}) \tag{2.34a}$$

$$|\boldsymbol{k}_0\rangle = \frac{1}{\sqrt{V}} \exp(\mathrm{i}\boldsymbol{k}_0\cdot\boldsymbol{r}) \tag{2.34b}$$

$\rho(\boldsymbol{k})$, the density of states of momentum $\boldsymbol{k}$, is evaluated in Appendix A (see also Marshall and Lovesey (1971)). It is given by:

$$\rho(\boldsymbol{k})\,\mathrm{d}\boldsymbol{k} = \frac{V}{(2\pi)^3}\, k^2\,\mathrm{d}\boldsymbol{\Omega}\,\mathrm{d}k. \tag{2.35}$$

Thus, the double differential cross section, $\dfrac{\partial^2\sigma}{\partial\boldsymbol{\Omega}\partial\omega}$, becomes

$$\frac{\partial^2\sigma}{\partial\boldsymbol{\Omega}\partial\omega} = \frac{1}{\mathrm{d}\boldsymbol{\Omega}\,\mathrm{d}\omega}\cdot\frac{I}{I_0}. \tag{2.36}$$

Using the expression (2.10) of the neutron–nucleus interaction potential

$$H_\mathrm{c} = \frac{2\pi\hbar^2}{m}\sum_i b_i\delta(\boldsymbol{r} - \boldsymbol{R}_i) \tag{2.37}$$

the matrix element between initial and final neutron states is simply given by

$$\begin{aligned}\bar{H}_\mathrm{c} &= \langle\boldsymbol{k}_0|H_\mathrm{c}|\boldsymbol{k}\rangle \\ &= \frac{2\pi\hbar^2}{mV}\sum_i b_i \exp(\mathrm{i}\boldsymbol{Q}\cdot\boldsymbol{R}_i)\end{aligned} \tag{2.38}$$

where we have introduced the neutron–wavevector transfer

$$\boldsymbol{Q} = \boldsymbol{k} - \boldsymbol{k}_0. \tag{2.39}$$

Therefore:

$$C_{H_\mathrm{c}H_\mathrm{c}}(t) = \frac{1}{V^2}\left(\frac{2\pi\hbar^2}{m}\right)^2\frac{1}{N}\sum_i\sum_j\langle b_i b_j \exp\{\mathrm{i}\boldsymbol{Q}\cdot\boldsymbol{R}_i(t)\}\exp\{-\mathrm{i}\boldsymbol{Q}\cdot\boldsymbol{R}_j(0)\}\rangle \tag{2.40}$$

and, using (2.36), (2.33), (2.30), (2.35) and (2.40), we get

$$\frac{\partial^2\sigma}{\partial\boldsymbol{\Omega}\partial\omega} = \frac{k}{k_0}\frac{1}{2\pi}\sum_i\sum_j\int_{-\infty}^{\infty}\frac{1}{N}\langle b_i b_j \exp\{\mathrm{i}\boldsymbol{Q}\cdot\boldsymbol{R}_i(t)\} \times \exp\{-\mathrm{i}\boldsymbol{Q}\cdot\boldsymbol{R}_j(0)\}\rangle\exp(-\mathrm{i}\omega t)\,\mathrm{d}t. \tag{2.41}$$

The thermal average in (2.41) holds not only for the positions of the sample nuclei, but also for all the spin states. In fact, the general rule is to assume that there is no coupling between the actual scattering length of each nucleus and its position. Under these conditions the average can

be performed independently on the spin states and on the nucleus locations. To introduce the definitions (2.11) of the coherent and incoherent scattering lengths into (2.41), we must make explicit in the double summation the terms which correspond to nuclei of identical nature. Let us assume that the sample is formed of n different types of atoms (i.e. H, D, C, etc) and let N_α, N_β be the number of atoms of type α, β. If there is no correlation between the values of the scattering lengths for different isotopes, the expression (2.41) can be split into two parts, namely:

$$\frac{\partial^2\sigma}{\partial\Omega\partial\omega} = \left(\frac{\partial^2\sigma}{\partial\Omega\partial\omega}\right)_{\text{coh}} + \left(\frac{\partial^2\sigma}{\partial\Omega\partial\omega}\right)_{\text{inc}} \tag{2.42}$$

The two terms on the r.h.s. of (2.42) are the coherent and incoherent cross sections, respectively.

$$\left(\frac{\partial^2\sigma}{\partial\Omega\partial\omega}\right)_{\text{coh}} = \frac{1}{N}\frac{k}{k_0}\sum_{\alpha=1}^{n}\sum_{\beta=1}^{n} b_\alpha^{\text{coh}} b_\beta^{\text{coh}} \sqrt{N_\alpha N_\beta}\; S^{\alpha\beta}(\boldsymbol{Q}, \omega) \tag{2.43a}$$

Here b_α^{coh} and b_β^{coh} are the coherent scattering lengths relative to isotopes α and β. The function

$$S^{\alpha\beta}(\boldsymbol{Q}, \omega) = \frac{1}{2\pi\sqrt{N_\alpha N_\beta}} \int_{-\infty}^{\infty} \sum_{i_\alpha=1}^{N_\alpha}\sum_{j_\beta=1}^{N_\beta} \langle \exp\{\mathrm{i}\boldsymbol{Q}\cdot\boldsymbol{R}_{i_\alpha}(t)\} \times \exp\{-\mathrm{i}\boldsymbol{Q}\cdot\boldsymbol{R}_{j_\beta}(0)\}\rangle \exp(-\mathrm{i}\omega t)\,\mathrm{d}t \tag{2.43b}$$

is called the scattering function (or the scattering law) relative to the components α and β. It is the time-Fourier transform

$$S^{\alpha\beta}(\boldsymbol{Q}, \omega) = \frac{1}{2\pi}\int_{-\infty}^{\infty} I^{\alpha\beta}(\boldsymbol{Q}, t)\exp(-\mathrm{i}\omega t)\,\mathrm{d}t \tag{2.44a}$$

of the intermediate function for α and β species:

$$I^{\alpha\beta}(\boldsymbol{Q}, t) = \frac{1}{\sqrt{N_\alpha N_\beta}} \sum_{i_\alpha=1}^{N_\alpha}\sum_{j_\beta=1}^{N_\beta} \langle \exp\{\mathrm{i}\boldsymbol{Q}\cdot\boldsymbol{R}_{i_\alpha}(t)\} \times \exp\{-\mathrm{i}\boldsymbol{Q}\cdot\boldsymbol{R}_{j_\beta}(0)\}\rangle \tag{2.44b}$$

Similarly, for the incoherent cross section, we can write

$$\left(\frac{\partial^2\sigma}{\partial\Omega\partial\omega}\right)_{\text{inc}} = \frac{1}{N}\frac{k}{k_0}\sum_{\alpha=1}^{n} b_\alpha^{\text{inc}}\, S_{\text{inc}}^{\alpha}(\boldsymbol{Q}, \omega) \tag{2.45a}$$

b_α^{inc} is the incoherent scattering length for the isotope α defined according to (2.11b). The function

$$S_{\text{inc}}^{\alpha}(\boldsymbol{Q}, \omega) = \frac{1}{2\pi N_\alpha}\int_{-\infty}^{\infty}\sum_{i_\alpha=1}^{N_\alpha} \langle \exp\{\mathrm{i}\boldsymbol{Q}\cdot\boldsymbol{R}_{i_\alpha}(t)\} \times \exp\{-\mathrm{i}\boldsymbol{Q}\cdot\boldsymbol{R}_{i_\alpha}(0)\}\rangle \exp(-\mathrm{i}\omega t)\,\mathrm{d}t \tag{2.45b}$$

is the incoherent scattering law, relative to the species α. Again, it is the time-Fourier transform

$$S^{\alpha}_{\text{inc}}(\boldsymbol{Q}, \omega) = \frac{1}{2\pi} \int_{-\infty}^{\infty} I^{\alpha}_{\text{inc}}(\boldsymbol{Q}, t) \exp(-i\omega t)\, dt \qquad (2.46a)$$

of the incoherent intermediate function for the nuclei of the type α:

$$I^{\alpha}_{\text{inc}}(\boldsymbol{Q}, t) = \frac{1}{N_{\alpha}} \sum_{i_{\alpha}=1}^{N_{\alpha}} \langle \exp\{i\boldsymbol{Q}\cdot\boldsymbol{R}_{i_{\alpha}}(t)\} \exp\{-i\boldsymbol{Q}\cdot\boldsymbol{R}_{i_{\alpha}}(0)\}\rangle. \qquad (2.46b)$$

Basically, $S^{\alpha\beta}(\boldsymbol{Q}, \omega)$ and $S^{\alpha}_{\text{inc}}(\boldsymbol{Q}, \omega)$ are quite different in nature. Indeed, $S^{\alpha\beta}(\boldsymbol{Q}, \omega)$ involves a sum over the phase-shifts of different atoms, and thus results in interference effects. On the other hand, the positions in the exponential terms in (2.46b) refer to the *same* nucleus at different times 0 and t. The relative magnitude of $S^{\alpha\beta}(\boldsymbol{Q}, \omega)$ and $S^{\alpha}_{\text{inc}}(\boldsymbol{Q}, \omega)$ mainly depends on the nature of the nuclei in the sample. If the system contains no hydrogen atoms, then it can be verified from table 2.2 that in most of the cases $b^{\text{coh}}_{\alpha} \ll b^{\text{inc}}_{\alpha}$: the spectra will be essentially coherent and will reflect collective atomic motions. Conversely, as soon as sample molecules contain hydrogen atoms, $b^{\text{inc}}_{\text{H}} \gg b^{\text{coh}}_{\alpha}$ and the scattering becomes incoherent. Incoherent neutron scattering from organic hydrogenated molecules provides a powerful tool in the analysis of the motions of one individual proton and, consequently, of the dynamics of the molecule itself.

It is worth noticing that $S^{\alpha}_{\text{inc}}(\boldsymbol{Q}, \omega)$ is already contained in $S^{\alpha\alpha}(\boldsymbol{Q}, \omega)$. Moreover, coherence effects tend to vanish at large Q and the difference between $S^{\alpha}_{\text{inc}}(\boldsymbol{Q}, \omega)$ and $S^{\alpha\alpha}(\boldsymbol{Q}, \omega)$ becomes negligible.

Expressions (2.43) to (2.46) deal with a multicomponent specimen. Actually, in this book we shall be essentially concerned with incoherent scattering from hydrogenous organic compounds, and the unique relevant isotope will be hydrogen. Therefore it is no use to remain in the framework of the most general case. So we shall go on introducing the basic quantities in neutron scattering under the assumption of a single component system. Further information concerning the case of several components can be found in the general textbooks (Lovesey 1984, Squires 1978, Kostorz 1978).

In the case of a single isotope, the double differential cross section can be written

$$\frac{\partial^2\sigma}{\partial\boldsymbol{\Omega}\partial\omega} = \frac{1}{4\pi N}\frac{k}{k_0}\left[\sigma_{\text{coh}} S(\boldsymbol{Q}, \omega) + \sigma_{\text{inc}} S_{\text{inc}}(\boldsymbol{Q}, \omega)\right] \qquad (2.47)$$

where σ_{coh} and σ_{inc} are the coherent and incoherent cross sections of the isotope. The scattering functions $S(\boldsymbol{Q}, \omega)$ and $S_{\text{inc}}(\boldsymbol{Q}, \omega)$ are the time-Fourier transforms

$$S(\boldsymbol{Q}, \omega) = \frac{1}{2\pi} \int_{-\infty}^{\infty} I(\boldsymbol{Q}, t) \exp(-i\omega t)\, dt \qquad (2.48a)$$

and

$$S_{\text{inc}}(\boldsymbol{Q}, \omega) = \frac{1}{2\pi} \int_{-\infty}^{\infty} I_{\text{inc}}(\boldsymbol{Q}, t) \exp(-\mathrm{i}\omega t)\, \mathrm{d}t \tag{2.48b}$$

with the intermediate functions

$$I(\boldsymbol{Q}, t) = \frac{1}{N} \sum_i \sum_j \langle \exp\{\mathrm{i}\boldsymbol{Q}\cdot\boldsymbol{R}_i(t)\} \exp\{-\mathrm{i}\boldsymbol{Q}\cdot\boldsymbol{R}_j(0)\}\rangle \tag{4.29a}$$

and

$$I_{\text{inc}}(\boldsymbol{Q}, t) = \frac{1}{N} \sum_i \langle \exp\{\mathrm{i}\boldsymbol{Q}\cdot\boldsymbol{R}_i(t)\} \exp\{-\mathrm{i}\boldsymbol{Q}\cdot\boldsymbol{R}_i(0)\}\rangle. \tag{2.49b}$$

At this point of our mathematical development, it may be worth discussing the physical significance which is attached to the functions we have defined above. Concerning the intermediate function $I(Q, t)$, we shall return to real space by taking its space-Fourier transform:

$$G(\boldsymbol{r}, t) = \frac{1}{(2\pi)^3} \int I(\boldsymbol{Q}, t) \exp(-\mathrm{i}\boldsymbol{Q}\cdot\boldsymbol{r})\, \mathrm{d}\boldsymbol{Q}. \tag{2.50a}$$

Introducing the definition of $I(\boldsymbol{Q}, t)$ given by (2.49a) in this expression we obtain $G(\boldsymbol{r}, t)$ under the form of a pair-correlation function:

$$G(\boldsymbol{r}, t) = \frac{1}{N} \sum_i \sum_j \int \langle \delta(\boldsymbol{r} - \boldsymbol{r}' + \boldsymbol{R}_i(0))\delta(\boldsymbol{r}' - \boldsymbol{R}_j(t))\rangle\, \mathrm{d}\boldsymbol{r}'. \tag{2.50b}$$

Derivation of (2.50b) is straightforward, but we must be careful because the two operators $\exp(\mathrm{i}\boldsymbol{Q}\cdot\boldsymbol{R}_j(t))$ and $\exp(-\mathrm{i}\boldsymbol{Q}\cdot\boldsymbol{R}_i(0))$ do not commute. Hence their product cannot be replaced by $\exp(-\mathrm{i}\boldsymbol{Q}\cdot[\boldsymbol{R}_i(0) - \boldsymbol{R}_j(t)])$. Now, if we define the microscopic particle density operator

$$p(\boldsymbol{r}, t) = \sum_i \delta(\boldsymbol{r} - \boldsymbol{R}_i(t)) \tag{2.51}$$

it follows that (2.50) can be written readily:

$$G(\boldsymbol{r}, t) = \frac{1}{N} \int \langle \rho(\boldsymbol{r}' - \boldsymbol{r}, 0)\rho(\boldsymbol{r}', t)\rangle\, \mathrm{d}\boldsymbol{r} \tag{2.52a}$$

with the condition of normalisation:

$$\int G(\boldsymbol{r}, t)\, \mathrm{d}\boldsymbol{r} = N. \tag{2.52b}$$

Thus, the scattering law becomes

$$S(\boldsymbol{Q}, \omega) = \frac{1}{2\pi N} \int \mathrm{d}t \exp(-\mathrm{i}\omega t) \int \mathrm{d}\boldsymbol{r} \int \langle \rho(\boldsymbol{r}' - \boldsymbol{r}, 0)\rho(\boldsymbol{r}', t)\rangle \exp(\mathrm{i}\boldsymbol{Q}\cdot\boldsymbol{r})\, \mathrm{d}\boldsymbol{r}'. \tag{2.53}$$

Introducing the Fourier components $\rho_K(t)$ of the particle density operator:

$$\rho(\boldsymbol{r}, t) = \frac{1}{(2\pi)^3} \int \rho_{\boldsymbol{K}}(t) \exp(\mathrm{i}\boldsymbol{K}\cdot\boldsymbol{r})\, \mathrm{d}\boldsymbol{K} \tag{2.54}$$

it follows that:

$$S(\boldsymbol{Q}, \omega) = \frac{1}{2\pi N} \int_{-\infty}^{\infty} \langle \rho_{\boldsymbol{Q}}(0)\rho_{-\boldsymbol{Q}}(t)\rangle \exp(-\mathrm{i}\omega t)\, \mathrm{d}t \tag{2.55}$$

and, for the intermediate function:

$$I(\boldsymbol{Q}, t) = \frac{1}{N} \langle \rho_{\boldsymbol{Q}}(0)\rho_{-\boldsymbol{Q}}(t)\rangle. \tag{2.56}$$

Equation (2.55) shows that $S(\boldsymbol{Q}, \omega)$ is the time-Fourier transform of a correlation function formed with the operator $\rho_{\boldsymbol{Q}}$ and its Hermitian conjugate $\rho_{\boldsymbol{Q}}^{+} = \rho_{-\boldsymbol{Q}}$. The reason for this result is that the Fermi pseudopotential couples the neutron to the density of the sample. Using the expression (2.37) for the neutron–nucleus interaction, averaged over various spin states and isotopes, and introducing the expression (2.51) of the microscopic particle density, we get, in the case of a single type of scatterer:

$$H_{\mathrm{c}} = \frac{2\pi\hbar^2}{m} b\rho(\boldsymbol{r}, t) \tag{2.57}$$

and

$$\bar{H}_{\mathrm{c}} = \frac{2\pi\hbar^2}{mV} \rho_{\boldsymbol{Q}}(t). \tag{2.58}$$

Assuming that the system under test obeys the fundamental condition of stationarity, i.e. that

$$\langle \rho_{\boldsymbol{Q}}(t')\rho_{\boldsymbol{Q}}^{+}(t + t')\rangle = \langle \rho_{\boldsymbol{Q}}(0)\rho_{\boldsymbol{Q}}^{+}(t)\rangle \tag{2.59}$$

for any arbitrary value of t', we obtain for the particular choice $t' = -t$:

$$\langle \rho_{\boldsymbol{Q}}(-t)\rho_{\boldsymbol{Q}}^{+}(0)\rangle = \langle \rho_{\boldsymbol{Q}}(0)\rho_{\boldsymbol{Q}}^{+}(t)\rangle. \tag{2.60}$$

Finally, expressing the correlation functions in terms of matrix elements, the complex conjugate of the density correlation function reads:

$$\begin{aligned} \langle \rho_{\boldsymbol{Q}}(0)\rho_{\boldsymbol{Q}}^{+}(t)\rangle^{*} &= \sum_{m} \langle m|\rho_{\boldsymbol{Q}}(0)\rho_{\boldsymbol{Q}}^{+}(t)|m\rangle^{*} \\ &= \sum_{m} \langle m|\{\rho_{\boldsymbol{Q}}(0)\rho_{\boldsymbol{Q}}^{+}(t)\}^{+}|m\rangle. \end{aligned}$$

And, because

$$\{\rho_{\boldsymbol{Q}}(0)\rho_{\boldsymbol{Q}}^{+}(t)\}^{+} = \{\rho_{\boldsymbol{Q}}^{+}(t)\}^{+}\rho_{\boldsymbol{Q}}^{+}(0)$$

we get the important relation

$$\langle \rho_{\boldsymbol{Q}}(0)\rho_{\boldsymbol{Q}}^{+}(t)\rangle^{*} = \langle \rho_{\boldsymbol{Q}}(t)\rho_{\boldsymbol{Q}}^{+}(0)\rangle \tag{2.61}$$

which, together with (2.55), allows the proof that $S(\boldsymbol{Q}, \omega)$ is a purely real function of time.

Using the definition of the thermal average in terms of the trace of the density operator and of the Heisenberg representation of operators we get

$$\langle \rho_{\boldsymbol{Q}}(0)\rho_{\boldsymbol{Q}}^{+}(t)\rangle = \frac{1}{Z_{\mathrm{R}}} \mathrm{Tr}\{\exp(-\beta H_{\mathrm{R}})\rho_{\boldsymbol{Q}}(0) \exp(-\mathrm{i}H_{\mathrm{R}}t)\rho_{\boldsymbol{Q}}^{+}(0) \exp(\mathrm{i}H_{\mathrm{R}}t)\}.$$

The trace is invariant in a cyclic permutation of the operators. Therefore

$$\begin{aligned}\langle \rho_{\boldsymbol{Q}}(0)\rho_{\boldsymbol{Q}}^{+}(t)\rangle &= \frac{1}{Z_{\mathrm{R}}} \mathrm{Tr}\{\exp(-\mathrm{i}H_{\mathrm{R}}t)\rho_{\boldsymbol{Q}}^{+}(0) \exp[\mathrm{i}H_{\mathrm{R}}(t + \mathrm{i}\beta)]\rho_{\boldsymbol{Q}}(0)\} \\ &= \frac{1}{Z_{\mathrm{R}}} \mathrm{Tr}\{\exp(-\beta H_{\mathrm{R}}) \exp[-\mathrm{i}H_{\mathrm{R}}(t + \mathrm{i}\beta)]\rho_{\boldsymbol{Q}}^{+}(0) \\ &\quad \times \exp[\mathrm{i}H_{\mathrm{R}}(t + \mathrm{i}\beta)]\rho_{\boldsymbol{Q}}(0)\}\end{aligned}$$

$$\langle \rho_{\boldsymbol{Q}}(0)\rho_{\boldsymbol{Q}}^{+}(t)\rangle = \langle \rho_{\boldsymbol{Q}}^{+}(t + \mathrm{i}\hbar\beta)\rho_{\boldsymbol{Q}}(0)\rangle. \tag{2.62}$$

Starting from (2.55) we can write

$$\begin{aligned}S(-\boldsymbol{Q}, -\omega) &= \frac{1}{2\pi N}\int_{-\infty}^{\infty} \langle \rho_{-\boldsymbol{Q}}(0)\rho_{\boldsymbol{Q}}(t)\rangle \exp(\mathrm{i}\omega t)\,\mathrm{d}t \\ &= \frac{1}{2\pi N}\int_{-\infty}^{\infty} \langle \rho_{\boldsymbol{Q}}^{+}(0)\rho_{\boldsymbol{Q}}(t)\rangle \exp(\mathrm{i}\omega t)\,\mathrm{d}t. \end{aligned} \tag{2.63}$$

Changing t into $-t$ in (2.63), and using (2.60), (2.61) and (2.62), we obtain

$$S(-\boldsymbol{Q}, -\omega) = \exp(-\beta\hbar\omega)\, S(\boldsymbol{Q}, \omega). \tag{2.64}$$

This relation is called the detailed balance condition. It gives the relation between the scattering cross sections in the cases of energy gain ($\hbar\omega > 0$) and energy loss ($\hbar\omega < 0$) of the neutron. Indeed, the relationship of the occupation numbers of the states of the sample is given by the Boltzmann distribution. For an energy difference between two states equal to $\hbar\omega$, the probability that the system is in the lower energy state is greater by a factor $\exp(\beta\hbar\omega)$ than the probability that it is in the higher energy state. Because transitions from the lower energy state to the higher energy state are more probable than the inverse, the function $S(\boldsymbol{Q}, \omega)$ is not symmetrical in ω.

2.4 Linear Response Function, Relaxation Function and Generalised Susceptibility

The main topic in this section is to relate the scattering function $S(\boldsymbol{Q}, \omega)$ to the usual functions defined in the linear response theory,

according to which the spectrum of spontaneous fluctuations in a variable, the particle density in our case, is proportional to the response of the sample to a weak external perturbation that couples to this variable. In the framework of the Van Hove formulation, equation (2.55) expresses the scattering function in terms of the spectrum of the particle density, which clearly describes the neutron–sample interaction. To establish the link between $S(\boldsymbol{Q}, \omega)$ and the various functions defined in the framework of the linear response may seem *a priori* a useless complication of the neutron scattering theory. However, it must be stressed that in most of the recent derivations of theories for the interpretation of neutron scattering experiments, it is sometimes more convenient to work in terms of the generalised susceptibility function, or in terms of relaxation functions. Therefore, we believe it is worth presenting some insight about these various approaches.

2.4.1 Response function

The linear response theory is a simple and practical way to describe the irreversible behaviour of a system out of equilibrium. We assume that at the time $t = -\infty$, the system is described by the hamiltonian H_0 and that external time-dependent perturbation $H_1(t)$ is slowly applied, so that the hamiltonian at time t is

$$H = H_0 + H_1(t). \tag{2.65}$$

Generally, we are concerned with perturbations where the external field is coupled to the dynamical variables, $\boldsymbol{B}_i$, of the system, according to

$$H_1(t) = -\boldsymbol{B}^+ \cdot \boldsymbol{F}(t) = -\sum_j B_j^+ F_j(t) \tag{2.66}$$

where $F_j(t)$ denotes the components of the external field coupled to the variables B_j. The response of the system is observed in the change of a variable A_i, which itself does not depend explicitly on time. In the framework of the linear response, the average value of A_i at time t, out of equilibrium is quite generally given by

$$\overline{A_i(t)} = \langle A_i \rangle + \int_{-\infty}^{t} \mathrm{d}t' \sum_j \phi_{A_i B_j^-}(t - t') F_j(t') \tag{2.67}$$

where the brackets denote the *equilibrium* average

$$\langle A_i \rangle = \mathrm{Tr}\{\hat{\rho}_0 A_i\} \tag{2.68}$$

with the equilibrium density matrix

$$\hat{\rho}_0 = \frac{1}{Z_0} \exp(-\beta H_0) \tag{2.69a}$$

and

$$Z_0 = \mathrm{Tr}\{\exp(-\beta H_0)\} \tag{2.69b}$$

$\phi_{A_iB_j^+}(t)$, the response function is one of the important quantities of the linear response. In the case of an impulse perturbation, localised at earlier time $t = 0$, $F_j(t) = \delta(t)$, equation (2.67) shows that $\phi_{A_iB_j^+}(t)$ is a measure of the change in A_i at time t:

$$\overline{A_i(t)} - \langle A_i \rangle = \sum_j \phi_{A_iB_j^+}(t) \tag{2.70}$$

An essential result of the linear response theory is that the response function to an external perturbation can be evaluated from the correlation functions of the dynamical variables of the system *at equilibrium*. A straightforward application of time-dependent perturbation theory yields (see, for example Kubo (1966))

$$\phi_{A_iB_j^+}(t) = \frac{\mathrm{i}}{\hbar} \langle [A_i(t),\, B_j^+(0)] \rangle = \frac{\mathrm{i}}{\hbar} \langle [A_i(0),\, B_j^+(-t)] \rangle. \tag{2.71}$$

According to (2.55) the spectrum of scattered neutrons in the Van Hove formulation is described by the spectrum of spontaneous density fluctuations $S(\boldsymbol{Q}, \omega)$. It can be related to the spectrum of the response function

$$\phi_{\boldsymbol{Q}\boldsymbol{Q}^+}(t) = \frac{\mathrm{i}}{\hbar} \langle [\rho_{\boldsymbol{Q}}(t),\, \rho_{\boldsymbol{Q}}^+(0)] \rangle \tag{2.72}$$

via the fluctuation–dissipation theorem (Lovesey 1980, 1984)

$$\frac{\mathrm{i}}{2\pi} \int_{-\infty}^{\infty} \phi_{\boldsymbol{Q}\boldsymbol{Q}^+}(t) \exp(\mathrm{i}\omega t)\, \mathrm{d}t = [\exp(-\beta\hbar\omega) - 1] S(\boldsymbol{Q}, \omega). \tag{2.73}$$

Equation (2.73) is easily demonstrated by using the identities (2.72) and (2.62) in (2.55). It relates the scattering function to the response to a perturbation in the density of the sample medium.

Using the identity (2.61), we can show that $\phi_{\boldsymbol{Q}\boldsymbol{Q}^+}(t)$ is purely real. According to (2.72)

$$\begin{aligned}
\phi^*_{\boldsymbol{Q}\boldsymbol{Q}^+}(t) &= \frac{-\mathrm{i}}{\hbar} \langle \{\rho_{\boldsymbol{Q}}(t)\rho_{\boldsymbol{Q}}^+(0)\}^+ - \{\rho_{\boldsymbol{Q}}^+(0)\rho_{\boldsymbol{Q}}(t)\}^+ \rangle \\
&= \frac{-\mathrm{i}}{\hbar} \langle \rho_{\boldsymbol{Q}}(0)\rho_{\boldsymbol{Q}}^+(t) - \rho_{\boldsymbol{Q}}^+(t)\rho_{\boldsymbol{Q}}(0) \rangle \\
&= \frac{\mathrm{i}}{\hbar} \langle [\rho_{\boldsymbol{Q}}^+(t),\, \rho_{-\boldsymbol{Q}}^+(0)] \rangle \\
&= \frac{\mathrm{i}}{\hbar} \langle [\rho_{-\boldsymbol{Q}}(t),\, \rho_{-\boldsymbol{Q}}^+(0)] \rangle \\
\phi^*_{\boldsymbol{Q}\boldsymbol{Q}^+}(t) &= \phi_{-\boldsymbol{Q}-\boldsymbol{Q}^+}(t) = \phi_{\boldsymbol{Q}\boldsymbol{Q}^+}(t).
\end{aligned} \tag{2.74}$$

The last equality in (2.74) assumes the existence of the inversion symmetry property for the system. Because $\phi_{QQ^+}(t)$ is real, and because $S(\boldsymbol{Q}, \omega)$ is also purely real, (2.73) can be written

$$[\exp(-\beta\hbar\omega) - 1]S(\boldsymbol{Q}, \omega) = \frac{1}{2\pi}\int_{-\infty}^{\infty} \phi_{QQ^+}(t) \sin \omega t \, dt \qquad (2.75a)$$

Therefore $\phi_{QQ^+}(t)$ is an odd function of the time t

$$\phi_{QQ^-}(t) = -\phi_{QQ^+}(-t) = -\phi^*_{QQ^-}(-t) \qquad (2.75b)$$

2.4.2 Relaxation function

Now we assume that the external perturbation has the following form

$$\boldsymbol{F}(t) = \boldsymbol{F}_0 = (F_{10}, F_{20}, \ldots, F_{j0}, \ldots) \qquad \text{if } t \leqslant 0 \qquad (2.75a)$$

and

$$\boldsymbol{F}(t) = 0 \qquad \text{if } t \geqslant 0 \qquad (2.76b)$$

In other words the perturbation has been applied for a long time and vanishes at $t = 0$. According to (2.67) the response of the system for the variable A_i is given by

$$\overline{A_i(t)} = \langle A_i \rangle + \int_{-\infty}^{0} dt' \sum_j \phi_{A_i B_j^+}(t - t') F_{j0} \, dt' \qquad (2.77a)$$

$$= \langle A_i \rangle + \sum_j \mathcal{R}_{A_i B_j^+}(t) F_{j0} \qquad (2.77b)$$

The relaxation function, defined by

$$\mathcal{R}_{A_i B_j^+}(t) = \int_t^{\infty} \phi_{A_i B_j^+}(t') \, dt' \qquad (2.78)$$

describes the behaviour of the change in the variable A_i after the external perturbation has been switched off, i.e. the return to the equilibrium value $\langle A_i \rangle$ from the initial value at $t = 0$

$$A_i(0) = \langle A_i \rangle + \sum_j \int_0^{\infty} \phi_{A_i B_j^+}(t') F_{j0} \, dt'$$

$$= \langle A_i \rangle + \sum_j \mathcal{R}_{A_i B_j^+}(0) F_{j0} \qquad (2.79)$$

A more useful form of the relaxation function is:

$$\frac{\partial}{\partial t} \mathcal{R}_{A_i B_j^+}(t) = -\phi_{A_i B_j^+}(t) \qquad (2.80)$$

Therefore, from the fluctuation–dissipation theorem, the scattering law

$S(\boldsymbol{Q}, \omega)$ can be written

$$S(\boldsymbol{Q}, \omega) = \frac{\omega}{\exp(-\beta\hbar\omega) - 1} \cdot \mathcal{R}_{\boldsymbol{Q}\boldsymbol{Q}^+}(\omega) \tag{2.81}$$

where $\mathcal{R}_{\boldsymbol{Q}\boldsymbol{Q}^+}(\omega)$ is the time-Fourier transform of the relaxation function, $\mathcal{R}_{\boldsymbol{Q}\boldsymbol{Q}^+}(t)$, related to the response function, $\phi_{\boldsymbol{Q}\boldsymbol{Q}^+}(t)$, i.e.:

$$\mathcal{R}_{\boldsymbol{Q}\boldsymbol{Q}^+}(\omega) = \frac{1}{2\pi} \int_{-\infty}^{\infty} \mathcal{R}_{\boldsymbol{Q}\boldsymbol{Q}^+}(t) \exp(-\mathrm{i}\omega t)\, \mathrm{d}t \tag{2.82}$$

and

$$\mathcal{R}_{\boldsymbol{Q}\boldsymbol{Q}^+}(t) = \int_t^{\infty} \phi_{\boldsymbol{Q}\boldsymbol{Q}^+}(t')\, \mathrm{d}t' \tag{2.83}$$

or else, using (2.72)

$$\mathcal{R}_{\boldsymbol{Q}\boldsymbol{Q}^+}(t) = \frac{\mathrm{i}}{\hbar} \int_t^{\infty} \langle [\rho_{\boldsymbol{Q}}(t'), \rho_{\boldsymbol{Q}}^-(0)] \rangle\, \mathrm{d}t' \tag{2.84}$$

In the classical limit, obtained with $\beta\hbar\omega \to 0$, we get from (2.81)

$$S^{\mathrm{cl}}(\boldsymbol{Q}, \omega) \to \frac{k_{\mathrm{B}}T}{\hbar} \mathcal{R}_{\boldsymbol{Q}\boldsymbol{Q}^+}(\omega) \tag{2.85}$$

which implies that $\mathcal{R}_{\boldsymbol{Q}\boldsymbol{Q}^+}(\omega)$ is an even function of ω:

$$\mathcal{R}_{\boldsymbol{Q}\boldsymbol{Q}^+}(-\omega) = \mathcal{R}_{\boldsymbol{Q}\boldsymbol{Q}^+}(\omega) \tag{2.86}$$

Given that property of $\mathcal{R}_{\boldsymbol{Q}\boldsymbol{Q}^-}(\omega)$, the detailed balance condition (2.64) appears as a direct consequence of (2.81). The function

$$[\exp(-\beta\hbar\omega) - 1]^{-1} \tag{2.87}$$

is generally referred to as the detailed balance factor.

2.4.3 *Generalised susceptibility*

Any time-dependent perturbation can, by Fourier transformation, be represented as a set of monochromatic periodical components, and the linear response of the system is the simple superposition of the responses to each individual component. Another prescription assumes that the perturbation is an adiabatic process, i.e. that at every time of its application the system remains in equilibrium. This condition is fulfilled if the perturbation increases very slowly with time, for instance with an overriding dependence of the form $\exp(\varepsilon t)$, $\varepsilon > 0$. So let us assume that a small periodical perturbation is applied to an isolated system initially at equilibrium, and couples with some dynamical variables, B_j, under the form

$$H_1(t) = -\sum_j B_j^+ F_j(t) \tag{2.88}$$

where

$$F_j(t) = \lim_{\varepsilon \to 0^+} F_{j0} \exp(-i\omega t) \exp(\varepsilon t) \tag{2.89}$$

ε being a small positive number.

The behaviour of any variable A_i, according to (2.81) is given by

$$\overline{A_i(t)} = \langle A_i \rangle + \lim_{\varepsilon \to 0^+} \int_{-\infty}^{\infty} \sum_j \phi_{A_i B_j^+}(t - t') F_{j0} \exp(-i\omega t' + \varepsilon t')\, dt'$$

or, after changing t' into $t - t'$ in the integral

$$\begin{aligned} \overline{A_i(t)} &= \langle A_i \rangle + \sum_j \chi_{A_i B_j^+}(\omega + i\varepsilon) F_{j0} \exp(-i\omega t + \varepsilon t) \\ &= \langle A_i \rangle + \sum_j \chi_{A_i B_j^+}(\omega + i\varepsilon)\, F_j(t) \end{aligned} \tag{2.91}$$

where, introducing $z = \omega + i\varepsilon$ ($\operatorname{Im} z > 0$), the Laplace transform of the response function:

$$\chi_{A_i B_j^+}(z) = \lim_{\varepsilon \to 0^+} \int_0^{\infty} \phi_{A_i B_j^+}(t') \exp(izt')\, dt' \tag{2.92}$$

is called the generalised susceptibility of the system.

Using the expression (2.71) of the response function, we can write

$$\chi_{A_i B_j^+}(z) = \frac{i}{\hbar} \int_0^{\infty} \langle [A_i(t'), B_j^+(0)] \rangle \exp(izt')\, dt' \tag{2.93}$$

and, in the case of neutron scattering:

$$\chi_{\varrho\varrho^+}(z) = \frac{i}{\hbar} \int_0^{\infty} \langle [\rho_{\varrho}(t'), \rho_{\varrho}^+(0)] \rangle \exp(izt')\, dt'. \tag{2.94}$$

Combining the definition of the generalised susceptibility in terms of the Laplace transform of the response function together with the relation (2.81) which relates the scattering function to the Fourier transform of this response function, it can be demonstrated, without any difficulty, that

$$S(\boldsymbol{Q}, \omega) = \frac{1}{\pi} \frac{1}{\exp(-\beta\hbar\omega) - 1} \chi''_{\varrho\varrho^+}(\omega) \tag{2.95}$$

where $\chi''_{\varrho\varrho^+}(\omega)$ denotes the imaginary part of the generalised susceptibility

$$\chi_{\varrho\varrho^+}(\omega) = \chi'_{\varrho\varrho^+}(\omega) + i\chi''_{\varrho\varrho^+}(\omega). \tag{2.96}$$

The real part of the susceptibility, $\chi'_{\varrho\varrho^+}(\omega)$, is related to $\chi''_{\varrho\varrho^+}(\omega)$ via the Kramers–Krönig relationship that we shall not give here because it is beyond the scope of this book.

Finally we shall conclude this section by giving the relation between the generalised susceptibility and the Laplace transform of the relaxation

function. Using (2.80) into (2.92), we get

$$\chi_{A_i B_j^+}(z) = -\int_0^\infty \frac{\mathrm{d}\mathcal{R}_{A_i B_j^+}}{\mathrm{d}t} \exp(\mathrm{i}zt)\, \mathrm{d}t. \tag{2.97}$$

Integrating the right-hand side, we obtain

$$\chi_{A_i B_j^+}(z) = -[\mathcal{R}_{A_i B_j^+}(z) \exp(\mathrm{i}zt)]_0^\infty + \mathrm{i}z \int_0^\infty \mathcal{R}_{A_i B_j^+}(t) \exp(\mathrm{i}zt)\, \mathrm{d}t. \tag{2.98}$$

If we define

$$\mathcal{R}_{A_i B_j^+}(z) = \int_0^\infty \mathcal{R}_{A_i B_j^+}(t) \exp(\mathrm{i}zt)\, \mathrm{d}t \tag{2.99}$$

taking into account that:

$$\mathcal{R}_{A_i B_j^+}(0) = \chi_{A_i B_j^+}(0) \tag{2.100}$$

and, from the definition of the relaxation function (2.78)

$$\mathcal{R}_{A_i B_j^+}(\infty) = 0 \tag{2.101}$$

we obtain

$$\mathcal{R}_{A_i B_j^+}(z) = \frac{1}{\mathrm{i}z} [\chi_{A_i B_j^+}(z) - \chi_{A_i B_j^+}(0)]. \tag{2.102}$$

To conclude this section, we shall point out that equations (2.73), (2.81) and (2.95) provide three possibilities of evaluating the scattering function $S(\boldsymbol{Q}, \omega)$, from the determination either of the response function to a small perturbation coupling with the density of the sample, or of the time-Fourier transform of the relaxation function or else from the dissipative part of the dynamical susceptibility. The choice of the most convenient function in which to couch the calculations is to a very large extent influenced by the specific nature of the problem.

2.5 Interpretation of the Correlation Functions in the Classical Approximation

The fundamental quantum-mechanical expression (2.50) for the pair-correlation function $G(\boldsymbol{r}, t)$ contains the Heisenberg operators $\boldsymbol{R}_i(0)$ and $\boldsymbol{R}_j(t)$ which do not commute, except for $t = 0$. In this special case, we can write

$$G(\boldsymbol{r}, 0) = \frac{1}{N} \sum_i \sum_j \langle \delta(\boldsymbol{r} + \boldsymbol{R}_i(0) - \boldsymbol{R}_j(0)) \rangle \tag{2.103}$$

$$= \delta(\boldsymbol{r}) + g(\boldsymbol{r}) \tag{2.104}$$

where we have defined

$$g(\boldsymbol{r}) = \frac{1}{N} \sum_i \sum_{j \neq i} \langle \delta(\boldsymbol{r} + \boldsymbol{R}_i(0) - \boldsymbol{R}_j(0)) \rangle \tag{2.105a}$$

$$= \sum_{j \neq 0} \langle \delta(\boldsymbol{r} + \boldsymbol{R}_0(0) - \boldsymbol{R}_j(0)) \rangle. \tag{2.105b}$$

In writing (2.105b) above, we have assumed that all particles were equivalent. This enables us to drop the averaging $(1/N)\ \Sigma_j$ in (2.105a).

The term $g(\boldsymbol{r})$ represents the static pair distribution function, which is well-known in x-ray diffraction: it can be interpreted as the probability of finding any particle in the volume unit around the position $\boldsymbol{r}$, if another particle is at the origin. By analogy with (2.50a) we also define the space-Fourier transform $G_{\text{inc}}(\boldsymbol{r}, t)$ of the incoherent intermediate scattering function $I_{\text{inc}}(\boldsymbol{Q}, t)$

$$G_{\text{inc}}(\boldsymbol{r}, t) = \frac{1}{(2\pi)^3} \int I_{\text{inc}}(\boldsymbol{Q}, t) \exp(-\mathrm{i}\boldsymbol{Q}\cdot\boldsymbol{r})\, \mathrm{d}\boldsymbol{Q}. \tag{2.106}$$

With $I(\boldsymbol{Q}, t)$ expressed as (2.49), $G_{\text{inc}}(\boldsymbol{r}, t)$ appears as a self-pair correlation function:

$$G_{\text{inc}}(\boldsymbol{r}, t) = \frac{1}{N} \sum_i \int \langle \delta\{\boldsymbol{r} - \boldsymbol{r}' + \boldsymbol{R}_i(0)\} \delta\{\boldsymbol{r}' - \boldsymbol{R}_i(t)\} \rangle\, \mathrm{d}\boldsymbol{r}' \tag{2.107}$$

with

$$\int G_{\text{inc}}(\boldsymbol{r}, t)\, \mathrm{d}\boldsymbol{r} = 1 \tag{2.108}$$

At time $t = 0$, $G_{\text{inc}}(\boldsymbol{r}, 0)$ is simply given by

$$G_{\text{inc}}(\boldsymbol{r}, 0) = \delta(\boldsymbol{r}). \tag{2.109}$$

Let us assume that the system under discussion is classical, i.e. that both the energy transfers $\hbar\omega$ and the momentum transfers $\hbar\boldsymbol{Q}$ are such that

$$|\hbar\omega| \ll \tfrac{1}{2} k_{\text{B}} T \tag{2.110a}$$

$$\frac{\hbar^2 Q^2}{2M} \ll \tfrac{1}{2} k_{\text{B}} T \tag{2.110b}$$

where M is the mass of the particle and $\frac{1}{2}k_{\text{B}}T$ corresponds to the thermal energy per degree of freedom. Therefore, $\boldsymbol{R}_i(0)$ and $\boldsymbol{R}_j(t)$ must be regarded simply as the position vectors of the particles i and j at times 0 and t, respectively, and we get:

$$G^{\text{cl}}(\boldsymbol{r}, t) = \sum_j \langle \delta(\boldsymbol{r} + \boldsymbol{R}_0(0) - \boldsymbol{R}_j(t)) \rangle \tag{2.111a}$$

$$G^{\text{cl}}_{\text{inc}}(\boldsymbol{r}, t) = \langle \delta(\boldsymbol{r} + \boldsymbol{R}_0(0) - \boldsymbol{R}_0(t)) \rangle. \tag{2.111b}$$

Thus $G^{\text{cl}}(\boldsymbol{r}, t)$ expresses the probability that, given a particle at the origin at time $t = 0$, any particle, including the reference particle, is to be found at the position $\boldsymbol{r}$, at the time t. Similarly, $G^{\text{cl}}_{\text{inc}}(\boldsymbol{r}, t)$ is just the

probability to find a particle at time t at the position $\boldsymbol{r}$, given that this same particle was at the origin at time $t = 0$.

In accordance with (2.108) and (2.109), the classical correlation functions have the following integral properties

$$\int G^{\mathrm{cl}}(\boldsymbol{r}, t)\, \mathrm{d}\boldsymbol{r} = N \tag{2.112a}$$

$$\int G^{\mathrm{cl}}_{\mathrm{inc}}(\boldsymbol{r}, t)\, \mathrm{d}\boldsymbol{r} = 1. \tag{2.112b}$$

When the classical approximation is used, it must be noted that $G^{\mathrm{cl}}(\boldsymbol{r}, t)$ is real and even in $\boldsymbol{r}$ and t. Then, from (2.49) and (2.48)

$$S^{\mathrm{cl}}(\boldsymbol{Q}, \omega) = S^{\mathrm{cl}}(-\boldsymbol{Q}, -\omega). \tag{2.113}$$

The classically evaluated scattering law $S^{\mathrm{cl}}(\boldsymbol{Q}, \omega)$ violates the principle of the detailed balance. In the limits of small energies and small momentum transfers mentioned above (2.110), the scattering function $S(\boldsymbol{Q}, \omega)$ can be considered to behave classically (i.e. for long times t and large values of $\boldsymbol{r}$). Conversely, for short times (large energies) and small distances (large momentum transfers), quantum effects are not negligible. In general, it is not possible to carry out the quantum-mechanical calculations from the atomic properties of the scattering system. Instead, the classically evaluated scattering function is derived from a physical model. In many cases, a very good approximation of the actual scattering function $S(\boldsymbol{Q}, \omega)$ is obtained by writing

$$S(\boldsymbol{Q}, \omega) = \exp\left(-\frac{\hbar\omega}{2k_{\mathrm{B}}T}\right) S^{\mathrm{cl}}(\boldsymbol{Q}, \omega) \tag{2.114}$$

which, according to (2.113) fulfils the detailed balance condition (2.64).

2.6 General Expression of the Incoherent Quasielastic Neutron Scattering for Molecules

In this section we consider the incoherent scattering function written under the form (2.49b). We investigate the different components of the position vector $\boldsymbol{r}(t)$ of an atom within the molecule and the origin of their time-dependence, i.e. the internal molecular vibrations and the external translational and rotational vibrations and motions. We state the hypotheses under which the dynamics of each kind of motion can be examined separately and we define the relevant scattering functions, which will be analysed separately in the next sections.

2.6.1 Separation of the different motions

The position vector of the scattering nucleus, $\boldsymbol{r}(t)$, can be separated into

two different components, essentially different in nature, according to:

$$\boldsymbol{r}(t) = \boldsymbol{r}_e(t) + \boldsymbol{u}(t) \tag{2.115}$$

$\boldsymbol{u}(t)$ is the displacement of the nucleus from its equilibrium position within the molecule, originating from internal vibrations, i.e. deformations of bond lengths and angles. $\boldsymbol{r}_e(t)$ indicates the instantaneous location of this equilibrium position, at time t, with respect to an external fixed coordinate system (for instance the set of lattice axes in the case of a crystalline material). $\boldsymbol{r}_e(t)$ is time-dependent via the motions of the molecule as a whole. With respect to lattice axes, $\boldsymbol{u}(t)$ depends on the time from both the internal molecular vibrations and the external whole-molecule motions.

External molecular motions are characteristic of the nature of the specimen under test. When dealing with liquid samples, they essentially consist of a translation of the molecule and a rotation about its centre of mass. So it is convenient to split $\boldsymbol{r}_e(t)$ into a translational component, $\boldsymbol{r}_T^G(t)$, and a rotational component, $\boldsymbol{r}_R(t)$:

$$\boldsymbol{r}_e(t) = \boldsymbol{r}_T^G(t) + \boldsymbol{r}_R(t) \tag{2.116}$$

$$\boldsymbol{r}(t) = \boldsymbol{r}_T^G(t) + \boldsymbol{r}_R(t) + \boldsymbol{u}(t). \tag{2.117}$$

$\boldsymbol{r}_R(t)$ is a vector, the modulus of which is constant, but which can access any orientation in space. Considering (2.117) the geometrical description of the motion of the nucleus is that of a point, moving on the neighbourhood of the surface of a sphere, while the centre of this sphere translates in all space.

When we are concerned with bulk samples, the centre of mass of the molecule cannot access any position in space and is restricted to the vicinity of well-located equilibrium positions, around which, from thermal agitation, small fluctuations are nevertheless allowed.

$$\boldsymbol{r}_T^G(t) = \boldsymbol{r}_e^G + \boldsymbol{u}_T^G(t). \tag{2.118}$$

At the same time, the rotation of the molecule about its centre of gravity is (generally) no more isotropic, because of the existence of strong intermolecular interactions. Schematically, three cases have to be considered.

(a) In orientationally ordered phases, each of the molecules has *one* precise equilibrium orientation, about which it undergoes small-amplitude oscillations (librations) originating from thermal agitation. Therefore the rotational component, $\boldsymbol{r}_R(t)$, becomes

$$\boldsymbol{r}_R(t) = \boldsymbol{r}_R^e + \boldsymbol{u}_R(t) \tag{2.119}$$

$\boldsymbol{r}_R^e$ is a constant vector which denotes the equilibrium position of the nucleus with respect to an external (lattice) frame. $\boldsymbol{u}_R(t)$ is the deviation of the actual nucleus position from this equilibrium position due to

thermal librations.

(b) In completely orientationally disordered phases, $\boldsymbol{r}_R(t)$ can still access any orientation in space. So the treatment of the dynamical behaviour of such phases can be apprehended from the method originally developed for liquids. However, it must be noticed that, whilst the nucleus can access any location on the surface of the sphere, the existence of weak molecular interactions yields a non-uniform probability distribution of presence on this surface. Consequently, neutron spectra will reveal marked differences as compared to the case of liquids.

(c) In the majority of cases of orientationally disordered phases, the most convenient description of the molecular rotational motions is based on the existence of *several* (generally distinct) equilibrium orientations for each molecule among which it reorients, by instantaneous jumps. When it is lying in a given orientation, the molecule undergoes small librations and now the rotational component $\boldsymbol{r}_R(t)$ becomes

$$\boldsymbol{r}_R(t) = \boldsymbol{r}_R^e(t) + \boldsymbol{u}_R(t). \tag{2.120}$$

Now the vector $\boldsymbol{r}_R^e(t)$ which denotes the equilibrium position of the nucleus is time-dependent, because it is a function of the equilibrium orientation that the molecule occupies at this time. Strictly speaking, the deviation vector $\boldsymbol{u}_R(t)$ also depends on the precise molecule orientation.

2.6.2 Separation of the contributions to the scattering law

An exact calculation of the incoherent intermediate scattering function

$$I_{inc}(\boldsymbol{Q}, t) = \langle \exp\{i\boldsymbol{Q}\cdot\boldsymbol{r}(t)\} \exp\{-i\boldsymbol{Q}\cdot\boldsymbol{r}(0)\}\rangle \tag{2.121}$$

taking into account all possible motions is very difficult (if feasible) and, to our knowledge, has not yet been attempted. The common method consists of a separation of $I_{inc}(\boldsymbol{Q}, t)$ into factors corresponding to different kinds of motion. We shall examine under what conditions this approximation holds. From our analysis of the various components of the motion, it is clear that, roughly speaking, we are concerned with two time-scales. First, internal vibrations, as well as external molecular librations, are generally very fast. Except for low-frequency acoustic modes, translational vibrations of the centre of gravity can also be considered as much more rapid than whole-molecule reorientations amongst equilibrium orientations. The main assumption is that neither the rotational motions of the molecule nor the lattice vibrations influence very much the intramolecular vibrations. This condition implies that the internal vibrational states correspond to energy values larger than both $k_B T$ and the energy transfers related to reorientational motions. This assumption is reasonable in practice, where vibration

energies are of the order of 100 meV while the quasielastic region under interest is only a few millielectronvolts.

Similarly, it is generally assumed that the coupling between the translation of the molecule (i.e. $\boldsymbol{u}_T^G(t)$), the librations ($\boldsymbol{u}_R(t)$), and the reorientations can be neglected. This second hypothesis, necessary for the calculations, is certainly less satisfactory. Especially it supposes that the molecules reorient independently from one another, a description which is certainly not true in the case of cooperative rotations.

Nevertheless, the dynamic independence being assumed, the intermediate scattering law, for a bulk sample, can be written (we restrict to the case of a single scatterer for simplicity)

$$I_{\text{inc}}(\boldsymbol{Q}, t) = I_{\text{inc}}^{L}(\boldsymbol{Q}, t) \cdot I_{\text{inc}}^{R}(\boldsymbol{Q}, t) \cdot I_{\text{inc}}^{V}(\boldsymbol{Q}, t) \tag{2.122}$$

where $I_{\text{inc}}^{L}(\boldsymbol{Q}, t)$ corresponds to the lattice contribution

$$\begin{aligned} I_{\text{inc}}^{L}(\boldsymbol{Q}, t) &= \langle \exp\{i\boldsymbol{Q}\cdot[\boldsymbol{r}_e^G + \boldsymbol{u}_T^G(t) + \boldsymbol{u}_R(t)]\} \\ &\quad \times \exp\{-i\boldsymbol{Q}\cdot[\boldsymbol{r}_e^G + \boldsymbol{u}_T^G(0) + \boldsymbol{u}_R(0)]\}\rangle \\ &= \langle \exp\{i\boldsymbol{Q}\cdot[\boldsymbol{u}_T^G(t) + \boldsymbol{u}_R(t)]\} \exp\{-i\boldsymbol{Q}\cdot[\boldsymbol{u}_T^G(0) + \boldsymbol{u}_R(0)]\}\rangle. \end{aligned} \tag{2.123}$$

$I_{\text{inc}}^{R}(\boldsymbol{Q}, t)$ corresponds to the reorientational term

$$I_{\text{inc}}^{R}(\boldsymbol{Q}, t) = \langle \exp\{i\boldsymbol{Q}\cdot\boldsymbol{r}_R^e(t)\} \exp\{-i\boldsymbol{Q}\cdot\boldsymbol{r}_R^e(0)\}\rangle \tag{2.124}$$

and $I_{\text{inc}}^{V}(\boldsymbol{Q}, t)$ is related to intramolecular vibrations

$$I_{\text{inc}}^{V}(\boldsymbol{Q}, t) = \langle \exp\{i\boldsymbol{Q}\cdot\boldsymbol{u}(t)\} \exp(-i\boldsymbol{Q}\cdot\boldsymbol{u}(0)\}\rangle. \tag{2.125}$$

In writing (2.122), the thermal averaging in (2.121) has been done separately for the different components. Moreover, the hypothesis of dynamical independence has enabled us to use the relation

$$\exp A_i \exp A_j = \exp(A_i + A_j) \tag{2.126}$$

between two operators A_i and A_j. Generally, the reorientational scattering function is calculated classically, and corrected for the factor $\exp[\beta(\hbar\omega/2)]$ in order to fulfil the detailed balance condition. So it can be written

$$I_{\text{inc}}^{R}(\boldsymbol{Q}, t) = \langle \exp\{i\boldsymbol{Q}\cdot[\boldsymbol{r}_R^e(t) - \boldsymbol{r}_R^e(0)]\}\rangle. \tag{2.127}$$

Conversely, neither $I_{\text{inc}}^{L}(\boldsymbol{Q}, t)$ nor $I_{\text{inc}}^{V}(\boldsymbol{Q}, t)$ can be written in this form, as we shall see in a later section. In the case of an orientationally ordered sample

$$\boldsymbol{r}_R^e(t) = \boldsymbol{r}_R^e(0) = \boldsymbol{r}_R^e \tag{2.128a}$$

and

$$I_{\text{inc}}^{R}(\boldsymbol{Q}, t) = 1. \tag{2.128b}$$

When the sample is a liquid, the independence of the translational and rotational motions of the molecules is generally assumed. The scattering law takes the form

$$I_{\text{inc}}(\boldsymbol{Q}, t) = I^{\text{T}}_{\text{inc}}(\boldsymbol{Q}, t) \cdot I^{\text{R}}_{\text{inc}}(\boldsymbol{Q}, t) \cdot I^{\text{V}}_{\text{inc}}(\boldsymbol{Q}, t) \tag{2.129}$$

with $I^{\text{R}}_{\text{inc}}(\boldsymbol{Q}, t)$ and $I^{\text{V}}_{\text{inc}}(\boldsymbol{Q}, t)$ given by (2.124) and (2.125), respectively, and

$$I^{\text{T}}_{\text{inc}}(\boldsymbol{Q}, t) = \langle \exp\{\text{i}\boldsymbol{Q} \cdot [\boldsymbol{r}^{\text{G}}_{\text{T}}(t) - \boldsymbol{r}^{\text{G}}_{\text{T}}(0)]\} \rangle . \tag{2.130}$$

In this book, we shall be concerned mainly with the incoherent reorientational scattering function, $I^{\text{R}}_{\text{inc}}(\boldsymbol{Q}, t)$ and also, to a smaller extent, with the translational scattering function. But, before dealing with these two aspects of the molecular motion, it is important to know the general features of the two remaining terms $I^{\text{V}}_{\text{inc}}(\boldsymbol{Q}, t)$ and $I^{\text{L}}_{\text{inc}}(\boldsymbol{Q}, t)$. The next section is devoted to the neutron spectroscopy of internal molecular modes. The scattered intensity will be found to consist of several lines located at high-energy transfers, with no direct influence in the quasielastic region, except for a Debye–Waller attenuation factor. Conversely, we shall see that $I^{\text{L}}_{\text{inc}}(\boldsymbol{Q}, t)$ leads to a wide band of scattered intensity in the immediate vicinity of the quasielastic region, with a small contribution under the elastic peak in the form of a nearly energy-independent flat background.

2.7 Neutron Spectroscopy of Internal Vibrations

A polyatomic molecule containing N_0 nuclei constitutes a system with $3N_0$ degrees of freedom. Three of them correspond to the rotational motions and three others to the vibrational motions of the system as a whole. Their contribution to the scattering function is considered in the terms $I^{\text{L}}_{\text{inc}}(\boldsymbol{Q}, \omega)$ and $I^{\text{R}}_{\text{inc}}(\boldsymbol{Q}, \omega)$ of the equation (2.122). The $3N_0-6$ remaining degrees of freedom correspond to the intramolecular vibrational motions. The effect of the coordinates corresponding to the translational and rotational motions of the system is to introduce constraints between the displacements $\boldsymbol{u}$ of the nuclei within the same molecule. In the framework of the harmonic approximation, the energy of the nuclei of a molecule, l, due to their small displacements can be written

$$E_l = \sum_{j\alpha} \tfrac{1}{2} m_j (\dot{u}^l_{j\alpha})^2 + \sum_{j\alpha} \sum_{k\beta} \tfrac{1}{2} C^{ll}_{jk\alpha\beta} u^l_{j\alpha} u^l_{k\beta} \tag{2.131}$$

where

$$u^l_{j\alpha}$$

denotes the α component of the atom j within the molecule l. m_j is the mass and

$$C^{l\,l}_{j\,k\,\alpha\beta}$$

a force constant. In writing (2.131) it is assumed that there is no coupling between the intramolecular displacements of the nuclei of different molecules. Therefore we can drop the index l in (2.131) and write, for any molecule:

$$E = \sum_{j\alpha} \tfrac{1}{2} m(\dot{u}^j_\alpha)^2 + \sum_{j\alpha} \sum_{k\beta} \tfrac{1}{2} C^{jk}_{\alpha\beta}\, u^j_\alpha\, u^k_\beta. \tag{2.132}$$

The derivation of the scattering function associated with vibrational motions of molecular nuclei can be found in many textbooks (Boutin and Yip 1968, Lovesey 1984). We shall just outline here the calculations, in order to point out the most characteristic features.

The first step is to express the displacements $\boldsymbol{u}^j$ in terms of the eigenmodes $\zeta^j(\mu)$, which verify

$$\sum_{j\alpha} \frac{1}{\sqrt{m_j m_k}}\, C^{jk}_{\alpha\beta}\, \zeta^j_\alpha(\mu) = \omega^2_\mu\, \zeta^k_\beta(\mu). \tag{2.133}$$

The index μ labels the different $3N_0-6$ eigenmodes. Moreover, the eigenmodes related to different eigenvalues ω^2_μ and ω^2_ν are orthogonal, i.e.

$$\sum_{j\alpha} \zeta^j_\alpha(\mu)\, \zeta^{k*}_\beta(\nu) = \delta_{\mu\nu}. \tag{2.134}$$

Group theory arguments provide a considerable help in the determination of the eigenmodes. These can be classified according to the irreducible representations of the symmetry group of the molecule in its equilibrium configuration. The hamiltonian corresponding to (2.132) can be written

$$H = \sum_{\mu=1}^{3N_0-6} (a^+_\mu a_\mu + \tfrac{1}{2})\hbar\omega_\mu \tag{2.135}$$

where a_μ and a^+_μ are the Bose operators, which satisfy the commutation relation

$$[a_\mu, a^+_\nu] = \delta_{\mu\nu} \tag{2.136}$$

and

$$\langle a^+_\mu a_\nu \rangle = \delta_{\mu\nu} n(\omega_\mu) \tag{2.137}$$

where $n(\omega_\mu)$ is the Bose occupation function

$$n(\omega_\mu) = \frac{1}{\exp(\beta\hbar\omega_\mu) - 1}. \tag{2.138}$$

Therefore the displacement of the atom j, becomes

$$\boldsymbol{u}^j(t) = \sum_{\mu=1}^{3N_0-6} \left(\frac{\hbar}{2m_j\omega_\mu}\right)^{1/2} \zeta^j(\mu) \left[a_\mu \exp(-i\omega_\mu t) + a_\mu^+ \exp(i\omega_\mu t)\right] \tag{2.139}$$

$\zeta^i(\mu)$ is the mass-weighted amplitude vector (in a molecule-fixed coordinate system) for the jth atom along the μth normal mode $Q_\mu(t)$,

$$Q_\mu(t) = \left(\frac{\hbar}{2m_j\omega_\mu}\right)^{1/2} \left[a_\mu \exp(-i\omega_\mu t) + a_\mu^+ \exp(i\omega_\mu t)\right] \tag{2.140}$$

$$\boldsymbol{u}^j(t) = \sum_{\mu=1}^{3N_0-6} \zeta^j(\mu) Q_\mu(t). \tag{2.141}$$

From the definition of the scattering function, the relevant correlation function

$$\langle \exp[-i\boldsymbol{Q}\cdot\boldsymbol{u}^j(0)] \exp[i\boldsymbol{Q}\cdot\boldsymbol{u}^k(t)]\rangle \tag{2.142}$$

can also be written

$$\langle \exp\{\tfrac{1}{2}[-i\boldsymbol{Q}\cdot\boldsymbol{u}^j(0), i\boldsymbol{Q}\cdot\boldsymbol{u}^k(t)]\} \exp\{-i\boldsymbol{Q}\cdot\boldsymbol{u}^j(0) + i\boldsymbol{Q}\cdot\boldsymbol{u}^k(t)\}\rangle. \tag{2.143}$$

In the derivation of this expression use has been made of the relation

$$\exp(A_j) \exp(A_k) = \exp\{\tfrac{1}{2}[A_j, A_k]\} \exp(A_j + A_k) \tag{2.144}$$

between two operators A_j and A_k which do not commute. This relation is valid if each of the two operators commutes independently with the commutator $[A_j, A_k]$. In the present case this condition is fulfilled because the commutator arising in the first exponential term of (2.143) reduces to a complex-number. Then, using the Bloch identity for an operator A which is a linear combination of the Bose operators a_μ and a_μ^+ (Lovesey 1984)

$$\langle \exp A\rangle = \exp(\tfrac{1}{2}\langle A\rangle) \tag{2.145}$$

we obtain

$$\langle \exp[-i\boldsymbol{Q}\cdot\boldsymbol{u}^j(0)] \exp[i\boldsymbol{Q}\cdot\boldsymbol{u}^k(t)]\rangle = \exp[-\tfrac{1}{2}\langle(\boldsymbol{Q}\cdot\boldsymbol{u}^j(0))^2\rangle - \tfrac{1}{2}\langle(\boldsymbol{Q}\cdot\boldsymbol{u}^k(t))^2\rangle + \langle(\boldsymbol{Q}\cdot\boldsymbol{u}^j(0))(\boldsymbol{Q}\cdot\boldsymbol{u}^k(t))\rangle]. \tag{2.146}$$

Introducing the expression of the displacements $\boldsymbol{u}^j(0)$ and $\boldsymbol{u}^k(t)$ in terms of a_μ and a_μ^+ given by (2.139) at times 0 and t, respectively, and using the relation (2.127), we get, without difficulty

$$\langle \exp[-i\boldsymbol{Q}\cdot\boldsymbol{u}^j(0)] \exp[i\boldsymbol{Q}\cdot\boldsymbol{u}^k(t)]\rangle = \exp[-W_j(\boldsymbol{Q}) - W_k(\boldsymbol{Q})]$$

$$\times \prod_{\mu=1}^{3N_0-6} \exp\left[\frac{\hbar(\boldsymbol{Q}\cdot\zeta^j(\mu))(\boldsymbol{Q}\cdot\zeta^k(\mu))}{2\omega_\mu\sqrt{m_j m_k}\sinh\{\beta(\hbar\omega_\mu/2)\}} \cosh\left(\beta\frac{\hbar\omega_\mu}{2} + i\omega_\mu t\right)\right] \tag{2.147}$$

where the Debye–Waller factor, $W_j(\boldsymbol{Q})$, for atom j, is

$$W_j(\boldsymbol{Q}) = \sum_{\mu=1}^{3N_0-6} \frac{\hbar}{4m_j\omega_\mu} |\boldsymbol{Q}\cdot\boldsymbol{\zeta}^j(\mu)|^2 \coth\left(\beta\frac{\hbar\omega_\mu}{2}\right). \tag{2.148}$$

Finally, we make use of the identity

$$\sum_{n=-\infty}^{\infty} I_n(y) \exp(nx) = \exp[y\cosh(x)] \tag{2.149}$$

where $I_n(y)$ denotes a Bessel function of the first kind and of order n, to write

$$\langle \exp[-i\boldsymbol{Q}\cdot\boldsymbol{u}^j(0)] \exp[i\boldsymbol{Q}\cdot\boldsymbol{u}^k(t)]\rangle$$

$$= \exp[-W_j(\boldsymbol{Q}) - W_k(\boldsymbol{Q})] \prod_{\mu=1}^{3N_0-6} \left\{\sum_{n_\mu} \exp\left(\beta\frac{\hbar\omega_\mu n_\mu}{2}\right)\right.$$

$$\left. \times I_{n_\mu}\left[\frac{\hbar(\boldsymbol{Q}\cdot\boldsymbol{\zeta}^j(\mu))(\boldsymbol{Q}\cdot\boldsymbol{\zeta}^k(\mu))}{2\omega_\mu\sqrt{m_j m_k}\sinh\{\beta(\hbar\omega_\mu/2)\}}\right] \exp(in_\mu\omega_\mu t)\right\} \tag{2.150}$$

where n_μ is the number of energy quanta of the μth mode. Equation (2.150) is the basis expression that is used in the following analysis.

In this section, we shall discuss the origin of the various contributions to the incoherent vibrational cross section:

$$\left(\frac{\partial^2\sigma}{\partial\boldsymbol{\Omega}\partial\omega}\right)_{\text{inc}}^{\text{V}} = \frac{k}{k_0}\sum_{j=1}^{N_0}\frac{\sigma_{\text{inc}}^j}{4\pi} S_{\text{inc}}^{\text{V}_j}(\boldsymbol{Q},\omega) \tag{2.151a}$$

where

$$S_{\text{inc}}^{\text{V}_j}(\boldsymbol{Q},\omega) = \frac{1}{2\pi}\int_{-\infty}^{\infty} \langle \exp\{-i\boldsymbol{Q}\cdot\boldsymbol{u}^j(0)\} \exp\{i\boldsymbol{Q}\cdot\boldsymbol{u}^j(t)\}\rangle \exp(-i\omega t)\, dt \tag{2.151b}$$

so that

$$\left(\frac{\partial^2\sigma}{\partial\boldsymbol{\Omega}\partial\omega}\right)_{\text{inc}}^{\text{V}} = \sum_j \sigma_{\text{inc}}^j \exp\{-2W_j(\boldsymbol{Q})\} \exp\left\{-\beta\frac{\hbar\omega}{2}\right\}$$

$$\times \prod_{\mu=1}^{3N_0-6} \sum_{n_\mu=-\infty}^{\infty} I_{n_\mu}\left[\frac{\hbar|\boldsymbol{Q}\cdot\boldsymbol{\zeta}^j(\mu)|^2}{2\omega_\mu m_j \sinh\{\beta(\hbar\omega_\mu/2)\}}\right] \delta\left(\omega - \sum_{\mu=1}^{3N_0-6} n_\mu\omega_\mu\right) \tag{2.151c}$$

$(\partial^2\sigma/\partial\boldsymbol{\Omega}\partial\omega)_{\text{inc}}^{V}$ consists of a sum over the N_0 atoms in the molecule. In fact, the dominance of the hydrogen incoherent cross section over those of the other elements means that for organic molecules the sum can be restricted to the hydrogens. The term $\exp\{-\frac{1}{2}\beta\hbar\omega\}$ expresses the usual detailed balance condition

$$S_{\text{inc}}^{\text{V}_j}(\boldsymbol{Q},\omega) = \exp\{-\beta\hbar\omega\} S_{\text{inc}}^{\text{V}_j}(\boldsymbol{Q},-\omega)$$

i.e. that, for a given transition, neutron energy gain, which requires the system to be in the higher energy state, is less frequent than neutron energy loss, in accord with the Boltzmann population factor. The delta function in (2.151) expresses energy conservation and shows that energy is exchanged only in discrete amounts corresponding to combinations of vibrational energy quanta. Thus the energy spectrum consists of a series of peaks located at discrete values of neutron energy transfers. The case $n_\mu = 0$ for all modes in (2.151) holds for elastic incoherent scattering. It gives rise to a peak at zero energy transfer

$$\left(\frac{\partial^2\sigma}{\partial\Omega\partial\omega}\right)_{\text{inc}}^{\text{V, el}} = \frac{1}{4\pi}\sum_j \sigma_{\text{inc}}^j \exp\{-2W_j(\boldsymbol{Q})\} \times \prod_{\mu=1}^{3N_0-6} I_0\left[\frac{\hbar|\boldsymbol{Q}\cdot\boldsymbol{\xi}^j(\mu)|^2}{2\omega_\mu m_j \sinh\{\beta(\hbar\omega_\mu/2)\}}\right]\delta(\omega). \quad (2.152)$$

If $n_\mu = \pm 1$ for one mode and zero for all the others then the neutron undergoes 'one-phonon' scattering. Conversely 'multiphonon' scattering is when $|n_\mu| > 2$ for one or more mode or also when $|n_\mu| \geqslant 1$ for two or more modes. Therefore the multiphonon peaks occur at harmonics and combination frequencies of the fundamental vibrational frequencies of the system.

The exponent, $-2W_j(\boldsymbol{Q})$, of the Debye–Waller factor is a sum of terms, one for each mode, each being the square displacement along $\boldsymbol{Q}$ of the jth nucleus in this mode. In the high-temperature limit, (2.148) reduces to the simple form

$$W_j(\boldsymbol{Q}) = \frac{1}{\beta}\sum_{\mu=1}^{3N_0-6}\frac{|\boldsymbol{Q}\cdot\boldsymbol{\xi}^j|^2}{m_j\omega_\mu^2}. \quad (2.153)$$

So, each mode μ contributes to the mean-square displacement, according to the energy equipartition law, by a factor $(\beta m_j\omega_\mu^2)^{-1}$.

The effect of the Debye–Waller factor is to attenuate the peak intensities at high momentum transfer. However, simultaneously the modified Bessel functions increase, and in most cases, the result is an increase of the scattering. In fact, it is impossible to increase the one-phonon scattering by increasing Q, without also increasing the multiphonon scattering. The reason is that multiphonon scattering involves modified Bessel functions $I_{n_\mu}(z)$ whose values are no more negligible at large values of their argument. To overcome this problem, experimental data are usually extrapolated to small Q. Anyway, combinations of 3, 4, ..., n vibrations give an intense background but without structure so that an interpretation of the neutron spectra in terms of the fundamental vibrations is possible.

When the arguments of the Bessel functions are small, a condition which is most often fulfilled under usual experimental conditions, the

scattered intensity relative to a fundamental mode, μ, becomes,

$$\left(\frac{\partial^2\sigma}{\partial\Omega\partial\omega}\right)_{\text{inc}}^{\text{V, inel}} = \frac{\hbar k}{k_0}\sum_{j=1}^{N_0}\frac{\sigma_{\text{inc}}^j}{4\pi}\exp\{-2W_j(\boldsymbol{Q})\}$$

$$\times\frac{(\boldsymbol{Q}\cdot\boldsymbol{\xi}^j(\mu))^2}{2m_j\omega_\mu}\cdot\frac{\delta(\omega-\omega_\mu)}{\exp\{\beta\hbar\omega\}-1} \tag{2.154a}$$

$$= \frac{k}{k_0}\sum_{j=1}^{N_0}\frac{\sigma_{\text{inc}}^j}{4\pi}S_{\text{inc}}^{\text{V, inel, }j}(\boldsymbol{Q},\omega) \tag{2.154b}$$

for a neutron creation process ($\omega = \omega_\mu$).

Simultaneously, we have for the elastic part:

$$\left(\frac{\partial^2\sigma}{\partial\Omega\partial\omega}\right)_{\text{inc}}^{\text{V, el}} = \frac{1}{4\pi}\sum_{j=1}^{N_0}\sigma_{\text{inc}}^j S_{\text{inc}}^{\text{V, el, }j}(\boldsymbol{Q},\omega) \tag{2.155a}$$

$$= \frac{1}{4\pi}\sum_{j=1}^{N_0}\sigma_{\text{inc}}^j\exp\{-2W_j(\boldsymbol{Q})\}\,\delta(\omega). \tag{2.155b}$$

So far, we have considered only single-crystal samples. When the experiment is carried out with a powder sample, an average has to be taken over all the possible directions of $\boldsymbol{Q}$ with respect to the crystal axes. We shall deal with that aspect in a later section.

Lastly, anticipating a later section, we examine the situation when other motions of the nuclei have to be included in the cross section. If these motions can be considered as independent of the vibrational motion, the resulting cross section is obtained after a convolution of (2.151) with the scattering law corresponding to their dynamics. Such motions will generally consist of translations or rotations of the molecules, with a diffusive nature, and occurring on a slower time-scale. Their effect is a broadening of the elastic and inelastic vibrational lines, whose width, related to the characteristic times of the slow motions, generally increases with the scattering vector. We shall turn back in more detail to this point in §2.9; but first we shall examine the feature of the contribution to the cross section originating from lattice vibrations.

2.8 Phonon Scattering

2.8.1 Harmonic lattice vibrations

Let us consider a molecular crystal, with n molecules within each cell. The displacement of the atom a, of the jth molecule in the mth cell, $\boldsymbol{u}(m, j, a)$ with respect to its equilibrium position can be separated into

two parts, under the hypothesis of small-amplitude rotations:

$$\boldsymbol{u}(m, j, a) = \boldsymbol{u}^{m}_{\mathrm{T}j} + \overline{\overline{\mathcal{J}}}(a)\boldsymbol{u}^{m}_{\mathrm{R}j}. \tag{2.156a}$$

$\boldsymbol{u}^{m}_{\mathrm{T}j}$ denotes the translational displacement of the centre of gravity of the molecule (m, j). Similarly, $\boldsymbol{u}^{m}_{\mathrm{R}j}$ corresponds to the rotational displacement. $\overline{\overline{\mathcal{J}}}(a)$ is an antisymmetrical tensor of rank 3, whose elements are given by

$$\overline{\overline{\mathcal{J}}}(a) = \begin{pmatrix} 0 & X_3(a) & -X_2(a) \\ -X_3(a) & 0 & X_1(a) \\ X_2(a) & -X_1(a) & 0 \end{pmatrix}. \tag{2.156b}$$

Here $X_\gamma(a)$ is the γth component of the position vector of the atom (a) in the molecule.

In the harmonic approximation, the potential energy, W, of a crystal composed of N rigid molecules in N' cells is expressed by truncating at the quadratic terms in the Taylor series

$$W = W_0 + \sum_{m,\,p=1}^{N'} \sum_{j,k=1}^{n} \sum_{\alpha,\beta=1}^{3} \left\{ W^{\mathrm{TT}}_{\substack{mj\alpha \\ pk\beta}} u_{\mathrm{T}}{}^{m}_{j\alpha}\, u_{\mathrm{T}}{}^{p}_{k\beta} + W^{\mathrm{TR}}_{\substack{mj\alpha \\ pk\beta}} u_{\mathrm{T}}{}^{m}_{j\alpha}\, u_{\mathrm{R}}{}^{p}_{k\beta} \right.$$

$$\left. + W^{\mathrm{RT}}_{\substack{mj\alpha \\ pk\beta}} u_{\mathrm{R}}{}^{m}_{j\alpha}\, u_{\mathrm{T}}{}^{p}_{k\beta} + W^{\mathrm{RR}}_{\substack{mj\alpha \\ pk\beta}} u_{\mathrm{R}}{}^{m}_{j\alpha}\, u_{\mathrm{R}}{}^{p}_{k\beta} \right\} \tag{2.157}$$

where W_0 is the potential energy of the crystal when all the molecules are in their equilibrium position. The coefficients

$$W^{\mathrm{TT}}_{\substack{mj\alpha \\ pk\beta}},\ W^{\mathrm{TR}}_{\substack{mj\alpha \\ pk\beta}},\ \ldots$$

etc are the double derivatives of the potential energy, the molecules being in their equilibrium position, i.e.:

$$W^{\mathrm{TT}}_{\substack{mj\alpha \\ pk\beta}} = \left(\frac{\partial^2 W}{\partial u_{\mathrm{T}}{}^{m}_{j\alpha}\, \partial u_{\mathrm{T}}{}^{p}_{k\beta}} \right)_0 \qquad W^{\mathrm{TR}}_{\substack{mj\alpha \\ pk\beta}} = \left(\frac{\partial^2 W}{\partial u_{\mathrm{T}}{}^{m}_{j\alpha}\, \partial u_{\mathrm{R}}{}^{p}_{k\beta}} \right)_0 \tag{2.158}$$

$$W^{\mathrm{RT}}_{\substack{mj\alpha \\ pk\beta}} = \left(\frac{\partial^2 W}{\partial u_{\mathrm{R}}{}^{m}_{j\alpha}\, \partial u_{\mathrm{T}}{}^{p}_{k\beta}} \right)_0 \qquad W^{\mathrm{RR}}_{\substack{mj\alpha \\ pk\beta}} = \left(\frac{\partial^2 W}{\partial u_{\mathrm{R}}{}^{m}_{j\alpha}\, \partial u_{\mathrm{R}}{}^{p}_{k\beta}} \right)_0$$

where the index 0 refers to the equilibrium configuration. First order derivatives do not occur in (2.157) because of the equilibrium condition. The coefficients

$$W^{\mathrm{TT}}_{\substack{mj\alpha \\ pk\beta}},\ W^{\mathrm{TR}}_{\substack{mj\alpha \\ pk\beta}},\ \ldots.$$

are generally called coupling parameters in the calculations of molecular crystal dynamics. By taking into account the crystal symmetry, it is

possible to deduce relations between these coefficients. Thus the number of relevant independent coefficients can be reduced.

The dynamical equations to be solved are

$$\begin{aligned} m_j \ddot{u}_{\mathrm{T}\alpha}^{j\,m} &= -\sum_{p=1}^{N'} \sum_{k=1}^{n} \sum_{\beta=1}^{3} \left\{ W_{\substack{mj\alpha \\ pk\beta}}^{\mathrm{TT}} u_{\mathrm{T}\beta}^{k\,p} + W_{\substack{mj\alpha \\ pk\beta}}^{\mathrm{TR}} u_{\mathrm{R}\beta}^{k\,p} \right\} \\ \sum_{\beta=1}^{3} I_{\alpha\beta}^{j} \ddot{u}_{\mathrm{R}\alpha}^{j\,m} &= -\sum_{p=1}^{N'} \sum_{k=1}^{n} \sum_{\beta=1}^{3} \left\{ W_{\substack{mj\alpha \\ pk\beta}}^{\mathrm{RT}} u_{\mathrm{T}\beta}^{k\,p} + W_{\substack{mj\alpha \\ pk\beta}}^{\mathrm{RR}} u_{\mathrm{R}\beta}^{k\,p} \right\} \end{aligned} \tag{2.159}$$

which hold for all the coordinates ($\alpha = 1, 2, 3$) of all the molecules (j) within all the lattice cell. $I_{\alpha\beta}^{j}$ denotes the elements of the inertia tensor of the molecule. If the reference axes are chosen to be coincident with the inertia principal axes, only the diagonal terms ($\alpha = \beta$) on the left-hand side of (2.159) are not vanishing.

Because of the translational symmetry of the lattice, the solutions of the set of differential equations are investigated in the form:

$$u_{\mathrm{T}\alpha}^{j\,m} = \frac{1}{\sqrt{m_j}} \xi_{\mathrm{T}\alpha}^{j}(\boldsymbol{q}) \exp\{\mathrm{i}[\boldsymbol{q}\cdot\boldsymbol{R}_m - \omega(\boldsymbol{q})t]\} \tag{2.160a}$$

$$u_{\mathrm{R}\alpha}^{j\,m} = \frac{1}{\sqrt{I_{\alpha\alpha}}} \xi_{\mathrm{R}\alpha}^{j}(\boldsymbol{q}) \exp\{\mathrm{i}[\boldsymbol{q}\cdot\boldsymbol{R}_m - \omega(\boldsymbol{q})t]\} \tag{2.160b}$$

where $\boldsymbol{R}_m$ corresponds to the origin of the mth lattice cell and $\boldsymbol{q}$ to a vector of the reciprocal lattice. Then we introduce the definitions:

$$D_{\substack{j\alpha \\ k\beta}}^{\mathrm{TT}}(\boldsymbol{q}) = \frac{1}{\sqrt{m_j m_k}} \sum_{p} W_{\substack{0j\alpha \\ pk\beta}}^{\mathrm{TT}} \exp\{\mathrm{i}\boldsymbol{q}\cdot(\boldsymbol{R}_p - \boldsymbol{R}_0)\} \tag{2.161a}$$

$$D_{\substack{j\alpha \\ k\beta}}^{\mathrm{TR}}(\boldsymbol{q}) = \frac{1}{\sqrt{m_j I_{\beta\beta}^{k}}} \sum_{p} W_{\substack{0j\alpha \\ pk\beta}}^{\mathrm{TR}} \exp\{\mathrm{i}\boldsymbol{q}\cdot(\boldsymbol{R}_p - \boldsymbol{R}_0)\} \tag{2.161b}$$

$$D_{\substack{j\alpha \\ k\beta}}^{\mathrm{RT}}(\boldsymbol{q}) = \frac{1}{\sqrt{I_{\alpha\alpha}^{j} m_k}} \sum_{p} W_{\substack{0j\alpha \\ pk\beta}}^{\mathrm{RT}} \exp\{\mathrm{i}\boldsymbol{q}\cdot(\boldsymbol{R}_p - \boldsymbol{R}_0)\} \tag{2.161c}$$

$$D_{\substack{j\alpha \\ k\beta}}^{\mathrm{RR}}(\boldsymbol{q}) = \frac{1}{\sqrt{I_{\alpha\alpha}^{j} I_{\beta\beta}^{k}}} \sum_{p} W_{\substack{0j\alpha \\ pk\beta}}^{\mathrm{RR}} \exp\{\mathrm{i}\boldsymbol{q}\cdot(\boldsymbol{R}_p - \boldsymbol{R}_0)\} \tag{2.161d}$$

and the 'generalised mass matrix', with its elements given by

$$m_{\substack{j\alpha \\ k\beta}}^{\mathrm{TT}} = \delta_{\alpha\beta}\delta_{jk} \tag{2.162a}$$

$$m_{\substack{j\alpha \\ k\beta}}^{\mathrm{RR}} = \frac{I_{\alpha\beta}^{j}}{\sqrt{I_{\alpha\alpha}^{j} I_{\beta\beta}^{k}}} \tag{2.162b}$$

$$m_{\substack{j\alpha \\ k\beta}}^{\mathrm{RT}} = m_{\substack{j\alpha \\ k\beta}}^{\mathrm{TR}} = 0 \tag{2.162c}$$

which reduces to the identity matrix when the directions of the system

axes correspond to the inertia principal axes of all the molecules. The set of differential equations (2.159) becomes

$$|\mathbf{D}(\boldsymbol{q}) - \omega^2(\boldsymbol{q})\cdot\mathbf{m}|\xi(\boldsymbol{q}) = 0 \tag{2.163}$$

with

$$\mathbf{D}(\boldsymbol{q}) = \begin{pmatrix} D^{TT}(\boldsymbol{q}) & D^{TR}(\boldsymbol{q}) \\ D^{RT}(\boldsymbol{q}) & D^{RR}(\boldsymbol{q}) \end{pmatrix} \qquad \mathbf{m} = \begin{pmatrix} m^{TT} & m^{TR} \\ m^{RT} & m^{RR} \end{pmatrix} \tag{2.164}$$

$$\xi(\boldsymbol{q}) = \begin{pmatrix} \xi_T(\boldsymbol{q}) \\ \xi_R(\boldsymbol{q}) \end{pmatrix}.$$

For each value of $\boldsymbol{q}$, there are $6n$ eigenvalues for $\omega^2(\boldsymbol{q}r)$ associated with orthogonal eigenmodes $\xi^j(\boldsymbol{q}r)$, $(r = 1, 6)$. An important consequence of the invariance of the potential energy by a simple crystal translation is the existence of three modes with a frequency equal to zero at the centre of the Brillouin zone ($\boldsymbol{q} = 0$). These modes are called acoustic modes. The $6n - 3$ other modes are called optical modes. They can be divided into $3n - 6$ translation optical modes and $3n$ rotation modes also called librations.

Actually, this distinction is rather formal. Indeed translational and optical modes are generally coupled together.

From the knowledge of the components $\xi_{T\alpha}^{j}(\boldsymbol{q}r)$ and $\xi_{R\alpha}^{j}(\boldsymbol{q}r)$ of the eigenvectors of the dynamical matrix, the components

$$u_{T\alpha}^{mj} \text{ and } u_{R\alpha}^{mj}$$

of the translational and rotational displacements of the molecule (m, j) can be derived, according to (2.160) and also the components of the displacement, $\boldsymbol{u}(m, j, a)$, will be written

$$\boldsymbol{u}(m, j, a) = \frac{1}{\sqrt{m_j}} \sum_{qr} \xi^j(\boldsymbol{q}ra) \exp\{i[\boldsymbol{q}\cdot\boldsymbol{R}_m - \omega(\boldsymbol{q}r)t]\}. \tag{2.165}$$

The connection between $\xi^j(\boldsymbol{q}ra)$ and $\xi_T^j(\boldsymbol{q}r)$ and $\xi_R^j(\boldsymbol{q}r)$ is straightforward.

In crystal dynamics studies, the calculation of most of the physical macroscopic quantities requires an addition over the normal mode frequencies. For any $\boldsymbol{q}$ direction, the consecutive values of $\omega(\boldsymbol{q}r)$ along each branch, r, are very close to each other; indeed the succession of values of $q = (2\pi l/N')\boldsymbol{a}^*$, $(l = 1, 2, \ldots$ and $\boldsymbol{a}^*$ being a vector of the reciprocal lattice) is very dense, because the number of cells, N', is very large. It is therefore more convenient to work with the frequency distribution function, $g(\omega)$, also called the frequency spectrum, which is defined in such a way that $g(\omega)\,d\omega$ is the fraction of normal modes whose values fall between ω and $\omega + d\omega$. Formally, we can write

$$g(\omega) = \frac{1}{6nv^*} \sum_{qr} \delta\{\omega - \omega(qr)\} \tag{2.166}$$

where v^* is the volume of the reciprocal unit cell. The sum runs over all the branches, r, and all the wavevectors, q, in the first Brillouin zone. The frequency distribution function is normalised:

$$\int_0^\infty g(\omega)\, \mathrm{d}\omega = 1 \tag{2.167}$$

The condition, $\omega = cte$, defines for each branch, r, a surface $S_r(\omega)$ in the reciprocal space. Let $\mathrm{d}S(\omega)$ denote an element of this surface, the number of frequencies within the infinitesimal volume with area $\mathrm{d}S_r(\omega)$ contained between the two surfaces $S_r(\omega)$ and $S_r(\omega + \mathrm{d}\omega)$ is equal to

$$\mathrm{d}n_{r,\omega} = \frac{N'}{v^*} \cdot \mathrm{d}S_r(\omega)\, \mathrm{d}\omega \cdot \frac{1}{|\mathbf{grad}_q \omega(qr)|} \tag{2.168}$$

Thus the fraction of the total $6nN'$ frequencies between ω and $\omega + \mathrm{d}\omega$ is obtained by summing over the $6n$ branches, after integrating over $S_r(\omega)$

$$g(\omega)\, \mathrm{d}\omega = \frac{1}{6nN'} \sum_r \int_{S_r(\omega)} \mathrm{d}n_{r,\omega} \tag{2.169}$$

and, from the expression of $\mathrm{d}n_{r,\omega}$ (2.168)

$$g(\omega) = \frac{1}{6nv^*} \sum_r \int_{S_r(\omega)} \frac{\mathrm{d}S_r(\omega)}{|\mathbf{grad}_q \omega(qr)|} \tag{2.170}$$

The important result of (2.170) is that $g(\omega)$ contains a number of singularities where $\mathbf{grad}_q \omega(qr) = 0$. The density of phonon states is large for phonon frequencies corresponding to the acoustic and optical branches at the limits of the Brillouin zone, and also to the optical branches at the centre of the Brillouin zone. As we shall see later, the incoherent neutron scattering is proportional to the phonon distribution $g(\omega)$. In the neighbourhood of these critical frequencies, large maxima appear in the scattered intensity, which give a rough insight into the phonon dispersion curves.

2.8.2 Neutron scattering law from lattice phonons

The derivation of the neutron scattering law originating from lattice (external) modes closely follows that for molecular internal modes, described in §2.7. The displacements $\boldsymbol{u}(m, j, a)$ are expressed in terms of the creation and annihilation operators relative to various modes $a^+(qr)$ and $a(qr)$,

$$u(m, j, a) = \sum_{qr} \left(\frac{\hbar}{2Nm_j\omega(qr)}\right)^{1/2} \Big[\xi^j(qra)a(qr) \exp\{i[q\cdot R_m - \omega(qr)t]\} + \xi^{j*}(qra)a^+(qr) \exp\{-i[q\cdot R_m - \omega(qr)t]\}\Big]. \quad (2.171)$$

The Bose operators fulfil the commutation relation

$$[a(qr), a^+(q'r')] = \delta_{rr'}\,\delta_{qq'}. \quad (2.172)$$

By analogy with the discussion of internal molecular modes, it follows that $a^+(qr)a(qr)$ is the number operator for the phonon described by q and r. Hence

$$H = \sum_{qr} [a^+(qr)a(qr) + \tfrac{1}{2}]\hbar\omega(qr) \quad (2.173)$$

$$\langle a^+(qr)a(q'r')\rangle = \delta_{rr'}\delta_{qq'}\, n(qr) \quad (2.174)$$

where $n(qr)$ is the Bose occupation function

$$n(qr) = \frac{1}{\exp\{\beta\hbar\omega(qr)\} - 1}. \quad (2.175)$$

The derivation of the neutron scattering law follows the method indicated in §2.7. The relevant correlation function in (2.123) can be written, using the relation (2.146):

$$\langle \exp\{iQ\cdot u(mja; 0)\} \exp\{-iQ\cdot u(pkb; t)\}\rangle = \exp\{-W_{ja}(Q)\} \exp\{-W_{kb}(Q)\} \exp\{\langle [Q\cdot u(mja; 0)][Q\cdot u(pkb;t)]\rangle\} \quad (2.176)$$

where the expression of the Debye–Waller factor, $W_{ja}(Q)$, relative to the atom (a) in the molecule (m, j), is:

$$W_{ja}(Q) = \frac{\hbar}{2N'} \sum_{qr} \frac{|Q\cdot\xi^j(qra)|^2}{m_j\omega(qr)} [n(qr) + \tfrac{1}{2}]. \quad (2.177)$$

To calculate the double differential cross section, the scattering lengths attenuated by the Debye–Waller factor, b'_{inc} and b'_{coh}

$$b'^{ja}_{\text{inc}} = b^{ja}_{\text{inc}} \exp\{-W_{ja}(Q)\} \quad (2.178a)$$

$$b'^{ja}_{\text{coh}} = b^{ja}_{\text{coh}} \exp\{-W_{ja}(Q)\} \quad (2.178b)$$

and the double differential coherent cross section becomes

$$\left(\frac{\partial^2\sigma}{\partial\Omega\partial\omega}\right)_{\text{coh}} = \frac{k}{k_0} \sum_{mjapkb} b'^{ja}_{\text{coh}} b'^{kb}_{\text{coh}} \exp\{-iQ\cdot(R_m + R_j + R_a - R_p - R_k - R_b)\} \times \frac{1}{2\pi} \int_{-\infty}^{\infty} \exp\{\langle [Q\cdot u(mja; 0)][Q\cdot u(pkb; t)]\rangle\} \exp(-i\omega t)\, dt. \quad (2.179)$$

Putting $(mja) = (pkb)$ in (2.179) above leads immediately to the incoherent cross section

$$\left(\frac{\partial^2\sigma}{\partial\boldsymbol{\Omega}\partial\omega}\right)_{\text{inc}} = \frac{k}{k_0}\sum_{mja}(b'^{ja}_{\text{inc}})^2\,\frac{1}{2\pi}\int_{-\infty}^{\infty}\exp\{\langle[\boldsymbol{Q}\cdot\boldsymbol{u}(mja;0)][\boldsymbol{Q}\cdot\boldsymbol{u}(mja;t)]\rangle\} \times \exp(-\mathrm{i}\omega t)\,\mathrm{d}t. \tag{2.180}$$

Then the method consists of an expansion of the exponential terms occurring in (2.179) and (2.180) in terms of the displacement correlation functions, with the expectation of a rapid convergence

$$\exp\{\langle[\boldsymbol{Q}\cdot\boldsymbol{u}(mja;0)][\boldsymbol{Q}\cdot\boldsymbol{u}(pkb;t)]\rangle\} = \exp\{\langle\ldots\rangle\} = 1 + \langle\ldots\rangle + \tfrac{1}{2}(\langle\ldots\rangle)^2 + \ldots. \tag{2.181}$$

The expansion of (2.179) according to (2.181) gives

$$\left(\frac{\partial^2\sigma}{\partial\boldsymbol{\Omega}\partial\omega}\right)_{\text{coh}} = \frac{k}{k_0}\sum_{mja}\sum_{pkb} b'^{ja}_{\text{coh}}\,b'^{kb}_{\text{coh}}\exp\{-\mathrm{i}\boldsymbol{Q}\cdot(\boldsymbol{R}_m + \boldsymbol{R}_j + \boldsymbol{R}_a - \boldsymbol{R}_p - \boldsymbol{R}_k - \boldsymbol{R}_b) \times\left[\delta(\omega) + \frac{1}{2\pi}\int_{-\infty}^{\infty}\langle\ldots\rangle\exp(-\mathrm{i}\omega t)\,\mathrm{d}t + \ldots\right] \tag{2.182}$$

Similarly

$$\left(\frac{\partial^2\sigma}{\partial\boldsymbol{\Omega}\partial\omega}\right)_{\text{inc}} = \frac{k}{k_0}\sum_{mja}(b'^{ja}_{\text{inc}})^2\left[\delta(\omega) + \frac{1}{2\pi}\int_{-\infty}^{\infty}\langle\ldots\rangle\exp(-\mathrm{i}\omega t)\,\mathrm{d}t + \ldots\right]. \tag{2.183}$$

The first zero order term on each of the right-hand sides of (2.182) and (2.183) gives rise to purely elastic scattering. The second (first order) term gives the one-phonon scattering, the next one the two-phonon scattering, etc . . . .

It is worth noting that, whilst the incoherent elastic scattering does not involve any selection rule concerning the scattering vector $\boldsymbol{Q}$, conversely, the coherent elastic scattering

$$\left(\frac{\partial^2\sigma}{\partial\boldsymbol{\Omega}\partial\omega}\right)^{\text{el}}_{\text{coh}} = \frac{k}{k_0}\sum_{m}\sum_{p}\left|\sum_{ja} b'^{ja}_{\text{coh}}\exp\{-\mathrm{i}\boldsymbol{Q}\cdot(\boldsymbol{R}_j + \boldsymbol{R}_a)\}\right|^2\exp\{-\mathrm{i}\boldsymbol{Q}\cdot(\boldsymbol{R}_m - \boldsymbol{R}_p)\}\,\delta(\omega) \tag{2.184a}$$

is zero, unless the scattering vector $\boldsymbol{Q}$ coincides with a vector of the

reciprocal lattice. Hence

$$\left(\frac{\partial^2\sigma}{\partial\Omega}\right)^{\text{el}}_{\text{coh}} = N'^2\,\frac{k}{k_0}\left|\sum_{ja} b'^{ja}_{\text{coh}}\exp\{-\mathrm{i}\boldsymbol{Q}\cdot(\boldsymbol{R}_j+\boldsymbol{R}_a)\}\right|^2\Delta(\boldsymbol{Q}) \quad (2.184b)$$

where $\Delta(\boldsymbol{Q})$ expresses the Bragg condition:

(i) $\Delta(\boldsymbol{Q}) = 1$, if $\boldsymbol{Q}$ is identical to any reciprocal lattice vector
(ii) $\Delta(\boldsymbol{Q}) = 0$, otherwise.

This relation gives the variation of the Bragg intensity for different reflections due to the interference of the atoms in the unit cell.

The expression of the displacement corrrelation function is easily evaluated from the relations (2.171) and (2.174):

$$\langle[\boldsymbol{Q}\cdot\boldsymbol{u}(mja;0)][\boldsymbol{Q}\cdot\boldsymbol{u}(pkb;t)]\rangle = \sum_{qr}\frac{\hbar[\boldsymbol{Q}\cdot\boldsymbol{\xi}^j(qra)][\boldsymbol{Q}\cdot\boldsymbol{\xi}^k(qrb)]}{2N'\omega(\boldsymbol{qr})\,(m_jm_k)^{1/2}}\cdot\exp\{-\mathrm{i}\boldsymbol{Q}\cdot(\boldsymbol{R}_m-\boldsymbol{R}_p)\} \quad (2.185a)$$
$$\times\left[(n(\boldsymbol{qr})+1)\exp(\mathrm{i}\omega(\boldsymbol{qr})t\} + n(\boldsymbol{qr})\exp\{-\mathrm{i}\omega(\boldsymbol{qr})t\}\right]$$

and the inelastic coherent partial cross section becomes

$$\left(\frac{\partial^2\sigma}{\partial\Omega\partial\omega}\right)^{\text{inel}}_{\text{coh}} = \frac{N'\hbar k}{2k_0}\sum_{qr}\left|\sum_{ja}\frac{b'^{ja}_{\text{coh}}\exp\{-\mathrm{i}\boldsymbol{Q}\cdot(\boldsymbol{R}_j+\boldsymbol{R}_a)\}\,(\boldsymbol{Q}\cdot\boldsymbol{\xi}^j(qra))}{[\,m_j\omega(\boldsymbol{qr})]^{1/2}}\right|^2$$
$$\times\left[(n(\boldsymbol{qr})+1)\,\delta\{\omega+\omega(\boldsymbol{qr})\} + n(\boldsymbol{qr})\,\delta\{\omega-\omega(\boldsymbol{qr})\}\right]\Delta(\boldsymbol{Q}-\boldsymbol{q}). \quad (2.185b)$$

The cross section appears as the sum of two terms, which contains respectively $\delta(\omega+\omega(\boldsymbol{qr}))$ and $\delta(\omega-\omega(\boldsymbol{qr}))$. Hence the first term represents the annihilation process of one phonon whilst the other corresponds to the one-phonon creation process. Another very important feature is the existence in (2.185b) of the function $\Delta(\boldsymbol{Q}-\boldsymbol{q})$ which is a momentum selection rule in the sense that it is zero, except if the difference $\boldsymbol{Q}-\boldsymbol{q}$ between the scattering vector and the wavevector of the phonon mode is coincident with a vector of the reciprocal lattice. An immediate consequence of these two conditions on the energy and momentum transfers of the neutron is that coherent inelastic scattering provides an extremely powerful tool for the measurement of phonon dispersion relations in the crystal, that is the determination of the phonon mode frequencies $\omega(\boldsymbol{qr})$ as a function of their wavevector $\boldsymbol{q}$. The technique of coherent inelastic scattering has been already described by many authors (Dolling 1974, Lovesey 1984). Because in this book we are mainly interested in the incoherent neutron scattering technique, we shall refer to these authors for more information and we shall focus our attention on the incoherent partial cross section which can be written, putting simply $(mja) = (pkb)$ in (2.185a)

$$\left(\frac{\partial^2\sigma}{\partial\Omega\partial\omega}\right)_{\text{inc}} = \frac{k}{k_0}\sum_{ja}(b'^{ja}_{\text{inc}})^2\left\{N'\delta(\omega) + \frac{\hbar}{2}\sum_{qr}\left|\frac{\boldsymbol{Q}\cdot\boldsymbol{\xi}^j(qra)}{[m_j\omega(qr)]^{1/2}}\right|^2\right.$$

$$\left.\times\,[(n(qr)+1)\,\delta(\omega+\omega(qr)) + n(qr)\,\delta(\omega-\omega(qr))]\right\}. \tag{2.186}$$

As for coherent scattering (see 2.185b), this formula contains two delta functions representing one-phonon annihilation and one-phonon creation processes. The major difference is that no momentum conservation condition is involved in incoherent scattering. Therefore, one-phonon incoherent scattering provides less detailed information than one-phonon coherent scattering. It is, however, of interest because it allows us to get an insight into vibration frequency distribution $g(\omega)$ as we shall see next.

The distribution of the q values in the Brillouin zone is very dense and can be considered as nearly continuous. It follows that the summation over qr in (2.186) can be replaced by an integral over the different values of $\omega(qr)$. Let us consider first the very simple case of a cubic crystal with one single atom per unit cell, for which the derivation is rigorous. The one-phonon creation of the incoherent partial derivative cross section becomes

$$\left(\frac{\partial^2\sigma}{\partial\Omega\partial\omega}\right)^{+1}_{\text{inc}} = \frac{N'\hbar k}{2k_0}\,\frac{(b_{\text{inc}})^2}{m}\exp\{-2W(\boldsymbol{Q})\}\int_0^{\omega_m}\frac{g(\omega')}{\omega'}\,\mathrm{d}\omega'$$

$$\times\sum_{qr}{}'\,|\boldsymbol{Q}\cdot\boldsymbol{\xi}(qr)|^2\,(n(qr)+1)\delta(\omega-\omega') \tag{2.187}$$

where the primed sum runs over modes qr at constant frequency, ω'. $g(\omega')$, the frequency distribution, is defined such that the fraction of eigenfrequencies $\omega(qr)$ between ω' and $\omega'+\mathrm{d}\omega'$ is equal to $g(\omega')\mathrm{d}\omega'$. For cubic crystals with one atom per unit cell, $|\boldsymbol{Q}\cdot\boldsymbol{\xi}(qr)|^2 = Q^2$. If we define

$$g(-\omega) = g(\omega) \tag{2.188}$$

it follows that the cross section is exactly similar in both the annihilation and creation cases, and is given by

$$\left(\frac{\partial^2\sigma}{\partial\Omega\partial\omega}\right)^{+1}_{\text{inc}} = \frac{N'\hbar k}{2k_0}\,\frac{(b_{\text{inc}})^2}{m}\exp\{-2W(\boldsymbol{Q})\}\,\frac{g(\omega)}{\omega}\,n(\omega). \tag{2.189}$$

According to (2.189) the one-phonon incoherent cross section is proportional to $g(\omega)$ and a measurement of the energy distribution of the scattered neutrons should yield a direct determination of the frequency distribution. A first difficulty arises because $g(\omega)$ also appears in the Debye–Waller factor, $\exp(-2W)$, which can be written:

$$W(\boldsymbol{Q}) = \frac{\hbar Q^2}{4m}\int_0^\infty \mathrm{d}\omega\,\frac{g(\omega)}{\omega}\coth\left(\beta\frac{\hbar\omega}{2}\right). \tag{2.190}$$

Therefore an approximate form for $g(\omega)$ must first be assumed; usually $g(\omega)$ is taken to be a Debye spectrum. In fact the influence of the Debye–Waller term is limited at small energy transfers and at low temperature.

These two conditions provide the other advantage of minimising the multiphonon effects, i.e. the contribution of the higher-order terms which have been neglected in the expansion (2.181). Multiphonon processes do not in general yield useful information, because they give rise to a smooth, structureless, inelastic spectrum, underlying the relevant one-phonon scattering, whose main features are essentially preserved.

So far, our derivation of equations (2.189) and (2.190) has been restricted to cubic monoatomic solids. For non-cubic lattices or for crystals with more than one atom per unit cell, and particularly for molecular crystals, which we are dealing with, it is impossible to eliminate the polarisation vectors in (2.186). However, in the case of polycrystalline substances some simplifications are possible. Then an average of (2.186) has to be taken over all the possible orientations of the grains of the powder specimen with respect to the direction of $\boldsymbol{Q}$. This procedure is equivalent to an averaging over all directions of $\boldsymbol{Q}$. The incoherent polycrystalline scattering law result is, for the inelastic part:

$$\left(\frac{\partial^2\sigma}{\partial\Omega\partial\omega}\right)_{\text{inc}}^{\text{inel}} = \frac{\hbar k}{k_0}\sum_{ja}(b_{\text{inc}}^{ja})^2\exp\{-2W_{ja}(Q)\}\;n(\omega)\;\frac{|\boldsymbol{Q}|^2 G_{ja}(\omega)}{2m_j\omega} \qquad (2.191)$$

where the density of states, weighted by the atomic amplitudes has been introduced:

$$\begin{aligned} G_{ja}(\omega) &= \frac{1}{6nN'}\sum_{qr}|\xi^j(qra)|^2\;\delta\{\omega-\omega(qr)\} \\ &= \frac{1}{6nN'}\sum_{r}\int_{S_r(\omega)}\frac{|\xi^j(qra)|^2}{|\mathbf{grad}_q\,\omega(qr)|}\,\mathrm{d}S_r(\omega). \end{aligned} \qquad (2.192)$$

It is worth noting that, even if the relation between $G_{ja}(\omega)$ and the true frequency distribution function is not easy, the scattered intensity exhibits maxima at critical frequencies such that $\mathbf{grad}_q\,\omega(qr) = 0$, i.e. for the limits of the optical and acoustic branches at the Brillouin zone boundaries and for the optical branches at the centre of zone. Thus inelastic incoherent scattering can provide a useful technique in the investigation of crystal dynamics, either in a first stage to get some idea about the phonon dispersion curves or when single crystals are not available, for instance in low-temperature phases, or else when the sample coherent cross section is too small. The expression (2.191) above is very similar to the expression of the incoherent partial differential cross section for intramolecular vibrations (equation 2.154).

Owing to the large incoherent cross section of hydrogen, in neutron inelastic experiments with hydrogenous organic molecules, only the hydrogen atoms are 'visible'. Therefore we can introduce

$$b_{\text{inc}}^{ia} = b_{\text{inc}} = 80 \text{ barns}$$

identical for all atoms (hydrogen) within all the molecules. Assuming moreover that all the molecules inside a unit cell are identical, the relation (2.191) becomes

$$\left(\frac{\partial^2\sigma}{\partial\Omega\partial\omega}\right)_{\text{inc}} = \frac{k}{k_0}(b_{\text{inc}})^2 S_{\text{inc}}(Q, \omega) \tag{2.193}$$

with

$$S_{\text{inc}}(Q, \omega) = \frac{\hbar Q^2}{2m}\exp\{-2W(Q)\}\,\bar{n}(\omega)\exp\left(-\beta\frac{\hbar\omega}{2}\right)G(\omega) \tag{2.194}$$

where

$$\bar{n}(\omega) = \left[\hbar\omega\sinh\left(\beta\frac{\hbar\omega}{2}\right)\right]^{-1} \tag{2.195a}$$

and

$$W(Q) = \frac{\hbar Q^2}{4m}\int_0^\infty \frac{G(\omega)}{\omega}\coth\left(\frac{\hbar\omega}{2k_{\text{B}}T}\right)\mathrm{d}\omega. \tag{2.195b}$$

If we define the function

$$p(\bar{\alpha}, \bar{\beta}) = 2\bar{\beta}\sinh\left(\frac{\bar{\beta}}{2}\right) S_{\text{inc}}^{\text{cl}}(Q, \omega) \tag{2.196}$$

in which (see 2.114)

$$S_{\text{inc}}(Q, \omega) = \exp\left\{-\beta\frac{\hbar\omega}{2}\right\} S_{\text{inc}}^{\text{cl}}(Q, \omega)$$

and

$$\bar{\alpha} = \frac{\hbar^2 Q^2}{2mk_{\text{B}}T} \tag{2.197a}$$

$$\bar{\beta} = \frac{\hbar\omega}{k_{\text{B}}T} \tag{2.197b}$$

it is clear that

$$\lim_{Q^2\to 0} p(\bar{\alpha}, \bar{\beta}) = G(\omega). \tag{2.198}$$

This method provides a determination of the frequency distribution $G(\omega)$.

Because we are mainly interested in the quasielastic part of the neutron spectra, it is useful to examine the intensity originating from lattice modes in the low-energy transfer region. Here we are essentially

concerned with acoustic lattice modes and the frequency distribution can be approximated by the usual Debye spectrum:

$$g_D(\omega) = 3\frac{\omega^2}{\omega_D^3} \tag{2.199}$$

which corresponds to a quadratic distribution up to a maximum Debye frequency, ω_D. Clearly, the Debye distribution is normalised

$$\int_0^{\omega_D} g_D(\omega)\, d\omega = 1. \tag{2.200}$$

There is a relation between the Debye–Waller term, $W(Q)$ and the Debye frequency, ω_D. According to (2.190)

$$\begin{aligned} 2W(Q) &= \frac{\hbar Q^2}{2m}\int_{-\omega_D}^{\omega_D}\frac{g_D(\omega)}{\omega}n(\omega)\, d\omega \\ &= \frac{\hbar Q^2}{2m}\int_{-\omega_D}^{\omega_D}\frac{1}{\omega}\cdot\frac{3\omega^2}{\omega_D^3}\,[\exp(\beta\hbar\omega)-1]^{-1}\, d\omega \end{aligned} \tag{2.201}$$

or

$$2W(Q) = \frac{\hbar Q^2}{2m}\cdot\frac{3}{\omega_D}\cdot\phi_1(\theta) \tag{2.202}$$

where θ is the temperature in reduced units

$$\theta = T/\theta_D \tag{2.203}$$

θ_D is the Debye temperature, defined by

$$k_B\theta_D = \hbar\omega_D. \tag{2.204}$$

The function $\phi_1(\theta)$ is defined by the integral (Marshall and Lovesey 1971)

$$\phi_1(\theta) = \int_{-1}^{1}\frac{u\, du}{\exp(u/\theta)-1}. \tag{2.205}$$

Plugging (2.199) and (2.202) into the expansion of the inelastic scattering function

$$S_{inc}(Q,\omega) = \exp(-2W)\delta(\omega) + \frac{\hbar^2Q^2}{2m}\exp(-2W)\frac{g(\omega)}{\omega}\cdot\frac{1}{\exp(\beta\hbar\omega)-1} + \ldots \tag{2.206}$$

we get

$$S_{inc}(Q,\omega) = \exp(-2W)\delta(\omega) + \frac{2W\exp(-2W)}{\omega_D^2\phi_1(\theta)}\cdot\frac{\omega}{\exp(\beta\hbar\omega)-1} + \ldots. \tag{2.207}$$

From the normalisation condition,

$$1 = \int_{-\infty}^{\infty} S_{\text{inc}}(Q, \omega)\, d\omega = \exp(-2W) + 2W\exp(-2W) + \ldots \qquad (2.208)$$

it appears that if the multiphonon terms are neglected, the resulting approximation is

$$2W\exp(-2W) \simeq 1 - \exp(-2W) \qquad (2.209)$$

which is certainly valid for small values of $2W$. Under these conditions (2.207) becomes

$$S_{\text{inc}}(Q, \omega) = \exp(-W)\delta(\omega) + \frac{1 - \exp(-2W)}{\omega_D^2 \phi_1(\theta)} \frac{\omega}{\exp(\beta\hbar\omega) - 1}$$

$$= \exp(-2W)\delta(\omega) + S_{\text{inc}}^{\text{inel}}(Q, \omega). \qquad (2.210)$$

Figure 2.2 illustrates the variation of $S_{\text{inc}}^{\text{inel}}(Q, \omega)$ as a function of both ω and Q. Clearly, in the quasielastic region this inelastic term appears as a small and slowly varying function of these variables, which is usually negligible providing that the experimental energy resolution is sufficiently high and also that the Q-range of analysis is not too large. We shall examine that point in more detail in the next section.

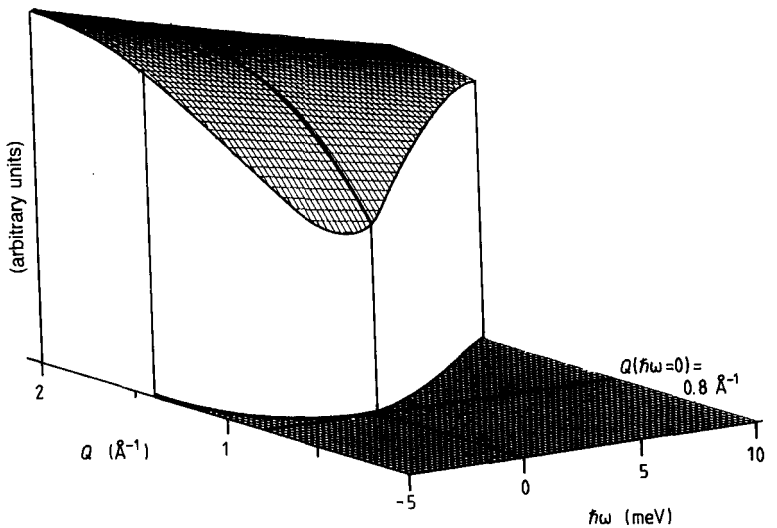

Figure 2.2 Variation of the inelastic incoherent scattering function originating from lattice vibrations as a function of both the energy and wavevector transfer. The frequency distribution is assumed to have the shape of a Debye spectrum. The surface has been truncated according to the condition $\phi = 30°$, where ϕ denotes the scattering angle. Thus the variation of the scattered intensity originating from phonons inside the usual spectrum recorded at constant angle is shown. In this figure, $\lambda = 4$ Å, $\hbar\omega_D = 10$ meV, $T = 300$ K and $m = 100$ atomic units.

2.9 Combination of the Different Kinds of Motions

In order to simplify the discussion and without any loss of generality, the analysis can be restricted to the case of identical molecules, in which only one kind of atom (for instance hydrogen) is visible. Moreover these atoms will be considered as dynamically equivalent. Thus all the scattering laws are restricted to the case of a single scatterer.

The hypothesis of dynamic independence for different molecular motions yielded to the formulation of the intermediate scattering law, in the case of a bulk sample:

$$I_{\text{inc}}(\boldsymbol{Q}, t) = I^{\text{L}}_{\text{inc}}(\boldsymbol{Q}, t) \cdot I^{\text{R}}_{\text{inc}}(\boldsymbol{Q}, t) \cdot I^{\text{V}}_{\text{inc}}(\boldsymbol{Q}, t) \tag{2.211a}$$

and for a liquid sample

$$I_{\text{inc}}(\boldsymbol{Q}, t) = I^{\text{T}}_{\text{inc}}(\boldsymbol{Q}, t) \cdot I^{\text{R}}_{\text{inc}}(\boldsymbol{Q}, t) \cdot I^{\text{V}}_{\text{inc}}(\boldsymbol{Q}, t). \tag{2.211b}$$

An alternative form is based on the convolution theorem for the Fourier transforms. In terms of the respective scattering functions, (2.111a) and (2.111b) become, respectively

$$S_{\text{inc}}(\boldsymbol{Q}, \omega) = S^{\text{L}}_{\text{inc}}(\boldsymbol{Q}, \omega) \otimes S^{\text{R}}_{\text{inc}}(\boldsymbol{Q}, \omega) \otimes S^{\text{V}}_{\text{inc}}(\boldsymbol{Q}, \omega) \tag{2.212a}$$

$$S_{\text{inc}}(\boldsymbol{Q}, \omega) = S^{\text{T}}_{\text{inc}}(\boldsymbol{Q}, \omega) \otimes S^{\text{R}}_{\text{inc}}(\boldsymbol{Q}, \omega) \otimes S^{\text{V}}_{\text{inc}}(\boldsymbol{Q}, \omega) \tag{2.212b}$$

where the symbol $\otimes$ denotes the convolution product, i.e.

$$S^{\text{A}}_{\text{inc}}(\boldsymbol{Q}, \omega) \otimes S^{\text{B}}_{\text{inc}}(\boldsymbol{Q}, \omega) = \int \mathrm{d}\omega' S^{\text{A}}_{\text{inc}}(\boldsymbol{Q}, \omega') \, S^{\text{B}}_{\text{inc}}(\boldsymbol{Q}, \omega - \omega'). \tag{2.213}$$

Referring to (2.151) and (2.186), the scattering functions related to molecular vibrations and lattice phonons, $S^{\text{V}}_{\text{inc}}(\boldsymbol{Q}, \omega)$ and $S^{\text{L}}_{\text{inc}}(\boldsymbol{Q}, \omega)$ can be separated formally into an elastic and a quasielastic part

$$S^{\text{V}}_{\text{inc}}(\boldsymbol{Q}, \omega) = \exp\{-2W^{\text{V}}(Q)\} \, [\delta(\omega) + S^{\text{V}}_{\text{inel}}(\boldsymbol{Q}, \omega)] \tag{2.214a}$$

$$S^{\text{L}}_{\text{inc}}(\boldsymbol{Q}, \omega) = \exp\{-2W^{\text{L}}(Q)\} \, [\delta(\omega) + S^{\text{L}}_{\text{inel}}(\boldsymbol{Q}, \omega)] \tag{2.214b}$$

where

$$2W^{\text{V}}(Q) = \langle u^2_{\text{V}} \rangle Q^2 \tag{2.215a}$$

and

$$2W^{\text{L}}(Q) = \langle u^2_{\text{L}} \rangle Q^2 \tag{2.215b}$$

are the Debye–Waller factors. $\langle u^2_{\text{V}} \rangle$ and $\langle u^2_{\text{L}} \rangle$ denote mean-square displacements of the atom. The former represents the effects of internal molecular vibrations. The second corresponds to whole-molecule translational vibrations and librations, originating from lattice modes. According to (2.151) $S^{\text{V}}_{\text{inel}}(\boldsymbol{Q}, \omega)$ is composed of a series of sharp lines (theoretically delta function) occurring at different energy values $\hbar\omega_\mu$, related to vibrational levels of the molecule. Therefore, when folded

with any scattering function expression $S_{inc}(\boldsymbol{Q}, \omega)$, this term will reproduce the same function, $S_{inc}(\boldsymbol{Q}, \omega - \omega_\mu)$, but centred at the different frequencies, ω_μ.

The result is a broadening of the inelastic spectral lines, but because these are located at rather high-energy transfer, there is no influence in the quasielastic region of interest.

We have shown that $S^{L}_{inel}(\boldsymbol{Q}, \omega)$ was a slowly varying term which, in the quasielastic region, takes the form of a small flat background. Characteristic structures associated with zone boundaries, limits of optical branches and upper pair of acoustic branches occur in the inelastic region. It can be considered that the convolution of $S^{L}_{inel}(\boldsymbol{Q}, \omega)$ with any quasielastic sharply peaked expression $S_{inc}(\boldsymbol{Q}, \omega)$ does not produce any major modification in the shape of $S^{L}_{inel}(\boldsymbol{Q}, \omega)$.

In conclusion, the result of the convolution (2.212), taking into account the expressions (2.214a) and (2.214b) and the discussion above, leads to writing the scattering law, for a bulk sample, in the form

$$S_{inc}(\boldsymbol{Q}, \omega) = \exp\{-\langle u^2 \rangle Q^2\} \, [S^{R}_{inc}(\boldsymbol{Q}, \omega) + S^{I}_{inc}(\boldsymbol{Q}, \omega)] \quad (2.216a)$$

where

$$\langle u^2 \rangle = \langle u^2_V \rangle + \langle u^2_L \rangle \quad (2.217b)$$

is the mean square vibration of the atom under the effects of internal molecular and external lattice modes. For a sample with long-range translation (i.e. a liquid), we get

$$S_{inc}(\boldsymbol{Q}, \omega) = \exp\{-\langle u^2_V \rangle Q^2\} \, [S^{T}_{inc}(\boldsymbol{Q}, \omega) \otimes S^{R}_{inc}(\boldsymbol{Q}, \omega) + S^{I}_{inc}(\boldsymbol{Q}, \omega)] \quad (2.217)$$

The term $S^{I}_{inc}(\boldsymbol{Q}, \omega)$ is an inelastic term which results from the convolution of $S^{V}_{inel}(\boldsymbol{Q}, \omega)$ and $S^{L}_{inel}(\boldsymbol{Q}, \omega)$ with $S^{R}_{inc}(\boldsymbol{Q}, \omega)$ (bulk samples), or of $S^{V}_{inel}(\boldsymbol{Q}, \omega)$ with $S^{T}_{inc}(\boldsymbol{Q}, \omega) \otimes S^{R}_{inc}(\boldsymbol{Q}, \omega)$ (liquids).

According to the discussion above, this term contributes only a little in the quasielastic region. It could, in any case, be taken into account by a Debye phonon density of states.

$S^{R}_{inc}(\boldsymbol{Q}, \omega)$ and, to a smaller extent $S^{T}_{inc}(\boldsymbol{Q}, \omega)$ are the two basic quantities which will be studied subsequently in this book. The translational scattering function is analysed in chapter 5, on the basis of several dynamical models. The rotational scattering function is the subject of chapter 6. New trends, special aspects and practical applications are presented in the other chapters. However, it is worth pointing out here and now the general properties of $S^{T}_{inc}(\boldsymbol{Q}, \omega)$ and $S^{R}_{inc}(\boldsymbol{Q}, \omega)$. In particular, we shall define a very important quantity, the elastic incoherent structure factor, which will rapidly appear in any experiment as the first information to be obtained before building any physical model capable of interpreting the data.

2.10 General Properties of the Rotational and Translational Scattering Functions

We shall again assume for simplicity that all the scatterers are dynamically equivalent. In any case because we are concerned with incoherent scattering, the resulting functions are simply the average of the different functions of the individual nuclei. We return to the expression (2.107) of the self-pair correlation function

$$G_{\text{inc}}(\boldsymbol{r}, t) = \frac{1}{n} \sum_i \int \langle \delta(\boldsymbol{r} - \boldsymbol{r}' + \boldsymbol{R}_i(0)) \delta(\boldsymbol{r}' - \boldsymbol{R}_i(t)) \rangle \, \mathrm{d}\boldsymbol{r}' \quad (2.218)$$

in which $\boldsymbol{R}_i(0)$ and $\boldsymbol{R}_i(t)$ are the positions at times 0 and t, respectively, of the ith nucleus. We assume that in $\boldsymbol{R}_i(0)$ and $\boldsymbol{R}_j(t)$ the vibration vectors $\boldsymbol{u}(t)$ and $\boldsymbol{u}_{\text{T}}^{\text{G}}(t)$ and $\boldsymbol{u}_{\text{R}}(t)$ (see §2.6.1.) are not involved and that the effects of internal molecular vibrations and external lattice modes have already been analysed elsewhere. We consider now the limit $t \to \infty$. Clearly, there is no correlation between $\boldsymbol{R}_i(0)$ and $\boldsymbol{R}_i(\infty)$ and hence

$$G_{\text{inc}}(\boldsymbol{r}, \infty) = \frac{1}{N} \sum_i \int \langle \delta(\boldsymbol{r} - \boldsymbol{r}' + \boldsymbol{R}_i(0)) \rangle \langle \delta(\boldsymbol{r}' - \boldsymbol{R}_i(0) \rangle \, \mathrm{d}\boldsymbol{r}' \quad (2.219)$$

From the relation (2.106) between the intermediate scattering function and the self-pair correlation function

$$I_{\text{inc}}(\boldsymbol{Q}, \infty) = \frac{1}{2\pi} \int G_{\text{inc}}(\boldsymbol{r}, \infty) \exp(-\mathrm{i}\boldsymbol{Q}\cdot\boldsymbol{r}) \, \mathrm{d}\boldsymbol{r} \quad (2.220a)$$

$$I_{\text{inc}}(\boldsymbol{Q}, \infty) = \frac{1}{N} \sum_i |\langle \exp(\mathrm{i}\boldsymbol{Q}\cdot\boldsymbol{R}_i) \rangle|^2. \quad (2.220b)$$

Splitting $I_{\text{inc}}(\boldsymbol{Q}, t)$ into its time-independent and time-dependent parts

$$I_{\text{inc}}(\boldsymbol{Q}, t) = I_{\text{inc}}(\boldsymbol{Q}, \infty) + I_{\text{inc}}^{\text{l}}(\boldsymbol{Q}, t) \quad (2.221)$$

and taking the time-Fourier transform, we get

$$S_{\text{inc}}(\boldsymbol{Q}, \omega) = I_{\text{inc}}(\boldsymbol{Q}, \infty)\delta(\omega) + S_{\text{inc}}^{\text{q}}(\boldsymbol{Q}, \omega). \quad (2.222)$$

The $S_{\text{inc}}(\boldsymbol{Q}, \omega)$ has been separated into a purely elastic component, $I_{\text{inc}}(\boldsymbol{Q}, \infty)\delta(\omega)$, superimposed on another one which, because it is the time-Fourier transform of a time-dependent term, possesses a non-vanishing broadening. The width of this quasielastic component provides information about the characteristic times of the motion. Conversely, the coefficient of the delta function is the space-Fourier transform of the final distribution of the scattering nuclei, averaged over all the nuclei, that is, because they are assumed all equivalent, averaged over all possible initial positions. It has the dimension of a structure factor and it is called the 'elastic incoherent structure factor' (EISF).

In the case of a sample with dynamical translational disorder,

$$G_{\text{inc}}(\boldsymbol{r}, \infty) = 0 \tag{2.223a}$$

and also

$$I_{\text{inc}}(\boldsymbol{r}, \infty) = 0. \tag{2.223b}$$

Therefore, a characteristic feature of the scattered intensity from a liquid or any material with dynamical disorder, like hydrogen in metals, superionic or protonic conductors, etc, is the absence of elastic peak. Conversely the existence of an elastic component in the scattered intensity clearly indicates the presence in the sample of a kind of scatterer, the motion of which is essentially located in space.

By integrating the incoherent scattering law over energy transfer ω at constant Q, we get, from the definition (2.48b).

$$\int_{-\infty}^{\infty} S^{\text{R}}_{\text{inc}}(\boldsymbol{Q}, \omega)\, \mathrm{d}\omega = \int_{-\infty}^{\infty} I^{\text{R}}_{\text{inc}}(\boldsymbol{Q}, t)\delta(t)\, \mathrm{d}t \tag{2.224a}$$

$$= I^{\text{R}}_{\text{inc}}(\boldsymbol{Q}, 0) = 1. \tag{2.224b}$$

Therefore the EISF is the fraction of the total quasielastic intensity contained in the purely elastic peak. The direct important consequence is that, providing that the separation between the sharp, purely elastic component and the wider, quasielastic contribution can be performed, by natural extrapolation or from computer techniques, the EISF is a measurable quantity, evaluated from the ratio

$$\mathcal{A}_0(Q) = \frac{\mathcal{S}^{\text{el}}(Q)}{\mathcal{S}^{\text{el}}(Q) + \mathcal{S}^{\text{q}}(Q)} \tag{2.225}$$

of the integrated intensities $\mathcal{S}^{\text{el}}(\boldsymbol{Q})$ and $\mathcal{S}^{\text{q}}(\boldsymbol{Q})$ corresponding to the elastic and quasielastic part of the spectra, respectively. However, we must make two remarks about the technical aspect of the experiments.

The instrument resolution is finite. That means that the elastic peak in the spectra does not appear as an infinitely sharp line but as a peak-shaped curve, often approximated by some triangle, lorentzian or gaussian function, with an energy width characteristic of the instrument (and sometime Q-dependent). This width defines the magnitude of the time-scale over which the motions are observable. For instance, the typical time-scale in backscattering technique is 10^{-10} s, while the time-of-flight method analyses motions over the 10^{-11}–10^{-12} s range. Motions too slow or too rapid are outside the instrument performances. Slow motions lead to quasielastic broadening negligible compared with the broadening due to the instrument energy-resolution. The corresponding scattered intensity is almost elastic. On the other hand, very fast motions produce considerable broadening and the related intensity tends to a flat background underlying the spectra. The first remark is

that any experimental determination of the EISF must not forget the typical instrumental time-scale. As an illustration, we mention an example often encountered in the study of liquids composed of large molecules. A determination of the EISF from a time-of-flight measurement, leads to a non-vanishing part of purely elastic intensity, because the translation of the molecules is too slow to be visible. The quasielastic broadening permits us to obtain the characteristic times of the rotation of the molecules about their centre of mass which appears as immobile. Conversely, the analysis of the spectra obtained by the backscattering technique clearly evidences that there is no elastic component; the measure of the broadening leads to the determination of the characteristic time related to the translation, the contribution originating from the rotation being much wider and taking the form of a flat background.

The second remark concerns the neutron detection geometry. In both the backscattering and the time-of-flight techniques the scattered neutrons are detected at constant angle. Because the momentum transfer $\boldsymbol{Q} = \boldsymbol{Q}(\phi, \omega)$ is a function of the scattering angle, ϕ, and of the energy transfer $\hbar\omega$, the later technique especially, provides a measurement of $S(\phi, \omega)$, where Q varies as a function of $\hbar\omega$, inside each spectrum at constant angle, according to

$$Q = Q(\phi, \omega) = \left(\frac{1}{2m\hbar^2}\left\{2E_0 + \hbar\omega - 2[E_0(E_0 + \hbar\omega)]^{1/2}\cos\phi\right\}\right)^{1/2} \tag{2.226}$$

where E_0 is the incident energy, m the neutron mass and ϕ the angle between the incident and scattered neutron directions (see figure 2.1). It results that a graphical EISF determination leads in fact to

$$\mathcal{A}_0(\phi) = \frac{\mathcal{S}^{el}(\phi)}{\mathcal{S}^{el}(\phi) + \mathcal{S}^{q}(\phi)} \tag{2.227}$$

which may be slightly different from $\mathcal{A}_0(Q)$ given by (2.225).

Moreover, on the neutron energy-loss side, the spectra are necessarily limited to $\hbar\omega = -E_0$, so that the integral (2.224) cannot actually be evaluated from $\hbar\omega = -\infty$. These two problems are sufficiently serious to have forbidden, in most cases, a simple determination of the EISF by taking directly the Fourier transform of the scattered intensity. We shall see later in this book, a more sophisticated method of extracting the EISF.

So far, we have considered in this chapter that an initially scattered neutron leaves the specimen without other scatterings. Before dealing with the problems of multiple scattering in chapter 4, we shall now turn to the technical aspects of neutron scattering with a description of some of the most powerful instruments in the field. This will be the subject of the next chapter.

Appendix A

The wavefunctions $\psi_k(\boldsymbol{r})$ associated with the neutron with wavevector $\boldsymbol{k}$ and energy $E = \hbar^2 k^2/2m$ are the eigenfunctions of the Schrödinger equation for a free particle

$$-\frac{\hbar^2}{2m}\Delta_r \psi_k(\boldsymbol{r}) = E\psi_k(\boldsymbol{r}) \tag{2.A.1}$$

where Δ_r denotes the laplacian operator. These eigenfunctions are

$$\psi_k(\boldsymbol{r}) = A \exp(\mathrm{i}\boldsymbol{k}\cdot\boldsymbol{r}) \tag{2.A.2}$$

A is a normalisation constant

$$\int \psi_k(\boldsymbol{r})\psi_k^*(\boldsymbol{r})\,\mathrm{d}\boldsymbol{r} = 1. \tag{2.A.3}$$

For a large box of volume $V = L^3$, the eigenfunctions are

$$\psi_k(\boldsymbol{r}) = \frac{1}{\sqrt{V}} \exp(\mathrm{i}\boldsymbol{k}\cdot\boldsymbol{r}). \tag{2.A.4}$$

In order to keep the solutions in the form of plane waves, periodic boundary conditions have to be applied, namely

$$\psi_k(\boldsymbol{r} + \boldsymbol{L}_\alpha) = \psi_k(\boldsymbol{r}) \tag{2.A.5}$$

where $\boldsymbol{L}_\alpha$ is any of the edge vectors of the cubic box. This leads to the expression of the wavevector as

$$\boldsymbol{k} = \frac{2\pi}{L^2}(m\boldsymbol{L}_x + n\boldsymbol{L}_y + p\boldsymbol{L}_z) \tag{2.A.6}$$

where m, n, p are integers.

Experimentally, one observes the number of neutrons scattered per unit of time in an element of solid angle $\mathrm{d}\Omega$ around the direction of $\boldsymbol{k}$, with an energy of between E and $E + \mathrm{d}E$. In the momentum space, this corresponds to the states within a volume element $\mathrm{d}\boldsymbol{k} = k^2\mathrm{d}\Omega\,\mathrm{d}k$. It follows from (2.A.6) that each extremity of a moment vector occupies in the reciprocal space a volume equal to $(2\pi/L)^3$ and the density of final states is such that

$$\rho(\boldsymbol{k})\,\mathrm{d}\boldsymbol{k} = \left(\frac{L}{2\pi}\right)^3 k^2\,\mathrm{d}\Omega\,\mathrm{d}k. \tag{2.A.7}$$

Chapter 3 Instruments and Methods in Cold Neutron Scattering

3.1 Introduction

In this chapter we shall give an account of the experimental apparatus to carry out measurements with cold neutrons inelastically scattered with low energy transfers. The neutron spectroscopy method consists in the measurement of changes in both energy and momentum of neutrons interacting with matter, in order to obtain information about the dynamics and the geometry of constituent atoms. For this purpose, neutrons are generally first collimated and monochromated to a defined initial wavevector state $\boldsymbol{k}_0$. After scattering by the sample, one collects the neutrons scattered with momenta between $\boldsymbol{k}_1$ and $\boldsymbol{k}_1 + \mathrm{d}\boldsymbol{k}_1$, for different scattering vectors $\boldsymbol{k}_1$. Thus, in reciprocal space, scattered neutrons are classified into small volumes d^3k_1 providing a more-or-less precise determination of the double differential cross section $\partial^2\sigma/\partial\Omega\,\partial\omega$.

Any machine used to carry out quasielastic neutron scattering experiments, on a steady state source, must perform three functions:

(i) the incident neutrons must be selected from the white beam from the reactor core in a small energy range between E_i and $E_i + \mathrm{d}E_i$ and in a small solid angle about the direction of $\boldsymbol{k}_0$.

(ii) the final energy E_f of the scattered neutrons must be analysed to

determine the energy change $\hbar\omega = E_f - E_i$.

(iii) the scattering angle with respect to the incident beam and with respect to the sample orientation must be measured to determine the momentum transfer $\boldsymbol{Q} = \boldsymbol{k}_1 - \boldsymbol{k}_0$.

In practice, these three conditions are achieved because of the physical properties of the neutron. This latter is a particle with spin $\frac{1}{2}$ (magnetic moment $\mu = -1.913$ nuclear magnetons), propagating at a finite velocity and to which the laws of kinematics can be applied. At the same time, it is a wave, whose wavelength is of the order of crystallographic spacings, for which the usual diffraction laws hold. Several experimental techniques make use of these two features. The wavelength of the neutron, λ, is related to its velocity, v, by:

$$\lambda = \frac{h}{mv} \tag{3.1}$$

with its mass $m = 1.675 \times 10^{-24}$ g, and to its energy, E, given by:

$$E = \tfrac{1}{2}mv^2. \tag{3.2}$$

Neutrons with different velocities have different wavelengths. The neutron velocities vary from 500 to 14,000 metres per second, therefore the neutron flight time is easily determined on sufficiently large lengths: a 5 Å wavelength neutron has a flight time $\tau = [L(\mathrm{m})/v(\mathrm{m\,s^{-1}})]$ of 1264 $\mu\mathrm{s\,m^{-1}}$.

Neutrons also obey Bragg's law, when diffracted by single crystals. The Bragg equation gives the relationship between wavelength $\lambda = h/mv$, distances between lattice parameters d_{hkl}, and the diffraction angle θ

$$\lambda = 2d_{hkl} \sin\theta. \tag{3.3}$$

Condition (i) is achieved from (3.1), by using mechanical velocity selectors like rotating phase choppers (see §3.3.1); or by associating (3.1) and (3.3) as in §3.3.2. Moreover, by working with θ near or equal to 90° in (3.3), high resolution is reached (§3.3.3) as is immediately seen by differentiation.

Condition (ii) is fulfilled via the relation (3.2) connecting the neutron velocity to its energy by simply measuring the time-of-flight $\tau = L/v$ over an accurately determined distance L. Machines with large dimensions (several metres: figure 3.6) allow precise measurement of the flight time of scattered neutrons from the sample to the detector.

It is worth noting that neutron spin–echo spectroscopy is somewhat different from the time-of-flight or backscattering techniques. This method compares directly the incident and scattered velocities of each individual neutron by counting neutron precessions in a magnetic field.

That turns out to be of major importance because the instrument resolution, i.e. the precision of the measurement of condition (ii), becomes basically independent of the beam monochromatisation (condition (i)).

Condition (iii) is simply achieved by counting the scattered neutrons with detectors located at accurate scattering angles.

Moderated nuclear fission reactors are still the most commonly used neutron sources. Here we shall concentrate only on the High Flux Reactor of the Institut Laue–Langevin (ILL) in Grenoble, France. This reactor acts as an intense continuous neutron source, especially designed for research with thermal neutrons. But also, thanks to a cold source and a hot source in the moderator, all the spectroscopy types are covered, with high- and low-energy transfers. Most of the experiments that we shall discuss in what follows in this book have been carried out with some of the 34 scheduled instruments of this institute (Maier 1983), (figure 3.1).

This book deals essentially with quasielastic neutron scattering and thus imposes evident limitations on the experimental methods we wish to look at in greater detail.

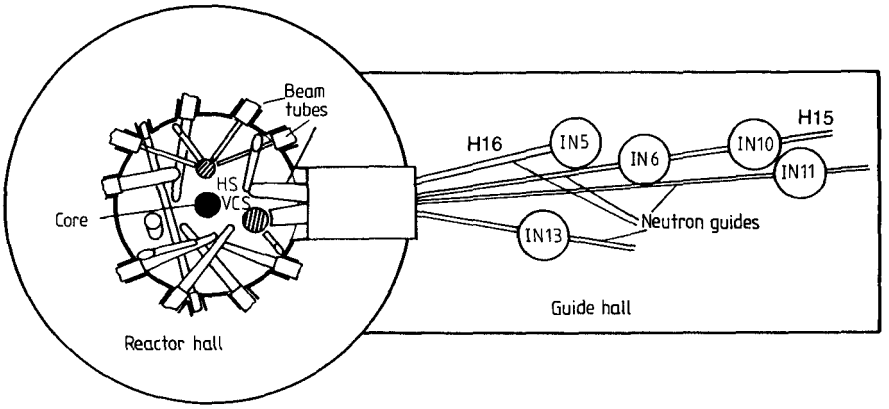

Figure 3.1 Schematic arrangements of beam tubes, hot source (HS) vertical cold source (VCS) and instruments at the high-flux reactor of the Institut Laue–Langevin, Grenoble (France).

3.1.1 The reactor. The hot and the cold source

The high neutron flux (1.5×10^{15} n cm^{-2} s^{-1}) is produced by the nuclear fission occurring in a 8.57 kg fuel element enriched to 93% of ^{235}U. The

fuel is embedded in zircalloy. D_2O acting as cooling medium and moderator, passes under pressure through it, in the reflector tank. Neutrons in thermal equilibrium with the moderator, have a maxwellian distribution. The flux $\Phi(v)$, i.e. the number of neutrons passing through unit area per second with velocities between v and $v + dv$, is given by:

$$\Phi(v) = \Phi \frac{1}{2} \left(\frac{m}{k_B T} \right)^2 v^3 \exp\left(- \frac{1}{2} \frac{mv^2}{k_B T} \right) \tag{3.4}$$

where k_B is the Boltzmann constant, Φ is the total flux originating from the core, m is the mass of the neutron, and T is the temperature of the moderator.

For a moderator at 300 K, the most probable wavelength is 1.45 Å. This is of the order of magnitude of the usual interatomic distances in solids and liquids and usual diffractometers are located on thermal beams.

For quasielastic experiments, i.e. for the purpose of high-energy resolution, low incident energy is needed.

Figure 3.2(*a*) shows the neutron intensity as a function of wavelength for a beam tube which faces a normal heavy water moderator at 300 K (full curve).

The hot source (HS in figure 3.1) is a graphite block of 10 litres in volume reaching a temperature of 2000 K by nuclear heating, which supplies neutrons of shorter wavelength (broken curve in figure 3.2(*a*)). Beyond 3 Å, the beam is very weak. The beam intensity can be moved to a longer wavelength by cooling a portion of the moderator by a 'cold source', VCS (i.e. vertical cold source) in figure 3.1 (Ageron *et al* 1971). This consists of an aluminium sphere filled with 2.5 l of liquid deuterium kept at 25 K, situated at 70 cm from the core, in the reflector; the deuterium cell is undissociably linked to the zircalloy vacuum enclosure and roughly acts as a cryostat installed in the reactor (figure 3.3). A helium refrigeration plant of 10 kW in power is necessary to keep this cold source at low temperature. Thermalisation shifts the Maxwell distribution to longer wavelengths. This source provides cold neutrons for the particular spectrometers linked to the core by neutron guides (see figure 3.1). In this book, we shall be more specifically interested in the spectrometers IN5, IN6, IN10, IN11 and also IN13 on the thermal guide.

The cold and the hot sources have spectral peaks at about 3.5 and 0.5 Å respectively. Figure 3.2 shows the improvement of fluxes given by the sources as compared with the heavy water moderator maintained at 300 K. The neutron velocity distribution, evaluated from (3.4), is illustrated in figure 3.2(b). The distributions corresponding to particular values $T = 25$, 300 and 2000 K have been highlighted.

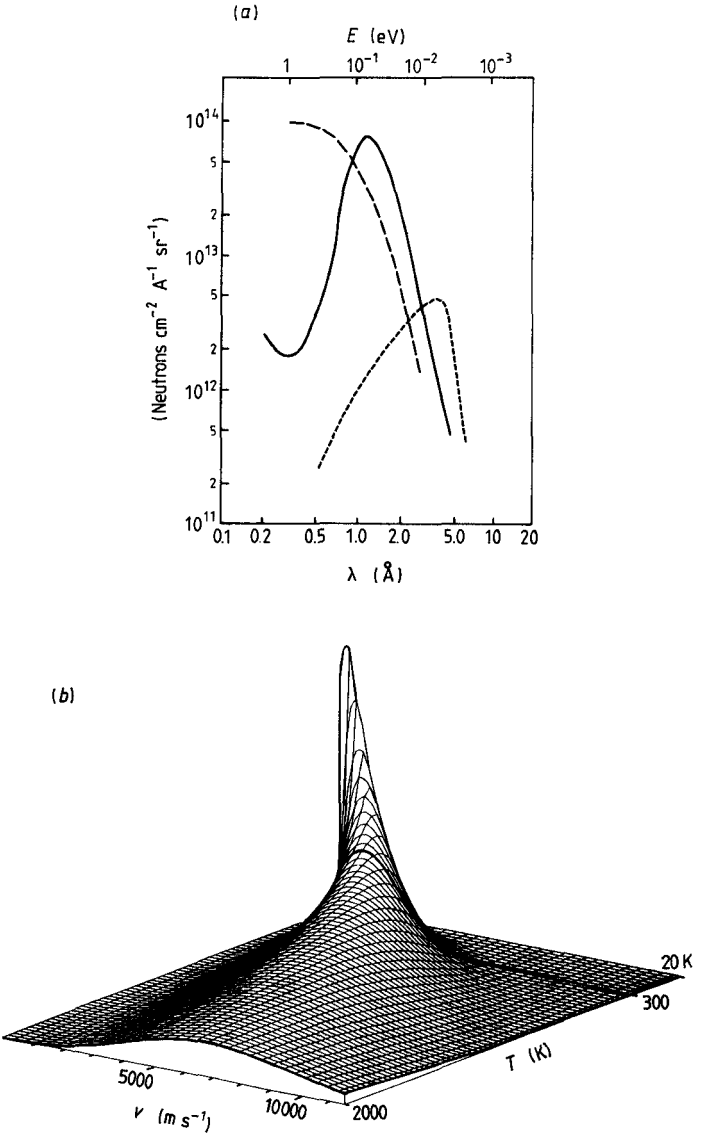

Figure 3.2 Illustration of the effects of the hot and vertical sources: (*a*) Neutron intensity as a function of energy and wavelength. The full curve corresponds to beam tubes facing the heavy water moderator at 300 K, the broken curve to those facing the hot source at 2000 K and the dotted curve to the beam tubes in front of the cold source (25 K). (*b*) Flux distribution of neutrons as a function of their velocity and of temperature, evaluated from equation (3.4). The distributions at $T = 20$, 300 and 2000 K are stressed.

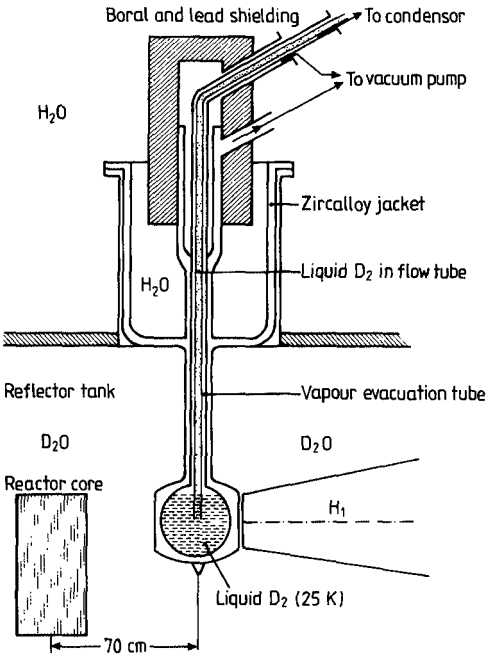

Figure 3.3 The cold source: the in-reflector part. The 2.5 l ball containing the liquid deuterium is isolated, by an evacuated double wall, from the H_2O swimming pool in the upper part and from the D_2O moderator of the reflector in the lower part.

3.1.2 The neutron guides

Thermal neutrons are extracted to the experimental hall, through the biological shielding, using beam tubes (see figure 3.1). The number of instruments around the reactor is essentially limited by their floorspace requirements. However, a system of neutron guide tubes permits transport of thermal and cold neutrons to other instruments situated at distances of several tens of metres from the core without excessive loss in intensity. The guide principle is based on the phenomenon of total reflection of neutrons. These guides are evacuated, rectangular glass tubes, with a cross section of $20 \times 3\ cm^2$. The inner surface is coated with an evaporated layer of nickel about 1000 Å thick (Jacrot 1970, Maier-Leibnitz and Springer 1963) which reflects more than 99% of neutrons incident at glancing angles below the limit refraction angle. Beam losses, resulting from non-perfect reflectivity are small, less than 1% per metre.

The guides can be curved in order not to see directly into the reactor

core. This suppresses considerably the background of fast neutrons and gamma rays, both having their origin in the core.

3.1.3 Detectors

Neutron detectors are based on the detection of the by products of nuclear reactions neutrons produce, such as the transformation of ^{10}B into ^{7}Li with the emission of an α-particle, or ^{3}He into ^{4}He and a proton, or ^{6}Li into ^{3}H and an α-particle. The subsequent charged particles or γ radiation are then detected.

The most commonly used detector in the past was the BF_3 gas-filled proportional counter. However, it is replaced now by ^{3}He-filled detectors, which have a higher absorption cross section and can be filled under a higher gas pressure. Furthermore they can be smaller in size, thus providing a better spatial and time-of-flight resolution.

3.1.4 Pulsed neutron sources

Neutron beams from reactors are limited by available thermal energies. The installation of cold and hot sources at reactors permits an extension of the window in the neutron spectrum on both sides of lower and higher energies. The continuous improvement in technology and spectrometer design yields an increase of the effective incident flux and of the amount of usable information extracted from the scattered neutron spectrum. The development of steady reactors followed the great success of the use of the neutron scattering technique in the investigation of chemical, biological and physical properties of matter. Time-of-flight technique turns out to be a very powerful method in the analysis of inelastic scattering processes, but leads to a considerable waste of neutrons (*ca* 96%). This is one of the reasons for the stimulation of the construction of pulsed neutron sources which promise at least an order of magnitude increase in peak fluxes. Among them, spallation sources appear to be the most efficient. The spallation reaction refers to the interaction of high-energy particles (*ca* 1 GeV protons) with a heavy metal target. The proton range is rather long, tens of centimetres, so many nuclei in the target are affected. Neutron production is high, around 30 neutrons per proton and, at the same time, the heat dissipated per neutron produced is smaller than in a steady reactor.

Today, there are operating facilities in the United States, at Argonne National Laboratory and at Los Alamos National Laboratory, in Japan at the National Laboratory for High Energy Physics, and in England, at the Rutherford Appleton Laboratory (Windsor 1981, Lovesey and Stirling 1984).

The Spallation Neutron Source at the Rutherford Appleton Labora-

tory is illustrated schematically in figure 3.4. It consists of a high intensity 800 MeV synchrotron in which 0.4 μs pulses of protons are accelerated and then guided through the extracted proton beam channel to the target station (Gray 1985). A 70 MeV injector accelerator adds protons into the bunches until they are repelled by the 'span charge' of protons already in the beam. To overcome this repulsion, H^- ions, protons with two orbital electrons, are injected and then the electrons are stripped off the protons by a thin foil. The compact target is made of plates of depleted uranium, clad with zircalloy. It is surrounded by four separate moderators. Their role is to shift the fast neutrons produced in the target downwards in energy to give an optimum neutron flux in the energy range of the experiment of interest. Above the target, there are two ambient-temperature water moderators and below there is a moderator of methane at 95 K and another of supercritical hydrogen at 25 K.

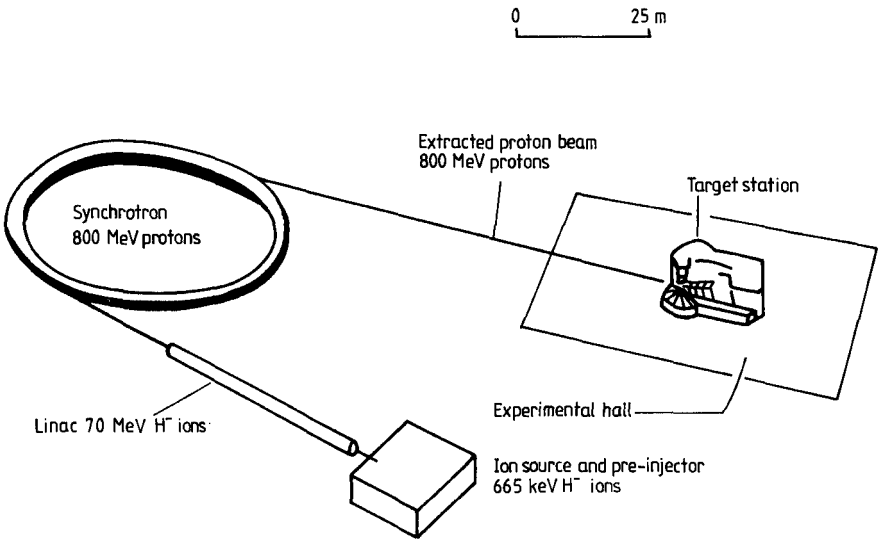

Figure 3.4 Schematic layout of the Spallation Neutron Source at the Rutherford Appleton Laboratory, Harwell (UK).

A reflector, made of beryllium rods cooled by D_2O, surrounds the target and the moderator, the whole assembly being at the centre of a steel vessel (3 m in diameter) filled with helium. A biological shield around the vessel attenuates the intense radiation, produced by the target, to a level causing negligible danger to experimentalists working at the spectrometers. Fast neutrons, with energies above 1 MeV, are the

most difficult radiations to shield. The biological shielding is pierced by 18 neutron beam holes.

The Intense Pulsed Neutron Source at the Argonne National Laboratory is also based on a proton accelerator installation. At Los Alamos, a big linear proton accelerator is used to accelerate protons to the full 800 MeV.

3.1.5 Instruments

The experimental methods at present used give energy resolutions from 10^{-4} eV to 10^{-8} eV ($1\text{ eV} \simeq 8000\text{ cm}^{-1}$). At ILL, two time-of-flight (t.o.f.) spectrometers, the multichopper IN5 and the time-focusing IN6, cover a range of energy transfers up to a few 10^{-2} eV with a resolution of about 10^{-4} eV. Another similar t.o.f. spectrometer (MIBEMOL) also exists on the cold source of the reactor Orphée in Saclay (France). Two backscattering spectrometers, IN10 and IN13, specially designed to have a very high energy resolution $\geqslant 0.15 \times 10^{-6}$ eV for IN10 and 4.10^{-6} eV for IN13 (h.w.h.m.), cover a much restricted energy transfer range ($|\hbar\omega| \leqslant 1.5 \times 10^{-5}$ eV or $|\hbar\omega| \leqslant 3 \times 10^{-4}$ eV, respectively). We shall also mention the backscattering spectrometer IRIS at the Spallation Neutron Source at the Rutherford Appleton Laboratory (UK).

The energy domain accessible to neutron spin–echo spectrometers extends from 10^{-4} eV to 10^{-8} eV, with an energy resolution $\geqslant 3 \times 10^{-8}$ eV. So far, two instruments of that type are available: the pioneering spectrometer, IN11, at ILL, and another recently built in Saclay.

Time-of-flight instruments are composed of a primary spectrometer producing the pulsed monochromatic beam, and of a secondary spectrometer, containing the sample table, the flight path and the ^{3}He detectors. The path between the sample and the detectors is sufficiently long (several metres) for measuring the time-of-flight of the scattered neutron directly linked to the energy change in the sample. The angular position of the detectors and the time-of-flight measurement permit the analysis of both the momentum transfer $\boldsymbol{Q}$ and the energy transfer $\hbar\omega$.

Conversely, in the backscattering technique, arrays of single crystals in the secondary spectrometer reflect neutrons with well-defined final energy, E_f, to the detectors. Complete analysis of the energy spectrum is realised by varying the energy of the incident neutrons around this value E_f, using different methods in the primary part of the spectrometer.

Neutron spin–echo spectroscopy presents a unique feature, in the sense that the neutron velocities are determined by using the Larmor spin precession as an internal clock attached to each neutron. This allows the direct comparison of the velocities after and before scattering, for each individual neutron. The energy resolution becomes in first

order independent of the monochromatisation. This method measures directly the time-dependent Fourier transform of the scattering function $S(\boldsymbol{Q}, \omega)$, i.e. the intermediate scattering function $I(\boldsymbol{Q}, t)$ defined in (2.46).

The specifications of each instrument are: the incident energy, the energy resolution, the accessible Q-range, the Q-resolution and the flux at the sample. A comparison of the range of energy transfer and scattering vector covered by the spectrometers at the Institut Laue–Langevin is given schematically in figure 3.5. These are described and compared with each other in the following sections.

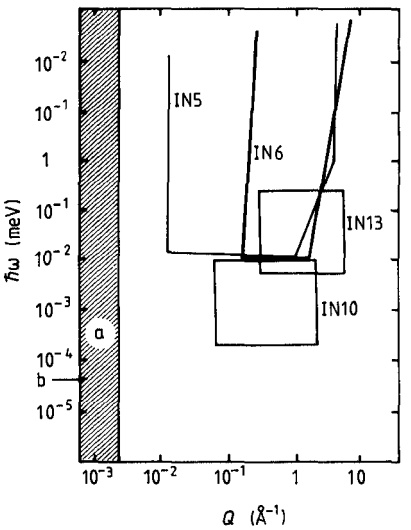

Figure 3.5 Range of energy transfer ($\hbar\omega$) and wavevector transfer (Q) covered by the time-of-flight, backscattering and spin–echo spectrometers available at the High Flux Reactor of the Institut Laue–Langevin, Grenoble (France).

3.2 Time-Of-Flight Spectrometers

We first consider the time-of-flight spectrometers which allow a determination of the final neutron energies through a direct measurement of their velocities. Three spectrometers will be described and their performances will be compared.

3.2.1 The multichopper IN5 (Lechner et al 1973)

The IN5 multichopper spectrometer is located at the end of the cold neutron guide H16 (figure 3.1) where a large range of wavelength is

available, with a distribution centred around an average wavelength of about 4.5 Å (4 meV).

The primary spectrometer 'monochromator' (Scherm and Springer 1967) comprises four disc choppers rotating around a horizontal axis. The first chopper and the fourth chopper (1, 4 in figure 3.6) define the desired wavelength. The principle of this mechanical velocity selector (Egelstaff 1954) is rather simple. A first chopper produces a pulse of white neutrons. Neutrons within the pulse have different energies and disperse according to their relative velocity: only those neutrons propagating with the appropriate velocity imposed by the phase shift $\Delta\phi$, between choppers 1 and 4 are passed by the second slit.

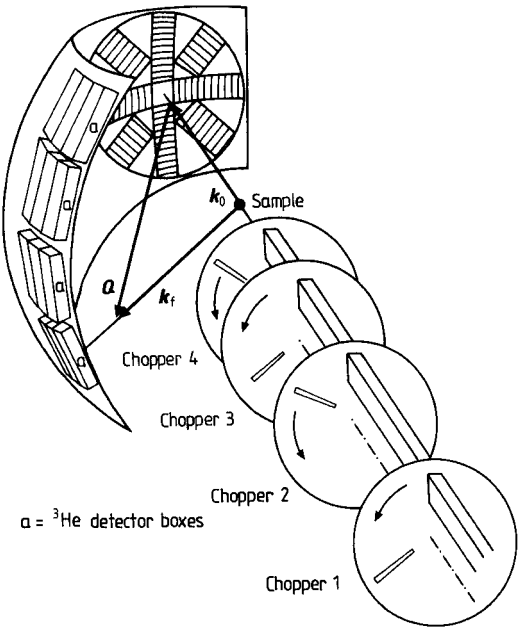

Figure 3.6 Schematic view of the time-of-flight multichopper spectrometer IN5 at the High Flux Reactor of the Institut Laue–Langevin, Grenoble (France). The wavelength of the neutrons incident on the sample is essentially determined by the phase angle between the two choppers 1 and 4. Chopper 2 eliminates higher-order contamination. Chopper 3 controls the repetition rate of the neutron bursts. After scattering from the sample, neutrons are detected by ^{3}He detectors placed at a distance of 4 m.

The time taken to reach the second chopper is inversely proportional to the velocity, v, of the neutron, as shown by the relation

$$\lambda = \frac{h}{mv} = \frac{h}{m\frac{L}{\tau}}$$

where τ is the flight time of the neutron, L the flight distance between the two choppers with m the neutron mass and h the Planck constant. We get $\tau = CL\lambda$ with $C = 256\ \mu s\, m^{-1}\, Å^{-1}$.

By selecting speed and phase of choppers 1 and 4, a sharp triangular pulse with a small spread of velocities is produced.

It is worth noting that the phase between choppers 1 and 4 is defined modulo 2π. Therefore, another chopper (number 2) running with the same velocity as choppers 1 and 4 is necessary for eliminating wavelengths of higher and lower order. A last chopper (number 3), can be rotated at a lower frequency than the others, in order to suppress intermediate pulses and to provide a time interval between two successive pulses. This interval must be sufficiently long to permit complete time analysis of each pulse, the neutron velocities having been spread by interaction with the sample. In other words, the role of this chopper is to prevent 'frame-overlap', i.e. to obviate fast neutrons arising from energy gain processes overtaking slow neutrons from the previous pulse.

The choppers are separated by nickel-coated glass guides of $2 \times 5\ cm^2$, which is the beam size at the sample.

Each chopper disc is made from aluminium alloy, covered with a neutron-absorbing material — gadolinium oxide — with two slots opening 2.7% of a period, rotating around a horizontal axis, and suspended by magnetic bearings.

The chopper speed can be varied continuously between 6000 and 20 000 rpm by computer control. The magnetically suspended chopper system runs under a vacuum of better than 10^{-2} Torr.

Choppers and guides are surrounded by concrete shielding as biological protection. The flux at the sample, as shown in figure 3.7 depends on the chopper speed, and the selected wavelength (the elastic resolution $\Delta E/E$ (figure 3.9)). The incident energy varies from 9 to 0.35 meV, the elastic resolution $\Delta E/E$ from 8 to 0.9%.

The $\hbar\omega$ and Q-measurements are achieved in the secondary spectrometer. A helium-filled aluminium box on a 4 m radius is the flight path for the neutrons. 1200 ^{3}He tube counters can be placed at almost any angular position corresponding to scattering angles smaller than 132° (see figure 3.8). These detectors can be grouped into a maximum of 128 spectra. Monitors placed in front of and behind the sample can be used for specimen transmission measurement and also for wavelength calibration by measuring the neutron flight time between these points.

Detectors and monitors are protected against neutrons, produced by the other experiments, by a cast shielding filled with paraffin wax.

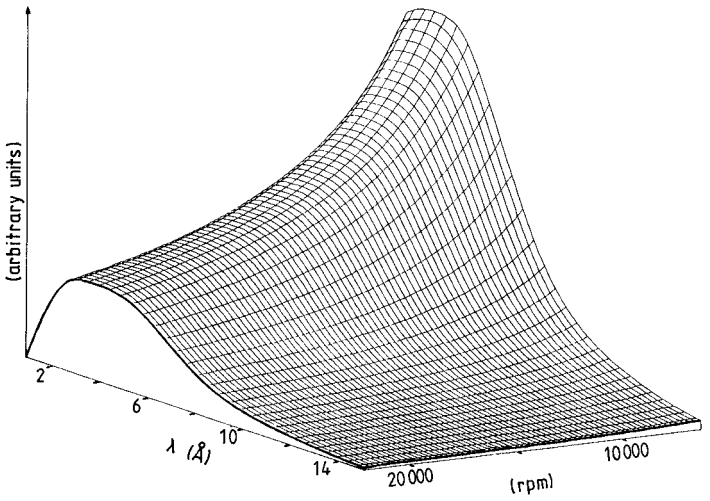

Figure 3.7 IN5 flux at the sample, as a function of the selected wavelength and of the velocity of the choppers.

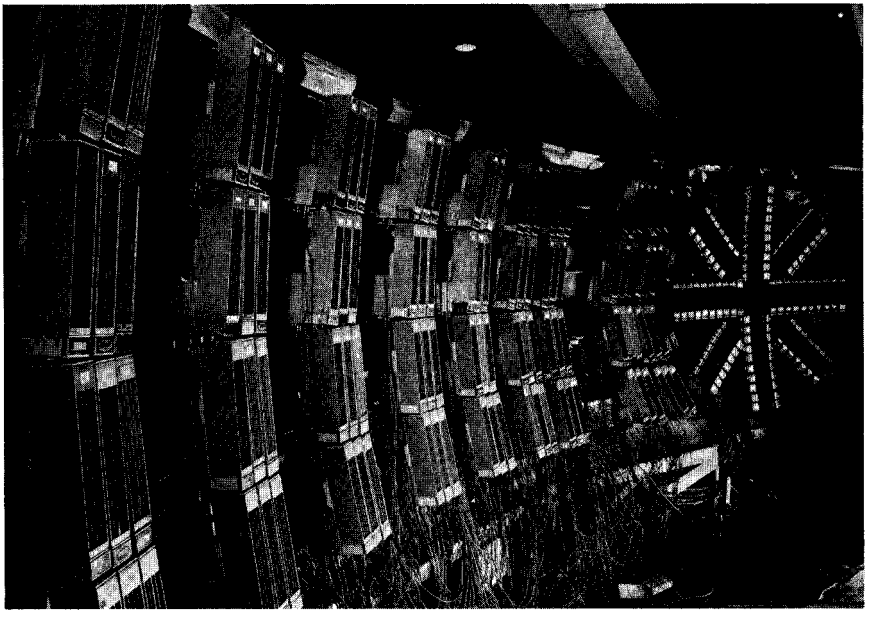

Figure 3.8 The IN5 spectrometer; view of the detector bank. (By permission of the Institut Laue–Langevin, Grenoble, France.)

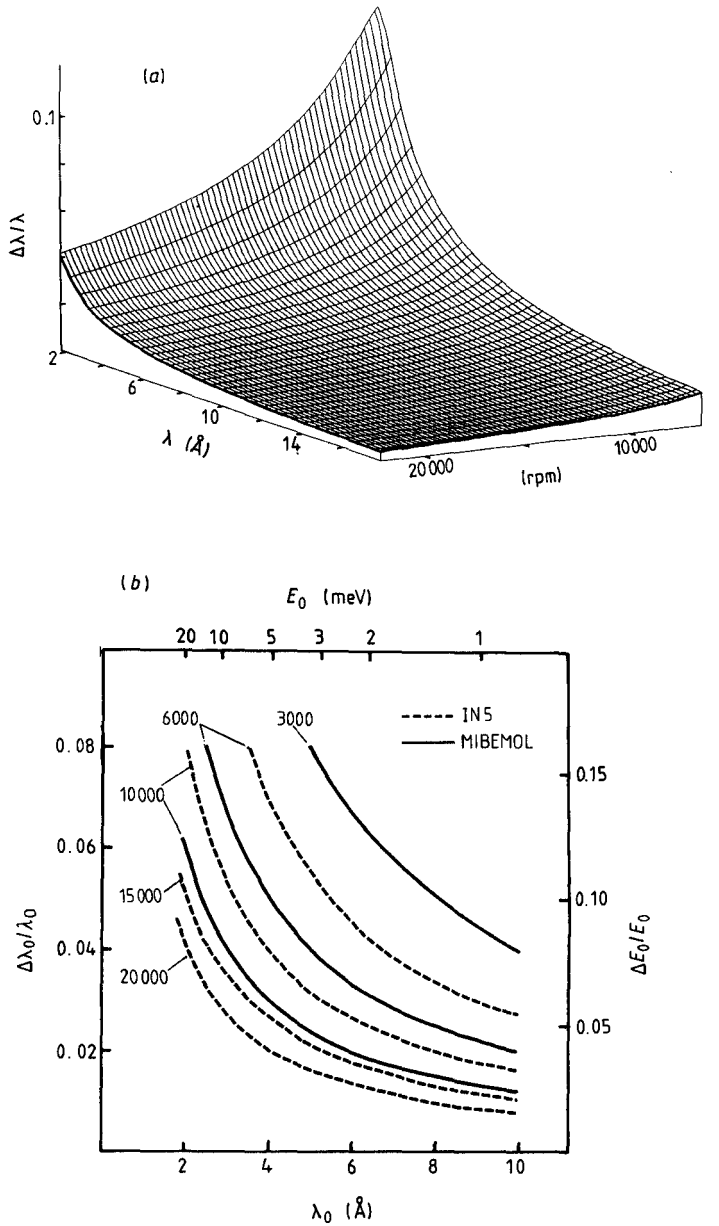

Figure 3.9 (*a*) Elastic energy resolution of IN5 as a function of the incident wavelength and of the velocity of the choppers. (*b*) Comparison of the elastic energy resolution of IN5 and MIBEMOL as a function of the selected wavelength and at various chopper rotation speeds.

3.2.2 The six-chopper time-of-flight spectrometer MIBEMOL

MIBEMOL has been placed at the end of the G6 guide of the Orphée reactor of the Laboratoire Léon Brillouin at the CEN in Saclay (France). This instrument (figure 3.10) is a variant of IN5 obtained by replacing the first and the last choppers by pairs of discs, closely spaced, and rotating in opposite directions. In spite of smaller disc diameters, combined with a maximum rotation speed of 10 000 rpm, it is possible to achieve a resolution which is about equal to that of IN5 at 15 000 rpm. Also with respect to IN5, the mechanics could be somewhat simplified.

The mechanical ball bearings and the motor armature run in air, the disc itself is separated by a labyrinth seal and operates under vacuum. The chopper discs are made of aluminium, the annulus rotating in front of the guide being covered with neutron-absorbing materials like a mixture of resin and gadolinium oxide. Two windows, at 180° from each other, are made in this layer.

By 1988 the aluminium discs of MIBEMOL should be replaced by fibre-glass discs, suspended by magnetic bearing as on IN5.

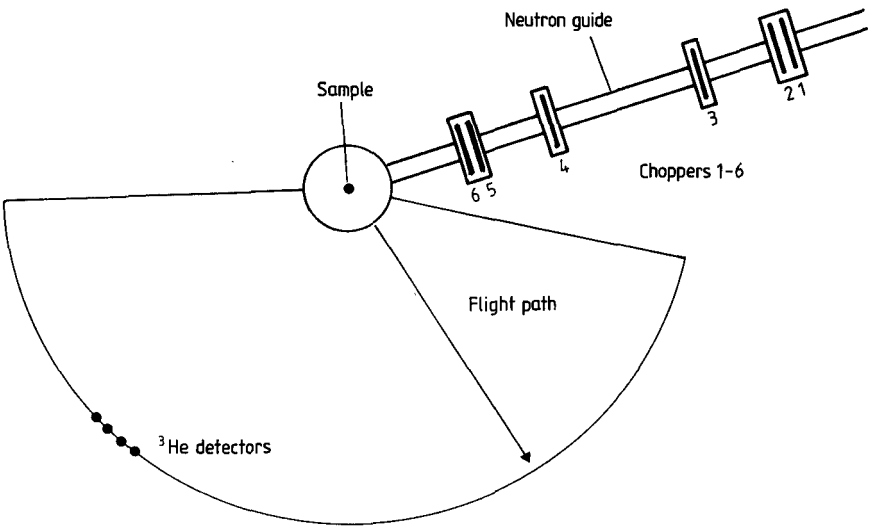

Figure 3.10 Schematic layout of the six-chopper time-of-flight spectrometer MIBEMOL at the Orphée reactor in Saclay (France). The energy of the neutrons incident on the sample is essentially determined by the phase angle between the two pairs of choppers 1 and 2, and 5 and 6. The resolution is dictated by the rotation speed chosen for these choppers. Higher-order contamination is eliminated by chopper 3 and the overall repetition rate of the neutron bursts is controlled by chopper 4 which may be allowed to rotate at a lower speed than the others. (from Hautecler *et al* 1984).

3.2.3 The time-focusing time-of-flight spectrometer IN6 (Scherm et al 1978)

The time-focusing spectrometer, IN6 (figures 3.11, 3.12), built to supplement IN5 at high incident energy, is implanted on the H15 guide (figure 3.1). The lack of a free neutron guide end made impossible the use of a multichopper monochromator. Static or rotating crystals were the only way for extracting from the guide neutrons with wavelength between 4 and 6 Å.

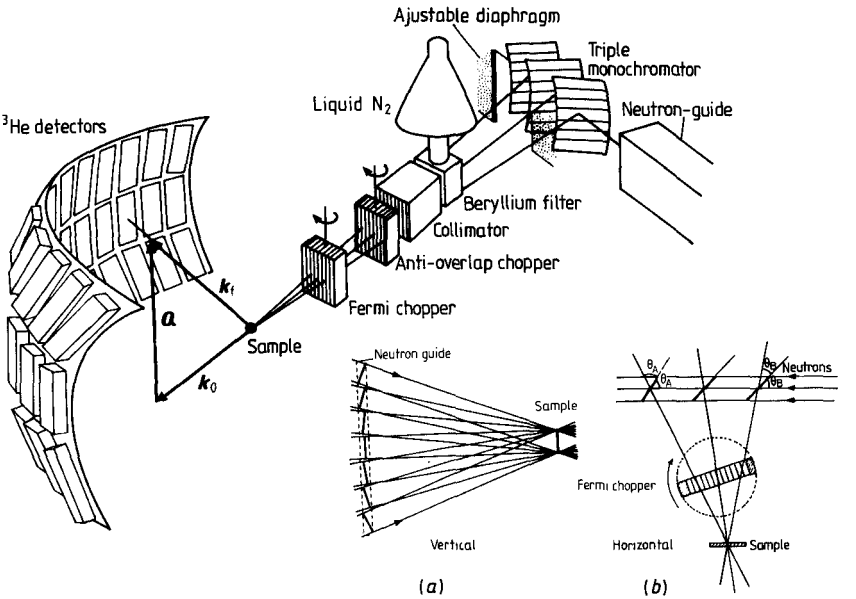

Figure 3.11 Schematic view of the time-of-flight time-focusing spectrometer IN6 at the High Flux Reactor of the Institut Laue–Langevin in Grenoble (France). The neutron beam H15 has been cut off for the IN6 monochromator. The scattered beam goes successively through an adjustable diaphragm, a cement shielding with four exit locks that can be closed (not represented), a beryllium filter at low temperature (80 K), a collimator, an anti-overlap chopper and a Fermi chopper, and then hits the sample in the changing sample hole. After scattering by the sample, the neutrons are detected by 337 fixed ^{3}He detectors placed at 2.466 m. *Inset:* Each group of the monochromator is composed of seven single crystals tangent to a circle, allowing neutron focalisation on the sample in the vertical plane. The beam size at the sample is restricted to 5 cm height and 3 cm width, given by the three monocrystal groups.

(a) The primary monochromator

The monochromator is composed of three groups of seven pyrolytic

graphite crystals placed successively in the path of the neutrons (see inset (a) in figure 3.11). Crystals are sheets of $2 \times 54 \times 29$ mm^3 with the 002 crystallographic plane parallel to the large face. The inter-reticular distance is 3.355 Å.

The mosaicity is of 23′ to 40′ for all the crystals. Each of the seven crystals is tangential to a circle of radius $R = 2D \sin\theta$ (D = sample monochromator length). Rotation (θ) of each of the three groups is possible and allows the wavelength selection. Because of this variation of θ, all the elements are set up on a mobile platform rotating around an axis centred on the monochromator, which can move on guide rails. It can be fixed at four positions related to four different wavelengths of the incident neutrons (4.1, 4.6, 5.1 and 5.9 Å). The focalisation increases the flux at the sample, at the expense of the energy resolution, but the time-focusing technique can fully compensate this energy resolution loss as we shall see next.

(b) The time-focusing principle

The beam from the neutron guide is collimated by the crystal system on the sample (see inset (b) in figure 3.11). Neutrons in the rays A and B have different directions $2\theta_A$ and $2\theta_B$, and according to the Bragg law, two different wavelengths.

$$\lambda = 2d \sin\theta. \qquad (3.3)(bis)$$

Let ϕ be the angular difference between A and B

$$\phi = 2\theta_A - 2\theta_B \qquad (3.5)$$

then

$$\Delta\lambda = 2d \cos\theta \frac{\phi}{2}. \qquad (3.6)$$

According to (3.1), λ can be expressed as a function of the velocity of the neutrons, ($\lambda = (Cv)^{-1}$ with $C = 2.56 \times 10^{-4}$ s m^{-1} Å^{-1}). The flight time, τ, for the distance, L, is:

$$\tau = CL\lambda \qquad (3.7)$$

The neutrons in A are slower than in B. Their difference in flight time is given by using (3.6) and (3.7).

$$\Delta\tau = CL2d \cos\theta \frac{\phi}{2}. \qquad (3.8)$$

The Fermi chopper rotating with angular velocity $2\pi\nu$, the A-beam passes Δt seconds earlier than the B-beam.

$$\Delta t = \frac{\phi}{2\pi\nu}. \qquad (3.9)$$

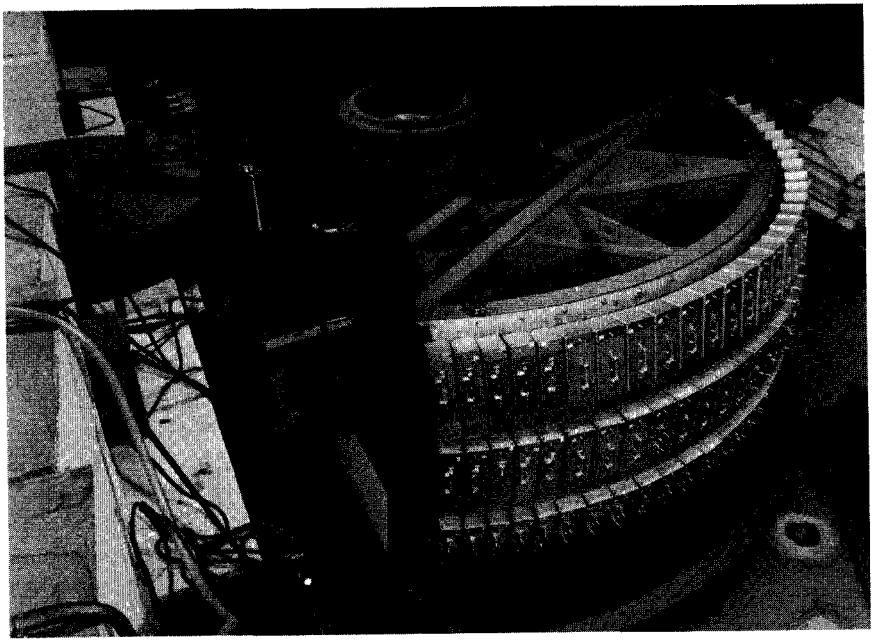

Figure 3.12 The IN6 spectrometer; view of the detector bank during building. (By permission of the Institut Laue–Langevin, Grenoble, France.)

The elastic focusing distance, F_{el}, is the distance, L, where the faster neutrons overtake the slower ones, that is when the delay Δt of the B-neutron burst with respect to the A-burst is just compensated by the difference in flight time, $\Delta\tau$, i.e. the distance of flight corresponding to

$$\Delta\tau = \Delta t. \tag{3.10}$$

Using (3.8) and (3.9) in (3.10), this elastic focusing distance is found to depend on the rotation speed of the chopper, namely

$$F_{el} = \frac{1}{2\pi\nu Cd\cos\theta}. \tag{3.11a}$$

Clearly, in most of the experiments, the time-focusing is achieved when the neutrons arrive at the detectors and F_{el} is chosen equal to the distance L between chopper and detectors. This latter is fixed, but the chopper velocity can be varied in order to fulfil the focusing condition:

$$2\pi\nu = \frac{1}{CLd\cos\theta}. \tag{3.11b}$$

(c) Inelastic focusing distance

Numerous experiments are concerned with the study of energy transfers $\hbar\omega = E_F - E_I > 2$ meV higher than in the quasielastic region, for

example, low-frequency modes in solids. The IN6 resolution, determined as before, is shown in figure 3.13. It appears very poor in this part of the $\hbar\omega$ space, but it can be considerably improved by focusing on the inelastic region of interest. The energy, E, of a neutron is related to its wavelength

$$E = \frac{\hbar^2}{2m}\left(\frac{2\pi}{\lambda}\right)^2. \tag{3.12}$$

In the inelastic region, for an energy transfer $E_F - E_I$, the wavelength of the scattered neutron is

$$\lambda_F = \lambda_I \left(1 + \frac{\hbar\omega}{2E_I}\right)^{-1/2}. \tag{3.13}$$

The distance L is the sum of the two lengths L_{CS} — distance from chopper to sample — and L_{SD} — distance from sample to detector.

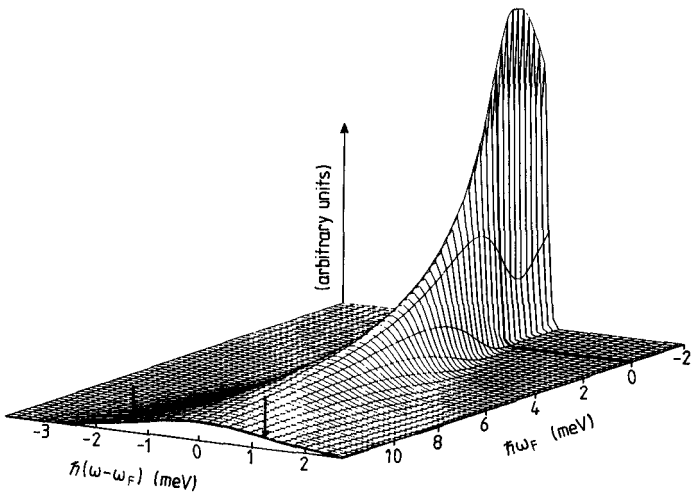

Figure 3.13 Shape of the energy resolution of the time-focusing spectrometer IN6, as a function of the neutron energy transfer $\hbar\omega_f$ after interaction with the sample. The velocity of the Fermi chopper is adjusted for elastic time focusing. The incident neutron wavelength is $\lambda = 5.1$ Å. The full width at half maximum of the instrument resolution (nearly gaussian) varies from $\simeq 80\,\mu$eV at $\hbar\omega_f = 0$ meV (elastic scattering) up to $\simeq 2500\,\mu$eV at $\hbar\omega_f = 12$ meV.

The associated flight times are

$$\tau_{CD} = \tau_{CS} + \tau_{SD}. \tag{3.14}$$

According to (3.7) and (3.13)

$$\tau_{CD} = \lambda_I C\left\{L_{CS} + L_{SD}\left(1 + \frac{\hbar\omega}{E_I}\right)^{-1/2}\right\}. \tag{3.15}$$

Keeping $\hbar\omega$ constant, one gets, with $E_I \simeq \frac{1}{\lambda^2}$

$$\frac{\partial\tau_{CD}}{\partial\lambda_I} = C\left\{L_{CS} + L_{SD}\left(1 + \frac{\hbar\omega}{E_I}\right)^{-3/2}\right\}. \tag{3.16}$$

As for elastic focusing, the inelastic focusing distance is then defined by combining (3.16) and (3.5).

$$\Delta\tau = C\left\{L_{CS} + L_{SD}\left(1 + \frac{\hbar\omega}{E_I}\right)^{-3/2}\right\} = \Delta t = \frac{\phi}{2\pi\nu}$$

$$L_{CS} + L_{SD}\left(1 + \frac{\hbar\omega}{E_I}\right)^{-3/2} = (2\pi\nu C d\cos\theta)^{-1} \tag{3.17}$$

L_{CS} and L_{SD} being fixed, the focusing is adjusted by changing the chopper speed ν.

When $\hbar\omega = 0$, one gets back the elastic focusing. Figure 3.14 shows an example of inelastic time-focusing. On the right-hand side of these time-of-flight spectra the sharpening of the inelastic peaks is clearly evidenced when the Fermi chopper speed is increased from 5000 rpm to 20 000 rpm.

To complete the description of this spectrometer, the neutron beams reflected by the three monochromators pass through a filter composed of a block of beryllium kept at liquid nitrogen temperature whose role is to eliminate higher-order harmonics. Intermediate pulses can be suppressed by a second chopper to avoid frame-overlap (see figure 3.11).

3.3 Backscattering Spectrometers

These spectrometers work in 'inverse spectroscopy': the final energy of the neutrons which are detected is in a narrow band of energy about some precise value. Conversely the initial energy of these neutrons is varied around this value. In the following we shall describe the two spectrometers IN10 and IN13 of the ILL.

These spectrometers are suited for the measurements of very small energy changes (of the order of one microelectronvolt for IN10, a few microelectronvolts for IN13). The high-energy resolution is achieved by working with the largest possible Bragg angle at the monochromator and at the analyser crystals ($\theta_M = \theta_A = 90°$).

Differentiating the Bragg relation $\lambda = 2d\sin\theta$, the expression of the energy resolution is deduced:

$$\frac{\Delta E}{E} = \frac{2\Delta\lambda}{\lambda} = 2\cot\theta\,\Delta\theta + \frac{2\Delta d}{d}. \tag{3.18}$$

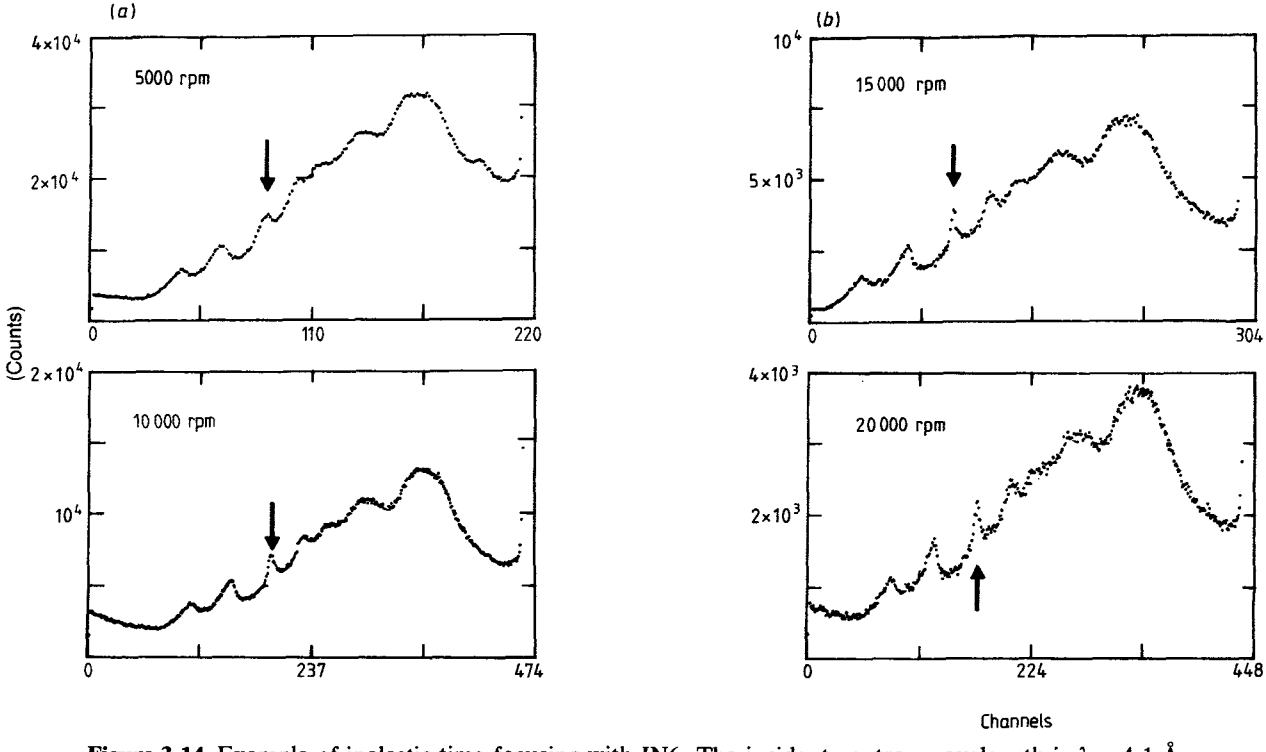

Figure 3.14 Example of inelastic time focusing with IN6. The incident neutron wavelength is $\lambda = 4.1$ Å.

The $\cot\theta$ term is minimised by working close to exact backscattering geometry ($\theta = 90°$). The second term is only dependent on the crystal quality. The energy of the incident neutrons is varied either:

(i) by a Doppler motion of the monochromator by a crank velocity drive on IN10, or
(ii) by modifying the lattice parameters of the monochromator by cooling or heating on IN13.

Only the neutrons which have lost in the sample the energy change given by one of these two processes, are reflected by the analyser crystals back into the detectors.

Each spectrometer is composed of the primary spectrometer with the specific monochromator and a secondary spectrometer, including the sample table, analyser and detectors.

3.3.1 The high resolution backscattering spectrometer IN10 (Birr et al 1971)

The spectrometer, shown schematically in figure 3.15, is located 50 m from the core (figure 3.1) on the curved neutron guide H15. The cold neutron beam has a total flux of about 2×10^9 n s^{-1} cm^{-2} with a spectral distribution around 6 Å. The beam width is 3 cm, the height 20 cm. Only the upper 5 cm of this beam are used on IN10. The beam travels along another straight neutron guide of 3×5 cm^2 cross section and 10 m length, followed by another one of the same width but 8 cm high and 6 m long. At this stage, the neutrons are backscattered from the monochromator mounted on a velocity drive.

Above 40% of the backscattered monochromatic beam is deflected by a (002)-oriented graphite crystal (situated just below the incoming primary beam) into a third neutron guide coated with supermirrors of 3×3 cm^2 and 4.25 m length.

The neutrons then pass through a chopper (the role of which is explained below) and a monitor, and hit the sample.

The scattered neutrons are analysed for changes in momentum and energy by analyser crystals. These are hexagonal-shaped silicon single crystal slices with a thickness of 0.4 mm and a diameter of 2 cm. The slices are attached in (111) or (311) orientation on the spherically curved surface of aluminium plates.

The spherical segments (50×50 cm^2), have a radius of curvature of 1.5 mm and are aligned such that the neutrons back-reflected from each analyser plate are focused onto a ^{3}He detector located behind the sample (see figure 3.16). For small-angle scattering experiments (from $Q = 0.07$ to 0.31 Å) an analyser system with seven concentric circles covered with Si(111) around the forward direction is available.

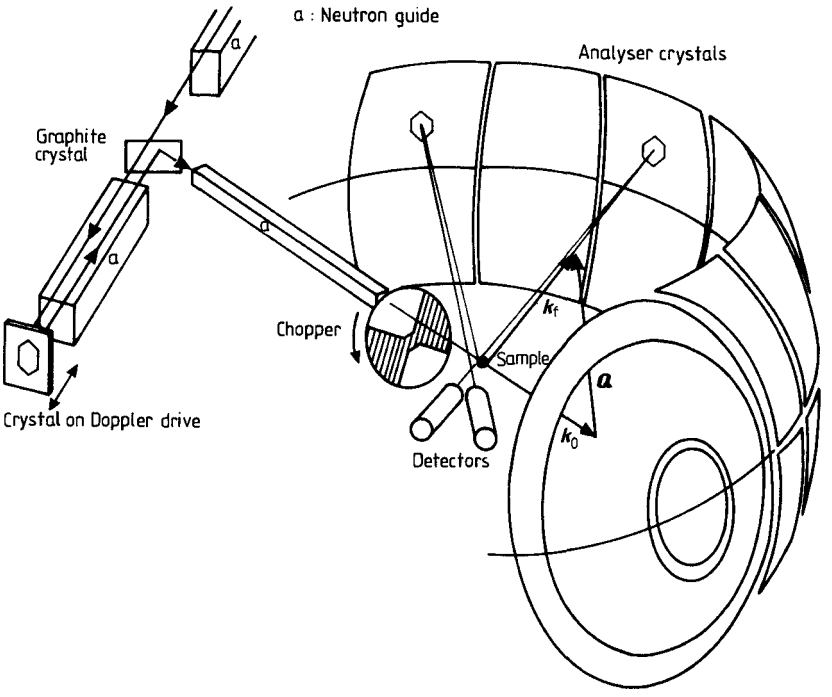

Figure 3.15 Schematic view of the backscattering spectrometer IN10 at the High Flux Reactor of the Institut Laue–Langevin, Grenoble (France). The neutron beam is backscattered by the monochromator mounted on a Doppler drive, deflected to the sample, scattered to the analysers and then backscattered again to the detectors located as close as possible to the sample position.

The detectors are filled with ^{3}He, at a pressure of two bars. Their size is 51 mm diameter, 50 mm length. Their efficiency is 97% for $\lambda = 6.27$ Å.

The flight path housing of the secondary spectrometer is filled with helium. It is entirely shielded with 1 mm of cadmium, 4 mm of boron carbide and 10 cm of paraffin.

The chopper interrupts the beam and is phased with the electronic counting circuits so that neutrons scattered into the detectors directly from the sample are not counted. The graphite crystal, the guide and the analyser house can be rotated around a vertical axis defined by the crossover of the midline of the main guide and the branching-off guide.

The Doppler velocity is measured with an induction coil rigidly connected to the monochromator. It induces a voltage directly proportional to the velocity of the monochromator. The output voltage is digitalised and, together with a detector code, defines the energy channel number into which the neutrons are stored. The monochromator crystals, on the front on the Doppler drive, are removable. Five types of crystals are available. Their characteristics are given in

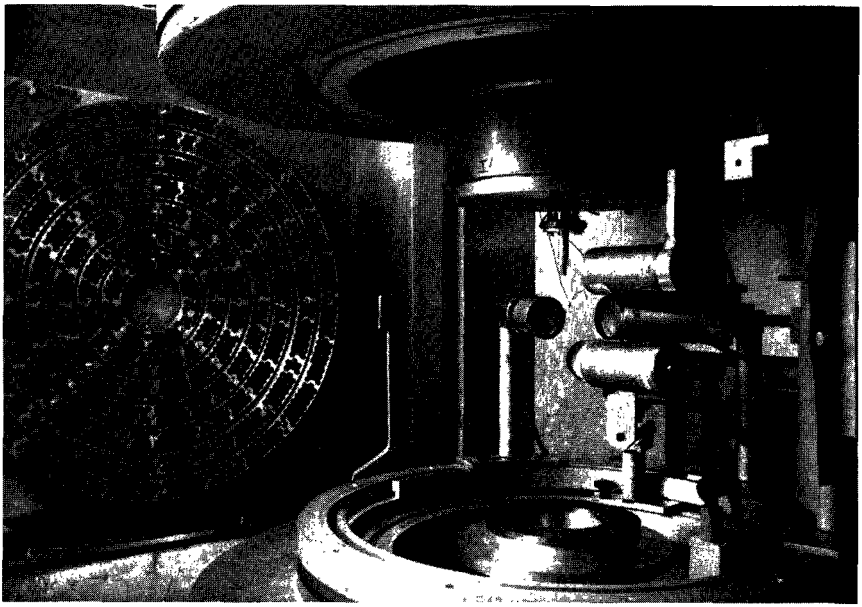

Figure 3.16 The backscattering spectrometer IN10 at the Institut Laue–Langevin. View of the analyser plates at small angles, and of the detectors. (By permission of the Institut Laue–Langevin, Grenoble, France.)

figure 3.17.

The main difference between Si(111) polished and unpolished is the mosaicity which is lower in the polished state and responsible for the high resolution of the spectrometer (0.35 μeV).

Si(311) with a 3.27 Å wavelength allows high Q values. However, the intensity loss at the sample position is high, and, even with the High Flux Reactor, such long measurements are limited to particular cases.

The modified version of IN10 proposed by Alefeld *et al* (1984) aimed to get a noticeable increase in the flux of detected neutrons by making use of the time structure of the neutron bursts issued from a pulsed source. This instrument was planned for the 'Spallation Neutronen Quelle' in Jülich (FRG). Whilst this project of an intense pulsed source is now abandoned, the basic idea on which the backscattering spectrometer was designed is still interesting: it consists in using a monochromator formed with several crystals with the same orientation but with slightly different lattice spacings, thus reflecting slightly different wavelengths. Owing to differences in path-length, neutrons with different wavelengths arrive at different times at the sample. The gain in the flux is equal to the number of crystals of the multimonochromator. The different lattice spacings can be produced by a temperature difference between the crystals or by using Si/Ge alloys with different concentrations.

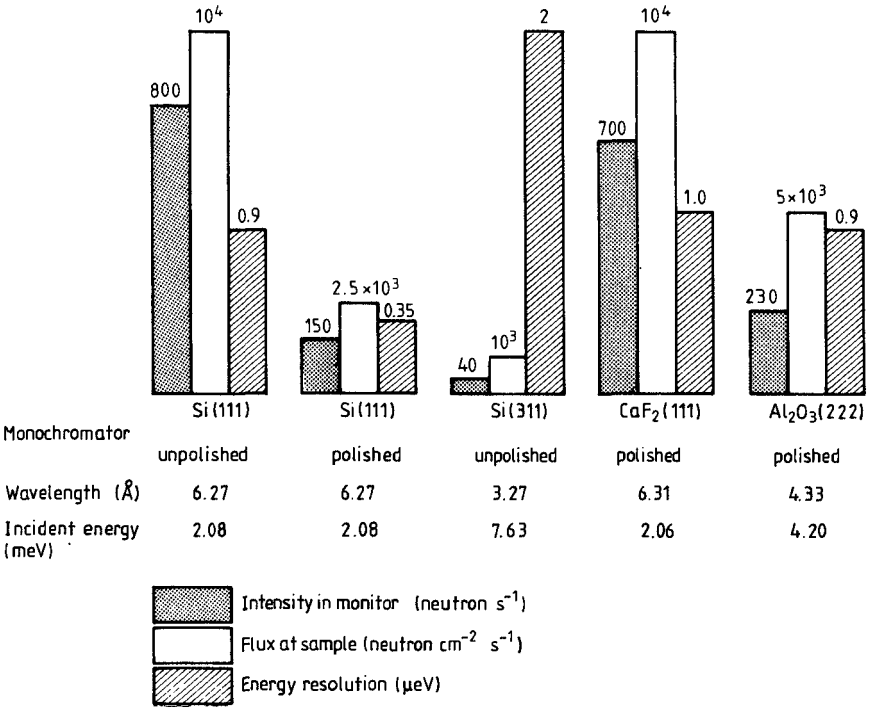

Figure 3.17 Characteristics of five types of monochromator crystal

3.3.2 The thermal backscattering IN13

(a) Principle

The main application of the spectrometer IN13 is the measurement of incoherent neutron scattering with microelectronvolt resolution at rather high momentum transfers between 0.5 and 5.5 $Å^{-1}$.

To achieve the large momentum transfers, a small wavelength has to be used. For that reason the spectrometer is installed at the thermal guide H24 (figure 3.1) with 3 cm width and 12.5 cm height.

The energy variation is performed by scanning the lattice parameter of the monochromator crystal via temperature changes. The neutrons are backscattered from the CaF_2 monochromator mounted in a cryofurnace and deflected by a vertically curved graphite crystal. The incident wavelength is about 2.23 Å, the incident energy 16.4 meV.

The neutrons pass through a chopper and a monitor (see figure 3.18) before hitting the sample in the secondary spectrometer. The scattered neutrons are analysed in momentum and energy transfers by a set of nine spherically curved composite CaF_2 crystal analysers. These crystals ($2 \times 2 \times 0.2\,cm^3$) are glued in the (422) orientation on the surface of

spherically curved concave aluminium plates (see figure 3.19). These plates are fixed on moving supports whose motion is correlated to the displacement of the graphite deflector. This deflector follows the wavelength variations induced by the change of lattice parameters of the heated monochromator crystals (broken line on figure 3.18). All these motions are computer controlled. (In fact, IN13 is very similar to a three-axis instrument under backscattering conditions.)

The backscattered neutrons are counted by three individual ^{3}He detectors (for the three small angles) and a cylindrical multidetector consisting of 32 ^{3}He detector tubes.

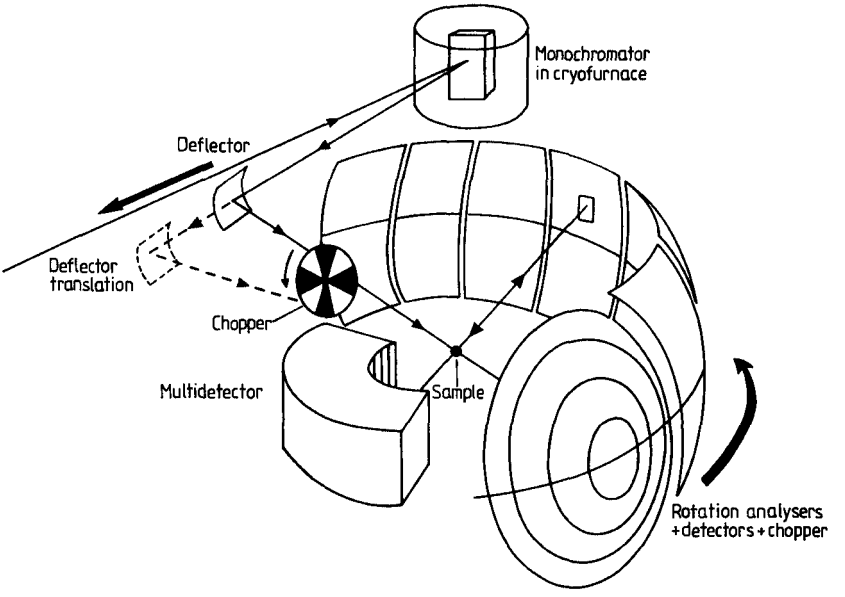

Figure 3.18 Schematic view of the backscattering spectrometer IN13 at the High Flux Reactor of the Institut Laue–Langevin, Grenoble (France). The neutron beam is backscattered by the monochromator in the furnace, deflected to the sample, scattered to the analysers and then backscattered again to the detector bank behind the sample.

(b) The monochromator

The Bragg equation including the temperature-dependent lattice spacing, d:

$$\lambda = 2d_{422}\left(1 + \beta_1 T + \frac{\beta_2 T^2}{2}\right)\sin\theta \qquad (3.19)$$

describes the wavelength at the sample, where β_1, and β_2 are expansion

coefficients. The fluorine crystals used on IN13 have large expansion coefficients:

$$\beta_1 = 1.9406 \times 10^{-5}(\mathrm{K}^{-1}) \tag{3.20a}$$

$$\beta_2 = 1.8744 \times 10^{-8}(\mathrm{K}^{-2}) \tag{3.20b}$$

The geometry in figure 3.18 shows that, at the monochromator, the exact backscattering condition is not fulfilled. The monochromator angle θ_M can be varied between 89° and 82°.

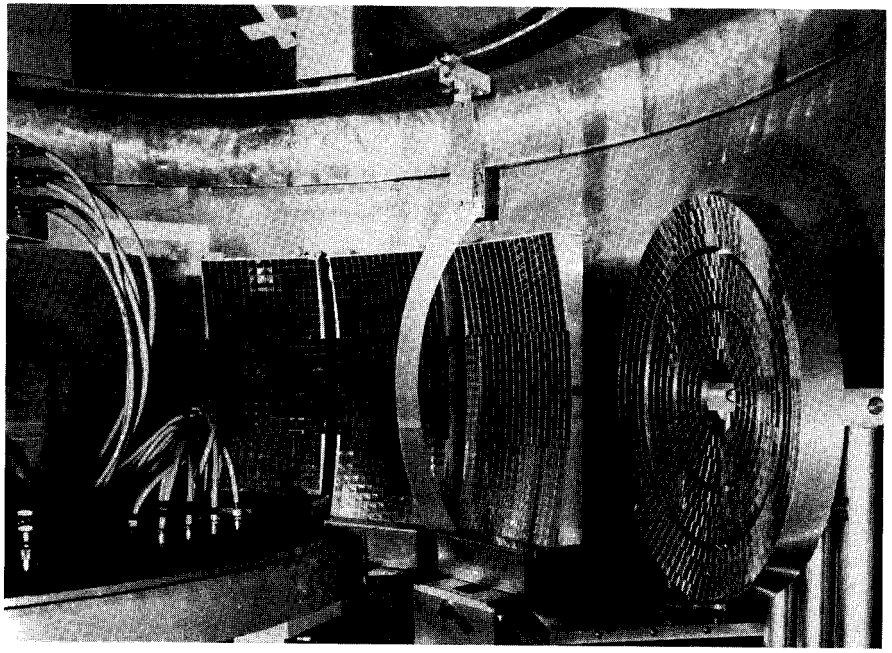

Figure 3.19 The backscattering spectrometer IN13 with its array of analyser crystals. (By permission of the Institut Laue–Langevin, Grenoble, France.)

The related resolution is given in figure 3.20 where the neutron energy change is given versus $2\theta_M$.

3.3.3 The IRIS spectrometer at the Rutherford Appleton laboratory

The High Resolution Inelastic Spectrometer IRIS (figure 3.21) is the time-of-flight spectrometer analogous to the backscattering spectrometers IN10 and IN13, on the Spallation Neutron Source at the Rutherford Appleton Laboratory, (UK), viewing the 25 K moderator.

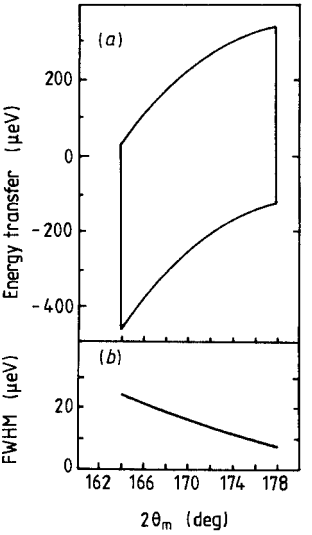

Figure 3.20 Energy range covered by the backscattering spectrometer IN13 and related resolution.

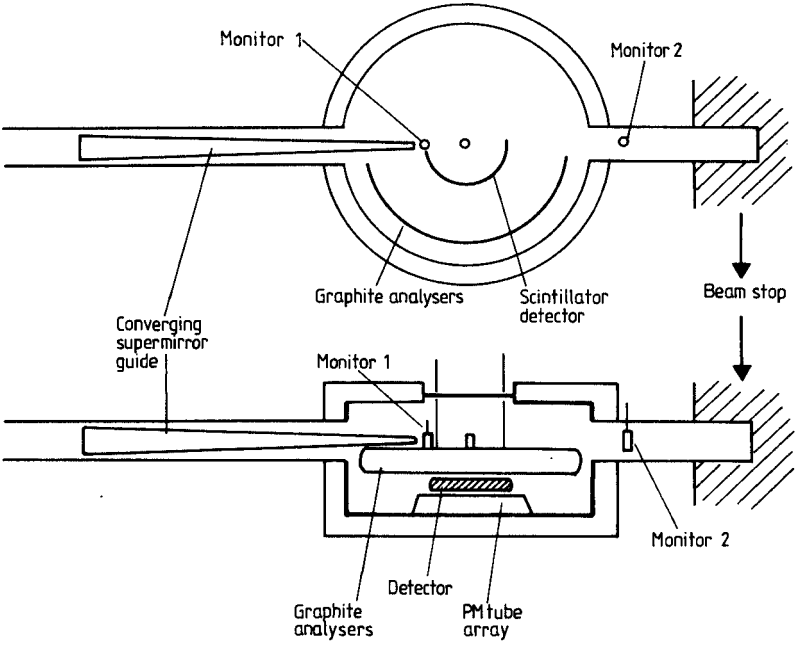

Figure 3.21 Schematic view of the High Resolution Inelastic Spectrometer IRIS at the Spallation Neutron Source of the Rutherford Appleton Laboratory in Harwell (UK).

By changing the neutron energy selector/analyser combination (graphite or Si(111)) a resolution ranging from 1 to 13 μeV can be selected. The two modes, both employ the same principle of mechanically selecting close to the moderator, a band of neutron energies ΔE having a time width $\delta t(E)$.

This band is allowed to disperse over 40 metres drift distance along a neutron guide to provide the required incident energy resolution. The incident energy window is then wider than that obtained on IN10.

Neutron detection follows the same principle as that of IN10. Sensitive scintillator detectors are used.

3.4 Neutron Spin–Echo Spectrometers

The key to high resolution in neutron spin–echo (NSE) technique is the *direct observation of the velocity change* of the neutron in the scattering process. Both the t.o.f. and the backscattering techniques use two separate steps, i.e. successive determination of the neutron initial and final energies in two distinct parts of the instrument (primary and secondary spectrometers, respectively). In NSE, the velocities of incoming and outgoing neutrons are directly compared in the following way. Before arriving at the sample, the neutrons perform Larmor precessions in a magnetic field. After scattering they are forced to precess in the opposite sense and the difference of the two precession angles is analysed at the detector.

3.4.1 The principle of neutron spin–echo

This technique has already been described in great detail (Mezei 1980, 1983). In this section, it will be sufficient to recall that in a neutron beam travelling through a magnetic field $\boldsymbol{H}_0$ (assumed to be homogeneous), and polarised perpendicular to the magnetic field direction, a Larmor precession is initiated (see figure 3.22). The precession angle, ϕ, for a given neutron at a distance l from the origin is given by

$$\phi = \gamma_L \frac{lH_0}{v} \tag{3.21}$$

where v is the neutron velocity and $\gamma_L = 2.916\,\text{kHz}\,\text{Oe}^{-1}$ is called the 'gyromagnetic ratio' of the neutron. The polarisation component, P_x, along a direction x perpendicular to $\boldsymbol{H}_0$ is the average

$$P_x = \langle \cos\phi \rangle = \int f(v) \cos \frac{\gamma_L l H_0}{v}\, dv \tag{3.22}$$

$f(v)$ being the velocity distribution function. Clearly, from (3.21), as l

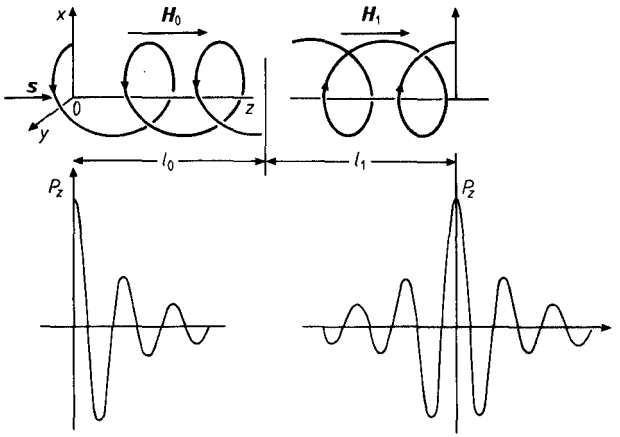

Figure 3.22 Larmor spin precession of neutrons in a magnetic field. The spin–echo principle.

increases, the Larmor precession angles for neutrons having different velocities become more and more out of phase and $P_x = \langle \cos \phi \rangle$ tends to zero. The echo principle eliminates this dephasing effect arising from the velocity distribution $f(v)$. It is realised by making the neutrons precess in the opposite sense after a certain time. The total Larmor precession angle now reads:

$$\phi = \phi_0 - \phi_1 = \gamma_L \left[\frac{l_0 H_0}{v_0} - \frac{l_1 H_1}{v_1} \right] = \phi(v_0, v_1) \qquad (3.23)$$

v_0 and v_1 are the incoming and outgoing neutron velocities, respectively, l_0 and l_1 are the travel lengths through the fields H_0 and H_1 (see figure 3.18). v_0 and v_1 are linked to the neutron incident and final energies E_0 and E_1 through

$$E_0 = \tfrac{1}{2} m v_0^2; \; E_1 = \tfrac{1}{2} m v_1^2. \qquad (3.24)$$

The relevant quantity in which we are interested is the neutron energy change $\hbar\omega$

$$\hbar\omega = E_1 - E_0 = \tfrac{1}{2} m (v_1^2 - v_0^2) = \hbar\omega(v_0, v_1). \qquad (3.25)$$

Thus the total Larmor precession angle $\phi = \phi_0 - \phi_1$ and the energy transfer $\hbar\omega$ are related together via (3.23) and (3.25). Let us consider neutron beams with average velocities $\bar{v}_0$ and $\bar{v}_1$ corresponding to $\hbar\bar{\omega}(\bar{v}_0, \bar{v}_1)$ and $\bar{\phi}(\bar{v}_0, \bar{v}_1)$. Small variations of the neutron velocities Δv_0 and Δv_1 about their average values will produce small changes of the energy transfer

$$\Delta(\hbar\omega) = m[\bar{v}_1 \Delta v_1 - \bar{v}_0 \Delta v_0] \tag{3.26}$$

and of the Larmor precession angle

$$\Delta\phi = \gamma_L \left[\frac{l_1 H_1}{\bar{v}_1^2} \Delta v_1 - \frac{l_0 H_0}{\bar{v}_0^2} \Delta v_0 \right]. \tag{3.27}$$

It follows that if the ratio of the magnetic fields H_0 and H_1 is chosen such that

$$\frac{l_0 H_0}{l_1 H_1} = \frac{\bar{v}_0^3}{\bar{v}_1^3} \tag{3.28}$$

the variation of the Larmor precession angle is just proportional to that of the energy transfer

$$\Delta\phi = \left[\gamma_L \frac{l_1 H_1}{v_1^3} \cdot \frac{h}{m} \right] \Delta(\omega) \tag{3.29}$$

where the first factor on the right-hand side of (3.29) has the dimension of time

$$\phi - \bar{\phi} = t(\omega - \bar{\omega}). \tag{3.30}$$

The distribution of ϕ in the scattered beam is simply given by the scattering function $S(\boldsymbol{Q}, \omega)$ which describes the probability that the neutrons are scattered with the energy change $\hbar\omega$. Consequently the polarisation component P_x given from (3.22)

$$P_x = \langle \cos(\phi - \bar{\phi}) \rangle = \frac{\int S(\boldsymbol{Q}, \omega) \cos[t(\omega - \bar{\omega})] \, d\omega}{\int S(\boldsymbol{Q}, \omega) \, d\omega} \tag{3.31a}$$

$$= \frac{I(\boldsymbol{Q}, t)}{I(\boldsymbol{Q}, 0)} \tag{3.31b}$$

is the normalised intermediate scattering function.

3.4.2 The spin–echo spectrometer IN11 (Mezei 1980)

The neutrons issued from the guide are first monochromatised by a helical selector giving a spectrum of $\lambda = \lambda_0 \pm 10\%$ within the range $4\ \text{Å} < \lambda < 9\ \text{Å}$. One obtains a 3 cm diameter beam, with a divergence of $0.5° \times 0.5°$ which is then polarised by an arrangement of two parallel supermirrors of 60 cm length, 1 cm apart. These supermirrors are mounted inside a solenoid 66 cm long; thus one obtains a longitudinally polarised beam with a very high polarisation.

A first $\pi/2$ coil converts this beam into a transversally polarised beam. Then the neutrons enter a Larmor precession field solenoid (H_0 in figure 3.23) consisting of three 66 cm long sections with 21 cm internal diameter. The wavelength spread gives a difference in the precession

angles of the neutron spins giving rise to a broadening of the initial distribution. A π-coil is placed as near as possible to the scattering sample. Its effect is to reverse the order of the spins compared to the order before the flipping, the most retarded becoming the most advanced. Afterwards, the neutrons traverse a second guide field (see figure 3.24). If this latter is equal to the first and if the neutron velocities are kept in the scattering process (elastic scattering) the differences will just cancel, and all the spins will be realigned when they reach the exit. The next stage is the second $\pi/2$ coil bringing the spin back to the longitudinal direction. If the scattering is not purely elastic, the neutron velocity is changed and the phase condition is not fulfilled at the end of the second guide field, and the longitudinal polarisation is only partly recovered. The final step is achieved at the analyser which transmits to the detector (maximum solid angle $1.2° \times 1.2°$) only the components of spin parallel to the guide field. Analysis of the final polarisation as a function of time yields the knowledge of the intermediate scattering function.

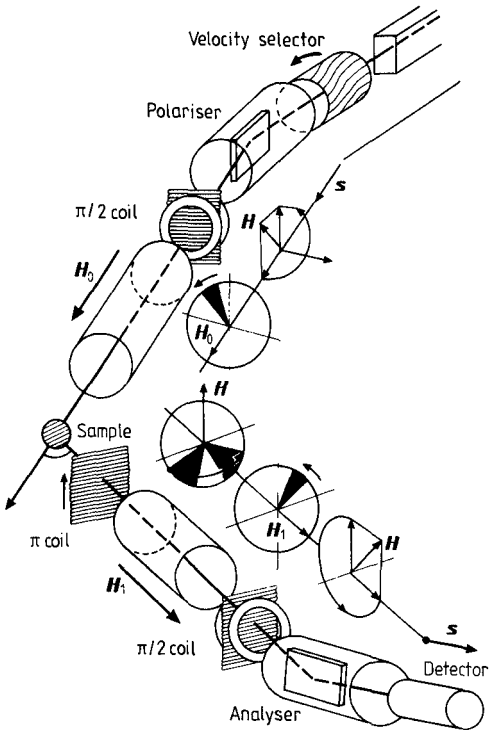

Figure 3.23 Schematic view of the neutron spin–echo spectrometer IN11 at the Institut Laue–Langevin. The successive transitions of the neutron spin in the different parts of the instrument are indicated.

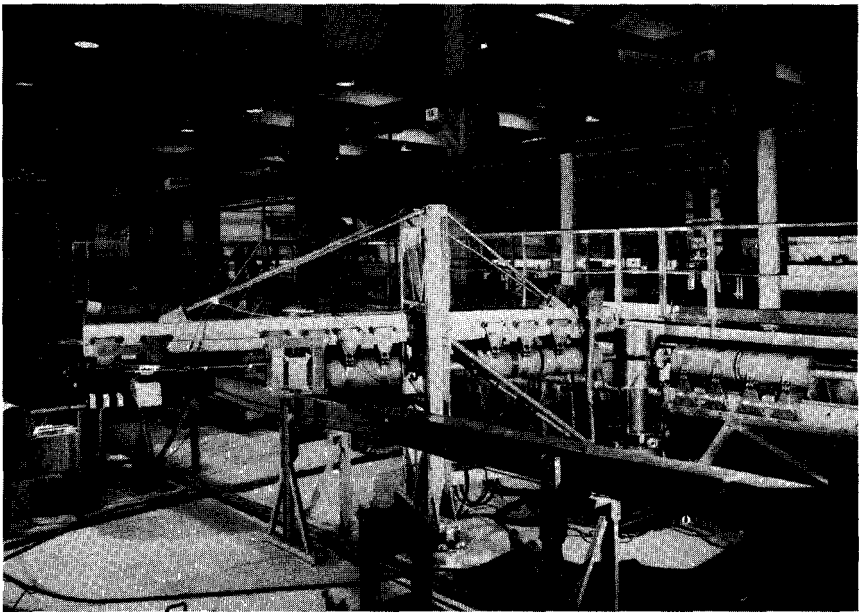

Figure 3.24 The spin–echo spectrometer IN11 on the guide H14 at the ILL. (By permission of the Institut Laue–Langevin, Grenoble, France.)

This instrument allows a spectral resolution ranging from 4×10^{-7} eV $< |\hbar\omega| < 4 \times 10^{-4}$ eV at incident wavelength $\lambda = 4$ Å to 8×10^{-9} eV $< |\hbar\omega| < 8 \times 10^{-5}$ eV at $\lambda = 8$ Å. The corresponding momentum transfer ranges are 3×10^{-2} Å$^{-1} < Q < 2.7$ Å^{-1} and 1.5×10^{-2} Å$^{-1} < Q < 1.35$ Å^{-1} respectively ($1.5° < 2\theta < 120°$).

The major limitation on performance was the use of a single detector of rather small solid angle which severely limits the data collection rate. A multiple detector bank with a wide angle magnet has been recently installed, which spans different scattering angles ($2\theta = 0.2° \pm 5°$) with a neutron beam cross section at each detector of 20×50 mm^2.

Numerous and significant results have been already obtained on IN11, where quasielastic linewidths of typically 2 to 100×10^{-9} eV are routinely measured. However, some recent investigations of macromolecular dynamics (polymers, biological matters, micelles, etc) require an even better energy and momentum resolution. A long wavelength NSE instrument (IN15) is under construction and should be operational by 1988. It is a version of IN11 optimised for neutron wavelengths around 20–30 Å. It will provide an order of magnitude higher energy resolution. The equivalent of the 'instrumental resolution broadening' is expected to be about 4×10^{-9} eV, thus extending the range of neutron inelastic scattering studies to characteristic frequencies as low as 25 kHz. The momentum resolution will be improved by a factor of 3, going from

2×10^{-3} Å^{-1} at the smallest scattering angles ($Q = 2 \times 10^{-3}$ Å^{-1}) to 5–10% at higher angles ($Q = 0.4$ Å^{-1} with $\lambda = 27$ Å at $2\theta = 120°$). An important improvement is the focusing of the incoming beam to the sample, for higher flux, or to the detector, for better angular resolution. This focusing will be achieved either by a superconducting hexapole magnet, or an assembly of eight mirrors with supermirror coating (both also act as polarisers).

For the time-of-flight mode an arrangement of five choppers is proposed: the velocity selector is replaced by a set of three choppers defining the width and the frequency repetition of the pulses. A set of two choppers acting as filter is located before the focusing device.

Simultaneously, Larmor precession field magnets of solenoidal form will be optimised for best field homogeneity. A 32×32 cm large multidetector will also be available.

3.4.3 The small-angle neutron spin–echo spectrometer at Saclay

A new small-angle, high-resolution neutron spin–echo spectrometer (see figure 3.25) has been built recently on a neutron guide of the Orphée reactor in Saclay (France), using both novel devices and new developments with respect to IN11. The main improvement with respect to this latter machine is the careful design of the precession magnets (solenoids).

Being twice as long and about twice as wide (4 m and diameter 370 mm, instead of 2 m and diameter 210 mm), they provide a precession field which is four times more homogeneous than IN11, resulting in a higher usable maximum axial magnetic field (1000 Oe) without destroying the polarisation of the neutron beam. Moreover, the total length from sample to analyser/polariser is greater (6 m instead of 3.5 m).

First tests have been successfully carried out and first echoes have been observed. Comparison with the IN11 spectrometer shows that both the spatial and spectral resolutions should be increased by at least a factor of two.

3.5 Conclusion

The major part of the experiments referenced in this book have been performed at the Institut Laue–Langevin. Therefore, this chapter has been essentially devoted to the equipments at the Institut. Those interested in a general view on neutron scattering facilities, can consult the review given by Pynn and Fender (1985). These authors looked in detail at neutron scattering in Europe, noting existing facilities and their plans for expansion.

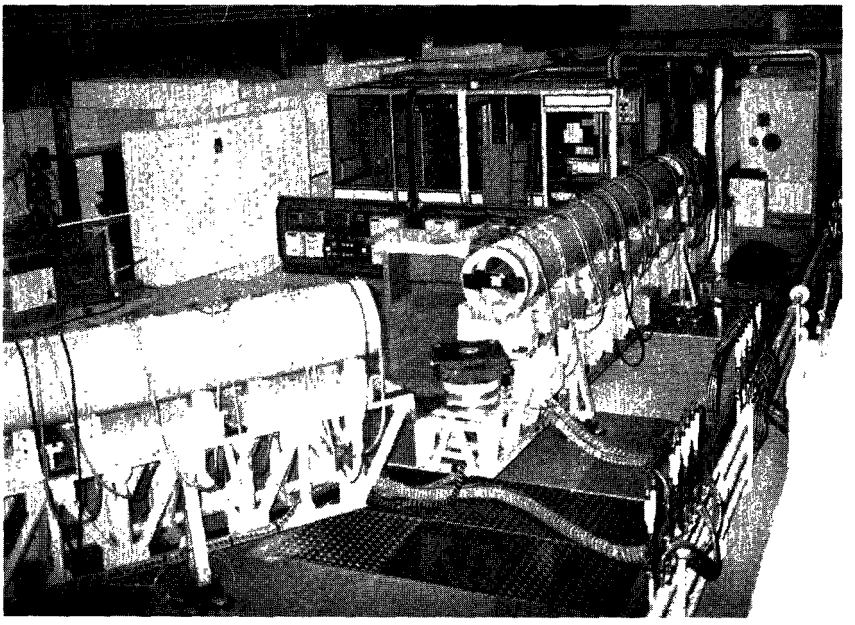

Figure 3.25 The spin–echo spectrometer at the Orphée reactor in Saclay. (By permission of the Laboratoire Léon Brillouin, Saclay, France.)

Pynn (1984) gives a more detailed description of a number of substantial improvements of neutron scattering instrumentation, which have allowed the extension of the application of neutron scattering to a wide range of scientific problems.

In the particular case of chemical applications of neutron scattering reference must also be made to the books of Bacon (1977), Egelstaff (1971), Marshall and Lovesey (1971), Willis (1973) and Windsor (1981), and to the recent review made by White and Windsor (1984) of neutron sources, modern techniques and their scientific impact, especially in chemistry and polymer science.

Chapter 4 Multiple Scattering Effects

4.1 Introduction

In chapter 2, it was shown how experimentally observed scattered-neutron intensities could be analysed in terms of scattering laws evaluated on the basis of various models in order to provide information about the molecular dynamics of the sample under test. However, expressions like (2.216) can be considered as describing idealised experimental requirements which are never achieved in practice, for instance a monoenergetic incident neutron beam and an infinite-resolution detector. Nevertheless, the instrument resolution functions are most often well known and their effects on the experimental data can be taken into account in a precise way in the analysis of the spectra. There are, however, some other effects, for which the corrections are much more difficult and imprecise. Indeed, when evaluating the scattering law, it is generally assumed that, once scattered, the neutron leaves the sample without being absorbed or further scattered. Expressions of the type (2.216) do not contain any term taking into account the attenuation of the incident or scattered beams. In fact, in slow-neutron scattering, the mean free path of the neutron in the sample is often comparable with the macroscopic dimensions of this latter. Therefore, analytical expressions of the scattering law should include the effects of second- and higher-order scattering. Because multiple scattering appears to be too complicated to be accounted for, it is hoped to make it small enough to be ignored, at least by employing samples with high transmission.

Although it is not always justified, this attitude is probably reasonable, as long as the molecular dynamical behaviour in the specimen is

unambiguous, and if the interest is restricted to the determination of physical parameters (characteristic times). Conversely, the neutron scattering technique is now usually used as a powerful tool to elucidate the exact mechanism of the dynamics of the molecules. Therefore a detailed, quantitative comparison with experiment is desirable. Physical information like EISF must be extracted with high precision in order to build molecular models capable of describing the data. This provides the incentive for having some physical understanding of the nature of multiple scattering and of its dependence on the size and shape of the sample.

Let us consider a flat-shaped sample, with thickness d, whose lateral dimensions are sufficiently large, as compared to the neutron beam section, to be supposed infinite. The mean free path of the neutron inside the sample, i.e. the averaged distance between two successive absorption or scattering processes is

$$l = \frac{1}{\Sigma} \tag{4.1}$$

where Σ is the total scattering cross section per volume unit. It is the sum

$$\Sigma = \Sigma_a + \Sigma_s \tag{4.2}$$

of the absorption cross section Σ_a and of the scattering cross section Σ_s, per unit volume. It is noteworthy that in the case of neutron scattering from hydrogenated samples, the absorption cross section is often negligible with respect to the (incoherent) scattering cross section. For instance, in the case of liquid H_2O, the incoherent scattering cross section per volume unit is easily evaluated. Starting from a density $\rho = 1\,\mathrm{g\,cm^{-3}}$, a molecular mass $m_{H_2O} = 18\,\mathrm{g}$, and the values of the atomic incoherent cross section for hydrogen $\sigma_{inc}(H) = 80$ barns and oxygen $\sigma_{inc}(O) \simeq 0$, we obtain

$$\Sigma_s = \Sigma_{inc} = \frac{\rho}{m_{H_2O}} N_a(\sigma_{inc}(O) + 2\sigma_{inc}(H)) \simeq 5\ \mathrm{cm^{-1}}$$

where $N_a = 6.02 \times 10^{23}$ is the Avogadro number.

Therefore the mean free path in the sample is about 2 mm.

More generally, for a flat-shaped sample, the transmission for a perpendicular incident beam is expressed as

$$T_\perp = \exp(-\Sigma d). \tag{4.3}$$

Then the mean free path is given by

$$l = -d/\log_e(T_\perp). \tag{4.4}$$

Its variation as a function of the specimen transmission $T_\perp$ is illustrated

in figure 4.1. Moreover, the path of the neutron inside the sample

$$L = x + \frac{d - x}{\cos \phi} \tag{4.5}$$

depends on the distance x from the entry face of the point at which the scattering process occurs. ϕ is the scattering angle. The value of L lies between d and $d/\cos\phi$.

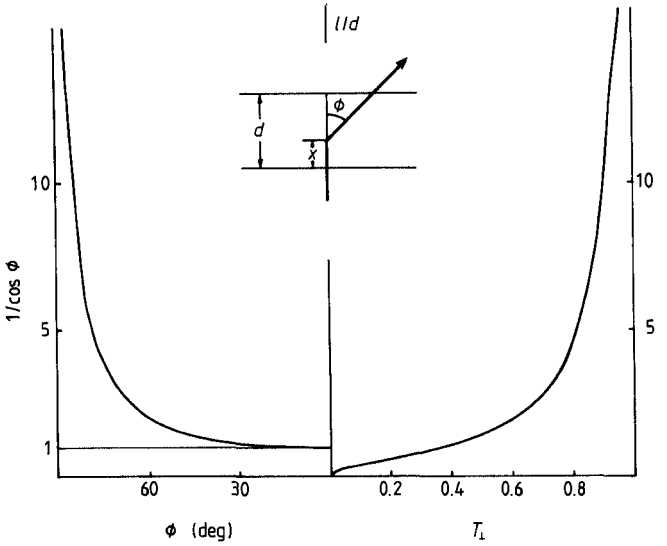

Figure 4.1 Mean free path in the sample, in units of the thickness, l/d, as a function of the specimen transmission when perpendicular to the beam $T_\perp$. The left-hand side illustrates the two limits of the neutron travel in the sample, L/d.

A typical value of the sample transmission in usual experiments is $T = 0.9$. From figure 4.1 the mean free path in the sample becomes comparable with the effective path in the sample for scattering angles $\phi \simeq 84°$. Using a specimen with a transmission $T = 0.8$, this angle is reduced to $\phi \simeq 75°$. Taking as a realistic limit that, to avoid multiple scattering, the mean free path must be at least four times the effective path in the sample, all the angles $\phi > 60°$ have to be considered carefully.

In fact, even with $T = 0.9$, a serious problem still persists: neutrons which have been scattered with an angle $\phi \simeq 90°$, i.e. in the plane of the sample, have most chance to be scattered again and then to leave the sample and to be detected, at some angle θ. Their contribution to the

scattered intensity observed at that angle cannot be evaluated from the analytical expression of $S(\boldsymbol{Q}, \omega)$ because both the final energy transfer value $\hbar\omega$ and the final wavevector transfer $\boldsymbol{Q}(\theta, \omega)$ are the result of two successive scattering processes.

The multiple scattering arising from neutrons scattered in the largest dimensions of the sample can be reduced considerably by partitioning the sample with absorbing spacers. This technique has been used in the past in most work on liquids (Cocking and Egelstaff 1968, Sköld *et al* 1972, Copley and Rowe 1974a, 1974b). The sample is divided by means of a set of parallel absorbing shieldings, with negligible thickness, oriented in the plane of scattering. In fact, this technique can greatly reduce the amount of multiple scattering, but not to the point where it is negligible. Therefore, residual corrections are often still required.

The multiple scattering corrections can be carried out using Monte Carlo simulation techniques. Several programs have been written. We shall mention MSC (Bischoff 1970, Bischoff *et al* 1972), MSCAT (Copley *et al* 1973, Copley 1974) and more particularly DISCUS (Johnson 1974) which will be used for the purpose of comparison. The advantages of the Monte Carlo techniques are that, because they effectively simulate the actual scattering experiment, they can be applied to several kinds of instrumental geometry. They constitute a reliable method but they often need long computing times. Furthermore, the evaluation of successive orders of scattering needs a precise knowledge of the single scattering function $S(\boldsymbol{Q}, \omega)$, i.e. of the correct dynamical model (especially the EISF) and of the characteristic times. This information is what has to be determined from the neutron experiment. Therefore, calculations are first performed on the basis of a set of parameters for the model estimated from a refinement before correction for multiple scattering. Then the sum of the different orders of scattering is compared with the experimental spectra. As long as they are different, the set of input parameters to the multiple scattering evaluation is modified. Several iterations are often necessary before the result of the comparison becomes satisfactory.

4.2 Expansion of the Effective Scattering Law

Firstly, we shall report on the general calculations derived by Sears (1975). We shall not go into all the mathematical details of this formalism but we shall concentrate upon the discussion of the main results. According to Sears, the double differential scattering cross section is written as

$$\frac{\mathrm{d}^2\sigma}{\mathrm{d}\Omega\,\mathrm{d}\omega} = V\frac{n\sigma}{4\pi}\cdot\frac{k}{k_0}\,s(\boldsymbol{k}_0, \boldsymbol{k}) \tag{4.6}$$

if $\boldsymbol{k} \neq \boldsymbol{k}_0$. Here V is the volume of the specimen assumed to be completely bathed in a uniform, monoenergetic beam of neutrons each with incident momentum $\boldsymbol{k}_0$. $\boldsymbol{k}$ is the final momentum of the neutrons, scattered into the solid angle element $\mathrm{d}\Omega$. n denotes the number of scatterers per volume unit in the sample (this sample is assumed to be formed of one type of scatterers only). $s(\boldsymbol{k}_0, \boldsymbol{k})$ is the effective scattering function, accounting for the presence of all the multiple-scattered fluxes, each of them being weighted by its attenuation due to absorption and self-shielding. This quantity is expanded into

$$s(\boldsymbol{k}_0, \boldsymbol{k}) = \sum_{j=1}^{\infty} s_j(\boldsymbol{k}_0, \boldsymbol{k}) \tag{4.7}$$

where $s_j(\boldsymbol{k}_0, \boldsymbol{k})$ is the contribution of the neutrons which have been scattered j times. We shall examine the conditions under which this expansion is rapidly convergent.

The effective scattering function for single scattering $s_1(\boldsymbol{k}_0, \boldsymbol{k})$ can be obtained in a straightforward way from the scattering law $S(\boldsymbol{Q}, \omega)$ evaluated on the basis of the model under test.

$$s_1(\boldsymbol{k}_0, \boldsymbol{k}) = S(Q, \omega)\, H_1(\boldsymbol{k}_0, \boldsymbol{k}) \tag{4.8}$$

$H_1(\boldsymbol{k}_0, \boldsymbol{k})$ describes the reduction in the single scattering due to the attenuation of both the incident and singly scattered beams in the sample. Similarly, the effective scattering functions for higher orders of scattering ($j \geqslant 2$) can be evaluated from

$$s_j(\boldsymbol{k}_0, \boldsymbol{k}) = \left[\frac{n\sigma_{\mathrm{inc}}}{4\pi}\right]^{j-1} \int\int \ldots \int \mathrm{d}\Omega_1\, \mathrm{d}\omega_1\, \mathrm{d}\Omega_2\, \mathrm{d}\omega_2 \ldots \mathrm{d}\Omega_{j-1}\, \mathrm{d}\omega_{j-1}$$
$$\times\, S(\boldsymbol{Q}_1, \omega_1)\, S(\boldsymbol{Q}_2, \omega_2) \ldots S(\boldsymbol{Q}_j, \omega_j)\, H_j(\boldsymbol{k}_0 \boldsymbol{k}_1 \boldsymbol{k}_2 \ldots \boldsymbol{k}_{j-1} \boldsymbol{k}_j) \tag{4.9}$$

where k_i is the momentum of the neutron following the ith collision and $\boldsymbol{Q}_i$, $\hbar\omega_i$ are the momentum and energy transfers in this collision, respectively. We have (see figure 4.2)

$$\boldsymbol{Q}_i = \boldsymbol{k}_i - \boldsymbol{k}_{i-1} \qquad i = 1, 2, \ldots, j \tag{4.10a}$$

$$\boldsymbol{k}_j \equiv \boldsymbol{k} \tag{4.10b}$$

$$\sum_{i=1}^{j} \boldsymbol{Q}_i \equiv \boldsymbol{Q} \tag{4.10c}$$

$$\hbar\omega_i = E_i - E_{i-1} \qquad i = 1, 2, \ldots, j \tag{4.10d}$$

$$\sum_{i=1}^{j} \omega_i = \omega. \tag{4.10e}$$

We shall now examine the conditions under which the expansion (4.7) is rapidly convergent. Referring to Sears (1975), the following inequality

$$0 \leqslant s_j(\boldsymbol{k}_0, \boldsymbol{k}) \leqslant \lambda^{j-1} \tag{4.11a}$$

holds for $j > 1$, where

$$\lambda = \frac{\Sigma_s}{4\pi} \int d\Omega \, \frac{1 - \exp\{-\Sigma(\boldsymbol{k})L(\boldsymbol{k})\}}{\Sigma(\boldsymbol{k})} < \frac{\Sigma_s}{\Sigma} < 1. \tag{4.11b}$$

Here the integral is performed over all possible directions of $\boldsymbol{k}$, and $L(\boldsymbol{k})$ is the linear dimension of the sample in that direction. Hence

$$s(\boldsymbol{k}_0, \boldsymbol{k}) \leqslant 1 + \lambda + \lambda^2 \ldots = \frac{1}{1 - \lambda}. \tag{4.12}$$

Therefore the expansion (4.7) is always convergent, but not necessarily rapidly so. There are two distinct cases for a rapid convergence:

(i) $\Sigma(\boldsymbol{k})L(\boldsymbol{k}) \ll 1$, i.e. if the linear dimensions of the sample are small in comparison with the mean free path $1/\Sigma$.

(ii) $\Sigma_a(\boldsymbol{k}) \gg \Sigma_s(\boldsymbol{k})$, i.e. if the absorption cross section is much larger than the scattering cross section. This suggests that the amount of multiple scattering can be reduced by increasing artificially the absorption cross section, either with an absorbing isotope or even by diluting another chemical element. For instance, Brockhouse *et al* (1963) lowered the transmission of their liquid tin specimen from 0.87 to 0.50 by adding about 0.8% cadmium. However, this technique also strongly reduces the singly scattered intensity.

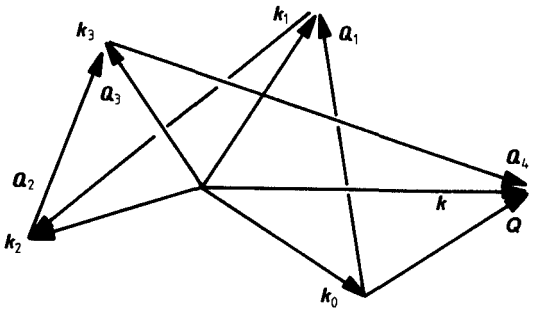

Figure 4.2 Example of successive wavevector transfers, in the case of a four-scattering process.

4.2.1 Expression of the transmission coefficients

(a) Infinite slab sample

We consider the case of an infinite plane slab of thickness d. The transmission factor for single scattering takes the form (see figure 4.3 for explanations of the symbols)

$$H_1(\boldsymbol{k}_0, \boldsymbol{k}) = u(\alpha - \alpha_0) \exp(-|\alpha| - |\alpha_0|) \tag{4.13}$$

where

$$u(x) = [\exp(x) - \exp(-x)]/2x \tag{4.14}$$

$$\alpha_0 = \Sigma_0 d/2 \cos \phi_0 \tag{4.15a}$$

and

$$\alpha = \Sigma d/2 \cos \phi \tag{4.15b}$$

Here Σ_0 and Σ denote the total collision cross section per unit volume for the incident and scattered wavevectors respectively

$$\Sigma = \Sigma(\boldsymbol{k}) = \Sigma_{\text{scat}}(\boldsymbol{k}) + \Sigma_{\text{abs}}(\boldsymbol{k}) \tag{4.16a}$$

$$\Sigma_0 = \Sigma(\boldsymbol{k}_0) \tag{4.16b}$$

in which the scattering collision cross section (assumed to be essentially incoherent)

$$\Sigma_{\text{scat}}(\boldsymbol{k}_0) = \frac{n\sigma_{\text{inc}}}{4\pi} \int \int \frac{k}{k_0} S_{\text{inc}}(\boldsymbol{Q}, \omega) \, \mathrm{d}\Omega \, \mathrm{d}\omega \tag{4.17}$$

differs somewhat from $n\sigma_{\text{inc}}$ because the scattering is not purely elastic. Then $\Sigma(\boldsymbol{k}_0)$ has to be calculated as a function of the incident wavelength. $\Sigma_{\text{abs}}(\boldsymbol{k})$ denotes the absorption cross section. In fact, this value must also take into account the neutrons which are scattered with an energy transfer outside the instrument scale.

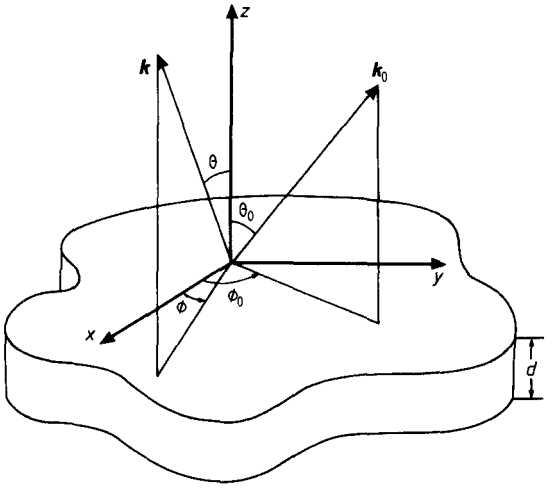

Figure 4.3 Spherical components of the wavevectors in a set of coordinates related to the sample. The slab normal is taken as the polar axis.

It is noteworthy that the first-order transmission factor $H_1(\boldsymbol{k}_0\boldsymbol{k})$ depends on the incident and final wavevector moduli, $|\boldsymbol{k}_0|$ and $|\boldsymbol{k}|$, only via the scattering and absorption cross sections $\Sigma_{\text{scat}}(\boldsymbol{k})$ and $\Sigma_{\text{abs}}(\boldsymbol{k})$. The expression becomes particularly simple in the case of experiments with weakly absorbing, purely incoherent samples. In this case

$$\Sigma_{\text{abs}}(\boldsymbol{k}) \ll 1 \tag{4.18a}$$

$$\Sigma_{\text{scat}}(\boldsymbol{k}) = \Sigma_{\text{inc}}(\boldsymbol{k}) = \Sigma = cte \tag{4.18b}$$

for any $\boldsymbol{k}$ value. Then, given the sample and the experiment geometry, $H_1(\boldsymbol{k}_0\boldsymbol{k})$ is a function of the orientations with respect to the sample of the incident and final wavevectors

$$H_1(\boldsymbol{k}_0\boldsymbol{k}) = H_1(\phi_0\phi) \tag{4.19}$$

where ϕ_0 and ϕ denote the angles with respect to the normal to the plane of $\boldsymbol{k}_0$ and $\boldsymbol{k}$, respectively (see figure 4.3).

Figure 4.4(a) illustrates the variation as a function of both ϕ and ϕ_0 of the transmission coefficient $H_1(\phi_0\phi)$ in the case $\Sigma d = 0.1$, i.e. for a sample whose normal transmission, when perpendicular to the beam, is about 0.9. The function sharply decreases down to zero for ϕ_0 or $\phi = 90°$, corresponding to scattering vectors in the plane of the sample. With more important values of Σd, the function varies more slowly, as shown in figure 4.4(b). The incident beam is perpendicular to the sample and the surface $H_1(\phi_0\phi)$ crosses the plane $\phi = 0$ according to the curve $H_1(0, 0) = \exp(-\Sigma d)$.

For higher orders of scattering ($j \geqslant 2$), the transmission factors are expressed by

$$H_j(\boldsymbol{k}_0\boldsymbol{k}_1\boldsymbol{k}_2 \ldots \boldsymbol{k}_{j-1}\boldsymbol{k}) = \exp(-|\alpha_0|\exp(-|\alpha|) \times \frac{\alpha_1\alpha_2 \ldots \alpha_{j-1}}{\Sigma_1\Sigma_2 \ldots \Sigma_{j-1}} U_j(\alpha_0\alpha_1\alpha_2 \ldots \alpha_{j-1}\alpha) \tag{4.20}$$

with the algebraic recursion formula

$$U_j(\alpha_0\alpha_1\alpha_2 \ldots \alpha_{j-1}\alpha) = \frac{1}{\alpha_1 - \alpha_0} \{U_{j-1}(\alpha_0\alpha_2 \ldots \alpha_{j-1}\alpha) - \exp[\zeta_1(\alpha_0 - \alpha_1)]\, U_{j-1}(\alpha_1\alpha_2 \ldots \alpha_{j-1}\alpha\}. \tag{4.21}$$

For second scattering we have

$$U_2(\alpha_0\alpha_1\alpha) = \frac{1}{\alpha_1 - \alpha_0} \{u(\alpha - \alpha_0) - \exp[\zeta_1(\alpha_0 - \alpha_1)]u(\alpha - \alpha_1)\} \tag{4.22}$$

with the following conventions:

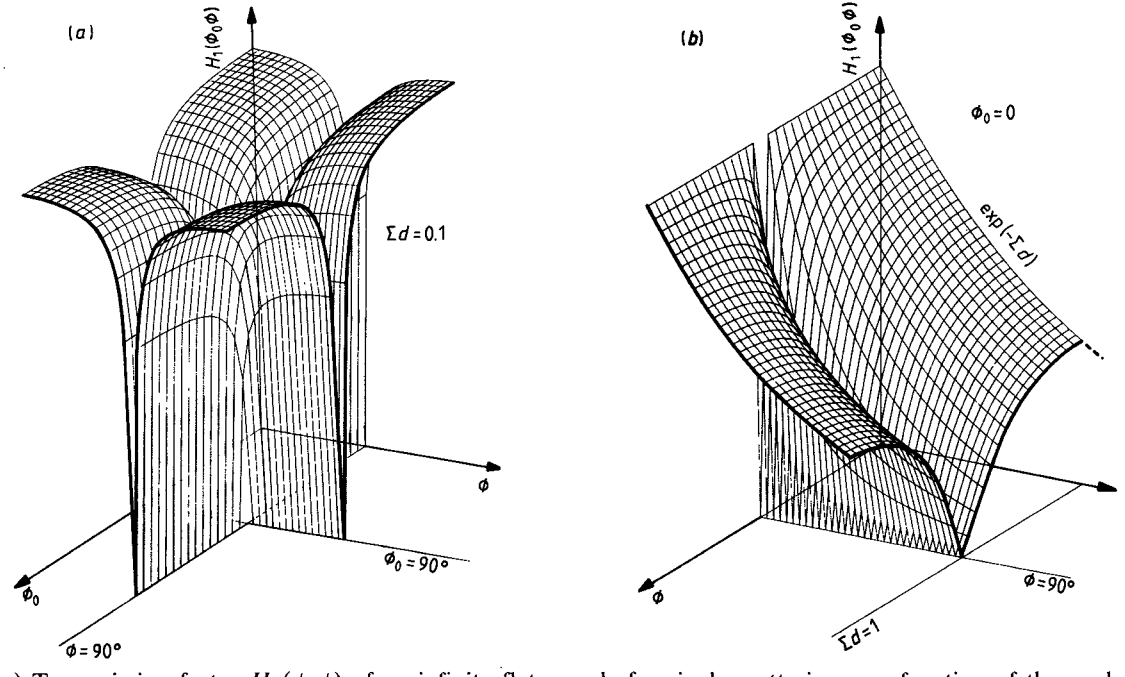

Figure 4.4 (*a*) Transmission factor $H_1(\phi_0\phi)$ of an infinite flat sample for single scattering as a function of the angles with respect to the normal to the plane of the incident beam (ϕ_0) and of the scattered beam (ϕ). The normal transmission when perpendicular to the beam is about 0.9 ($\Sigma d = 1$). (*b*) Transmission factor $H_1(\phi_0\phi)$ of an infinite flat sample as a function of the scattering angle ϕ and of the product Σd (Σ, total cross section per volume unit; d, thickness). The sample plane is assumed to be normal to the incident beam ($\phi_0 = 0$).

$$\alpha_i = \Sigma(\boldsymbol{k}_i)d/2\cos\phi_i \tag{4.23}$$

$$\zeta_1 = 1 \qquad \text{if } \alpha_i > 0 \qquad \left(\phi_1 < \frac{\pi}{2}\right) \tag{4.24a}$$

$$\zeta_1 = -1 \qquad \text{if } \alpha_1 < 0 \qquad \left(\phi_1 > \frac{\pi}{2}\right). \tag{4.24b}$$

In the case of third scattering

$$U_3(\alpha_0\alpha_1\alpha_2\alpha) = \frac{1}{\alpha_1 - \alpha_0}\,[U_2(\alpha_0\alpha_1\alpha) - \exp[\zeta_1(\alpha_0 - \alpha_1)]U_2(\alpha_1\alpha_2\alpha)]. \tag{4.25}$$

Likewise in the case of the first-order transmission factor $H_1(\boldsymbol{k}_0\boldsymbol{k})$, the various coefficients $H_j(\boldsymbol{k}_0\boldsymbol{k}_1 \ldots \boldsymbol{k}_{j-1}\boldsymbol{k})$ depend on the wavevector moduli $|\boldsymbol{k}_0|$, $|\boldsymbol{k}_1|$ ... etc, only via the scattering and absorption cross sections. Therefore, for weakly absorbing, purely incoherent specimens, equation (4.18) holds for any intermediate wavevector and we have

$$H_j(\boldsymbol{k}_0\boldsymbol{k}_1\boldsymbol{k}_2 \ldots \boldsymbol{k}_{j-1}\boldsymbol{k}) = H_j(\phi_0\phi_1\phi_2 \ldots \phi_{j-1}\phi). \tag{4.26}$$

Figure 4.5 illustrates the variation of the second-order transmission factor $H_2(\phi_0\phi_1\phi)$ as a function of both the final (ϕ) and intermediate (ϕ_1) scattering angles. The product Σd has again been chosen equal to 0.1 and the plane of the sample is assumed to be perpendicular to the incident neutron beam. Clearly, the values of $H_2(\phi_0\phi_1\phi)$ are much smaller than the values of $H_1(\phi_0\phi)$ corresponding to the same experimental conditions (see figure 4.4). Furthermore, they strongly depend on the direction of the intermediate scattering. The existence of the narrow peak centred on $\phi_1 = 90°$, independent of the precise value of ϕ, clearly indicates that the intermediate scattering processes which mainly contribute to the twice-scattered flux, are those occurring parallel to the sample plane. Indeed, for a once-scattered neutron in a direction perpendicular to the slab, the probability of emerging from the sample without being rescattered increases as the thickness decreases, as illustrated in figure 4.4 where the singly-scattered flux is maximum for $\phi = 0$. Conversely, a neutron which is scattered parallel to the sample plane must be scattered at least once again to emerge and thus contributes to increase the multiple scattering. Otherwise it will be absorbed.

The variation of the third-order transmission coefficient $H_3(\phi_0\phi_1\phi_2\phi)$ is illustrated in figure 4.6, the incident and final wavevectors $\boldsymbol{k}_0$ and $\boldsymbol{k}$ both being normal to the sample, as a function of the intermediate scattering angles ϕ_1 and ϕ_2. Here also, the surface is sharply peaked around $\phi_1 = \phi_2 = 90°$, evidencing the important role of the intermediate scatterings arising in the plane of the specimen. Conversely, the absolute amplitude is one order of magnitude smaller than the amplitude of $H_2(\phi_0\phi_1\phi)$.

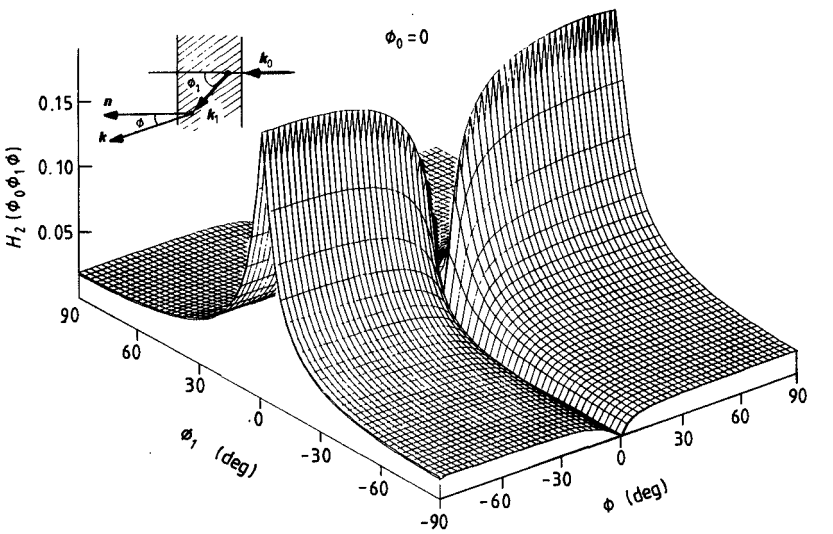

Figure 4.5 Second-order transmission factor $H_2(\phi_0\phi_1\phi)$ of an infinite flat sample as a function of the angles with respect to the normal to the slab plane of the final direction of scattering (ϕ) and of the intermediate direction of scattering in the sample (ϕ_1). The incident neutron beam is perpendicular to the slab ($\phi_0 = 0$).

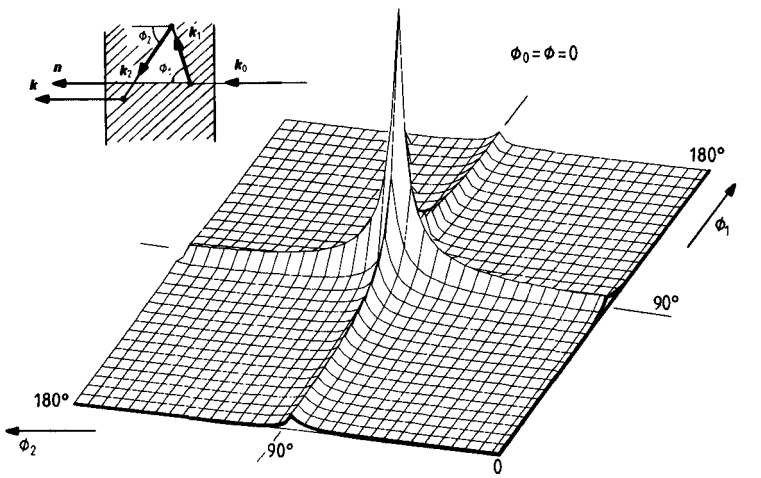

Figure 4.6 Third-order transmission factor $H_3(\phi_0\phi_1\phi_2\phi)$ for an infinite flat sample as a function of the angles ϕ_1 and ϕ_2 with respect to the normal to the slab plane of the intermediate scattering directions. The incident and final directions of the neutron are both normal to the slab ($\phi_0 = \phi = 0°$).

(b) Spherical sample

Suppose the sample takes the form of a sphere of radius r. The first-order transmission factor values are tabulated by Kasper and Lonsdale (1959). They are shown in figure 4.7 as a function of both the scattering angle ϕ and the product Σr (i.e. the radius of the sphere expressed in units of the mean free path in the sample Σ^{-1}). The intersection of the surface with the plane $\phi = 0$ is given analytically by (Sears 1975):

$$H_1(\boldsymbol{k}\boldsymbol{k}) = 1 - \tfrac{3}{2}\Sigma r + \tfrac{6}{5}(\Sigma r)^2 - \ldots \tag{4.27}$$

while for scattering in the backward direction ($\phi = 180°$)

$$H_1(\boldsymbol{k} - \boldsymbol{k}) = 1 - \tfrac{3}{2}\Sigma r + \tfrac{8}{5}(\Sigma r)^2 - \ldots. \tag{4.28}$$

It is worth noting that $H_1(\boldsymbol{k}_0\boldsymbol{k}) = 1$ if $\Sigma r = 0$. More precisely, in the case of a small sample ($\Sigma r \ll 1$), the first-order transmission factor is almost isotropic

$$H_1(\boldsymbol{k}_0\boldsymbol{k}) = 1 - \tfrac{3}{2}\Sigma r + \tfrac{7}{5}(\Sigma r)^2. \tag{4.29}$$

For arbitrary values of $\boldsymbol{k}_0, \boldsymbol{k}_1, \boldsymbol{k}_2, \ldots, \boldsymbol{k}_{j-1}$ and $\boldsymbol{k}$, the transmission factors $H_j(\boldsymbol{k}_0\boldsymbol{k}_1\boldsymbol{k}_2 \ldots \boldsymbol{k}_{j-1}\boldsymbol{k})$ can be evaluated analytically only in the case of an infinite plane slab. However, providing that some approximations are made, the second-order transmission coefficient can be written (refer to Sears original paper for more information)

$$H_2(\boldsymbol{k}_0\boldsymbol{k}_1\boldsymbol{k}) = H_1(\boldsymbol{k}_0\boldsymbol{k})B(\boldsymbol{k}_1) \tag{4.30}$$

where the coefficient

$$B(\boldsymbol{k}_1) = \frac{45}{76\Sigma}\left[1 - \exp(-\tfrac{19}{15}\Sigma r)\right] \tag{4.31}$$

is isotropic in the spherical case.

(c) Cylindrical sample

We now consider the case when the sample takes the form of a cylinder of radius r and height d. The study will be restricted to directions of the incident and scattered wavevectors both perpendicular to the axis. Figure 4.8 illustrates the values of the first-order transmission factor tabulated by Kasper and Lonsdale (1959), as a function of both Σr and Σd. The transmission factors in the forward and backward directions are given by (Sears 1975):

$$H_1(\boldsymbol{k}\boldsymbol{k}) = 1 - \frac{16}{3\pi}\Sigma r + \frac{3}{2}(\Sigma r)^2 \tag{4.32}$$

for $\phi = 0$, and by,

$$H_1(-\boldsymbol{k}\boldsymbol{k}) = 1 - \frac{16}{3\pi}\Sigma r + 2(\Sigma r)^2 \tag{4.33}$$

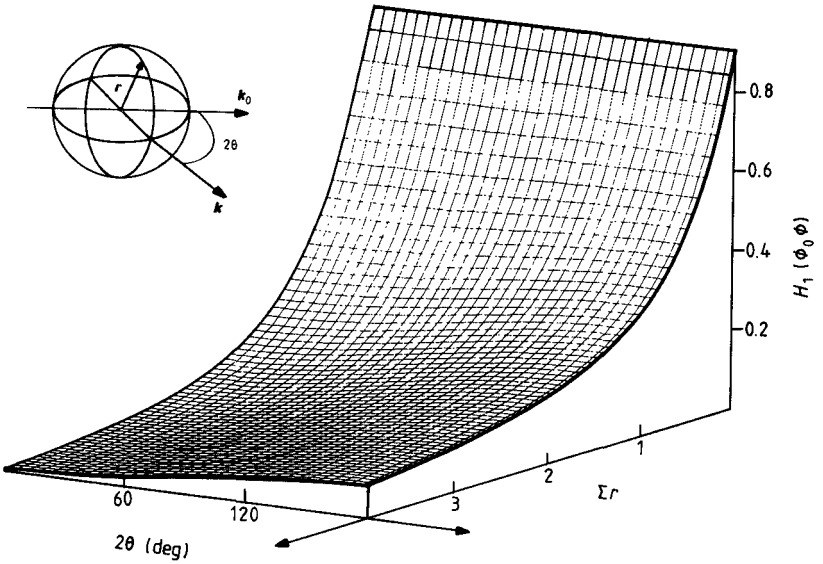

Figure 4.7 First-order transmission factor for a sphere as a function of both the scattering angle $2\theta = \phi - \phi_0$ and the product Σr of the radius of the sphere, r, and the total scattering cross section per volume unit of the specimen Σ (from the values tabulated by Kasper and Lonsdale 1959).

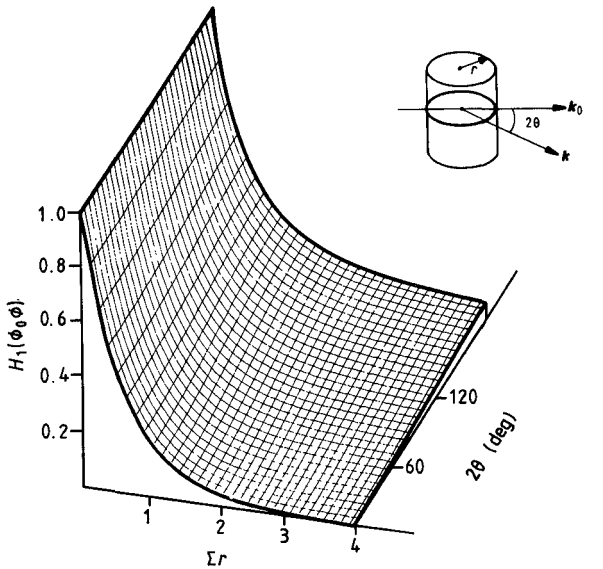

Figure 4.8 First-order transmission factor for a cylinder as a function of both the scattering angle $2\theta = \phi - \phi_0$ and the product Σr, r is the radius of the cylinder, while Σ stands for total scattering cross section per volume unit of the specimen (from the values tabulated by Kasper and Lonsdale 1959).

for $\phi = 180°$. As in the case of a spherical sample, $H_1(\boldsymbol{k}_0\boldsymbol{k}) = 1$ if $\Sigma r = 0$ and for a small specimen ($\Sigma r \ll 1$), the transmission is almost isotropic

$$H_1(\boldsymbol{k}\boldsymbol{k}) = 1 - \frac{16}{3\pi}\Sigma r + \frac{7}{4}(\Sigma r)^2 \tag{4.34}$$

Again, the second- and higher-order transmission factors $H_j(\boldsymbol{k}_0, \boldsymbol{k}_1, \boldsymbol{k}_2, \ldots, \boldsymbol{k}_{j-1}, \boldsymbol{k})$, $(j > 2)$ cannot be evaluated analytically for arbitrary values of $\boldsymbol{k}_0, \boldsymbol{k}_1, \boldsymbol{k}_2, \ldots, \boldsymbol{k}_{j-1}$ and $\boldsymbol{k}$. Employing the approximate theory developed by Sears, it is possible to write

$$H_2(\boldsymbol{k}_0\boldsymbol{k}_1\boldsymbol{k}) = H_1(\boldsymbol{k}_0\boldsymbol{k})B(\boldsymbol{k}_1) \tag{4.35}$$

with the expression of $B(\boldsymbol{k}_1)$

$$B(\boldsymbol{k}_1) = B_{\parallel}(\phi_1) = B_{\parallel}(\pi - \phi_1) = \frac{p_{\parallel}}{\Sigma}\left[1 - \exp\left(-\frac{q_{\parallel}\Sigma d}{\cos\phi_1}\right)\right] \tag{4.36a}$$

if $0 \leqslant \phi \leqslant \beta$

$$B(\boldsymbol{k}_1) = B_{\perp}(\phi_1) = B_{\perp}(\pi - \phi_1) = \frac{p_{\perp}}{\Sigma}\left[1 - \exp\left(-\frac{2q_{\perp}\Sigma r}{\sin\phi_1}\right)\right] \tag{4.36b}$$

if $\beta \leqslant \phi_1 \leqslant \pi/2$. Here the angle β is defined by

$$\beta = \arctan\left(\frac{2r}{d}\right) \tag{4.37}$$

while $p_{\parallel} = \frac{3}{4}$, $q_{\parallel} = \frac{2}{3}$, $p_{\perp} = \frac{16}{9\pi^2 - 64}$, $q_{\perp} = \frac{9\pi^2 - 64}{12\pi}$.

The variation of $B(\boldsymbol{k}_1)$ as a function of ϕ_1 and Σd is illustrated in figure 4.9. There the value $\Sigma r = 1$ was taken. It appears that in the limit $\Sigma d \to 0$, i.e. when the sample has the shape of a small disc, $B(\boldsymbol{k}_1)$ is sharply peaked at $\phi_1 = 90°$, as in the case of an infinite flat slab. Conversely, when Σd increases, i.e. for rod-shaped samples, $B(\boldsymbol{k}_1)$ tends to become independent of ϕ_1.

4.2.2 Importance and nature of multiple scattering

There are rather few examples in the literature where multiple scattering corrections are reported in full detail. Using the quasi-isotropic approximation (Vineyard 1954) which consists in setting arbitrarily

$$S(\boldsymbol{Q}, \omega) = \delta(\omega) \tag{4.38}$$

for all the directions and moduli of the momentum transfer, the ratio of double to single scattering can be easily evaluated. Indeed,

$$\tilde{s}(\boldsymbol{k}_0, \boldsymbol{k}) = \sum_{j=1}^{\infty} s_j(\boldsymbol{k}_0, \boldsymbol{k}) \tag{4.39}$$

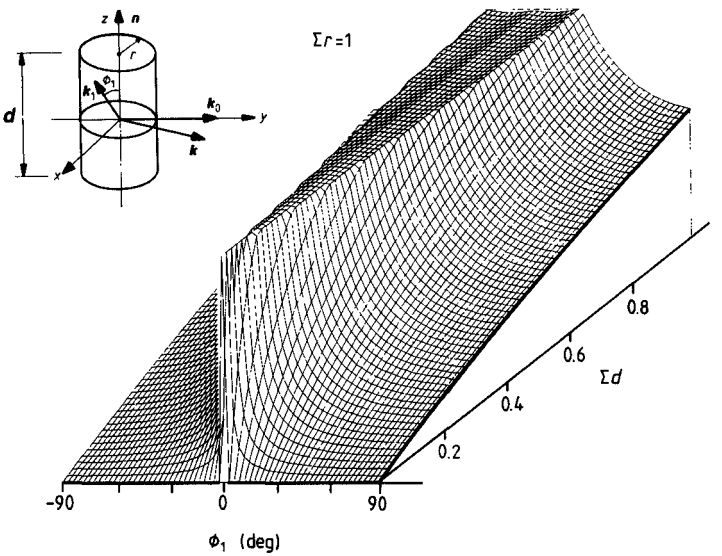

Figure 4.9 Variation of $B(\boldsymbol{k}_1)$, for a cylindrical sample of radius r and height d, (equation (4.36)), as a function of the angle ϕ_1 of the intermediate wavevector $\boldsymbol{k}_1$ with the axis of the cylinder and also as a function of the product Σd. Σ is the total cross section per sample volume unit, and $\Sigma r = 1$.

where

$$\tilde{s}_1(\boldsymbol{k}_0, \boldsymbol{k}) = H_1(\boldsymbol{k}_0, \boldsymbol{k}) \tag{4.40}$$

and

$$s_j(\boldsymbol{k}_0\boldsymbol{k}) = \left[\frac{n\sigma}{4\pi}\right]^{j-1} \int\int \ldots \int \mathrm{d}\Omega_1 \, \mathrm{d}\Omega_2 \ldots \mathrm{d}\Omega_{j-1} H(\boldsymbol{k}_0\boldsymbol{k}_1\boldsymbol{k}_2 \ldots \boldsymbol{k}_{j-1}\boldsymbol{k}) \tag{4.41}$$

for $j \geqslant 2$. The tilde refers to the quasi-isotropic approximation. Moreover, under these conditions the moduli of the wavevectors are all equal

$$|\boldsymbol{k}_0| = |\boldsymbol{k}_1| = \ldots = |\boldsymbol{k}_{j-1}| = |\boldsymbol{k}| \tag{4.42}$$

and now, according to (4.17)

$$\Sigma_{\mathrm{scat}}(\boldsymbol{k}_0) = n\sigma. \tag{4.43}$$

Sears (1975) tabulated this ratio δ in the particular case of a cylindrical specimen, as a function of both the radius r and the height d of the cylinder. These values are reported in figure 4.10, where the influence of the geometry of the sample is clearly evidenced. For rod-shaped samples (i.e. $\Sigma r \to 0$, figure 4.10), δ appears almost independent of the height d, whilst for disc-shaped samples (i.e. $\Sigma d \to 0$, figure 4.10), δ is, conversely, nearly independent of the radius r.

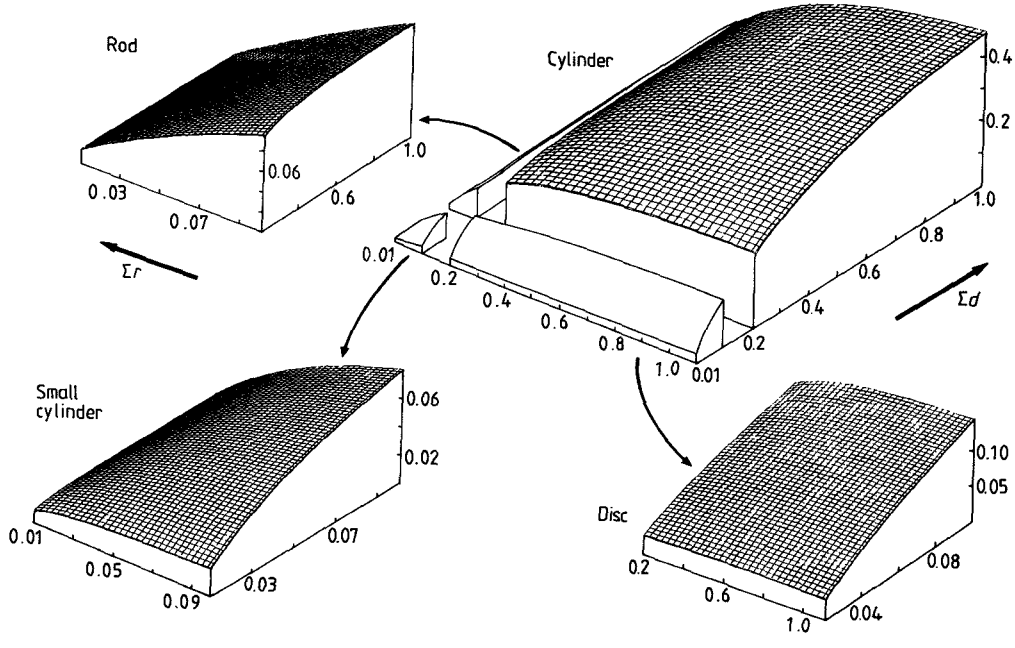

Figure 4.10 Ratio of the double-to-single scattering in the quasi-isotropic approximation, for a cylindrical sample (from the values tabulated by Sears 1975).

However, in the framework of the quasi-isotropic approximation, it is impossible to obtain any insight into the energy-dependence of the multiple-scattering. Before dealing with that aspect in the next section, we shall outline some general features, referring to an IQNS study of methyl group reorientations (Bée *et al* 1984b). The relevant scattering law was

$$S(\boldsymbol{Q}, \omega) = \frac{1}{3}[1 + 2j_0(\boldsymbol{Q}r\sqrt{3})]\delta(\omega) + \frac{2}{3}[1 - 2j_0(\boldsymbol{Q}r\sqrt{3})]\frac{1}{\pi} \cdot \frac{\tau}{1 + \omega^2\tau^2} \tag{4.44}$$

which is a typical expression in IQNS. Here $j_0(x) = \sin x/x$ is the zero order Bessel function. $r = 0.998$ is the distance from each proton of a methyl group to its centre of gravity. The value of the characteristic time, τ, was found to lie at about 7.4×10^{-11} s at $T = 300$ K. According to (4.44) the scattering function appears to be composed of a sharp elastic peak $\delta(\omega)$ superimposed on a broad component, yielding to intensity outside $\hbar\omega = 0$, the relative intensity between these two components being Q-dependent.

In figure 4.11 the values of the ratio of the singly-scattered flux, J_1, over the sum $J_1 + J_2$ of the singly- and twice-scattered fluxes, are reported, as a function of both the energy transfer $\hbar\omega$ and the scattering angle $2\theta = \phi - \phi_0$. For $2\theta = 0$, the single scattering is purely elastic and

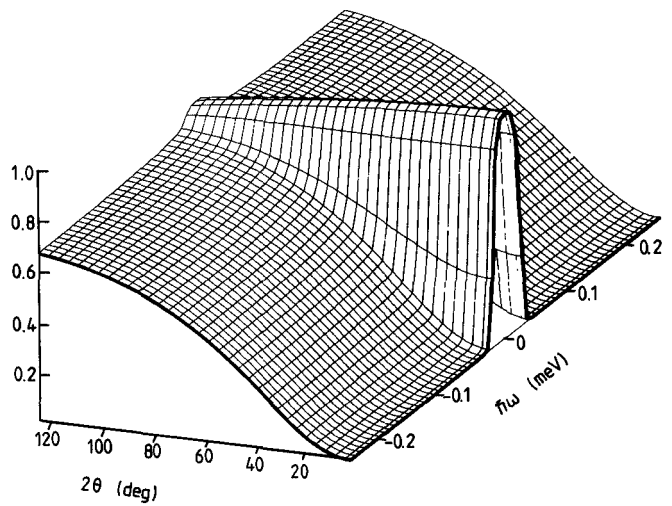

Figure 4.11 Ratio of the single scattering over the total scattering (evaluated up to second order) as a function of both the energy transfer $\hbar\omega$ and the scattering angle $2\theta = \phi - \phi_0$. The sample is a powder of trimethylsulphoxonium iodide (Bée *et al* 1985b).

the energy spectrum is a Dirac delta-function. Conversely the twice-scattered flux not only results from two successive scattering processes with no wavevector change, but also from contributions in which a neutron, first scattered with a momentum transfer $\boldsymbol{Q}_1 \neq 0$ is next scattered with $\boldsymbol{Q}_2 = -\boldsymbol{Q}_1$. Neither process is necessarily purely elastic and their succession leads to a non-vanishing resulting energy transfer. Consequently, whilst the fraction of second scattering is only a few per cent at $\hbar\omega = 0$, it increases up to 100% as soon as $\hbar\omega \neq 0$; the wings of the experimental spectra, outside the resolution range, at small scattering angles, are mainly due to multiple scattering. For larger values of the scattering angle $2\theta = \phi - \phi_0$, the quasielastic contribution to the singly-scattered flux increases and the fraction of multiple scattering in the wings of the spectra decreases noticeably.

4.3 Evaluation of the Scattered Fluxes of Successive Orders in the Particular Case of Quasielastic Incoherent Scattering

We shall turn to the evaluation of the second and higher orders of scattering in the case where the scattering law (assumed *a priori* incoherent) can be written in the form

$$S(\boldsymbol{Q}, \omega) = A_0(\boldsymbol{Q})\delta(\omega) + \sum_{i=1}^{N} A_i(\boldsymbol{Q})L_i(\omega) \tag{4.45}$$

where we have defined

$$A_0(\boldsymbol{Q}) = a_0(\boldsymbol{Q}) \exp(-\langle u^2 \rangle Q^2). \tag{4.46}$$

The term $a_0(\boldsymbol{Q})$ is the elastic incoherent structure factor (EISF) already defined in chapter 2. This term always exists when the space accessible to the scatterer in the specimen is restricted to a finite region of space. For instance the scattering laws related to rotations of molecules, molecular groups, or also to diffusion of particles inside a restricted volume, lead to an EISF in their expression. Conversely, this term vanishes in the case of long-range diffusion (assuming that the motion is sufficiently fast to be resolved on the instrument time-scale). Many other physical systems also lead to the presence of a purely elastic term in the expression of the scattered intensity. Most often, in the study of adsorbed species, an elastic contribution occurs from the scattering of the substrate. Also, coherent elastic scattering can arise, as a consequence of long-range translational order, in the form of more or less intense Bragg peaks well-localised in space, but, sometimes, for disordered materials, in the form of broad diffuse bands. Therefore, the presence in the scattering law of a purely elastic term (represented

by a Dirac delta function), whose contribution is Q-dependent (according to $a_0(Q)$) can be considered as a general feature of the IQNS technique.

The Debye–Waller factor $\exp(-\langle u^2 \rangle Q^2)$ takes into account the decrease of the quasielastic intensity versus Q, arising from the existence of fast motions giving intensity outside the quasielastic region. Generally, $\langle u^2 \rangle$ is considered as a mean square amplitude for vibrational motions (internal vibrations, lattice vibrations, molecular librations). In fact, any important quasielastic broadening of the spectra which lies largely outside the instrument energy range will be responsible for an attenuation of the intensity.

The second term in (4.45) is a quasielastic contribution which appears as a sum of N lorentzian functions

$$L_i(\omega) = \frac{1}{\pi} \frac{\tau_i}{1 + \omega^2 \tau_i}. \tag{4.47}$$

These are all normalised to unity

$$\int_{-\infty}^{\infty} L_i(\omega)\, d\omega = 1. \tag{4.48}$$

Their half-width at half-maximum τ_i^{-1} together with their respective weights as a function of Q, predicted by $a_i(Q)$, depend on the model under consideration. We shall treat in full detail the different possible expressions of the scattering law according to the physical situation of interest in a following chapter. In this section, it is sufficient for our purpose to notice that we are mainly concerned with two cases:

(i) Long-range translational motion. Assuming that this motion is diffusive and characterised by a diffusion coefficient D_T, then (4.45) reduces to

$$S(Q, \omega) = \frac{1}{\pi} \frac{D_T Q^2}{(D_T Q^2)^2 + \omega^2} \tag{4.49}$$

i.e. the neutron spectra are single lorentzian lines whose full-width at half-maximum is $2D_T Q^2$. However, a significant broadening of the spectra will be seen only if $2D_T Q^2$ is larger than the energy resolution of the spectrometer (or at least comparable).

(ii) Motion confined in a restricted region of space. A common case for such motion is the rotation of whole molecules or of inner molecular groups. Then the scattering law is formally expressed by the expansion (4.45), where the half-widths, τ_i^{-1}, of the lorentzian function involve a set of jump-probabilities, characteristic of the model under test. It should be noticed that some models (i.e. the rotational diffusion model) lead to an expansion over an infinite number of terms. However, as will be shown in the following chapters, in the Q-range accessible to the

instrument, these can be restricted to a finite number of significant terms.

Therefore, in the remainder of this chapter, we shall take as a basic statement that the first-order scattering function can be written in the form (4.45). This will enable us to obtain some useful insight into the two following questions in connection with the dependence on the detailed form of the effective scattering function on the amount of multiple scattering.

(i) How are the respective contributions of the purely elastic scattered intensity and of the quasielastic scattered intensity modified?
(ii) How is the shape of the quasielastic part of the spectra modified?

4.3.1 Second scattering

Let us consider first the case of second-order scattering. According to (4.9), the effective scattering function reads:

$$s_2(\boldsymbol{Q}, \omega) = \frac{n\sigma}{4\pi} \int\int \mathrm{d}\Omega_1 \, \mathrm{d}\omega_1 \, S(\boldsymbol{Q}_1, \omega_1) \, S(\boldsymbol{Q}_0, \omega_2) \, H_2(\boldsymbol{k}_0 \boldsymbol{k}_1 \boldsymbol{k}) \tag{4.50}$$

where the following wavevector transfers have been introduced:

$$\boldsymbol{Q}_1 = \boldsymbol{k}_1 - \boldsymbol{k}_0 \tag{4.51a}$$

$$\boldsymbol{Q}_2 = \boldsymbol{k} - \boldsymbol{k}_1 \tag{4.51b}$$

$$\boldsymbol{Q} = \boldsymbol{k} - \boldsymbol{k}_0 = \boldsymbol{Q}_1 + \boldsymbol{Q}_2 \tag{4.51c}$$

together with the energy transfers:

$$\hbar\omega_1 = E_1 - E_0 \tag{4.52a}$$

$$\hbar\omega_2 = E - E_1 \tag{4.52b}$$

$$\hbar\omega = E - E_0 = \hbar(\omega_1 + \omega_2). \tag{4.52c}$$

Here E_0 and E_1 denote the initial and final values of the neutron energy, respectively. E_1 is the energy after the first scattering process. Introducing the expression (4.45) for the quasielastic scattering function, the right-hand side of (4.50) can be separated into four terms:

$$s_2(\boldsymbol{Q}, \omega) = s_{\mathrm{EE}}(\boldsymbol{Q}, \omega) + s_{\mathrm{EI}}(\boldsymbol{Q}, \omega) + s_{\mathrm{IE}}(\boldsymbol{Q}, \omega) + s_{\mathrm{II}}(\boldsymbol{Q}, \omega) \tag{4.53}$$

with the following definitions:

$$s_{\mathrm{EE}}(\boldsymbol{Q}, \omega)$$

$$= \frac{n\sigma}{4\pi} \int \mathrm{d}\Omega_1 \, \mathrm{d}\omega_1 A_0(\boldsymbol{Q}) A_0(\boldsymbol{Q} - \boldsymbol{Q}_1) \delta(\omega_1) \delta(\omega - \omega_1) H_2(\boldsymbol{k}_0 \boldsymbol{k}_1 \boldsymbol{k}) \tag{4.54a}$$

$$s_{\mathrm{EI}}(\boldsymbol{Q}, \omega) = \frac{n\sigma}{4\pi}\int \mathrm{d}\Omega_1\, \mathrm{d}\omega_1 A_0(\boldsymbol{Q}_1) \sum_{i=1}^{N} A_i(\boldsymbol{Q} - \boldsymbol{Q}_1)\delta(\omega_1) L_i(\omega - \omega_1) H_2(\boldsymbol{k}_0\boldsymbol{k}_1\boldsymbol{k}) \tag{4.54b}$$

$$s_{\mathrm{IE}}(\boldsymbol{Q}, \omega) = \frac{n\sigma}{4\pi}\int \mathrm{d}\Omega_1\, \mathrm{d}\omega_1 \sum_{i=1}^{N} A_i(\boldsymbol{Q}) A_0(\boldsymbol{Q} - \boldsymbol{Q}_1)\, L_i(\omega_1)\delta(\omega - \omega_1) H_2(\boldsymbol{k}_0\boldsymbol{k}_1\boldsymbol{k}) \tag{4.54c}$$

$$s_{\mathrm{II}}(\boldsymbol{Q}, \omega) = \frac{n\sigma}{4\pi}\int \mathrm{d}\Omega_1\, \mathrm{d}\omega_1 \sum_{j=1}^{N}\sum_{i=1}^{N} A_i(\boldsymbol{Q}) A_j(\boldsymbol{Q} - \boldsymbol{Q}_1) L_i(\omega_1) L_j(\omega - \omega_1) H_2(\boldsymbol{k}_0\boldsymbol{k}_1\boldsymbol{k}) \tag{4.54d}$$

Thus, the second scattering has been separated into four contributions of a different nature: the term s_{EE} corresponds to two successive purely elastic scatterings of the same neutron whilst $s_{\mathrm{II}}(\boldsymbol{Q}, \omega)$ represents the opposite case of two inelastic collisions. Both other terms $s_{\mathrm{EI}}(\boldsymbol{Q}, \omega)$ and $s_{\mathrm{IE}}(\boldsymbol{Q}, \omega)$ arise from mixed situations, i.e. one of the collisions is purely elastic and the other is inelastic.

The set of equations (4.54) involves integrals over all the possible values of the energy transfer $\hbar\omega_1$ and of the wavevector transfer $\boldsymbol{Q}_1$ occurring in the first collision. Both $\boldsymbol{Q}$ and $\boldsymbol{Q}_1$ also depend on ω and ω_1, respectively. We shall write this dependence explicitly:

$$\boldsymbol{Q} = \boldsymbol{Q}(\theta, \phi, \omega) = \boldsymbol{Q}^{\omega} \tag{4.55a}$$

$$\boldsymbol{Q}_1 = \boldsymbol{Q}_1(\theta_1, \phi_1, \omega_1) = \boldsymbol{Q}_1^{\omega} \tag{4.55b}$$

similarly, for purely elastic scattering

$$\boldsymbol{Q}(\theta, \phi, 0) = \boldsymbol{Q}^0 \tag{4.56a}$$

$$\boldsymbol{Q}_1(\theta_1, \phi_1, 0) = \boldsymbol{Q}_1^0. \tag{4.56b}$$

The second-order transmission factors $H_2(\phi_0\phi_1\phi)$ depend on ω and ω_1 via the module of the wavevector transfers $|\boldsymbol{k}_1|$ and $|\boldsymbol{k}|$. We shall write

$$H_2(\boldsymbol{k}_0\boldsymbol{k}_1\boldsymbol{k}) = H_2(\phi_0\phi_1\phi;\, \omega_1\omega). \tag{4.57}$$

Using this notation, the contribution to second scattering arising from elastic processes becomes

$$s_{\mathrm{EE}}(\boldsymbol{Q}, \omega) = \frac{n\sigma}{4\pi}\int \mathrm{d}\Omega_1 A_0(\boldsymbol{Q}^{\omega} - \boldsymbol{Q}_1^0)\, H_2(\phi_0\phi_1\phi;\, \omega\omega)\delta(\omega) \tag{4.58a}$$

$$s_{\mathrm{EE}}(\boldsymbol{Q}, \omega) = B_{00}(\boldsymbol{Q}^0)\delta(\omega) \tag{4.58b}$$

where we have introduced

$$B_{00}(\boldsymbol{Q}^0) = \frac{n\sigma}{4\pi} \int \mathrm{d}\Omega_1 A_0(\boldsymbol{Q}_1^0)\,(A_0(\boldsymbol{Q}^0 - \boldsymbol{Q}_1^0) H_2(\phi_0\phi_1\phi;\, 0\ 0). \tag{4.59}$$

This coefficient is similar to an elastic incoherent structure factor for the twice-scattered flux. It is the result of the convolution over all the possible directions of the scattering vector resulting from the first collision, of the EISF of the single-scattering law with itself, and weighted by the transmission factor for second order. Correspondingly, using the following definitions analogous to (4.59).

$$B_{0i}(\boldsymbol{Q}^\omega) = \frac{n\sigma}{4\pi} \int \mathrm{d}\Omega_1 A_0(\boldsymbol{Q}_1^0) A_i(\boldsymbol{Q}^\omega - \boldsymbol{Q}_1^0) H_2(\phi_0\phi_1\phi;\, 0\ \omega) \tag{4.60a}$$

$$B_{i0}(\boldsymbol{Q}^\omega) = \frac{n\sigma}{4\pi} \int \mathrm{d}\Omega_1 A_i(\boldsymbol{Q}_1^\omega) A_0(\boldsymbol{Q}^\omega - \boldsymbol{Q}_1^\omega) H_2(\phi_0\phi_1\phi;\, \omega\ \omega) \tag{4.60b}$$

the contributions of the processes involving an elastic and an inelastic scattering can be written

$$s_{\mathrm{EI}}(\boldsymbol{Q},\, \omega) = \sum_{i=1}^{N} B_{0i}(\boldsymbol{Q}^\omega) L_i(\omega) \tag{4.61a}$$

$$s_{\mathrm{IE}}(\boldsymbol{Q},\, \omega) = \sum_{i=1}^{N} B_{i0}(\boldsymbol{Q}^\omega) L_i(\omega). \tag{4.61b}$$

4.3.2 Simplified form of second scattering

According to the expressions (4.60a) and (4.60b) above, the evaluation of the terms s_{EI} and s_{IE} requires an integration for each value of the final energy transfer $\hbar\omega$. In the particular case of quasielastic scattering, we are mainly concerned with small values of these energy transfers. Under these conditions, it can be taken as a realistic assumption that the wavevector transfer $\boldsymbol{Q}^\omega$ varies little inside an experimental spectrum recorded at constant angle, and therefore

$$\boldsymbol{Q}^\omega \simeq \boldsymbol{Q}^0 \tag{4.62a}$$

and

$$\boldsymbol{Q}_1^\omega \simeq \boldsymbol{Q}_1^0. \tag{4.62b}$$

Consequently, if the structure factors $A_i(\boldsymbol{Q})$ related to first-order scattering vary slowly as a function of the modulus of $\boldsymbol{Q}$, they can be expanded into a Taylor series about the precise value $\boldsymbol{Q}^0$.

$$A_i(\boldsymbol{Q}^\omega) = A_i(\boldsymbol{Q}^0) + \left[\frac{\mathrm{d}A_i(\boldsymbol{Q}^\omega)}{\mathrm{d}\omega}\right]_{\omega=0} \omega + \frac{1}{2!}\left[\frac{\mathrm{d}^2 A_i(\boldsymbol{Q}^\omega)}{\mathrm{d}\omega^2}\right]_{\omega=0} \omega^2 + \ldots . \tag{4.63}$$

Under these conditions, the set of equations (4.60) becomes

$$s_{\mathrm{EI}}(\boldsymbol{Q}, \omega) = \sum_{i=1}^{N} [B_{0i}(\boldsymbol{Q}^0) + B_{0i}^{(1)}(\boldsymbol{Q}^0)\omega + B_{0i}^{(2)}(\boldsymbol{Q}^0)\omega^2 + \ldots]L_i(\omega) \tag{4.64a}$$

$$s_{\mathrm{IE}}(\boldsymbol{Q}, \omega) = \sum_{i=1}^{N} [B_{i0}(\boldsymbol{Q}^0) + B_{i0}^{(1)}(\boldsymbol{Q}^0)\omega + B_{i0}^{(2)}(\boldsymbol{Q}^0)\omega^2 + \ldots]L_i(\omega) \tag{4.64b}$$

with the general definition

$$B_{0i}^{(m)}(\boldsymbol{Q}^0) = \frac{n\sigma}{4\pi} \int \mathrm{d}\Omega_1 \frac{1}{m!} \left\{ \frac{\mathrm{d}^m}{\mathrm{d}\omega^m} \left[A_0(\boldsymbol{Q}_1^0) A_i(\boldsymbol{Q}^\omega - \boldsymbol{Q}_1^0) H_2(\phi_0\phi_1\phi; 0\omega) \right] \right\}_{\omega=0} \tag{4.65a}$$

$$B_{i0}^{(m)}(\boldsymbol{Q}^0) = \frac{n\sigma}{4\pi} \int \mathrm{d}\Omega_1 \frac{1}{m!} \left\{ \frac{\mathrm{d}^m}{\mathrm{d}\omega^m} \left[A_i(\boldsymbol{Q}_1^\omega) A_0(\boldsymbol{Q}^\omega - \boldsymbol{Q}_1^\omega) H_2(\phi_0\phi_1\phi; \omega\,\omega) \right] \right\}_{\omega=0}. \tag{4.65b}$$

Providing that the terms $B_{0i}^{(m)}$ and $B_{i0}^{(m)}$ converge to zero rapidly enough when m increases, the Taylor expansions occurring in the set of equations (4.63) can be truncated to a restricted number of terms to be evaluated. Moreover these terms have to be calculated for the particular value $\boldsymbol{Q}^0$ corresponding to $\hbar\omega = 0$, only. Another simplification occurs with weakly absorbing, purely incoherent specimens, whose total cross section can be considered independent of the energy (equation 4.18); where consequently,

$$H_2(\phi_0\phi_1\phi; \omega_1\omega) = H_2(\phi_0\phi_1\phi) \tag{4.66}$$

and (4.65) becomes:

$$B_{0i}^{(m)}(\boldsymbol{Q}^0) = \frac{n\sigma}{4\pi} \int \mathrm{d}\Omega_1 \frac{1}{m!} \left\{ \frac{\mathrm{d}^m}{\mathrm{d}\omega^m} \left[A_0(\boldsymbol{Q}_1^0) A_i(\boldsymbol{Q}^\omega - \boldsymbol{Q}_1^0) \right] \right\}_{\omega=0} H_2(\phi_0\phi_1\phi) \tag{4.67a}$$

$$B_{i0}^{(m)}(\boldsymbol{Q}^0) = \frac{n\sigma}{4\pi} \int \mathrm{d}\Omega_1 \frac{1}{m!} \left\{ \frac{\mathrm{d}^m}{\mathrm{d}\omega^m} \left[A_i(\boldsymbol{Q}_1^\omega) A_0(\boldsymbol{Q}^\omega - \boldsymbol{Q}_1^\omega) \right] \right\}_{\omega=0} H_2(\phi_0\phi_1\phi). \tag{4.67b}$$

Otherwise, it is often sufficient, at least in a first approach of the problem, to restrict the expansion (4.67) to the zero order approximation and to write:

$$s_{\mathrm{EI}}(\boldsymbol{Q}, \omega) = \sum_{i=1}^{N} B_{0i}(\boldsymbol{Q}^0) L_i(\omega) \tag{4.68a}$$

$$s_{\mathrm{IE}}(\boldsymbol{Q}, \omega) = \sum_{i=1}^{N} B_{i0}(\boldsymbol{Q}^0) L_i(\omega). \tag{4.68b}$$

The evaluation of the remaining term $s_{II}(\boldsymbol{Q}, \omega)$, related to the succession of two inelastic scatterings of the neutron, is based upon similar hypotheses. Assuming that the lorentzian functions occurring in (4.45) have a value small enough to be negligible when $\hbar\omega_1$ increases, the integrals over the energy transfers and over the orientations of the intermediate scattering vector $\boldsymbol{k}_1$ can be separated from each other. With the restriction to the zero order approximation, we shall write:

$$s_{II}(\boldsymbol{Q}, \omega) = \sum_{i=1}^{N} \sum_{j=1}^{N} B_{ij}(\boldsymbol{Q}^0) L_{ij}(\omega) \tag{4.69}$$

where, by definition,

$$B_{ij}(\boldsymbol{Q}^0) = \frac{n\sigma}{4\pi} \int \mathrm{d}\Omega_1 \, A_i(\boldsymbol{Q}_1^0) A_j(\boldsymbol{Q}^0 - \boldsymbol{Q}_1^0) H_2(\phi_0 \phi_1 \phi; 0\ 0) \tag{4.70}$$

and

$$L_{ij}(\omega) = \int_{-E_0}^{\infty} \mathrm{d}\omega_1 L_i(\omega_1) L_j(\omega - \omega_1). \tag{4.71}$$

Here, the lower limit of the integral for the convolution product $L_{ij}(\omega)$ is given by the finite value E_0 of the incident energy. Providing that the lorentzian functions $L_i(\omega_1)$ and $L_j(\omega - \omega_1)$ tend rapidly to zero when $\omega_1 \to \infty$, this lower limit can be extended to $-\infty$ and then

$$L_{ij}(\omega) = \int_{-\infty}^{\infty} \mathrm{d}\omega_1 L_i(\omega_1) L_j(\omega - \omega_1) = \frac{1}{\pi} \frac{\tau_{ij}}{1 + \omega^2 \tau_{ij}^2} \tag{4.72}$$

where

$$\tau_{ij}^{-1} = \tau_i^{-1} + \tau_j^{-1}. \tag{4.73}$$

Finally, from the equations (4.58), (4.68) and (4.70), the second-order scattering can be put into a form similar to the single scattering one:

$$s_2(\boldsymbol{Q}, \omega) = B_{00}(\boldsymbol{Q}^0)\delta(\omega) + \sum_{i=1}^{N} [B_{0i}(\boldsymbol{Q}^0) + B_{i0}(\boldsymbol{Q}^0)] L_i(\omega) + \sum_{i=1}^{N} \sum_{j=1}^{N} B_{ij}(\boldsymbol{Q}^0) L_{ij}(\omega). \tag{4.74}$$

4.3.3 Third scattering

The cases of third and higher orders of scattering are similar and the same hypotheses and approximations are involved. For instance, on the basis of the zero order approximation, the scattering function for third scattering is written:

$$s_3(\boldsymbol{Q}, \omega) = \sum_{i=0}^{N} \sum_{j=0}^{N} \sum_{k=0}^{N} C_{ijk}(\boldsymbol{Q}^0) L_{ijk}(\omega) \tag{4.75}$$

where:

$$L_{ijk}(\omega) = \frac{1}{\pi} \frac{\tau_{ijk}}{1 + \omega^2 \tau_{ijk}^2} \qquad \text{if } \tau_{ijk}^{-1} = \tau_i^{-1} + \tau_j^{-1} + \tau_k^{-1} \neq 0 \quad (4.76a)$$

and

$$L_{ijk}(\omega) = \delta(\omega) \qquad \text{if } \tau_{ijk}^{-1} = 0. \quad (4.76b)$$

The coefficients $C_{ijk}(\boldsymbol{Q}^0)$ are defined by

$$C_{ijk}(\boldsymbol{Q}^0) = \left[\frac{n\sigma}{4\pi}\right]^2 \iint d\Omega_1 \, d\Omega_2 A_i(\boldsymbol{Q}_1^0) A_j(\boldsymbol{Q}_2^0) A_k(\boldsymbol{Q}^0 - \boldsymbol{Q}_1^0 - \boldsymbol{Q}_2^0) H_3(\phi_0 \phi_1 \phi_2 \phi, 000). \quad (4.77)$$

If the various possible combinations of three successive scatterings are separated (elas–elas–elas, elas–elas–inel, . . . etc.)

$$\begin{aligned} s_3(\boldsymbol{Q}, \omega) = {} & s_{\mathrm{EEE}}(\boldsymbol{Q}, \omega) \\ & + s_{\mathrm{EEI}}(\boldsymbol{Q}, \omega) + s_{\mathrm{EIE}}(\boldsymbol{Q}, \omega) + s_{\mathrm{IEE}}(\boldsymbol{Q}, \omega) \\ & + s_{\mathrm{EII}}(\boldsymbol{Q}, \omega) + s_{\mathrm{IEI}}(\boldsymbol{Q}, \omega) + s_{\mathrm{IIE}}(\boldsymbol{Q}, \omega) \\ & + s_{\mathrm{III}}(\boldsymbol{Q}, \omega) \end{aligned} \quad (4.78)$$

with the following expressions for each contribution:

$$s_{\mathrm{EEE}}(\boldsymbol{Q}, \omega) = C_{000}(\boldsymbol{Q}^0)\delta(\omega) \quad (4.79a)$$

$$s_{\mathrm{EEI}}(\boldsymbol{Q}, \omega) = \sum_{i=1}^{N} C_{00i}(\boldsymbol{Q}^0) L_i(\omega) \quad (4.79b)$$

$$s_{\mathrm{EII}}(\boldsymbol{Q}, \omega) = \sum_{i=1}^{N} \sum_{j=1}^{N} C_{0ij}(\boldsymbol{Q}^0) L_{ij}(\omega) \quad (4.79c)$$

$$s_{\mathrm{III}}(\boldsymbol{Q}, \omega) = \sum_{i=1}^{N} \sum_{j=1}^{N} \sum_{k=1}^{N} C_{ijk}(\boldsymbol{Q}^0) L_{ijk}(\omega). \quad (4.79d)$$

4.3.4 Summary

According to (4.9) the multiple scattering can be evaluated from the single-scattering law, taking into account the experimental geometry by means of transmission factors like H_2 and H_3. Moreover, when the scattering law takes the form (4.45), it is possible to separate, in the evaluation of the multiple-scattered fluxes, the integrals over the orientations of the different momentum transfers (i.e. the geometrical aspect of the problem) from the integral over the energy exchanges (i.e. the time aspect). Under these conditions, the higher orders of scattering

can be expressed in a form analogous to (4.45), introducing coefficients B_{ij} and C_{ijk} which stand for generalised second- and third-order structure factors, respectively. These can be evaluated independently of the knowledge of the jump probabilities. Therefore the total scattering function (4.7), after folding with the instrument resolution function, can be refined directly to the experimental data, to obtain the relevant characteristic times.

In most cases, the amplitude of the coefficients B_{ij} and C_{ijk}, when compared with first-order structure factors A_i, permits their evaluation for the particular value $Q^0 = Q(\phi, \omega = 0)$. If this zero order approximation is not sufficient (i.e. if the experimental spectra recorded at constant angle have to be analysed up to very large energy transfers, or if a very precise study of their shape has to be performed), use can be made of the Taylor expansion (4.63). Even in that situation, the number of coefficients to be evaluated remains small enough to carry out the multiple scattering corrections in this way, rather than performing the numerical integral given by (4.9).

We conclude this section with a remark concerning the expansion of the total scattering function according to the various scattering processes. Each of the scattering orders is partly similar to the preceding orders. Indeed, the second-scattering function involves lorentzian and Dirac delta functions which already appear in the single-scattering expression (s_{EE}, s_{IE} and s_{EI}), while the third-scattering function involves both those of first order (s_{EEI}, s_{EIE} and s_{EEE}) and of second order (s_{EII}, s_{IEI} and s_{IIE}). Moreover, for each order, an additional contribution exists, for which the lorentzian function widths are linear combinations of those of lower order (s_{II} and s_{III} for second and third scattering, respectively). Therefore, the more the order of scattering increases, the more the scattering function broadens. That aspect will be examined in the following example.

4.4 Examples of the Application of the Quasielastic Approximation

Let us return to the scattering law related to CH_3-reorientational jumps among three orientations (see equation (4.44)). In figure 4.12 the second scattering intensity has been expanded into the different scattering processes. Clearly, the curve labelled $s_{EI} + s_{IE}$, which results from the combination of the elastic–quasielastic type, has a shape and a width at half-maximum very similar to those of the single-scattering intensity. Conversely, the width of the curve labelled s_{II} and corresponding to two quasielastic processes is roughly wider by a factor of two. The final wavevector transfer in figure 4.12 is $Q = 0.92\ \text{Å}^{-1}$. For the three-site jump model under consideration, we are dealing with a rather important

contribution of the purely elastic part in the scattering law, according to the EISF (see (4.44))

$$a_0(Q) = \tfrac{1}{3}[1 + j_0(Qr\sqrt{3})]. \tag{4.80}$$

Therefore, the second-order quasielastic structure factors $B_{01}(Q)$ and $B_{10}(Q)$, evaluated from (4.47) with

$$A_0(Q) = a_0(Q) \exp(-Q^2 \langle u^2 \rangle) \tag{4.81a}$$

$$A_1(Q) = a_1(Q) \exp(-Q^2 \langle u^2 \rangle) = (1 - a_0(Q)) \exp(-Q^2 \langle u^2 \rangle) \tag{4.81b}$$

have larger values than the structure factor $B_{11}(Q)$ given by (4.70). (see figure 4.13). Consequently, at least in this Q-range, the resulting width of the quasielastic part of the second scattering is nearly equal to the width of the quasielastic part of the single-scattering.

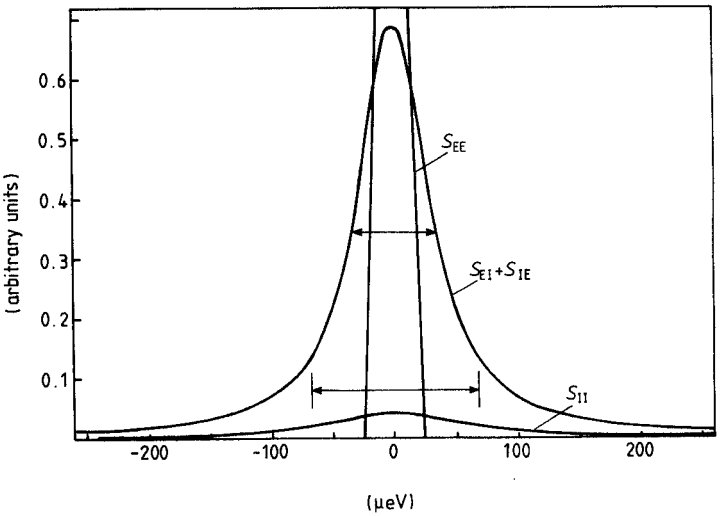

Figure 4.12 Expansion of second scattering into different scattering processes. The sample is a powder of trimethyloxosulphonium iodide (Bée *et al* 1985a).

In figure 4.13 some other features of the generalised structure factors are also evidenced.

(i) The structure factors for second scattering $B_{ij}(Q)$, as well as those for upper orders of scattering, are slowly varying with Q.

(ii) Their values at $Q = 0$ are different from zero. Thus they are responsible for a quasielastic contribution in the spectra recorded at small scattering angles, and, even though their values are rather small,

they are nevertheless larger than that of the first-order coefficient $a_1(Q)$ in that Q-range, and their contribution is predominating.

(iii) The ratio of $B_{00}(Q)$ to the sum of all the $B_{ij}(Q)$ differs radically from $a_1(Q)$. It is a characteristic feature of multiple scattering to change the apparent EISF noticeably.

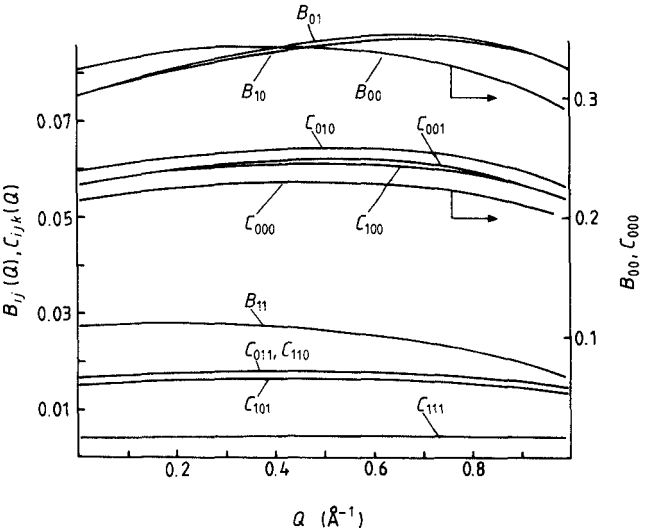

Figure 4.13 Variation as a function of Q of the generalised structure factors $B_{ij}(Q)$ and $C_{ijk}(Q)$ for second- and third-order scattering, respectively. The sample is a powder of trimethylsulphoxonium iodide (Bée *et al* 1985a).

In figure 4.14 are reported experimental EISF values extracted from the spectra obtained from a measurement with triethylenediamine (Bée *et al* 1985b). The full curve is the theoretical EISF predicted by the first-order scattering law. Clearly, large deviations exist in the range of small momentum transfers. All the models describing rotational motions lead to an EISF equal to 1 at $Q = 0$. Here a limiting value of 0.72 is found experimentally. These deviations were attributed to the existence of an important amount of multiple scattering, as suggested by the small transmission coefficient ($T = 0.8$). Multiple scattering corrections were performed by the method described here, up to the third order of scattering. The broken curve in figure 4.14 illustrates the resulting apparent EISF, i.e. the ratio of the elastic to the total scattering when the multiple scattering is included. The agreement with experimental values is remarkable, especially bearing in mind that the transmission coefficient is the single experimental data which was introduced in the evaluation.

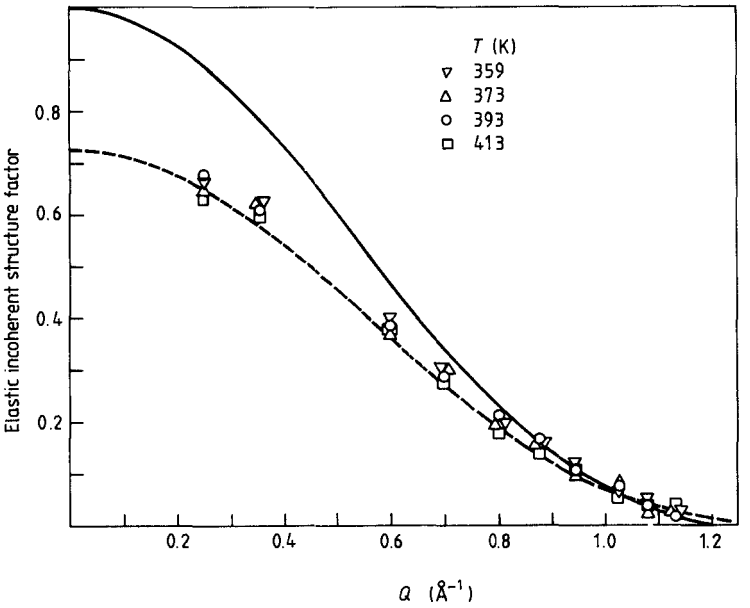

Figure 4.14 Experimental values of the ratio of purely elastic to quasielastic scattering obtained from an IQNS measurement with triethylenediamine (Bée *et al* 1985b). The full curve is the theoretical EISF when taking into account single scattering only. The broken curve is the EISF when considering also the multiple scattering.

In figure 4.15 some typical spectra have been reported. The multiple scattering contribution is indicated, and the elastic intensity has been separated from the quasielastic intensity. The broken curves represent the part of the multiple scattering involving more than one quasielastic process (i.e. s_{II}, s_{EII}, s_{IEI}, s_{IIE} and s_{III}). This is shown to produce a large broadening of the signal and to constitute a nearly flat background underlying the spectra. The other part of the multiple scattering quasielastic intensity has roughly the same width as the first order quasielastic part.

Finally, we shall try to give some answer to the question of the accuracy and validity of the physical parameters refined to experimental data not corrected for multiple scattering effects, where these are known to be significant. The insight into the nature of multiple scattering effects in quasielastic experiments that we have just given can be summarised in three points:

(i) the true first-order EISF is not respected in the total scattering.

(ii) a part of the multiple scattering has nearly the same width as the first-order scattering.

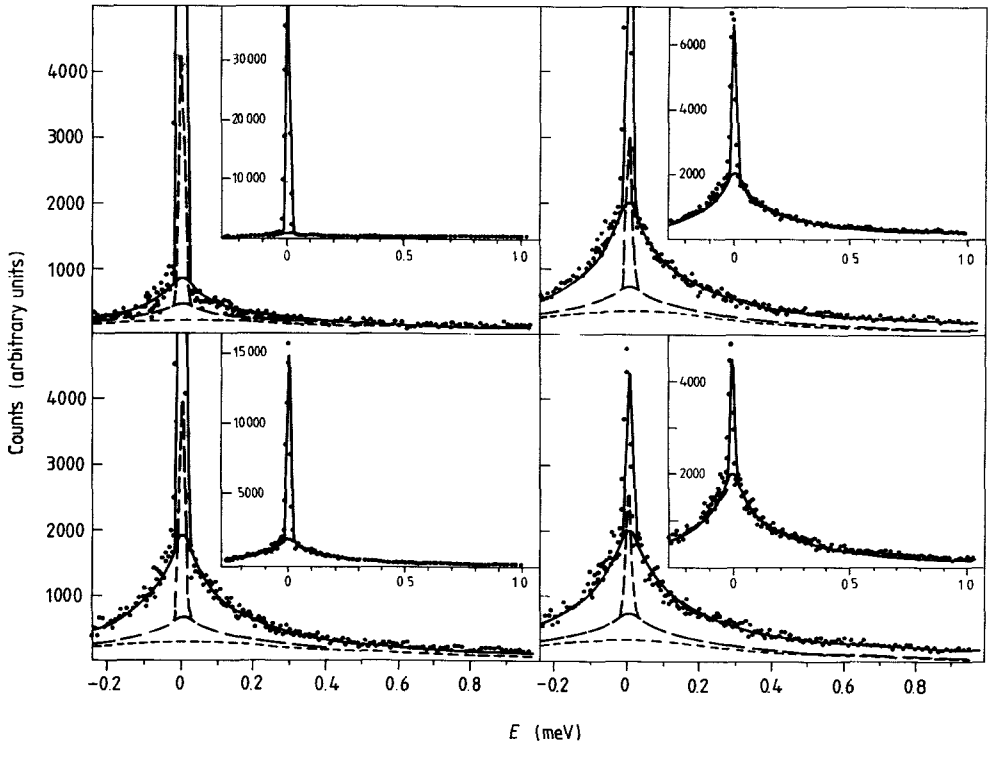

Figure 4.15 IQNS energy spectra for triethylenediamine (Bée *et al* 1985b). The multiple scattering contribution has been indicated. The purely elastic contribution is separated into both total and multiple scattering. The broken curves represent the part of the intensity involving more than one quasielastic process.

(iii) the rest of the multiple scattering is much wider and, especially when the third scattering contribution is also significant, it can be considered as a sort of flat background underlying the spectra.

Now there are two cases to be distinguished:

(i) If the model for describing the dynamical behaviour under test is unknown and has to be determined from experimental data, use cannot be made of the experimental EISF.

(ii) On the other hand, if the model is unambiguous, and if only values of the relevant characteristic times are sought, refinements of the model to experimental data can be envisaged, providing that the amount of elastic scattering is controlled by a weight parameter and allowed to vary from the value predicted by the model. However, even in that case, the widest part of the spectra due to the succession of quasielastic processes will have to be taken into account. The simplest way to account for it is to introduce a flat background parameter and to refine it.

In figure 4.16 we report on the comparison which was made of the values of the correlation time associated with the uniaxial rotation of the molecule about its symmetry axis. These were obtained in three different ways (Bée *et al* 1980a):

(a) by taking into account the multiple scattering.

(b) without accounting for the multiple scattering, but introducing a weight parameter for the elastic part and a flat background as explained in (ii).

(c) as in (b) but with a weight parameter for the elastic part only, and no flat background.

Method (a) leads to the correct values of the correlation time. Method (b) accounts for the intensity in the wings of the spectra by the background parameter and consequently, yields a value of the characteristic time slower than in reality. Conversely, in method (c) the widest components in the quasielastic part have to be taken into account by the first-order scattering law and the resulting correlation time is too fast. However, whilst the deviations between the characteristic times determined from these three methods are rather small (less than 10%), it must be emphasised that the model which was refined, involved only one correlation time, and was unambiguous. Often, we are dealing with more complicated systems, where IQNS is used precisely to distinguish between several kinds of reorientations and where two or even more characteristic times are involved. Refinement of experimenal data with a non-negligible amount of multiple scattering becomes intractable. Besides, in order to correctly describe the wings of the spectra, the widths of the lorentzian functions with the weakest weight in the first-order

scattering law (i.e. associated to the smallest structure factors) tend to become artificially large, yielding final values of the correlation times which are largely erroneous.

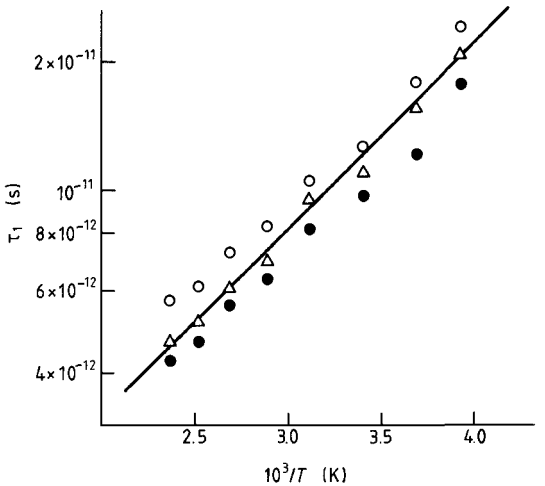

Figure 4.16 Jump rate in cyanoadamantane as a function of the inverse of the temperature (Bée *et al* 1980a). The triangles correspond to the values obtained after multiple scattering corrections have been performed. The circles indicate the values obtained without these corrections. Open (full) symbols indicate that a flat background (no flat background) was introduced in the refinements.

4.5 Monte Carlo Simulation Techniques

4.5.1 Description

Typically, a simple Monte Carlo simulation consists in sampling a succession of events for a neutron and in following its history. More precisely, the incident beam is assumed to be uniform and the point at which the neutron enters the specimen, with incident momentum $\boldsymbol{k}_0$, is first sampled. Then are sampled successively:

(a) the position of the first even along the direction of the neutron velocity, which is compared with the distance to the external surface of the specimen;

(b) the nature of this event, i.e. a scattering or an absorption; in the latter case, the history of another neutron is started;

(c) providing that the event is a scattering process, the value of the

energy exchange $\hbar\omega$ and the wavevector transfer $\boldsymbol{Q}$, from the scattering law $S(\boldsymbol{Q}, \omega)$.

A further event is next considered by returning to point (a). This series of loops ends:

(i) in point (a) if the scattering event would occur outside the sample. In that case the event does not take place and the neutron is added to the spectrum of the suitable detector according to its final trajectory. Furthermore, it is classified according to its final energy (and also its number of collisions).

(ii) in point (b) where its history ends in the case of an absorption process.

By considering the histories of a large number of incident neutrons, it is possible to obtain, for each detector of the instrument, the neutron fluxes corresponding to one, two, . . . etc successive scatterings. This method is very expensive in computing time because many neutrons either (i) are not scattered within the sample or (ii) are absorbed in the sample before or after scattering or (iii) are scattered into a solid angle which does not correspond to a detector. Therefore, major economy in time can be made by forcing the neutron (i) to experience relevant events and (ii) to travel along useful trajectories leading to detectors. After that a correction is made for this constraint by assigning a suitable statistical weight to this neutron history.

Figure 4.17 illustrates a simplified flow-chart diagram of the program DISCUS (Johnson 1974). The original version enables calculation of the ratio of once-scattered to twice-scattered neutrons, for any sample for which the scattering law is of the form $S(|\boldsymbol{Q}|, \omega)$. It can be easily modified to account for further orders of scattering (R.E. Lechner, private communication). Other Monte Carlo codes have also to be mentioned.

Furthermore, the sample is very often surrounded by a container which contributes to single and multiple scattering and which further attenuates the beam. Container scattering contributes significantly to the measured cross section in experiments where, for instance, the container is made of a refractory metal, for high temperature measurements, or else where it is thick, for high pressure experiments. Analytical expressions for these corrections are given in the Appendix at the end of this chapter, for simple geometries. A modified version of the original program MSC written by Bischoff (1970), was developed by Copley (1974), with the provision for a container surrounding the sample. This program MSCAT, in addition to other improvements, allows any combination of elastic coherent scattering, elastic incoherent scattering and inelastic scattering in the specimen and/or in the container. The program was extended to treat the case of slab geometry (Copley 1975a)

and also of a target consisting of multiple cylinders with axes normal to the scattering plane or, conversely, in the scattering plane (Copley 1975b).

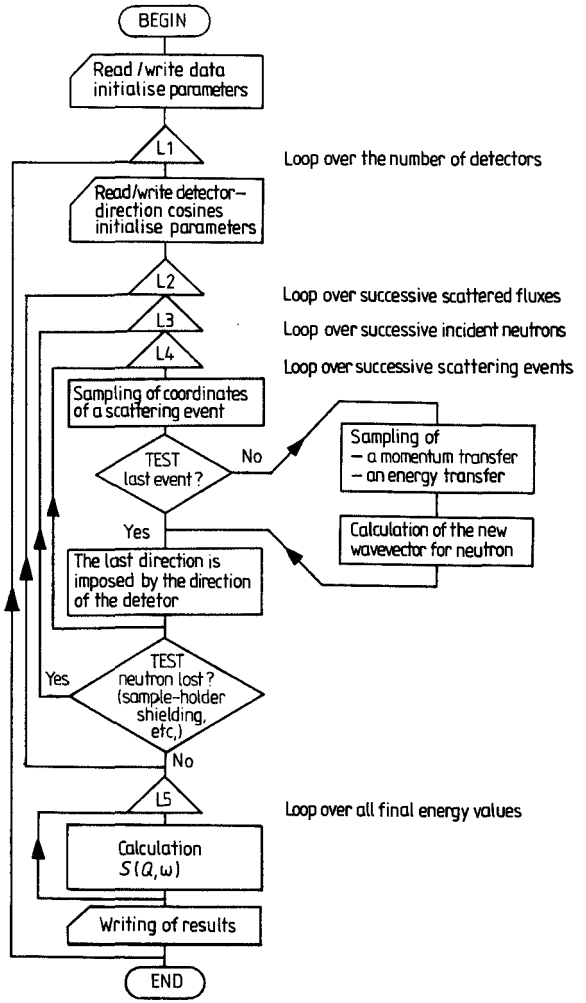

Figure 4.17 Flow chart diagram (simplified) for the program DISCUS (Johnson 1974).

4.5.2 Comparison with Sears' analytical method

The chosen example refers to a study of water dynamics in silica gels

(Ramsay *et al* 1985). Under the assumption that there is no coupling between the rotational and translational motions of the water molecules, the scattering law can be expanded into the convolution product:

$$S(Q, \omega) = \exp\{-Q^2\langle u^2\rangle\}\ [S^{\mathrm{R}}(Q, \omega) \otimes S^{\mathrm{T}}(Q, \omega)] \qquad (4.82)$$

where $\langle u^2\rangle$ is the mean-square vibrational amplitude while $S^{\mathrm{R}}(Q, \omega)$ and $S^{\mathrm{T}}(Q, \omega)$ refer to the scattering laws describing the rotational and translational motions of the water molecules, respectively. From the translational part arises a quasielastic term,

$$S^{\mathrm{T}}(Q, \omega) = \frac{1}{\pi} \frac{\gamma(Q)}{\omega^2 + \gamma^2(Q)} \qquad (4.83)$$

which is a lorentzian function of the energy transfer whose Q-dependent width is given, in the case of a random-diffusion jump model, by (Egelstaff 1967)

$$\gamma(Q) = \frac{DQ^2}{\omega^2 + \tau_0 DQ^2}. \qquad (4.84)$$

Here τ_0 is the mean residence time and D the translational constant.

Conversely, the rotational motion of the water molecules is essentially localised and the corresponding scattering law (in the framework of the isotropic rotational model (Sears 1966)), involves a purely elastic term and a quasielastic part

$$S^{\mathrm{R}}(Q, \omega) = j_0^2(Qr)\delta(\omega) + \sum_{l=1}^{\infty} (2l + 1) j_l^2(Qr) \cdot \frac{1}{\pi} \frac{l(l + 1)D_{\mathrm{R}}}{\omega^2 + l^2(l + 1)^2 \mathrm{D}_{\mathrm{R}}^2}. \qquad (4.85)$$

Here r stands for the water-molecule radius, $j_l(x)$ is a Bessel function and D_{R} is the rotational diffusion constant. It is noteworthy that the widths of the lorentzian functions occurring in (4.85) do not depend on Q. However, owing to the Q-dependence of the translational part (4.83), the integrals over Ω_1 and ω_1 occurring in (4.54) cannot be performed separately. Therefore, multiple scattering corrections were carried out by a Monte Carlo method, using the program DISCUS (Johnson 1974). At the same time, the second-scattering flux was evaluated from the general expressions derived by Sears (4.9). The ratio of the single scattering over the total scattering obtained from both methods is reported in figure 4.18, for several values of the scattering angle. Clearly, the agreement between the two results is satisfactory, and consequently, the validity of both methods is confirmed. We shall mention that the Monte Carlo technique was still faster than the integral evaluation by roughly a factor of 2, even taking account of several successive calculations to avoid systematic errors in the statistics.

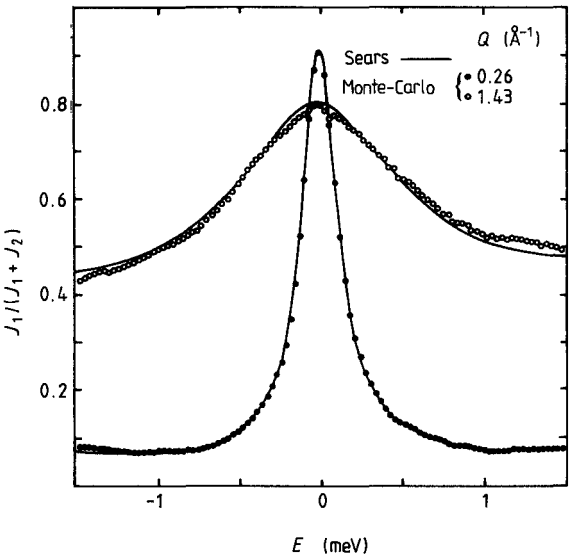

Figure 4.18 Ratio of the single over total scattering from water in silica gels (Ramsay *et al* 1985). Values obtained from a Monte-Carlo simulation (circles) are compared with the results of the evaluation according to Sears' calculations (full curves).

4.5.3 Conclusion

Monte Carlo methods are reliable methods for making multiple-scattering corrections. With modern computers, they become relatively fast. They are applicable to a large variety of geometries and it is realistic to conceive the use of these methods to investigate the effects of experimental errors such as miscentring of the sample or the influence of the instrument technical characteristics: the angular divergence of the incident beam, the incident beam intensity profile or the size of the detectors. Anyway everything can be simulated, but to the detriment of computing time.

Appendix: Evaluation of the Attenuation Corrections for Single Scattering From Samples Confined Within Containers

The samples analysed by the neutron scattering technique are usually contained in a sample holder. Then experimentally measured spectra have to be corrected not only for the effects of the absorption and self-shielding of the specimen itself but also for the scattering and the

absorption effects of the container. This correction cannot be performed by simply subtracting from the sample + container spectrum, the container spectrum obtained by a 'background measurement' of the scattering from the container alone. Besides, the experimental spectrum measured from the sample in the can I^{S+C}_{S+C} is the sum of the scattering from the sample in the presence of the can, I^{S}_{S+C}, and from the can in the presence of the sample, I^{C}_{S+C}

$$I^{S+C}_{S+C} = I^{S}_{S+C} + I^{C}_{S+C}. \tag{4.A.1}$$

Let us denote by I^S the theoretically scattered intensity from the sample if there were no absorption or self-shielding of the primary and scattered fluxes, neither from the sample itself nor from the container. Therefore I^S is the relevant quantity to be compared with the scattering law

$$I^{S}_{S+C} = A^{S}_{S+C} I^{S} \tag{4.A.2}$$

where A^{S}_{S+C} is an attenuation coefficient to be determined for each scattering angle and for each final energy value of the neutron. Similarly, we denote by I^C the theoretical intensity which would be scattered from the container, if there were no attenuation

$$I^{C}_{S+C} = A^{C}_{S+C} I^{C}. \tag{4.A.3}$$

Here A^{C}_{S+C} is the attenuation of the intensity scattered by the can, when the sample is inside the can. From the experiment with the can alone, another intensity I^{C}_{C} is measured

$$I^{C}_{C} = A^{C}_{C} I^{C} \tag{4.A.4}$$

where A^{C}_{C} is the attenuation due to the can alone. Combining (4.A.1), (4.A.2), (4.A.3) and (4.A.4) the theoretical scattering from the sample can be obtained

$$I^{S} = \frac{1}{A^{S}_{S+C}} \left(I^{S}_{S+C} - \frac{A^{C}_{S+C}}{A^{C}_{C}} I^{C}_{C} \right). \tag{4.A.5}$$

Therefore, we are led to the evaluation of three attenuation coefficients A^{S}_{S+C}, A^{C}_{S+C} and A^{C}_{C}, which depend on the nature of the specimen and of the can (i.e. on their absorption and scattering cross sections) and also on their geometrical shape, and on their orientation with respect to the incident neutron beam. These calculations have to be performed for each scattering angle and for all the values of the energy transfer.

Before dealing with the evaluation of these coefficients for simple-geometry cases, it is noteworthy that (4.A.5) is based on the assumption of a single scattering of the neutron, either by the container or by the sample. This equation also holds for multiple scattering if cross effects (e.g. a first scattering from the sample followed by another from the can) can be neglected.

A.1 Infinite slab geometry

We consider the case of an infinite plane specimen, with thickness d, which is itself enclosed between the two plane walls of a container, each of them with thickness c and also with infinite lateral extent (figure 4.A.1). The total scattering cross sections per volume unit are denoted by $\Sigma^S(\boldsymbol{k})$ and $\Sigma^C(\boldsymbol{k})$, respectively.

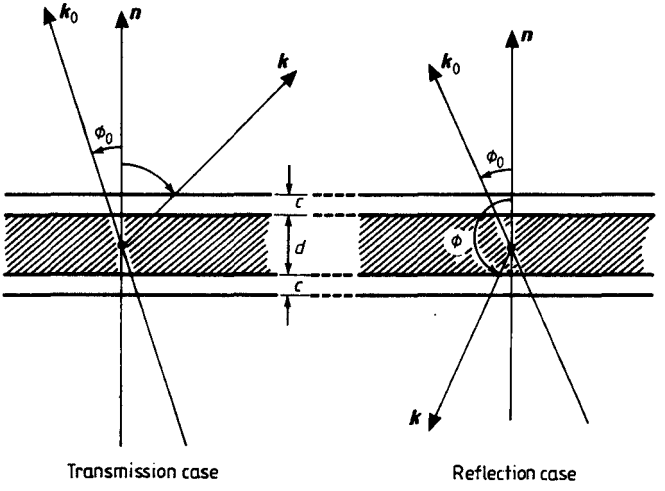

Figure 4.A.1 Single scattering from a flat sample confined between two walls.

In the experiment with the container alone, the total thickness is $2c$ and the attenuation coefficient A_C^C is given by (4.13).

$$A_C^C = H_1(2\alpha_0^C, 2\alpha^C) = \exp(-2|\alpha_0^C| - 2|\alpha^C|)u(2\alpha^C - 2\alpha_0^C) \quad (4.A.6)$$

with

$$\alpha^C = \frac{\Sigma^C(\boldsymbol{k})c}{2\cos\phi} \qquad \alpha_0^C = \frac{\Sigma^C(\boldsymbol{k}_0)c}{2\cos\phi}. \quad (4.A.7)$$

Similarly the attenuation coefficient for the scattering arising from the specimen resulting from absorption and self-shielding due to the sample itself is

$$H_1(\alpha_0^S\alpha^S) = \exp(-|\alpha_0^S| - |\alpha^S|)u(\alpha^S - \alpha_0^S) \quad (4.A.8)$$

with

$$\alpha^S = \frac{\Sigma^S(\boldsymbol{k})d}{2\cos\phi} \qquad \alpha_0^S = \frac{\Sigma^S(\boldsymbol{k}_0)d}{2\cos\phi_0}. \quad (4.A.9)$$

In the presence of the can, the incident beam is attenuated by the first wall and the scattered beam by the second wall. Therefore

$$A^{S}_{S+C} = \exp(-2|\alpha^{C}_{0}|)H_1(\alpha^{S}_{0}\alpha^{S}) \exp(-2|\alpha^{C}|). \quad (4.A.10)$$

Let us denote by $I^{C/2}$ the theoretical intensity which would be scattered by a half-container if there were no absorption nor self-shielding. The flux scattered by the first wall is attenuated by the sample and the second wall, while the incoming flux on the second wall has been attenuated by the first wall and by the sample. Then the flux scattered by the container, in the presence of the sample is

$$I^{C}_{S+C} = I^{C/2}H_1(\alpha^{C}_{0}\alpha^{C}) [\exp(-2|\alpha^{S} + \alpha^{C}|) + \exp(-2|\alpha^{S}_{0} + \alpha^{C}_{0}|)] \quad (4.A.11)$$

with

$$I^{C} = 2I^{C/2} \quad (4.A.12)$$

$$A^{C}_{S+C} = \tfrac{1}{2}H_1(\alpha^{C}_{0}\alpha^{C}) [\exp(-2|\alpha^{S} + \alpha^{C}|) + \exp(-2|\alpha^{S}_{0} + \alpha^{C}_{0}|)]. \quad (4.A.13)$$

In the reflection geometry, the first wall attenuates both the incident beam on the specimen and the scattered beam from this latter. Therefore the expression for A^{S}_{S+C} is still given by

$$A^{S}_{S+C} = \exp(-2|\alpha^{C}_{0}|)H_1(\alpha^{S}_{0}\alpha^{S}) \exp(-2|\alpha^{C}|). \quad (4.A.14)$$

Furthermore, the scattered flux from the first wall is not attenuated further while the first wall and the sample attenuate both the incident beam on the second wall and the scattered flux from it. The coefficients A^{C}_{S+C} and A^{C}_{C} are given by

$$A^{C}_{C} = H_1(\alpha^{C}_{0}\alpha^{C}) [1 + \exp(-|\alpha^{C}_{0} + \alpha^{C}|)] \quad (4.A.15)$$

and

$$A^{C}_{S+C} = H_1(\alpha^{C}_{0}\alpha^{C}) [1 + \exp(-2|\alpha^{C}_{0} + \alpha^{C}|) \exp(-2|\alpha^{S}_{0} + \alpha^{S}|)]. \quad (4.A.16)$$

Similar expressions were found by Dianoux *et al* (1975) in their analysis of data from t.o.f. experiments.

A.2 Cylindrical samples

When the sample takes the shape of a cylinder confined within a cylindrical container of radii R_1 and R_2, the corrections cannot be performed analytically. These reduce to the evaluation of the three attenuation factors (Paalman and Pings 1962, Poncet 1976, Poncet 1977a)

$$A^{C}_{C} = \frac{1}{\pi(R_2^2 - R_1^2)} \int_{R_1}^{R_2} r\,dr \int_{0}^{2\pi} d\beta \exp(-\Sigma^{C}(\boldsymbol{k}_0)l^{C}_{0} - \Sigma^{C}(\boldsymbol{k})l^{C}) \quad (4.A.17)$$

$$A^{C}_{S+C} = \frac{1}{\pi(R_2^2 - R_1^2)} \int_{R_1}^{R_2} r\,dr \int_0^{2\pi} d\beta \exp(-\Sigma^C(\boldsymbol{k}_0) l_0^C - \Sigma^S(\boldsymbol{k}_0) l_0^S - \Sigma^S(\boldsymbol{k}) l^S - \Sigma^C(\boldsymbol{k}) l^C) \tag{4.A.18}$$

$$A^{S}_{S+C} = \frac{1}{\pi R_1^2} \int_0^{R_1} r\,dr \int_0^{2\pi} d\beta \exp(-\Sigma^C(\boldsymbol{k}_0) l_0^C - \Sigma^S(\boldsymbol{k}_0) l_0^S - \Sigma^C(\boldsymbol{k}) l^S - \Sigma^C(\boldsymbol{k}) l^C) \tag{4.A.19}$$

for each scattering angle. The path lengths l_0^C, l^C, l_0^S, l^S occurring in (4.A.17), (4.A.18), (4.A.19) are defined in figure 4.A.2. They depend on the position of the point (r, β) where the scattering occurs, and on the scattering angles. The index 0 refers to the distance travelled before reaching the point (r, β). The linear attenuation coefficients $\Sigma^S(\boldsymbol{k}_0)$, $\Sigma^S(\boldsymbol{k})$, $\Sigma^C(\boldsymbol{k}_0)$ and $\Sigma^C(\boldsymbol{k})$ are defined according to (4.16).

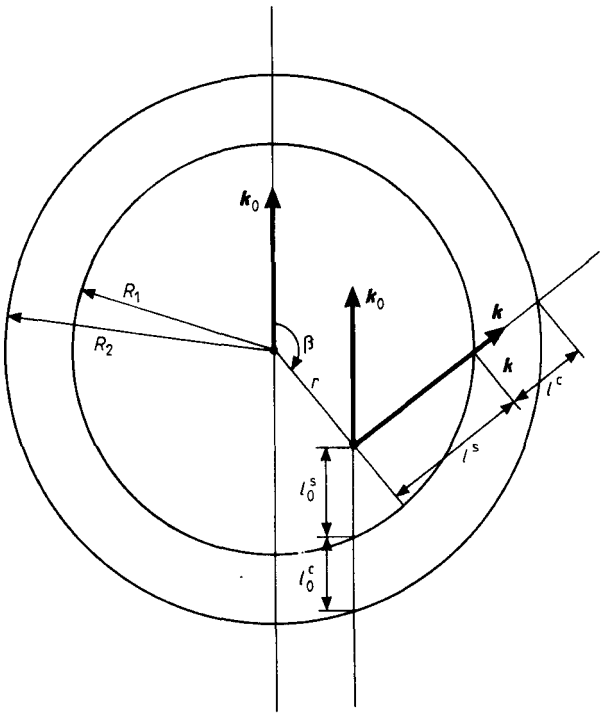

Figure 4.A.2 Single scattering from a cylindrical sample confined between two coaxial cylinders.

These calculations have been extended to the case of samples confined within two coaxial cylinders (Poncet 1977b, Poncet 1978a) and also to partly irradiated samples (Poncet 1978b).

Chapter 5 Long-Range Translational Diffusion

Long-range diffusion motions are associated with transport phenomena. Their understanding is of major interest in the field of applied research, for instance when dealing with the problem of hydrogen diffusion in metals or displacements of ions in solid electrolytes. The quasielastic neutron scattering technique, in conjunction with NMR, provides information on the spatial and temporal aspects of the elementary mechanisms of diffusion.

In a liquid, in the presence of a macroscopic gradient of concentration, a flux of atoms occurs, taking a direction in order to reduce the concentration gradient, and proportional to it: the constant of proportionality is denoted D. The concentration fluctuations in a volume element $d\boldsymbol{r}$ at $\boldsymbol{r}$ is given by $D\nabla^2 G_s$ and is equal to the time rate of change of concentration

$$D\nabla^2 G_s(\boldsymbol{r}, \tau) = \frac{\partial}{\partial t} G_s(\boldsymbol{r}, \tau) \tag{5.1}$$

This equation is known as Fick's law. It was derived by assuming that the liquid behaves like a macroscopic continuum. The translational Brownian motion provides a description on the microscopic scale, by calculating the joint probability density for the positions and velocities of the constituent particles. The relation between the diffusion coefficient D of a Brownian particle and the viscous friction constant, η, was early pointed out by Einstein (1905)

$$D = \frac{k_B T}{m\eta} \tag{5.2}$$

where m is the particle mass, T the temperature, and k_B the Boltzmann constant.

Kubo (1966) showed that the Brownian motion is described by the simplest example of the Langevin equation

$$\frac{d\boldsymbol{v}}{dt} = \eta \boldsymbol{v} + \frac{1}{m} f(t) \tag{5.3}$$

which is nothing other than a formulation of Newton's second law with the assumption that the force acting on the particle is the sum of a retarding force proportional to its velocity, $\boldsymbol{v}$, and a random force $f(t)$ due to collisions with the surrounding particles. Equation (5.3) will be discussed in detail in chapter 7. Using the Langevin equation, it is possible to derive a Fokker–Planck equation for the distribution function of position and velocity. Kubo demonstrated also that the mobility $\mu = |m\eta|^{-1}$ is the response function of the system and is related to the fluctuations of the velocity, i.e.:

$$\mu = \frac{1}{m\eta} = \frac{D}{k_B T} = \frac{1}{k_B T} \int_0^\infty \langle \boldsymbol{v}(0)\boldsymbol{v}(t) \rangle \, dt. \tag{5.4}$$

Equation (5.4) is a manifestation of the fluctuation dissipation theorem.

Equation (5.1) yields a very simple neutron scattering law where the broadening of the spectra varies as a function of the momentum transfer, $\boldsymbol{Q}$, according to the well-known DQ^2 law. Actually, it turns out that this continuous stochastic motion can describe the diffusional motion only in the case of very weak interparticle interactions and very small random displacements. An excellent example is provided by liquid argon (Dasannacharya and Rao 1965).

Deviations from Fick's law arise when the strength of the interparticle interactions increases. The damping term in the Langevin equation, introduced to take into account such effects, completely neglects the structure of the liquid. De Gennes (1967) reviewed neutron data about motions in normal liquids and pointed out that, for the larger Q-values, the major effects were related to the existence of two characteristic times: the jump time τ_J during which the particle diffuses and the residence time τ_0 during which, it remains in the immediate vicinity of any point $\boldsymbol{r}$, about which it undergoes oscillatory motions. This was first observed in the case of water by Brockhouse (1958) and Singwi and Sjölander (1960).

The jump-diffusion model was developed by Chudley and Elliott (1961) and later Egelstaff (1967). This formalism was originally introduced to describe deviation from Fick's law for structured liquids. Then, it was extended to hydrogen diffusion in metals. It corresponds to the case when the jump time τ_J is negligible as compared to the residence time τ_0. The original formalism of Chudley and Elliott deals with an

atom diffusing by jumps to nearest neighbour sites on a Bravais lattice. Improvements of this model were performed later by considering non-equivalent sites located on a non-Bravais lattice, namely tetrahedral and octahedral sites in a bcc lattice (Rowe *et al* 1971). Recently a model was developed in the case of particles jumping between sites on different sublattices, each of which may have a different residence time (Anderson *et al* 1984). Gissler and Stumpf (1973) considered the case of higher hydrogen concentrations, and took into account interactions between diffusing particles.

The jump models lead to scattering laws in which the quasielastic broadening at large Q value noticeably deviates from the DQ^2 law. However, at small Q values, i.e. so far as long distances are considered, the details of the elementary jump processes are no longer observed and all these scattering laws reduce to Fick's law. Therefore, whatever the model, the diffusion coefficient D is deduced from the width (h.w.h.m. $\Delta\omega = DQ^2$) of the energy distribution of the neutrons at low Q values.

5.1 The Continuous Diffusion Model

5.1.1 Einstein's random walk theory

The most simple motion occurring in a bath of particles in very low interactions is the Brownian motion, discovered by Brown in 1827 and quantitatively described by Einstein in 1905 (figure 5.1).

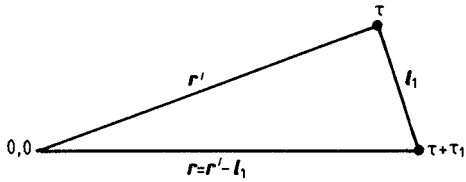

Figure 5.1 Illustration of the random-walk model.

In Brownian motion, the basic idea is that the particles move under the influence of the forces arising from the collisions between them. Between two collisions one particle moves along a straight line. After a collision it goes in another random direction, independent of the previous one: the particle has forgotten its previous history. The requirement of a 'loss of memory' between two steps allows the minimum length and time involved in the motion to be defined.

Let us denote by $G_s(\boldsymbol{r}, t)$ the probability for a particle to be at $\boldsymbol{r}$ at

the time t, independently of its previous history and especially of the number of collisions that it has experienced. We also introduce $P(\boldsymbol{l}, \tau)$, the probability of a particle travelling along $\boldsymbol{l}$, during the time τ, after a collision located at $\boldsymbol{l} = 0$. Clearly, because the collisions between the particles are frequent, both $\boldsymbol{l}$ and τ are small and, in any case, much smaller than $\boldsymbol{r}$ and t, respectively. The probability of finding the particle at $\boldsymbol{r}$ at time $t + \tau$ is thus related to the probability of finding it at the neighbouring points $\boldsymbol{r} - \boldsymbol{l}$ at the previous time t, according to

$$G_s(\boldsymbol{r}, t + \tau) = \int_v G(\boldsymbol{r} - \boldsymbol{l}, t) P(\boldsymbol{l}, \tau)\, \mathrm{d}\boldsymbol{l} \tag{5.5}$$

where the integral runs over all the space. Because $\boldsymbol{l}$ and τ have been introduced as small quantities, the left-hand side of (5.5) may be expanded about τ and the right-hand side about $\boldsymbol{r}$, leading to

$$G_s(\boldsymbol{r}, t + \tau) = G_s(\boldsymbol{r}, t) + \tau \frac{\partial}{\partial t} G_s(\boldsymbol{r}, t) + \ldots \tag{5.6a}$$

and

$$\int_v G_s(\boldsymbol{r} - \boldsymbol{l}, \tau) P(\boldsymbol{l}, \tau)\, \mathrm{d}\boldsymbol{l} = \int_v P(\boldsymbol{l}, \tau)\, \mathrm{d}\boldsymbol{l}$$
$$\times \left[G_s(\boldsymbol{r}, t) - \boldsymbol{l} \cdot \nabla G_s(\boldsymbol{r}, t) + \frac{1}{2} \sum_{i=1}^{3} \sum_{j=1}^{3} l_i l_j \frac{\partial^2 G_s(\boldsymbol{r}, t)}{\partial x_i \partial x_j} + \ldots \right] \tag{5.6b}$$

where l_1, l_2 and l_3 are the components of $\boldsymbol{l}$ and x_1, x_2, x_3 those of $\boldsymbol{r}$. The integral of $P(\boldsymbol{l}, \tau)$ over space is unity and the first terms in both expansions are equal and cancel together. Moreover, $P(\boldsymbol{l}, \tau)$ being isotropic, the second term on the r.h.s. of (5.6b) vanishes, and also the crossed terms in $l_i l_j$ if $i \neq j$. Neglecting higher order terms, (5.6) yields

$$\tau \frac{\partial G_s(\boldsymbol{r}, t)}{\partial t} = \int_v \sum_{i=1}^{3} l_i^2 \frac{\partial^2 G_s}{\partial x_i^2} P(\boldsymbol{l}, \tau)\, \mathrm{d}\boldsymbol{l}. \tag{5.7}$$

Because $P(\boldsymbol{l}, \tau)$ is isotropic

$$\langle l_i^2(\tau) \rangle = \int_v l_i^2 P(\boldsymbol{l}, \tau)\, \mathrm{d}\boldsymbol{l} \tag{5.8}$$

$$= \frac{1}{3} \langle l^2(\tau) \rangle \tag{5.9}$$

where

$$\langle l^2(\tau) \rangle = \langle l_1^2(\tau) \rangle + \langle l_2^2(\tau) \rangle + \langle l_3^2(\tau) \rangle \tag{5.10}$$

is the mean square displacement between τ. One gets

$$\tau \frac{\partial G_s(\boldsymbol{r}, t)}{\partial t} = \frac{\langle l^2(\tau) \rangle}{6} \nabla^2 G_s(\boldsymbol{r}, t) \tag{5.11}$$

which is Fick's law (5.1). A solution of (5.11) can be obtained,

providing that it can be shown that the ratio $\langle l(\tau)^2\rangle/6\tau$ is independent of τ and could be specified by any pair of values of $\langle l(\tau)^2\rangle$ and τ. Let us consider p successive diffusion steps $\boldsymbol{l}_n(\tau)$, $n = 1, 2, \ldots, p$.

$$\boldsymbol{l}(p\tau) = \sum_{n=1}^{p} \boldsymbol{l}_n(\tau) \tag{5.12}$$

$$\langle|\boldsymbol{l}(p\tau)|^2\rangle = \langle|\sum_{n=1}^{p} \boldsymbol{l}_n(\tau)|\rangle \tag{5.13}$$

$$= \langle\sum_{n=1}^{p} l_n^2(\tau)\rangle + \langle\sum_{n\neq m}\sum \boldsymbol{l}_n(\tau)\boldsymbol{l}_m(\tau)\rangle. \tag{5.14}$$

If the successive steps are uncorrelated, clearly

$$\langle \boldsymbol{l}_n(\tau)\boldsymbol{l}_m(\tau)\rangle = 0 \tag{5.15}$$

and

$$\langle|\boldsymbol{l}(p\tau)|^2\rangle = p\langle|\boldsymbol{l}(\tau)|^2\rangle. \tag{5.16}$$

Therefore the ratio $\langle l(p\tau)^2\rangle/6p\tau$ is independent of the number of steps. It is generally named as the 'diffusion constant', D, and obtained from the smallest values $\langle l^2\rangle$ and τ for which the condition of loss of memory is satisfied

$$D = \frac{\langle l^2\rangle}{6\tau}. \tag{5.17}$$

Equation (5.17) is Einstein's relation. It is another expression of Fick's law.

5.1.2 Solution of the diffusion equation

The solution of the equation (5.11) must fulfil the following conditions. At initial time, the particle is assumed to be located at the origin of coordinates

$$G_s(\boldsymbol{r}, 0) = \delta(\boldsymbol{r}). \tag{5.18}$$

Furthermore, at any time t, when integrating over all space

$$\int G_s(\boldsymbol{r}, t)\, \mathrm{d}\boldsymbol{r} = 1. \tag{5.19}$$

A solution can be found, with expression

$$G_s(\boldsymbol{r}, t) = (4\pi Dt)^{-3/2} \exp(-r^2/4Dt). \tag{5.20}$$

We point out that

$$\langle r^2\rangle = \int |\boldsymbol{r}|^2 G_s(\boldsymbol{r}, t)\, \mathrm{d}\boldsymbol{r} = 6Dt \tag{5.21}$$

in agreement with equation (5.8). Fourier transformations in both $\boldsymbol{Q}$

space and time of (5.20) lead successively to the intermediate scattering function

$$I_{\text{inc}}(\boldsymbol{Q}, t) = \int G_s(\boldsymbol{r}, t) \exp(-i\boldsymbol{Q}\cdot\boldsymbol{r})\, d\boldsymbol{r} \tag{5.22a}$$

$$= \exp(-DQ^2t) \tag{5.22b}$$

and to the scattering law

$$S_{\text{inc}}(\boldsymbol{Q}, \omega) = \frac{1}{\pi} \cdot \frac{DQ^2}{\omega^2 + (DQ^2)^2}. \tag{5.23}$$

The energy spectrum of the scattered neutrons exhibits the shape of a lorentzian function whose half-width at half-maximum increases with the momentum transfer according to a DQ^2 law (figure 5.2). Thus incoherent neutron scattering provides a rather direct determination of the diffusion coefficient, but measurements must be restricted to small Q values and small energy transfer, as already discussed in the introduction to this chapter.

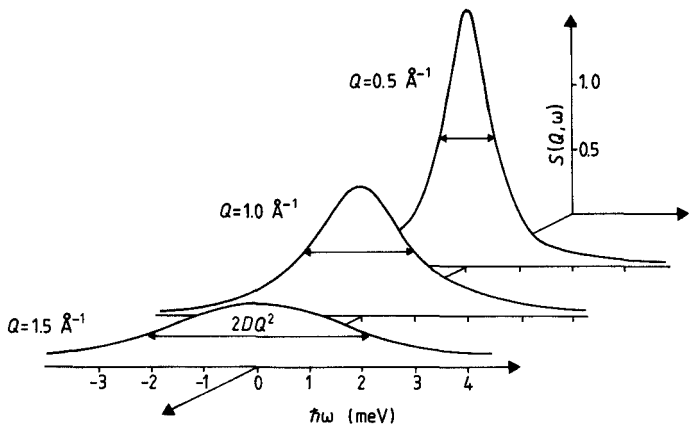

Figure 5.2 Scattering law corresponding to the continuous diffusion model.

Examples of purely stochastic diffusive motions are rare. Nevertheless, such a situation is encountered in the case of the liquid phase of argon that we are going to examine now.

5.1.3 Diffusive motion in liquid argon

Argon is probably the simplest liquid to understand theoretically. Studies in the gas and solid phases led to the knowledge of the

interatomic potential. The liquid phase was investigated by neutron scattering by Dasannacharya and Rao (1965). In particular, the width of the self-correlation function $G_{inc}(r, t)$, deduced from the measured $S_{inc}(Q, \omega)$, was found to follow the Q-dependence predicted by Fick's law, suggesting that in liquid argon the diffusion mechanism was a simple process, unlike that in other liquids (molten metals or water).

However, argon is not a purely incoherent scatterer ($\sigma_{coh} = 2.4$ barns, $\sigma_{inc} = 0.27$ barns). The partial differential scattering cross section of neutrons is the sum of the incoherent differential cross section:

$$\left(\frac{\partial^2\sigma}{\partial\omega\partial\Omega}\right)_{inc} = \frac{\sigma_{inc}}{4\pi N} \cdot \frac{k}{k_0} \cdot S_{inc}(\boldsymbol{Q}, \omega) \tag{5.24a}$$

and of the coherent differential cross section:

$$\left(\frac{\partial^2\sigma}{\partial\omega\partial\Omega}\right)_{coh} = \frac{\sigma_{coh}}{4\pi N} \cdot \frac{k}{k_0} \cdot S(\boldsymbol{Q}, \omega). \tag{5.24b}$$

$S_{inc}(\boldsymbol{Q}, \omega)$ and $S(\boldsymbol{Q}, \omega)$, i.e. the scattering functions for incoherent and coherent scattering, are connected to the Van Hove correlation functions $G_{inc}(r, t)$ (the self-correlation function) and $G(r, t)$ (the pair-correlation function) by time and space Fourier transformation

$$G_{inc}(r, t) = \left(\frac{1}{2\pi}\right)^3 \int S_{inc}(\boldsymbol{Q}, \omega) \exp[-i(\boldsymbol{Q}\cdot\boldsymbol{r} - \omega t)]\, d\boldsymbol{Q}\, d\omega \tag{5.25a}$$

$$G(r, t) = \left(\frac{1}{2\pi}\right)^3 \int S(\boldsymbol{Q}, \omega) \exp[-i(\boldsymbol{Q}\cdot\boldsymbol{r} - \omega t)]\, d\boldsymbol{Q}\, d\omega. \tag{5.25b}$$

As already shown in chapter 2, $G_{inc}(r, t)$ represents the probability of finding an atom at the position r at time t if it was at the origin at time $t = 0$. $G(r, t)$ represents the probability of finding any atom at r at time t, given there was an atom at the origin at time zero. Therefore $G(r, t)$ includes $G_{inc}(r, t)$ and it is more convenient to write

$$G(r, t) = G_s(r, t) + G_d(r, t) \tag{5.26}$$

where the subscripts 's' and 'd' refer to the terms 'self' and 'distinct', respectively. Clearly, $G_s(r, t)$ is identical to $G_{inc}(r, t)$. $G_d(r, t)$ represents the probability, given an atom at the origin at $t = 0$, of finding a different atom at the position r at a later time t.

Liquid argon provides an interesting example where $G_s(r, t)$ and $G_d(r, t)$ can be separated. Indeed $S_{inc}(\boldsymbol{Q}, \omega)$ and $S(\boldsymbol{Q}, \omega)$ predominate at different Q ranges, as illustrated by the diffraction pattern in figure (5.3). At small Q values, the scattered intensity remains nearly constant and can be considered as almost completely incoherent. Conversely, when the modulus of the momentum transfer becomes larger than $1.6\,\text{Å}^{-1}$, a large maximum appears in the scattered intensity, originating from coherent effects. Figure 5.4 represents the scattering function for

liquid argon, plotted as a function of the momentum transfer and of the energy transfer. The broken line at $Q = 0$ and $Q = 2\ \text{Å}^{-1}$ indicates the resolution function of the spectrometer. It turns out that the broadening of the spectra vanishes at $Q = 0$ and increases with Q. Simultaneously, from $Q = 0$ to $Q = 1.6\ \text{Å}^{-1}$, the overall intensity of the spectra (convoluted with the experimental resolution) remains constant, in accordance with the incoherent nature of the scattering. For higher values of the momentum transfer, coherent effects are responsible for the strong increase in the intensity around $Q = 2.0\ \text{Å}^{-1}$. Moreover the presence of coherent scattering leads to oscillations of the width of the spectra with respect to the DQ^2 law (figure 5.5), which, conversely, is followed when incoherent scattering predominates ($Q < 1.6\ \text{Å}^{-1}$).

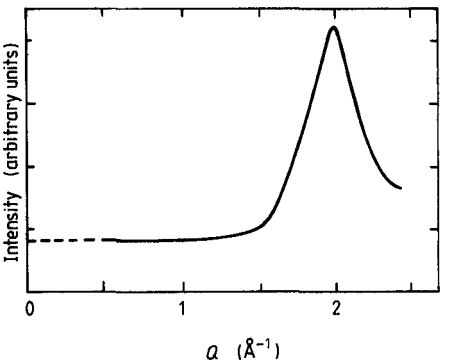

Figure 5.3 Diffraction pattern of liquid agron obtained with a wavelength of 4 Å (Dasannacharya and Rao 1965).

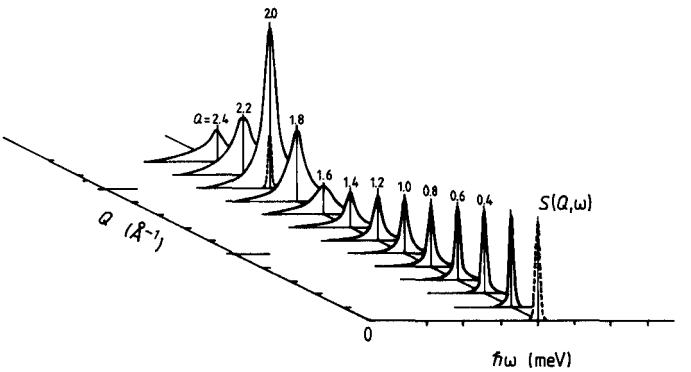

Figure 5.4 The scattered intensity for liquid argon plotted as a function of wavevector transfer Q and energy transfer $\hbar\omega$ (the dotted line represents the resolution function).

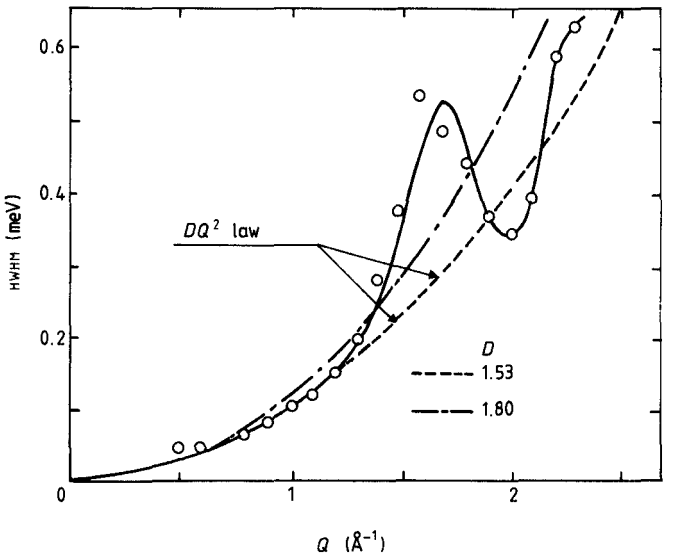

Figure 5.5 Half-width at half-maximum of the spectrum of liquid argon plotted as a function of Q. The diffusion constant D is expressed in units of 10^{-5} cm^2 s^{-1}. The maximum of width at exactly 2 Å^{-1} is predicted by de Gennes and known as 'de Gennes narrowing', in the case of coherent diffusion.

5.2 The Jump-Diffusion Model

In the case of Brownian motion, the jump length $|l|$ of the diffusing particle is assumed to be small compared to the distance $|r|$ of this particle from the origin, or compared to any relevant distance between two positions at two well-separated times: in other words, the diffusion is assumed to occur via infinitely small, elementary jumps. This description leads to a linear variation of the broadening as a function of Q^2. As long as we are concerned with small Q values, the exact mechanisms of the diffusion are not revealed and Fick's law is fulfilled. Actually, at large values of the momentum transfer, the continuous diffusion model appears no more true: the evaluation of the scattering law requires a more precise description of the details of the elementary diffusive steps.

Chudley and Elliott (1961) evaluated the scattering law for a simple model in which the liquid was assumed to have an appreciable short-range order. It turns out that their description deals with a liquid in a quasicrystalline form and that it found many applications in the case of atoms diffusing in lattices.

This model is based on the following hypotheses. For a time interval

τ, an atom remains on a given site, vibrating about a centre of equilibrium, building up a thermal cloud. After this time, the atom moves rapidly to another site, in a negligible jump-time. The length of the jump vector between these two sites, $|\boldsymbol{l}|$, is assumed to be much larger than the dimensions of the thermal cloud.

5.2.1 The Chudley–Elliott model

The calculations are usually derived under the hypothesis that the equilibrium sites for the particles are located over a Bravais lattice. Simplifications occur when it is assumed that the allowed jumps are restricted to being towards nearest neighbours only. The rate equation for the probability $P(\boldsymbol{r}, t)$ of finding an atom on a site at a distance $\boldsymbol{r}$ from an arbitrarily chosen origin is

$$\frac{\partial}{\partial t} P(\boldsymbol{r}, t) = \frac{1}{n\tau} \sum_{l_i} [P(\boldsymbol{r} + \boldsymbol{l}_i, t) - P(\boldsymbol{r}, t)] \tag{5.27}$$

where the sum runs over the set of n vectors $\boldsymbol{l}_i$ connecting a site to its nearest neighbours. Because all sites are equivalent, the set of nearest neighbours is identical for all of them. Moreover, in (5.27), the jump rate, τ^{-1}, is assumed to be the same for all neighbours, whatever the jump direction.

The self-correlation function, $G_{\text{inc}}(\boldsymbol{r}, t)$, is the probability of finding the atom at $\boldsymbol{r}$ at the time t, after averaging over all possible starting positions. Clearly, all initial sites are equivalent and

$$G_{\text{inc}}(\boldsymbol{r}, t) \equiv P(\boldsymbol{r}, t). \tag{5.28}$$

Introducing this identity in (5.27), a space-Fourier transformation yields the rate equation for the intermediate function $I_{\text{inc}}(\boldsymbol{Q}, t)$:

$$\frac{\partial}{\partial t} \int \exp(\mathrm{i}\boldsymbol{Q}\cdot\boldsymbol{r}) G_{\text{inc}}(\boldsymbol{r}, t)\, \mathrm{d}\boldsymbol{r}$$

$$= \frac{1}{n\tau} \sum_{l_i} \left[\int \exp(\mathrm{i}\boldsymbol{Q}\cdot\boldsymbol{r}) G_{\text{inc}}(\boldsymbol{r} + \boldsymbol{l}_i, t)\, \mathrm{d}\boldsymbol{r} - \int \exp(\mathrm{i}\boldsymbol{Q}\cdot\boldsymbol{r}) G_{\text{inc}}(\boldsymbol{r}, t)\, \mathrm{d}\boldsymbol{r} \right] \tag{5.29}$$

$$\frac{\partial}{\partial t} \mathrm{I}_{\text{inc}}(\boldsymbol{Q}, t) = \frac{1}{n\tau} \sum_{l_i} I_{\text{inc}}(\boldsymbol{Q}, t)[\exp(-\mathrm{i}\boldsymbol{Q}\cdot\boldsymbol{l}_i) - 1] \tag{5.30}$$

with the boundary condition, corresponding to $G_s(\boldsymbol{r}, 0) = \delta(\boldsymbol{r})$:

$$I_{\text{inc}}(\boldsymbol{Q}, 0) = 1. \tag{5.31}$$

Denoting by

$$\Delta\omega(\boldsymbol{Q}) = \frac{1}{n\tau} \sum_{l_i} [1 - \exp(-\mathrm{i}\boldsymbol{Q}\cdot\boldsymbol{l}_i)] \tag{5.32}$$

the solution is straighforward, yielding:

$$I_{\text{inc}}(\boldsymbol{Q}, t) = I_{\text{inc}}(\boldsymbol{Q}, 0) \exp[-\Delta\omega(\boldsymbol{Q})t]. \tag{5.33}$$

The scattering law is the time-Fourier transform of $I(\boldsymbol{Q}, t)$

$$S_{\text{inc}}(\boldsymbol{Q}, \omega) = \frac{1}{\pi} \frac{\Delta\omega(\boldsymbol{Q})}{[\Delta\omega(\boldsymbol{Q})]^2 + \omega^2} \tag{5.34}$$

which is a lorentzian function, with h.w.h.m. $\Delta\omega(\boldsymbol{Q})$. This width depends on the mean residence time τ, but also on the geometry of the lattice sites. For Bravais lattices, each site is an inversion centre. The distances $\boldsymbol{l}_i$ and $-\boldsymbol{l}_i$ occur equally in (5.32) and we obtain

$$\Delta\omega(\boldsymbol{Q}) = \frac{1}{n\tau}\left[n - 2\sum_{l_i>0} \cos(\boldsymbol{Q}\cdot\boldsymbol{l}_i)\right] \tag{5.35a}$$

$$= \frac{4}{n\tau} \sum_{l_i>0} \sin^2 \frac{\boldsymbol{Q}\cdot\boldsymbol{l}_i}{2} \tag{5.35b}$$

where the sum runs over all the next-neighbouring sites located within one half-space. The width of the quasielastic spectrum is an oscillatory function of the momentum transfer, with nodes at the reciprocal lattice points

$$\boldsymbol{Q} = \frac{2\pi\boldsymbol{l}_i}{|\boldsymbol{l}_i|^2}. \tag{5.36}$$

The case of hydrogen atoms dissolved in palladium provides an example of description of long-range diffusion in terms of the Chudley–Elliott model. Many metals can dissolve hydrogen interstitially. Let us mention, for instance, bcc metals V, Nb, Ta, etc, or fcc metals like Pd. The values of the diffusion constant determined at room temperature are of the same order of magnitude as in liquids (between 10^{-6} cm^2 s^{-1} and 10^{-5} cm^2 s^{-1}) corresponding to jump rates of the order of 10^{11} s^{-1} and 10^{10} s^{-1}, respectively. Many microscopic details of hydrogen diffusion were resolved using the IQNS technique.

In palladium, hydrogen atoms occupy interstitial sites with octahedral symmetry (figure 5.6), and, in the dilute α-phase, hop randomly between the available sites. Around each site there are twelve nearest-neighbouring other sites, in the [110] directions.

From (5.35), the width of the quasielastic line is

$$\Delta\omega(\boldsymbol{Q}) = \frac{1}{3\tau}\left\{\sin^2\left[\frac{(Q_y + Q_z)a}{2\sqrt{2}}\right] + \sin^2\left[\frac{(Q_x + Q_z)a}{2\sqrt{2}}\right] + \sin^2\left[\frac{Q_x + Q_y)a}{2\sqrt{2}}\right]\right. \tag{5.37}$$

where a is the metal lattice parameter and Q_x, Q_y, Q_z the components of the momentum transfer with respect to lattice axes. Figure 5.7 shows

the variations of $\Delta\omega(\boldsymbol{Q})$ as a function of Q for several directions of this scattering vector.

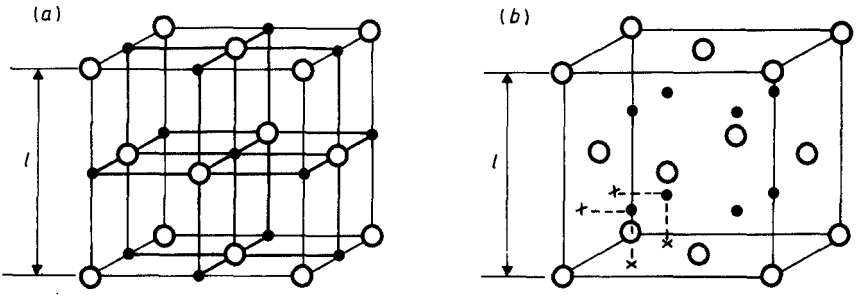

Figure 5.6 The octahedral (a) and tetrahedral (b) sites in a fcc lattice of palladium. Pd atoms are in open circles and sites correspond to full dots. (Reproduced by permission of Springer Verlag.)

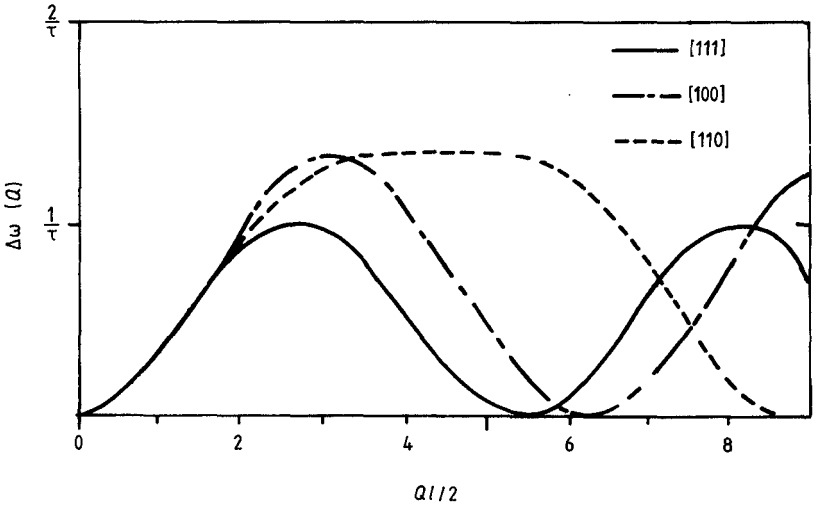

Figure 5.7 H.w.h.m. of the quasi-elastic line for random jumps between octahedral sites in a fcc lattice, for three directions of the momentum transfer vector.

The first experiment on hydrogen diffusion in metals was carried out by Sköld and Nelin using a polycrystalline sample of Pd with small hydrogen concentration (0.02–0.04). In that case (5.32) has to be averaged over all possible directions of the scattering vector. Because all the nearest neighbour sites correspond to the same jump-length l, one gets

$$\Delta\omega(\boldsymbol{Q}) = \frac{1}{4\pi}\int_0^{2\pi} d\varphi \int_0^{\pi} d\theta \sin\theta[1 - \exp(-iQl\cos\theta)] \qquad (5.38)$$

where (θ, φ) are the angular coordinates of $\boldsymbol{Q}$ and where the jump vector $\boldsymbol{l}$ has been taken as Oz-axis. The result is

$$\Delta\omega(Q) = \frac{1}{\tau}\left[1 - \frac{\sin Ql}{Ql}\right]. \qquad (5.39)$$

In figure 5.8 the results of Sköld and Nelin for quasielastic linewidths are illustrated and compared with theoretical variations predicted by the Chudley–Elliott model assuming either jumps between octahedral sites or jumps between tetrahedral sites. Their results were confirmed in a subsequent single crystal experiment by Rowe *et al* (1972) as illustrated in figure 5.9. For scattering vectors $\boldsymbol{Q}$ along the [100] directions, both the model based on diffusion between octahedral sites and the model assuming tetrahedral sites yield the same results. Conversely, the experiment with $\boldsymbol{Q}$ along [110] directions allows the distinction.

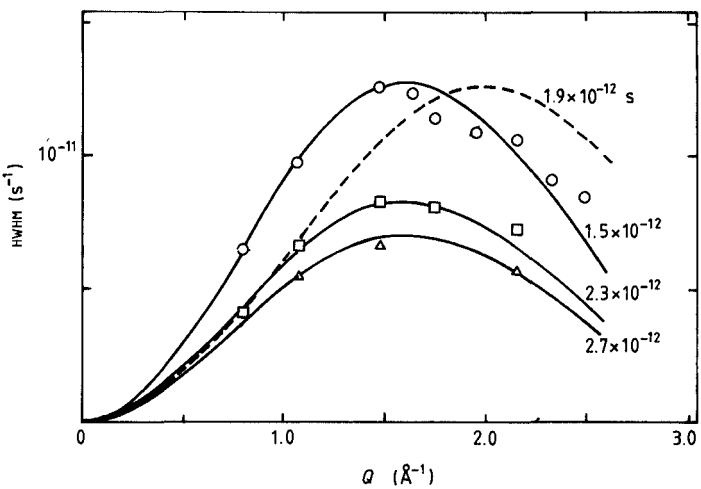

Figure 5.8 H.w.h.m. of the quasielastic lines for neutron scattering from hydrogen in Pd, measured by Sköld and Nelin (1967). The curves correspond to theoretical calculations based on the Chudley–Elliott model assuming jumps between either octahedral (full curves) or tetrahedral (broken curves) sites. Values of τ are given on the curves.

Finally, it is worth pointing out that in the low-Q limit an expansion of (5.39) in terms of Ql, up to third order, gives

$$\Delta\omega(Q) = \frac{Q^2 l^2}{6\tau}. \tag{5.40}$$

We again obtain a DQ^2 variation with a diffusion constant

$$D = \frac{l^2}{6\tau}. \tag{5.41}$$

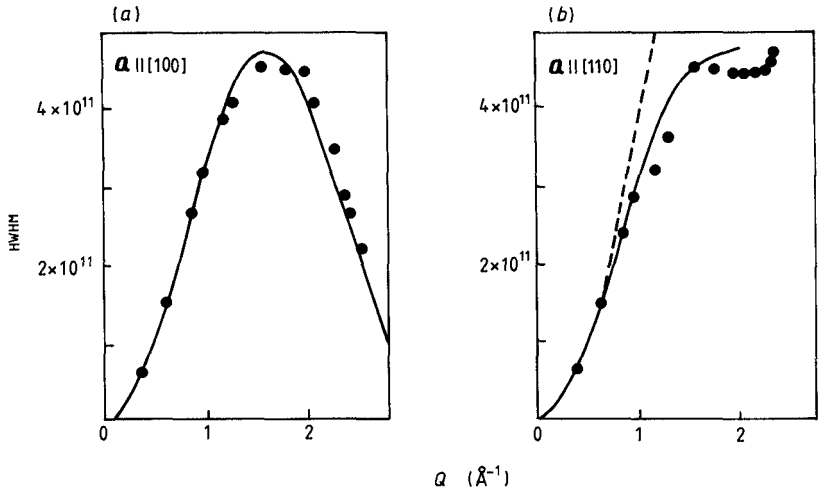

Figure 5.9 H.w.h.m. of the quasielastic lines for neutron scattering from hydrogen in Pd, measured by Rowe *et al* (1972). The lines are calculated from the Chudley–Elliott model, assuming either jumps over octahedral sites (full curves, $\tau = 2.8$ ps) or jumps over tetrahedral sites (broken line, $\tau = 1.4$ ps). In (*a*) both curves are identical.

5.2.2 Diffusive motions in a bcc lattice

Other investigations of hydrogen diffusion were carried out with different bcc metals (e.g. V, Nb and Ta). As in fcc metals, the particle may occupy sites of either tetrahedral or octahedral symmetry (see figure 5.10). But a complication occurs because the sites do not form a Bravais lattice. The extension of the Chudley–Elliott model is due to Rowe *et al* (1972).

Because the sites do not form a Bravais lattice, the m inequivalent sites per primitive unit cell must be labelled. Also, the set of jump vectors for each site will, in general, connect two inequivalent sites. The notation $\boldsymbol{l}_{ijk}$ is introduced, referring to the jump vector which connects the site of local symmetry i to the k^{th} site of local symmetry j. To simplify the calculations, the model is restricted to nearest-neighbour jumps only and a single jump rate τ^{-1} is introduced. In other words, the

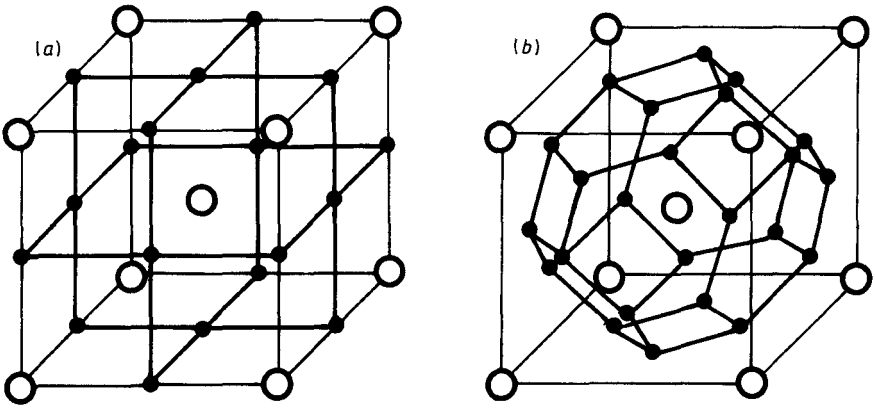

Figure 5.10 The octahedral sites (*a*) and the tetrahedral sites (*b*), in a unit cell of a bcc metal lattice. (From Springer 1972, reproduced by permission of Springer Verlag)

same probability is attributed to all the jumps, even if they occur to different sites with different symmetry. This assumption can be considered as realistic so far as we deal with small concentrations of diffusing species, without interactions between the particles. The probability of finding a hydrogen atom at $\boldsymbol{r}$, on a site with local symmetry i, $P_i(\boldsymbol{r}, t)$ follows an equation analogous to (5.27):

$$\frac{\partial}{\partial t}P_i(\boldsymbol{r}, t) = \frac{1}{n\tau}\sum_{jk}[P_j(\boldsymbol{r} + \boldsymbol{l}_{ijk}, t) - P(\boldsymbol{r}, t)]. \tag{5.42}$$

The sum over j, k runs over all the n nearest-neighbour sites of the site i. The index $i (i = 1, 2, \ldots, m)$ enables a distinction to be made between inequivalent types of sites, and we can write m equations analogous to (5.42) to describe the probability of occupation of each type of site. The probability of finding the atom at $\boldsymbol{r}$, on any kind of site is

$$P(\boldsymbol{r}, t) = \sum_{i=1}^{m} P_i(\boldsymbol{r}, t). \tag{5.43}$$

But $P(\boldsymbol{r}, t)$ is not equivalent to $G_{\text{inc}}(\boldsymbol{r}, t)$. Indeed, as defined in (5.28), $G_{\text{inc}}(\boldsymbol{r}, t)$ is the probability of finding the atom at $\boldsymbol{r}$, averaged over all possible starting sites for this atom, and assuming an equal probability for each type of site. More precisely, if we consider a solution of (5.42) subject to the initial conditions

$$P_i(\boldsymbol{r}, 0) = \delta(\boldsymbol{r}) \qquad \text{if } i = j \tag{5.44a}$$

and

$$P_i(\boldsymbol{r}, 0) = 0 \qquad \text{if } i \neq j \tag{5.44b}$$

we can define the probability if being at $\boldsymbol{r}$ at the time t, on a site with

any local symmetry, given that the atom was on a site of local symmetry j at time zero, $P^j(\boldsymbol{r}, t)$, as

$$P^j(\boldsymbol{r}, t) = \sum_{i=1}^{m} P_i(\boldsymbol{r}, t) \tag{5.45}$$

therefore

$$G_{\text{inc}}(\boldsymbol{r}, t) = \frac{1}{m} \sum_{j=1}^{m} P^j(\boldsymbol{r}, t). \tag{5.46}$$

The set of vectors $\boldsymbol{l}_{ijk}$ connects different unit cells as well as different sites in the cell. Therefore (5.42) corresponds to an infinite set of coupled differential equations which can be resolved by Fourier transformation. Introducing

$$I_i(\boldsymbol{Q}, t) = \int P_i(\boldsymbol{r}, t) \exp(\mathrm{i}\boldsymbol{Q}\cdot\boldsymbol{r})\, \mathrm{d}\boldsymbol{r} \tag{5.47}$$

we get

$$\frac{\partial}{\partial t} I_i(\boldsymbol{Q}, t) = \frac{1}{n\tau} \sum_{jk} [\exp(-\mathrm{i}\boldsymbol{Q}\cdot\boldsymbol{l}_{ijk}) I_j(\boldsymbol{Q}, t) - I_i(Q, t)] \tag{5.48a}$$

$$= \frac{1}{n\tau} \sum_{j} I_j(\boldsymbol{Q}, t) \left\{ \sum_{k} \exp(-\mathrm{i}\boldsymbol{Q}\cdot\boldsymbol{l}_{ijk}) \right\} - \frac{1}{\tau} I_i(Q, t). \tag{5.48b}$$

This set of equations can be written in matrix form, i.e.

$$[A][I] = \frac{\partial}{\partial t} [I] \tag{5.49}$$

where $[A]$ is a $m \times m$ matrix, with elements

$$A_{ij} = \frac{1}{n\tau} \sum_{k} \exp(-i\boldsymbol{Q}\cdot\boldsymbol{l}_{ijk}) - \frac{1}{\tau} \delta_{ij}. \tag{5.50}$$

Similarly, $[I]$ is a column vector, with elements $I_i(\boldsymbol{Q}, t)$ and $i = 1, 2, \ldots, m$.

The differential equations (5.48) or (5.49) are of first order, linear with constant coefficients. Their solutions are subject to boundary conditions, corresponding to the Fourier transformation of equations (5.44a) and (5.44b), namely

$$I_i(\boldsymbol{Q}, 0) = 0 \qquad \text{if } i \neq j \tag{5.51a}$$

$$I_i(\boldsymbol{Q}, 0) = 1 \qquad \text{if } i = j \tag{5.51b}$$

The intermediate function

$$I_{\text{inc}}(\boldsymbol{Q}, t) = \int G_{\text{inc}}(\boldsymbol{r}, t) \exp(\mathrm{i}\boldsymbol{Q}\cdot\boldsymbol{r})\, \mathrm{d}\boldsymbol{r} \tag{5.52}$$

is obtained by taking the average according to the Fourier transformation of (5.45) and (5.46), respectively

$$I^j(Q, t) = \sum_i I_i(Q, t) \tag{5.53}$$

and

$$I_{\text{inc}}(Q, t) = \frac{1}{m} \sum_j I^j(Q, t). \tag{5.54}$$

The solutions of (5.49), obtained from standard methods, are of the form:

$$[I] = \sum_{j=1}^{m} C_j[V_j] \exp(\Delta\omega_j t). \tag{5.55}$$

Here $[V_j]$ is a column vector. It is the eigenvector of $[A]$ related to the j^{th} eigenvalue, $\Delta\omega_j$. The m constants, C_j, are determined from (5.51), (5.53) and (5.54). More precisely, at initial time, (5.55) reduces to

$$[I] = \sum_j C_j[V_j] \tag{5.56a}$$

$$\equiv [V].[C] \tag{5.56b}$$

$[I]$ is a column vector with m elements $I_i(Q, 0)$. $[V]$ is a $m \times m$ matrix, formed with the components V_{ij} of the eigenvectors $[V_j]$. $[C]$ is an m-component vector with elements C_j; thus

$$[C] = [V]^{-1}[I]. \tag{5.57}$$

If the eigenvalues $[V_j]$ are orthonormal

$$[V]^{-1} = [V]^{+} \tag{5.58}$$

with

$$([V]^{+})_{ij} = V^*_{ij}. \tag{5.59}$$

This model was derived by Rowe *et al* (1972) for the calculation of the scattering law for hydrogen diffusion in the bcc lattice of vanadium. Referring to figure (5.10), and denoting by a the lattice parameter, the three octahedral sites within one primitive cell can be labelled

$$(a/2, 0, 0) = 1$$

$$(0, a/2, 0) = 2$$

$$(0, 0, a/2) = 3.$$

The jumps occur from octahedral or tetrahedral sites in one primitive cell towards another neighbouring cell, i.e. $k = 1, 2$. The l_{ijk} values are listed explicitly in table 5.1. Let

$$C_x = \cos(Q_x\, a/2) \tag{5.60a}$$

$$C_y = \cos(Q_y\, a/2) \tag{5.60b}$$

$$C_z = \cos(Q_z\, a/2). \tag{5.60c}$$

Table 5.1 List of the l_{ijk} values

i	j	k	l_{ijk}		
1	2	1	0	0	$a/2$
		2	0	0	$-a/2$
	3	1	0	$a/2$	0
		2	0	$-a/2$	0
2	1	1	0	0	$a/2$
		2	0	0	$-a/2$
	3	1	$a/2$	0	0
		2	$-a/2$	0	0
3	1	1	0	$a/2$	0
		2	0	$-a/2$	0
	2	1	$a/2$	0	0
		2	$-a/2$	0	0

The matrix $[A]$ defined by (5.50) takes the form

$$[A] = \frac{1}{2\tau}\begin{pmatrix} -2 & C_z & C_y \\ C_z & -2 & C_x \\ C_y & C_x & -2 \end{pmatrix}. \tag{5.61}$$

In the particular case of a scattering vector oriented along any [111] direction, i.e. with $Q = (Q/\sqrt{3}, Q\sqrt{3}, Q\sqrt{3})$, this matrix reduces to

$$[A] = \frac{1}{2\tau}\begin{pmatrix} -2 & C & C \\ C & -2 & C \\ C & C & -2 \end{pmatrix} \tag{5.62}$$

where $C = \cos(Qa/2\sqrt{3})$. The intermediate function is:

$$I_{\text{inc}}(\boldsymbol{Q}, t) = \exp\left[-(1 - C)\frac{t}{\tau}\right]. \tag{5.63}$$

One verifies easily that at $Q = 0$

$$I_{\text{inc}}(0, t) = 1. \tag{5.64}$$

Moreover, for small values of Q, the term $(1 - C)$ tends to $Q^2a^2/24$. Therefore,

$$\lim_{Q\to 0} I(\boldsymbol{Q},t) = \exp\left(-\frac{a^2Q^2}{24\tau}t\right). \tag{5.65}$$

Thus, when the scattering vector is oriented along one of the [111] directions, the variation of the broadening of the scattering law as a function of Q follows again a DQ^2 law, in the limit of small momentum transfers. The diffusion constant, D, is expressed in terms of the lattice parameters, a, and of the residence time, τ, according to

$$D = \frac{a^2}{24\tau}. \tag{5.66}$$

For the jumps between tetrahedral sites, the matrix $[A]$ is evaluated in the same way:

$$[A] = \frac{1}{\tau} \begin{pmatrix} -1 & 0 & T_{yz} & \bar{T}_{\bar{y}z} & \bar{T}_{xz} & \bar{T}_{\bar{x}z} \\ 0 & -1 & T_{\bar{y}z} & \bar{T}_{yz} & T_{\bar{x}z} & T_{xz} \\ \bar{T}_{yz} & T_{\bar{y}z} & -1 & 0 & T_{xy} & T_{\bar{x}y} \\ \bar{T}_{\bar{y}z} & T_{yz} & 0 & -1 & \bar{T}_{\bar{x}y} & \bar{T}_{xy} \\ T_{xz} & \bar{T}_{\bar{x}z} & \bar{T}_{xy} & T_{\bar{x}y} & -1 & 0 \\ T_{\bar{x}z} & \bar{T}_{xz} & \bar{T}_{\bar{x}y} & T_{xy} & 0 & -1 \end{pmatrix} \tag{5.67}$$

with the following notation:

$$\begin{aligned} T_{yz} &= \frac{1}{4}\exp[ia(Q_y + Q_z)/4] & T_{\bar{y}z} &= \frac{1}{4}\exp[ia(-Q_y + Q_z)/4] \\ T_{xz} &= \frac{1}{4}\exp[ia(Q_x + Q_z)/4] & T_{\bar{x}z} &= \frac{1}{4}\exp[ia(-Q_x + Q_z)/4] \\ T_{xy} &= \frac{1}{4}\exp[ia(Q_x + Q_y)/4] & T_{\bar{x}y} &= \frac{1}{4}\exp[ia(-Q_x + Q_y)/4] \end{aligned} \tag{5.68}$$

and where $\bar{T}_{\alpha\beta}$ denotes the complex conjugate of $T_{\alpha\beta}$.

The intermediate function, obtained from (5.53) and (5.54) after solution of (5.49) is

$$I_{\text{inc}}(\boldsymbol{Q}, t) = \frac{1}{m}\sum_{j=1}^{m} \left|\sum_i V_{ij}\right|^2 \exp(\Delta\omega_j t) \tag{5.69}$$

where V_{ij} is the ith component of the jth orthonormal eigenvector corresponding to the eigenvalue $\Delta\omega_j$ of the hermitian matrix $[A]$. The Fourier transform of (5.69) leads to the scattering function

$$S_{\text{inc}}(\boldsymbol{Q}, \omega) = \frac{1}{m}\sum_{j=1}^{m} \left|\sum_i V_{ij}\right|^2 \frac{1}{\pi} \cdot \frac{\Delta\omega_j(Q)}{\omega^2 + [\Delta\omega_j(Q)]^2} \tag{5.70}$$

where the Q-dependence of the eigenvalues has been written.

In the particular case of a wavevector transfer oriented along any [100] direction, $\boldsymbol{Q} = (\boldsymbol{Q}, 0, 0)$ and the matrix $[A]$ becomes

$$[A] = \frac{1}{\tau} \begin{pmatrix} -1 & 0 & 0 & 0 & t & t^* \\ 0 & -1 & 0 & 0 & t^* & t \\ 0 & 0 & -1 & 0 & t & t^* \\ 0 & 0 & 0 & -1 & t^* & t \\ t & t^* & t & t^* & -1 & 0 \\ t^* & t & t^* & t & 0 & -1 \end{pmatrix} \tag{5.71}$$

with $t = \frac{1}{4}\exp[i(Qa/4)]$ and where t^* denotes the complex conjugate of

t. However, the behaviour of the eigenvalues of $[A]$ in the low-Q limit is not so straightforward as in the case of octahedral sites.

5.3 Diffusive Motion in Water

Water has been the subject of numerous studies for a long time, and cold neutron scattering has been used for the last thirty years to analyse atomic motions in the liquid phase. As compared with other ordinary liquids, water exhibits many anomalous physical properties. In some aspects, it behaves more like a solid than like a liquid and this behaviour makes it more amenable for mathematical calculations. However, many problems are not yet perfectly resolved and, in particular, the nature of the diffusive motion of the molecules in liquid water is not yet fully understood.

The earliest neutron experiments were performed in the 1950s by Brockhouse (1958), Vineyard (1958), Singwi and Sjölander (1960), Egelstaff (1956) and Cribier and Jacrot (1960). More accurate measurements were recently carried out by Chen *et al* (1982) and Texeira *et al* (1982, 1985) with the high resolution time-of-flight spectrometer available at the Institut Laue–Langevin.

5.3.1 The model of Singwi and Sjölander (1960)

The original model proposed by Bernal and Fowler (1933) and later modified by Lennard-Jones and Pople (1951), described water as a network of linked molecules, each of them being surrounded tetrahedrally by four others, held together by hydrogen bonds, which can more or less bend, according to the temperature. Hydrogen bonds are continuously breaking and reforming, such that, on a slower time-scale, the molecules undergo a diffusion mechanism through large, independent jumps corresponding to their mean distance in the network.

In contrast to this model, it was proposed that liquid water consists of clusters of bonded molecules, mixed with non-bonded fluid. The corresponding diffusion mechanism would then be more complex, water molecules sharing their time between an oscillatory motion and/or free diffusion motion.

Using the expression for the self-diffusion function obtained as a solution of the classical diffusion equation (5.11) Vineyard (1958) calculated the broadening in the continuous case. But measurements performed later by Brockhouse (1959) show that the observed line broadening is somewhat less than that predicted by this simple diffusion theory. It was concluded that this hypothesis does not provide an adequate description of the mechanism of diffusion of water and,

furthermore, that a variety of diffusive motions might occur.

Hugues *et al* (1959) indicated later that their experiments show no evidence of broadening related to diffusive motions, and predicted an experimental broadening smaller at least by a factor of three than the theoretical value of Vineyard. In view of these contradictions, Singwi and Sjölander performed a more theoretical study and proposed the following description of liquid water.

A molecule executes an oscillatory motion for a mean time τ_0. Then it diffuses by continuous motion for a mean time τ_1. This sort of motion is continuously repeated. On the basis of these hypotheses Singwi and Sjölander evaluated the differential scattering cross section for cold neutrons.

To calculate $G_s(\boldsymbol{r}, t)$ they divide the motion into steps numbered 0, 1, 2, ..., $2N$. At initial time $t = 0$, the particle is assumed to oscillate about the origin $\boldsymbol{r} = 0$. At a later time t it could have arrived at the point $\boldsymbol{r}$ after making 0, 1, 2, ..., $2N$ steps. Zero step corresponds to the oscillatory motion, step 1 to the succeeding diffusive motion, step 2 again to oscillatory motion, step 3 to diffusive motion. Then $G_s(\boldsymbol{r}, t)$ is given by an expansion into probabilities related to the different processes

$$G_s(\boldsymbol{r}, t) = \sum_{i=0}^{\infty} F_i(\boldsymbol{r}, t). \tag{5.72}$$

This relation is defined only at positive times. The successive $F_i(\boldsymbol{r}, t)$ are evaluated as follows. Starting from the origin at time $t = 0$, one gets for step 0:

$$F_0(\boldsymbol{r}, t) = g(\boldsymbol{r}, t) \cdot p(t) \tag{5.73}$$

$g(\boldsymbol{r}, t)$ is the probability of finding a particle at the position $\boldsymbol{r}$ at time t, when it is performing an oscillatory motion about an equilibrium position, starting from the origin at initial time $t = 0$. $p(t)$ gives the probability that the particle remains in the same oscillatory motion at a later time t, if it starts from as oscillatory motion at time $t = 0$. Singwi and Sjölander assumed for $p(t)$ the simple form:

$$p(t) = \exp(-t/\tau_0) \tag{5.74}$$

where τ_0 is the lifetime of the oscillatory motion which can be identified with the residence time in the Chudley–Elliott model.

The time τ_0 is much greater than the period of the oscillatory motion and, during this time, the motion of the molecule is very similar to what it is in its solid state. Therefore, the form chosen for $g(\boldsymbol{r}, t)$ is the same as for an atom in a solid. Singwi and Sjölander pointed out that this description would probably be incorrect for liquids other than water. $g(\boldsymbol{r}, t)$ can be calculated rigorously, on the basis of the Debye description of a solid. Starting from the equations (2.194) and (2.195) for the

incoherent scattering function and introducing the Debye density of states (2.199), one gets, after two successive Fourier transformations with respect to energy and momentum

$$g(\boldsymbol{r}, t) = [2\pi\gamma(t)]^{-3/2} \exp\left(-\frac{r^2}{2\gamma(t)}\right) \tag{5.75}$$

where $\gamma(t)$ is the oscillatory width (Vineyard 1958)

$$\gamma(t) = \gamma_\infty\left[1 - \frac{\sin \omega_D t}{\omega_D t}\right] \tag{5.76}$$

ω_D is the characteristic frequency for a harmonic Debye crystal and

$$\gamma_\infty = \langle u^2 \rangle = \frac{3k_B T}{M\omega_D^2} \tag{5.77}$$

is the mean-square amplitude for the vibrating atom.

The probability for step 1 is of the form:

$$F_1(\boldsymbol{r}, t) = -\int_0^t \mathrm{d}t_1 \int \mathrm{d}\boldsymbol{r}_1 q(t - t_1) h(\boldsymbol{r} - \boldsymbol{r}_1, t - t_1) p'(t_1) \cdot g(\boldsymbol{r}_1, t_1). \tag{5.78}$$

Here $h(\boldsymbol{r}, t)$ is the probability of finding a particle at the position $\boldsymbol{r}$ at time t, when it is performing a diffusive motion between two equilibrium positions, starting from the origin at time $t = 0$. $h(\boldsymbol{r}, t)$ is the solution of the usual equation of diffusion (5.11). Like $g(\boldsymbol{r}, t)$, $h(\boldsymbol{r}, t)$ is isotropic, i.e.

$$h(\boldsymbol{r}, t) = h(r, t) = (4\pi D_1 t)^{-3/2} \exp\left(-\frac{r^2}{4D_1 t}\right) \tag{5.79}$$

D_1, the diffusion coefficient, is defined according to $D_1 = \langle l^2 \rangle / 6\tau_1$, where $\langle l^2 \rangle$ is the mean square displacement in the time τ_1 during which the continuous diffusion takes place. $q(t)$ gives the probability that the particle remains in the same state of diffusive motion at a later time (t) when it starts from a state of diffusive motion at time $t = 0$. It is assumed to have the same form as $p(t)$

$$q(t) = \exp(-t/\tau_1). \tag{5.80}$$

The probability that the particle has left its oscillatory state during the time interval between t and $(t + \mathrm{d}t)$ and has gone into a diffusive state is given by the change

$$p'(t)\,\mathrm{d}t = p(t + \mathrm{d}t) - p(t) \tag{5.81}$$

in the value of the probability to remain in the oscillatory motion. Similarly, for step 2, we write:

$$F_2(\boldsymbol{r}, t) = (-1)^2 \int_0^t \mathrm{d}t_2 \int_0^{t_2} \mathrm{d}t_1 \int \mathrm{d}\boldsymbol{r}_2 \int \mathrm{d}\boldsymbol{r}_1\, p(t - t_2) \times g(|\boldsymbol{r} - \boldsymbol{r}_2|, t - t_2) q'(t_2 - t_1) h(|\boldsymbol{r}_2 - \boldsymbol{r}_1|, t_2 - t_1) p'(t_1) \cdot g(r_1, t_1). \tag{5.82}$$

In this expression, another term has been introduced, namely $q'(t)$, which is defined by the difference

$$q'(t)\,\mathrm{d}t = q(t + \mathrm{d}t) - q(t) \tag{5.83}$$

and which represents the probability that the particle has left its diffuse state during the time interval between t and $t + \mathrm{d}t$ and has gone into an oscillatory state.

In a general way, for step $2N$, we have:

$$F_{2N}(\boldsymbol{r}, t) = (-1)^{2N} \int_0^t \mathrm{d}t_{2N} \int_0^{t_{2N}} \mathrm{d}t_{2N-1} \ldots \int_0^{t_2} \mathrm{d}t_1 \int \mathrm{d}\boldsymbol{r}_{2N} \int \mathrm{d}\boldsymbol{r}_{2N-1} \ldots \int \mathrm{d}\boldsymbol{r}_1$$
$$p(t_2 - t_{2N})g(|\boldsymbol{r} - \boldsymbol{r}_{2N}|, t - t_{2N})q'(t_{2N} - t_{2N-1})h(|\boldsymbol{r}_{2N} - \boldsymbol{r}_{2N-1}|, t_{2N} - t_{2N-1})$$
$$\ldots p'(t_1)g(r, t_1). \tag{5.84}$$

By substituting the F_i in (5.66), it is possible to calculate $G_s(\boldsymbol{r}, t)$ and therefrom its time-space-Fourier transform, $S(\boldsymbol{Q}, \omega)$. After making the following change of variables

$$\begin{aligned} t - t_{2N} &= \tau_{2N+1} \\ t_{2N} - t_{2N-1} &= \tau_{2N} \\ &\vdots \\ t_2 - t_1 &= \tau_2 \\ t_1 &= \tau_1 \end{aligned} \tag{5.85}$$

for the time integral, and in a similar way

$$\begin{aligned} \boldsymbol{r} - \boldsymbol{r}_{2N} &= \boldsymbol{\xi}_{2N+1} \\ \boldsymbol{r}_{2N} - \boldsymbol{r}_{2N-1} &= \boldsymbol{\xi}_{2N} \\ \boldsymbol{r}_2 - \boldsymbol{r}_1 &= \boldsymbol{\xi}_2 \\ \boldsymbol{r}_1 &= \boldsymbol{\xi}_1 \end{aligned} \tag{5.86}$$

for the space integrals, the integrals in (5.76) can be factorised, leading to the evaluation of the four following terms:

$$A = \int_0^\infty \mathrm{d}t \int \mathrm{d}\boldsymbol{r} \exp[\mathrm{i}(\boldsymbol{Q}\cdot\boldsymbol{r} - \omega t)]\, p(t)g(\boldsymbol{r}, t)$$
$$= \exp\left[-\frac{1}{2} Q^2\gamma_\infty\right] \frac{\tau_0}{1 + \mathrm{i}\omega\tau_0} \tag{5.87a}$$
$$B = \int_0^\infty \mathrm{d}t \int \mathrm{d}\boldsymbol{r} \exp[\mathrm{i}(\boldsymbol{Q}\cdot\boldsymbol{r} - \omega t)]\, q(t)h(\boldsymbol{r}, t)$$
$$= \tau_1/[1 + Q^2 D_1 \tau_1 + \mathrm{i}\omega\tau_1] \tag{5.87b}$$

$$C = -\int_0^\infty \mathrm{d}t \int_0 \mathrm{d}\boldsymbol{r} \exp[\mathrm{i}(\boldsymbol{Q}\cdot\boldsymbol{r} - \omega t)]\, p'(t) g(\boldsymbol{r}, t)$$

$$= A/\tau_0 \tag{5.87c}$$

$$D = -\int_0^\infty \mathrm{d}t \int \mathrm{d}\boldsymbol{r} \exp[\mathrm{i}(\boldsymbol{Q}\cdot\boldsymbol{r} - \omega t)] q'(t) h(\boldsymbol{r}, t)$$

$$= B/\tau_1. \tag{5.87d}$$

With these notations, we can write:

$$\int_0^\infty \mathrm{d}t \int \mathrm{d}\boldsymbol{r} \exp[\mathrm{i}(\boldsymbol{Q}\cdot\boldsymbol{r} - \omega t)] F_{2N}(\boldsymbol{r}, t) = AC^N D^N \tag{5.88}$$

and

$$\int_0^\infty \mathrm{d}t \int \mathrm{d}\boldsymbol{r} \exp[\mathrm{i}(\boldsymbol{Q}\cdot\boldsymbol{r} - \omega t)] F_{2N+1}(\boldsymbol{r}, t) = BC^{N+1} D^N. \tag{5.89}$$

So that the time- space-Fourier transform of $G_s(\boldsymbol{r}, t)$ is given by

$$\int_0^\infty \mathrm{d}t \int \mathrm{d}\boldsymbol{r} \exp[\mathrm{i}(\boldsymbol{Q}\cdot\boldsymbol{r} - \omega t)] \sum_{N=0}^{\infty} F_N(\boldsymbol{r}, t)$$

$$= A \sum_{N=0}^{\infty} (CD)^N + BC \sum_{N=0}^{\infty} (CD^N) + \ldots \tag{5.90}$$

$$= \frac{A + BC}{1 - CD} + \ldots. \tag{5.91}$$

This expression was derived under the assumption that, at time $t = 0$, all the particles start with an oscillatory motion. Clearly, the same treatment has to be applied, with particles starting their motion as free diffusing particles. The final expression, analogous to (5.91) is

$$\int_0^\infty \mathrm{d}t \int \mathrm{d}\boldsymbol{r} \exp[\mathrm{i}(\boldsymbol{Q}\cdot\boldsymbol{r} - \omega t)] \sum_{N=0}^{\infty} F_N(\boldsymbol{r}, t) = \frac{B + AD}{1 - CD} + \ldots. \tag{5.92}$$

The final scattering law is expressed as the weighted sum of the expressions (5.91) and (5.92), i.e. by taking into account the fractions of particles performing an oscillatory or a diffusive motion

$$S(\boldsymbol{Q}, \omega) = \frac{1}{2\pi} \left\{ \frac{\tau_0}{\tau_1 + \tau_0} \frac{A[1 + B\tau_0^{-1}]}{1 - \dfrac{AB}{\tau_0 \tau_1}} + \frac{\tau_1}{\tau_1 + \tau_0} \frac{B[1 + A\tau_1^{-1}]}{1 - \dfrac{AB}{\tau_0 \tau_1}} \right\} \tag{5.93}$$

where account has been taken of the relations (5.87b) and (5.87d) between the terms A, C and B, D.

Substituting into (5.93) the expression of the Debye–Waller factor in a solid, i.e.

$$2W = \tfrac{1}{2} Q^2 \langle u^2 \rangle = \tfrac{1}{2} Q^2 \gamma_\infty \tag{5.94}$$

together with the values of A, B, C and D, one obtains:

$$S(\boldsymbol{Q}, \omega) = \frac{1}{\pi} \frac{\exp(-2W)\tau_0}{1 + \dfrac{\tau_1}{\tau_0}} \frac{(c + d\omega^2\tau_0^2)b}{b^2 + \omega^2\tau_0^2(f + \omega^2\tau_0^2 g)} \tag{5.95}$$

where

$$b = 1 + Q^2 D_1 \tau_1 - \exp(-2W) \tag{5.96a}$$

$$c = 1 + Q^2 D_1 \tau_1 + 2\frac{\tau_1}{\tau_0} + \left(\frac{\tau_1}{\tau_0}\right)^2 \exp(2W) \tag{5.96b}$$

$$d = \left(\frac{\tau_1}{\tau_0}\right)^2 2W \tag{5.96c}$$

$$f = (1 + Q^2 D_1 \tau_1)^2 + \left(\frac{\tau_1}{\tau_0}\right)^2 + 2\frac{\tau_1}{\tau_0} \exp(-2W) \tag{5.96d}$$

$$g = \left(\frac{\tau_1}{\tau_0}\right)^2. \tag{5.96e}$$

Clearly, the shape of the scattering function differs from a lorentzian. If $\langle \bar{R}^2 \rangle$ is the mean square radius of the thermal cloud developed in the oscillatory motion, the actual diffusion coefficient D, taking into account both the diffusive and oscillatory states, is given by

$$D = \frac{\langle R^2 \rangle + \langle l^2 \rangle}{6(\tau_0 + \tau_1)} \tag{5.97}$$

and differs from the diffusion constant $D_1 = \langle l^2 \rangle / 6\tau_1$ defined in the time τ_1 during which continuous diffusion takes place. Because the radius of the thermal cloud is assumed to be small compared with the mean length of continuous diffusion, $\langle R^2 \rangle \ll \langle l^2 \rangle$,

$$D_1 \tau_1 \simeq D\tau_0 \left(1 + \frac{\tau_1}{\tau_0}\right). \tag{5.98}$$

Let us consider first the limiting case when the time interval during which continuous diffusion occurs is much longer than the time interval of the oscillatory state, i.e. the situation where $\tau_1 \gg \tau_0$. Neglecting τ_1/τ_0 in (5.98), the scattering law (5.95) reduces to

$$S(\boldsymbol{Q}, \omega) = \frac{1}{\pi} \cdot \frac{DQ^2}{\omega^2 + (DQ^2)^2} \tag{5.99}$$

which is the usual scattering law corresponding to Fick's equation. Conversely, if we assume that the particle oscillates for a much longer time than it diffuses, $\tau_1 \ll \tau_0$, and we get:

$$S(\boldsymbol{Q}, \omega) = \exp(-2W) \cdot \frac{\tau_0}{\pi} \cdot \frac{1 - \dfrac{\exp(-2W)}{1 + Q^2 D\tau_0}}{\omega^2\tau_0^2 + \left[1 - \dfrac{\exp(-2W)}{1 + Q^2 D\tau_0}\right]} \tag{5.100}$$

The shape of the quasielastic peak is lorentzian. The h.w.h.m. is given by

$$\Delta\omega = \frac{1}{\tau_0}\left[1 - \frac{\exp(-2W)}{1 + Q^2 D\tau_0}\right] \tag{5.101}$$

with the Debye–Waller term

$$2W = \tfrac{1}{2}Q^2\gamma_\infty \tag{5.102a}$$

$$= \tfrac{1}{2}Q^2\langle R^2\rangle. \tag{5.102b}$$

Also, because $Q^2 D\tau_0 = Q^2\langle l^2\rangle/6$, we have from (5.101) and (5.102)

$$2W = Q^2 D\tau_0 \frac{\langle R^2\rangle}{\langle l^2\rangle} \ll Q^2 D\tau_0. \tag{5.103}$$

In the limit of small momentum transfers, $Q^2 D\tau_0 \ll 1$ and the expression (5.101) of the h.w.h.m. of the quasielastic peak reduces to:

$$\Delta\omega = DQ^2 \tag{5.104}$$

which is the expression of the broadening predicted by the simple diffusion theory. On the contrary, if $Q^2 D\tau_0 \gg 1$, the broadening tends to the asymptotic value

$$\Delta\omega = \frac{1}{\tau_0} \tag{5.105}$$

independent of the momentum transfer.

In figure 5.11, the broadening of the quasielastic peak is plotted as a function of $Q^2 D\tau_0$, for different values of τ_0 and τ_1. It is seen that, at small momentum transfers, all the curves lead to the same broadening. Conversely, at large Q values, the broadening as given by the curves corresponding to $\tau_1 = 0$ is much less than that given by the other curves and clearly tends to the asymptotic value $1/\tau_0$. Another striking feature in figure 5.11 is that, even if the particle spends the same time in its oscillatory states as in its diffusive states, ($\tau_1/\tau_0 = 1$, curve C), the increase of the broadening is less than 20% over that corresponding to the pure oscillatory behaviour ($\tau_1/\tau_0 = 0$).

When Singwi and Sjölander performed their calculations, no spectrometer with sufficient resolution was available to check their results with accuracy. Recently, Texeira *et al* (1982) obtained high-quality quasielastic incoherent scattering data for water in the temperature range extending from room temperature down to −20 °C in the supercooled liquid state, using the time-focusing time-of-flight spectrometer IN6 at the Institut Laue–Langevin.

5.3.2 The dynamics of supercooled water

Texeira *et al* (1982), from the analysis of their IQNS data, identified two

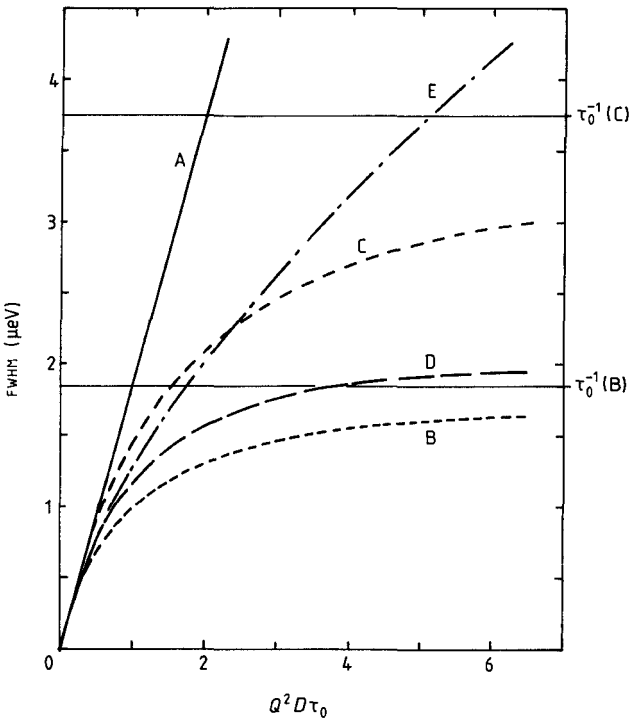

Figure 5.11 Broadening of the quasielastic peak versus $Q^2D\tau_0$ as predicted by the Singwi–Sjölander model. The curve A corresponds to the Fick's law. D is taken equal to 1.85×10^{-5} cm^2 s^{-1}, $\tau_0 = 3.6 \times 10^{-12}$ s. Curves B and C are given by equation (5.101) with $\tau_0 = 3.6 \times 10^{-12}$ s and $\tau_0 = 1.8 \times 10^{-12}$ s, respectively. Curve D is the broadening obtained with $\tau_1 = \tau_0 = 3.6 \times 10^{-12}$ s. Curve E corresponds to $\tau_0 = 1.25 \times 10^{-12}$ s and $\tau_1 = 1.16 \times 10^{-12}$ s (Texeira *et al* 1985, see figure 5.12).

relaxation times on two different time-scales. The shorter time was attributed to the rotation of the groups of water molecules linked by hydrogen bonds about their centre of mass or of individual molecules about the different hydrogen bonds. The longer relaxation time was associated with jump-diffusion. Under the assumption of a complete decoupling between these two motions, the relevant scattering function could be expressed as the convolution product of the scattering laws associated with each motion (see chapter 2).

$$S_{\text{inc}}(Q, \omega) = S^{\text{R}}_{\text{inc}}(Q, \omega) \otimes S^{\text{T}}_{\text{inc}}(Q, \omega) \tag{5.106}$$

where $S^{\text{R}}_{\text{inc}}(Q, \omega)$ and $S^{\text{T}}_{\text{inc}}(Q, \omega)$ denote the rotational and translational scattering function, respectively.

Chen *et al* (1982) pointed out the fact that the rapid completion of hydrogen bonding in supercooled water below 0 °C could be effectively used to separate the two mechanisms and to identify their respective temperature-dependence. Figure 5.12 illustrates the variation of the linewidth as a function of Q^2, for different temperatures of experiment. Clearly, after an initial linear variation, the curves noticeably deviate from Fick's law and tend asymptotically to a constant value $1/\tau_0$, especially at the lowest temperatures. These results tend to confirm the validity of the jump model. But special points, like for instance the temperature-dependence of the residence time τ_0 as a function of the temperature, still require some explanation.

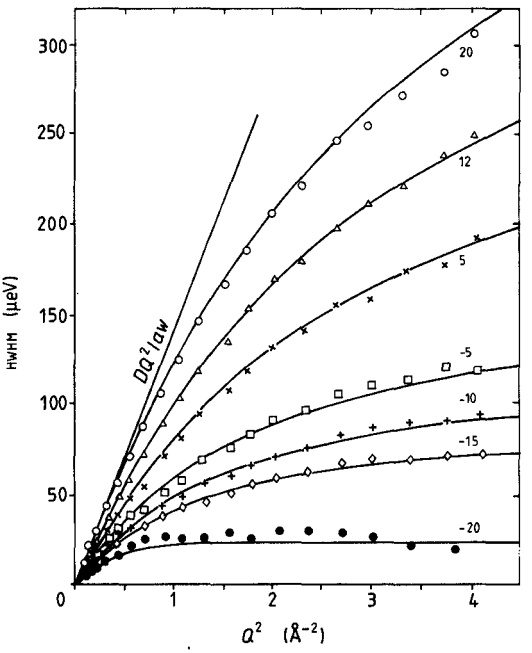

Figure 5.12 Half-width at half-maximum of the translational component of the scattering law for water, as a function of Q^2, measured at different temperatures (given in °C on curves) (Texeira *et al* 1985). The straight line corresponds to the DQ^2 law.

Chapter 6 Molecular Reorientations in Orientationally Disordered Crystals

According to the character of their translational and rotational degrees of freedom, molecular solids are usually classified in three main classes: brittle, liquid and plastic crystals. Brittle crystals are fully ordered, i.e. apart from thermal fluctuations, they exhibit a translational and orientational order of their molecules when passing from one lattice cell to another. Conversely, liquid crystals are orientationally ordered but translationally disordered, and in plastic crystals the orientational order is lost whilst the translational order remains. Simultaneous disorder of both rotational and translational degrees of freedom corresponds to isotropic molecular liquids. In this chapter, we are mainly concerned with the orientationally disordered (plastic) phases.

6.1 Rotational Potential in Plastic Crystals

The essential feature of plastic crystals is that the molecules have their centres of mass well located in space on a crystalline lattice, but their orientations vary from one site to another and change with time. Classically, these phases consist of globular or highly symmetrical molecules. (Timmermans 1938, 1961). Typical examples are norbornane,

adamantane, cyclohexane (Clark *et al* 1974). Molecular reorientations occur among a set of distinguishable equilibrium positions so that the average lattice symmetry is generally high (often cubic or hexagonal). Nonetheless, molecules not very globular in their shape, but with internal degrees of freedom, sometimes evidence a plastically crystalline phase: the bcc phase of succinonitrile $NC(CH_2)_2CN$ is shown to be highly disordered, composed of a temperature-dependent, equilibrium mixture of *cis* and *trans* geometrical isomers. The disorder arises from (i) changes between these forms by 120° rotation of the CH_2CN groups with respect to each other and (ii) rigid rotations of the *trans* molecules about their principal axis (Bée *et al* 1980b, Bée *et al* 1983a). In pivalic acid $(CH_3)_3CCOOH$ (Bée *et al* 1983b) methyl groups, the whole t-butyl group or the carboxylic group may rotate. Although the various molecular conformations occurring may be of fairly low symmetry, the average shape of the molecule due to the internal rotations remains close to spherical and sometimes permits a 'tumbling' motion of the whole molecule. Beyond classical molecular van der Waals-type crystals, there is another important class of polyatomic ions in ionic crystals. For instance, the disorder of the ammonium ion in $NH_4^+Cl^-$ (Töpler *et al* 1978) and that of the trimethylsulphoxonium ion in $(CH_3)_3SO^+I^-$ (Sourisseau *et al* 1985, Bée *et al* 1985a).

With decreasing the temperature, order is usually achieved in several stages, i.e. several orientational phase transitions may be observed with a stepwise reduction of the orientational disorder. Whole-reorientations disappear first, because they mainly depend upon intermolecular forces. Conversely, inner rotations may persist at low temperature. However, it is noteworthy that in low-symmetry, ordered phases, reorientations of chemical groups, or even whole-bodies, can still occur between well-defined, indistinguishable equilibrium positions. For instance the triclinic phase ($T < 278$ K) of pivalic acid (Bée *et al* 1983b) or the low-temperature phase of 1-bromo-adamantane $C_{10}H_{15}Br$ and other 1-adamantyl halides (Virlet *et al* 1983).

Structural, thermodynamic and motional properties of the 'rotator' molecular crystal phases may be understood semi-quantitatively by use of intermolecular potentials. The weak, non-isotropic interactions mainly originate from the weak van der Waals' forces, reflecting both the symmetry of the molecule and that of its surroundings. The radial part of the potential is responsible for the translational order, whilst the angle-dependent part of the potential governs the orientational ordering of the molecules.

The dynamics of disordered crystalline phases is a very active field of research and important progress has been made in recent years. However, the weakness of the intermolecular forces allows large displacements and the dynamics of these crystals cannot be treated in the

harmonic approximation. Moreover, the molecular rotations couple to the translational modes (phonons) which complicates the picture. Considerable work was done on the microscopic approach to the problem (Michel and Kroll 1976, Kroll and Michel 1977, Michel and Naudts 1977, Michel and Naudts 1978, Naudts and Michel 1978, Michel *et al* 1978). From an intermolecular hamiltonian, using Mori's projection operator technique (Mori 1965), coupled dynamical equations for translations and rotations were derived, and transport coefficients were evaluated. The incoherent neutron scattering law for rotational motion of a dumbbell molecule in an octahedral potential was formulated in terms of symmetry adapted functions, the relevant correlation functions being classified according to the irreducible representations (De Raedt and Michel 1979). More recently, the neutron-scattering law was formulated for arbitrary molecular symmetry (Yvinek and Pick 1980, Pick and Yvinec 1980). Both site and molecular symmetry are taken into account to derive a complete set of independent correlation functions, and to determine those which are accessible through neutron coherent and incoherent scattering experiments.

The microscopic approach is very attractive. But final expressions are very complicated and cannot be easily evaluated. Another method of investigation is to simulate the motion on a computer. Molecular dynamics calculations were used in the case of $NH_4^+Cl^-$ (Gerling and Hüller 1983) and solid bicyclo(2,2,2)octane (Neusy *et al* 1984). Although this method may appear as very fruitful, in most cases until now, experimental data are interpreted on the basis of phenomenological descriptions. Various models have been proposed in which adjustable coefficients have been introduced which may in the future be related to the intermolecular potential.

Many experimental techniques, like IQNS, look at only one molecule, individually. In a crystal lattice, the angular motion of such a molecule is strongly affected by the interactions with neighbouring atoms and molecules which produce an orientational crystal field. This potential reflects both the symmetry of the molecule and that of its surroundings (site symmetry). Generally, several equilibrium orientations are determined by the minima of the potential. These are separated by potential barriers. The natural unit to measure the height of these barriers is $\hbar^2/2I$ where I is the relevant moment of inertia. Orientational motions can be classified with regard to the height of the hindrance potential.

If the height of the hindrance potential is large compared with the rotational constant $\hbar^2/2I$, the molecule is captured in the orientations which correspond to the minima of the potential. Around this equilibrium orientation the molecule performs small angular oscillations with high frequency (librations). A quantum mechanics analysis shows that the wavefunctions are essentially localised in the minima of the potential

and that the low energy levels are much smaller than the barriers. However, at sufficiently low temperature, the overlap of the wavefunctions in adjacent potential minima, produces a tunnelling splitting of the librational levels (Press 1981, Hüller 1977, Hüller and Press 1981, Müller and Hüller 1982, Clough *et al* 1980).

In the high-temperature limit, thermal excitations of the molecule are of the same order of magnitude as the rotational potential. Molecules jump over the barrier amongst the set of preferential orientations. Frenkel's model is the most commonly used (Frenkel 1935). Jumps are assumed to be instantaneous and decoupled from the oscillations of the molecule in the minima. No attempt is made to describe the motion of the molecule when passing from one orientation to another. Introducing a probability of reorientation per unit time, $1/\tau$, where τ is the average time between two successive jumps, it is possible to write stochastic differential equations for the orientational distribution function. The characteristic time τ is found to follow an Arrhenius law

$$\tau = \tau_0 \exp(\Delta H / k_B T)$$

where ΔH is the activation energy, i.e. the difference between the height of the potential and the librational ground state energy. In spite of the fact that in reality the jumps are not instantaneous and that the orientational probability is a continuous function, the number of molecules performing a reorientation is much smaller than the number of molecules in the minima. Even when the real motion is complicated, in most cases until now it was possible to give an adequate description of the motions on the basis of jump models with a set of discrete orientations located on the maxima of the continuous distribution function.

The opposite situation corresponds to the case when the rotational potential is small in comparison to the rotational constant $\hbar^2/2I$. At low temperature, well-defined rotational quantum states appear. These are only slightly shifted in energy with respect to the levels of a free rotator. Such states are called 'rotational tunnelling' because lower energy levels are below the top of the hindrance barrier. Neutron spectroscopy permits the observation of transitions between these states. On the contrary, in the high-temperature limit, large fluctuations of the potential barrier occur caused by the interactions between the rotations and the thermal lattice vibrations or by reorientations of neighbouring molecules. Then the molecular motion is often described on the basis of the rotational diffusion model (Debye 1929, Furry 1957, Sears 1966, Sears 1967), in which the molecules are assumed to perform continuous small-angle rotations and then, on a time average, to have no preferred orientation in space. We point out the interesting extended diffusion models (Gordon 1966).

Neither the rotational diffusion model, nor the jump model are fully satisfactory. The former totally ignores the existence of preferred orientations of the molecule. The second restricts the angular displacements to a set of rotations corresponding to well-defined trajectories for each atom of the molecules. Models have been formulated which take into account molecular librations around quasi-equilibrium positions between two rotational motions (Dahlborg *et al* 1970, Larsson 1970).

More recently, Dianoux and Volino (1977) have treated the case of a rotation with one degree of freedom in an N-fold cosine potential, assuming that the evolution of the orientational distribution follows a Fokker–Planck equation involving a phenomenological, frequency-independent diffusion coefficient. According to the height of the potential, the free-rotational diffusion model or the jump model among equidistant sites is found as the limiting case. This model was generalised to the three-dimensional case, (Bée 1982) by introducing rotator functions taking into account both molecular and site symmetries and by expanding the potential on the basis of Wigner functions $D^l_{mn}(\mathbf{\Omega})$ of the Euler angles $\mathbf{\Omega}$. These more sophisticated analyses will be considered in the following chapter. Here we shall deal essentially with the classical models for molecular motions, i.e. the rotational diffusion model and the reorientational jump model.

6.2 Isotropic Rotational Diffusion

In this model, molecular reorientation is assumed to take place through small-angle, random rotations. Then, on a time average, no most probable orientation exists. In the study of the plastically crystalline phases, this assumption is often in conflict with the orientational probability obtained from x-ray structure analysis.

Indeed, Seymour and Pryor (1970), Press and Hüller (1973) have developed a general method to obtain the crystallographic structure of orientationally disordered phases from neutron or x-ray scattering measurements. From the analysis of the intensity of the Bragg peaks, it is possible to determine the coefficients $A^l_{mm'}$, of the expansion

$$P(\mathbf{\Omega}) = \sum_{lmm'} \frac{(2l+1)}{8\pi^2} A^l_{mm'} R^l_{mm'}(\mathbf{\Omega}) \tag{6.1}$$

of the orientational probability of the molecule $P(\mathbf{\Omega})$ on the basis of the rotator functions $R^l_{mm'}(\mathbf{\Omega})$ (Amoureux *et al* 1981a). An isotropic orientational probability corresponds to

$$A^l_{mm'} = \delta_{l,0}. \tag{6.2}$$

Then, the importance of the molecule delocalisation is evidenced by

both the sign and the amplitude of the relevant coefficients $A^l_{mm'}$. Typical values found in plastic crystals differ significantly from (6.2). Usually, intermediate values are obtained between 0 and the precise value corresponding to a molecule *rigidly fixed* in an equilibrium orientation.

Values of the coefficients $A^l_{mm'}$ experimentally found with bicyclo(2,2,2)octane at $T = 300$ K, are listed in table 6.1, together with the values corresponding to a molecule whose threefold axis would be fixed along [111]. Differences between the two sets evidence a strong molecular delocalisation. However, experimental values are not small enough to allow a description of the dynamics of the bicyclo(2,2,2)octane molecule on the basis of the isotropic rotational diffusion model. Nevertheless, this model is more likely to be valid at higher temperature in the plastic phase, in the vicinity of the melting point.

Table 6.1 Coefficients of the expansion of the orientational probability in the case of bicyclo(2,2,2)octane (after Sauvajol and Amoureux 1981).

	Experimental	Molecule along [111]	Isotropic
A^0_{11}	1	1	1
A^4_{11}	-0.382 ± 0.024	$\sqrt{21}/9 = 0.509$	0
A^6_{11}	0.350 ± 0.040	$4\sqrt{2}/9 = 0.628$	0
A^8_{11}	0.07 ± 0.01	$\sqrt{33}/27 = 0.213$	0

We will not present a detailed derivation of this model which was formulated by Sears (1966) and we restrict ourselves to its main results.

We return to the expression of the intermediate scattering function $I^R_{inc}(\boldsymbol{Q}, t)$

$$I^R_{inc}(\boldsymbol{Q}, t) = \sum_{\boldsymbol{\Omega}_0} \sum_{\boldsymbol{\Omega}} \exp\{i\boldsymbol{Q}\cdot[\boldsymbol{R}(\boldsymbol{\Omega}) - \boldsymbol{R}(\boldsymbol{\Omega}_0)]\}\ P(\boldsymbol{\Omega}, \boldsymbol{\Omega}_0, t)\ P(\boldsymbol{\Omega}_0). \quad (6.3)$$

The sums are taken over all initial ($\boldsymbol{\Omega}_0$) and final ($\boldsymbol{\Omega}$) equilibrium orientations of the molecule. $\boldsymbol{R}(\boldsymbol{\Omega})$ is the position vector (from the molecule centre of mass) of the proton being considered for the orientation $\boldsymbol{\Omega}$. $P(\boldsymbol{\Omega}_0)$ is the distribution of the initial orientations, whilst $P(\boldsymbol{\Omega}, \boldsymbol{\Omega}_0, t)$ is the conditional probability of finding the molecule at time t in the orientation $\boldsymbol{\Omega}$ if it was in $\boldsymbol{\Omega}_0$ at $t = 0$. It can be expanded in terms of the Wigner rotation matrices (Rose 1957) in the form

$$P(\boldsymbol{\Omega}, \boldsymbol{\Omega}_0, t) = \sum_{lmm'} \frac{2l+1}{8\pi^2} F^l_{mm'}(t) \sum_n D^l_{mn}(\boldsymbol{\Omega}) D^{l*}_{m'n}(\boldsymbol{\Omega}_0). \tag{6.4}$$

The conditions which $P(\boldsymbol{\Omega}, \boldsymbol{\Omega}_0, t)$ and the $F^l_{mm'}(t)$ must satisfy are

(i) *normalisation*

$$\int P(\boldsymbol{\Omega}, \boldsymbol{\Omega}_0, t)\, \mathrm{d}\boldsymbol{\Omega} = 1. \tag{6.5}$$

The orthogonality of the Wigner rotation matrices (Rose 1957)

$$\int \mathrm{d}\boldsymbol{\Omega}\, D^l_{mn}(\boldsymbol{\Omega}) D^{l'}_{m'n'}(\boldsymbol{\Omega}) = \frac{8\pi^2}{2l+1} \delta_{ll'} \delta_{mm'} \delta_{nn'} \tag{6.6}$$

lead to

$$F^0_{00}(t) = 1 \tag{6.7}$$

(ii) *initial condition*

$$P(\boldsymbol{\Omega}, \boldsymbol{\Omega}_0, 0) = (\boldsymbol{\Omega} - \boldsymbol{\Omega}_0) \tag{6.8}$$

where $\delta(\boldsymbol{\Omega} - \boldsymbol{\Omega}_0)$ is the delta function in the space of the Euler angles.

From the relation

$$\sum_{lmm'} \frac{2l+1}{8\pi^2} D^l_{mm'}(\boldsymbol{\Omega}) D^l_{mm'}(\boldsymbol{\Omega}_0) = \delta(\boldsymbol{\Omega} - \boldsymbol{\Omega}_0) \tag{6.9}$$

one obtains

$$F^l_{mm'}(0) = \delta_{mm'}. \tag{6.10}$$

The exponential in (6.3) can be expanded in spherical harmonics in the form

$$\exp\{\mathrm{i}\boldsymbol{Q}\cdot\boldsymbol{R}(\boldsymbol{\Omega})\} = \sum_{lm} \left(\frac{2l+1}{4\pi}\right)^{1/2} \mathrm{i}^l j_l(QR) Y^m_l(\theta', \varphi')\, D^l_{0m}(\boldsymbol{\Omega})^* \tag{6.11}$$

where θ', φ' are the polar angles of $\boldsymbol{R}(\Omega)$ in the molecular system. The $j_l(QR)$ are the spherical Bessel functions.

Substituting (6.4) and (6.11) into (6.3), we find, using the orthogonality of the rotation matrices and the spherical harmonic addition theorem (Rose 1957)

$$I^{\mathrm{R}}_{\mathrm{inc}}(Q, t) = \sum_{l=0}^{\infty} (2l+1)\, j^2_l(QR) F^l_{00}(t). \tag{6.12}$$

For the rotational diffusion of the molecule, the orientational distribution function satisfies the differential equation

$$D_{\mathrm{R}} \Delta(\boldsymbol{\Omega})\, P(\boldsymbol{\Omega}, \boldsymbol{\Omega}_0, t) = \frac{\partial}{\partial t} P(\boldsymbol{\Omega}, \boldsymbol{\Omega}_0, t) \tag{6.13}$$

where $\Delta(\mathbf{\Omega})$ is the Laplace operator in the space of the Euler angles

$$\Delta(\mathbf{\Omega}) = \frac{1}{\sin^2\beta}\left[\left(\frac{\partial}{\partial\alpha} - \cos\beta\,\frac{\partial}{\partial\gamma}\right)^2 + \left(\sin\beta\,\frac{\partial}{\partial\beta}\right)^2\right] + \frac{\partial^2}{\partial\gamma^2} \quad (6.14)$$

D_R is the isotropic rotational diffusion constant. Using the expansion (6.4) and the initial condition (6.8), one obtains

$$F^l_{00}(t) = \exp[-l(l+1)D_R t]. \quad (6.15)$$

By taking the time-Fourier transform it is usual to write the scattering function in the form

$$S(Q, \omega) = A_0(Q)\,\delta(\omega) + \sum_{l=1}^{\infty} A_l(Q) \times \frac{1}{\pi} \times \frac{\tau_l}{1 + \omega^2\tau_l^2} \quad (6.16)$$

with the elastic and quasielastic structure factors respectively given by

$$A_0(Q) = j_0^2(Qr) \quad (6.17a)$$

$$A_l(Q) = (2l+1)j_l^2(QR) \quad (6.17b)$$

and where we have introduced the correlation time τ_l for the spherical harmonic of order l:

$$\tau_l = l(l+1)D_R. \quad (6.18)$$

6.3 Examples of Molecular Isotropic Rotational Diffusion

There are few examples of molecules whose dynamical behaviour can be described properly as an isotropic rotational diffusion. Some cases are, however, encountered.

6.3.1 Octaphenylcyclotetrasiloxane

Octaphenylcyclotetrasiloxane (OPCTS) $[SiO(C_6H_5)_2]_4$ is a symmetrical-top molecule, where, as shown in figure 6.1, eight phenyl rings are attached to a central tetrasiloxane ring. Between 300 K and 483 K, three solid phases can be observed (Keyes and Daniels 1975, Smith 1979). The room temperature phase is monoclinic (a, b, c = 21.962, 10.139, 21.722 Å, β = 115°99, space group $P_{21/c}$, Z = 4). The siloxane ring is almost planar, with the eight phenyl groups roughly pointing towards the vertex of a parallepiped, with approximate dimensions 6.5 × 6.5 ×4.7 Å (Volino and Dianoux 1978, Hossain *et al* 1979). Long-range translational order also exists in the intermediate phase (349 K < T < 461 K) which can also be considered as a normal molecular crystal, while more symmetric or disordered. On the contrary, the

mesophase between 461 K and 478 K is highly disordered. This phase appears optically isotropic and, owing to large amplitude molecular motions, Bragg peaks are too weak to be detected by neutron diffraction (Volino and Dianoux 1978). Furthermore, the melting entropy, obtained from differential scanning calorimetry (DSC) (Keyes and Daniels 1975), is found to be one of the lowest ever measured for any crystalline species ($\Delta S_m/R = 0.49$).

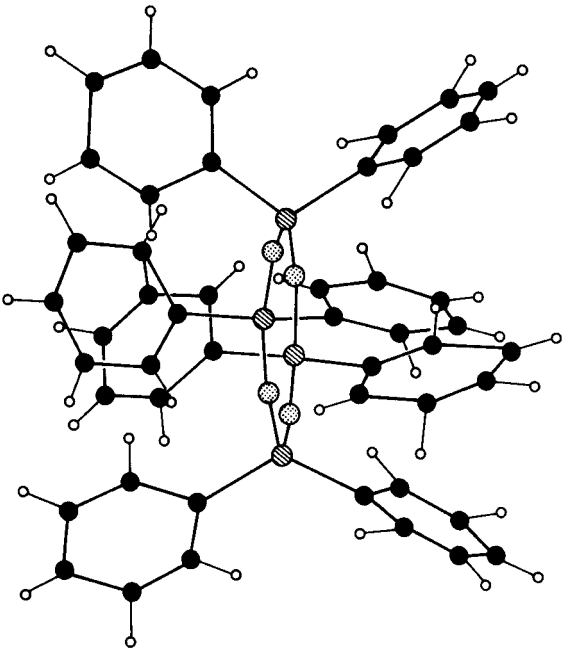

Figure 6.1 The OPCTS molecule. Silicon atoms are dotted, oxygens are dashed, carbons are full circles and hydrogens are open circles.

Experimental values of the EISF extracted from the spectra obtained with the backscattering spectrometer IN10 of the Institut Laue–Langevin are shown in figure 6.2. These values are close to the theoretical curve corresponding to an isotropic rotational diffusion of the whole molecule. The best agreement is obtained at the highest temperature of measurement. Furthermore, no discontinuity is found for D_R at the mesophase–liquid phase transition, and the results can be described by a unique Arrhenius law (Bée *et al* 1984)

$$D_R = 0.86 \times 10^{13} \exp(-\Delta H_R/RT)\ \mathrm{s}^{-1}$$

with $\Delta H_R = 33.8\ \mathrm{kJ\ mol}^{-1}$.

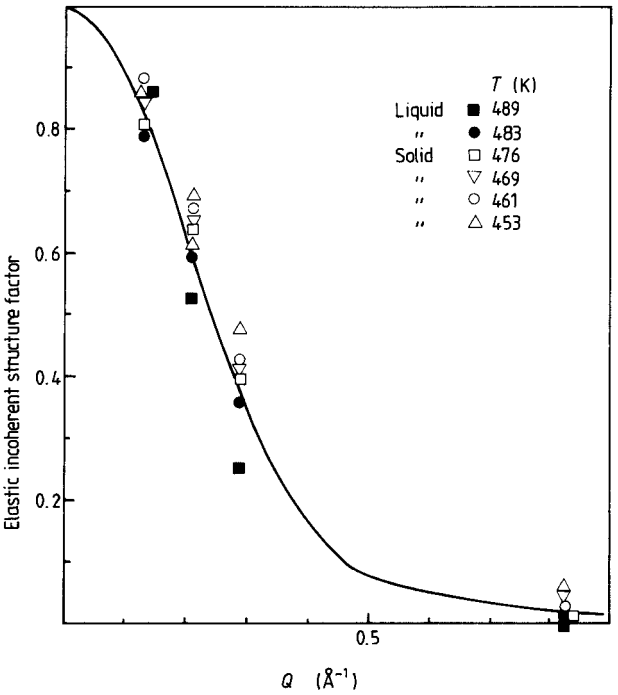

Figure 6.2 Determination of the experimental EISF from the back-scattering technique, in both the solid and liquid phases of OPCTS. Measurements at $T = 453$ K correspond to the supercooled meso-phase. The full curve is the theoretical EISF for the isotropic rotational diffusion model (Bée *et al* 1984).

6.3.2 Norbornane

Norbornane, bicyclo(2,2,1)heptane, (see figure 6.3) appears to be a particularly interesting candidate for molecular motion studies because it exhibits a phase transition at $T = 306$ K separating two plastic phases. The low-temperature plastic phase, which exists from 131 K to 306 K has a hcp structure ($a = 6.17$ Å, $c = 10.03$ Å) while the high-temperature phase is fcc ($a = 8.73$ Å) and exists up to the melting point ($T_m = 360$ K).

The molecular disorder is clearly evidenced by light spectroscopy techniques (Folland *et al* 1975). NMR techniques were also extensively used (Folland *et al* 1973a, Folland *et al* 1973b) but could not provide precise information on the molecular dynamics because the relaxation is mainly influenced by self-diffusion of the molecules (Chadwick and Forrest 1978). Recently IQNS was used to study the rotational behaviour of norbornane and of the other two related bridged cyclic molecules

norbornene and norbornadiene (see figure 6.3). Especially, in the case of norbornane, it was shown that in the fcc plastic phase and at the highest temperatures in the hcp phase, the rotational diffusion model is well adapted to describe the motions of the molecules. Furthermore, the temperature evolution of the rotational diffusion constant D_R does not show any discontinuity at the hcp–fcc phase transition, following the unique relation (Bée *et al* 1986a)

$$D_R = 2.03 \times 10^{12} \exp(\Delta H_R/RT)\ \mathrm{s}^{-1}$$

with $\Delta H_R = 6.14\ \mathrm{kJ\,mol}^{-1}$.

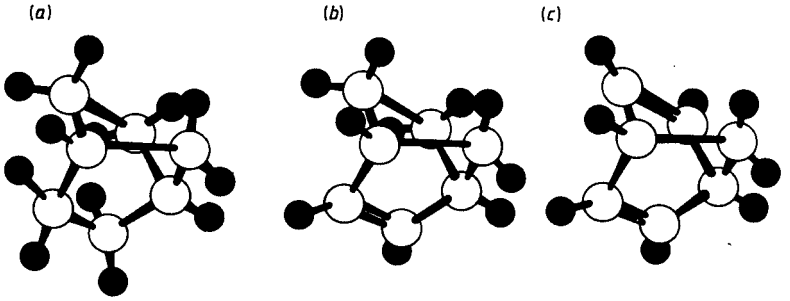

Figure 6.3 The norbornane, (*a*), norbornene, (*b*), and norbornadiene, (*c*), molecules. Carbons are full circles and hydrogens open circles.

6.4 Continuous Rotational Diffusion On a Circle

Let us consider the case where the diffusional motion is confined to a circle of radius r. Therefore, the orientational distribution function follows a differential equation analogous to (6.13).

$$D_r \frac{\partial^2 P(\phi, \phi_0, t)}{\partial \phi^2} = \frac{\partial}{\partial t} P(\phi, \phi_0, t) \qquad (6.19)$$

where D_r is the rotational diffusion constant. ϕ and ϕ_0 are the angular positions of the scatterer on the circle, at time t and 0, respectively. The solution is (Dianoux *et al* 1975)

$$P(\phi, \phi_0, t) = \frac{1}{2\pi} \sum_{n=-\infty}^{\infty} \exp[im(\phi - \phi_0)t] \exp(-D_r n^2 |t|). \qquad (6.20)$$

It is necessary to consider the relative orientation of the scattering vector and of the circle. We choose a set of coordinates with axis Oz along the rotation axis. The direction of $\boldsymbol{Q}$ is given by its polar angles θ

and φ (figure 6.4). The scalar products occurring in the intermediate scattering law

$$I(\boldsymbol{Q}, t) = \int \mathrm{d}\phi_0 \int \mathrm{d}\phi \exp\{\mathrm{i}\boldsymbol{Q}\cdot[\boldsymbol{R}(\phi) - \boldsymbol{R}(\phi_0)]\}\ P(\phi, \phi_0, t)P(\phi_0) \quad (6.21)$$

are easily evaluated

$$\boldsymbol{Q}\cdot\boldsymbol{R}(\phi) = Qr\sin\theta\cos(\phi - \varphi) \quad (6.22a)$$

$$\boldsymbol{Q}\cdot\boldsymbol{R}(\phi_0) = Qr\sin\theta\cos(\phi_0 - \varphi). \quad (6.22b)$$

Since at equilibrium all the positions on the circle are equiprobable,

$$P(\phi_0) = \frac{1}{2\pi}. \quad (6.23)$$

We make use of the expansion

$$\exp\{\mathrm{i}Qr\sin\theta\cos(\phi - \varphi)\} = \sum_{m=-\infty}^{\infty} \mathrm{i}^m \exp[-\mathrm{i}m(\phi - \varphi)]J_m(Qr\sin\theta) \quad (6.24)$$

where J_m is a Bessel function of the first kind and order m, to obtain

$$I(\boldsymbol{Q}, t) = \sum_{m=-\infty}^{\infty} J_m^2(Qr\sin\theta)\exp(-D_r m^2|t|). \quad (6.25)$$

By taking the Fourier transform

$$S(\boldsymbol{Q}, \omega) = J_0^2(Qr\sin\theta)\delta(\omega) + 2\sum_{m=1}^{\infty} J_m^2(Qr\sin\theta) \times \frac{1}{\pi}\frac{D_r m^2}{(D_r m^2)^2 + \omega^2}. \quad (6.26)$$

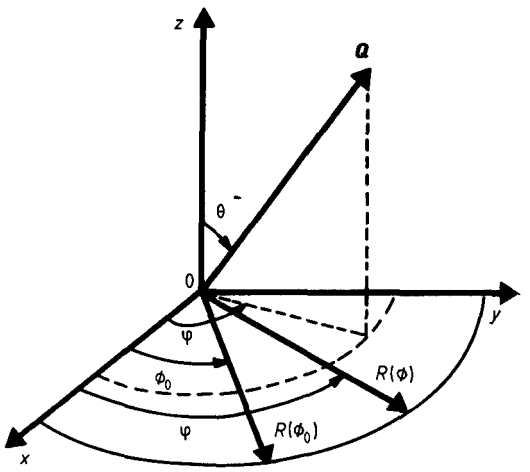

Figure 6.4 Spherical coordinates for proton and momentum transfer vector $\boldsymbol{Q}$. Symbols are defined in the text.

Now the behaviour of the elastic and quasielastic structure factors, strongly depends on the angle θ between the direction of $\boldsymbol{Q}$ and the axis of rotation. Figure 6.5 shows their variation, as function of Qr, for a series of values of θ. For a powder sample, one has to take an isotropic average over the angle θ. Unfortunately, no formal expression exists for the average and the result is not simple. However, as it will be shown in a later section, it is possible to use expressions of the structure factors for a jump model over N equally spaced sites. At any given Q, with N sufficiently large, the scattering law becomes independent of further increase in N. Structure factor variations for the powder case have also been reported in figure 6.5.

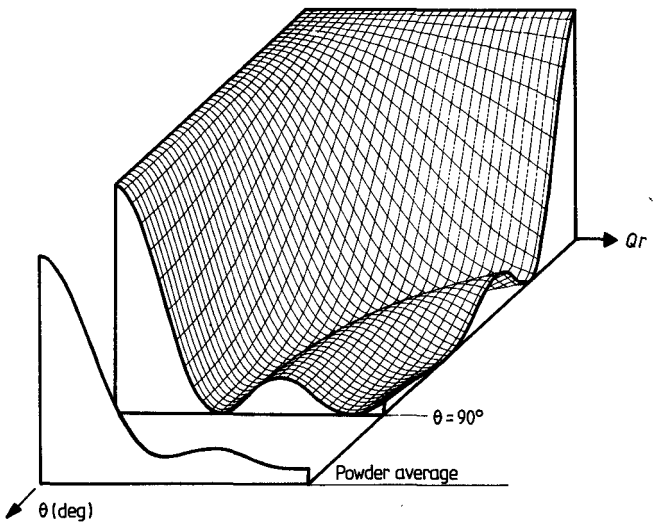

Figure 6.5 EISF for continuous uniaxial rotational diffusion over a circle as function of Qr (r, rotation radius) for different values of the angle θ between the direction of $\boldsymbol{Q}$ and the axis of rotation.

In the case of crystalline samples, use can be made of the dependence of the structure factors on the orientation of $\boldsymbol{Q}$ with respect to the sample (equation (6.26)), in order to enhance or reduce the elastic or quasielastic contribution. In the same way, anisotropic effects or preferential orientations of crystallites in a powder sample will be evidenced if, when rotating the specimen with respect to the incident beam, subsequent modifications appear in the spectra recorded at the same scattering angle. Oriented samples are the subject of another chapter and, in this section, we shall restrict our analysis to the perfectly polycrystalline specimen.

6.5 Jump Model Among Two Sites

6.5.1 Neutron scattering law for two equivalent sites

Let us denote by $p(\boldsymbol{r}_1, t)$ and $p(\boldsymbol{r}_2, t)$ the probability of finding the particle (proton) at time t, at sites $\boldsymbol{r}_1$ and $\boldsymbol{r}_2$, respectively. Then $p(\boldsymbol{r}_1, t)$ and $p(\boldsymbol{r}_2, t)$ follow a set of rate equations

$$\frac{\mathrm{d}}{\mathrm{d}t} p(\boldsymbol{r}_1, t) = -\frac{1}{\tau} p(\boldsymbol{r}_1, t) + \frac{1}{\tau} p(\boldsymbol{r}_2, t) \tag{6.27a}$$

$$\frac{\mathrm{d}}{\mathrm{d}t} p(\boldsymbol{r}_2, t) = \frac{1}{\tau} p(\boldsymbol{r}_1, t) - \frac{1}{\tau} p(\boldsymbol{r}_2, t) \tag{6.27b}$$

where τ^{-1} is the jump rate probability from one site to the other (assumed to be equal). We immediately get

$$\frac{\mathrm{d}}{\mathrm{d}t} [p(\boldsymbol{r}_1, t) + p(\boldsymbol{r}_2, t)] = 0 \tag{6.28b}$$

$$p(\boldsymbol{r}_1, t) + p(\boldsymbol{r}_2, t) = cte = 1. \tag{6.28b}$$

The solutions for $p(\boldsymbol{r}_1, t)$ and $p(\boldsymbol{r}_2, t)$ are of the form:

$$p(\boldsymbol{r}_1, t) = A + B\, \mathrm{e}^{-2t/\tau} \tag{6.29a}$$

$$p(\boldsymbol{r}_2, t) = A - B\, \mathrm{e}^{-2t/\tau} \tag{6.29b}$$

where the coefficients A and B are determined from initial conditions.

Assuming that the particle was initially at $\boldsymbol{r}_1$ at time $t = 0$

$$p(\boldsymbol{r}_1, 0) = A + B = 1 \tag{6.30a}$$

$$p(\boldsymbol{r}_2, 0) = A - B = 0 \tag{6.30b}$$

we obtain

$$p(\boldsymbol{r}_1, t; \boldsymbol{r}_1, 0) = \tfrac{1}{2}[1 + \exp(-2t/\tau)] \tag{6.31a}$$

$$p(\boldsymbol{r}_2, t; \boldsymbol{r}_1, 0) = \tfrac{1}{2}[1 - \exp(-2t/\tau)] \tag{6.31b}$$

where $p(\boldsymbol{r}_i, t; \boldsymbol{r}_j, 0)$ denotes the probability that the proton is at $\boldsymbol{r}_i$ at time t, under the condition that it was at $\boldsymbol{r}_j$ at $t = 0$. The probabilities $p(\boldsymbol{r}_1, t; \boldsymbol{r}_2, 0)$ and $p(\boldsymbol{r}_2, t; \boldsymbol{r}_2, 0)$ for the case of a proton at $\boldsymbol{r}_2$ at $t = 0$ are easily found by simply interchanging the indices

$$p(\boldsymbol{r}_1, t; \boldsymbol{r}_2, 0) = \tfrac{1}{2}[1 - \exp(-2t/\tau)] \tag{6.32a}$$

$$p(\boldsymbol{r}_2, t; \boldsymbol{r}_2, 0) = \tfrac{1}{2}[1 + \exp(-2t/\tau)]. \tag{6.32b}$$

The equilibrium distribution is obtained by taking $t \to \infty$

$$p(\boldsymbol{r}_1, \infty) = p(\boldsymbol{r}_2, \infty) = \tfrac{1}{2} \tag{6.33}$$

independently of the initial site for the proton.

Now the intermediate scattering function $I(\boldsymbol{Q}, t)$ can be evaluated

$$I(\boldsymbol{Q}, t) = \langle e^{i\boldsymbol{Q}\cdot\boldsymbol{r}(t)}\, e^{-i\boldsymbol{Q}\cdot\boldsymbol{r}(0)}\rangle \tag{6.34}$$
$$= [p(\boldsymbol{r}_1, t; \boldsymbol{r}_1, 0) + p(\boldsymbol{r}_2, t; \boldsymbol{r}_1, 0)\, e^{i\boldsymbol{Q}\cdot(\boldsymbol{r}_2-\boldsymbol{r}_1)}]\, p(\boldsymbol{r}_1, 0)$$
$$+ [p(\boldsymbol{r}_1, t; \boldsymbol{r}_2, 0)\, e^{i\boldsymbol{Q}\cdot(\boldsymbol{r}_1-\boldsymbol{r}_2)} + p(\boldsymbol{r}_2, t; \boldsymbol{r}_2, 0)]\, p(\boldsymbol{r}_2, 0).$$

Assuming that the system was in equilibrium at $t = 0$

$$p(\boldsymbol{r}_1, 0) = p(\boldsymbol{r}_2, 0) = \tfrac{1}{2} \tag{6.35}$$

we obtain

$$I(\boldsymbol{Q}, t) = A_0(\boldsymbol{Q}) + A_1(\boldsymbol{Q}) \exp(-2t/\tau) \tag{6.36}$$

with:

$$A_0(\boldsymbol{Q}) = [1 + \cos \boldsymbol{Q}\cdot(\boldsymbol{r}_2 - \boldsymbol{r}_1)]/2 \tag{6.37a}$$

$$A_1(\boldsymbol{Q}) = [1 - \cos \boldsymbol{Q}\cdot(\boldsymbol{r}_2 - \boldsymbol{r}_1)]/2. \tag{6.37b}$$

The structure factors $A_0(Q)$ and $A_1(Q)$ fulfil the relation

$$A_0(\boldsymbol{Q}) + A_1(\boldsymbol{Q}) = 1. \tag{6.38}$$

Fourier transformation with respect to time finally gives

$$S(\boldsymbol{Q}, \omega) = A_0(\boldsymbol{Q})\delta(\omega) + A_1(\boldsymbol{Q}) \frac{1}{\pi} \frac{2\tau}{4 + \omega^2\tau^2}. \tag{6.39}$$

Integrating over all possible values for ω leads to

$$\int_{-\infty}^{\infty} S(\boldsymbol{Q}, \omega)\, d\omega = A_0(Q) + A_1(Q) = 1. \tag{6.40}$$

In the case of a powder specimen, an average has to be taken over all possible orientations of $\boldsymbol{Q}$

$$S(Q, \omega) = \frac{1}{4\pi} \int_0^{2\pi} d\varphi \int_{-\pi}^{\pi} S(\boldsymbol{Q}, \omega) \sin\theta\, d\theta\, d\varphi \tag{6.41}$$

$$S(Q, \omega) = A_0(Q)\delta(\omega) + A_1(Q) \frac{1}{\pi} \frac{2\tau}{4 + \omega^2\tau^2} \tag{6.42}$$

with:

$$A_0(Q) = \tfrac{1}{2}[1 + j_0(Qd)] \tag{6.43a}$$

$$A_1(Q) = \tfrac{1}{2}[1 - j_0(Qd)] \tag{6.43b}$$

$j_0(x)$ is a Bessel function of zero order and $d = |\boldsymbol{r}_2 - \boldsymbol{r}_1|$ is the jump distance between the two sites.

6.5.2 Two non-equivalent sites

Suppose that we are concerned with two different transition rates.

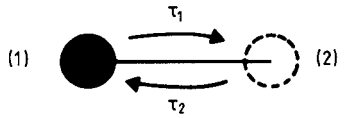

Figure 6.6 Jump model between two sites. τ_1 and τ_2 are the mean residence times in each site. The corresponding jump probabilities are $\tau_1^{-1}(1 \to 2)$ and $\tau_2^{-1}(2 \to 1)$.

Denoting by τ_1^{-1} (respectively τ_2^{-1}) the probability for the particle to jump from site 1 to site 2 (respectively from site 2 to site 1) (figure 6.6) the rate equations (6.27) become

$$\frac{\mathrm{d}}{\mathrm{d}t} p(\boldsymbol{r}_1, t) = -\frac{1}{\tau_1} p(\boldsymbol{r}_2, t) + \frac{1}{\tau_2} p(\boldsymbol{r}_2, t), \tag{6.44a}$$

$$\frac{\mathrm{d}}{\mathrm{d}t} p(\boldsymbol{r}_2, t) = \frac{1}{\tau_1} p(\boldsymbol{r}_1, t) - \frac{1}{\tau_2} p(\boldsymbol{r}_2, t) \tag{6.44b}$$

The equilibrium solution, obtained by setting right-hand sides of (6.44) to zero, reads:

$$p(\boldsymbol{r}_1, 0) = p(\boldsymbol{r}_1, \infty) = \frac{1}{1 + \rho} \tag{6.45a}$$

$$p(\boldsymbol{r}_2, 0) = p(\boldsymbol{r}_2, \infty) = \frac{\rho}{1 + \rho} \tag{6.45b}$$

where $\rho = \tau_1/\tau_2$. In (6.45) we have assumed the system initially at equilibrium at $t = 0$. Resolution of (6.44) is straightforward, and quite analogous to calculations developed in §6.5.1. The relevant reciprocal correlation times are given by:

$$\alpha_1 = 0 \tag{6.46a}$$

$$\alpha_2 = \frac{1}{\tau_1} + \frac{1}{\tau_2} = \frac{1}{\tau_1}(1 + \rho). \tag{6.46b}$$

The expressions of the corresponding structure factors are:

$$A_1(\boldsymbol{Q}) = \frac{1}{(1 + \rho)^2} [1 + \rho^2 + 2\rho \cos(\boldsymbol{Q} \cdot \boldsymbol{r})] \tag{6.47a}$$

$$A_2(\boldsymbol{Q}) = \frac{2\rho}{(1 + \rho)^2} [1 - \cos(\boldsymbol{Q} \cdot \boldsymbol{r})] \tag{6.47b}$$

with $\boldsymbol{r} = \boldsymbol{r}_2 - \boldsymbol{r}_1$. Taking the powder average,

$$A_1(Q) = \frac{1}{(1 + \rho)^2} [1 + \rho^2 + 2\rho j_0(Qd)] \tag{6.48a}$$

$$A_2(Q) = \frac{2\rho}{(1 + \rho^2)} [1 - j_0(Qd)]. \tag{6.48b}$$

The structure factors are function of the correlation times τ_1 and τ_2 via the ratio $\rho = \tau_1/\tau_2$. Their variations as a function of Qd are drawn in figure 6.7 for different ρ values. Equations (6.36), (6.37) and (6.43) are retrieved by putting $\rho = 1$.

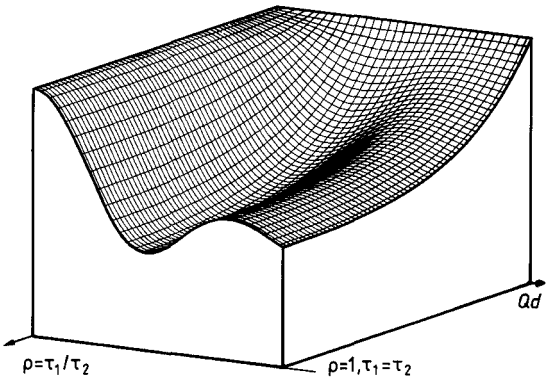

Figure 6.7 The EISF for the jump model between two sites, as a function of Qd (d, jump distance) for different values of the ratio $\rho = \tau_1/\tau_2$ of the two residence times in each site τ_1 and τ_2.

6.5.3 Example of two-site jump-model: $CsOH{\cdot}H_2O$

A good example of application of the two-site jump model is provided by Stahn *et al* (1983) who studied the dynamics of the hydrogen bond in caesium hydroxide monohydrate, $CsOH{\cdot}H_2O$. Above 340 K, the crystalline structure is hexagonal (space group P6/mmm), with alternate layers of Cs^+ and $H_3O_2^-$ (Harbrecht 1981). Within each $H_3O_2^-$ layer, all the protons appear to be equivalent, with no distinct OH^- and H_2O groups. A good description of these layers is that of a two-dimensional net, with pairs of neighbouring O atoms connected by hydrogen bonds (figure 6.8).

Since the O–O distance (2.64 Å) is larger than twice the O–H bond length (0.96 Å) each H atom is located in one of the minima of a symmetric double well potential between a pair of neighbouring O atoms. The P6/mmm crystal symmetry is fulfilled when assuming a dynamical disorder of the protons among the minima which, on a time average, appear to be equally occupied. Stahn *et al* (1983) have considered several hypotheses for the jump process. The first is a simple two-site jump between neighbouring O atoms. Another model describes the process as a 120° jump rotation of each proton around an oxygen atom to which it is bound. In that case, both OH^- ions and H_2O

molecules would rotate. Finally, translational diffusion would appear if the rotating entities were exchanging atoms.

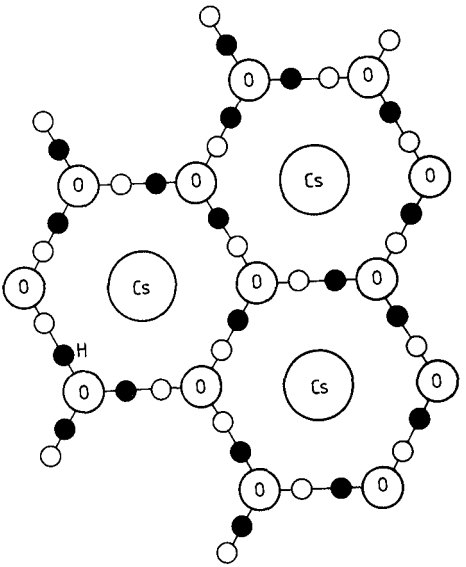

Figure 6.8 Random distribution of the hydrogen atoms between the oxygen atoms in CsH_3O_2. Each hydrogen can occupy two sites symbolised by full and open small circles between two neighbouring oxygen atoms. The Cs atoms define the unit cell. Oxygen and hydrogen atoms are located in an upper layer at the coordinate $\frac{1}{2}$.

A careful EISF analysis ruled out models based on rotational motion. The conclusion was that the main process related to proton disorder is a two-site jump model between adjacent oxygen atoms, with a jump rate of $8.0 \times 10^{10}\ s^{-1}$. The vibrational mean square displacement in each of the potential minima was found equal to 0.07 $Å^2$ at 402 K. At the same time, the jump distance was found to be relatively large (1.03 Å). That result was interpreted by assuming a non-linear H bond, with a bending angle $\alpha \simeq 20°$ and a H–O–H angle of $\simeq 110°$ for a H_2O molecule.

6.5.4 Proton dynamics in solid carboxylic acids

An IQNS study of terephthalic acid at 220 K (Meier *et al* 1984) has provided information on the dynamics mechanism in hydrogen-bonded carboxylic acid dimers. The double proton-exchange mechanism amongst the minima of a double well potential between oxygen atoms of

the O–H. . . O bonds was supported by NMR measurements of p-toluic acid (Meier *et al* 1982), benzoic acid (Nagaoka *et al* 1983) and several other carboxylic acids (Meier *et al* 1983, Graf *et al* 1981, Nagaoka *et al* 1983). Conversely interpretation of the infrared spectrum of benzoic acid (Furic 1984) led to the alternative suggestion of 180° rotations of the entire hydrogen-bonded eight-membered ring. From IQNS measurements, the determination of the experimental EISF leads to a jump distance of about 0.7 Å, which is support for the proton exchange mechanism in a double well potential.

6.6 Jumps Among Three Equivalent Sites Equally Spaced on a Circle

6.6.1 Scattering law

The incoherent scattering law corresponding to a proton jumping between three equidistant equivalent sites (figure 6.9) can be evaluated by resolving the set of rate equations:

$$\frac{\mathrm{d}}{\mathrm{d}t}p(\boldsymbol{r}_1, t) = \frac{1}{\tau}[-2p(\boldsymbol{r}_1, t) + p(\boldsymbol{r}_2, t) + p(\boldsymbol{r}_3, t)] \quad (6.49a)$$

$$\frac{\mathrm{d}}{\mathrm{d}t}p(\boldsymbol{r}_2, t) = \frac{1}{\tau}[p(\boldsymbol{r}_2, t) - 2p(\boldsymbol{r}_2, t) + p(\boldsymbol{r}_3, t)] \quad (6.49b)$$

$$\frac{\mathrm{d}}{\mathrm{d}t}p(\boldsymbol{r}_3, t) = \frac{1}{\tau}[p(\boldsymbol{r}_1, t) + p(\boldsymbol{r}_2, t) - 2p(\boldsymbol{r}_3, t)] \quad (6.49c)$$

where τ^{-1} is the jump-rate probability from one site to another.

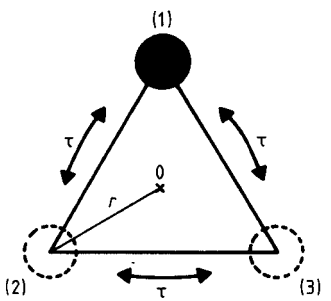

Figure 6.9 Jump model among three equivalent sites on a circle with radius r. τ is the mean residence time on each site.

Assuming the system initially at equilibrium at $t = 0$, i.e.

$$p(\boldsymbol{r}_1, 0) = p(\boldsymbol{r}_2, 0) = p(\boldsymbol{r}_3, 0) = \tfrac{1}{3} \quad (6.50)$$

and following the method indicated in §6.5.1, we obtain, in the powder case:

$$S(Q, \omega) = A_0(Q)\delta(\omega) + A_1(Q)\frac{1}{\pi}\frac{3\tau}{9 + \omega^2\tau^2} \tag{6.51}$$

with

$$A_0(Q) = \tfrac{1}{3}[1 + 2j_0(Qr\sqrt{3})] \tag{6.52a}$$

and

$$A_1(Q) = \tfrac{2}{3}[1 - j_0(Qr\sqrt{3})]. \tag{6.52b}$$

6.6.2 Example: methyl 120° jumps in trimethyloxosulphonium ion

The most common example of three-site jump-model is certainly that of methyl groups reorienting by 120° jumps about their threefold symmetry axis. There are numerous IQNS studies of such rotating CH_3 groups but often other kinds of molecular motion are observed simultaneously and thus are superimposed in the experimental results. Then neutron data become difficult to interpret. Sometimes, partial deuteration of the sample makes separation of different kinds of motion possible. In the case of solid para-azoxyanisole (Hervet *et al* 1976), this technique enabled the separation of the methyl group motion from the motion of the whole molecule. There are some cases, however, where methyl group motions can be observed alone because random motions occur on a quite different time-scale (slower).

The trimethyloxosulphonium (TMOS) ion $(CH_3)_3SO^+$ is almost globular in shape (figure 6.10) with all three methyl groups bonded directly to the sulphur atom. Calorimetric measurements over the 10–450 K temperature range, evidenced for TMOS iodide two solid–solid phase transitions, at about 200 K and 250 K. Infrared, Raman and inelastic neutron scattering studies (Sourisseau *et al* 1985) proved that the low-temperature (III) phase is completely ordered. Methyl group reorientations are mainly involved in the phase (III) → phase (II) transition, while whole-cation motions are partly involved in the phase (II) → phase (I) transition. A recent NMR study (Jurga *et al* 1981) for the different TMOS halides alluded to the occurrence of 120° reorientational jumps of methyl groups in TMOS iodide, over an energy barrier estimated equal to 10.9 kJ mol^{-1}, in agreement with the barrier height against methyl torsion derived from light-scattering study ($E_a \simeq$ 13.3 kJ mol^{-1}), and with a correlation time $\tau_c \simeq 9.6 \times 10^{-11}$ s at $T = 300$ K. 120° jumps of the whole cation were also evidenced but over a noticeably higher energy barrier ($E_a = 48$ kJ mol^{-1}) and at a much slower rate ($\tau \simeq 1.75 \times 10^{-5}$ s at $T = 300$ K).

These conclusions concerning the dynamical disorder of methyl groups

and TMOS ion were confirmed by more recent IQNS experiments (Bée *et al* 1985a).

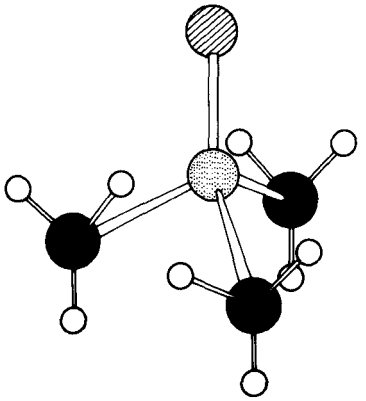

Figure 6.10 Sketch of the trimethyloxosulphonium (TMOS) ion. Carbon atoms are full circles, oxygen dashed circles and sulphur dotted circles. Hydrogen atoms are open circles.

In figure 6.11 the EISF corresponding to 120° methyl jumps is drawn, evaluated from (6.52) with a value $r = 0.99$ Å of the rotation radius of hydrogen. For the model based on 120° jumps of the whole cation alone, the protons rotate on two distinct circles. Then the one-proton scattering function involves averaged structure factors

$$A_0(Q) = \tfrac{1}{9}[3 + 2j_0(Qr_1\sqrt{3}) + 4j_0(Qr_2\sqrt{3})] \qquad (6.53a)$$

$$A_1(Q) = \tfrac{2}{9}[3 - j_0(Qr_1\sqrt{3}) - 2j_0(Qr_2\sqrt{3})] \qquad (6.53b)$$

where $r_1 = 1.433$ Å and $r_2 = 2.110$ Å. The EISF corresponding to simultaneous occurrence of both types of motions is also drawn, evaluated from the method based upon group theory (Thibaudier and Volino 1973, Rigny 1972). (Refer to §6.10 for more information.) The large difference between the three model curves is due to appreciable difference in the relevant rotation radii of the protons. Experimental determination of $A_0(Q)$, at several temperatures clearly proves the existence, in the three phases, of methyl groups reorientations alone. As predicted by NMR, whole-cation jumps are too slow to produce any quasielastic broadening. Moreover, the methyl dynamics is well described by a unique Arrhenius law, without any discontinuity at the transitions:

$$\tau = 1.05 \times 10^{-12} \exp(E_a/RT) \text{ s},$$

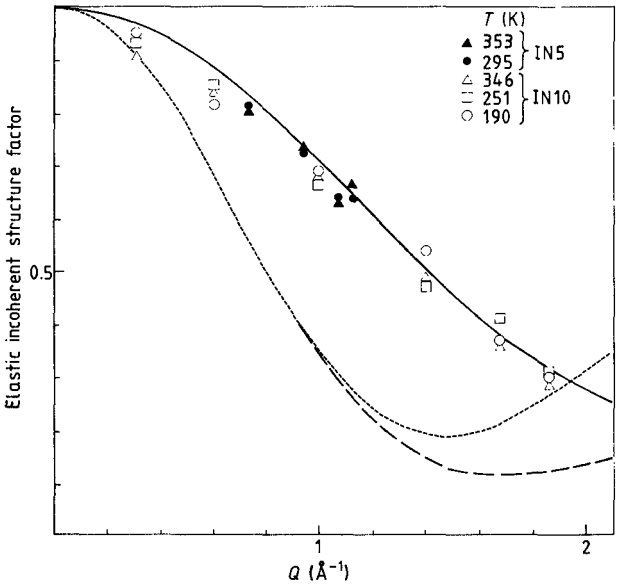

Figure 6.11 EISF for different models of rotations in TMOS-iodide, as functions of Q. Full curve corresponds to methyl $\frac{2}{3}\pi$ rotations alone, dotted curve to $\frac{2}{3}\pi$ jumps of the cation about its threshold axis. The broken curve corresponds to simultaneous occurrence of these motions. Experimental values are indicated (Béc *et al* 1985a).

with an activation energy $E_a = 10.6\ \text{kJ mol}^{-1}$.

These results differ from the conclusions of IQNS studies of other compounds where three methyls are bounded to the same atom. More precisely, in the case of t-butyl cyanide (Frost *et al* 1980a, Frost *et al* 1982) and t-butyl chloride (Frost *et al* 1980b) it was concluded that the correlation time for methyl rotation was longer than that for t-butyl rotation, in conflict with previous NMR results (O'Reilly *et al* 1973). IQNS measurements with trimethylammonium ion led to similar conclusions (Schlaak *et al* 1977). In the disordered phase above $T = 308$ K, quasielastic broadening was interpreted by a rotational diffusion of the whole cation about its threefold axis. Methyl reorientations were found to occur on a longer time-scale, outside the instrument time-analysis range.

6.7 Jump Model Among N Equivalent Sites on a Circle

When the number of sites is greater than three, use can be made of the

general relations derived by Barnes (1973) in the study of the 'rotator' phase transition in *n*-nonadecane. Consider a particle located at the *i*th site among N equivalent sites equally distributed on a circle of radius r. The particle is allowed to perform a random walk among these sites. Jumps are restricted to neighbouring sites. The average time spent by a proton in a site between two successive jumps is τ. The probability that the particle is on the jth site at time t, $p_j(t)$, satisfied a jump rate equation (Dianoux *et al* 1975)

$$\frac{\mathrm{d}}{\mathrm{d}t} p_j(t) = \frac{1}{2\tau} [p_{j-1}(t) - 2p_j(t) + p_{j+1}(t)] \tag{6.54}$$

The resulting expression of the scattering law is, for a powder sample (Barnes 1973, Dianoux *et al* 1975, Leadbetter and Lechner 1979)

$$S_{\mathrm{inc}}(Q, \omega) = A_0(Q)\delta(\omega) + \sum_{l=1}^{N-1} A_l(Q) \frac{1}{\pi} \frac{\tau_l}{1 + \omega^2\tau_l^2} \tag{6.55}$$

with

$$A_l(Q) = \frac{1}{N} \sum_{n=1}^{N} j_0(Qr_n) \cos\left(\frac{2ln\pi}{N}\right). \tag{6.56}$$

The r_n are the jump distances under the effect of $(2n\pi/N)$ rotations (see figure 6.12)

$$r_n = 2r \sin\left(\frac{n\pi}{N}\right). \tag{6.57}$$

The correlation times are evaluated from (Barnes 1973)

$$\tau_l^{-1} = 2\tau^{-1} \sin^2\left(\frac{\pi l}{N}\right). \tag{6.58}$$

Table 6.2 gives the widths of the relevant lorentzian functions and the expressions of the structure factors for a series of models corresponding to a number of equivalent sites from three to six. Structure factors related to the same value of the correlation time evaluated from (6.58) have been added together. The value $\tau_0^{-1} = 0$ corresponds to purely elastic scattering, i.e. to the delta function in (6.55). It is obtained from equation (6.58) in both cases $l = 0$ or $l = 6$, i.e. in the cases where the proton remains fixed or undergoes a jump returning it to its original position.

Variations of the structure factors as function of Q are illustrated in figure 6.13, in a range $Qr \leqslant 4.0$. Clearly, at least in this Q range, models based upon a number of sites $N \geqslant 6$ lead to practically the same EISF.

Two-site and three-site jump-models involve a single lorentzian function in the quasielastic part of their scattering law. The width of the broadened spectra remains constant as function of Q. Conversely,

four-site and six-site models involve two and three lorentzian functions respectively. Furthermore, their relative weights, i.e. the quasielastic structure factors, strongly depend on Q (figure 6.13). The resulting width of the quasielastic scattering is no longer constant and varies as a function of the momentum transfer (figure 6.14).

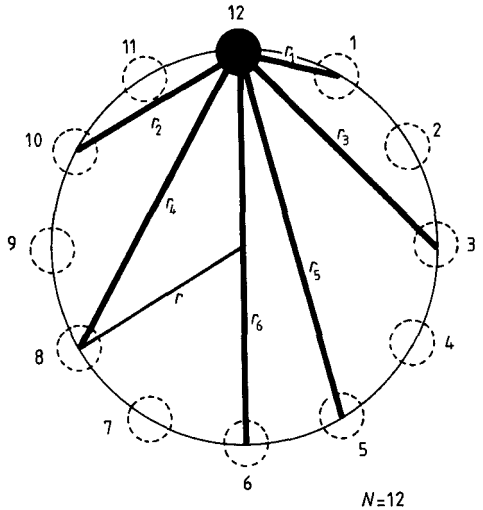

Figure 6.12 Jump model among twelve equivalent sites equally spaced on a circle with radius r. Possible jump distances r_1, r_2 . . ., r_6 are indicated. To simplify the figure, only one of each of them is illustrated. However, for instance, r_1 also corresponds to the distance between sites 11 and 12. The same remark holds for r_2, r_3, r_4 and r_5.

If the number of equilibrium positions is sufficiently large, the scattering function for a jump model is nearly identical to that of a continuous rotation (Dianoux *et al* 1975, Leadbetter and Lechner 1979) at least in the limit $Qr < \pi$. Under these conditions, the rotational diffusion constant D_r can be identified with the jump-rate probability $1/\tau_1$ obtained from (6.58)

$$D_r \simeq \frac{1}{\tau_1} = \frac{2}{\tau} \sin^2\left(\frac{\pi}{N}\right). \tag{6.59}$$

Then the correlation times τ_l are most often expressed as

$$\tau_l = \tau_1 \frac{\sin^2(\pi/N)}{\sin^2(l\pi/N)}. \tag{6.60}$$

Table 6.2 Widths of the lorentzian functions and expressions of the elastic (EISF) and quasielastic structure factors, corresponding to uniaxial rotational jump models between N sites equally spaced on a circle of radius r. The terms $a_l(Q)$ can be calculated from (6.56) and (6.57). τ is the mean residence time. Characteristic times τ_l can be evaluated from (6.58).

	$N = 2$	
$\frac{1}{\tau_0} = 0$	$A_0(Q) = a_0(Q)$	$= \frac{1}{2}[1 + j_0(2Qr)]$
$\frac{1}{\tau_1} = \frac{2}{\tau}$	$A_1(Q) = a_1(Q)$	$= \frac{1}{2}[1 - j_0(2Qr)]$
	$N = 3$	
$\frac{1}{\tau_0} = 0$	$A_0(Q) = a_0(Q)$	$= \frac{1}{3}[1 + 2j_0(Qr\sqrt{3})]$
$\frac{1}{\tau_1} = \frac{1}{\tau_2} = \frac{1.5}{\tau}$	$A_1(Q) = a_1(Q) + a_2(Q)$	$= \frac{2}{3}[1 - j_0(Qr\sqrt{3})]$
	$N = 4$	
$\frac{1}{\tau_0} = 0$	$A_0(Q) = a_0(Q)$	$= \frac{1}{4}[1 + 2j_0(Qr\sqrt{2}) + j_0(2Qr)]$
$\frac{1}{\tau_1} = \frac{1}{\tau_3} = \frac{1}{\tau}$	$A_1(Q) = a_1(Q) + a_3(Q)$	$= \frac{1}{2}[1 - j_0(2Qr)]$
$\frac{1}{\tau_2} = \frac{2}{\tau}$	$A_2(Q) = a_2(Q)$	$= \frac{1}{4}[1 - 2j_0(Qr\sqrt{2}) + j_0(2Qr)]$

Table 6.2 (*cont.*)

$N = 6$		
$\frac{1}{\tau_0} = 0$	$A_0(Q) = a_0(Q)$	$= \frac{1}{6}[1 + 2j_0(Qr) + 2j_0(Qr\sqrt{3}) + j_0(2Qr)]$
$\frac{1}{\tau_1} = \frac{1}{\tau_5} = \frac{0.5}{\tau}$	$A_1(Q) = a_1(Q) + a_5(Q)$	$= \frac{1}{6}[2 + 2j_0(Qr) - 2j_0(Qr\sqrt{3}) - 2j_0(2Qr)]$
$\frac{1}{\tau_2} = \frac{1}{\tau_4} = \frac{1.5}{\tau}$	$A_2(Q) = a_2(Q) + a_4(Q)$	$= \frac{1}{6}[2 - 2j_0(Qr) - 2j_0(Qr\sqrt{3}) + 2j_0(2Qr)]$
$\frac{1}{\tau_3} = \frac{2}{\tau}$	$A_3(Q) = a_3(Q)$	$= \frac{1}{6}[1 - 2j_0(Qr) + 2j_0(Qr\sqrt{3}) - j_0(2Qr)]$

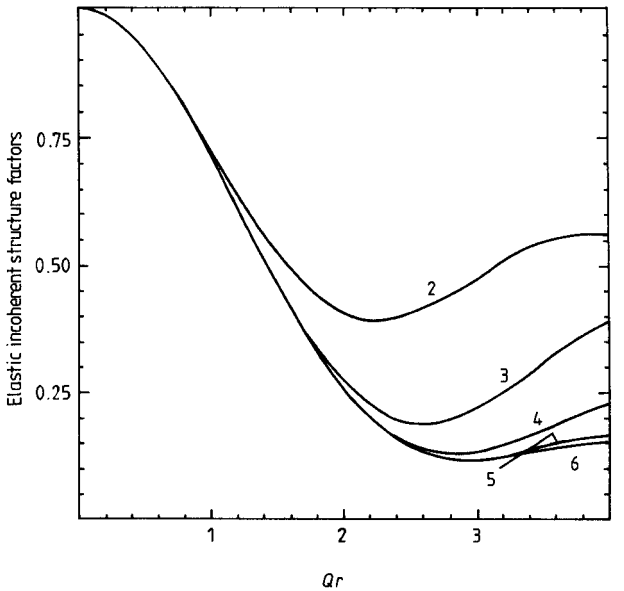

Figure 6.13 EISF and quasielastic structure factors for jump models over N sites equally spaced on a circle. Values of N are shown on curves.

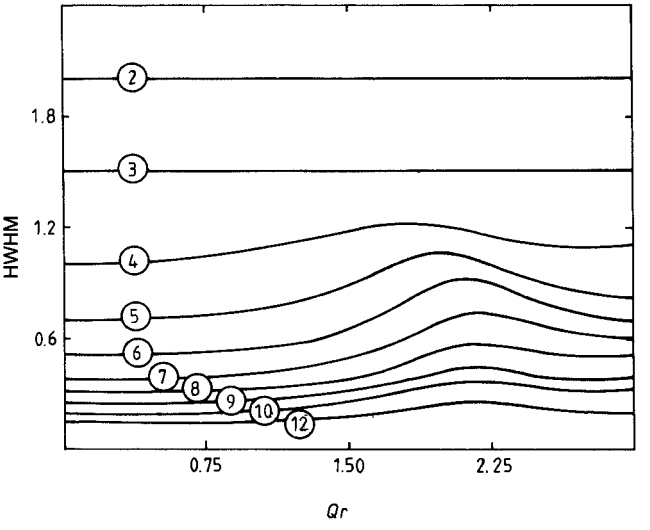

Figure 6.14 Half-widths at half-maximum, as functions of Qr for the quasielastic part of the spectra, for jump models over N sites equally spaced on a circle. They are expressed in units of τ^{-1}, where τ is the mean residence time between two successive jumps.

Considerable uncertainty exists, in the literature, concerning the exact meaning of the correlation times. It is worth noting that both Dianoux *et al* (1975) and Leadbetter and Lechner (1979) define τ as the average time spent by a nucleus in an equilibrium site. In other words, τ is the time between its arrival in this site and and its departure under the effect of a $2\pi/N$ or $-2\pi/N$ rotation. Barnes (1973) defines τ^{-1} as a rate constant, i.e. $\tau^{-1}\Delta t$ is the probability for a $2\pi/N$ jump to occur during the time Δt, which is equal to the probability for a $-2\pi/N$ jump to occur during the same time interval. Consequently, the correlation time τ of Barnes (1973) is twice the value of τ according to Dianoux *et al* or Leadbetter and Lechner.

Applying the general relation (6.60) to the simple case $N = 3$, leads immediately to two identical correlation times corresponding to $l = 1$ or $l = 2$:

$$\tau_1 = \tau_2 = \tfrac{2}{3}\tau. \tag{6.61}$$

Direct calculation from jump-rate equations performed in §6.6.1 leads to a double eigenvalue $\alpha = 3/\tau$, because τ^{-1} was introduced as a jump-rate probability from one site to another. Summing the structure factors related to τ_1 and τ_2, evaluated from (6.56), leads to expressions identical to (6.26).

Conversely, in the case of two sites over a circle, application of (6.60) leads to a single correlation time

$$\tau_1 = \frac{\tau}{2} \tag{6.62}$$

in accordance with §6.5.1. This is because the model presented in that section is a two-site model where τ^{-1} is the probability of going from one site to another, in a straight path, without introducing the concept of rotation over a circle, and consequently without any consideration of sense of rotation. Then τ was defined, according to Dianoux *et al* (1975) or Leadbetter and Lechner (1979), as the mean time spent in one of the two sites.

6.8 Examples of Jump Models Over a Circle

6.8.1 Nickelocene

Nickelocene $Ni(C_5H_5)_2$ belongs to the metallocene family, i.e. one metal sandwiched by two cyclopentadienyl rings (figure 6.15). Whilst the crystal structure remains monoclinic from 100 K to 300 K (Chhor *et al* 1982), anomalies were observed in the structural parameters and in the heat capacity curve in the 170 K–240 K temperature range. Because the

variation of entropy was found to correspond with $\Delta S = R \ln 2$, an interpretation was given in terms of a second-order-like transition, related to the existence of two distinct configurations (Azokpota *et al* 1976). In the low-temperature phase, molecules are in nearly eclipsed conformation (Clech and Calvarin 1981) with D_5 symmetry, as evidenced by Raman spectroscopy (Chhor *et al* 1981). First IQNS results were reported by Gardner *et al* (1981). Then Sourisseau *et al* (1983) could draw precise conclusions about the nature of the reorientational process, i.e. (i) to determine the precise number of equilibrium positions among which the ring jumps occur (five or ten) and (ii) to compare the dynamical disorder of both rings of a given molecule.

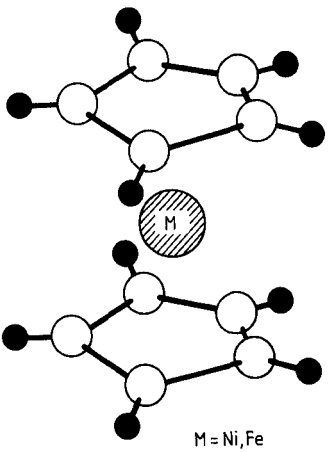

Figure 6.15 Sketch of the nickelocene $(C_5H_5)_2Ni$ or ferrocene $(C_5H_5)_2Fe$ molecules.

As already pointed out in §6.7 both $2\pi/5$- and $2\pi/10$-jump models lead to practically the same EISF curve while $Qr \leqslant 3$. In the case of a rotating C_5H_5 ring, distinction becomes possible only for $Q \geqslant 1.6$ Å^{-1}, as shown in figure 6.16. Experimental values obtained by Sourisseau *et al* at $T = 300$ K are in agreement with $2\pi/5$ jumps. Furthermore, the correlation time of the process deduced from an extensive analysis using t.o.f. and backscattering technique, was found to follow the Arrhenius law

$$\tau_c = 3.3 \times 10^{-13} \exp(\Delta H/RT) \text{ s} \tag{6.63}$$

with $\Delta H = 6.3$ kJ mol^{-1}, below and above the diffuse phase transition at about 200 K. Thus reorientations of all the protons are governed by the same mechanism over the whole 100–300 K temperature range. At

$T = 300$ K. $\tau_c = 4 \times 10^{-12}$ s in agreement with the value of 3×10^{-12} s reported by Gardner *et al* (1981). The activation energy is of the same order of magnitude as the potential barrier hindering the C_5H_5 ring reorientations (5.0 kJ mol^{-1}) derived from Raman spectroscopy (Sourisseau *et al* 1983). The difference could arise from the contribution of the reorientational motions of molecules as a whole, which are not observed by vibrational spectroscopy, but also from intermolecular interaction.

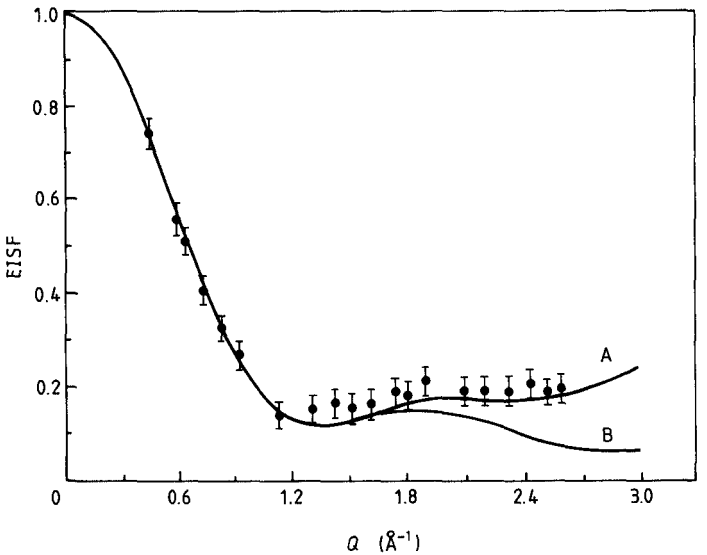

Figure 6.16 EISF for different reorientational motions of the protons of C_2H_5 rings of nickelocene $(C_2H_5)_2Ni$, on a circle of radius 2.15 Å: Curves A and B correspond to $\frac{2}{5}\pi$ and $\frac{2}{10}\pi$ jumps, respectively. Experimental values extracted from the spectra are indicated (after Sourisseau *et al* 1983).

However, the absence of discontinuity in the Arrhenius law cannot explain the anomaly in the heat-capacity measurement. A qualitative interpretation was given (Chhor *et al* 1981, Chhor 1982), describing the potential by an asymmetric double-well function obtained by the superposition of a V_5 (five-fold) and a V_{10} (ten-fold) potential, with a dephasing roughly equal to about 12°. This leads to a tilt angle of $\simeq 9°$ between both rings within a molecule. Under these conditions, the C_p anomaly is related to the coexistence of some rings undergoing small-amplitude oscillations in the lower part of the potential, while other rings oscillate around another position corresponding to the upper part

of the well. This small asymmetry cannot be evidenced in the IQNS measurement.

6.8.2 Ferrocene

At $T = 164$ K, ferrocene $Fe(C_5H_5)_2$ (see figure 6.15) undergoes a transition (Edwards *et al* 1959) from a high-temperature, monoclinic form, into a low-temperature, triclinic phase. Below 250 K, both forms appear to be metastable with respect to an orthorhombic form (Barar *et al* 1980, Ogasahara *et al* 1979), after cooling below 164 K and then annealing at about 200 K for several hours. The room-temperature, monoclinic phase is disordered, as shown by x-ray and neutron diffraction (Seiler and Dunitz 1979, Takusagawa and Koetzle 1979). Electron diffraction experiments have shown that, in the gas phase, cyclopentadienyl rings can rotate with an activation energy of 3.8 kJ mol^{-1}. Ring reorientations were also detected by NMR in the low-temperature phase. Above 164 K, several relaxation times were detected. X-ray and neutron diffraction experiments in the high-temperature phase were explained by a disorder model involving two different molecular orientations, i.e. ten equilibrium sites, for the rings. Conversely, proton jumps amongst five-fold sites were detected by IQNS (Gardner *et al* 1981), but the possibility of a slower relaxation between two sets of five-fold sites belonging to different molecular orientations was not excluded.

Independently of the precise nature of the reorientation ($2\pi/5$ and/or $2\pi/10$ jumps), an activation energy of 4.4 kJ mol^{-1} was derived with a pre-exponential factor $\tau_0 = 8 \times 10^{-13}$ s in the case of $2\pi/5$ jumps. At low temperature, an inelastic feature appears at 2.7 meV, which was attributed to the frequency of the libration in one of the wells. For this energy transfer, a characteristic time of 3.75×10^{-13} s is obtained which, following Brot (1969) is in agreement with $\tau_0/2$, thus confirming the $2\pi/5$-jump model. Below 164 K, a small broadening of the IQNS spectra is still visible. Since the crystalline structure of the low-temperature phase appears to be ordered (Seiler and Dunitz 1979), the reorientation is almost certainly between five indistinguishable sites.

6.8.3 Arene metal tricarbonyl compounds

The dynamics of aromatic rings was also investigated in the arene metal tricarbonyl compounds $C_6H_6Cr(CO)_3$ and $(C_5H_5)Mn(CO)_3$.

Raman-band broadenings evidence the existence in these complexes of a low barrier height and thus the possibility of ring jumps (Chhor *et al* 1981).

For $C_6H_6Cr(CO)_3$, no anomaly exists in the heat-capacity curve,

which would indicate the existence of distinguishable configurations of molecules in the crystal. Then $2\pi/6$ ring reorientations and/or $2\pi/3$ whole-molecule reorientations can both be envisaged, as long as they keep the crystal invariant. NMR measurements (Delise *et al* 1975) give an activation energy and a residence time at $T = 300$ K equal to 17.6 kJ mol^{-1} and 4.6×10^{-11} s, respectively. IQNS data at $T = 300$ K (Chhor *et al* 1984, Lucazeau 1983) permit the determination of an EISF corresponding to $2\pi/6$ uniaxial jumps of the aromatic rings. The residence time was found equal to 4.8×10^{-11} s and the activation energy was estimated equal to 15.5 kJ mol^{-1}, in agreement with NMR and with the torsional potential barrier calculated from the torsional frequency (86.5 cm^{-1}).

For $C_5H_5Mn(CO)_3$, a very small anomaly is observed between 75 K and 300 K (Chhor and Pommier 1984) which was not interpreted in terms of distinguishable configurations. Whole-molecule reorientations are forbidden and only $2\pi/5$ ring-reorientations are allowed. From NMR measurements (Butler *et al* 1983) an activation energy of 7.2 kJ mol^{-1} associated with a correlation time of 6.4×10^{-13} s at $T = 300$ K, was obtained for ring reorientations. IQNS results confirm the $2\pi/5$ jump model of ring reorientations whilst the value of the activation energy (16.8 kJ mol^{-1}) is far from both the NMR value and the value deduced from the torsional frequency ($\simeq 10$ kJ mol^{-1} at $T = 300$ K). This inaccuracy can be explained by the rather restricted temperature range of investigation.

6.8.4 1-Cyanoadamantane

From the point of view of steric hindrance, the 1-cyanoadamantane molecule (figure 6.17) exhibits a general globular shape on which is bound a linear group. A weakly first-order phase transition occurs at $T = 228$ K between a low-temperature, monoclinic ordered phase, and a high-temperature, fcc, plastic phase. Crystal structure determinations (Amoureux and Bée 1979, Amoureux *et al* 1981a) have shown that several equilibrium orientations are accessible to the same molecule. First, the C≡N group can occupy six possible equilibrium orientations along the three fourfold axes of the cubic cell, in one of the octahedral sites of the lattice. Moreover, around one precise [100] axis, each molecule can occupy four distinct equilibrium orientations. Taking into account the C_{3v} molecular symmetry, there are twelve accessible orientations equally spaced by 30° about each of these directions.

NMR experiments, together with dielectric relaxation measurements have evidenced two types of motions: first a rapid rotation of the molecule around its threefold axis ($\tau \simeq 10^{-12}$ s at 300 K) and also a tumbling of the CN group between the [100] axes, but at a much slower

rate ($\tau > 10^{-8}$ s at the melting point). The IQNS technique was used to investigate the uniaxial rotation of the molecule (Bée *et al* 1980a). Variations of the structure factors as function of Q, evaluated from (6.56) and averaged over the three values of rotation radius for the protons, are illustrated in figure 6.18. Considering the large number of equilibrium positions about the fourfold lattice axis and the fact that only a small 30° rotation is sufficient to jump from one position to a neighbouring one, it may be assumed that the molecular motion will approach rotational uniaxial diffusion. Under these conditions, it would be possible to describe the incoherent rotational scattering law by the expression (6.26). Corresponding structure factors are illustrated in figure 6.18, whilst correlation times are reported in table 6.3. Clearly, the widths of the three first lorentzian functions coincide with those calculated from (6.58). Other values differ noticeably but their related structure factors contribute less to the scattered intensity in the momentum transfer range of the experiment.

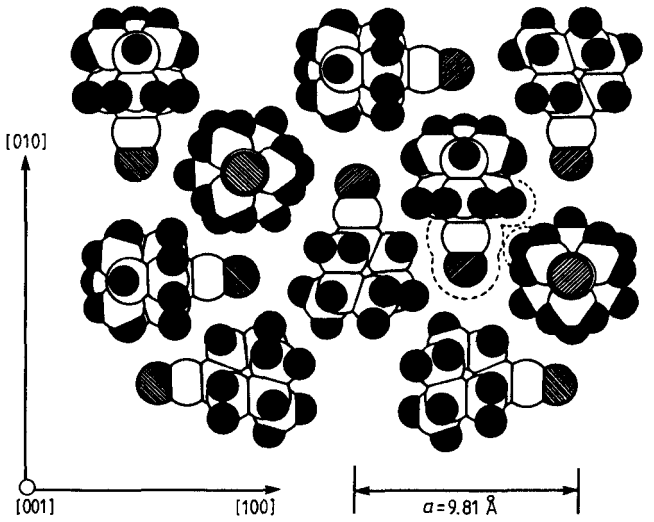

Figure 6.17 An example of the possible local order of the cyanoadamantane molecule along the [100] axes of the fcc lattice. In order to clarify the figure, van der Waals radii have been reduced in the ratio $\frac{2}{3}$. The exact steric hindrance is illustrated by the broken line. It is evidence that uniaxial rotations about the molecular threefold axis are only weakly hindered. Conversely, tumbling reorientations of neighbouring molecules among [100] lattice directions are strongly correlated.

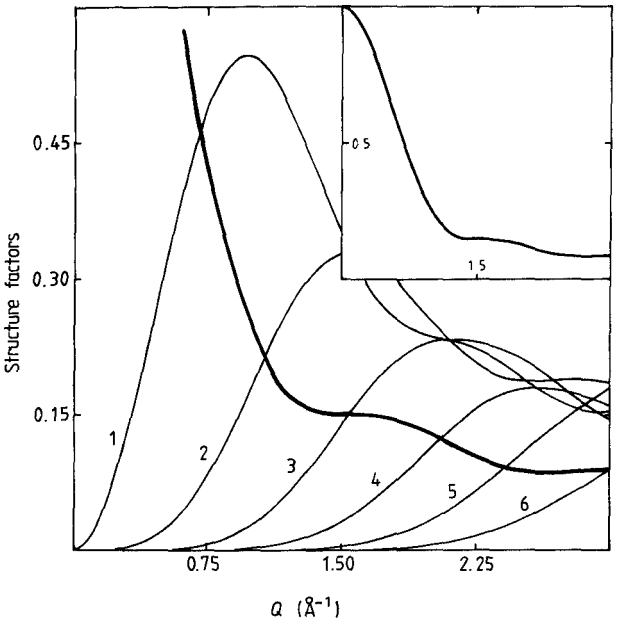

Figure 6.18 Elastic and quasielastic structure factors as a function of the modulus of the scattering vector, Q, in the case of a model based on 30° jumps of the 1-cyanoadamantane molecule about its threshold symmetry axis (full curves). These curves are coincident with the structure factors evaluated from equation (6.26) on the basis of the rotational diffusion model ($l = 1, 2, \ldots$, etc (shown on curves)).

6.9 Reorientations of a Molecule About Several Different Axes in Space

Until now, we have considered reorientations of whole molecules or of parts of them which occur by rotation about one single axis. However, in many cases, molecular reorientations in disordered phases occur about several (crystallographic) axes. More precisely in a cubic lattice, there are three equivalent [100] directions, four [111] diagonal and six [110] axes. Molecules with spherical shape, can *a priori* rotate about all of these axes. Calculation of models taking into account all possibilities of reorientation, with corresponding correlation times is tedious work when starting from the set of rate equations for jump probabilities (see §6.5.1).

A formalism using group theory, was developed to calculate correlation functions resulting from molecular reorientations in crystals (Rigny

Table 6.3 Comparison of the widths of the lorentzian functions for a rotational diffusion model and a jump model between twelve equilibrium positions equally spaced on a circle. Explanations of symbols are given in the text

m	$m^2 D_r$	$\frac{m^2}{\tau_l}$	$\frac{1}{\tau_m}$ (jump model)
0	0	0	0
1	D_r	$\frac{0.134}{\tau}$	$\frac{0.134}{\tau}$
2	$4D_r$	$\frac{0.536}{\tau}$	$\frac{0.5}{\tau}$
3	$9D_r$	$\frac{1.206}{\tau}$	$\frac{1}{\tau}$
4	$16D_r$	$\frac{2.144}{\tau}$	$\frac{1.5}{\tau}$
5	$25D_r$	$\frac{3.35}{\tau}$	$\frac{1.866}{\tau}$
6	$36D_r$	$\frac{4.824}{\tau}$	$\frac{2}{\tau}$

1972). Characteristic times are simply calculated with the help of the character tables. Next, calculations were generalised (Thibaudier and Volino 1973) and extended to models permitting reorientations around both fixed (crystallographic) and mobile (molecular) axes.

This method has proved to be very fruitful in many complicated cases of reorientations in molecular crystals, especially for molecules containing side groups reorienting about their own symmetry axis, in the same time that whole-molecule reorientations occur. Assuming that the two types of jumps occur independently this formalism allows characteristic times related to each process to be obtained.

6.9.1 Application of group theoretical method. The formalism of Rigny

In the case of incoherent quasielastic scattering, the relevant quantity to be evaluated is the autocorrelation function

$$I(\boldsymbol{Q}, t) = \langle e^{i\boldsymbol{Q}\cdot\boldsymbol{r}(t)}\, e^{-i\boldsymbol{Q}\cdot\boldsymbol{r}(0)} \rangle .$$

From the reorientational motion of the molecule, $e^{i\boldsymbol{Q}\cdot\boldsymbol{r}(t)}$ is a random function of time. More generally, we consider a function $f(t)$, depending on the molecule orientation, which can take n equally probable values f_i. These values f_i are assumed to correspond with one another under

the effects of the rotations of a finite group G.

We define $p_{ij}(t)$, the conditional probability that $f(t) = f_j$ at time t if $f(0) = f_i$ at time 0:

$$f_i(t) = \sum_j p_{ij} f_j. \tag{6.64}$$

The correlation function for $f(t)$ is given by

$$F(t) = \langle f^*(0) f(t) \rangle = \frac{1}{n} \sum_{ij} f_i^* p_{ij}(t) f_j = \frac{1}{n} \sum_i f_i^* f_i(t). \tag{6.65}$$

Now we suppose that the probability for one particular rotation of the class Q of the group G to occur in the time interval $\mathrm{d}t$ is $\mathrm{d}t/\tau_q$ i.e. the same for all rotations in the class. The probability for any one rotation of the n_q rotations of the class Q to occur in this time interval is $n_q \mathrm{d}t/\tau_q$. The quantities f_i define a representation $\langle\langle f \rangle\rangle$ with dimension n of the group G.

Suppose now that we introduce n linear combinations of the f_i

$$\varphi_k = \sum_{j=1}^{n} \alpha_{kj} f_j \tag{6.66}$$

and

$$\varphi_k(t) = \sum_{j=1}^{n} \alpha_{kj} f_j(t) \tag{6.67a}$$

$$\varphi_k(0) = \varphi_k \tag{6.67b}$$

which are time-dependent, together with the conditional probabilities

$$\Pi_{kl}(t) = \sum_{ij} \alpha_{ki} p_{ij}(t) \alpha_{jl}^*. \tag{6.68}$$

So, we can write

$$\varphi_k(t) = \sum_{l=1}^{n} \Pi_{kl}(t) \varphi_l \tag{6.69}$$

and the correlation function $F(t)$ is given by

$$F(t) = \frac{1}{n} \sum_{kl} \varphi_{kl}^* \Pi_{kl}(t) \varphi_l = \frac{1}{n} \sum_{k=1}^{n} \varphi_k^* \varphi_k(t) \tag{6.70}$$

providing that the transformation $f \rightarrow \varphi$ is unitary, i.e.

$$\sum_{j=1}^{n} \alpha_{ij} \alpha_{jk}^* = \delta_{ik}. \tag{6.71}$$

Suppose now that the linear combination φ_k are the basis functions for a decomposition of the representation $\langle\langle f \rangle\rangle$ of the group G into irreducible components. So we introduce a notation with two indices φ_k^μ, where μ denotes the irreducible representation.

Any rotation $\mathcal{R}$ of G transforms the function φ_l^ν into a linear combination $\mathcal{R}\varphi_l^\nu$ of the function φ_l^ν which are in the same representation. So, we have

$$\Pi_{kl}^{\mu\nu}(t) = \Pi_{kl}^{\mu\mu}(t)\delta_{\mu\nu} \tag{6.72a}$$

and

$$\varphi_k^\mu(t) = \sum_{l=1}^{n_\mu} \Pi_{kk}^{\mu\mu}(t)\varphi_l^\mu. \tag{6.72b}$$

We consider the effect of the n_q rotations of the class Q of the group G.

$$\varphi_k^\mu(t + dt) = \varphi_k^\mu(t)\left(1 - n_q \frac{dt}{\tau_q}\right) + \frac{dt}{\tau_q}\sum_{\mathcal{R}\in Q}\mathcal{R}\left(\sum_{lv}\Pi_{kl}^{\mu\nu}(t)\varphi_l^\nu\right) \tag{6.73a}$$

$$= \varphi_k^\mu(t)\left(1 - n_q \frac{dt}{d\tau_q}\right) + \frac{dt}{\tau_q}\sum_{\mathcal{R}\in Q}\mathcal{R}(\varphi_k^\mu). \tag{6.73b}$$

The first term is the probability that none of the n_q rotations of the class Q occurs during the time dt. Moreover, because the φ_l^ν form the basis functions of an irreducible representation, $\mathcal{R}$ is the matrix $D_\mu(\mathcal{R})$ representative of the rotation $\mathcal{R}$ in the irreducible representation μ. Moreover, from Schur's lemma II:

$$\sum_{\mathcal{R}\in Q} D_\mu(\mathcal{R})\varphi_k^\mu = n_q \frac{\chi_q^\mu}{\chi_E^\mu}\varphi_k^\mu \tag{6.74}$$

where E denotes the identity operation.

$$\frac{d}{dt}\varphi_k^\mu(t) = -\frac{n_q}{\tau_q}\left(1 - \frac{\chi_q^\mu}{\chi_E^\mu}\right)\varphi_k^\mu(t). \tag{6.75}$$

Adding together the effects of the different classes of the group, we obtain:

$$F(t) = \frac{1}{n}\sum_{k\mu}[\varphi_k^{\mu *}\ \varphi_k^\mu]\exp(-|t|/\tau_\mu) \tag{6.76a}$$

with

$$\tau_\mu^{-1} = \sum_q \frac{n_q}{\tau_q}\left(1 - \frac{\chi_q^\mu}{\chi_E^\mu}\right) \tag{6.76b}$$

It is worth pointing out:

(a) If μ is the identity representation $\chi_q^\mu = \chi_E^\mu = 1$. Then $1/\tau_E = 0$, and the corresponding term is

$$\frac{1}{n}(\varphi_E^*\varphi_E) = \sum_i \left[\frac{f_i}{n}\right]^2 \tag{6.77}$$

independent of the time.

(b) It is possible to obtain $1/\tau_\mu = 0$ for other representations.

(c) If all the rotations of the group occur with the same probability, according to

$$\sum_q n_q \chi_q^\mu = 0 \qquad \text{(for } \mu \neq \text{identity representation)} \tag{6.78}$$

then

$$\frac{1}{\tau_\mu} = \frac{1}{\tau}\sum_q n_q\left(1 - \frac{\chi_q^\mu}{\chi_1^\mu}\right) = \frac{1}{\tau}\sum_q n_q = \frac{g}{\tau} \tag{6.79}$$

and $1/\tau_\mu$ becomes independent of μ. In that case

$$F(t) = \left|\frac{1}{n}\sum_i f_i\right|^2 + \left[\frac{1}{n}\sum_i |f_i|^2 - \left|\frac{1}{n}\sum_i f_i\right|^2\right] e^{-|t|/\tau} \tag{6.80}$$

(d) Cyclic groups have complex characters. However, rotations $\mathcal{R}$ corresponding to these characters are not discernible from rotations $\mathcal{R}^{-1}$ whose characters are complex conjugated. Associating these rotations we are led to a time constant with real values.

(e) The correlation function generally involves several exponential decays.

6.9.2 *Example: reorientations according to the rotations of the group 32 ($\mathcal{D}_3$)*

This group has six rotations (see figure 6.19): the identity operation E, two rotations C_3 and C_3^2 of $+120°$ and $-120°$ about a threefold axis (Oz)

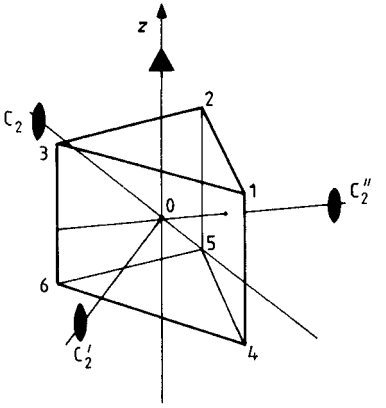

Figure 6.19 Possible reorientations and accessible positions in the case of the group $\mathcal{D}_3$.

and three 180° rotations C_2, C_2' and C_2'' about three twofold axes perpendicular to the Oz axis. Considering any point 1, 2, . . ., 6 successive applications of all these rotations generates the others. The six functions

$$f_i = \exp(i\boldsymbol{Q}\cdot\boldsymbol{r}_i) \qquad i = 1, 2, 3, 4, 5, 6$$

form the basis of a representation of the group $\mathcal{D}_3$, on which the matrices representing the rotations take the form

$$D(E) = \left(\begin{array}{c:c} 100 & 000 \\ 010 & 000 \\ 001 & 000 \\ \hdashline 000 & 100 \\ 000 & 010 \\ 000 & 001 \end{array}\right) \qquad D(C_3) = \left(\begin{array}{c:c} 001 & 000 \\ 100 & 000 \\ 010 & 000 \\ \hdashline 000 & 001 \\ 000 & 100 \\ 000 & 010 \end{array}\right) \qquad D(C_3^2) = \left(\begin{array}{c:c} 010 & 000 \\ 001 & 000 \\ 100 & 000 \\ \hdashline 000 & 010 \\ 000 & 001 \\ 000 & 100 \end{array}\right)$$

$$D(C_2) = \left(\begin{array}{c:c} 000 & 100 \\ 000 & 001 \\ 000 & 001 \\ \hdashline 100 & 000 \\ 001 & 000 \\ 010 & 000 \end{array}\right) \qquad D(C_2') = \left(\begin{array}{c:c} 000 & 001 \\ 000 & 010 \\ 000 & 100 \\ \hdashline 001 & 000 \\ 010 & 000 \\ 100 & 000 \end{array}\right) \qquad D(C_2'') = \left(\begin{array}{c:c} 000 & 010 \\ 000 & 100 \\ 000 & 001 \\ \hdashline 010 & 000 \\ 100 & 000 \\ 001 & 000 \end{array}\right)$$

from which the characters of this representation are easily evaluated:

$$\chi(E) = 6 \qquad \chi(C_3) = \chi(C_3^2) = \chi(C_2') = \chi(C_2'') = \chi(C_2''') = 0.$$

The problem is to find a basis for an irreducible representation.

Having three different classes, the group $\mathcal{D}_3$ possesses three irreducible representations, the characters of which are listed in table 6.4. Now we apply the general relation which gives the number of times n_α any irreducible representation labelled α occurs in the decomposition of $\Gamma = \{f_1, f_2, \ldots, f_6\}$, namely

$$n_\alpha = \frac{1}{g}\sum_q n_q \chi^\alpha(C_q)\chi(C_q) \tag{6.81}$$

where the sum runs over all the classes of the group, n_q is the number of rotations in the class q; g is the group order; $\chi^\alpha(C_q)$ and $\chi(C_q)$ denote the characters of the class q in the irreducible representation α and in the reducible representation Γ, respectively. We get,

$$n_{A_1} = \tfrac{1}{6}\{1 \times 1 \times 6 + 2 \times 1 \times 0 + 3 \times 1 \times 0\} = 1$$

$$n_{A_2} = \tfrac{1}{6}\{1 \times 1 \times 6 + 2 \times 1 \times 0 + 3 \times (-1) \times 0\} = 1$$

$$n_E = \tfrac{1}{6}\{1 \times 2 \times 6 + 2 \times (-1) \times 0 + 3 \times 0 \times 0\} = 2$$

and we write

$$\Gamma = A_1 + A_2 = 2E.$$

To obtain the basis function of these irreducible representations, we apply the projection operator

$$\mathcal{P}^{(\alpha)} = \frac{n_\alpha}{g} \sum_{\mathcal{R}} \chi^{\alpha *}(\mathcal{R}) \mathcal{O}_{\mathcal{R}} \tag{6.82}$$

where $\mathcal{O}_{\mathcal{R}}$ is the operator of the rotation $\mathcal{R}$

$$\varphi_i^\alpha = \mathcal{P}^{(\alpha)} f_i. \tag{6.83}$$

We can build three operators

$$P^{(A_1)} = \tfrac{1}{6} [E + C_3 + C_3^2 + C_2 + C_2' + C_2''] \tag{6.84a}$$

$$P^{(A_2)} = \tfrac{1}{6} [E + C_3 + C_3^2 - C_2 - C_2' - C_2''] \tag{6.84b}$$

$$P^{(E)} = \tfrac{1}{3} [2E - C_3 - C_3^2] \tag{6.84c}$$

which enable six functions to be obtained, providing the basis of the irreducible representations:

$$\begin{aligned}
\varphi^{A_1} &= f_1 = \tfrac{1}{6}[f_1 + f_2 + f_3 + f_4 + f_5 + f_6] \\
\varphi^{A_2} &= P^{(A_2)} f_1 = \tfrac{1}{6}[f_1 + f_2 + f_3 - f_4 - f_5 - f_6] \\
\varphi_1^E &= P^{(E)}(f_1 + f_4) = \tfrac{1}{6}[2f_1 - f_2 - f_3 + 2f_4 - f_5 - f_6] \\
\varphi_2^E &= P^{(E)}(f_2 + f_5) = \tfrac{1}{6}[-f_1 + 2f_2 - f_3 - f_4 + 2f_5 - f_6] \\
\varphi_1^{E'} &= P^{(E)}(f_1 - f_4) = \tfrac{1}{6}[2f_1 - f_2 - f_3 - 2f_4 + f_5 + f_6] \\
\varphi_2^{E'} &= P^{(E)}(f_2 - f_5) = \tfrac{1}{6}[-f_1 + 2f_2 - f_3 + f_4 - 2f_5 + f_6].
\end{aligned} \tag{6.85}$$

Evaluation of the correlation times from (6.76b) is straightforward

$$A_1 \rightarrow \tau_{A_1}^{-1} = 0 \tag{6.86a}$$

$$A_2 \rightarrow \tau_{A_2}^{-1} = \frac{2}{\tau_{C_3}} \left(1 - \frac{1}{1}\right) + \frac{3}{\tau_{C_2}} \left(1 - \frac{(-1)}{1}\right) = \frac{6}{\tau_{C_2}} \tag{6.86b}$$

$$E, E' \rightarrow \tau_E^{-1} = \frac{2}{\tau_{C_3}} \left(1 - \frac{(-1)}{2}\right) + \frac{3}{\tau_{C_2}} \left(1 - \frac{0}{2}\right) = \frac{3}{\tau_{C_3}} + \frac{3}{\tau_{C_2}}. \tag{6.86c}$$

Table 6.4 Character table for the group $\mathcal{D}_3$

$32(\mathcal{D}_3)$	E	$2C_3$	$3C_2$
A_1	1	1	1
A_2	1	1	−1
E	2	−1	0
$\Gamma = \{f_1, f_2, \ldots, f_6\}$	6	0	0

Thus we can express explicitly

$$\left.\begin{aligned}
&\varphi^{A_1}(t) = \varphi^{A_1}(0)\\
&\varphi^{A_2}(t) = \varphi^{A_2}(0)\exp(-6t/\tau_{C_2})\\
&\varphi_i^{E}(t) = \varphi_i^{E}(0)\exp(-3t/\tau_{C_3} - 3t/\tau_{C_2})\\
&\varphi_i^{E'}(t) = \varphi_i^{E'}(0)\exp(-3t/\tau_{C_3} - 3t/\tau_{C_2})
\end{aligned}\right\} i = 1, 2. \tag{6.87}$$

Finally, the relevant correlation function

$$\begin{aligned}
F(t) &= \langle \exp\{i\boldsymbol{Q}\cdot\boldsymbol{r}(t)\}\exp\{-i\boldsymbol{Q}\cdot\boldsymbol{r}(0)\}\rangle\\
&= \frac{1}{6}\sum_{\mu k}\varphi_k^{\mu *}(0)\varphi_k^{\mu}(t)
\end{aligned} \tag{6.88}$$

is given by

$$\begin{aligned}
F(t) = {} & |\varphi^{A_1}(0)|^2 + |\varphi^{A_2}(0)|^2\exp(-6t/\tau_{C_2})\\
& + \{|\varphi_1^{E}(0)|^2 + |\varphi_2^{E}(0)|^2 + |\varphi_1^{E'}(0)|^2 + |\varphi_2^{E'}(0)|^2\}\\
& \times \exp(-3t/\tau_{C_3} - 3t/\tau_{C_2}).
\end{aligned} \tag{6.89}$$

The different square moduli in this expression are easily evaluated from the relations (6.85) between the set of functions φ^{A_1}, φ^{A_2}, . . . etc and the $f_i = \exp(i\boldsymbol{Q}\cdot\boldsymbol{r}_i)$. Finally, we obtain

$$\begin{aligned}
F(t) = {} & A^{A_1}(\boldsymbol{Q}) + A^{A_2}(\boldsymbol{Q})\exp(-6t/\tau_{C_2})\\
& + A^{E}(\boldsymbol{Q})\exp(-3t/\tau_{C_3} - 3t/\tau_{C_2})
\end{aligned} \tag{6.90}$$

where, if we introduce the jump distances $\boldsymbol{r}_{ij} = \boldsymbol{r}_j - \boldsymbol{r}_i$, and the definitions

$$\begin{aligned}
A_3(\boldsymbol{Q}) = {} & \cos\boldsymbol{Q}\cdot\boldsymbol{r}_{21} + \cos\boldsymbol{Q}\cdot\boldsymbol{r}_{31} + \cos\boldsymbol{Q}\cdot\boldsymbol{r}_{32}\cos\boldsymbol{Q}\cdot\boldsymbol{r}_{54} + \cos\boldsymbol{Q}\cdot\boldsymbol{r}_{64} + \cos\boldsymbol{Q}\cdot\boldsymbol{r}_{65}
\end{aligned} \tag{6.91a}$$

$$\begin{aligned}
A_2(\boldsymbol{Q}) = {} & \cos\boldsymbol{Q}\cdot\boldsymbol{r}_{41} + \cos\boldsymbol{Q}\cdot\boldsymbol{r}_{51} + \cos\boldsymbol{Q}\cdot\boldsymbol{r}_{61} + \cos\boldsymbol{Q}\cdot\boldsymbol{r}_{42} + \cos\boldsymbol{Q}\cdot\boldsymbol{r}_{52}\\
& + \cos\boldsymbol{Q}\cdot\boldsymbol{r}_{62} + \cos\boldsymbol{Q}\cdot\boldsymbol{r}_{43} + \cos\boldsymbol{Q}\cdot\boldsymbol{r}_{53} + \cos\boldsymbol{Q}\cdot\boldsymbol{r}_{63}
\end{aligned} \tag{6.91b}$$

$$A^{A_1}(\boldsymbol{Q}) = \tfrac{1}{18}[3 + A_3(Q) + A_2(Q)] \tag{6.92a}$$

$$A^{A_2}(\boldsymbol{Q}) = \tfrac{1}{18}[3 + A_3(Q) - A_2(Q)] \tag{6.92b}$$

$$A^{E}(\boldsymbol{Q}) = \tfrac{1}{9}[6 - A_3(Q)]. \tag{6.92c}$$

6.9.3 Application of group theoretical methods

We denote by G the group of the full set of instantaneous reorientations $\mathcal{R}$ of a molecule, and by $p(\mathcal{R})$ the probability per unit time that the

rotation $\mathcal{R}$ occurs. The probability $P(\mathcal{R}, t)$ that the molecule has been brought, by the rotation $\mathcal{R}$, from its orientation at time $t = 0$, to its actual orientation at time t, follows a Fokker–Planck equation

$$\frac{\mathrm{d}}{\mathrm{d}t} P(\mathcal{R}, t) = \int p(\mathcal{R}\mathcal{S}^{-1})\, P(\mathcal{S}^{-1}, t) d\mathcal{S} - P(\mathcal{R}, t) \int p(\mathcal{S})\, \mathrm{d}\mathcal{S}. \quad (6.93)$$

Using group-theoretical arguments, Thibaudier and Volino obtained the explicit form of $P(\mathcal{R}, t)$

$$P(\mathcal{R}, t) = \exp(-pt) \sum_{\alpha} d_{\alpha} \mathrm{Tr}\left[\exp\left(\frac{Q_{\alpha}}{d_{\alpha}} t\right) \Gamma^{(\alpha)}(\mathcal{R})\right] \quad (6.94)$$

where

$$p = \int p(\mathcal{S})\, \mathrm{d}\mathcal{S}. \quad (6.95)$$

The sum over α runs over the irreducible representations $\Gamma^{(\alpha)}$ of the group G, with dimension d_{α}. The symbol Tr denotes the trace operator. Q_{α} is a matrix, with dimension d_{α}, defined by

$$Q = d_{\alpha} \int \Gamma^{(\alpha)}(\mathcal{R}^{-1})\, p(\mathcal{R})\, \mathrm{d}\mathcal{R}. \quad (6.96)$$

This expression (6.94) permits calculation of the correlation functions $F(t)$ of any function $f(\boldsymbol{R})$ of a molecular point, from a knowledge of the expressions $p(\mathcal{R})$:

$$F(t) = \int f^{*}(\boldsymbol{R})\, f(\mathcal{R}\boldsymbol{R})\, P(\mathcal{R}, t)\, \mathrm{d}\mathcal{R} \quad (6.97)$$

where $\mathcal{R}\boldsymbol{R}$ is the point deduced from $\boldsymbol{R}$ by the rotation $\mathcal{R}$.

Now we assume that all the rotations belonging to the same class occur with the same probability, independently of the equilibrium orientation. This is not always the case, especially for molecules of low symmetry. We shall discuss this point in the following. The expression (6.94) becomes

$$P(\mathcal{R}, t) = \sum_{\alpha} d_{\alpha} \exp\left[\left(\frac{q_{\alpha}}{d_{\alpha}} - p\right)t\right] \chi_{\alpha}(\mathcal{R}) \quad (6.98)$$

where $\chi_{\alpha}(\mathcal{R})$ is the character of the rotation $\mathcal{R}$ in the irreducible representation $\Gamma^{(\alpha)}$, and also

$$q_{\alpha} = \int \chi_{\alpha}(\mathcal{R}^{-1})\, p(\mathcal{R})\, \mathrm{d}\mathcal{R}. \quad (6.99)$$

Let us consider the case of a finite group. The probability per unit time of a well-defined rotation belonging to the class μ is τ_{μ}^{-1}, where τ_{μ} is the average time between two successive jumps of this class. If n_{μ} is the number of rotations in this class, the characteristic time τ_{α} associated to the irreducible representation $\Gamma^{(\alpha)}$ is given by an expression identical to that derived by Rigny:

$$\frac{1}{\tau_\alpha} = p - \frac{q_\alpha}{d_\alpha} = \sum_\mu \frac{n_\mu}{\tau_\mu}\left(1 - \frac{\chi_\alpha^\mu}{\chi_\alpha^E}\right) \tag{6.100}$$

where E is the identity operation. The sum runs over all the classes of the group. The intermediate rotational scattering function is the self-correlation function of $\exp(i\boldsymbol{Q}\cdot\boldsymbol{R})$ then

$$I_{\text{inc}}^{R}(\boldsymbol{Q}, t) = \sum_\alpha \frac{\chi_\alpha^E}{g}\left(\sum_\mu \sum_{\mathcal{R}_\mu} \exp(i\boldsymbol{Q}\cdot(\boldsymbol{R} - \mathcal{R}_\mu\boldsymbol{R}))\chi_\alpha^\mu\right)\exp(-t/\tau_\alpha) \tag{6.101}$$

where the elastic and quasielastic structure factors are

$$A_\alpha(\boldsymbol{Q}) = \frac{\chi_\alpha^E}{g}\sum_\mu \sum_{R_\mu} \exp(i\boldsymbol{Q}\cdot(\boldsymbol{R} - \mathcal{R}_\mu\boldsymbol{R}))\chi_\alpha^\mu. \tag{6.102}$$

The sums over μ and $\mathcal{R}_\mu$ run over all the classes μ and over all the rotations $\mathcal{R}_\mu$ of the class μ respectively. g is the order of the group. When the sample is in a powder form, one obtains after averaging over all the directions of $\boldsymbol{Q}$

$$A_\alpha(Q) = \frac{\chi_\alpha^E}{g}\sum_\mu \sum_{R_\mu} \chi_\alpha^\mu j_0(Q|\boldsymbol{R} - \mathcal{R}_\mu\boldsymbol{R}|). \tag{6.103}$$

6.9.4 Equivalence of the two formalisms

To make the comparison with the method developed by Rigny, we shall first evaluate the structure factors for a molecule reorienting under the rotations of the group $\mathcal{D}_3$. Contrarily to the method of Rigny, the formalism of Thibaudier and Volino does not require the evaluation of the basis functions of the irreducible representations. Application of the relation (6.102) needs only the knowledge of how the equilibrium positions are transformed under the effects of the rotations of the group $\mathcal{D}_3$. These transformations are summarised in table 6.5. Clearly, application of (6.102) is straightforward and immediately yields the expressions (6.92).

To prove the equivalence of the two formalisms, we must show that the two expressions of the correlation function $F(t)$ given by (6.76a) and (6.102) are identical. Let us consider the projector

$$\mathcal{P}^{(\mu)} = \frac{\chi_\mu^E}{g}\sum_{\mathcal{R}} \chi_\mu(\mathcal{R})\mathcal{O}_{\mathcal{R}} \tag{6.104}$$

where $\mathcal{O}_{\mathcal{R}}$ is the operator of the rotation $\mathcal{R}$. This projector acts on a function $f_i = f(\boldsymbol{r}_i)$ according to

$$\mathcal{P}^{(\mu)}f(\boldsymbol{r}_i) = \frac{\chi_\mu^E}{g}\sum_{\mathcal{R}} \chi_\mu(\mathcal{R})f(\mathcal{R}\boldsymbol{r}_i). \tag{6.105}$$

If φ_k^μ are the basis functions of the irreducible representation μ, deduced

from the f_is by a unitary transformation

$$f_i = \sum_{\mu' k} \alpha_i^{\mu' k *} \varphi_k^{\mu'} \tag{6.106}$$

we have

$$\mathcal{P}^{(\mu)} \varphi_k^{\mu'} = \delta_{\mu\mu'} \varphi_k^{\mu} \tag{6.107}$$

therefore

$$\begin{aligned} \mathcal{P}^{(\mu)} f(\boldsymbol{r}_i) &= \mathcal{P}^{(\mu)} \left[\sum_{\mu' k} \alpha_i^{\mu' k *} \varphi_k^{\mu'} \right] \\ &= \sum_{\mu' k} \alpha_i^{\mu' k} \mathcal{P}^{(\mu)} \varphi_k^{\mu'} = \sum_k \alpha_i^{\mu k *} \varphi_k^{\mu}. \end{aligned} \tag{6.108}$$

Multiplying both sides of (6.105) by $f^*(\boldsymbol{r}_i)$ and summing over i, we obtain, after using (6.108)

$$\begin{aligned} \frac{\chi_\mu^{\mathrm{E}}}{g} \sum_{\mathcal{R}} \chi_\mu(\mathcal{R}) f^*(\boldsymbol{r}_i) f(\mathcal{R}\boldsymbol{r}_i) &= \sum_i f_i(\boldsymbol{r}_i) \sum_k \alpha_i^{\mu k *} \varphi_k^{\mu} \\ &= \sum_i \sum_k \sum_{\mu' k'} \alpha_i^{\mu' k'} \alpha_i^{\mu k *} \varphi_{k'}^{\mu' *} \varphi_k^{\mu} \\ &= \sum_k \varphi_k^{\mu *} \varphi_k^{\mu} \end{aligned} \tag{6.109}$$

where account has been taken of the unitary property. This equality proves the identity of the two formulations. Nevertheless, the formalism of Thibaudier and Volino is more direct and more useful in practice for the calculation of the scattering laws.

Table 6.5 Positions accessed by a proton under the rotations of the group $\mathcal{D}_3(32)$

Position at $t = 0$		Position after the rotations					
		E	C_3	C_3^2	C_2	C_2'	C_2''
1		1	2	3	4	6	5
2		2	3	1	6	5	4
3		3	1	2	5	4	6
4		4	5	6	1	3	2
5		5	6	4	3	2	1
6		6	4	5	2	1	3
Character table	A_1	1	1	1	1	1	1
	A_2	1	1	1	$\bar{1}$	$\bar{1}$	$\bar{1}$
	E	2	$\bar{1}$	$\bar{1}$	0	0	0

6.9.5 Application to uniaxial reorientations; comparison with Barnes formalism

The models described in §6.7 for reorientations occurring amongst N equivalent sites equally spaced on a circle are step-models in which the scatterer is allowed to reorient only to next-neighbouring sites. However, it is conceivable that reorientations of $(2\pi n/N)$ with $n = 2, 3, \ldots, N-1$ also occur. The method based upon group theory can take into account such reorientations, introducing for each of them a jump probability.

Consider for example the case of the six-site model. In the time-interval Δt, a particle initially located at 1 (figure 6.20) is allowed to undergo any rotation bringing it into any other site 2, 3, . . ., 6 with a related probability τ_2^{-1}, τ_3^{-1}, . . ., τ_6^{-1}. Clearly, we are concerned with $(2\pi n/6)$ -rotations, in any direction, i.e. the rotations of the $\mathscr{C}^6$ group.

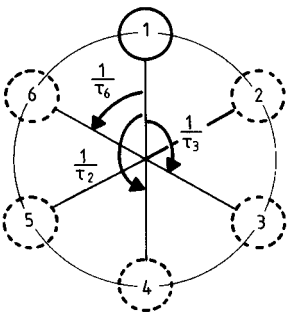

Figure 6.20 Jump model among six sites equally spaced on a circle and taking into account the possible occurrence of 60, 120 and 180° reorientations. The corresponding jump probabilities are indicated (τ_6^{-1}, τ_3^{-1} and τ_2^{-1} respectively).

$\mathscr{C}^6$ group has six classes and six irreducible representations (Γ_0, . . ., Γ_5), whose characters are given in table 6.6. From a knowledge of this character set, the relevant correlation times can be evaluated from (6.100). The intermediate scattering law given by (6.101), does not depend explicitly on the path followed by the scatterer to go from the site $\boldsymbol{r}_i$ at time zero to the site $\boldsymbol{r}_j$ at time t. It is usual to consider that $\pi/6$ rotations in the direct sense are in fact $2\pi/6$ rotations in the inverse sense. Taking as a realistic assumption that any rotation of $+\alpha$ with $\alpha = \pi/3, 2\pi/3, \pi$ has an equal probability of occurring as a rotation of $-\alpha$, we define three jump probabilities $1/\tau_6$, $1/\tau_3$, $1/\tau_2$. Using (6.100)

the relevant jump rates are obtained

$$\Gamma_0: 0 \tag{6.110a}$$

$$\Gamma_1, \Gamma_5: \frac{1}{\tau_6} + \frac{3}{\tau_3} + \frac{2}{\tau_2} \tag{6.110b}$$

$$\Gamma_2, \Gamma_4: \frac{3}{\tau_6} + \frac{3}{\tau_3} \tag{6.110c}$$

$$\Gamma_3: \frac{4}{\tau_6} + \frac{2}{\tau_2}. \tag{6.110d}$$

Thus complex conjugated representations are related to the same expressions of the jump rate. The character of any cyclic group $\mathcal{C}^N$ can be written in the form

$$\chi_\mu^\eta = \exp\left(\mathrm{i}\,\frac{2\pi\eta\mu}{N}\right) \tag{6.111}$$

where indices η and μ refer to the rotation and to the irreducible representation, respectively. Assuming, as in §6.7, that only $\pi/3$ rotations can occur, i.e. that $\tau_3^{-1} = \tau_2^{-1} = 0$, we obtain

$$\frac{1}{\tau_\mu} = \frac{2}{\tau_6}\left(1 - \cos\frac{\pi\mu}{3}\right) = \frac{4}{\tau_6}\sin^2\frac{\pi\mu}{6}. \tag{6.112}$$

This expression is analogous to (6.58), where $\tau = \tau_6/2$ is the mean residence time between two successive jumps of $\pi/3$, without any consideration of direction.

Table 6.6 Character table for the group $\mathcal{C}^6$. $\omega = \exp\left(\mathrm{i}\frac{\pi}{3}\right) = \frac{1}{2} + \mathrm{i}\frac{\sqrt{3}}{2}$

		E	C_6^1	C_6^2	C_6^3	C_6^4	C_6^5
	η	0	1	2	3	4	5
	μ						
Γ_0	0	1	1	1	1	1	1
Γ_1	1	1	ω	$-\omega^*$	-1	$-\omega$	ω^*
Γ_2	2	1	$-\omega^*$	$-\omega$	1	$-\omega^*$	$-\omega$
Γ_3	3	1	-1	1	-1	1	-1
Γ_4	4	1	$-\omega$	$-\omega^*$	1	$-\omega$	$-\omega^*$
Γ_5	5	1	ω^*	$-\omega$	-1	$-\omega^*$	ω

The elastic and quasielastic structure factors, evaluated from (6.103) lead to the expressions of table 6.2.

6.9.6 Reorientations about axes of a cubic lattice

Let us return to the evaluation of the incoherent neutron scattering law when a molecule undergoes reorientations about several crystallographic lattice directions. The most general case is that of a molecule in a cubic lattice reorienting about [100], [110] and [111] axes, according to the rotations of the symmetry-group $\mathbb{O}$. Explicitly, we are concerned with five classes of rotations E, C_2, C_2', C_3 and C_4. E is the identity operation. The four other classes are formed by π rotations about [100] directions, π rotations about [110], $2\pi/3$ rotations about [111] and $\pi/2$ rotations about [100] axes, respectively. To these four last classes are associated the average times between two successive molecular rotations τ_{C_2}, $\tau_{C_2'}$, τ_{C_3} and τ_{C_4}. The group $\mathbb{O}$ allows five irreducible representations, Γ_μ, $\mu = 1, 2, \ldots, 5$. For each of them, using the character set given in table 6.7, corresponding jump rates τ^{-1} are easily evaluated from (6.100):

$$\frac{1}{\tau_1} = 0 \tag{6.113a}$$

$$\frac{1}{\tau_2} = \frac{2}{\tau_{C_2'}} + \frac{2}{\tau_{C_4}} \tag{6.113b}$$

$$\frac{1}{\tau_3} = \frac{2}{\tau_{C_2'}} + \frac{3}{2\tau_{C_3}} + \frac{1}{\tau_{C_4}} \tag{6.113c}$$

$$\frac{1}{\tau_4} = \frac{4}{3\tau_{C_2}} + \frac{2}{3\tau_{C_2'}} + \frac{1}{\tau_{C_3}} + \frac{4}{3\tau_{C_4}} \tag{6.113d}$$

$$\frac{1}{\tau_5} = \frac{4}{3\tau_{C_2}} + \frac{4}{3\tau_{C_2'}} + \frac{1}{\tau_{C_3}} + \frac{4}{3\tau_{C_4}} \tag{6.113e}$$

Expressions of the structure factors, evaluated from (6.103), essentially depend on the molecule geometry. For a particle initially located at point M in space, with general coordinates x, y, z, there are, in the case of a powder sample, 16 non-vanishing jump distances. These are listed in table 6.8 and the expressions of the elastic and quasielastic structure factors, corresponding to characteristic times of (6.113) are given in table 6.9.

Table 6.7 Character set for the group $\mathbb{O}$

θ	E	$8C_3$	$3C_2$	$6C_4$	$6C_2'$
A_1	1	1	1	1	1
A_2	1	1	1	−1	−1
E	2	−1	2	0	0
T_1	3	0	−1	1	−1
T_2	3	0	−1	−1	1

Table 6.8 General expressions of the jump distances for a particle initially located at point M(x, y, z) under the action of the rotation of the group $\mathbb{O}$.

Rotations			Distances
E			0
C_4	$[100]$ $[\bar{1}00]$	r_1	$[(y+z)^2+(y-z)^2]^{1/2}$
	$[010]$ $[0\bar{1}0]$	r_2	$[(y+x)^2+(z-x)^2]^{1/2}$
	$[00\bar{1}]$ $[001]$	r_3	$[(x+y)^2+(x-y)^2]^{1/2}$
C_3		r_4	$[(x-y)^2+(y-z)^2+(z-x)^2]^{1/2}$
		r_5	$[(x+y)^2+(y+z)^2+(z-x)^2]^{1/2}$
		r_6	$[(x+y)^2+(y-z)^2+(z+x)^2]^{1/2}$
		r_7	$[(x-y)^2+(y+z)^2+(z+x)^2]^{1/2}$
C_2	$[100]$ $[\bar{1}00]$	r_8	$2[y^2+z^2]^{1/2}$
	$[010]$ $[0\bar{1}0]$	r_9	$2[z^2+x^2]^{1/2}$
	$[001]$ $[00\bar{1}]$	r_{10}	$2[x^2+y^2]^{1/2}$
C_2'		r_{11}	$[4x^2+2(y-z)^2]^{1/2}$
		r_{12}	$[4x^2+2(y+z^2]^{1/2}$
		r_{13}	$[4y^2+2(z-x)^2]^{1/2}$
		r_{14}	$[4y^2+2(z+x^2]^{1/2}$
		r_{15}	$[4z^2+2(x-y)^2]^{1/2}$
		r_{16}	$[4z^2+2(x+y)^2]^{1/2}$

Table 6.9 Elastic and quasielastic structure factors for a particle reorienting under the effects of the rotations of the group $\mathbb{O}$. J_ν is a shorthand notation for $j_0(Qr_\nu)$. Jump distances $r_\nu(\nu = 1, \ldots, 16)$ are listed in table 6.8. $j_0(x)$ is the Bessel function.

$\frac{1}{24}[1 + 2A + B + C + 2D]$
$\frac{1}{24}[1 + 2A + B - C - 2D]$
$\frac{1}{24}[4 - 4A + 4B]$
$\frac{1}{24}[9 - 3B + 3C - 6D]$
$\frac{1}{24}[9 - 3B - 3C + 6D]$

$$A = \sum_{\nu=4}^{7} J_\nu \qquad C = \sum_{\nu=11}^{16} J_\nu$$

$$B = \sum_{\nu=8}^{10} J_\nu \qquad D = \sum_{\nu=1}^{3} J_\nu$$

$$J_\nu = j_0(Qr_\nu)$$

6.9.7 Reorientations in plastic adamantane

Adamantane $C_{10}H_{16}$ (tricyclo[3,3,1,$1^{3,7}$]decane), is the simplest saturated polycyclic hydrocarbon. The cage-like molecule (figure 6.21) has tetrahedral symmetry (Td). At $T = 208.6$ K a phase transition occurs (Chang and Westrum 1960) with an associated entropy change $\Delta S_t = 16.2\,\mathrm{J\,mol^{-1}\,K^{-1}}$, between a low-temperature bc tetragonal cell with symmetry $P\bar{4}2_1c$ (Nordman and Schmitkons 1965) and a high temperature fcc phase (Nordman and Schmitkons 1965, Amoureux *et al* 1980a) with symmetry Fm3m, stable until the melting point $T_m = 540$ K ($\Delta S_m = 20.9\,\mathrm{J\,mol^{-1}\,K^{-1}}$). This phase is disordered, the molecules are randomly distributed among two distinguishable orientations, related to each other by 90°-rotations about their twofold symmetry axes. These are parallel to the [100] directions of the cubic cell, so that the molecule and lattice threefold symmetry axes are coincident.

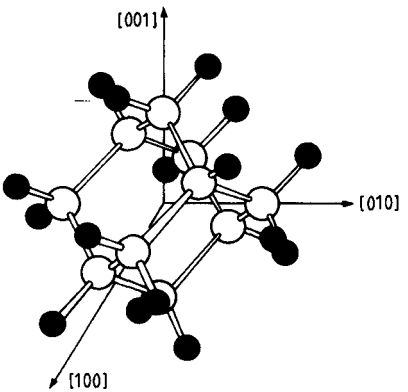

Figure 6.21 The adamantane molecule, in one of its equilibrium orientations with respect to the fcc lattice, symbolised by its [100], [010] and [001] directions.

NMR studies have evidenced the dynamical nature of the disorder in the room-temperature phase (McCall and Douglass 1960, Resing 1969, Amoureux *et al* 1980b). Furthermore, a detailed x-ray diffraction analysis has made it possible to obtain the time-averaged angular distribution for a molecule (Amoureux and Bée 1980a).

Adamantane was studied early on by the IQNS technique (Stockmeyer and Stiller 1968, Stockmeyer 1969). In a more recent study (Lechner 1976, Lechner and Heidemann 1976), the EISF was determined and a certain number of details concerning the rotational motion could be revealed. The problem was fully solved in a further experiment using a

single crystal (Bée *et al* 1980c). In this section we shall be concerned with the conclusions of the powder experiments. The results of the single-crystal analysis will be reported in chapter 8.

Considering the expressions of the jump rates given by (6.113) different situations can be envisaged, according to the occurrence or, conversely, the lack, of some particular rotations. More precisely, three models can be envisaged.

(i) C_4 and/or C_2' rotations occur. Independently of the simultaneous existence of other rotations,

$$\tau_1^{-1} = 0 \tag{6.114a}$$

$$\tau_j^{-1} \neq 0 \qquad j = 2, 3, 4, 5 \tag{6.114b}$$

and

$$S_{\text{inc}}^{\text{R}}(Q, \omega) = a_1(Q)\delta(\omega) + \sum_{j=2}^{5} a_j(Q) \frac{1}{\pi} \frac{\tau_j}{1 + \omega^2\tau_j^2}. \tag{6.115}$$

The corresponding EISF

$$a_0(Q) = a_1(Q) \tag{6.116}$$

is drawn in figure 6.22 (model A).

(ii) C_4 and C_2' rotations do not occur; the molecule is allowed to perform C_3 and C_2 rotations, then

$$\tau_1^{-1} = \tau_2^{-1} = 0, \tag{6.117a}$$

$$\tau_j^{-1} \neq 0 \qquad j = 3, 4, 5 \tag{6.117b}$$

and

$$S_{\text{inc}}^{\text{R}}(Q, \omega) = a_0(Q)\delta(\omega) + \sum_{j=3}^{5} a_j(Q) \frac{1}{\pi} \frac{\tau_j}{1 + \omega^2\tau_j^2} \tag{6.118}$$

with the corresponding EISF (model B)

$$a_0(Q) = a_1(Q) + a_2(Q). \tag{6.119}$$

(iii) Only 180° rotations about the [100] axes occur. Then

$$\tau_1^{-1} = \tau_2^{-1} = \tau_3^{-1} = 0, \tag{6.120a}$$

$$\tau_j^{-1} \neq 0 \qquad j = 4, 5 \tag{6.120b}$$

and

$$S_{\text{inc}}^{\text{R}}(Q, \omega) = a_0(Q)\delta(\omega) + \sum_{j=4}^{5} a_j(Q) \frac{1}{\pi} \frac{\tau_j}{1 + \omega^2\tau_j^2} \tag{6.121}$$

with the EISF (model C)

$$a_0(Q) = a_1(Q) + a_2(Q) + a_3(Q). \tag{6.122}$$

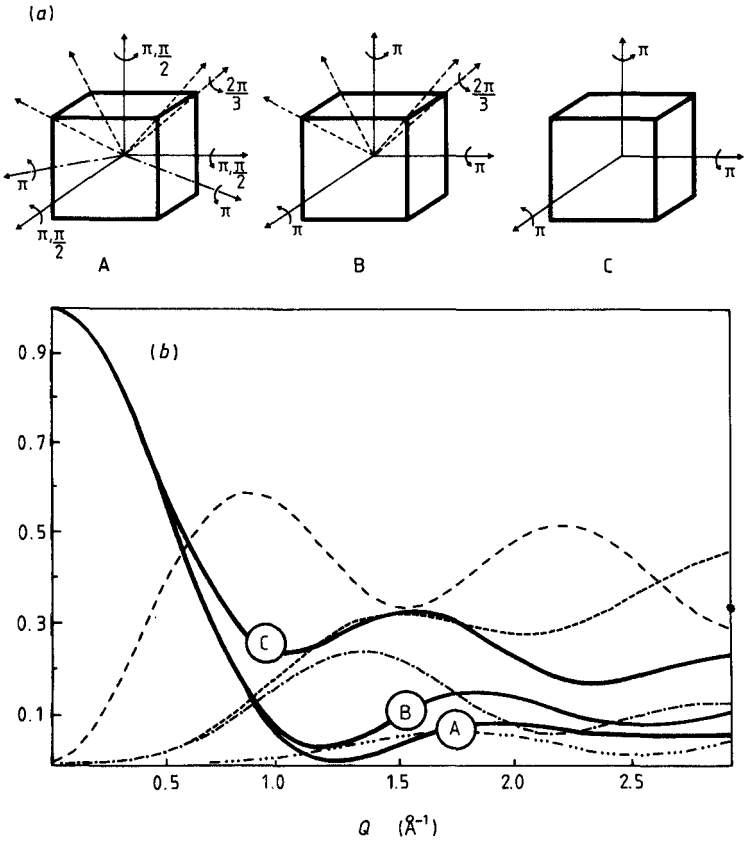

Figure 6.22 (*a*) A schematic representation of possible reorientations of the adamantane molecule, according to the three models A, B and C under consideration. (*b*) Elastic (EISF) and quasielastic structure factors for powder adamantane, as functions of the modulus of the momentum transfer, Q. EISF curves have been denoted by A, B and C, according to the three possible models. Curve B can be retrieved by adding to the EISF related to the model A the quaiselastic structure factor $a_2(Q)$ (chain curve with triple dots). Similarly, curve C is obtained when adding to the EISF related to the model B the quasielastic structure factor $a_3(Q)$ (chain curve). Broken curves with short dashes and long dashes correspond to $a_4(Q)$ and $a_5(Q)$ respectively.

In figure 6.22, the curves describing the EISF variations for models A, B and C are shown, together with the quasielastic structure factors. Model C differs strongly from the others. But the curves related to model A

and B are close to each other.

The expansion of the angular density function in terms of cubic harmonics (Amoureux and Bée 1980a) evidences very sharp maxima of the orientational probability density $P(\mathbf{\Omega})$, corresponding to a librational amplitude less than ten degrees. Starting from the expansion (for a single particle)

$$P(\mathbf{\Omega}) = \sum_{lm} C_{lm} K_{lm}(\mathbf{\Omega}) \tag{6.123}$$

where $\mathbf{\Omega}$ holds for spherical coordinate of the particle with respect to lattice axes, x-ray or neutron diffraction experiments permit the values of the coefficients C_{lm} to be obtained. These involve the particle coordinates in a frame tied to the molecule. Then, making use of the following expression for $\exp(i\boldsymbol{Q}\cdot\boldsymbol{r})$ (Sears 1966),

$$\exp(i\boldsymbol{Q}\cdot\boldsymbol{r}) = 4\pi \sum_{lm} j_l(Qr) i^l K(\mathbf{\Omega}_Q) K_{lm}(\mathbf{\Omega}) \tag{6.124}$$

in the expression

$$\langle \exp(i\boldsymbol{Q}\cdot\boldsymbol{r}) \rangle = \int P(\mathbf{\Omega}) \exp(i\boldsymbol{Q}\cdot\boldsymbol{r})\, d\mathbf{\Omega}. \tag{6.125}$$

We derive an expression for the EISF

$$a_0(Q) = j_0^2(Qr) + 4\pi \left[C_{41}^2 j_4^2(Qr) + C_{61}^2 j_6^2(Qr) + C_{81}^2 j_8^2(Qr) + C_{101}^2 j_{10}^2(Qr) + \ldots\right]. \tag{6.126}$$

Derivations between this curve and the model A are small and restricted to the higher momentum transfer values. They are at least partly due to the fact that the cubic harmonic expansion is restricted to a finite number of terms namely $l \leqslant 10$.

EISF values were experimentally obtained (Lechner and Heidemann 1976). Considering the agreement with theoretical curve predicted by model A, they concluded that either C_4 or C_2' rotations, or both, must play a dominant role on the time-scale of their experiment. Conversely, C_3 and/or C_2 rotations, if they exist, certainly do not occur alone. Since the molecular symmetry is somewhat closer to fourfold symmetry along the [110] axes, their preference was given to C_4 rotations. Under these assumptions, from the quasielastic part of the scattering, the temperature-dependence of the correlation time τ_{C_4} was described by an Arrhenius law

$$\tau_{C_4} = 0.192 \times 10^{-12} \exp(1350/T) \text{ s}$$

with a barrier height $\Delta H = 11.2 \text{ kJ mol}^{-1}$. Their conclusions were confirmed by a further IQNS experiment using a single crystal (Bée 1980c).

6.10 Reorientations About Mobile and Fixed Axes

Until now we have only considered reorientations about axes which were fixed with respect to a laboratory frame. More precisely, molecules reorienting in disordered phases were rotating about *fixed* crystallographic directions. In the case of intramolecular rotating groups, the molecule itself was assumed to be static with respect to the lattice. Performing the powder average introduces a time-independent average with respect to the Q direction of all possible orientations of the crystallite axes, i.e. an average over all possible orientations of the lattice axes with respect to a set of coordinates tied to the instrument. A more complicated situation can be encountered when chemical groups can rotate inside a molecule which is itself reorienting in the lattice. Then we are concerned with two kinds of rotation axes: fixed (crystallographic) axes and mobile (molecular) axes.

Thibaudier and Volino (1973) extended their application of the group theory to this situation. Their method can be of considerable help in most cases, provided that some basic hypotheses are respected. We shall discuss this point further in the following chapter.

6.10.1 The scattering law

When rotations about molecular axes and about crystal lattice directions occur simultaneously, the relevant correlation times are evaluated from the relation

$$\frac{1}{\tau_\mu} = \sum_\nu \frac{n_\nu}{\tau_\nu}\left(1 - \frac{\chi_\mu^{\nu e}}{\chi_\mu^{Ec}}\right) + \sum_\eta \frac{n_\eta}{\tau_\eta}\left(1 - \frac{\chi_\mu^{E\eta}}{\chi_\mu^{Ee}}\right). \tag{6.127}$$

Here $\chi_\mu^{\nu\eta}$ is the character of the product of the two rotations C and M belonging to the crystal symmetry group and to the molecule group, respectively, in the irreducible representation Γ_μ. This itself represents the direct product

$$\Gamma_\mu = \Gamma_{\mu_C} \otimes \Gamma_{\mu_M} \tag{6.128}$$

of the two irreducible representations Γ_{μ_C} of the crystal group and Γ_{μ_M} of the molecule group. These characters are the products

$$\chi_\mu^{\nu\eta} = \chi_{\mu_C}^{\nu} \times \chi_{\mu_M}^{\eta} \tag{6.129}$$

E denotes the identity operation of the crystal group and, as above, e is that for the molecular group. In (6.127) above, the sums over ν and η run, respectively, over all the classes of these groups. n_ν and n_η are the number of rotations in the classes.

The elastic and quasielastic incoherent structure factors can be calculated from the general relation (Thibaudier and Volino 1973)

$$A_\mu(Q) = \frac{\chi_\mu^{Ee}}{g} \sum_\nu \sum_\eta \chi_\mu^{\nu\eta} \sum_{C_\nu} \sum_{M_\eta} \exp[i\boldsymbol{Q}\cdot(\boldsymbol{R} - C_\nu M_\eta \boldsymbol{R})]. \quad (6.130)$$

As previously, the sums over ν and η run over all the classes of both crystal and molecule groups, respectively. The two others correspond to summations over all the rotations, C_ν, of the crystal class, ν, and over all the rotations, M_η, of the molecule class, η. The order of the group product is g. Taking into account a polycrystalline nature of the sample leads to an average over all possible directions of the momentum transfer. One obtains:

$$A_\mu(Q) = \frac{\chi_\mu^{Ee}}{g} \sum_\nu \sum_\eta \chi_\mu^{\nu\eta} \sum_{C_\nu} \sum_{M_\eta} j_0(Q|\boldsymbol{R} - C_\nu M_\eta \boldsymbol{R}|). \quad (6.131)$$

6.10.2 Application: methyl group reorientations in trimethyl compounds

We shall give an application of this method to the investigation of the dynamics of three methyl groups directly bonded to the same atom. Such a situation is often encountered. Let us mention for example the trimethyloxosulphonium $(CH_3)_3SO^+$ already discussed in this chapter. Schlaak *et al* (1977) analysed the dynamical behaviour of the trimethylammonium ion $(CH_3)_3NH^+$. t-butyl compounds were studied by Frost *et al* (1980a, 1980b) who considered $(CH_3)_3CCN$ and $(CH_3)_3CCl$. It should be noted that in the case of a t-butyl group, rotations of this group about its own symmetry axis can also appear as intramolecular reorientations, whilst the whole molecule can also rotate. In the plastic phase of pivalic acid $(CH_3)_3CCOOH$ ($278\ K < T < 310\ K$) or of hexamethylethane $(CH_3)_3CC(CH_3)_3$, any proton belonging to a methyl group can be considered as reorienting under the effect of methyl, t-butyl and whole-molecule reorientations. However, these motions often occur on different time-scales, so that, in most cases, we are dealing with two simultaneous types of rotations only.

In figure 6.23 a $(CH_3)_3A$ group is shown, where A can be any atom, bonded or not to the rest of a molecule. We shall suppose that only 120° jumps of both methyl and the whole group about their respective threefold axes can occur. Then reorientations occur between indistinguishable configurations. Possible positions for an individual proton are numbered from 1 to 9. Table 6.10 gives a list of final positions accessed by the protons of one methyl group after successive applications of an operation of the C_3 symmetry group about each of the rotation axes, together with the corresponding jump distances which can be restricted to a set of eight different values. Each methyl group leads to the same set of jump distances.

We denote by τ_M^{-1} the probability of a $\pm 120°$ jump for a methyl group and by τ_G the corresponding probability for the whole group. After

application of (6.127) four correlation times are involved because the two complex conjugated representations lead to the same expressions.

$$\tau_1^{-1} = 0 \tag{6.132a}$$

$$\tau_2^{-1} = \tfrac{3}{2}\tau_M^{-1} \tag{6.132b}$$

$$\tau_3^{-1} = \tfrac{3}{2}\tau_G^{-1} \tag{6.132c}$$

$$\tau_4^{-1} = \tfrac{3}{2}\tau_M^{-1} + \tfrac{3}{2}\tau_G^{-1}. \tag{6.132d}$$

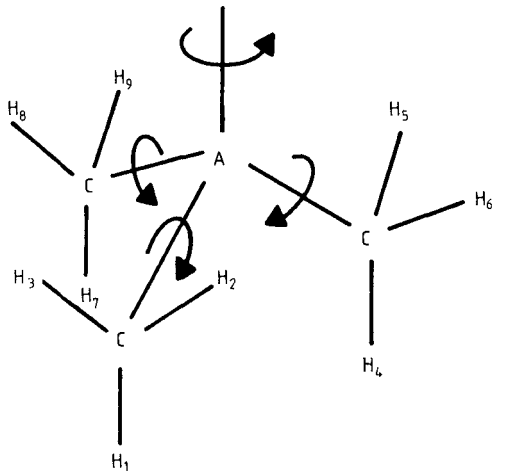

Figure 6.23 Sketch of the $(CH_3)_3A$ group. The equilibrium positions of the hydrogen atoms are numbered. Possible rotations are indicated by arrows.

From the results of table 6.11 and using (6.131) the evaluation of the elastic and quasielastic structure factors is straightforward. Adding together the expressions related to identical jump-rate values, we obtain the four expansions listed in table 6.11. Their variation as a function of Q is illustrated in figure 6.24, using a set of jump distances corresponding to a t-butyl group. Clearly, $A_2(Q)$ and $A_4(Q)$ which are related to correlation times involving the dynamics about the methyl axis, mainly contribute at large Q-value ($Q > 1.7$ Å^{-1}). Conversely, $A_3(Q)$ is larger at intermediate Q values ($0.8 < Q < 1.2$ Å^{-1}) and the scattering law will be more sensitive to the motion of the whole group in this Q range.

6.10.3 Methyl group and t-butyl group reorientations in pivalic acid

In 1976 Albert *et al* investigated both low- and high-temperature phases of trimethylacetic (pivalic) acid $(CH_3)_3CCOOH$, using pulsed and

Table 6.10 Geometrical information for a proton of a methyl group reorienting by 120° jumps about the methyl axis and about the whole $(CH_3)_3A$ threefold axis. The third column indicates the final position accessed after the application of the corresponding whole-group and methyl rotation (figure 6.23). Corresponding distances are in column 4.

Initial positions of the proton	Whole rotations	Final positions: Methyl rotations E	C_3 $(\frac{2}{3}\pi)$	C_3^2 $(\frac{4}{3}\pi)$	Jump distances: Methyl rotations E	C_3 $(\frac{2}{3}\pi)$	C_3^2 $(\frac{4}{3}\pi)$
	E	1	3	2	0	R_2	R_2
1	C_3 $(\frac{2}{3}\pi)$	4	6	5	R_3	R_4	R_5
	C_3^2 $(\frac{4}{3}\pi)$	7	9	8	R_3	R_5	R_4
	E	2	1	3	0	R_2	R_2
2	C_3 $(\frac{2}{3}\pi)$	5	4	6	R_8	R_4	R_7
	C_3^2 $(\frac{4}{3}\pi)$	8	7	9	R_8	R_5	R_6
	E	3	2	1	0	R_2	R_2
3	C_3 $(\frac{2}{3}\pi)$	6	5	4	R_8	R_6	R_5
	C_3^2 $(\frac{4}{3}\pi)$	9	8	7	R_8	R_7	R_4

$R_1 = R_{11} = R_{22} = R_{33} = 0$
$R_2 = R_{12} = R_{13} = R_{23} = R_{32} = R_{31} = R_{21}$
$R_3 = R_{14} = R_{17}$
$R_4 = R_{16} = R_{18} = R_{24} = R_{34}$
$R_5 = R_{15} = R_{19} = R_{27} = R_{34}$
$R_6 = R_{29} = R_{35}$
$R_7 = R_{26} = R_{38}$
$R_8 = R_{25} = R_{28} = R_{36} = R_{39}$

Table 6.11 Expressions of the elastic and quasielastic structure factors in the case of three methyl groups, bonded directly to the same atom (figure 6.23) and reorienting by 120° jumps about their own threefold axis and about the whole group axis

A ⊗ A	$A_1(Q) = \frac{1}{27}[3 + 6j_2 + 2j_3 + 4j_4 + 4j_5 + 2j_6 + 2j_7 + 4j_8]$
A ⊗ E	$A_2(Q) = \frac{1}{27}[6 - 6j_2 + 4j_3 - 4j_4 - 4j_5 - 2j_6 - 2j_7 + 8j_8]$
E ⊗ A	$A_3(Q) = \frac{1}{27}[6 + 12j_2 - 2j_3 - 4j_4 - 4j_5 - 2j_6 - 2j_7 - 4j_8]$
E ⊗ E	$A_4(Q) = \frac{1}{27}[12 - 12j_2 - 4j_3 + 4j_4 + 4j_5 + 2j_6 + 2j_7 - 8j_8]$

$A_2(Q) = A_{A\otimes E_1}(Q) + A_{A\otimes E_2}(Q)$
$A_3(Q) = A_{E_1\otimes A}(Q) + A_{E_2\otimes A}(Q)$
$A_4(Q) = A_{E_1\otimes E_1}(Q) + A_{E_1\otimes E_2}(Q) + A_{E_2\otimes E_1}(Q) + A_{E_2\otimes E_2}(Q)$

continuous wave proton magnetic resonance methods. For the partially deuterated form, $(CH_3)_3CCOOD$, below the phase transition at 280 K, the second moment and the spin lattice relaxation time of the protons are in agreement with a combination of methyl group and t-butyl group

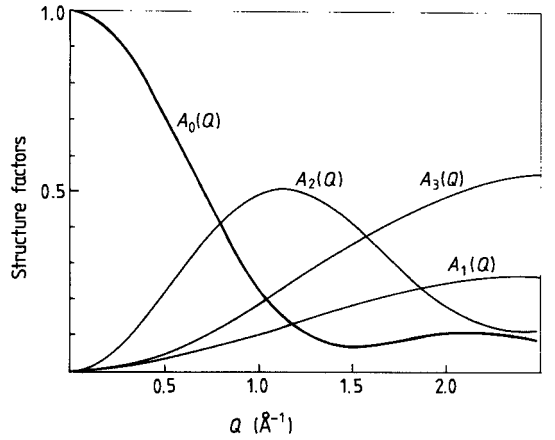

Figure 6.24 Elastic (EISF) and quasielastic structure factor variations as a function of the modulus of the momentum transfer, Q, for a $(CH_3)_3A$ group undergoing 120° reorientations about its threshold axis simultaneously with 120° inner reorientations of the methyl groups. The jump distances used in the evaluation correspond to a t-butyl $(CH_3)_3C$ group.

reorientations having activation energies of $\Delta H_1 = 9.835\ \text{kJ mol}^{-1}$ and $\Delta H_2 = 16.75\ \text{kJ mol}^{-1}$, respectively. Using IQNS technique, the molecular dynamics of this compound was also investigated (Bée *et al* 1983b). NMR results were confirmed. Determination of the experimental EISF unambiguously proves the existence of 120° reorientations of both groups. Measurements at 178 K, 215 K and 254 K lead to the Arrhenius laws:

$$\tau_M = 2.6 \pm 0.2 \times 10^{-12} \exp(\Delta H_M/RT)\ \text{s}$$

with $\Delta H_M = 9.34 \pm 0.15\ \text{kJ mol}^{-1}$, for the methyl reorientations, and

$$\tau_B = 1.3 \pm 0.1 \times 10^{-13} \exp(\Delta H_B/RT)\ \text{s}$$

with $\Delta H_B = 16.7 \pm 0.2\ \text{kJ mol}^{-1}$, for the t-butyl reorientations. In the analysis of their spin-lattice relaxation measurements, Albert *et al*, on the basis of the same model, obtained:

$$\tau_M = 2.32 \times 10^{-12} \exp(\Delta H_1/RT)\ \text{s}$$

and

$$\tau_B = 15.60 \times 10^{-12} \exp(\Delta H_2/RT)\ \text{s}.$$

An extensive IQNS analysis of trimethylacetic acid (Bée *et al* 1986b) in its plastic phase ($280\ \text{K} < T < 310\ \text{K}$), using different partially deuter-

ated samples, has shown that no change occurs in the dynamical behaviour of methyl groups at the phase transition. Conversely the jump rate for whole t-butyl considerably increases ($\tau_B \simeq 10^{-11}$ s at 300 K) and the motion tends to uniaxial diffusion. No tumbling was found in the plastic phase on a time-scale of 10^{-11} s , in agreement with the value $\tau = 2 \times 10^{-9}$ s obtained by Albert *et al* (1976), for the correlation time associated with overall tumbling.

These results have to be compared to conclusions of IQNS studies of other trimethyl compounds. We have already seen (§6.6.2) that in the case of trimethyloxosulphonium ion, the quasielastic broadening essentially results from methyl group 120° reorientations. These reorientations were found to play no part in the successive phase transitions. Similar conclusions were drawn in the case of trimethylammonium (Schlaak *et al* 1977). Low temperature IQNS data are in agreement with a model of 120° jump of both the cation and the methyl groups with correlation times of about the same value at 273 K ($\tau \simeq 4 \times 10^{-10}$ s) for the two motions. Above the transition at $T = 308$ K, methyl groups were found too slow to produce a quasielastic broadening detectable by the t.o.f. experiment. The results were described by a rotational diffusion of the whole cation about its threefold axis. Lately, in a recent series of papers, a detailed neutron scattering investigation of the t-butyl group in t-butyl cyanide (Frost *et al* 1980a, Frost *et al* 1982), t-butyl chloride (Frost *et al* 1980b) and t-butyl bromide (Richardson and Taylor 1984) has been published. In the case of $(CH_3)_3CCN$, above 130 K, whole-body reorientations were found to be faster than the methyl reorientations. The residence time between two methyl jumps, obtained from a backscattering technique analysis from 218 K to 270 K follows the Arrhenius law

$$\tau = 3.0 \pm 0.2 \times 10^{-13} \exp(\Delta H_M/RT) \text{ s}$$

with an activation energy

$$\Delta H_M = 16.3 \pm 0.15 \text{ kJ mol}^{-1}$$

in agreement with the value obtained from the analysis of the torsional frequencies. No discontinuity was found at $T = 233$ K at the transition between the ordered and disordered phases.

Similar results were obtained for t-butyl chloride and t-butyl bromide, which confirm the intramolecular nature of the potential acting on methyl groups in trimethyl compounds.

6.10.4 Simultaneous reorientations of whole molecules about their own axis and about lattice axes

The group theory method can also be applied when a molecule, in

addition to reorientations amongst lattice directions, undergoes whole-reorientations about one of its own axes. Then the two sets of rotations to be considered are the group of the rotations about this particular molecule (symmetry) axis and the group of the rotations which bring this precise axis from one crystallographic direction to another. However, the method has to be applied with caution.

The main hypothesis (Thibaudier and Volino 1973) is that all the rotations belonging to the same class occur with the same probability per unit time, independently of the precise molecule equilibrium orientation. This assumption is not always fulfilled, especially for molecules with low symmetry. Let us consider for example the case of a symmetrical-top molecule, whose axis is aligned along the [100] direction of a cubic lattice. Then possible reorientational motions can be classified into

(i) rotations about the molecule axis;
(ii) reorientations of the molecule axis amongst the different lattice directions

If we assume that the motions of two neighbouring molecules are uncorrelated, the probability of any rotation about the molecule axis can be considered as independent of the precise lattice direction along which the molecule is lying. Conversely, if the molecule is lying along [100], the probability of any rotation about this particular axis is *a priori* not equal to the probability of the same rotation about any of the two other directions [010] or [001] because the corresponding moments of inertia are different. The same remark holds for the [110] twofold symmetry axes. Rigorously, rotations about [111] axes alone can be considered to occur with the same probability.

Similarly, assuming that the molecules are in an equilibrium orientation when their axes are lying along any of the [111] lattice directions, it is only in the case of rotations about the [100] directions that all the probabilities are equal.

Evaluation of the relevant correlation times from (6.91) involves a jump-rate parameter for each of the molecular and crystalline classes. Refinement of these parameters simultaneously from experimental data is rather difficult, especially in the powder case, where the Q direction dependence of the structure factors is lost (see chapter 8). Molecules jump over the potential barrier between two equilibrium orientations under the effect of thermal motions. It is quite reasonable to assume the weakest probabilities for the largest angular motions. In the case of the symmetrical-top molecule described above, when the equilibrium directions of the axis are directed along [100] lattice axes, 180° rotations about [100] or [110] axes can be ruled out of the model, at least in a first step. Moreover, calculation of the different moment of inertia

about [111] or [100] axes, together with steric hindrance considerations, enable us to assume that 90° rotations around any of the fourfold lattice axes along which the molecule is not lying have little chance of occurring and the allowed rotations about lattice axes are restricted to 120° jumps about [111] directions. On the basis of these assumptions, all the jump probabilities belonging to the same class are equal. Despite these drastic simplifications, a serious difficulty occurs. Indeed, the set of rotations we have restricted does not constitute a group. Nevertheless, it is possible to overcome this difficulty by using the full group $\mathcal{O}$ of all the rotations about crystal axes, and, after the calculations have been performed, assuming a vanishing jump probability for all non-relevant classes.

6.10.5 Substituted derivatives of adamantane

The original work concerning the dynamical behaviour of adamantane within its plastic phase was followed by an extensive study of its substituted derivatives: adamantane-halides (Bée and Amoureux 1983a, Bée and Amoureux 1983b), adamantanone (Bée and Amoureux 1982), and adamantane-carbonitrile (Bée *et al* 1980a). Noticeable differences were evidenced, for example the existence of successive phase transitions between ordered, intermediate (partially orientationally disordered) or fully disordered phases. Furthermore, glassy-crystal phases have more recently been obtained by rapid quenching of specimens (Foulon *et al* 1983). Numerous experimental techniques were used in these investigations: calorimetry, light scattering, dielectric relaxation and NMR. Obviously IQNS was also extensively used to study the molecular motions in the different phases. IQNS proved to be one of the most powerful tools because the molecular motions mostly occur within a time-scale accessible to experimental conditions. We shall report on the main results obtained from this technique.

The series of 1-halide-adamantane is of particular interest. Indeed, according to the nature of the halogen atom substituted for one hydrogen of a tertiary carbon of adamantane, the departure from the globular symmetry is of more or less importance (figure 6.25). Steric hindrance effects can be investigated, with a general molecule symmetry $\mathcal{C}_{3v}$. (The distortion of the adamantyl skeleton resulting from the substitution is negligible.) Also, considering the dipole–dipole interactions, this series exhibits different values of the molecular dipole moment along the threefold symmetry axis.

Fluoroadamantane $C_{10}H_{15}F$ (1-fluoro-tricyclo[3,3,1,1]decane) undergoes a solid–solid phase transition at 221.6 K and melts at 442.5 K (Clark *et al* 1977). The structure of the room-temperature phase

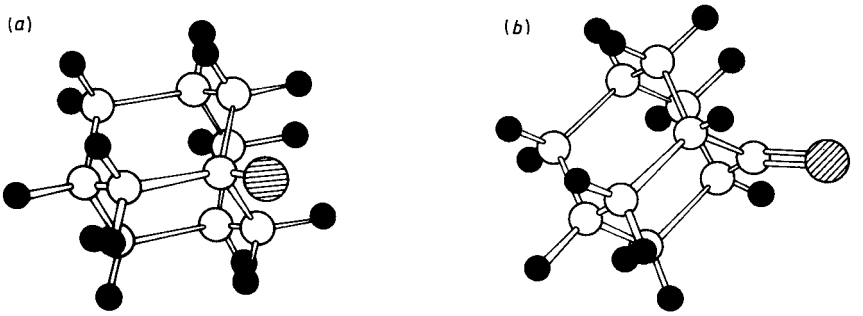

Figure 6.25 (*a*) Sketch of the 1-halide-adamantane molecule. Carbon atoms are open circles and hydrogen atoms are full circles. The halide atom is shown dashed. (*b*) Sketch of the adamantanone molecule. Carbon and hydrogen atoms as in (*a*). The oxygen atom is dashed.

obtained from x-ray scattering (Amoureux *et al* 1982a) is fcc, space group Fm3m with parameter $a = 9.54$ Å and four molecules in the unit cell. Each molecule can occupy eight distinct equilibrium positions, corresponding to the C–F bond along one of the [111] directions of the cubic lattice. As in adamantane, the twofold symmetry axes of the adamantyl cage coincide with the [100] directions of the lattice.

Chloroadamantane $C_{10}H_{15}Cl$ (1-chloro-tricyclo[3,3,1,1]decane) undergoes at $T = 224.2$ K a solid–solid phase transition $\Delta H = 6.01$ kJ mol^{-1} to a disordered fcc phase ($a = 9.974$ Å, Fm3m, $Z = 4$) which is stable up to the melting point ($T = 442.5$ K, $\Delta H = 4.87$ kJ mol^{-1} (Clark *et al* 1977)). Owing to steric hindrance, the threefold molecular symmetry axis is unusual in lying along the [100] lattice axes, and the chlorine atom is located in one octahedral site. Moreover each molecule can occupy four distinct equilibrium positions around one [100] axis (Amoureux *et al* 1982b).

When the steric hindrance increases, intermediate semi-ordered phases appear. Bromoadamantane $C_{10}H_{15}Br$ (1-bromo-tricyclo[3,3,1,1]decane) exhibits three different solid phases. The low-temperature phase is monoclinic (space group $P2_1c_n$, $a = 10.12$ Å, $b = 6.81$ Å, $c = 13.60$ Å, $\beta = 90.22°$, $Z = 4$). At $T = 279$ K, a nearly second-order displacive transition occurs. The intermediate phase ($279\text{ K} < T < 310$ K) is orthorhombic ($a = 10.12$ Å, $b = 6.81$ Å, $c = 13.60$ Å, space group $Pna2_1$, $Z = 4$). The molecules have two discernible equilibrium orientations differing from each other by a 60° uniaxial rotation around their threefold axis. The high-temperature fcc phase is disordered ($a = 10.10$ Å, Fm3m, $Z = 4$) and persists up to the melting point $T_m = 496$ K.

Iodoadamantane $C_{10}H_{15}I$ (1-iodo-tricyclo[3,3,1,1]decane) undergoes at $T = 211$ K a phase transition from a low-temperature phase whose structure is still unknown into an orthorhombic disordered phase ($a = 6.70$ Å, $b = 8.86$ Å, $c = 8.675$ Å, $Pmn2_1$). Each molecule in the cell has four discernible equilibrium orientations about its threefold axis, differing from each other by 30°. No fully disordered phase exists (with whole-molecule tumbling). Melting occurs at $T_m = 347$ K.

Adamantanone $C_{10}H_{14}O$ (2-one-tricyclo[3,3,1,1]decane) can be obtained from adamantane by substituting an oxygen atom for the two hydrogens of a secondary carbon. The room-temperature phase is orientationally disordered. It is stable from 178 K where a transition occurs to a low-temperature ordered phase ($\Delta H = 4.85$ kJ mol^{-1}), up to the liquid phase ($T_m = 529$ K). The structure at $T = 300$ K is fcc ($a = 9.524$ Å, Fm3m, $Z = 4$). Each molecule has 12 distinguishable equilibrium orientations, the C=0 bond lying along one of the six [100] directions (Amoureux and Bée 1980b). As in the case of fluoroadamantane and adamantane, the twofold symmetry axes of the adamantyl group are aligned with the [100] directions.

1-cyanoadamantane $C_{10}H_{15}CN$ (tricyclo[3,3,1,$1^{3,7}$]decane 1-carbonitrile) where the radical —C≡N is substituted for one hydrogen of a tertiary carbon, exhibits the general shape of a linear group bound on a spherical cage. From the existence of the C≡N radical, the whole molecule bears a large dipole moment. A weakly first-order phase transition occurs at 228 K. The structure of the room-temperature phase is identical with that of 1-chloro-adamantane (Amoureux and Bée 1979, Amoureux *et al* 1981a).

The dynamical nature of the disorder is clearly shown by NMR. The analysis of the second moment of the absorption line proves the existence, in the room-temperature phase of fluoroadamantane and adamantanone of endospherical reorientations ($M_2 = 1.0$ G^2 and $M_2 = 0.7$ G^2, respectively). Below the transition, the value of M_2 increases suddenly towards the rigid-lattice value ($M_2 = 22$ G^2).

Proton spin-lattice relaxation time T_1 measurements (Amoureux *et al* 1982a) and dielectric studies (Amoureux *et al* 1984a) confirm this result. Conversely NMR and dielectric relaxation experiments performed with chloroadamantane prove the existence of a dynamical disorder not only in the room-temperature phase but also below the transition at 244.2 K, where M_2 jumps abruptly from 0.85 G^2 to 5.3 G^2 indicating a uniaxial rotation of the molecules. M_2 remains nearly constant down to 170 K and then slowly increases to the rigid-lattice value ($M_2 = 21$ G^2 at $T = 130$ K). Similar conclusions were drawn in the case of cyanoadamantane, in which, furthermore, the frequency of the occurrence of the molecule axis reorientations in the plastic phase was found to be very

low (less than 10^8 Hz) at the melting point (Amoureux *et al* 1981b, Amoureux *et al* 1983, Amoureux *et al* 1984).

For bromoadamantane, between 310 K and 180 K, the experimental value of the second moment shows a plateau ($M_2 = 5.1\ G^2$), with no discontinuity at the transition ($T_t = 279$ K) and which agrees well with that calculated for uniaxial rotations of the molecules (Virlet *et al* 1983). In the cubic high-temperature phase, fast endospherical reorientations were evidenced ($M_2 = 0.65\ G^2$). Corresponding measurements for iodoadamantane agree with the existence of threefold uniaxial rotations in the low-temperature phase and of 12-fold uniaxial rotations above the transition ($M_2 = 4.9\ G^2$). In the case of both ADMBr and ADMI measurements confirmed these conclusions.

IQNS technique was extensively used to investigate the dynamics of these molecules in their different solid phases. Systematic extraction of EISF values from experimental spectra recorded at various scattering angles led to an analysis of the motions in terms of jump models allowing reorientations about molecule and crystal axes. More precisely, in the case of fluoroadamantane (Bée and Amoureux 1983a), molecular motions were assumed to comprise: (a) 60° jumps about the molecule threefold axis, itself coincident with a [111] lattice axis, and (b) 90° jumps of the molecule axis about [100] directions from one [111] direction to another. Conversely, in adamantanone allowed jumps were: (a) 90° jumps about the C = 0 axis and (b) 120° jumps of this C = 0 axis about [111] lattice directions, from one [100] lattice axis to another (Bée and Amoureux, 1982).

Relevant correlation times are given in table 6.12 for both cases. Corresponding structure factors, averaged over all types of protons in the molecule, are shown in figure 6.26.

Correlation times associated with each type of motion were found to follow the Arrhenius laws (see figure 6.26):

$$\tau_{C_4} = 9.3 \pm 0.1 \times 10^{-15} \exp(\Delta H_c/RT)\ \text{s}$$

with $\Delta H_c = 24.4 \pm 0.1\ \text{kJ mol}^{-1}$ and

$$\tau_{M_3} = 5.92 \pm 0.05 \times 10^{-13} \exp(\Delta H_M/RT)\ \text{s}$$

with $\Delta H_M = 13.3 \pm 0.1\ \text{kJ mol}^{-1}$ for fluoroadamantane. For adamantanone, the following variations were obtained:

$$\tau_{C_3} = 5.11 \times 10^{-14} \exp(\Delta H_c/RT)\ \text{s}$$

$$\tau_{M_4} = 3.17 \times 10^{-13} \exp(\Delta H_M/RT)\ \text{s}$$

with respectively the two activation energies $\Delta H_C = 19.71\ \text{kJ mol}^{-1}$ and $\Delta H_M = 9.81\ \text{kJ mol}^{-1}$.

In figure 6.27 it is seen that, near the melting point, both types of motion tend to occur with the same values of the correlation times.

Table 6.12 Relevant correlation times for IQNS in the case of fluoroadamantane and adamantanone

Crystal group representations	Fluoroadamantane		Adamantanone		
	Molecular group representations		Molecular group representations		
	A	E	A	B	E
A_1	$\tau_1^{-1} = 0$	$\tau_{i+5}^{-1} =$	$\tau_1^{-1} = 0$	$\tau_{i+5}^{-1} =$	$\tau_{i+10}^{-1} =$
A_2	$\tau_2^{-1} = 2\tau_{C_4}^{-1}$	$\tau_i^{-1} + 3\tau_{M_3}^{-1}$	$\tau_2^{-1} = 2\tau_{C_4}^{-1}$	$\tau_i^{-1} + 4\tau_{M_4}^{-1}$	$\tau_i^{-1} + 2\tau_{M_4}^{-1}$
E	$\tau_3^{-1} = \tau_{C_4}^{-1}$	$i = 1, \ldots, 5$	$\tau_3^{-1} = \tau_{C_4}^{-1}$	$i = 1, .., 5$	$i = 1, .., 5$
T_1	$\tau_4^{-1} = \frac{2}{3}\tau_{C_4}^{-1}$		$\tau_4^{-1} = \frac{2}{3}\tau_{C_4}^{-1}$		
T_2	$\tau_5^{-1} = \frac{4}{3}\tau_{C_4}^{-1}$		$\tau_5^{-1} = \frac{4}{3}\tau_{C_4}^{-1}$		

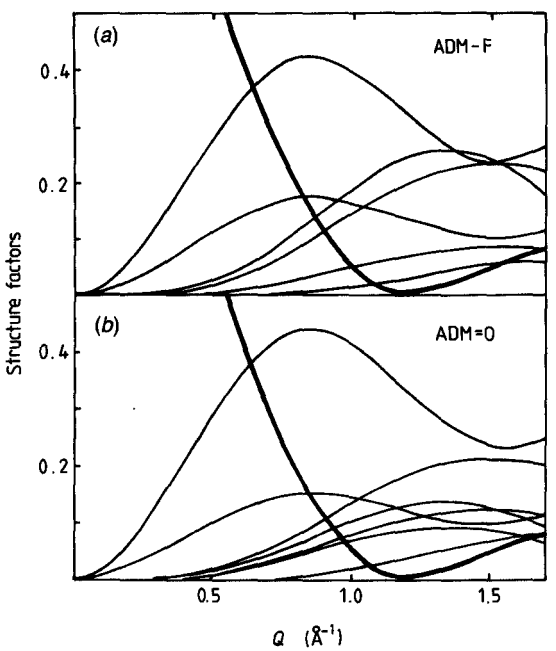

Figure 6.26 Variations of the elastic (EISF) and quasielastic structure factors as functions of Q, in the case of fluoroadamantane (a) and adamantanone (b). Seven and eight curves are illustrated, respectively. The other structure factors are strictly vanishing. The corresponding correlation times are indicated in table 6.12.

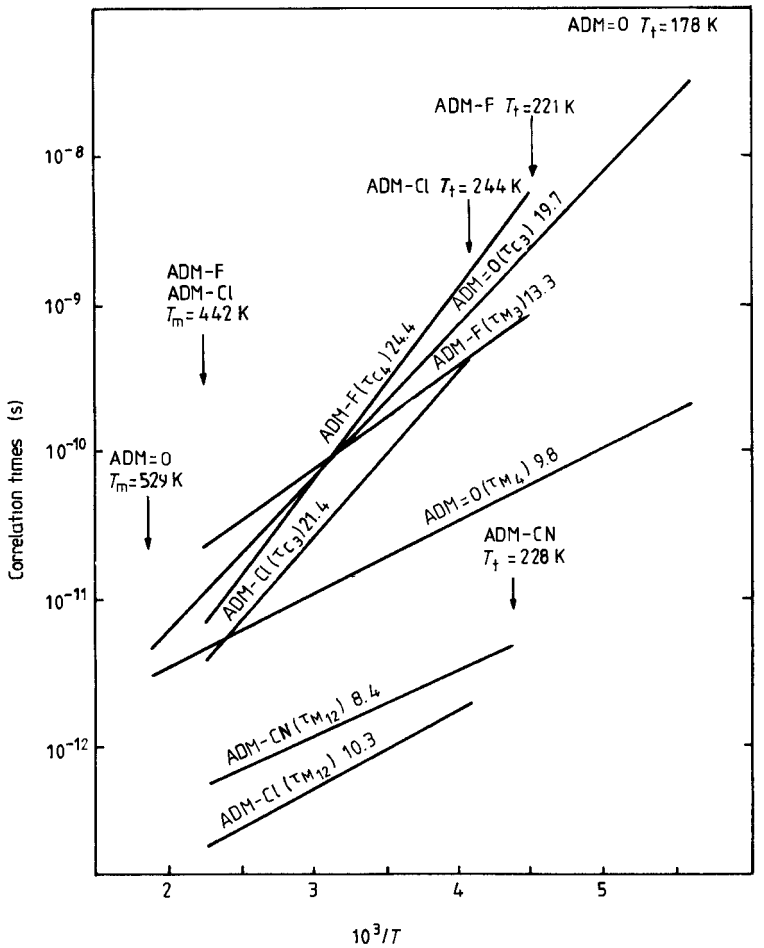

Figure 6.27 Temperature dependence of the correlation times related to reorientations of various adamantane derivative molecules about their own symmetry axis (M_3, M_4, M_{12}) and about lattice directions (C_3, C_4). The numbers on the curves are the values of ΔH in kJ mol^{-1}.

Then the motion can be described as an isotropic rotational diffusion.

Although their crystallographic equilibrium positions are identical, in their fcc lattice cells having nearly the same parameters, and although their respective molecular masses are close to each other, chloroadamantane and cyanoadamantane have a net difference in their dynamical behaviour. In both cases, the molecules undergo rapid 30° jump reorientations about their symmetry axis and their motion tends to approach isotropic rotational diffusion (see §6.8.4). The corresponding correlation times vary as follows:

$$\tau_{M_{12}} = 1.23 \times 10^{-14} \exp(\Delta H_M/RT) \text{ s}$$

with a barrier height $\Delta H_M = 10.3 \text{ kJ mol}^{-1}$ for chloroadamantane (Bée and Amoureux 1983b), and

$$\tau_{M_{12}} = 5.64 \times 10^{-14} \exp(\Delta H_M/RT) \text{ s}$$

with an activation energy $\Delta H_M = 8.4 \text{ kJ mol}^{-1}$ for cyanoadamantane (Bée *et al* 1980a). But the tumbling of the molecule axis occurs on two different time-scales. In the case of chloroadamantane, it is visible on the time-scale of the t.o.f. experiment, following the Arrhenius law:

$$\tau = 1.09 \times 10^{-14} \exp(\Delta H_c/RT) \text{ s}$$

with $\Delta H_c = 21.4 \text{ kJ mol}^{-1}$. On the other hand, the frequency of occurrence of cyanoadamantane-axis jumps, as obtained from dielectric relaxation measurements, is very low (less than 10^8 Hz at the melting point) and rapidly decreases at room temperature. Just above the transition ($T = 228$ K) these jumps are almost non-existent.

6.10.6 Bicyclooctane, triethylenediamine and quinuclidine

Recently, IQNS data were measured for two similar molecules: bicyclo[2,2,2]octane (BCO) (Bée *et al* 1982, Leadbetter *et al* 1982) and diazobicyclo-octane (also triethylenediamine (TEDA) (Bée *et al* 1985b). These molecules are shown in figure 6.28. Both are approximately spherical, with a cage-like skeleton. Furthermore, in both cases, a phase transition occurs from a low-temperature, hexagonal, ordered phase, to a high-temperature, cubic (Fm3m, $Z = 4$), plastic phase. However, the transition temperatures are different: $T_t = 164$ K for BCO and $T_t = 351$ K for TEDA. In the two cases x-ray structure analysis at room temperature (Sauvajol and Amoureux 1981, Nimmo and Lucas 1976), leads to the conclusion that the molecule at each lattice site undergoes hindered reorientations between eight, equally weighted, equilibrium orientations, all centred on the site with coincident threefold molecular and crystal axes. About each [111] direction, two orientations exist; the molecule can jump from one to another under the effects of the rotations of the $\mathfrak{C}^6$ group.

IQNS data were interpreted on the basis of a model assuming $\pm 60°$ about the molecular axis and $\pm 90°$ jump around [100] lattice axes from one [111] direction to another.

Brot *et al* (1979) have investigated the room-temperature (plastic) phase of azobicyclo[2,2,2]octane (quinuclidine (QND); see figure 6.28). They found that the situation which was more likely to be valid was described by a model allowing for 90° jumps about lattice [100] axes and 120° reorientations about the molecular axis.

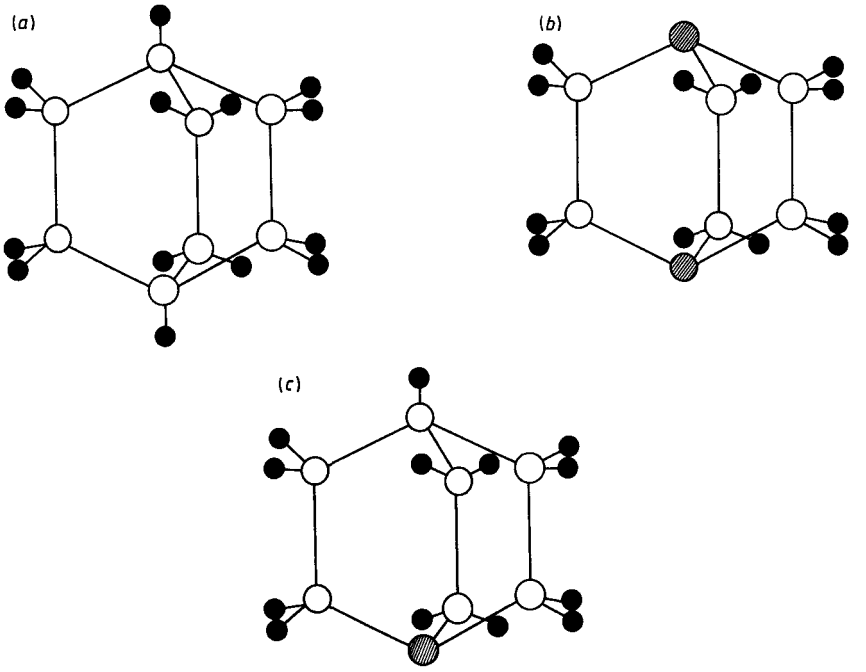

Figure 6.28 The three related molecules: bicyclo[2,2,2]octane (*a*), triethylenediamine (*b*) and quinuclidine (*c*). Carbon atoms are open circles, hydrogen atoms are full circles and nitrogen atoms are dashed circles.

Results are summarised in figure 6.29, where Arrhenius plots are illustrated for orientations of BCO and TEDA about molecule or crystalline axes. Correlation time values for QND at $T = 300$ K have also been reported.

Comparison of the activation energies suggests a stronger steric hindrance in TEDA than in BCO. This is consistent with the values of the lattice parameters at $T = 300$ K: $a = 8.86$ Å, 8.96 Å, 9.10 Å for TEDA, QND, BCO, respectively, whilst the sizes of the molecules are identical. Moreover, the correlation times for QND at $T = 300$ K are intermediate between that for BCO and TEDA. In other words, the interatomic potential between nitrogen atom and the other atoms is evidenced to play a dominant role in the dynamics of these molecules.

6.11 Extension of the Application of Group-Theory Formalism for the Evaluation of the Neutron Scattering Law

Recently Beaufils (1985) has developed a generalisation of the formal-

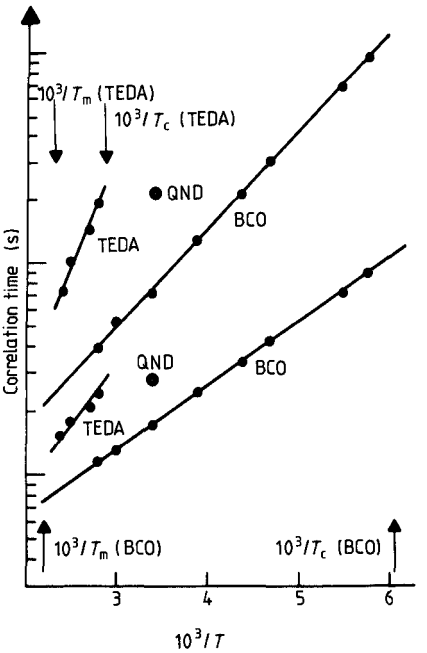

Figure 6.29 Temperature dependence of the correlation times, related to reorientations of bicyclo[2,2,2]octane, quinuclidine and triethylenediamine molecules about their threshold axis and about lattice [100] directions.

ism of Thibaudier and Volino (1973), which can be used to describe a great variety of complex physical situations. The basic idea is the introduction of several *states* of the scattering species within each equilibrium *site* (i.e. orientation or position). Transitions between states are considered together with jumps between sites. Thus more information about the circumstances of the jumps between sites can be taken into account. For instance, the possibility is given to treat the dynamical coupling of two neighbouring molecules, by associating to each equilibrium orientation of the first molecule a set of states associated to the different possible orientations of the other. Furthermore this formalism allows memory effects to be taken into account: a molecule can 'remember' whether its last jump took place recently or not. This is described by associating to the molecule, after each of its jumps, an 'excited' state and a transition rate to a 'relaxed' state. Assuming that the jump probabilities are different in both states, the probability of the occurrence of multiple jumps (i.e. successive jumps with short residence times between them) can become significant. This possibility of memory has been already pointed out (Brot 1969, Brot *et al* 1979) and recently confirmed from molecular simulations (Gerling and Hüller 1983).

The mathematical treatment follows the calculations developed in §6.9.3. The probability $\mathcal{P}(\mathcal{R}, t)$ for a molecule to have been brought, by the rotation $\mathcal{R}$, from its position at time $t = 0$ into its orientation at time t, must be replaced by $\mathcal{P}_{\lambda\mu}(\mathcal{R}, t)$ which is the probability that, simultaneously, it has changed from the state λ to the state μ. $\mathcal{P}_{\lambda\mu}$ follows a Fokker–Planck equation, which is a generalisation of (6.63):

$$\frac{\mathrm{d}}{\mathrm{d}t}\mathcal{P}_{\lambda\mu}(\mathcal{R}, t) = \sum_{\mathcal{S}}\sum_{\nu=1}^{N} p_{\nu\mu}(\mathcal{R}\mathcal{S}^{-1})\mathcal{P}_{\lambda\nu}(\mathcal{S}, t) \tag{6.133}$$

$p_{\nu\mu}(\mathcal{R})$ is the probability per time-unit that the rotation $\mathcal{R}$ occurs with, in the same time, a change from state ν to state μ. The sums run over all the operations $\mathcal{S}$ of the group and over all the possible states ν. The probability per time-unit that neither a rotation nor a state change occurs, $p_{\lambda\lambda}(E)$, (E is the identity element of the group of rotations) is defined by

$$p_{\lambda\lambda}(E) = \sum_{\mathcal{S}}\sum_{\mu=1}^{N'} p_{\lambda\mu}(\mathcal{S}) \tag{6.134}$$

where the prime indicates that the term $\mu = \lambda$ is excluded in the summation if $\mathcal{S} = E$.

Equation (6.133) above can be put in a compact form by introducing the matrices $[\mathcal{P}(\mathcal{R}, t)]$ and $[p(\mathcal{S})]$ whose elements are $\mathcal{P}_{\lambda\mu}(\mathcal{R}, t)$ and $p_{\lambda\mu}(\mathcal{S})$, respectively:

$$\frac{\mathrm{d}}{\mathrm{d}t}[\mathcal{P}(\mathcal{R}, t)] = \sum_{\mathcal{S}}[\mathcal{P}(\mathcal{S}, t)][p(\mathcal{R}\mathcal{S}^{-1})]. \tag{6.135}$$

A solution of (6.135) can be obtained, by following the calculations of Thibaudier and Volino (1973). Introducing the operator $K_{\lambda\mu}$ such that for any function $f_{\lambda\mu}(\mathcal{R})$

$$(Kf)_{\lambda\mu}(\mathcal{R}) = \frac{1}{g}\sum_{\mathcal{S}}\sum_{\nu} K^{(1)}_{\lambda\nu}(\mathcal{R}, \mathcal{S})f_{\nu\mu}(\mathcal{S}) \tag{6.136}$$

with the kernel

$$K^{(1)}_{\lambda\mu}(\mathcal{R}, \mathcal{S}) = p_{\lambda\mu}(\mathcal{R}\mathcal{S}^{-1}) \tag{6.137}$$

equation (6.135) above can be expressed as:

$$\frac{\mathrm{d}}{\mathrm{d}t}[\mathcal{P}(\mathcal{R}, t)] = [K]\,[\mathcal{P}(\mathcal{R}, t)] \tag{6.138}$$

$[K]$ is a matrix operator, whose elements are $K_{\lambda\mu}$. The formal solution is

$$[\mathcal{P}(\mathcal{R}, t)] = \exp\{[K]t\}\,[\mathcal{P}(\mathcal{R}, 0)] \tag{6.139}$$

with the initial conditions at $t = 0$

$$\mathcal{P}_{\lambda\mu}(\mathcal{R}, 0) = \delta_{\lambda\mu}\delta_{\mathrm{E}}(\mathcal{S}) \tag{6.140}$$

or else

$$[\mathcal{P}(\mathcal{R}, 0)] = [I]\delta_E(\mathcal{S}) \tag{6.141}$$

where $[I]$ is the identity matrix and $\delta_E(\mathcal{S})$ the Dirac function at the identity element E.

To obtain the explicit form of $[\mathcal{P}(\mathcal{R}, t)]$, the operator $\exp([K]t)$ has to be evaluated. It can be expressed from a kernel $\exp\{[K]t\}$ $(\mathcal{R}, \mathcal{S})$ such that

$$(\exp\{[K]t\}f)_{\lambda\mu}(\mathcal{R}) = \frac{1}{g}\sum_{\mathcal{S}}\sum_{\nu}(\exp\{[K]t\}(\mathcal{R}, \mathcal{S}))_{\lambda\mu}f_{\nu\mu}(\mathcal{S}). \tag{6.142}$$

This kernel is itself expressed from the iterated kernels $K^{(n)}_{\lambda\mu}(\mathcal{R}, \mathcal{S})$

$$[\exp\{[K]t\}\ (\mathcal{R}, \mathcal{S})] = \sum_{n=0}^{\infty}[K^{(n)}(\mathcal{R}, \mathcal{S})]\frac{t^n}{n!} \tag{6.143}$$

with

$$[K^{(n)}(\mathcal{R}, \mathcal{S})] = \frac{1}{g}\sum_{\mathcal{C}}[K^{(n-1)}(\mathcal{R}, \mathcal{C})]\,[K^{(1)}(\mathcal{C}, \mathcal{S})] \tag{6.144}$$

$$[K^{(1)}(\mathcal{C}, \mathcal{S})] = [p(\mathcal{C}\mathcal{S}^{-1})] \tag{6.145}$$

$$[K^{(0)}(\mathcal{R}, \mathcal{S})] = [I]\delta_{\mathcal{R}}(\mathcal{S}). \tag{6.146}$$

Let us denote by $\Gamma^{(\alpha)}_{(\mathcal{R})}$ the irreducible matrix representations of the group, of dimension d_α. According to the theorem of Peter Weyl any function $f(\mathcal{R})$ defined on the group, can be expressed as a linear combination of the matrix elements of the representation:

$$f(\mathcal{R}) = \sum_{\alpha}\mathrm{Tr}\left\{\frac{d_\alpha}{g}\sum_{\mathcal{S}}\Gamma^{(\alpha)}(\mathcal{S}^{-1})f(\mathcal{S})\Gamma^{(\alpha)}(\mathcal{R})\right\}. \tag{6.147}$$

Therefore taking

$$p_{\mu\nu}(\mathcal{R}) = f(\mathcal{R}) \tag{6.148}$$

$$p_{\mu\nu}(\mathcal{R}) = \sum_{\alpha}\mathrm{Tr}\{Q^{(\alpha)}_{\mu\nu}\Gamma^{(\alpha)}(\mathcal{R})\} \tag{6.149}$$

where

$$Q^{(\alpha)}_{\mu\nu} = \frac{d_\alpha}{g}\sum_{\mathcal{S}}\Gamma^{(\alpha)}(\mathcal{S}^{-1})p_{\mu\nu}(\mathcal{S})$$

is an element of the supermatrix $[Q^{(\alpha)}]$. The symbol Tr denotes the trace operator. The jump rate $p_{\mu\nu}(\mathcal{S})$ depends only on the class of the operation $\mathcal{R}$. If we add all the matrices corresponding to rotations $\mathcal{S}_q$ of the class q, we obtain a matrix

$$\Gamma^{(\alpha)}_q = \sum_{\mathcal{S}_q}\Gamma^{(\alpha)}(\mathcal{S}^{-1}) \tag{6.150}$$

which commutes with all the matrices of the representation. According to Schur's lemma II, $\Gamma_q^{(\alpha)}$ is a multiple of the identity matrix $[I^\alpha]$ with dimension d_α, and $Q_{\mu\nu}^{(\alpha)}$ is a scalar matrix of the form

$$Q_{\mu\nu}^{(\alpha)} = q_{\mu\nu}^{\alpha}[I^\alpha] \tag{6.151}$$

with

$$q_{\mu\nu}^{\alpha} = \frac{1}{g}\sum_{\mathcal{S}} \chi^{(\alpha)}(\mathcal{S}^{-1}) p_{\mu\nu}(\mathcal{S}) \tag{6.152}$$

being the elements of a matrix $[q^\alpha]$ with dimension d_α. The second iterated kernel $K_{\lambda\mu}^{(2)}(\mathcal{R}, \mathcal{S})$ becomes

$$K_{\lambda\mu}^{(2)}(\mathcal{R}, \mathcal{S}) = \frac{1}{g}\sum_{\mathscr{C}}\sum_{\nu=1}^{N} p_{\lambda\nu}(\mathscr{C}\mathcal{S}^{-1}) p_{\nu\mu}(\mathcal{R}\mathscr{C}^{-1}) \tag{6.153}$$

$$= \frac{1}{g}\sum_{\alpha} d_\alpha \sum_{\nu=1}^{N} \mathrm{Tr}\left\{\frac{q_{\lambda\nu}^{(\alpha)}}{d_\alpha}\frac{q_{\nu\mu}^{(\alpha)}}{d_\alpha}\Gamma^{(\alpha)}(\mathcal{R}\mathcal{S}^{-1})\right\} \tag{6.154}$$

$$[K^{(2)}(\mathcal{R}, \mathcal{S})] = \frac{1}{g}\sum_{\alpha} d_\alpha \chi^{(\alpha)}(\mathcal{R}\mathcal{S}^{-1})\left(\frac{[q^\alpha]}{d_\alpha}\right)^2. \tag{6.155}$$

We can easily demonstrate, for arbitrary n,

$$[K^{(n)}(\mathcal{R}, \mathcal{S})] = \frac{1}{g}\sum_{\alpha} d_\alpha \chi^{(\alpha)}(\mathcal{R}\mathcal{S}^{-1})\left(\frac{[q^\alpha]}{d_\alpha}\right)^n. \tag{6.156}$$

An immediate consequence of (6.147) is that, putting $f(\mathcal{R}) = \delta_{\mathcal{R}}(\mathcal{S})$

$$\delta_{\mathcal{R}}(\mathcal{S}) = \frac{1}{g}\sum_{\alpha} d_\alpha \mathrm{Tr}\{\sum_{\mathcal{S}} \Gamma^{(\alpha)}(\mathcal{S}^{-1})\Gamma^{(\alpha)}(\mathcal{R})\delta_{\mathcal{R}}(\mathcal{S})\} \tag{6.157}$$

$$= \frac{1}{g}\sum_{\alpha} d_\alpha \chi^{(\alpha)}(\mathcal{R}). \tag{6.158}$$

Now, defining

$$[\mathcal{U}^{(\alpha)}(t)] = [I] + \sum_{n=1}^{\infty}\left(\frac{[q^\alpha]}{d_\alpha}\right)^n \frac{t^n}{n!} \tag{6.159}$$

and using (6.139), (6.143), (6.146) and (6.156), we obtain

$$[\mathcal{P}(\mathcal{R}, t)] = \frac{1}{g}\sum_{\alpha} d_\alpha [\mathcal{U}^{(\alpha)}(t)]\chi^{(\alpha)}(\mathcal{R}). \tag{6.160}$$

In theory, calculating the $[q^\alpha]$, the matrix elements $\mathcal{U}_{\lambda\mu}^{\alpha}$ can be determined from (6.159) and hence, the elements of the probability matrix can be evaluated. In practice, it is worth noting that there are solutions of

$$\frac{\mathrm{d}}{\mathrm{d}t}[\mathcal{U}^{(\alpha)}(t)] = \frac{1}{d_\alpha}[\mathcal{U}^{(\alpha)}(t)]\,[q^\alpha] \tag{6.161}$$

with the initial solution (resulting from (6.141), (6.158) and (6.160))

$$[\mathcal{U}^{(\alpha)}(0)] = [I^{\alpha}]. \tag{6.162}$$

We pause at this point to note that, according to (6.161), we have now to solve, for each irreducible representation of the rotation group, a system of linear equations, whose dimension is equal to the number of possible states in each site. The solution can be obtained by standard methods and formally written:

$$[\mathcal{U}^{(\alpha)}(t)] = [\mathcal{H}^{(\alpha)-1}]\,[\mathcal{V}^{(\alpha)}(t)]\,[\mathcal{H}^{(\alpha)}] \tag{6.163}$$

where $\mathcal{V}^{(\alpha)}(t)$ is a matrix whose elements

$$\mathcal{V}^{(\alpha)}_{\lambda\mu}(t) = \delta_{\lambda\mu} \exp(-\mathcal{V}^{(\alpha)}_{\lambda} t) \tag{6.164}$$

depend on the different eigenvalues. Correspondingly, the matrix is formed by the eigenvalues related to the $\mathcal{V}^{(\alpha)}_{\lambda}$. When all the probabilities $\mathcal{P}_{\lambda\mu}(\mathcal{R}, t)$ have been evaluated, the correlation function of any variable $f_{\mu}(\boldsymbol{r})$ attached to the molecule and depending on its orientation and state can be obtained according to

$$\langle f(0)f(t)\rangle = \sum_{\mathcal{R}} \sum_{\lambda=1}^{N} \sum_{\mu=1}^{N} f^{*}_{\lambda}(\boldsymbol{r}) f_{\mu}(\mathcal{R}\boldsymbol{r}) w_{\lambda} \mathcal{P}_{\lambda\mu}(\mathcal{R}, t). \tag{6.165}$$

The first summation runs over all possible rotations of the molecule, the two others run over all possible initial and final states. Equation (6.165) is simply a generalisation of (6.65), with, however, the introduction of weights, w_{λ}, of the different states, λ. These weights are the limit at infinite time

$$w_{\lambda} = \lim_{t\to\infty} \mathcal{P}_{\lambda\mu}(\mathcal{R}, t) = \mathcal{P}_{\lambda\mu}(\mathcal{R}, \infty) \tag{6.166}$$

of the probabilities of a change for the molecule. With this stationary condition

$$\lim_{t\to\infty} \frac{\mathrm{d}}{\mathrm{d}t} \mathcal{P}_{\lambda\mu}(\mathcal{R}, t) = 0. \tag{6.167}$$

Equation (6.133) becomes

$$0 = \sum_{\nu=1}^{N} w_{\nu} \sum_{\mathcal{S}} p_{\nu\mu}(\mathcal{S}^{-1}) \tag{6.168}$$

Or in matrix form:

$$[0] = \sum_{\mathcal{S}} [p(\mathcal{S}^{-1})]\,[\mathcal{W}] \tag{6.169}$$

where the elements of the diagonal matrix $[\mathcal{W}]$ are $\mathcal{W}_{\lambda\mu} = w_{\lambda}\delta_{\lambda\mu}$. The weights of the possible states appear as the components of an eigenvector of the matrix

$$\sum_{\mathcal{S}} [p(\mathcal{S}^{-1})]$$

associated to the eigenvalue 0. They are determined from the transition probabilities $p_{\lambda\mu}$ between the different states. Finally, introducing the matrices $[\mathcal{F}(\mathcal{R})]$, with elements

$$\mathcal{F}_{\lambda\mu}(\mathcal{R}) = f_\lambda^*(\boldsymbol{r}) f_\mu(\mathcal{R}\boldsymbol{r}) \tag{6.170}$$

the correlation function becomes

$$\langle f(0)f(t)\rangle = \frac{1}{g} \sum_{\alpha} \sum_{\mathcal{R}} d_\alpha \chi^{(\alpha)}(\mathcal{R}) \times \mathrm{Tr}\{[\mathcal{H}^{(\alpha)}][\mathcal{F}(\mathcal{R})][\mathcal{W}][\mathcal{H}^{(\alpha)-1}][\mathcal{V}^{(\alpha)}(t)]\}. \tag{6.171}$$

According to the definition of $[\mathcal{V}^{(\alpha)}]$, it appears as an expansion into exponential terms. Each of them corresponds to an eigenvalue $\mathcal{V}_\lambda^{(\alpha)}$ of the matrices $[q^\alpha]$ associated to each irreducible representation $\Gamma^{(\alpha)}$. When evaluating the scattering law, taking the Fourier transform of each of the exponential term leads to a series of lorentzian functions $\mathcal{L}(\mathcal{V}_\lambda^{(\alpha)}, \omega)$

$$S(\boldsymbol{Q}, \omega) = \sum_{\alpha} \sum_{\lambda} A_\lambda^{(\alpha)} \mathcal{L}(\mathcal{V}_\lambda^{(\alpha)}, \omega) \tag{6.172}$$

$$\mathcal{L}(\mathcal{V}_\lambda^{(\alpha)}, \omega) = \frac{1}{\pi} \frac{\mathcal{V}_\lambda^{(\alpha)}}{(\mathcal{V}_\lambda^{(\alpha)})^2 + \omega^2}. \tag{6.173}$$

The structure factors $A_\lambda^{(\alpha)}$ are expressed by

$$A_\lambda^{(\alpha)} = \frac{d_\alpha}{g} \left\{ [\mathcal{H}^{(\alpha)}] \sum_{\mathcal{R}} \chi^{(\alpha)}(\mathcal{R}) \, [\mathcal{F}(\mathcal{R})] \, [\mathcal{W}] \, [\mathcal{H}^{(\alpha)-1}] \right\}. \tag{6.174}$$

In his original paper, Beaufils (1985) applies his formalism to the influence of rotation–translation coupling on incoherent neutron scattering. The case of a homonuclear diatomic molecule is considered. This molecule is assumed to have three possible equilibrium orientations on each site of a cubic lattice, i.e. it can be aligned along each of the lattice axes (figure 6.30.) Reorientations among these orientations can occur, at a rate $\gamma_{\mathcal{R}}$. Simultaneously, displacements of the molecule from one site to any of the six next-neighbouring ones are allowed, but with different rates γ_+ or γ_- depending on whether the displacement is parallel to the molecule axis, or not. The difference between γ_+ and γ_- accounts for the coupling between rotation and translation.

To apply the formalism previously described, the two types of motion are treated on different grounds: (i) the group of the operation $\mathcal{R}$ is the group of lattice translations, whose irreducible representations are labelled by a vector $\boldsymbol{k}$ in the reciprocal space and whose characters are

$$\chi^{\boldsymbol{k}}(\mathcal{R}) = \exp(-\mathrm{i}\boldsymbol{k}\cdot\mathcal{R})$$

$\mathcal{R}$ being a lattice vector. (ii) The three possible orientations of the molecule are described as three states within each lattice site.

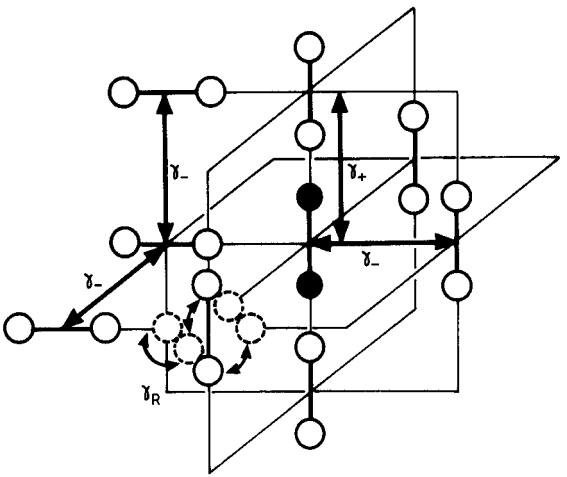

Figure 6.30 Rotation–translation coupling of a dumbbell molecule.

The effects of the coupling were clearly evidenced, on both the EISF and the widths of the quasielastic components, these latter being drastically reduced. The difference between the coupled model ($\gamma_+ \neq \gamma_-$) and the not-coupled model ($\gamma_+ = \gamma_-$) are obviously most marked when $\gamma_{\mathcal{R}} \gg \gamma_+$. However, both models lead to a similar behaviour if $\gamma_{\mathcal{R}} \gg \gamma_+$: when the rotation is fast compared to the residence time in a site, each molecule is seen as a sphere from the neighbouring sites.

6.12 Conclusion

In this chapter, numerous IQNS studies of organic compounds have been presented. They provide good illustrations of the calculation of the rotational incoherent scattering laws based on different possibilities of molecular motions. In most cases, the models exposed in this chapter are enable to give an adequate interpretation of the experimental results. However, other situations exist, in which a description in terms of these models is inadequate. We shall be concerned with these features of quasielastic scattering in the next chapter.

Chapter 7 Recent Developments in the Investigation of Orientationally Disordered Phases

7.1 Introduction

In this chapter, we present some of the most recent developments in the interpretation of neutron scattering data. Indeed, neither the rotational-diffusion model nor the jump model are fully satisfying. Owing to the interactions with its neighbours, a molecule embedded in a crystal is never able to rotate freely. The opposite situation of molecules rigidly aligned along some preferential orientations and experiencing instantaneous reorientations is no more realistic. Numerous studies of orientationally disordered phases have established the existence of large-amplitude librations of the molecules, which can hardly be taken into account by a simple Debye–Waller term. Many authors have derived various methods to overcome the difficulties encountered in the interpretation of their specific data. An exhaustive report of all these mathematical calculations would be impossible, within the compass of a

single chapter. We restrict our objective to a general survey of the formalisms which are now the most commonly used. We start with simple improvements of the rotational diffusion model derived in the investigation of liquid-crystal phases, which consist in the introduction of a non-uniform distribution of the scattering particle over a circle or over a sphere. Octaphenylcyclotetrasiloxane and pivalic acid provide two examples where the experimental EISF can be interpreted on the basis of this description. A more rigorous treatment takes into account an average static potential acting on the molecule and originating from its neighbours. For that purpose we are led to state the stochastic Langevin, Fokker–Planck and Smoluchowski equations. The one-dimensional case is illustrated by the solution in the case of a potential with a cosine form. Both the rotational case (Dianoux and Volino 1977) and the translational case (Volino *et al* 1979) are considered. The extension to the three-dimensional case requires the introduction of symmetry-adapted (rotator) functions to get a simple formulation of the neutron scattering law in terms of correlation functions of these functions. They appear very useful because, by definition, they possess both the symmetry of the molecule and that of the site. They form an orthogonal basis on which the equilibrium orientational probability and the potential can be expanded. We demonstrate how it is possible to determine the numerical values of the leading coefficients in these expansions from an analysis of x-ray or neutron crystallographic structure measurements and also from the study of the EISF in quasielastic neutron scattering.

The microscopic approach (De Raedt and Michel 1979) also uses the symmetry-adapted functions in the expansion of the neutron scattering law. The Mori–Zwanzig projection-operator technique is used to derive an expression of the correlation functions of these symmetry-adapted functions in terms of their moments. As a concrete example, the case of a dumbbell molecule in an octahedral potential is considered. The most striking feature is that, according to the height of the potential (or equivalently, according to the value of the temperature), correlation functions are found to have a diffusive or an oscillatory character, corresponding, either to reorientational motions of the molecule or to librations about the potential minima, respectively.

The next section deals with the investigation of orientational disorder by Raman and infrared spectroscopies. Recent studies have evidenced that, from the analysis of the integrated intensity and of the shape of internal modes, it is possible to get information about the numerical values of the coefficients of the expansion of the orientational probability into rotator functions and also about the dynamical aspect of the molecular motion. Examples are given and the results are compared with the conclusions of x-ray and neutron scattering studies.

7.2 Uniaxial Rotation with Non-uniform Distribution

The neutron scattering law for the case of uniform rotational motion over a circle has been established in chapter 6. The orientational distribution function $P(\phi, \phi_0, t)$ is the solution of a Fokker–Planck type equation (6.19)

$$\frac{\partial}{\partial t}P(\phi, \phi_0, t) = D_r\frac{\partial^2 P(\phi, \phi_0, t)}{\partial \phi^2} \tag{7.1}$$

in which D_r is the rotational diffusion constant, ϕ and ϕ_0 denote the angular position of the scatterer on the circle, at time t and zero, respectively. The initial distribution $P(\phi_0)$ is uniform

$$P(\phi_0) = \frac{1}{2\pi}. \tag{7.2}$$

The corresponding scattering law is (see equation (6.26))

$$S(\boldsymbol{Q}, \omega) = J_0^2(Qr\sin\theta)\delta(\omega) + 2\sum_{m=1}^{\infty} J_m^2(Qr\sin\theta)\frac{1}{\pi}\frac{D_r m^2}{(D_r m^2)^2 + \omega^2}. \tag{7.3}$$

Here r is the radius of the circle and θ the angle between the scattering vector $\boldsymbol{Q}$ and the rotation axis. This scattering law was found to be equivalent to that derived for a jump motion among a sufficiently large number, N, of sites, equivalent and equally spaced on the circle. In other words, the discrete distribution

$$P_N(\phi_0) = \frac{1}{N}\sum_{n=1}^{N}\delta(\phi_0 - \phi_n) \tag{7.4}$$

is such that

$$\lim_{N\to\infty} P_N(\phi_0) = P(\phi_0). \tag{7.5}$$

If the points are not equally weighted over the circle one should rather take a peaked distribution. But the introduction of an order parameter leads to major difficulties in calculating the self-correlation function of the scatterer. The EISF can nevertheless be obtained because it is the limit at infinite time of the intermediate scattering law.

$$I(\boldsymbol{Q}, \infty) = \int d\phi_0 \int d\phi \exp\{i\boldsymbol{Q}\cdot[\boldsymbol{R}(\phi) - \boldsymbol{R}(\phi_0)]\}P(\phi, \phi_0, \infty)P(\phi_0) \tag{7.6}$$

and therefore it may be calculated without resolving the equation of motion. We then choose the orientational distribution, peaked at $\phi = 0$,

$$P(\phi, \phi_0, \infty) = \frac{1}{A}\sum_{n=1}^{N}\delta(\phi - \phi_n)\exp\left[\beta' \cos\left(\frac{2\pi n}{N} + \phi_0\right)\right]. \tag{7.7}$$

Here β' characterises the width of the angular distribution. A is a normalising constant given by (Hervet *et al* 1975)

$$A = NI_0(\beta') \tag{7.8}$$

where I_0 is the zero-order modified Bessel function of the first kind. It is possible to define an orientational order parameter

$$\beta = \langle \cos\phi \rangle = \frac{I_1(\beta')}{I_0(\beta')}. \tag{7.9}$$

If the initial distribution $P(\phi_0)$ is chosen such that

$$P(\phi_0) = \frac{1}{2\pi I_0(\beta')} \exp(\beta' \cos\phi_0) \tag{7.10}$$

the calculation of the EISF can be performed exactly. The result is in the powder case:

$$A_0(Q) = \frac{1}{NI_0^2(\beta')} \sum_{n=1}^{N} j_0\left(2Qr \sin\frac{\pi n}{N} I_0\left(2\beta' \left|\cos\frac{\pi n}{N}\right|\right)\right) \tag{7.11}$$

where $j_0(x)$ is the Bessel function of the first kind and r the circle radius. If there is no orientational order, $\beta' = 0$, and the result of §6.7 (equation (6.56)) is recovered. The continuous limit when $N \to \infty$ is

$$A_0(Q) = \frac{1}{\pi I_0^2(\beta')} \int_0^{\pi} j_0(2Qr \sin x) I_0(2\beta' \cos x)\, dx. \tag{7.12}$$

This formalism was used to investigate the nature of the molecular alignment in the smectic-H phase of TBBA (Hervet *et al* 1975).

7.3 Rotation over a Sphere with Non-uniform Distribution

7.3.1 Theoretical background

Let us now turn to the three-dimensional case, i.e. when the particle motion occurs on a sphere. In the preceding chapter, it has been seen that in the case of uniform diffusion over the sphere, the orientational distribution function $P(\boldsymbol{\Omega}, \boldsymbol{\Omega}_0, t)$ satisfies the differential equation (6.13)

$$\frac{\partial}{\partial t} P(\boldsymbol{\Omega}, \boldsymbol{\Omega}_0, t) = D_R \Delta(\boldsymbol{\Omega}) P(\boldsymbol{\Omega}, \boldsymbol{\Omega}_0, t) \tag{7.13}$$

in which D_R is the rotational diffusion constant. $\Delta(\boldsymbol{\Omega})$ is the Laplace operator in the space of the Euler angles. $\boldsymbol{\Omega}$ and $\boldsymbol{\Omega}_0$ denote these angles for the position of the scatterer on the sphere at times t and 0, respectively. The corresponding scattering law was derived in §6.2:

$$S(Q, \omega) = j_0^2(QR)\delta(\omega) + \sum_{l=1}^{\infty} (2l+1) j_l^2(QR) \frac{1}{\pi} \frac{l(l+1)D_R}{[l(l+1)D_R]^2 + \omega^2}. \tag{7.14}$$

Here we are interested in the case when all the points on the sphere are not equally weighted, i.e. when the distribution is rather peaked about some direction in space. Taking this direction as z-axis, and denoting by θ and ϕ the spherical coordinates of the scatterer (see figure 7.2), we suppose for the distribution $P(\theta, \phi)$ peaked at $\theta = 0$, the following (normalised) function

$$P(\theta, \phi) = P(\theta) = \frac{\delta}{2sh\delta} \exp(\delta \cos\theta). \tag{7.15}$$

As in the uniaxial case, the derivation of the complete scattering law is extremely difficult and we shall restrict ourselves to the evaluation of the EISF. We make use of the expansion

$$\exp(i\boldsymbol{Q}\cdot\boldsymbol{R}) = 4\pi \sum_{l=0}^{\infty} \sum_{m=-l}^{l} i^l j_l(QR) Y_l^{m*}(\theta_Q, \phi_Q) Y_l^m(\theta, \phi) \tag{7.16}$$

where θ_Q and ϕ_Q are the polar and azimuthal angles of the scattering vector $\boldsymbol{Q}$ (see figure 7.1). For the evaluation of the average

$$\langle \exp(i\boldsymbol{Q}\cdot\boldsymbol{R}) \rangle = \frac{1}{2\pi} \int_0^{2\pi} d\phi \int_0^{\pi} d\theta \sin\theta \exp(i\boldsymbol{Q}\cdot\boldsymbol{R}) \frac{\delta}{2sh\delta} \exp(\delta \cos\theta) \tag{7.17}$$

it is worth replacing the spherical harmonics by Legendre functions P_l^m, according to

$$Y_l^m(\theta, \phi) = (-1)^m \left[\frac{2l+1}{4\pi} \frac{(l-m)!}{(l+m)!} \right]^{1/2} P_l^m(\cos\theta) e^{im\phi}. \tag{7.18}$$

When averaging over the polar (uniform) angular distribution,

$$\frac{1}{2\pi} \int_0^{2\pi} Y_l^m(\theta, \phi)\, d\phi = \left[\frac{2l+1}{4\pi} \right]^{1/2} P_l(\cos\theta) \delta_{m0} \tag{7.19}$$

where $P_l(\cos\theta) = P_l^0(\cos\theta)$ are the Legendre polynomials, so that we obtain:

$$\langle \exp(i\boldsymbol{Q}\cdot\boldsymbol{R}) \rangle = \sum_{l=0}^{\infty} [4\pi(2l+1)]^{1/2} i^l j_l(QR) Y_l^{0*}(\theta_Q, \phi_Q) S_l(\delta) \tag{7.20}$$

in which we have defined:

$$S_l(\delta) = \frac{\delta}{2sh\delta} \int_0^{\pi} P_l(\cos\theta) \exp(\delta \cos\theta)\, d\theta. \tag{7.21}$$

To obtain the EISF, we take the modulus squared of the r.h.s of (7.20). In the powder case, we obtain after an average over all the possible directions of $\boldsymbol{Q}$:

$$A_0(Q) = \sum_{l=0}^{\infty} (2l+1) j_l^2(QR) S_l^2(\delta). \tag{7.22}$$

To get this result, the orthogonality properties of the Y_l^m have been taken into account.

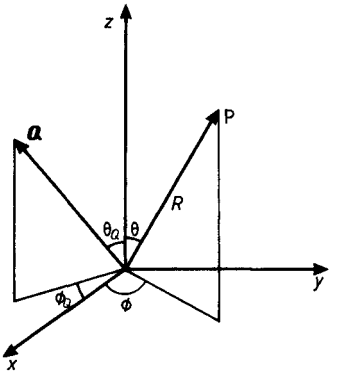

Figure 7.1 Polar coordinates notation for a particle P moving on the surface of a sphere with radius R.

The $S_l(\delta)$ are orientational order parameters. They follow the recurrence relation (Volino *et al* 1976b)

$$S_{l+1}(\delta) = -\frac{2l+1}{\delta} S_l(\delta) + S_{l-1}(\delta) \tag{7.23}$$

with the explicit definitions for $l = 0$ and $l = 1$

$$S_0(\delta) = 1 \tag{7.24a}$$

$$S_1(\delta) = \langle \cos\theta \rangle = \coth\delta - \frac{1}{\delta}. \tag{7.24b}$$

The parameter δ is related to the width of the distribution (7.15). In the case $\delta = 0$ (uniform distribution), we get

$$S_l(0) = \delta_{l0} \tag{7.25}$$

and (7.22) reduces to

$$A_0(Q) = j_0^2(QR) \tag{7.26}$$

which is the EISF of a sphere of radius R (equation (6.17a)). Variations of the EISF as a function of QR are illustrated in figure 7.2, for several values of δ.

More sophisticated models assume different combinations of motions. For instance, the scatterer is assumed to perform a uniform rotation on a circle of radius r, while the axis of this circle itself fluctuates in space.

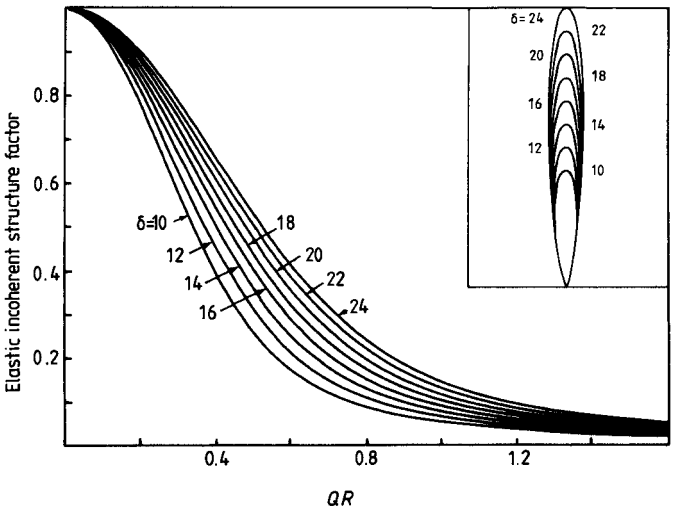

Figure 7.2 EISF variations as a function of the modulus of the scattering vector Q, in the case of a particle moving on the surface of a sphere with radius R, with a position distribution peaked at one point (equation (7.15)). Different cases of the distribution width δ have been considered.

Such a situation can be encountered when a group of atoms can rotate about some bond inside a molecule, and when the whole-molecule orientation can simultaneously fluctuate. Figure 7.3 summarises the notations. The relation

$$Y_l^m(\theta, \phi) = \sum_{n=-l}^{l} D_{mn}^{l*}(\mathbf{\Omega}) Y_l^n(\theta', \phi') \tag{7.27}$$

relates the spherical harmonics expressed as function of the spherical coordinates of the scatterer in the laboratory frame (θ, ϕ) and in the mobile frame (θ', ϕ'). The D_{mn}^l are the Wigner matrices. $\mathbf{\Omega}$ are the Euler angles which bring the two frames in coincidence. Plugging (7.27) into (7.16), we get

$$\exp(\mathrm{i}\boldsymbol{Q}\cdot\boldsymbol{R}) = 4\pi \sum_{l=0}^{\infty} \sum_{m=-l}^{l} \sum_{n=-l}^{l} \mathrm{i}^l j_l(QR) Y_l^{m*}(\theta_Q, \phi_Q) D_{mn}^l(\mathbf{\Omega}) Y_l^n(\theta', \phi'). \tag{7.28}$$

Using (7.19) and performing the average over ϕ' with the uniform distribution

$$P(\phi') = \frac{1}{2\pi} \tag{7.29}$$

which leaves only the term $n = 0$, we get

$$\langle \exp(i\boldsymbol{Q}\cdot\boldsymbol{R})\rangle_{\phi'} = \sum_{l=0}^{\infty}\sum_{m=-l}^{l} i^l j_l(QR) Y_l^{m*}(\theta_Q, \phi_Q) \times D^l_{m0}(\boldsymbol{\Omega})[4\pi(2l+1)]^{1/2} P_l(\cos\theta'). \tag{7.30}$$

Now, we use the following relation

$$D^l_{m0}(\boldsymbol{\Omega}) = \left[\frac{4\pi}{2l+1}\right]^{1/2} Y_l^m(\theta'', \phi'') \tag{7.31}$$

and perform the averages over ϕ'' and θ'', with the distributions

$$P(\phi'') = \frac{1}{2\pi} \tag{7.32a}$$

$$P(\theta'') = \frac{\delta}{2sh\delta}\exp(\delta\cos\theta''). \tag{7.32b}$$

The first one leaves only the term $m = 0$. The calculations are exactly the same as previously. We finally obtain the EISF

$$A_0(Q) = \sum_{l=0}^{\infty}(2l+1) j_l^2(QR) S_l^2(\delta) P_l^2(\cos\theta''). \tag{7.33}$$

Putting $\cos\theta'' = 1$ (i.e. $r = 0$) in this equation leads to the recovery of (7.22), i.e. motion on a sphere on which the orientational distribution is peaked at one point. Moreover, when $\delta = 0$, we have $S_l(0) = \delta_{l0}$ and the Sears expression (7.26) is obtained. Conversely, the situation $\delta \to \infty$ corresponds to uniform uniaxial rotation on the circle of radius r. Volino *et al* verified numerically that boundary condition which is clearly seen in figure 7.4 where the EISF curves have been illustrated for a series of values of δ.

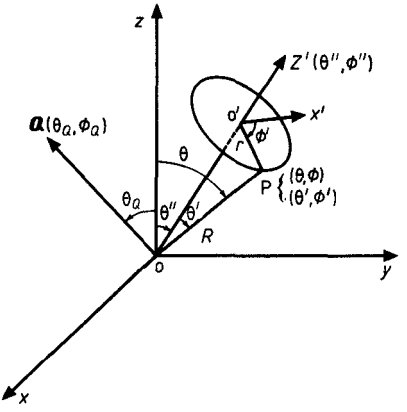

Figure 7.3 Polar coordinates notation for a particle P, rotating over a circle of radius r, the axis of which simultaneously fluctuates in space.

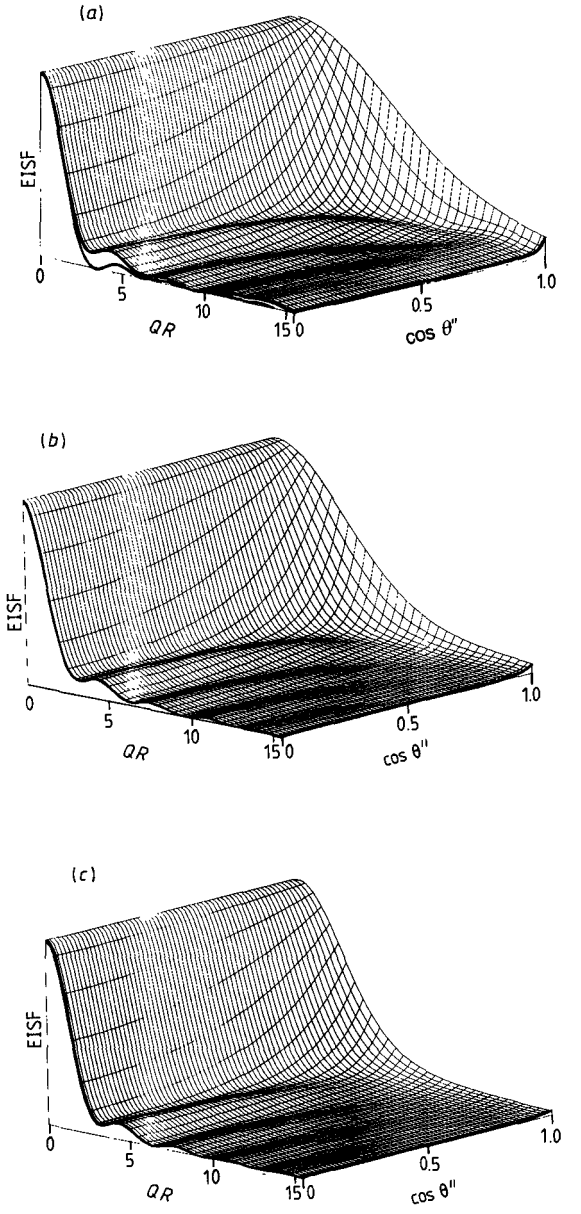

Figure 7.4 EISF variations as a function of the modulus of the scattering vector Q, in the case of a particle rotating over a circle of radius r, the axis of which simultaneously fluctuates in space. Different cases are illustrated corresponding to different values of the width, δ, of the distribution of the fluctuations: (a), $\delta = 50$; (b), $\delta = 24$; (c), $\delta = 10$; (d), $\delta = 5$; (e), $\delta = 2$; (f), $\delta = 0.5$.

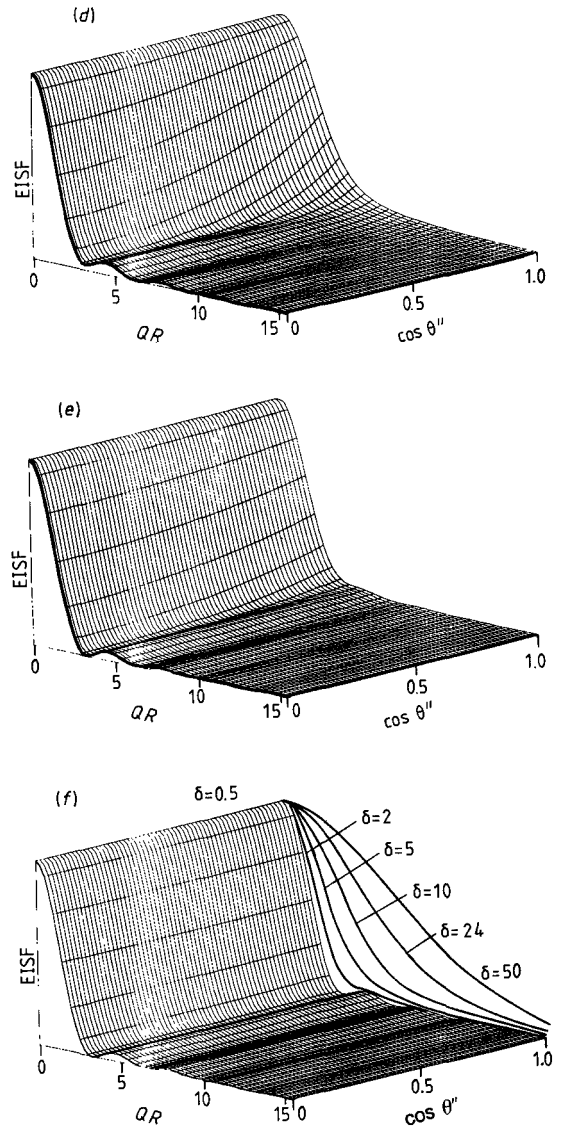

Figure 7.4 (*cont.*)

7.3.2 Octaphenylcyclotetrasiloxane

Results of the investigation of the dynamics of the octaphenylcyclotetrasiloxane (OPCTS) molecule (see figure 6.1) using the backscattering technique have been reported in §6.3.1. It was shown that, on the 10^{-9} s time-scale, the motions could be described as a rotational diffusion

about the molecular centre of gravity, in both the isotropic and liquid phase, with apparently no change at the melting point. OPCTS was also analysed on the time scale of 10^{-11} s, using time-of-flight neutron spectroscopy (Bée *et al* 1984). Experimental values of the EISF extracted from the spectra were compared to theoretical values predicted by two models. The first model is based on large amplitude oscillations of the para-axes of the phenyl rings. This hypothesis was supported by the consideration that the siloxane ring is not rigid and that rotations around the Si–O bonds can easily occur, with simultaneously an exchange of the ring between two equivalent boat forms, via a chain form. In the same time, large librations of the phenyl groups about their para-axes are probable, although a complete rotation is rather improbable owing to steric hindrance. The corresponding EISF of this model is expressed as (7.22).

The second model, in addition to rapid fluctuations of the phenyl para-axes, assumes a rotation of the whole molecule around the siloxane axis and yields to the EISF given by (7.33). Comparison of theoretical curves with experimental values is shown in figure 7.5. It is seen that both models agree well with the experimental data. Using expression (7.33) for the EISF, $\Delta\alpha$ varies from $\simeq 15°$ in the mesophase to $\simeq 24°$ in the liquid phase, with no apparent discontinuity at the melting temperature. When using the model based upon (7.22), the agreement is a little worse, though it is still reasonable, with $\Delta\alpha$ varying from $\simeq 40°$ at 416 K to $\simeq 47°$ at 483 K. The distinction between both models could be made from an analysis of the intensity of the spectra measured by the backscattering technique. The decrease of this intensity as a function of Q was found consistent with an oscillational amplitude of $\simeq 15°$, in accordance with the first model.

7.3.3 Pivalic acid

Pivalic acid $(CH_3)_3CCOOH$ (figure 7.6) undergoes at $T = 280$ K a solid–solid phase transition between a low-temperature, triclinic phase and an orientationally disordered, cubic phase (Longueville *et al* 1978, Longueville and Fontaine 1976). In this latter phase, the molecules are associated in non-polar dimer units, formed by two nearest-neighbour molecules linked by two hydrogen bonds, as evidenced from dielectric relaxation measurements (Kondo and Oda 1954). The long axes of the dimeric units are aligned along either of the [110] directions. The existence of a dynamical disorder was clearly shown by NMR (Jackson and Strange 1971, Albert *et al* 1976, Hasebe *et al* 1980). Characteristic times and activation energies were obtained, corresponding to reorientations of the whole molecule or of its different parts and also to translational self-diffusion of the molecules further studied by radio-

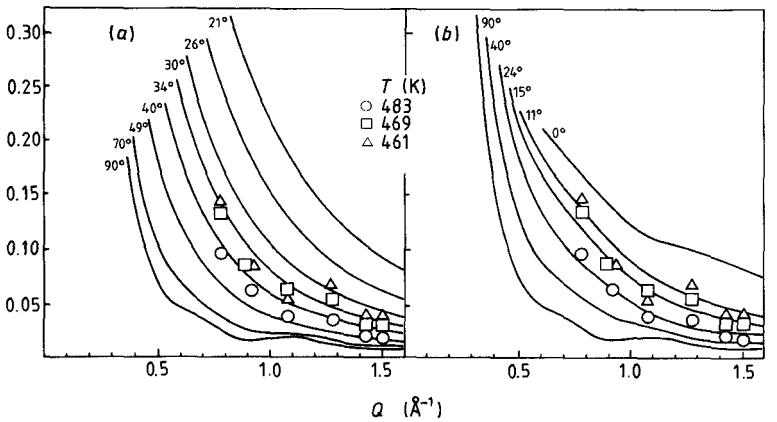

Figure 7.5 Comparison of experimental EISF values with theoretical curves in the case of octaphenylcyclotetrasiloxane (Bée *et al* 1984). Models are based upon fluctuations of the orientations of the phenyl ring axes (*a*), with a possible rotation of the whole molecule about the siloxane ring axis (*b*).

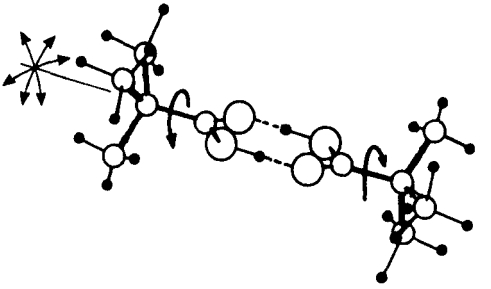

Figure 7.6 Sketch of a dimeric unit of pivalic acid.

tracer experiments (Hawthorne and Sherwood 1970, Brissaud-Lancin *et al* 1982). Pivalic acid was also the subject of several IQNS studies (Leadbetter and Turnbull 1977, Urban *et al* 1983). More recently, the partial deuteration method was used to investigate in a precise way the motions of the different parts of the molecule (Bée *et al* 1983b, 1986b, Longueville *et al* 1986). The extraction of an experimental EISF over a very large energy-transfer range up to 10 meV, permitted the conclusion that, on the 10^{-11}–10^{-13} s time-scale, large-amplitude oscillations exist. These can be attributed, either to whole dimers, or to each part of the dimer unit with a deformation of the central hydrogen-bonded carboxylic ring. Simultaneously, uniform rotations of the protons of the t-butyl groups occur, as a result of the rotation of the whole dimer or of the

individual t-butyl groups. Rotations of methyl groups appear too slow to be visible on the instrument time-scale. A mean amplitude of about 10° was found for the oscillations (figure 7.7). Pivalic acid was extensively studied using Raman scattering (Longueville and Fontaine 1976, Longueville *et al* 1982). This technique provided a detailed description of intramolecular motions. Especially, torsional oscillations of t-butyl and methyl groups were found to occur at low-frequency ($\langle 40\,\text{meV} \simeq 320\,\text{cm}^{-1}$), which should be visible in the inelastic part of the neutron spectrum because the instrument resolution is still reasonable in that range.

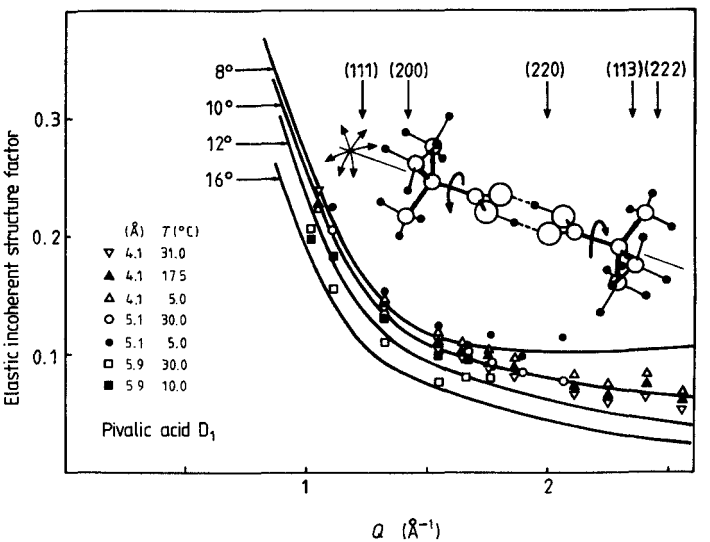

Figure 7.7 Comparison of experimental EISF values deduced from an experiment on pivalic acid, with the theoretical curves predicted by a model allowing a uniaxial rotation of the dimer units about their long axis together with fluctuations of the orientation of this axis.

So far, we have not been dealing with this inelastic part of the spectrum, looking only at the region near the elastic line, where the contribution to the scattered intensity originating from vibrations can generally be approximated by some flat background. In the case of pivalic acid, this contribution was found to be, conversely, extremely important. The main reason lies in the large dimension of the dimeric units in the direction of their long axis. Thus small angular librations yield to considerable displacements of the protons of the t-butyl groups.

Because the inelastic intensity is proportional to the displacement self-correlation function (equation 2.183)), it becomes very large in this case, so that the usual separation according to (2.212) of the inelastic and quasielastic scattering law is no longer valid. We emphasise somewhat the analysis of the inelastic part because it is a nice example of how the same information can be obtained by two very different techniques: neutron spectroscopy and Raman scattering. In neutron inelastic scattering spectroscopy it is usual to consider the function (Boutin and Yip 1968)

$$P(\bar{\alpha}, \bar{\beta}) = \frac{\omega^2}{Q^2} S(Q, \omega) \tag{7.34}$$

where

$$\bar{\alpha} = \frac{\hbar^2 Q^2}{2k_B T} \tag{7.35a}$$

and

$$\bar{\beta} = \frac{\hbar\omega}{k_B T}. \tag{7.35b}$$

Its limit when $Q^2 \to 0$,

$$\lim_{Q^2 \to 0} P(\alpha, \beta) = G(\omega) \tag{7.36}$$

is the generalised frequency distribution (chapter 2). Figure 7.8 illustrates the function $P(\bar{\alpha}, \bar{\beta})$, versus the energy transfer $\hbar\omega$, for several values of the scattering angle, in both the low-temperature and plastic phases. In the range 20–40 meV (160–320 cm^{-1}), a pronounced, wide band appears, composed of several, unresolved peaks. From Raman-analysis conclusions, contributions from CH_3 torsional modes should be expected at 256 cm^{-1} and 263 cm^{-1} but also deformations $\delta_{C'CC}$ of the C'—C—(CH_3) system at 248 cm^{-1} and vibrations at 287 cm^{-1} involving methyl-torsions and rotations of the C—C_3 group. In the low-frequency range (0–20 meV), the instrument resolution is better. Four peaks are revealed. The line at 130 cm^{-1} corresponds to the stretching of the hydrogen bonds ν(OH---O);Ag in which the two parts of the dimer move with respect to each other. The peak at 55 cm^{-1} can be attributed to the mode β(O---O) (observed at 59 and 56 cm^{-1} by IR and Raman spectroscopy). But the vibration ν(OH---O);Bu, predicted at 107 cm^{-1}, is not visible. At 91 cm^{-1} a torsional mode of the C'—C bond appears between the carboxylic group and the t-butyl group, also involved in the peak at 37 cm^{-1} where it is coupled to a deformation of the carboxylic ring (t(OH---O);Au).

With the fully deuterated isotope, the intensity in the region 100–320 cm^{-1} is strongly reduced, but some structures remain. At about

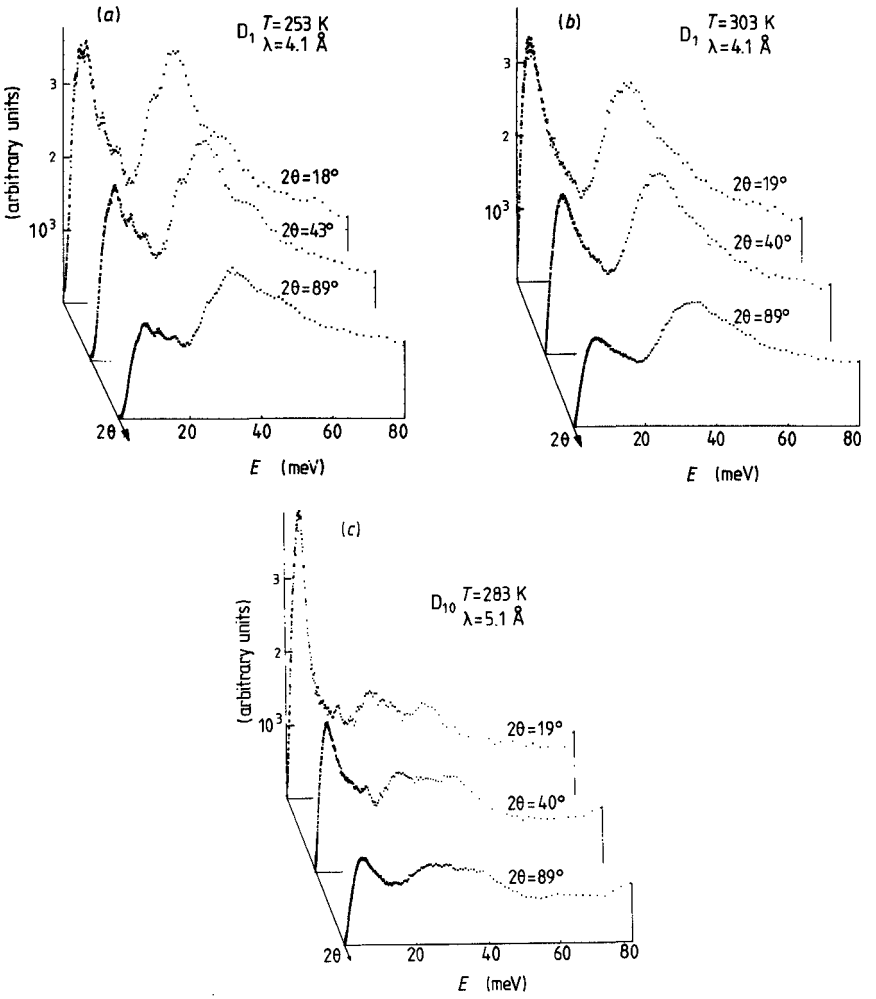

Figure 7.8 Experimental values of the $P(\bar{\alpha}, \bar{\beta})$ function (equation (7.34)) in the case of pivalic acid isotopes, for several values of the scattering angle, in the low-temperature ($T = 253$ K) and plastic ($T = 303, 283$ K) phases: (*a*) $(CH_3)_3COOH$, $T = 253$ K, (*b*) $(CD_3)_3COOD$, $T = 303$ K, (*c*) $(CH_3)_3COOH$, $T = 283$ K.

118 cm^{-1}, a small peak corresponds to the ν(OD---O) mode. Owing to mass effect, CH_3 torsions are shifted from 256 cm^{-1} to 185 cm^{-1}. Conversely, vibrations $\delta_{C'CC}$ and rotations of the CC_3 groups suffer only small change and correspond to the region 245–300 cm^{-1}.

Above the phase transition, the peaks disappear in the low-frequency region. The general shape of the spectra is a single broad band. That means that the deformations of the central hydrogen-bonded carboxylic

ring become strongly anharmonic, in accordance with the existence of large oscillations of the two parts of the dimers with respect to each other. A phenomenological description of this part of the spectrum was proposed in terms of a single overdamped oscillator (Bée *et al* 1986b). It yields an average value of 8° for the amplitude of the oscillations, which, in addition, are strongly overdamped. This conclusion is in perfect agreement with the first description in terms of dimer-axis fluctuations.

7.4 Stochastic equations

A molecule embedded in a crystal experiences, in addition to a periodic potential, fluctuating torques from the thermal motion of its neighbours. The static potential reflects the symmetry of the molecule and the symmetry of its surroundings. We shall deal with the consequences originating from the symmetry of the potential later in this chapter. For the moment, we do not precisely define its explicit form and we concentrate on the fluctuating part, reflecting the fact that the molecules are not at rest.

We look only at one molecule whose motion is described as a random process. The small fluctuations of the potential are simulated by a heat bath, which represents all other degrees of freedom of the crystal. The probability function which describes a stochastic process obeys a rate equation. We shall study first the Langevin equation, which differs from the classical equation of motion by only a friction term and a stochastic term. Then we shall discuss the Fokker–Planck equation and the Smoluchowski equation which appear to be the same formulation, apart from the fact that the former is derived in the velocity space while the latter holds in ordinary coordinate space. The basic assumptions concerning the slow variation of the probability distribution will lead us to examine also the general 'master-equation' and to show how jump models or diffusion models can be recovered. All these calculations will be performed in the one-dimensional case; the case of three dimensions, which is involved to account for the symmetry of the potential and the introduction of 'symmetry-adapted functions', will be considered later, in §7.7. An example of description in terms of the Smoluchowski diffusion equation is given in the next section, where we report on the solution given by Dianoux and Volino (1977), for a potential with a cosine form.

7.4.1 The Langevin equation

The Langevin equation is a stochastic equation of motion. A free particle, of mass m, is in contact with a bath. The interaction between the particle and the bath is described by a stochastic force F, which

depends on the time t and on the velocity $\dot{x}(t')$ for times t' prior to t. The velocity follows a non-linear and retarded rate equation:

$$m\ddot{x}(t) = F(t, \dot{x}(t')). \tag{7.37}$$

The random force F is characterised by its mean value $\bar{F}$, which is not explicitly time-dependent, and also by the self-correlation of its fluctuations $f(t) = F - \bar{F}$

$$G(t) = \langle f(0)f(t)\rangle. \tag{7.38}$$

The spectrum of the fluctuations of the force, $G(t)$, defines the correlation time of the random force, τ_c characteristic of the bath, and corresponding to the minimum time-scale of the problem.

In the derivation of the Langevin equation, the first approximation concerns the short memory of the particle, i.e. that the velocity $\dot{x}(t)$ does not change appreciably during the time interval τ_c. This assumption is justified if the random force is so weak that it produces only small variations of $\dot{x}(t)$ during small time intervals. Therefore, we are concerned with an instantaneous equation of motion

$$m\ddot{x}(t) = F(t, \dot{x}(t)) \tag{7.39}$$

and with a white spectrum of the fluctuations

$$\langle f(0)f(t)\rangle = G(\dot{x})\delta(t). \tag{7.40}$$

The second assumption is that the particle velocity is much smaller than the mean thermal velocity of the particles in the bath. Expanding $\bar{F}$ and G with respect to $\dot{x}$

$$\bar{F}(x) = F_0 - m\gamma\dot{x} \tag{7.41a}$$

$$G(\dot{x}) = G + \ldots \tag{7.41b}$$

we obtain the usual Langevin equation

$$\frac{d^2x}{dt^2} = -\gamma\frac{dx}{dt} + \frac{1}{m}f(t) + F_0. \tag{7.42}$$

The frictional force exerted by the bath is represented by the first term on the r.h.s., and the second term $(1/m)f(t)$ represents the random force due to the random collisions with the particles of the bath. Because γ and $f(t)$ have the same physical origin, they are related to each other, through the fluctuation-dissipation theorem.

Equation (7.42) is not deterministic, because $f(t)$ is not a deterministic function of time. Only ensemble averages are known. By definition, the average value of the fluctuating part of the force (noise) is zero,

$$\langle f(t)\rangle = 0. \tag{7.43}$$

Moreover, the values of $f(t)$ at different times are completely uncorrelated

$$\langle f(t)f(t')\rangle = G\delta(t - t'). \tag{7.44}$$

Here, the averaging is performed over a time interval which is long compared to the rapid variation in $f(t)$ and short compared to the damping time γ^{-1}.

A solution $x(t)$ or $\dot{x}(t)$ of (7.42) does not exist, but ensemble averages can be calculated. A formal (because $f(t)$ is unknown) solution of (7.42) is:

$$\dot{x}(t) = \exp(-\gamma t)\left[\dot{x}(0) + \frac{1}{m}\int_0^t dt' f(t')\exp(\gamma t')\right] \tag{7.45}$$

and so

$$\langle \dot{x}(t)^2\rangle = \exp(-2\gamma t)\left\{\langle \dot{x}(0^2)\rangle + \frac{1}{m}\int_0^t dt' \int_0^t dt''\langle f(t')f(t'')\rangle \exp[\gamma(t' + t'')]\right\}$$

$$= \langle \dot{x}(0)^2\rangle \exp(-2\gamma t) + \frac{G}{2m\gamma}[1 - \exp(-2\gamma t)]. \tag{7.46}$$

In the limit $\gamma t \to \infty$, the initial values have damped out:

$$\langle x(\infty)^2\rangle = \frac{G}{2m\gamma}. \tag{7.47}$$

Assuming that the system is returned to equilibrium so that the law of equipartition of energy holds

$$\tfrac{1}{2}m\langle x(\infty)^2\rangle = \tfrac{1}{2}k_B T \tag{7.48}$$

$$G = 2k_B T\gamma \tag{7.49}$$

(7.49) above is an expression of the fluctuation–dissipation theorem, which related the spectrum of spontaneous fluctuations (G) to the response of the system to an applied force (the drift coefficient γ). The constant part, F_0, can be identified as a static force which arises from a static potential. It is possible that F is a function of x. Using a potential $V(x)$, the static part can be written

$$F_0 = -\frac{\partial V(x)}{\partial x}. \tag{7.50}$$

This yields the expression of the Langevin equation

$$\frac{d^2x}{dt^2} = -\gamma\frac{dx}{dt} - \frac{1}{m}\frac{\partial V(x)}{\partial x} + \frac{1}{m}f(t). \tag{7.51}$$

7.4.2 Markovian processes

The probability distribution of the velocity is defined according to

$$P(v, t) = \langle \delta(v - u(t))\rangle \tag{7.52}$$

$u(t)$ is the velocity of the brownian particle at time t. The average is

evaluated over the bath, for an initial condition. Clearly, $P(v, t)$ is the probability of finding the velocity of the particle at time t in the interval between v and $v + dv$. From this follows the equation

$$P(v, t) = \int dv' \langle \delta(v' - u(t'))\delta(v - v' - \Delta u) \rangle \tag{7.53a}$$

with

$$\Delta u = u(t) - u(t') = \frac{1}{m}\int_{t'}^{t} F(\tau)\, d\tau. \tag{7.53b}$$

Here $F(\tau)$ is the stochastic force acting on the particle (see equation (7.37)), which depends on τ and on the prior history $u(\tau')$. We assume, as in the derivation of the Langevin equation, the existence of two distinct time-scales:

(i) a fast scale, with characteristic time τ_c. τ_c can be either the correlation time of the random force, or the time of an individual collision, in the case of well-separated collisions.

(ii) a slow scale, with characteristic time τ_R. τ_R denotes the relaxation time of the velocity, or also the time-interval between two collisions.

Furthermore, if $\tau_c \ll \tau_R$, the interval of integration $t - t'$ in (7.53b) can be chosen such that it is sufficiently large compared to τ_c and there is no correlation between $F(\tau)$ and the fluctuations at time t', but also sufficiently small when compared to τ_R and $P(v, t)$ varies only little in the time $t - t'$. Under these conditions, the two delta functions in (7.53a) are statistically independent and it is possible to write

$$P(v, t) = \int dv' P(v', t')p(v', v, t - t') \tag{7.54}$$

where $p(v', v, t - t')$ is the transition probability from v' to v in the time interval $t - t'$. More precisely, $p(v', v, t - t')\, dv'$ is the probability of finding the particle velocity, at time t', in the interval v' and $v' + dv'$, if it was v at time t.

$$p(v', v, \tau) = \left\langle \delta\left(v - v' - \frac{1}{m}\int_0^{\tau} F(\tau)\, d\tau\right)\right\rangle \tag{7.55}$$

Such a process without memory is called a markovian process.

At this stage, it is worth pointing out that the hypothesis of a small variation of $P(v, t)$ over a time interval equal to the correlation time τ_c can be satisfied in two ways.

(i) The velocity $u(t)$ varies only little, as in the Langevin case of a heavy particle in a bath of light particles. The noise is permanent, but small.

(ii) The velocity $u(t)$ varies only rarely. The noise is formed of strong pulses, but well separated in time. Therefore the probability of the

occurrence of a velocity change is small.
These two possibilities lead to two different situations, that we shall examine now.

7.4.3 The Fokker–Planck equation

Let us write (7.54) as a function of the velocity transfer $w = v - v'$ and of the initial velocity v'

$$P(v, t + \tau) = \int \mathrm{d}w P(v - w, t) p(w, v - w, \tau). \tag{7.56}$$

At short time τ, P and p being slow functions of v', they can be expanded as a function of w,

$$p(w, v - w, \tau) = p(w, v, \tau) - w\frac{\partial p}{\partial v} + \frac{1}{2}w^2\frac{\partial^2 p}{\partial v^2} + \ldots \tag{7.57a}$$

$$P(v - w, t) = P(v, t) - w\frac{\partial P}{\partial v} + \frac{1}{2}w^2\frac{\partial^2 P}{\partial v^2} + \ldots \tag{7.57b}$$

so that, limiting the expansion to second order in w,

$$\begin{aligned} P(v, t + \tau) = {} & P(v, t)\int \mathrm{d}w\, p(w, v, \tau) \\ & -\left[\frac{\partial P}{\partial v} + P(v, t)\frac{\partial}{\partial v}\right]\int \mathrm{d}w\, w p(w, v, \tau) \\ & + \left[\frac{1}{2}\frac{\partial^2 P}{\partial v^2} + \frac{\partial P}{\partial v}\frac{\partial}{\partial v} + \frac{1}{2}P\frac{\partial^2}{\partial v^2}\right]\int \mathrm{d}w\, w^2 p(w, v, \tau). \end{aligned} \tag{7.58}$$

Introducing the mean velocity transfer

$$\langle w \rangle = \int \mathrm{d}w\, w p(w, v, \tau) \tag{7.59a}$$

and the mean square displacement of the velocity

$$\langle w^2 \rangle = \int \mathrm{d}w\, w^2 p(w, v, \tau) \tag{7.59b}$$

$$\begin{aligned} P(v, t + \tau) = {} & P(v, t) - \frac{\partial P}{\partial v}\langle w \rangle - P\frac{\partial \langle w \rangle}{\partial v} \\ & + \frac{1}{2}\frac{\partial^2 P}{\partial v^2}\langle w^2 \rangle + \frac{\partial P}{\partial v}\frac{\partial \langle w^2 \rangle}{\partial v} + \frac{1}{2}P\frac{\partial^2 \langle w^2 \rangle}{\partial v^2}. \end{aligned} \tag{7.60}$$

Let us assume that the particle velocity follows a Langevin equation:

$$\dot{v}(t) + \gamma v(t) = \frac{1}{m}f(t) \tag{7.61}$$

with δ-correlated noise:

$$\langle f(t)f(t_0)\rangle = G\delta(t - t_0) \tag{7.62a}$$

of zero mean:

$$\langle f(t)\rangle = 0. \tag{7.62b}$$

The mean value $\langle w\rangle$ and $\langle w^2\rangle$ are easily evaluated

$$\langle w\rangle = -v(t)\gamma\tau \tag{7.63a}$$

$$\langle w^2\rangle = G\tau = \frac{2k_BT}{m}\gamma\tau \tag{7.63b}$$

and

$$\frac{\partial\langle w\rangle}{\partial v} = -\gamma\tau \tag{7.64a}$$

$$\frac{\partial\langle w^2\rangle}{\partial v} = 0 \tag{7.64b}$$

$$\frac{\partial^2\langle w^2\rangle}{\partial v^2} = 0. \tag{7.64c}$$

Equation (7.60) becomes:

$$\frac{\partial P}{\partial t} = \gamma P + \gamma v\frac{\partial P}{\partial v} + \frac{1}{2}G\frac{\partial^2 P}{\partial v^2} \tag{7.65}$$

$$\frac{\partial P}{\partial t} = \frac{\partial}{\partial v}(\gamma v P) + \frac{\partial^2}{\partial v^2}\left(\frac{1}{2}GP\right). \tag{7.66}$$

Equation (7.66) is a particular case of the general Fokker–Planck equation

$$\frac{\partial P(v,t)}{\partial t} = \frac{\partial}{\partial v}\left\{D^{(1)}(v,t)P(v,t) + \frac{\partial}{\partial v}[D^{(2)}(v,t)P(v,t)]\right\} \tag{7.67}$$

The time-evolution of $P(v, t)$ appears as a continuous flow in the velocity space. The first term on the r.h.s corresponds to a convection, the second to a diffusion. $D^{(1)}(v, t)$ and $D^{(2)}(v, t)$ are, respectively, the drift and diffusion coefficients in this space.

The solution of (7.66) is

$$P(v,t) = \left\{\frac{2\pi k_BT}{m}[1 - \exp(-2\gamma t)]\right\}^{-1/2}\exp\left\{-\frac{m[v - v_0\exp(-\gamma t)]^2}{2k_BT[1 - \exp(-\gamma t)]}\right\} \tag{7.68}$$

where it has been assumed that the probability distribution is sharply peaked around v_0 at $t = 0$

$$P(v, 0) = \delta(v - v_0). \tag{7.69}$$

The limit at infinite time of $P(v, t)$ is the solution of the stationary equation. It is the Boltzmann distribution

$$P(v, \infty) = \left[\frac{m}{2\pi k_B T}\right]^{1/2} \exp\left\{-\frac{mv^2}{2k_B T}\right\}. \tag{7.70}$$

The evolution as a function of time of the probability distribution given by (7.68) is illustrated in figure 7.9.

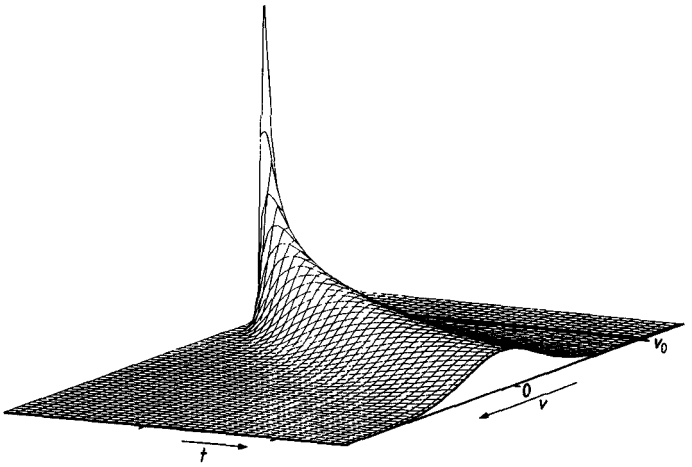

Figure 7.9 Evolution as a function of the time of the probability distribution $P(v, t)$, evaluated from (7.68).

7.4.4 Presence of a potential; the Smoluchowski equation

If we assume that the particle under test experiences a potential $V(x)$, the Langevin equation is

$$\dot{v}(t) + \gamma v(t) = \frac{1}{m} f(t) - \frac{1}{m}\frac{\partial V}{\partial x}. \tag{7.71}$$

The derivation of a Fokker–Planck equation follows exactly the same procedure. By analogy with the preceding paragraph, we define the probability density $P(x, v; t)$ of finding the particle at time t, in the abscissa interval between x and $x + dx$, and with a velocity between v and $v + dv$. Using the same hypothesis, the following relation, analogous to (7.56)

$$P(x, v; t + \tau) = \int\int P(x - s, v - w; t) p(x - s, v - w; s, w)\, ds\, dw \tag{7.72}$$

can be expanded as a function of both w and s, second order. This yields

$$P(x, v; t + \tau) = P(x, v; t) - \frac{\partial P}{\partial x}\langle s\rangle - \frac{\partial P}{\partial v}\langle w\rangle + \frac{1}{2}\frac{\partial^2 P}{\partial v^2}\langle w^2\rangle - P\frac{\partial\langle w\rangle}{\partial v} \tag{7.73}$$

where

$$\langle s\rangle = \int\int \mathrm{d}s\,\mathrm{d}w\, s\, p(x - s, v - w; s, w). \tag{7.74}$$

Evaluation of the mean values $\langle s\rangle$, $\langle w\rangle$ and $\langle w^2\rangle$, now gives

$$\langle w\rangle = -\gamma v(t)\tau - \frac{\tau}{m}\frac{\partial V}{\partial x} \tag{7.75a}$$

$$\frac{\partial\langle w\rangle}{\partial v} = -\gamma\tau \tag{7.75b}$$

$$\langle w^2\rangle = G\tau = \frac{2k_{\mathrm{B}}T}{m}\gamma\tau \tag{7.75c}$$

$$\langle s\rangle = v\tau \tag{7.75d}$$

$$\frac{\partial\langle s\rangle}{\partial v} = \tau \tag{7.75e}$$

and finally

$$\frac{\partial P(x, v; t)}{\partial t} = \gamma\frac{\partial}{\partial v}\left(vP + \frac{k_{\mathrm{B}}T}{m}\frac{\partial P}{\partial v}\right) - v\frac{\partial P}{\partial x} - \frac{1}{m}\frac{\partial V}{\partial x}\frac{\partial P}{\partial v}. \tag{7.76}$$

The stationary solution is of the form

$$P(x, v; t) = C\exp\left\{-\frac{\frac{1}{2}mv^2 + V(x)}{k_{\mathrm{B}}T}\right\}. \tag{7.77}$$

Introducing the probability distribution in ordinary space

$$P(x, t) = \int \mathrm{d}v\, P(x, v; t) \tag{7.78}$$

we obtain the Smoluchowski equation

$$\frac{\partial P(x, t)}{\partial t} = \frac{1}{m\gamma}\left\{\frac{\partial}{\partial x}\left[\frac{\partial V}{\partial x}P(x, t)\right] + k_{\mathrm{B}}T\frac{\partial}{\partial x}P(x, t)\right\} \tag{7.79}$$

or

$$\frac{1}{D_{\mathrm{r}}}\frac{\partial}{\partial t}P(x, t) = \frac{\partial}{\partial x}\left[\frac{\partial}{\partial x}P(x, t) + \frac{1}{k_{\mathrm{B}}t}\left(\frac{\partial V}{\partial x}\right)P(x, t)\right] \tag{7.80}$$

where the diffusion coefficient (in coordinate space) is

$$D_{\mathrm{r}} = \frac{k_{\mathrm{B}}T}{m\gamma}. \tag{7.81}$$

If the potential vanishes, (7.1) is retrieved.

7.4.5 The master equation

The derivation of the Fokker–Planck and Smoluchowski equation was based on the fundamental hypothesis of a slow variation of the velocity and the position, i.e. in each collision, the corresponding transfers were small. Now we consider the inverse case, namely the situation in which the collisions rarely occur, but are very strong. Consequently, the Kramers–Moyal expansion (7.57) is not possible.

Consider for example a scatterer (particle), which, under the effect of the successive collisions, moves among different locations in space, quite distinct, schematically represented in figure 7.10.

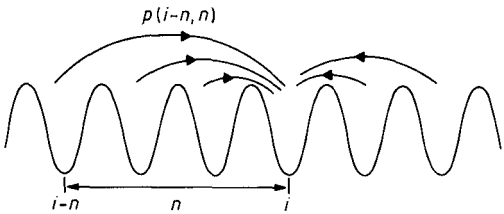

Figure 7.10 Schematic illustration of the physical situation of a particle moving among quite distinct locations.

We are interested in the changes occurring in an arbitrary short time interval τ, but chosen sufficiently large with respect to the transition duration. The probability that the particle is at (i) at time $t + \tau$ is

$$P(i;\, t + \tau) = \sum_n P(i - n;\, t)p(i - n;\, n) \tag{7.82}$$

where $p(i - n, n)$ is the probability of going from $(i - n)$ to (i), under the collision effects. We have:

$$\sum_n p(i;\, n) = p(i,\, 0) + \sum_{n\neq 0}{}' p(i;\, n) = 1. \tag{7.83}$$

Here the left-hand side summation is the probability of going anywhere, $p(i; 0)$ is the probability of remaining at (i) and the primed summation corresponds to the probability of going somewhere else. Rewriting (7.82) in the form

$$P(i;\, t + \tau) = P(i;\, t)\, p(i;\, 0) + \sum_{n\neq 0}{}' P(i - n;\, t)p(i - n;\, n) \tag{7.84}$$

and introducing the expression of $p(i, 0)$ deduced from (7.83) above we obtain:

$$P(i; t + \tau) - P(i; t) = -P(i; t)\sum_{n\neq 0}{}'p(i; n) + \sum_{n\neq 0}{}'P(i - n; t)p(i - n; n). \quad (7.85)$$

Now, if we assume an infinitesimal time interval τ, and introducing the usual transition rates from one site to another $\gamma(i - n; n)$ through the definition:

$$p(i - n; n) = \tau\gamma(i - n; n) \quad (7.86)$$

we are led to the master equation

$$\frac{\partial}{\partial t}P(i; t) = -\sum_{n\neq 0}{}'\gamma(i; n)P(i; t) + \sum_{n\neq 0}{}'\gamma(i - n; n)P(i - n; t). \quad (7.87)$$

This equation is based on the unique hypothesis of well-separated transitions. The first term on the right-hand side of (7.87) corresponds to the transitions from the site (i), which decrease $P(i, t)$ whilst the second sum describes the increase in $P(i, t)$ arising from the transitions to the site (i). If we restrict our considerations to transitions to adjacent sites only, and if the sites are equivalent so that all the transition rates $(i \pm 1; \pm 1)$ can be considered as equal to the same value, γ:

$$\frac{\partial}{\partial t}P(i; t) = \gamma[P(i + 1; t) - 2P(i; t) + P(i - 1; t)] \quad (7.88)$$

which is nothing else than the Barnes equation (6.54) already encountered. Equation (7.88) can be formally written

$$\frac{\partial}{\partial t}P(i; t) = \gamma l^2 \frac{P(i + 1; t) - 2P(i; t) + P(i - 1; t)}{l^2} \quad (7.89)$$

where l is the distance between two sites. We go to the continuous limit when assuming that the distance l is infinitely short. Then

$$\lim_{l\to 0}\frac{P(i + 1; t) - 2P(i; t) + P(i - 1; t)}{l^2} = \frac{\partial^2 P(x, t)}{\partial x^2} \quad (7.90)$$

and (7.89) becomes

$$\frac{\partial}{\partial t}P(x; t) = \gamma l^2 \frac{\partial^2 P(x; t)}{\partial x^2} \quad (7.91)$$

which is the Smoluchowski equation without potential, the diffusion coefficient $D = \gamma l^2$ being expressed in $\mathrm{cm^2\ s^{-1}}$. Now, in the presence of a potential $V(x)$, slowly varying with regard to the distance l, the transition rates at various sites are connected by

$$\gamma(i \pm 1; \pm 1) = \gamma\exp\left\{-\frac{V(i \pm 1) - V(i)}{k_B T}\right\} \quad (7.92)$$

$$\simeq \gamma\left[1 \mp \frac{l}{k_B T}\frac{\partial V}{\partial x}\right]. \quad (7.93)$$

The expansion (7.93), introduced in (7.89) leads to the Smoluchowski equation with a potential (7.80).

We shall conclude this section with two remarks.

(i) So far, we have considered transitions among discrete sites in coordinate space. It is possible to derive a master equation for a continuous distribution of positions, namely

$$\frac{\partial}{\partial t}P(x, t) = \int \mathrm{d}s[P(x - s; t)p(x - s; s) - P(x; t)p(x; s)] \quad (7.94)$$

(ii) Calculations performed in coordinate space can also be carried out in the velocity space and follow exactly the same procedure. Moreover, if the collisions correspond to small velocity transfers, the continuous limit leads to the Fokker–Planck equation (7.67).

7.5 Neutron Scattering Law for a Uniaxial Rotator in an N-fold Potential

7.5.1 Expansion of the scattering law

Evaluation of the scattering law requires the calculation of the intermediate scattering function

$$I(\boldsymbol{Q}, t) = \langle \exp(\mathrm{i}\boldsymbol{Q}\cdot\boldsymbol{R}(t)) \exp(-i\boldsymbol{Q}\cdot\boldsymbol{R}(0)) \rangle \quad (7.95)$$

for which we closely follow the lines of Gerling (1981) and Dianoux and Volino (1977). Since we are concerned with the rotation of molecules about some axis, we take this axis as the Oz coordinate such that $\boldsymbol{R}(t)$ has the form $(R\cos\phi(t), R\sin\phi(t), 0)$ where $\phi(t)$ is the rotational angle (see figure 7.11). Writing $\boldsymbol{Q}$ in this coordinate system, with polar angles θ and α, we easily obtained the scalar product

$$\boldsymbol{Q}\cdot\boldsymbol{R}(t) = QR\sin\theta\cos(\phi(t) - \alpha). \quad (7.96)$$

Making use of the expansion (Abramovitz and Stegun 1965)

$$\exp(\pm\, \mathrm{i}x\cos\psi) = \sum_{n=-\infty}^{\infty} \pm\, \mathrm{i}^n J_n(x)\exp(\mathrm{i}n\psi) \quad (7.97)$$

where $J_n(t)$ is a Bessel function of first kind and order n, (7.94) becomes:

$$I(\boldsymbol{Q}, t) = \sum_{n,m=-\infty}^{\infty} -\mathrm{i}^{n+m} J_n(QR\sin\theta)J_m(QR\sin\theta) \times \langle \exp[\mathrm{i}n(\phi(t) - \alpha)]\exp[\mathrm{i}m(\phi(0) - \alpha)] \rangle_{\phi\phi_0} \quad (7.98)$$

where the average is taken over all possible values ϕ, ϕ_0 of $\phi(t)$ and $\phi(0)$ at time t and zero, respectively.

Restricting our calculations to the powder case, an average has to be

taken over θ and α to account for all possible orientations of the scatterers with respect to $\boldsymbol{Q}$

$$I(\boldsymbol{Q}, t) = \frac{1}{4\pi}\int_0^{2\pi} \mathrm{d}\alpha \int_0^{\pi} I(\boldsymbol{Q}, t) \sin\theta \,\mathrm{d}\theta. \tag{7.99}$$

In practice, this model is applicable to semi-ordered phases in which some kind of order exists along one direction. Therefore, it is worthwhile introducing an intermediate average over all the values of α, the circles being assumed to be distributed at random in the (x, y) plane,

$$I(\boldsymbol{Q}, t)\,|_{\alpha} = \frac{1}{2\pi}\int_0^{2\pi} I(\boldsymbol{Q}, t)\,\mathrm{d}\alpha \tag{7.100}$$

one obtains:

$$I(\boldsymbol{Q},t)|_{\alpha} = \sum_{n=-\infty}^{\infty} J_n^2(QR\sin\theta)\langle \exp\{in[\phi(t) - \phi(0)]\}\rangle_{\phi\phi_0} \tag{7.101}$$

and for the full powder average (Gerling 1981)

$$I(\boldsymbol{Q}, t) = A_0(QR) + 2\sum_{k=1}^{\infty} A_k(QR)\Gamma_k(t) \tag{7.102}$$

where we have introduced the correlation functions

$$\Gamma_k(t) = \langle \cos n[\phi(t) - \phi(0)]\rangle_{\phi\phi_0} \tag{7.103}$$

and the coefficients

$$A_n(QR) = \frac{1}{\pi}\int_0^{\pi} j_0(2QR\sin x)\cos(2nx)\,\mathrm{d}x \tag{7.104a}$$

$$= \sum_{l=0}^{\infty} \frac{(-1)^l (QR)^{2(l+n)}}{[2(l+n)+1]l!(2n+l)!} \tag{7.104b}$$

and the EISF:

$$A_0(QR) = \frac{1}{\pi I_0^2(\gamma'_N)}\int_0^{\pi} j_0(2QR\sin x) I_0(2\gamma'_N \cos Nx)\,\mathrm{d}x. \tag{7.104c}$$

An illustration of the variation of these coefficients $A_n(QR)$ versus QR is given in figure 7.12, where it clearly appears that only the first terms in the expansion are relevant to get a good approximation of the scattering law, at least in the usual accessible Q range.

The EISF is the long-time limit $I(Q, \infty)$ of the intermediate scattering law. Therefore it is helpful to make apparent the asymptotic limit of the correlation functions (7.103). Writing

$$\Gamma_k(t) = \Gamma'_k(t) + \Gamma_k(\infty) \tag{7.105}$$

we get the EISF

$$I(\boldsymbol{Q}, \infty) = A_0(QR) + 2\sum_{k=1}^{\infty} A_k(QR)\Gamma_k(\infty) \tag{7.106}$$

and, from the usual Fourier transformation

$$S(Q, \omega) = I(Q, \infty)\delta(\omega) + 2\sum_{k=1}^{\infty} A_k(QR)\mathcal{F}[\Gamma'_k(t)] \qquad (7.107)$$

where $(\Gamma'_k(t))$ denotes the Fourier transform of $\Gamma'_k(t)$.

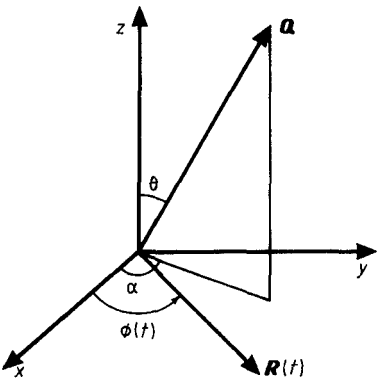

Figure 7.11 Set of coordinates for an N-fold uniaxial rotator.

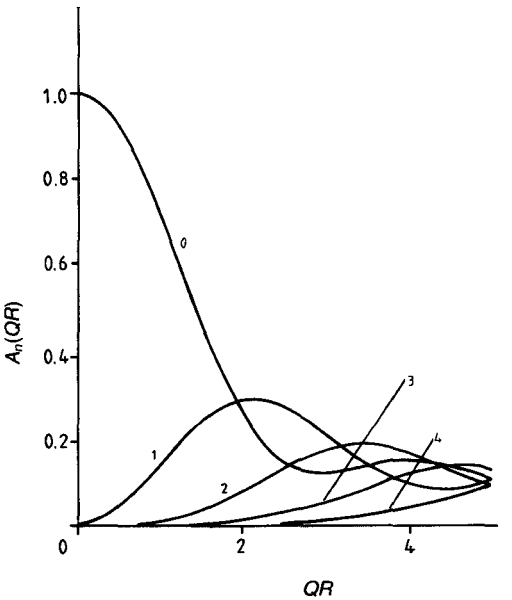

Figure 7.12 Illustration of the variation of the coefficients $A_n(QR)$, evaluated from (7.104), as a function of the product QR of the scattering vector modulus, Q, by the radius of gyration R (Gerling 1981).

Equation (7.107) above requires two remarks:

(i) No specific model assumptions have been made, and (7.107) is applicable to any description of the molecule rotation for which it is possible to calculate the correlation functions $\Gamma_k(t)$. We shall see an application to the case of the Smoluchowski equation in the next section.

(ii) Using (7.97) the intermediate scattering law has been expanded on a basis of symmetry-adapted functions, which in this case are just the cylindrical harmonics $\exp(im\psi)$. For more complicated geometries, the same procedure holds and one has to find the correct symmetry-adapted functions onto which $I(\boldsymbol{Q}, t)$ can be conveniently expanded.

7.5.2 *Evaluation of the correlation functions for the diffusion of a uniaxial rotator in an N-fold potential*

The molecular potential takes into account the symmetry of the rotating molecule and of the surrounding. It depends only on a single variable, i.e. the rotation angle ϕ and should be periodic. Because any periodic potential of arbitrary shape can always be expanded into Fourier components:

$$V(\phi) = \sum_{N=1}^{\infty} \frac{V_N}{2} \cos N\phi \tag{7.108}$$

the problem of finding a solution to (7.80) can be restricted, without a loss of generality, to the case of a potential with a simple cosine form:

$$V(\phi) = -\frac{V_N}{2} \cos N\phi. \tag{7.109}$$

We shall just outline the calculations, referring to the original work for more information (Dianoux and Volino 1977). Our aim is rather to point out and to analyse the principal results, than to report in full details the mathematical development. The problem is to evaluate the correlation functions $\Gamma_k(t)$. In fact, it is not necessary to solve the rate equation (7.80), for which a solution has been presented, for different initial conditions, by Byung *et al* (1976). Any function can be expanded in a series of symmetry-adapted functions, which in the present case of cylindrical symmetry are the trigonometric functions $\cos(n\phi)$ and $\sin(n\phi)$. Using a procedure similar to the one already used (in liquid crystal studies) (Brondeau and Goulon, 1975), we are led to solve an infinite system of linear equations governing the time dependence of $\langle \cos(n\phi) \rangle$ and $\langle \sin(n\phi) \rangle$. Dianoux and Volino introduce the following quantities

$$c_n(t) = \langle \cos n\phi \rangle_\phi = \int_0^{2\pi} \mathrm{d}\phi \cos n\phi P(\phi, \phi_0, t) \tag{7.110a}$$

$$s_n(t) = \langle \sin n\phi \rangle_\phi = \int_0^{2\pi} \mathrm{d}\phi \sin n\phi P(\phi, \phi_0, t). \tag{7.110b}$$

The limit at infinite time of $c_n(t)$ and $s_n(t)$ depends on the boundary condition

$$\lim_{t\to\infty} P(\phi, \phi_0, t) = P(\phi) = \frac{1}{Z}\exp\left\{-\frac{V(\phi)}{k_B T}\right\} \tag{7.111a}$$

with

$$Z = \int_0^{2\pi} d\phi \exp(\gamma'_N \cos n\phi) = \frac{1}{2\pi I_0(\gamma'_N)}. \tag{7.111b}$$

Here we have defined

$$\gamma'_N = \frac{V_N}{2k_B T} \tag{7.112}$$

and $I_k(x)$ the modified Bessel function of the first kind and of order k. In the infinite-time limit, (7.110) yields:

$$c_n(\infty) = \frac{I_k(\gamma'_N)}{I_0(\gamma'_N)}\delta_{n,\,kN} \tag{7.113a}$$

$$s_n(\infty) = 0. \tag{7.113b}$$

It is preferable to deal with correlation functions which tend to zero at infinite time. Therefore, Dianoux and Volino introduce the quantities

$$\tilde{c}_n(t) = c_n(t) - c_n(\infty) \tag{7.114a}$$

and, by analogy:

$$\tilde{s}_n(t) = s_n(t) - s_n(\infty). \tag{7.114b}$$

The following properties are easily demonstrated

$$\tilde{c}_0(t) = 0, \tag{7.115a}$$

$$\tilde{c}_n(\infty) = 0, \tag{7.115b}$$

$$\tilde{c}_{-n}(t) = \tilde{c}_n(t), \tag{7.115c}$$

$$\tilde{s}_0(t) = 0, \tag{7.116a}$$

$$\tilde{s}_n(\infty) = 0, \tag{7.116b}$$

$$\tilde{s}_{-n}(t) = -\tilde{s}_n(t). \tag{7.116c}$$

Gerling (1981) has generalised the formalism to the case of the so-called Sack equation (Sack 1956). The mathematical development follows exactly the calculations of Dianoux and Volino. We shall not discusss the Sack equation. Nevertheless for a more general development, we introduce at this time the operator

$$H_t = \frac{\partial}{\partial t} \tag{7.117}$$

so that the equation (7.80) becomes

$$\frac{1}{D_r}H_t P = \frac{\partial}{\partial\phi}\left[\frac{\partial P}{\partial\phi} + \frac{1}{k_B T}\left(\frac{\partial V}{\partial\phi}\right)P\right]. \tag{7.118}$$

Multiplying by $\cos(n\phi)$ from the left side, and integrating over ϕ yields:

$$\frac{1}{D_r}H_t c_n(t) = \int_0^{2\pi} d\phi \cos n\phi \frac{\partial}{\partial\phi}\left[\frac{\partial P}{\partial\phi} + \frac{1}{k_B T}\left(\frac{\partial V}{\partial\phi}\right)P\right]. \tag{7.119}$$

Making use of the expression of the derivative of the potential with respect to:

$$\frac{\partial V}{\partial\phi} = -\frac{NV_N}{2}\sin N\phi \tag{7.120}$$

and integrating by parts, we obtain after some easy trigonometric manipulations

$$-\frac{1}{D_r}H_t c_n(t) = -n\frac{N\gamma'_N}{2}c_{n-N}(t) + n^2 c_n(t) + n\frac{N\gamma'_N}{2}c_{n+N}(t). \tag{7.121}$$

Using the identity (Abramovitz and Stegun 1965)

$$I_{k+1}(\gamma'_N) - I_{k-1}(\gamma'_N) = -\frac{2k}{\gamma'_N}I_k(\gamma'_N) \tag{7.122}$$

in the case for $n = kN$, it is easily seen that the $\tilde{c}_n(t)$ satisfies the same equation:

$$-\frac{1}{D_r}H_t \tilde{c}_n(t) = -n\frac{N\gamma'_N}{2}\tilde{c}_{|n-N|}(t) + n^2 \tilde{c}_n(t) + n\frac{N\gamma'_N}{2}\tilde{c}_{n+N}(t). \tag{7.123}$$

Calculation of the self-correction function $\tilde{s}_n(t)$ is quite similar. The only important difference is the odd parity for sine functions (7.115c) whilst cosine functions are even (7.116c). They verify the recurrence relation

$$-\frac{1}{D_r}H_t \tilde{s}_n(t) = -\frac{(n-N)N\gamma'_N}{|n-N|}\tilde{s}_{n-N}(t) + n^2 \tilde{s}_n(t) + \frac{nN\gamma'_N}{2}\tilde{s}_{n+N}(t). \tag{7.124}$$

Equations (7.123) and (7.124) can be written in matrix form

$$-\frac{1}{D}H_t \tilde{C}(t) = [M]\tilde{C}(t) \tag{7.125a}$$

$$-\frac{1}{D}H_t \tilde{S}(t) = [N]\tilde{S}(t) \tag{7.125b}$$

where the components of the vectors $\tilde{C}(t)$ and $\tilde{S}(t)$ are the functions $\tilde{c}_n(t)$ and $\tilde{s}_n(t)$, respectively. The matrices $[M]$ and $[N]$ are given by

$$M_{m,n} = m^2\delta_{m,n} + \frac{mN\gamma'_N}{2}[\delta_{m+N,n} - \delta_{|m-N|,n}], \tag{7.126a}$$

$$N_{m,n} = m^2\delta_{m,n} + \frac{mN\gamma'_N}{2}\left[\delta_{m+N,n} - \frac{m-N}{|m-N|}\delta_{|m-N|,n}\right]. \tag{7.126b}$$

Let λ_p and V_{np} be the eigenvalues and eigenvectors of matrix $[M]$. The formal solution of (7.125a) is

$$\tilde{c}_n(t) = \sum_p V_{np} d_p(0) \exp\{-D_r\lambda_p t\} \tag{7.127a}$$

where the $d_p(0)$ are the components of the vector $D(0)$ defined by

$$\tilde{C}(0) = [V]D(0). \tag{7.127b}$$

These constants $d_p(0)$ are determined by the initial conditions. Similarly, the formal solution of (7.125b) is,

$$\tilde{s}_n(t) = \sum_p W_{np} f_p(0) \exp\{-D_r\mu_p t\} \tag{7.128a}$$

where μ_p and W_{np} denote the eigenvalues and the eigenvectors of matrix $[N]$ and where the components $f_p(0)$ of the vector $F(0)$ defined such that

$$\tilde{S}(0) = [W]F(0) \tag{7.128b}$$

are determined from the conditions at $t = 0$. More precisely, the initial distribution is

$$P(\phi, \phi_0, 0) = \sum_{k=-\infty}^{\infty} \delta(\phi - \phi_0 + 2k\pi). \tag{7.129}$$

Therefore, from the definitions of the $\tilde{c}_n(t)$ and $\tilde{s}_n(t)$ (7.114)

$$\tilde{c}_n(0) = \sum_p V_{np} d_p(0) = \cos n\phi_0 - \frac{I_k^0(\gamma'_N)}{I_0(\gamma'_N)}\delta_{n,kN} \tag{7.130a}$$

$$\tilde{s}_n(0) = \sum_p W_{np} f_p(0) = \sin n\phi_0. \tag{7.130b}$$

In fact, instead of evaluating the $d_p(0)$ and $f_p(0)$ from these equations it is worth noticing that the calculation of the correlation function

$$\Gamma_n(t) = \langle \cos n(\phi - \phi_0) \rangle_{\phi\phi_0} = \langle \cos n\phi \cos n\phi_0 \rangle_{\phi\phi_0} - \langle \sin n\phi \sin n\phi_0 \rangle_{\phi\phi_0} \tag{7.131}$$

involves the averages over initial distribution

$$\langle c_n(t) \cos n\phi_0 \rangle_{\phi_0} = \langle \tilde{c}_n(t) \cos n\phi_0 \rangle_{\phi_0} + \langle c_n(\infty) \cos n\phi_0 \rangle_{\phi_0} \tag{7.132a}$$

$$\langle s_n(t) \sin n\phi_0 \rangle_{\phi_0} = \langle \tilde{s}_n(t) \sin n\phi_0 \rangle_{\phi_0}. \tag{7.132b}$$

The second term on the r.h.s of (7.132a) is easily obtained, using (7.130a):

$$\langle c_n(\infty)\cos n\phi_0\rangle_{\phi_0} = \int_0^{2\pi} d\phi_0 p(\phi_0)\frac{I_k(\gamma'_n)}{I_0(\gamma'_n)}\delta_{n,\,kN}\cos n\phi_0 \quad (7.133a)$$

$$\langle c_n(\infty)\cos n\phi_0\rangle_{\phi_0} = \left[\frac{I_k(\gamma'_n)}{I_0(\gamma'_N)}\right]\delta_{n,\,kN}. \quad (7.133b)$$

Multiplying both sides of equations (7.130a) and (7.130b) by $\cos(m\phi)$ and $\sin(m\phi_0)$ respectively, and averaging over the initial distribution $P(\phi_0)$, we obtain:

$$\langle \tilde{c}_n(0)\cos m\phi_0\rangle_{\phi_0} = \sum_p V_{np}T_{pm} = \Omega^c_{nm} \quad (7.134a)$$

$$\langle \tilde{s}_n(0)\sin m\phi_0\rangle_{\phi_0} = \sum_p W_{np}U_{pm} = \Omega^s_{nm} \quad (7.134b)$$

where Ω^c_{nm} and Ω^s_{nm} are the respective elements of two matrices $[\Omega^c]$ and $[\Omega^s]$, whose explicit expressions are

$$\Omega^c_{nm} = \frac{1}{2}\frac{I_k(\gamma'_N)}{I_0(\gamma'_N)}\delta_{|m-n|,\,kN} + \frac{1}{2}\frac{I_k(\gamma'_N)}{I_0(\gamma'_N)}\delta_{m+n,\,k'N} - \frac{I_{k''}(\gamma'_N)I_{k'''}(\gamma'_N)}{I_0^2(\gamma'_N)}\delta_{n,\,k''N}\delta_{m,k'''N} \quad (7.135a)$$

$$\Omega^s_{nm} = \frac{1}{2}\frac{I_k(\gamma'_N)}{I_0(\gamma'_N)}\delta_{|n-m|,\,kN} - \frac{1}{2}\frac{I_{k'}(\gamma'_N)}{I_0(\gamma'_N)}\delta_{n+m,\,k'N}. \quad (7.135b)$$

After evaluating the constants T_{pm} and U_{pm} from (7.134a) and (7.135b), the correlation function $\Gamma_n(t)$ reads:

$$\Gamma_n(t) = \frac{I_k^2(\gamma'_N)}{I_0^2(\gamma'_N)}\delta_{n,\,kN} + \sum_p V_{np}T_{pn}\exp(-D_r\lambda_p t) + \sum_p W_{np}U_{pn}\exp(-D_r\mu_p t). \quad (7.136)$$

The complete scattering law is obtained from the general relation (7.107). It can be demonstrated (see the original paper by Dianoux and Volino, 1977) that, in the case of a semi-oriented sample, the expression of the scattering function can be written as:

$$S(Q,\omega)|_\alpha = A_0(QR)|_\alpha\delta(\omega) + \frac{2}{\pi}\sum_p\left[\sum_{n=1}^{\infty}A_n(QR)|_\alpha V_{np}T_{pn}\right]\frac{D_r\lambda_p}{(D_r\lambda_p)^2+\omega^2} + \frac{2}{\pi}\sum_p\left[\sum_{n=1}^{\infty}A_n(QR)|_\alpha W_{np}U_{pn}\right]\frac{D_r\mu_p}{(D_r\mu_p)^2+\omega^2} \quad (7.137a)$$

with the EISF:

$$A_0(QR)|_\alpha = \frac{1}{\pi I_0^2(\gamma'_N)} \int_0^\pi J_0(2QR \sin\theta \sin x) I_0(2\gamma'_N \cos Nx)\, dx \qquad (7.137b)$$

and

$$A_n(QR)|_\alpha = \frac{1}{\pi} \int_0^\pi J_0(2QR \sin\theta \sin x) \cos(2nx)\, dx. \qquad (7.137c)$$

The corresponding expression for the complete powder average (i.e. the average over θ) is formally identical to (7.137a) with $A_0(Qr)|_\alpha$ and $A_n(QR)|_\alpha$ replaced by $A_0(QR)$ and $A_n(QR)$ given by (7.104).

7.5.3 Analysis of the eigenvalues

The aim of this section is to discuss in more detail the properties of the scattering function we have just established, as a function of the relative barrier height γ'_2, for the case $N = 2$, which turned out to be of practical importance for a liquid-crystal study (Dianoux and Volino 1977). In their original paper, these authors evaluated the behaviour of the eigenvalues λ_p and μ_p, which is reported in figure 7.13. In the low-barrier limit ($\gamma'_2 = 0$) the values of λ_p and μ_p are just identical and such that $\lambda_p = \mu_p = p^2$, so that the classical rotational diffusion model is retrieved (see section 6.2). When the relative barrier height γ'_2 increases, results of numerical calculation show some striking features:

(i) Dianoux and Volino found numerically that $\lambda_{2p} = \mu_{2p}$;

(ii) all the eigenvalues λ_p and μ_p, except λ_1, increase with γ'_2;

(iii) λ_1 strongly decreases as a function of γ'_2 and rapidly tends to zero;

(iv) common limiting values appear in the high-barrier limit, e.g.:

$$\mu_1 \to \lambda_2 = \mu_2$$

$$\mu_3 \to \lambda_2 = \mu_2$$

$$\lambda_3 \to \lambda_4 = \mu_4$$

Figure 7.14 shows the variations of the quantities $V_{np}T_{pn}$ and $W_{np}U_{pn}$ which contribute to the weights of the lorentzian functions of width $\lambda_p D_r$ and $\mu_p D_r$ in the scattering law. All these terms are found to tend to zero in the high-barrier limit, except for the terms $V_{2p+1,1}T_{1,2p+1}$ related to λ_1, which always increase and tend to 1, the predominating term being $V_{11}T_{11}$. Therefore the quasielastic part of the spectrum can be considered as being composed of a single lorentzian function, superimposed on a much broader component with much smaller intensity. Dianoux and Volino demonstrated that, in the high-barrier limit,

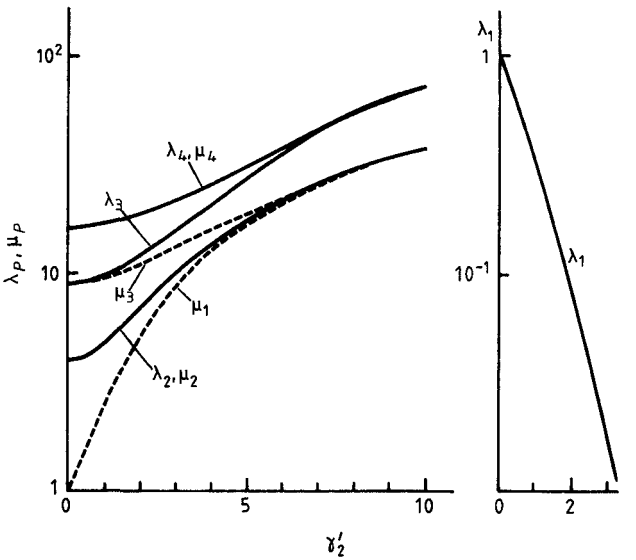

Figure 7.13 Variations of the eigenvalues λ_p and μ_p of the matrices $[M]$ and $[N]$ given by (7.126), in the case of a twofold potential V_2, as a function of $\gamma_2' = V_2(2k_BT)^{-1}$, according to Dianoux and Volino (1977). (Reproduced by permission of Taylor & Francis Ltd.)

$\gamma_2' \to \infty$, the EISF given by (7.137) tends to the expression

$$\lim_{\gamma_2' \to \infty} A_0(\boldsymbol{Q})|_\alpha = \frac{1}{2}[1 + J_0(2Qa \sin\theta)] = A_0^{(2)}(\boldsymbol{Q}). \tag{7.138a}$$

Simultaneously,

$$\lim_{\gamma_2' \to \infty} 2\sum_{n=1}^{\infty} A_n(\boldsymbol{Q})|_\alpha V_{n1} T_{1n} = 1 - A_0^{(2)}(\boldsymbol{Q}). \tag{7.138b}$$

Clearly, the high-barrier limit corresponds to the jump model between two sites, for which the scattering law was stated in chapter 6 (equation 6.37). Dianoux and Volino also investigated the general case of arbitrary N. In their numerical study, they recovered the jump model among N equidistant sites on a circle. More precisely, for N even and odd, they found $N/2$ or $(N-1)/2$ eigenvalues, respectively, which tend to zero when γ_N' increases. The corresponding coefficients $V_{np}T_{np}$ and $W_{np}U_{pn}$ tend to finite values whilst the others vanish. Also the ratios of the eigenvalues, τ_p^{-1} were found in accordance, for $\gamma_2' \to \infty$, with the relation (6.60)

$$\tau_p^{-1} = \tau_1^{-1} \frac{\sin^2 \pi p/N}{\sin^2 \pi/N}. \tag{7.139}$$

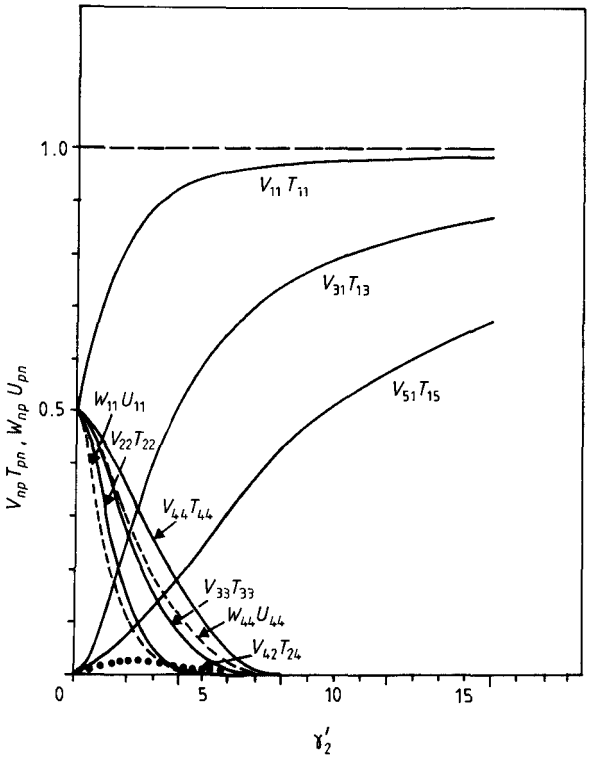

Figure 7.14 Variations of the coefficients $V_{np}T_{pn}$ and $W_{np}U_{pn}$ corresponding to the weights of the lorentzian functions of width $\lambda_p D_r$ and $\mu_p D_r$ in the expansion of the scattering law for a uniaxial rotation in a twofold potential V_2 as a function of $\gamma_2' = V_2(2k_B T)^{-1}$ according to Dianoux and Volino (1977). (Reproduced by permission of Taylor & Francis Ltd).

7.5.4 Application: orientational order in tilted smectic phases

The nature of the molecular ordering in the tilted smectic phases has been the subject of considerable work. The existence of an orientational ordering of the molecules about their long axis was a fundamental feature of the former microscopic mean-field theories (Meyer and McMillan 1974, Meyer 1975). This ordering was associated with the existence of a strong intermolecular dipole–dipole interaction responsible for the tilted character of these phases. However, the subject was very controversial because numerous experimental results do not support the hypothesis of such an order: x-ray (Doucet *et al* 1974a, 1974b, 1975), NMR (Luz and Meiboom 1973, Luz *et al* 1974, Deroche *et al* 1975), ESR (Meirovitch and Luz 1975), Raman (Dvorjetski *et al* 1975) experiments led to the development of other theories which do not

contain this feature (Priest 1976, Cabib and Benguigui 1977). Dianoux and Volino have performed an extensive investigation of terephtal-bis-butyl-aniline (TBBA) in its crystalline (Volino *et al* 1975) and various smectic phases (Hervet *et al* 1974, 1975, Volino *et al* 1975, 1976a, 1976b). They conclude that in the C and H phases, the molecules rotate rapidly about their long axis, with, simultaneously, rapid fluctuations of this axis about its equilibrium mean orientation. Rapid rotational motions still exist in the smectic-VI phase, but they appear less uniform than rotational diffusion, a feature which could be explained by some orientational ordering around the long axis.

A more detailed analysis of quasi-elastic scattering data in the supercooled smectic-H, smectic-VI and smectic-VII phases was performed, in terms of the model described in §7.5.2. Figure 7.15 illustrates the experimental EISF values as a function of the temperature deduced from spectra taken at $Q = 1.03\ \text{Å}^{-1}$. It is seen that the EISF increases as the temperature is decreased with definite jumps at 89 °C and 68 °C. We have also reported the range in which the theoretical EISF, given by (7.104c) and averaged over the different kinds of proton in the TBBA molecule, can vary with γ'_N, for the value $Q = 1.03\text{Å}^{-1}$. The limit $\gamma'_N = 0$ is the same for all N. It appears to be identical to the limit $\gamma'_N \to \infty$, for values of $N > 4$, evaluated from (7.104c). Clearly, the following conclusions can be drawn:

(i) Down to 89 °C, in the supercooled H phase, the value of N appears large, suggesting uniaxial rotational motion and a very weak, orientational ordering. Dianoux and Volino attributed the small decrease of the EISF between 89 °C and 102 °C to fluctuations of the long axis (Volino *et al* 1976a).

(ii) In the smectic-VI phase, between 89 °C and 68 °C, some kind of orientational order seems to exist, because the experimental points lie systematically above the limit $\gamma'_N \to 0$. However, the value of the EISF alone cannot permit determination of the value of N.

(iii) Below 68 °C, in the smectic-VII phase, only the case $N = 1$ is possible.

Dianoux and Volino analysed the shape of the quasielastic spectra, on the basis of the scattering law given by, for the cases $N = 1$ and $N = 2$. The case $N = 1$ corresponds to the microscopic theories (Meyer and McMillan 1974, Meyer 1975), where the molecules are allowed to perform large fluctuations around their long axis, about some equilibrium orientation $\phi = 0$. The case $N = 2$ corresponds to oscillations of the molecules about two opposite equilibrium positions ($\phi = 0$ and $\phi = \pi$), and to jumps between these two positions. For the smectic-H phase, previous conclusions obtained in the normal state (Hervet *et al* 1974, 1975) were confirmed in the supercooled phase: molecules rotate

around their long axis and the orientational ordering is quasi-negligible. In the smectic-VI phase, model $N = 1$ led to large angular fluctuations whose average amplitude varies from $\pm 60°$ to $\pm 80°$ when the temperature increases from 68 °C to 89 °C. Conversely, the twofold model yields fluctuations of smaller amplitude, the average value varying from $\pm 20°$ to nearly 0 over the same temperature range. From x-ray results (Doucet *et al* 1974a) and also from conclusions of similar neutron measurements with other liquid crystals (Leadbetter *et al* 1976), preference was given to the twofold model.

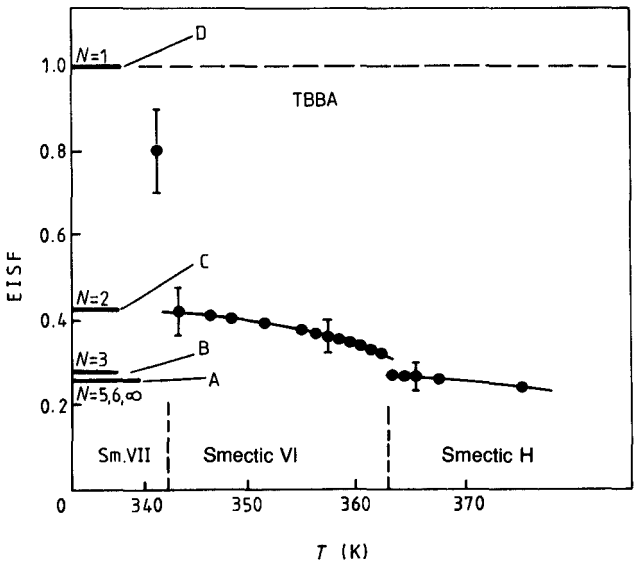

Figure 7.15 Experimental values of the EISF for TBBA, at $Q = 1.03$ Å, as a function of the temperature. These are compared with extremal theoretical limits predicted in several cases of the N-fold potential. (Reproduced by permission of Taylor & Francis Ltd.)

7.6 IQNS Law for a Particle Diffusing in a Cosine Potential in One Dimension

7.6.1 Theoretical background

Dianoux and Volino extended their formalism for the derivation of the scattering law for uniaxial rotational diffusion in an N-fold cosine potential to the case of translational motion. Results were used to

discuss the problem of diffusion through the layers, in smectic phases (Volino and Dianoux 1978).

The particle is assumed to diffuse along a straight line, taken as the Oz axis, and is acted upon by a potential $V(z)$ whose periodicity is a. Since any periodic function can be expanded in Fourier series, Volino and Dianoux limited their calculation to the case of a simple cosine form

$$V_N(z) = -\frac{V_N}{2}\cos(Nq_c z) \tag{7.140a}$$

where

$$q_c = \frac{2\pi}{a}. \tag{7.140b}$$

The equation governing the distribution function $P(z, z_0, t)$ is derived from (7.119) with ϕ replaced by z.

$$\frac{1}{D_T}\frac{\partial}{\partial t}P(z, z_0, t) = \frac{\partial}{\partial z}\left[\frac{\partial}{\partial z}P(z, z_0, t)N\gamma'_N q_c \sin(Nq_c z)P(z, z_0, t)\right] \tag{7.141}$$

with

$$\gamma'_N = \frac{V_N}{2k_B T}. \tag{7.142}$$

The relevant functions whose correlations have to be evaluated are the eigenfunctions of the translation operator. So the following intermediate averages are introduced

$$c_n(t) = \langle \exp\{i(Q + nq_c)z\}\rangle_z \tag{7.143a}$$

$$= \int_{-\infty}^{\infty} \exp\{i(Q + nq_c)z\}P(z, z_0, t)\,dz \tag{7.143b}$$

together with

$$\tilde{c}_n(t) = c_n(t) - c_n(\infty). \tag{7.144}$$

These functions are found to satisfy a set of linear equations analogous to (7.123)

$$-\frac{1}{D_T q_c^2}\frac{\partial \tilde{c}_n(t)}{\partial t} = -\left(\frac{Q}{q_c} + n\right)\frac{N\gamma'_N}{2}\tilde{c}_{n-N}(t) + \left(\frac{Q}{q_c} + n\right)^2 \tilde{c}_n(t) + \left(\frac{Q}{q_c} + n\right)\frac{N\gamma'_N}{2}\tilde{c}_{n+N}(t) \tag{7.145}$$

which can be written in matrix form:

$$-\frac{1}{D_T q_c^2}\frac{\partial}{\partial t}\tilde{C}(t) = [M]\tilde{C}(t). \tag{7.146}$$

Here $\tilde{C}(t)$ is a vector with components $\tilde{c}_n(t)$. The problem reduces to finding the eigenvalues, λ_p, and eigenvectors, V_{np}, of the matrix $[M]$, whose elements are

$$M_{mn} = \left(\frac{Q}{q_c} + m\right)^2 \delta_{m,n} + \frac{N\gamma'_N}{2}\left(\frac{Q}{q_c} + m\right)\left[\delta_{m+N,n} - \delta_{m-N,n}\right] \quad (7.147)$$

truncated at some range, depending upon the Q value and the desired accuracy. Then the correlation functions

$$\Gamma_n(t) = \langle c_n(t) c_n^*(0)\rangle_{z_0} \quad (7.148)$$

are evaluated in a manner similar to that in §7.5.2.

We introduce a matrix $[\Omega]$ whose elements, Ω_{nm}, are (see(7.135)):

$$\Omega_{nm} = \frac{I_{n-m}(\gamma'_n)}{I_0(\gamma'_N)} - \frac{I_{k+n}(\gamma'_N) I_{k+m}(\gamma'_N)}{I_0^2(\gamma'_N)} \delta\left(\frac{Q}{q_c} - kN\right) \quad (7.149)$$

k being any arbitrary integer. We calculate the constants T_{pn}, elements of the matrix $[T]$ such that

$$[V][T] = [\Omega] \quad (7.150)$$

where $[V]$ is formed with the eigenvectors V_{np} (see (7.134)). The final result is:

$$\Gamma_n(t) = \frac{I_{k+m}^2(\gamma'_N)}{I_0^2(\gamma'_N)} \delta\left(\frac{Q}{q_c} - kN\right) + \sum_{p=-\infty}^{\infty} V_{np} T_{pn} \exp(-D_T q_c^2 \lambda_p t). \quad (7.151)$$

Then the IQNS law can be evaluated. Assuming axial symmetry around Oz, for a scattering vector Q along Oz, we have

$$S(Q, \omega) = \frac{1}{2\pi} \int \langle \exp\{i Q \cdot (z - z_0)\}\rangle_{zz_0} \exp(-i\omega t)\, dt \quad (7.152a)$$

$$= \frac{1}{2\pi} \int \Gamma_0(t) \exp(-i\omega t)\, dt \quad (7.152b)$$

$$= A_0(Q)\delta(\omega) + \frac{1}{\pi} \sum_{p=-\infty}^{\infty} V_{0p} T_{p0} \frac{D_T q_c^2 \lambda_p}{(D_T q_c^2 \lambda_p^2)^2 + \omega^2} \quad (7.153)$$

with

$$A_0(Q) = \frac{I_k^2(\gamma'_N)}{I_0^2(\gamma'_N)} \delta\left(\frac{Q}{q_c} - kN\right) \quad (7.154)$$

is related to the kth translational order parameter γ_{Nk} defined as the average of $\cos(kNq_c z)$:

$$\gamma_{Nk} = \langle \cos(kNq_c z)\rangle = \frac{I_k(\gamma'_N)}{I_0(\gamma'_N)}. \quad (7.155)$$

This EISF is zero everywhere except at the lattice points in reciprocal space such that $Q = kNq_c$, where its value is equal to the square of the corresponding order parameter. This is an important difference from the

rotational case, where the EISF was non-zero for all Q values.

Furthermore, while for rotation, only the amplitudes of the lorentzian functions were Q-dependent, in the translational case, both their amplitudes and their widths depend on Q and on γ'_N.

We shall not here go into a discussion of the mathematical aspect of the scattering law and we refer to the original paper of Volino and Dianoux (1978) for more information. However, we shall examine the behaviour at low Q, namely that for $Q/q_c \to 0$. The lineshape tends towards a single lorentzian with a width of DQ^2 such that

$$D = \frac{D_T}{I_0^2(\gamma'_N)}. \tag{7.156}$$

7.6.2 Application to self-diffusion in smectic phases

These expressions have been used to analyse the self-diffusion across the layers in the smectic phase of the liquid crystal TBBA (Volino *et al* 1979). That turns out to be a typical case which can be approached using this formalism. Indeed, the large size of the TBBA molecules justifies the diffusive character. These are aligned, on average, along a unique direction and stacked into layers, leading to the existence of a periodic potential. Therefore, the theoretical scattering law given by (7.153) with $N = 1$ was applied to analyse neutron spectra obtained from aligned smectic-A phases, the neutron momentum transfer Q being normal to the smectic planes. The refined value of γ'_1 was found equal to about 0.6, with $D = (2.55 \pm 0.55) \times 10^{-6}\,\mathrm{cm^2\,s^{-1}}$, in perfect agreement with spin-echo measurement (Kruger *et al* 1976). The potential V_1, which maintains the molecules in layers in smectic-A TBBA at $T_c = 184\,^\circ\mathrm{C}$ is about $1.2\,k_B T_c$, where T_c is the smectic-A to nematic transition temperature. One deduces that the order parameter

$$\langle \cos q_c z \rangle = \frac{I_1(\gamma'_1)}{I_0(\gamma'_1)} \simeq 0.29.$$

This value corresponds to a mean-square displacement Δz of the molecules along the normal to the smectic planes of about 6 Å. This is in agreement with the one deduced from x-ray diffraction data ($\Delta z \geqslant 5$ Å) to explain the lack of the second-order reflection peak on the smectic planes.

7.7 Rotational Diffusion in a Three-Dimensional Potential

Our aim in this section is to generalise the calculations of Dianoux and Volino to the three-dimensional case. That will allow us to evaluate the

correlation functions appearing in the expansion of the scattering law derived by Yvinec and Pick (1980). The first step consists in expanding the static potential $V(\mathbf{\Omega})$ experienced by the molecule on the basis of the Wigner functions $D^l_{mn}(\mathbf{\Omega})$ of the Euler angles $(\mathbf{\Omega})$ characteristic of the molecule orientation. The evaluation of the correlation functions of the $D^l_{mn}(\mathbf{\Omega})$ is straightforward. Then we show how the problem can be much simplified when taking into account both molecule and site symmetries and using rotator functions (Bée 1982).

7.7.1 Three-dimensional rotational diffusion equation

In the case of rotations in three dimensions, it is possible to derive a Smoluchowski equation, analogous to (7.67)

$$\frac{\partial}{\partial t}P(\mathbf{\Omega}, \mathbf{\Omega}_0, t) = [\mathrm{i}\hat{L} \cdot \mathbf{D}^{(1)}(\mathbf{\Omega}) - \hat{L} \cdot \mathbf{D}^{(2)}(\mathbf{\Omega})\hat{L}]P(\mathbf{\Omega}, \mathbf{\Omega}_0, t) \tag{7.157}$$

where $\hat{L}$ is the quantum mechanical angular momentum operator in units of $\hbar$. $P(\mathbf{\Omega}, \mathbf{\Omega}_0, t)$ is the conditional probability of finding the molecule with the orientation $\mathbf{\Omega}$ at time t if it had the orientation $\mathbf{\Omega}_0$ at time zero. $\mathbf{D}^{(1)}(\mathbf{\Omega})$ and $\mathbf{D}^{(2)}(\mathbf{\Omega})$ are the drift and diffusion tensors, respectively, expressed as the two moments

$$\mathbf{D}^{(1)}(\mathbf{\Omega}) = \lim_{\tau \to 0} \frac{1}{\tau} \int \xi p(\xi, \mathbf{\Omega}, \tau)\, \mathrm{d}\xi \tag{7.158a}$$

$$\mathbf{D}^{(2)}(\mathbf{\Omega}) = \lim_{\tau \to 0} \frac{1}{\tau} \int \xi \cdot \xi p(\xi, \mathbf{\Omega}, \tau)\, \mathrm{d}\xi. \tag{7.158b}$$

Here $p(\xi, \mathbf{\Omega}, \tau)$ is the probability of the rotation ξ occurring in the time interval τ. These two moments are related together because the Boltzmann distribution

$$p(\mathbf{\Omega}) = \frac{1}{Z} \exp\left(-\frac{V(\mathbf{\Omega})}{k_B T}\right) \tag{7.159}$$

with

$$Z = \int P(\mathbf{\Omega})\, \mathrm{d}\mathbf{\Omega} \tag{7.160}$$

must be a stationary solution of (7.157) above.

$$\mathrm{i}\mathbf{D}^{(1)}(\mathbf{\Omega}) = -\mathbf{D}^{(2)}(\mathbf{\Omega}) \cdot \hat{L}\left\{\frac{V(\mathbf{\Omega})}{k_B T}\right\}. \tag{7.161}$$

For nearly spherical molecules, the $\mathbf{D}^{(2)}(\mathbf{\Omega})$ tensor is nearly a scalar

$$\mathbf{D}^{(2)}(\mathbf{\Omega}) \simeq D_R[I] \tag{7.162}$$

where $[I]$ is the identity matrix and D_R the rotational diffusion constant. We shall make this assumption, which provides a great simplification of

the calculations, without restricting the validity of the method. Following Brondeau and Goulon (1975) and Dianoux and Volino (1977), we introduce the conditional averages of any function $f(\mathbf{\Omega}, t)$

$$\langle f(\mathbf{\Omega}, t)\rangle_{\mathbf{\Omega}} = \int P(\mathbf{\Omega}, \mathbf{\Omega}_0, t) f(\mathbf{\Omega}, t)\, \mathrm{d}\mathbf{\Omega} \tag{7.163a}$$

$$\langle f(\mathbf{\Omega}_0, 0) f(\mathbf{\Omega}, t)\rangle = \int \mathrm{d}\mathbf{\Omega}_0 P(\mathbf{\Omega}_0) f(\mathbf{\Omega}_0, 0)\langle f(\mathbf{\Omega}, t)\rangle_{\mathbf{\Omega}}. \tag{7.163b}$$

The quantum mechanical angular momentum operator is hermitian. Therefore

$$\int f^* \hat{L} f \,\mathrm{d}\mathbf{\Omega} = \int f \hat{L}^* f^* \,\mathrm{d}\mathbf{\Omega} \tag{7.164}$$

and we obtain from (7.157) and (7.163a) above

$$\frac{\partial}{\partial t}\langle f(\mathbf{\Omega}, t)\rangle_{\mathbf{\Omega}} = \int P(\mathbf{\Omega}, \mathbf{\Omega}_0, t)[\mathrm{i}\hat{L}\cdot\mathbf{D}^{(1)}(\mathbf{\Omega}) - \hat{L}\cdot\mathbf{D}^{(2)}(\mathbf{\Omega})\cdot\hat{L}] f(\mathbf{\Omega}, t)\,\mathrm{d}\mathbf{\Omega}. \tag{7.165}$$

Hereafter, we shall drop the index $\mathbf{\Omega}$ in the notation of the conditional averages $\langle f(\mathbf{\Omega}, t)\rangle_{\mathbf{\Omega}}$.

7.7.2 Correlation functions for elements of Wigner matrices

An important theorem in group theory (theorem of Peter Weyl) states that, given a group, any function defined on the group can be expanded on the elements of the matrices representing the operations of the group. Because the Wigner matrices $D^l_{mm'}(\mathbf{\Omega})$ provide a representation of the rotation group, we shall expand the potential $V(\mathbf{\Omega})$ in the form

$$\frac{1}{k_B T} V(\mathbf{\Omega}) = \sum_l \sum_m \sum_{m'} a_l^{mm'} D^l_{mm'}(\mathbf{\Omega}). \tag{7.166}$$

In fact, the potential $V(\mathbf{\Omega})$ is not invariant under all the operations of the full rotation group. Therefore some relations exist between the $a_l^{mm'}$. We shall examine the consequences of the symmetry elements later. The elements of the Wigner matrices are the eigenfunctions of the angular momentum operator. Denoting by $\hat{L}_x$, $\hat{L}_y$ and $\hat{L}_z$ the components of the operator L in the lattice coordinates, we have

$$\hat{L}^2 D^k_{nn'}(\mathbf{\Omega}) = k(k+1) D^k_{nn'}(\mathbf{\Omega}) \tag{7.167a}$$

$$\hat{L}_z D^k_{nn'}(\mathbf{\Omega}) = n D^k_{nn'}(\mathbf{\Omega}). \tag{7.176b}$$

Furthermore, the operators

$$\hat{L}_1 = -(\hat{L}_x + \mathrm{i}\hat{L}_y)/\sqrt{2} \tag{7.168a}$$

and

$$\hat{L}_{\bar{1}} = (\hat{L}_x - i\hat{L}_y)/\sqrt{2} \tag{7.168b}$$

act on the $D^k_{nn'}(\mathbf{\Omega})$ according to:

$$\hat{L}_1 D^k_{nn'}(\mathbf{\Omega}) = \frac{-1}{\sqrt{2}}[k(k+1) - n(n+1)]D^k_{n+1,n'}(\mathbf{\Omega}) \tag{7.169a}$$

$$\hat{L}_{\bar{1}} D^k_{nn'}(\mathbf{\Omega}) = \frac{1}{\sqrt{2}}[k(k+1) - n(n-1)D^k_{n-1,n'}(\mathbf{\Omega}). \tag{7.169b}$$

Using for the potential $V(\mathbf{\Omega})$ the expansion (7.166), one finds

$$\frac{-1}{D_R}\frac{\partial}{\partial t}\langle D^k_{nn'}\rangle = k(k+1)\langle D^k_{nn'}\rangle + \sum_{lmm'} a^{mm'}_l \langle \hat{L}D^k_{nn'} \cdot \hat{L}D^l_{mm'}\rangle. \tag{7.170}$$

The scalar product in (7.170) can be expressed as

$$\langle \hat{L}D^k_{nn'} \cdot \hat{L}D^l_{mm'}\rangle = \hat{L}_z D^k_{nn'} \hat{L}_z D^l_{mm'} - \hat{L}_1 D^k_{nn'} \hat{L}_{\bar{1}} D^l_{mm'} - \hat{L}_{\bar{1}} D^k_{nn'} \hat{L} D^l_{mm'}. \tag{7.171}$$

The following relation holds between the Wigner matrices:

$$D^k_{nn'} D^l_{mm'} = \sum_{j=|k-l'}^{k-l} (klnm|jp) D^j_{pp'}(kln'm')|jp') \tag{7.172}$$

in which the notation $(klnm|jp)$ denotes the Clebsch–Gordan coefficients (Rose 1957).

Making use of (7.169) and (7.172) in (7.171) and of the property of the Clebsch–Gordan coefficients

$$\begin{aligned}[j(j+1) - p(p+1) - k(k+1) + n(n+1) - l(l+1) + m(m+1)](klnm|jp) \\ = [k(k+1) - n(n+1)]^{1/2}[l(l+1) - m(m-1)]^{1/2}(kln+1\, m-1|jp) \\ + [k(k+1) - n(n-1)]^{1/2}[l(l+1) - m(m+1)]^{1/2}(kln-1\, m+1|jp)\end{aligned} \tag{7.173}$$

one obtains finally

$$\begin{aligned}-\frac{1}{D_R}\frac{\partial}{\partial t}\langle D^k_{nn'}\rangle &= k(k+1)\langle D^k_{nn'}\rangle \\ &+ \sum_{lmm'} a^{mm'}_l \sum_{j=|k-l|}^{k+l} \frac{j(j+1) - k(k+1) - l(l+1)}{2}(klnm|jp) D^l_{pp'}(kln'm'|jp').\end{aligned} \tag{7.174}$$

Equation (7.174) represents an infinite set of linear differential equations for whose solution it is required to find the eigenvalues of the eigenvectors of the matrix $[M]$, with elements

$$\begin{aligned}M_{KJ} &= \{k(k+1)\,\delta_{KJ} \\ &+ \sum_{lmm'} a^{mm'}_l \sum_{j=|k-l}^{k+l} \frac{j(j+1) - k(k+1) - l(l+1)}{2}(klnm|jp)(kln'm'|jp').\end{aligned} \tag{7.175}$$

K and J are shorthand notations for the composite indexes (k, n, n')

and (j, p, p'), respectively. The conditional averages $\langle D^k_{mn'}(\Omega)\rangle_\Omega$ can therefore be considered as the components $D_K(t)$ of a vector $\boldsymbol{D}(t)$ such that

$$\frac{1}{D_R}\boldsymbol{D}(t) = [M]\boldsymbol{D}(t). \tag{7.176}$$

If $[P]$ is the transformation matrix from the basis $\boldsymbol{D}(t)$ to another $\boldsymbol{F}(t)$ on which the matrix $[M]$ takes diagonal form $[\Lambda]$

$$\boldsymbol{D}(t) = [P]\boldsymbol{F}(t) \tag{7.177a}$$

$$[\Lambda] = [P]^{-1}[M][P]. \tag{7.177b}$$

The formal solution of (7.176) is

$$D_K(t) = \sum_J P_{KJ}F_J(0)\exp(-D_R\Lambda_J t) \tag{7.178}$$

where the constants $F_J(0)$ are determined by the initial conditions.

We shall conclude this section with two remarks.

Firstly, the solution of the eigenvalue problem requires us to truncate the infinite $[M]$ matrix at some l value. However, even when truncating at small values of l, the order of the matrix remains large. Namely, $l = 4$ leads to a 25×25 matrix. Fortunately, many of its elements vanish because of the restriction $|k - l| < j < k + l$ and also owing to the particular $a_l^{mm'}$ values in the potential expansion. It should be helpful to find linear combinations of the D^l to form a basis on which the matrix $[M]$ would be expressed in a more tractable form.

The second remark deals with the determination of the complete correlation functions (7.163b) which lead to the evaluation of initial averages at $t = 0$ of the form

$$\int P(\Omega_0)D^k_{nn'}(\Omega_0)D^l_{mm'}(\Omega_0)\,d\Omega_0. \tag{7.179}$$

The equilibrium distribution of orientation $P(\Omega_0)$ can be obtained from x-ray or neutron scattering (Seymour and Prior 1970), in terms of symmetry-adapted rotator functions. Moreover, the potential itself can be expanded conveniently on the basis of these functions, which account for the symmetries of both the molecule and the lattice. In particular, an expression for the neutron scattering function was recently given by Yvinec and Pick (1980) in terms of these functions. Therefore it appears worthwhile to provide some insight into their properties.

7.7.3 Symmetry-adapted functions; rotator functions

Symmetry-adapted functions are appropriate linear combinations of

spherical harmonics with the same l. For each value of l, there are $2l + 1$ functions, adapted to the lattice (L) symmetry

$$L_{lp}(\theta, \phi) = \sum_{m=-l}^{l} S^{l}_{mp}(L) Y_{lm}(\theta, \phi) \tag{7.180a}$$

and $2l + 1$ functions adapted to the molecule (M) symmetry:

$$M_{lq}(\theta, \phi) = \sum_{m=-l}^{l} S^{l}_{mq}(M) Y_{lm}(\theta, \phi). \tag{7.180b}$$

They form the bases for irreducible representations of the symmetry groups of the lattice, L, and the molecule, M. Selection of linear combinations of Y_{lm} for different symmetry groups has been given by Kurki-Suonio (1967, 1968) and Bradley and Cracknell (1972). The matrices $S^{l}_{mp}(L)$ and $S^{l}_{mq}(M)$ are unitary. Symmetry-adapted functions are also named surface harmonics. They are orthogonal and normalised

$$\int L^{*}_{lp}(\theta, \phi) L_{l'p'}(\theta, \phi) \sin\theta \, d\theta \, d\phi = \delta_{ll'}\delta_{pp'} \tag{7.181a}$$

$$\int M^{*}_{lq}(\theta, \phi) M_{l'q'}(\theta, \phi) \sin\theta \, d\theta \, d\phi = \delta_{ll'}\delta_{qq'}. \tag{7.181b}$$

In general θ and ϕ will be the polar and azimuthal angle either of the scattering vector in the lattice frame or of the position vector $\boldsymbol{R}'$ of the scatterer in the molecular frame.

Table 7.1 gives the list of the first symmetry-adapted functions for several crystallographic groups. Clearly, the case $l = 0$ leads to a unique function $K_{01}(\theta, \phi) = M_{01}(\theta, \phi) = Y_{00}(\theta, \phi) = 1/\sqrt{4\pi}$ which corresponds to the fully symmetric identical representation (A, Ag, A_1, A_{1g} according to the precise point-group). For $l = 1$, considering the cubic group, we are concerned with three cubic harmonics $K_{11}(\theta, \phi)$, $K_{12}(\theta, \phi)$, $K_{13}(\theta, \phi)$ which transform into one another under the effect of the symmetry operations of the cubic groups and therefore form the basis of a three-dimensional representation. Depending on the exact group symmetry, i.e. $\mathcal{T}$, $\mathcal{T}_h$, $\mathcal{T}_d$, $\mathcal{O}$ or $\mathcal{O}_h$, the symmetry will be T, T_u, T_2, T_1 or T_{1u}, respectively. Conversely, when dealing with surface harmonics for the C_{3v} group, we are concerned, for $l = 1$, with two irreducible representations. Clearly, $M_{11}(\theta, \phi)$ which can be identified with the z coordinate along the threefold axis, is invariant under all the operations of the group and is the basis of a one-dimensional, fully symmetric representation (A_1). $M_{12}(\theta, \phi)$ and $M_{13}(\theta, \phi)$ transform into each other and correspond to a two-dimensional irreducible representation, with symmetry E. Similarly, for higher l values the expressions of other symmetry-adapted functions, with their symmetries, are indicated in table 7.1.

Table 7.1 Surface harmonics for the C_{3v} and cubic groups. The convention for spherical harmonics is that of Bradley and Cracknell (1972)

	Group C_{3v}		Cubic groups	$\mathcal{O}_h$	$\mathcal{O}$	$\mathcal{T}_d$	$\mathcal{T}_h$	$\mathcal{T}$
$l = 0$	$M_{01} = Y_{00}$	A_1	$K_{01} = Y_{00}$	A_{1g}	A_1	A_1	A_g	A
	$M_{11} = Y_{10}$	A_1	$K_{11} = (Y_{11} + Y_{1\bar{1}})/\sqrt{2}$					
$l = 1$	$M_{12} = (Y_{11} + Y_{1\bar{1}})/\sqrt{2}$	E	$K_{12} = -\mathrm{i}(Y_{11} - Y_{1\bar{1}})/\sqrt{2}$	T_{1u}	T_1	T_2	T_u	T
	$M_{13} = -\mathrm{i}(Y_{11} - Y_{1\bar{1}})/\sqrt{2}$		$K_{13} = Y_1^0$					
	$M_{21} = Y_{20}$	A_1	$K_{21} = Y_{20}$	E_g	E	E	^1E_g	^1E
	$M_{22} = (Y_{21} + Y_{2\bar{1}})/\sqrt{2}$	E	$K_{22} = (Y_{22} + Y_{2\bar{2}})/\sqrt{2}$					
$l = 2$	$M_{23} = -\mathrm{i}(Y_{21} - Y_{2\bar{1}})/\sqrt{2}$		$K_{23} = -\mathrm{i}(Y_{21} - Y_{2\bar{1}})/\sqrt{2}$					
	$M_{24} = (Y_{22} + Y_{2\bar{2}})/\sqrt{2}$	E	$K_{24} = (Y_{21} + Y_{2\bar{1}})/\sqrt{2}$	T_{2g}	T_2	T_2	T_g	T
	$M_{25} = \mathrm{i}(Y_{22} - Y_{2\bar{2}})/\sqrt{2}$		$K_{25} = -\mathrm{i}(Y_{22} - Y_{2\bar{2}})/\sqrt{2}$					
	$M_{31} = Y_{30}$	A_1	$K_{31} = \sqrt{\frac{3}{16}}(Y_{31} + Y_{2\bar{1}}) - \frac{5}{16}(Y_{33} + Y_{3\bar{3}})$					
	$M_{32} = (Y_{33} + Y_{3\bar{3}})/\sqrt{2}$	A_1	$K_{32} = -\mathrm{i}\sqrt{\frac{3}{16}}(Y_{31} - Y_{3\bar{3}}) - \mathrm{i}\sqrt{\frac{5}{16}}(Y_{33} - Y_{3\bar{3}})$	T_{1u}	T_1	T_2	T_u	T
	$M_{33} = -\mathrm{i}(Y_{33} - Y_{3\bar{3}})/\sqrt{2}$	A_2	$K_{33} = -Y_{30}$					
$l = 3$	$M_{34} = (Y_{31} + Y_{3\bar{1}})/\sqrt{2}$	E	$K_{34} = -\sqrt{\frac{5}{16}}(Y_{31} + Y_{3\bar{1}}) - \sqrt{\frac{3}{16}}(Y_{33} + Y_{3\bar{3}})$					
	$M_{35} = -\mathrm{i}(Y_{31} - Y_{3\bar{3}})/\sqrt{2}$		$K_{35} = -\mathrm{i}\sqrt{\frac{5}{16}}(Y_{31} + Y_{3\bar{1}}) + \mathrm{i}\sqrt{\frac{5}{16}}(Y_{33} - Y_{3\bar{3}})$	T_{2u}	T_2	T_1	T_u	T
	$M_{36} = (Y_{32} + Y_{3\bar{2}})/\sqrt{2}$	E	$K_{36} = (Y_{32} + Y_{3\bar{2}})/\sqrt{2}$					
	$M_{37} = \mathrm{i}(Y_{32} - Y_{3\bar{2}})/\sqrt{2}$		$K_{37} = -\mathrm{i}(Y_{32} - Y_{3\bar{2}})/\sqrt{2}$	A_{2u}	A_2	A_1	A_u	A
	$M_{41} = Y_{40}$	A_1	$K_{41} = \sqrt{\frac{7}{12}}Y_{40} + \sqrt{\frac{7}{12}}(Y_{44} + Y_{4\bar{4}})/\sqrt{2}$	A_{1g}	A_1	A_1	A_g	A
	$M_{42} = (Y_{43} + Y_{4\bar{3}})/\sqrt{2}$	A_1	$K_{42} = \sqrt{\frac{5}{12}}Y_{40} - \sqrt{\frac{5}{12}}(Y_{44} + Y_{4\bar{4}})/\sqrt{2}$	E_g	E	E	^1E_g	^1E
	$M_{43} = -\mathrm{i}(Y_{43} - Y_{4\bar{3}})/\sqrt{2}$	A_2	$K_{43} = -(Y_{42} + Y_{4\bar{2}})/\sqrt{2}$					
	$M_{44} = (Y_{41} + Y_{4\bar{1}})/\sqrt{2}$	E	$K_{44} = -\frac{1}{4}(Y_{41} - Y_{4\bar{1}}) + \mathrm{i}\sqrt{\frac{7}{4}}(Y_{43} - Y_{4\bar{3}})$					
$l = 4$	$M_{45} = -\mathrm{i}(Y_{41} - Y_{4\bar{1}})/\sqrt{2}$		$K_{45} = \frac{1}{4}(Y_{41} + Y_{4\bar{1}}) + \sqrt{\frac{7}{4}}(Y_{43} + Y_{4\bar{3}})$	T_{2g}	T_2	T_2	T_g	T
	$M_{46} = (Y_{44} + Y_{4\bar{4}})/\sqrt{2}$	E	$K_{46} = -(Y_{44} + Y_{4\bar{4}})/\sqrt{2}$					
	$M_{47} = -\mathrm{i}(Y_{44} - Y_{4\bar{4}})/\sqrt{2}$		$K_{47} = \mathrm{i}\sqrt{\frac{7}{4}}(Y_{41} - Y_{4\bar{1}}) + \frac{1}{4}(Y_{43} - Y_{4\bar{3}})$					
	$M_{48} = (Y_{42} + Y_{4\bar{2}})/\sqrt{2}$	E	$K_{48} = \sqrt{\frac{7}{4}}(Y_{41} + Y_{4\bar{1}}) - \frac{1}{4}(Y_{43} + Y_{4\bar{3}})$	T_{1g}	T_1	T_1	T_g	T
	$M_{49} = \mathrm{i}(Y_{42} - Y_{4\bar{2}})/\sqrt{2}$		$K_{49} = -\mathrm{i}(Y_{44} - Y_{4\bar{4}})/\sqrt{2}$					

Wigner matrices are defined as the representations of the rotation operations on the basis of the spherical harmonics.

$$Y_{lm}(\theta', \phi') = \sum_{n=-l}^{l} Y_{ln}(\theta, \phi) D^{l}_{nm}(\mathbf{\Omega}). \tag{7.182}$$

Unprimed coordinates (θ, ϕ) refer to an orthogonal coordinate system (Ox, Oy, Oz) fixed in the crystal, primed ones (θ', ϕ') to an analogous system (Ox', Oy', Oz') fixed in the molecule. $\mathbf{\Omega}$ is the set of Eulerian angles transforming (Ox, Oy, Oz) into (Ox', Oy', Oz'). Plugging the expressions (7.180) of the symmetry-adapted functions into (7.182), we easily obtain

$$M_{lq}(\theta', \phi') = \sum_{p=1}^{2l+1} L_{lp}(\theta, \phi) R^{l}_{pq}(\mathbf{\Omega}) \tag{7.183}$$

where the molecular-lattice rotator functions are defined by

$$R^{l}_{pq}(\mathbf{\Omega}) = \sum_{n=-l}^{l} \sum_{m=-l}^{l} S^{l*}_{mp}(L) D^{l}_{mn}(\mathbf{\Omega}) S^{l}_{nq}(M) \tag{7.184}$$

in terms of Wigner functions. Because Wigner functions are orthogonal, i.e.

$$\int D^{l*}_{mn}(\mathbf{\Omega}) D^{l'}_{m'n'}(\mathbf{\Omega})\, \mathrm{d}\mathbf{\Omega} = \frac{8\pi^2}{2l+1} \delta_{ll'} \delta_{mm'} \delta_{nn'} \tag{7.185}$$

the rotator function of lowest order ($l = 0$) is found to be a constant

$$R^{0}_{11}(\mathbf{\Omega}) = 1 \tag{7.186}$$

for an arbitrary pair of lattice and molecule groups. Moreover, rotator functions are also orthogonal

$$\int R^{l*}_{mn}(\mathbf{\Omega}) R^{l'}_{m'n'}(\mathbf{\Omega})\, \mathrm{d}\mathbf{\Omega} = \frac{8\pi^2}{2l+1} \delta_{ll'} \delta_{mm'} \delta_{nn'}. \tag{7.187}$$

The tetrahedral rotator functions introduced by James and Keenan (1959) and the cubic rotator functions of Press and Hüller (1973) are particular cases of rotator functions with cubic point groups.

7.7.4 Calculation of the molecular rotational potential from Bragg scattering data

In crystal structure analysis, mean positions of individual atoms and mean square amplitude of their thermal motion can be obtained from analysis of Bragg scattering data from x-ray or neutron diffraction experiments. This conventional method is not applicable to crystals with orientational disorder or strongly librating molecules; and we are concerned rather with the determination of a rotational density distribution. The structure factor formalism developed by Press and Hüller

(1973) and Press (1973) for a cubic crystalline field was then extended to more general molecule and site symmetries (Amoureux and Bée 1980a, Amoureux *et al* 1981a, Prandl 1981). It was also possible, to a certain extent, to account for rotational-translational coupling for the molecular motion (Press *et al* 1979).

The structure factor for an orientationally disordered crystal of rigid molecules can be written as

$$F(\boldsymbol{\Omega}) = \sum_j \Xi(\boldsymbol{Q}) F_j^{\mathrm{rot}}(\boldsymbol{Q}) \exp(\mathrm{i}\boldsymbol{Q}\cdot\boldsymbol{m}_j) \tag{7.188}$$

where $\boldsymbol{m}_j$ is the position vector of the centre of gravity of the molecule j.

$\Xi(\boldsymbol{Q})$ is the temperature factor due to translations. In the harmonic approximation, it corresponds to the usual Debye–Waller factor. The rotational form factor $F_j^{\mathrm{rot}}(\boldsymbol{\Omega})$ can be written as

$$F^{\mathrm{rot}}(\boldsymbol{Q}) = \sum_{\mu=1}^{s} n_\mu f_\mu(Q) \int_{\mathrm{cell}} C_\mu(\boldsymbol{R}) \exp(\mathrm{i}\boldsymbol{Q}\cdot\boldsymbol{R})\, \mathrm{d}\boldsymbol{R}. \tag{7.189}$$

Here the index j has been dropped. The molecule consists of s shells of atoms with n_μ equivalent atoms on the μth shell. $f_\mu(Q)$ and $C_\mu(\boldsymbol{R})$ are the atomic x-ray scattering factor (in electrons) and the positional probability of an atom of the shell μ, with respect to average crystal structure, respectively. Expanding $C_\mu(\boldsymbol{R})$ into lattice symmetry-adapted functions $L_{lm'}$, we get:

$$C_\mu(\boldsymbol{R}) = \frac{1}{R^2}\delta(R - R_\mu) C_\mu(\theta, \phi) \tag{7.190a}$$

$$= \frac{1}{R^2}\delta(R - R_\mu) \sum_{l,m} C_{lm}^\mu L_{lm}(\theta, \phi) \tag{7.190b}$$

where R_μ is the radius of the shell μ, and θ and ϕ are polar angles of the vector $\boldsymbol{R}$. Therefore the rotational structure factor reads

$$F^{\mathrm{rot}}(\boldsymbol{Q}) = 4\pi \sum_{\mu=1}^{s} n_\mu f_\mu(Q) \sum_{l,m} \mathrm{i}^l j_l(QR_\mu) C_{lm}^\mu L_{lm}(\theta_Q, \phi_Q) \tag{7.191}$$

where θ_Q and ϕ_Q are polar angles of the scattering vector $\boldsymbol{Q}$, and j_l is the spherical Bessel function of order l.

The expansion coefficients C_{lm}^μ can be calculated as follows. The atomic density distribution of the shell μ, with respect to a coordinate system (primed) tied to the molecule and rotating with it is

$$B_\mu(\boldsymbol{R}') = \frac{1}{R'^2}\delta(R' - R_\mu) B_\mu(\theta', \phi') \tag{7.192a}$$

$$= \frac{1}{R'^2}\delta(R' - R_\mu) \sum_{l'm'} B_{l'm'}^\mu M_{l'm'}(\theta', \phi'). \tag{7.192b}$$

If $P(\Omega)$ is the orientational probability of the molecular system we have (Press and Hüller 1973)

$$C_\mu(\boldsymbol{R}) = \int P(\Omega) B_\mu(\boldsymbol{R}')\, \mathrm{d}\Omega \tag{7.193}$$

and, using the relation (7.26) between molecule and lattice symmetry-adapted functions

$$C^\mu_{lm} = \sum_{m'} B^\mu_{lm'} \int P(\Omega) R^l_{mm'}(\Omega)\, \mathrm{d}\Omega \tag{7.194a}$$

$$= \sum_{m'} B^\mu_{lm'} \langle R^l_{mm'}(\Omega) \rangle. \tag{7.194b}$$

Expression (7.194) is plugged into the expansion (7.191) of the rotational structure factors. Then theoretical values predicted by (7.188) are compared with the observed data and the expectation values $\langle R^l_{mm'}(\Omega) \rangle$ are refined.

In their original method, Press and Hüller (1973) expanded $P(\Omega)$ into cubic rotator functions. For the case of arbitrary molecule and site symmetries, we write (Amoureux *et al* 1981a)

$$P(\Omega) = \frac{1}{8\pi^2} \sum_{lmm'} (2l + 1) A^l_{mm'} R^l_{mm'}(\Omega) \tag{7.195a}$$

with

$$A^0_{11} = R^0_{11}(\Omega) = 1. \tag{7.195b}$$

This expansion was mentioned in §6.2. An isotropic orientational probability corresponds to

$$A^l_{mm'} = \delta_{l,0}. \tag{7.196}$$

However, the density distribution resulting from a refinement of the coefficients $A^l_{mm'}$ may not be positive-definite over the whole space of Eulerian angles (Hüller and Press 1979). A positive-definite expression of $P(\Omega)$ is guaranteed from the start if, instead of expanding $P(\Omega)$ into rotator functions, one deals with the potential acting on the molecule itself. Indeed, this potential is invariant under the symmetry operations of the molecule and of the lattice groups, and we can write

$$\frac{1}{k_B T} V(\Omega) = \sum_{lmm'} b^{mm'}_l R^l_{mm'}(\Omega).$$

It is worth pointing out that, because both $P(\Omega)$ and $V(\Omega)$ are invariant by the molecule and site symmetry operations, the only non-vanishing coefficients A^l and $b^{mm'}_l$ in (7.195a) and (7.197) above correspond to rotator functions belonging to the identical representation of the product of the molecule and site 'reduced' point group. A rigorous discussion of

the relevant terms was given by Yvinec and Pick (1980). 'Reduced' point group denotes the group of proper operations. For instance, in the case of a molecule with symmetry C_{3v} in a cubic site, the first terms in the expansion are

$$\frac{1}{k_B T} V(\Omega) = b_0^{11} R_{11}^0(\Omega) + b_{11}^4 R_{11}^4(\Omega) + b_4^{12} R_{12}^4(\Omega) + \ldots . \quad (7.198)$$

Using (7.198) and (7.166), and from the definition of the rotator functions (7.184), we easily demonstrate that the coefficients $b_l^{mm'}$ are related to the $a_l^{mm'}$ by

$$a_l^{mm'} = \sum_{pp'} S_{mp}^{l*}(L) b_l^{pp'} S_{m'p'}^{l}(M). \quad (7.199)$$

There are several examples of application of this method which is now commonly employed for structure determinations of orientationally disordered phases (Amoureux *et al* 1981a, 1982b, Sauvajol and Amoureux 1981). Vogt and Prandl (1983) obtained the shape of the potential acting on the NH_4 molecule in $(NH_4)_2SnCl_6$. Hoser *et al* (1985) investigated the case of NO_3 and NH_3 disorder in nickel(II) hexammine nitrate $Ni(NH_3)_6(NO_3)_2$.

We have somewhat emphasised the definitions and properties of the surface harmonics and rotator functions because they are not very familiar. They appear to be very helpful, enabling us to account for the symmetries of the problem and, consequently, introducing large simplifications for solving it. That will clearly appear in the following; but we shall now turn to the expansion of the scattering law in terms of these functions.

7.7.5 The neutron scattering law in terms of symmetry-adapted functions

We start with the expansion into spherical harmonics (Sears 1966)

$$\exp(i\boldsymbol{Q}\cdot\boldsymbol{R}) = 4\pi \sum_{l,m} i^l j_l(QR) Y_{lm}(\theta_Q, \phi_Q) Y_{lm}^*(\theta, \phi). \quad (7.200a)$$

The polar and azimuthal angles (θ, ϕ) of the scatterer in the crystal axes can be deduced from the corresponding angles (θ', ϕ') in molecule axes (see 7.182)

$$Y_{lm}(\theta, \phi) = \sum_{n=-l}^{l} Y_{ln}(\theta', \phi') D_{mn}^{l}(\Omega)$$

where Ω is the rotation characterising the orientation of the molecule. Thus

$$\exp(i\boldsymbol{Q}\cdot\boldsymbol{R}) = 4\pi \sum_{lmm'} i^l j_l(QR) Y_{lm}(\theta_Q, \phi_Q) D_{mn}^{l}(\Omega) Y_{ln}^*(\theta', \phi'). \quad (7.200b)$$

If we use the definitions of the surface harmonics (7.180a) and (7.180b) and of the molecule-lattice rotator functions, (7.184) we get

$$\exp(\mathrm{i}\boldsymbol{Q}\cdot\boldsymbol{R}) = 4\pi\sum_{lpq}\mathrm{i}^l j_l(QR)M_{lq}(\theta', \phi')R^l_{qp}(\boldsymbol{\Omega})L_{lp}(\theta_Q, \phi_Q) \quad (7.201)$$

and the incoherent rotational intermediate scattering law, after summing over all the atoms in the molecule, can be expressed as (Pick and Yvinec 1980)

$$I^{\mathrm{R}}_{\mathrm{inc}}(\boldsymbol{Q}, t) = \sum_j |b^j_{\mathrm{inc}}|^2\langle\exp[\mathrm{i}\boldsymbol{Q}\cdot\boldsymbol{R}(0)]\exp[-\mathrm{i}\boldsymbol{Q}\cdot\boldsymbol{R}(t)]\rangle \quad (7.202a)$$

$$= \sum_{lpq}\sum_{l'p'q'} L^*_{lp}(\theta_Q, \phi_Q)L_{l'p'}(\theta_Q, \phi_Q)H^{pp'}_{ll'}(Q) \quad (7.202b)$$
$$\times \langle R^l_{pq}(\boldsymbol{\Omega}(0))R^l_{p'q'}(\boldsymbol{\Omega}(t))\rangle$$

with

$$H^{pp'}_{ll'}(Q) = 16\pi^2\sum_j |b^j_{\mathrm{inc}}|^2(-\mathrm{i})^{l+l'}j_l(QR_j)j_{l'}(QR_j)M_{lq}(\theta', \phi')M^*_{l'q'}(\theta', \phi'). \quad (7.202c)$$

This last factor involves a summation over the j atoms of the molecule and reflects the full molecular symmetry. In the case of a powder sample, when averaging over all possible directions of $\boldsymbol{Q}$

$$\int \mathrm{d}\boldsymbol{\Omega}_Q L^*_{lp}(\theta_Q, \phi_Q)L_{l'p'}(\theta_Q, \phi_Q) = \delta_{ll'}\delta_{pp'}. \quad (7.203)$$

Thus only the terms $l = l'$ and $p = p'$ remain in (7.202a)

$$I^{\mathrm{R}}_{\mathrm{inc}}(Q, t) = \sum_{lpqq'} H^{pp}_{ll}(Q)\langle R^l_{pq}(\boldsymbol{\Omega}(0))R^l_{pq'}(\boldsymbol{\Omega}(t))\rangle \quad (7.204a)$$

and

$$H^{pp}_{ll}(Q) = 16\pi^2\sum_j |b^j_{\mathrm{inc}}|^2 j_l^2(QR_j)M_{lq}(\theta', \phi')M^*_{lq'}(\theta', \phi'). \quad (7.204b)$$

7.7.6 Evaluation of correlation functions for rotator functions

Inserting the relations (7.184), (7.197) and (7.199) into (7.174), we can write the time-evolution of the conditional averages of the rotator functions:

$$\frac{1}{D_r}\frac{\partial}{\partial t}\langle R^k_{qq'}\rangle = k(k+1)\langle R^k_{qq'}\rangle \quad (7.205)$$
$$+ \sum_{jrr'}\langle R^j_{rr'}\rangle\sum_{l=|k-j|}^{k+j}\frac{j(j+1) - k(k+1) - l(l+1)}{2}\sum_{ss'}C^{klj*}_{qsr}(L)b^{ss'}_l C^{klj}_{q's'r'}(M).$$

In the derivation of the above expression, the equivalence of the two summations

$$\sum_{l} \sum_{j=|k-l|}^{k+l} \quad \text{and} \quad \sum_{j} \sum_{l=|k-j}^{k+j}$$

has been taken into account. The coefficients $C^{klj}_{qsr}(L)$ and $C^{klj}_{q's'r'}(M)$ are functions of the Clebsch–Gordan coefficients:

$$C^{klj}_{qsr}(L) = \sum_{nmp} S^{k}_{nq}(L) S^{l}_{ms}(L) S^{j*}_{pr}(L)(klnm|jp) \tag{7.206a}$$

$$C^{klj}_{q's'r'}(M) = \sum_{n'm'p'} S^{k}_{n'q'}(M) S^{l}_{m's'}(M) S^{j*}_{p'r'}(M)(kln'm'|jp'). \tag{7.206b}$$

The set of linear differential equations (7.207) is apparently much more complicated than the preceding one. In fact, rotator functions belonging to different irreducible representations or to different columns of the same irreducible representation do not couple together. The infinite set of equations reduces itself into several irreducible subsystems, which also are infinite but involve only rotator functions with the same symmetry.

For instance, we consider again the case of a molecule with C_{3v} symmetry in a cubic site $\mathbb{O}_h$. Expressions of the surface harmonics are given in table 7.1. The rotator functions are calculated from (7.184), using the elements of the unitary matrices given in this table. In fact, for our purpose, the explicit form of the rotator functions is not needed. We shall restrict our study to the first terms in the expansion of the potential, namely $l < 4$. In this limit, we are concerned with only two rotator functions with full symmetry: A_{1g} for crystal and A_1 for molecule. These are R^0_{11} and R^4_{11}. They lead to a set of two linear differential equations:

$$\begin{pmatrix} \dfrac{d}{dt}\langle R^0_{11}\rangle \\ \dfrac{d}{dt}\langle R^4_{11}\rangle \end{pmatrix} = M(A_{1g}, A_1) \begin{pmatrix} \langle R^0_{11}\rangle \\ \langle R^4_{11}\rangle \end{pmatrix}$$

which can easily be solved once the coefficients of the matrices $M(A_{1g}, A_1)$ have been calculated. In the same manner, one finds a 3×3 matrix coupling the rotator functions of (T_{1u}, A_1) symmetry. This matrix holds for the three columns of the T_{1u} irreducible representation, i.e. for the three bases

$$(\langle R^1_{11}\rangle, \langle R^3_{21}\rangle, \langle R^3_{22}\rangle)$$
$$(\langle R^1_{21}\rangle, \langle R^3_{31}\rangle, \langle R^3_{32}\rangle)$$
$$(\langle R^1_{31}\rangle, \langle R^3_{41}\rangle, \langle R^3_{42}\rangle).$$

Another 3×3 matrix couples together rotator functions of (T_{1u}, E).

There are six possible bases. For example R^1_{12} and R^1_{13}, which are the two E partners for $l = 1$ in the C_{3v} group have the same time evolutions. More generally, rotator functions belonging to the same column of the same irreducible representations for both molecular and lattice group, but with different l values, are coupled together.

Table 7.2 shows all the possible matrices with their corresponding bases. Let us give just one explicit form:

$$M(T_{1u}, A_1) = \begin{pmatrix} 2 & \frac{10}{9}\sqrt{\left(\frac{7}{9}\right)}b_4^{11} & \frac{35}{18\sqrt{3}}b_4^{12} \\ \frac{10}{\sqrt{21}}b_4^{11} & 12 - \frac{10}{11}\sqrt{\left(\frac{7}{3}\right)}b_4^{11} & \frac{35}{11\sqrt{3}}b_4^{12} \\ \frac{5}{2\sqrt{3}}b_4^{12} & \frac{35}{11\sqrt{3}}b_4^{12} & 12 - \frac{5}{11}\sqrt{\left(\frac{7}{3}\right)}b_4^{11} \end{pmatrix}.$$

Obviously, if we make the assumption $b_4^{11} = b_4^{12} = 0$, we find the case of free rotational diffusion

Table 7.2 The M matrices and their bases

Symmetry and dimension		Bases
$M(A_{1g}, A_1)$	1	(R^0_{11}, R^4_{11})
$M(T_{1u}, A_1)$	3	$(R^1_{11}, R^3_{21}, R^3_{22})(R^1_{21}, R^3_{31}, R^3_{32})(R^1_{31}, R^3_{41}, R^3_{42})$
$M(T_{1u}, E)$	3	$R(^1_{12}, R^3_{24}, R^3_{26})(R^1_{22}, R^3_{34}, R^3_{36})(R^1_{32}, R^3_{44}, R^3_{46})$
		$(R^1_{13}, R^3_{25}, R^3_{27})(R^1_{23}, R^3_{35}, R^3_{37})(R^1_{33}, R^3_{45}, R^3_{47})$
$M(E_g, A_1)$	2	$(R^2_{11}, R^4_{21})(R^2_{21}, R^4_{31})$
$M(E_g, E)$	5	$(R^2_{12}, R^2_{14}, R^4_{24}, R^4_{26}, R^4_{28})(R^2_{13}, R^2_{15}, R^4_{25}, R^4_{27}, R^4_{29})$
		$(R^2_{22}, R^2_{24}, R^4_{34}, R^4_{36}, R^4_{38})(R^2_{23}, R^2_{25}, R^4_{35}, R^4_{37}, R^4_{39})$
$M(T_{2g}, A_1)$	1	$(R^2_{31})(R^2_{41})(R^2_{51})$
$M(T_{2g}, E)$	5	$(R^2_{32}, R^2_{34}, R^4_{44}, R^4_{46}, R^4_{48})(R^2_{33}, R^2_{35}, R^4_{45}, R^4_{47}, R^4_{49})$
		$(R^2_{42}, R^2_{44}, R^4_{54}, R^4_{56}, R^4_{58})(R^2_{43}, R^2_{45}, R^4_{55}, R^4_{57}, R^4_{59})$
		$(R^2_{52}, R^2_{54}, R^4_{64}, R^4_{66}, R^4_{68})(R^2_{53}, R^2_{55}, R^4_{65}, R^4_{67}, R^4_{69})$
$M(A_{2u}, A_1)$	2	(R^3_{11}, R^3_{12})
$M(A_{2u}, A_2)$	1	(R^3_{13})
$M(A_{2u}, E)$	2	$(R^3_{14}, R^3_{16})(R^3_{15}, R^3_{17})$
$M(T_{1u}, A_2)$	1	$(R^2_{23})(R^3_{33})(R^3_{43})$
$M(T_{2u}, A_2)$	2	$(R^3_{51}, R^3_{52})(R^3_{61}, R^3_{62})(R^3_{71}, R^3_{72})$
$M(T_{2u}, A_2)$	1	$(R^3_{53})(R^3_{63})(R^3_{73})$
$M(T_{2u}, E)$	2	$(R^3_{54}, R^3_{56})(R^3_{55}, R^3_{57})$
		$(R^3_{64}, R^3_{66})(R^3_{65}, R^3_{67})$
		$(R^3_{74}, R^3_{76})(R^3_{75}, R^3_{77})$

$$\left.\begin{aligned}\langle R^1_{11}(\boldsymbol{\Omega}(t))\rangle &= \langle R^1_{11}(\boldsymbol{\Omega}(0))\rangle \exp(-2D_R t)\\ \langle R^3_{21}(\boldsymbol{\Omega}(t))\rangle &= \langle R^3_{21}(\boldsymbol{\Omega}(0))\rangle \exp(-12D_R t)\\ \langle R^3_{22}(\boldsymbol{\Omega}(t))\rangle &= \langle R^3_{22}(\boldsymbol{\Omega}(0))\rangle \exp(-12D_R t)\end{aligned}\right\} \quad \begin{aligned} l &= 1,\ l(l+1) = 2\\ l &= 3,\ l(l+1) = 12.\end{aligned}$$

The other case, where $b_4^{11} \neq 0$ and $b_4^{12} = 0$, corresponds to the possibility of free rotational diffusion around the molecular axis while the diffusion of this axis from one crystallographic direction to another is hindered. In this case one finds

$$\langle R^3_{22}(\boldsymbol{\Omega}(t))\rangle = \langle R^3_{22}(\boldsymbol{\Omega}(0))\rangle \exp\{-(12 - \tfrac{5}{11}\sqrt{\tfrac{7}{3}} b_4^{11}) D_R t)\}.$$

We return to the general case. Determining the eigenvalues of the M matrices, and accounting for the initial conditions at $t = 0$, then we have to evaluate integrals of the form (see (7.204a))

$$\langle R^l_{pq}(\boldsymbol{\Omega}(0)) R^l_{pq'}(\boldsymbol{\Omega}(t))\rangle = \int R^l_{pq}(\boldsymbol{\Omega}(0)) \langle R^l_{pq'}(\boldsymbol{\Omega}(t))\rangle P(\boldsymbol{\Omega}(0))\, \mathrm{d}\boldsymbol{\Omega}(0) \tag{7.207}$$

in which the intermediate conditional averages $\langle R^l_{pq}(\boldsymbol{\Omega}(t))\rangle$ defined according to (7.163a) are linear combinations of their expressions at $t = 0$. In fact no integration has to be made, providing that we make use of an expansion of $P(\boldsymbol{\Omega})$ on the basis of rotator functions, analogous to (7.195a), whose coefficients A^l_{mn} are obtained from analysis of Bragg peak intensities.

Writing

$$P(\boldsymbol{\Omega}) = \frac{1}{8\pi^2} \sum_{l''p''q''} (2l'' + 1) A^{l''}_{p''q''} R^{l''}_{p''q''}(\boldsymbol{\Omega})$$

we get

$$\langle R^l_{pq}(\boldsymbol{\Omega}(0)) R^l_{pq'}(\Omega(t))\rangle = \frac{1}{8\pi^2} \sum_{l''p''q''} (2l'' + 1) A^{l''}_{p''q''} \int R^l_{pq}(\boldsymbol{\Omega}(0)) \langle R^l_{pq'}(\boldsymbol{\Omega}(t))\rangle R^{l''}_{p''q''}(\boldsymbol{\Omega}(0))\, \mathrm{d}\boldsymbol{\Omega}(0). \tag{7.208}$$

In fact, the evaluation of the integrals is not necessary. Indeed, the relation for Wigner matrices

$$\int D^k_{nn'}(\boldsymbol{\Omega}) D^l_{mm'}(\boldsymbol{\Omega}) D^{j*}_{pp'}(\boldsymbol{\Omega})\, \mathrm{d}\boldsymbol{\Omega} = \frac{8\pi^2}{2j+1} (klnm|jp)(kln'm'|jp')$$

becomes for rotator functions

$$\int R^k_{qq'}(\boldsymbol{\Omega}) R^l_{ss'}(\boldsymbol{\Omega}) R^{j*}_{rr'}(\boldsymbol{\Omega}) = \frac{8\pi^2}{2j+1} C^{klj*}_{qsr}(L) C^{klj}_{q's'r'}(M) \tag{7.210}$$

where the coefficients $C^{klj}_{qsr}(L)$ and $C^{klj}_{q's'r'}(M)$ are defined by (7.206). This equation is very useful because

(i) it makes possible the calculation of the correlation functions of the rotator functions without any knowledge of their explicit form as function of the Euler's angles;

(ii) using the well-known properties of the Clebsch–Gordan coefficients the vanishing correlation functions are easily predicted and the eigenvalue problem of the matrices M have to be solved for only the relevant intermediate conditional averages.

Another very useful application of the relation (7.128) above is encountered in the evaluation of the EISF from the knowledge of the equilibrium orientational probability $P(\mathbf{\Omega})$ determined, for instance, from an x-ray or neutron crystallographic structure analysis. Indeed, we have defined in chapter 2 the EISF as the limit at infinite time ($I(\mathbf{Q}, \infty)$) of the intermediate scattering law, given for instance by (7.202)

$$I^{\mathrm{R}}_{\mathrm{inc}}(\mathbf{Q}, \infty) = \sum_{lpq} \sum_{l'p'q'} L^{*}_{lp}(\theta_Q, \phi_Q) L_{l'p'}(\theta_Q, \phi_Q) H^{pp'}_{ll'}(Q) \times \langle R^{l}_{pq}(\mathbf{\Omega}(0)) R^{l'}_{p'q'}(\mathbf{\Omega}(0)) \rangle \tag{7.211}$$

where $H^{pp'}_{ll'}(Q)$ is given by (7.202c). Using the expansion (7.195) of $P(\mathbf{\Omega})$ into rotator functions:

$$P(\mathbf{\Omega}) = \frac{1}{8\pi^2} \sum_{l''p''q''} (2l'' + 1) A^{l''}_{p''q''} R^{l''}_{p''q''}(\mathbf{\Omega})$$

on the evaluation of the thermal averages

$$\langle R^{l}_{pq}(\mathbf{\Omega}) R^{l'}_{p'q'}(\mathbf{\Omega}) \rangle = \frac{1}{8\pi^2} \sum_{l''p''q''} (2l'' + 1) A^{l''}_{p''q''} \int R^{l}_{pq}(\mathbf{\Omega}) R^{l'}_{p'q'}(\mathbf{\Omega}) R^{l''}_{p''q''}(\mathbf{\Omega}) \, \mathrm{d}\mathbf{\Omega} \tag{7.212}$$

we get, with the aid of (7.218)

$$I(\mathbf{Q}, \infty) = \sum_{lpq} \sum_{l'p'q'} \sum_{l''p''q''} A^{l''}_{p''q''} C^{ll'l''*}_{pp'p''}(L) C^{ll'l''}_{qq'q''}(M) \times L^{*}_{lp}(\theta_Q, \phi_Q) L_{l'p'}(\theta_Q, \phi_Q) H^{pp'}_{ll'}(Q). \tag{7.213}$$

This expression is easier to calculate than it *a priori* looks because

(i) the number of coefficients in the expansion (7.213) is generally limited (restricted to the rotator functions which are both in the molecule and in the lattice identity representation);

(ii) from the properties of the Clebsch–Gordan coefficients, many of the terms $C^{ll'l''}_{pp'p''}(L)$ and $C^{ll'l''}_{qq'q''}(L)$ and $C^{ll'l''}_{qq'q''}(M)$ are vanishing.

It is worth pointing out that, instead of evaluating the EISF from a given equilibrium distribution, the relation (7.213) makes it possible, in

principle, to determine the coefficients $A^{l''}_{p''q''}$ of the expansion of $P(\boldsymbol{\Omega})$, from the measurement of the EISF in an IQNS experiment. However, to our knowledge, such a determination has not yet been attempted. This method would require us to obtain experimental EISF values over a large Q range and, preferably, to carry out the experiment with a single crystal to take advantage of the $\boldsymbol{Q}$-direction-dependence. We shall see in §7.9 that analogous analyses have been made using Raman spectroscopy. The large size and the small thickness of the single crystal necessary to perform precise IQNS measurements are certainly an obstacle to such experiments.

7.8 The Microscopic Approach

In this section we recall some well-known results of the Mori–Zwanzig formalism. We shall give a rather abstract but very general formulation which can easily be applied to a large variety of physical systems.

The projection-operator technique assumes that, for the time-scale under interest, the dynamics of the system is essentially described by a finite set of variables $\{A_i\}$, $i = 1, 2, \ldots, n$, leading to more-or-less immediate physical measurements, which we called secular variables. These relevant variables define an n-dimensional Hilbert subspace $\mathcal{H}_P$ of the Hilbert space $\mathcal{H}$ of all the operators A_μ; $\mu = 1, 2, \ldots$. The Mori–Zwanzig projection-operator technique enables us to extract from the general evolution of the system the dynamics of the secular variables.

The quantity of interest for neutron scattering is the (incoherent) scattering law $S(\boldsymbol{Q}, \omega)$ which can be expressed formally as (see §7.7.5)

$$S(\boldsymbol{Q}, \omega) = \sum_i \sum_j a_{ij}(\boldsymbol{Q}) C_{ij}(\omega) \tag{7.214}$$

in terms of Fourier transforms $C_{ij}(\omega)$:

$$C_{ij}(\omega) = \frac{1}{2\pi} \int_{-\infty}^{\infty} C_{ij}(t) \exp(-i\omega t)\, dt \tag{7.215}$$

of correlation functions $C_{ij}(t)$ of symmetry adapted functions $U_i(t)$:

$$C_{ij}(t) = \langle U_i(t) U_j(0) \rangle . \tag{7.216}$$

Since these correlation functions are the experimentally relevant quantities, the corresponding symmetry-adapted functions will be chosen as secular variables, together with their time derivatives $\dot{U}_i = (d/dt) U_i$. In the framework of the Mori–Zwanzig method, it is more convenient to calculate the Laplace transform, $\mathcal{R}_{ij}(z)$, of the Kubo's relaxation function, $\mathcal{R}_{ij}(t)$ (see §2.4):

$$\mathcal{R}_{ij}(z) = \int_0^\infty \mathrm{d}t \exp(\mathrm{i}zt)\mathcal{R}_{ij}(t) \tag{7.217a}$$

$$\mathcal{R}_{ij}(z) = \frac{\mathrm{i}}{\hbar}\int_0^\infty \mathrm{d}t \exp(\mathrm{i}zt)\int_t^\infty \langle [U_i(\tau),\, U_j(0)]\rangle \,\mathrm{d}\tau \tag{7.217b}$$

with $z = \omega + \mathrm{i}\varepsilon$, $\varepsilon \to 0^+$ and to determine $C_{ij}(\omega)$ by means of the fluctuation–dissipation theorem (see equation (2.81)):

$$C_{ij}(\omega) = \frac{-\omega}{\exp\left(\dfrac{\hbar\omega}{k_\mathrm{B}T}\right) - 1}\,\mathcal{R}''_{ij}(\omega) \tag{7.218}$$

where $\mathcal{R}''_{ij}(\omega)$ denotes the imaginary part of $\mathcal{R}_{ij}(\omega)$

$$\mathcal{R}''_{ij}(\omega) = \frac{1}{2\mathrm{i}}\,[\mathcal{R}_{ij}(\omega + \mathrm{i}\varepsilon) - \mathcal{R}_{ij}(\omega - \mathrm{i}\varepsilon)]. \tag{7.219}$$

In the Hilbert space of operators, $\mathcal{H}$, the time-evolution of any operator, U, is determined by the hermitian Liouville operator, $\mathcal{L}$, related to the hamiltonian, H, of the system by

$$\mathcal{L}U = \frac{\mathrm{d}}{\mathrm{d}t}\dot{U} = [H,\, U] \tag{7.220a}$$

or, also:

$$U(t) = \exp(\mathrm{i}\mathcal{L}t)U(0) = \exp(\mathrm{i}Ht)U(0)\exp(-\mathrm{i}Ht). \tag{7.220b}$$

In this space, the scalar product of two operators is defined as the static susceptibility

$$(U_i,\, U_j) = \int_0^\beta \langle \mathrm{e}^{\lambda\mathcal{L}}U_i^+ U_j\rangle \,\mathrm{d}\lambda \tag{7.221a}$$

$$= \chi_{U_i^+ U_j}(z = 0) = \chi_{ij}^0. \tag{7.221b}$$

Equation (7.217b) can be written, after the change of the variable τ into $t + t'$

$$\mathcal{R}_{ij}(z) = \frac{\mathrm{i}}{\hbar}\int_0^\infty \mathrm{d}t \exp(\mathrm{i}zt)\int_0^\infty \langle [U_i(t'),\, U_j(-t)]\rangle \,\mathrm{d}t' \tag{7.222a}$$

$$\mathcal{R}_{ij}(z) = \frac{\mathrm{i}}{\hbar}\int_0^\infty \mathrm{d}t' \langle [U_i(t'),\, \int_0^\infty \mathrm{d}t \exp(\mathrm{i}zt)U_j(-t)]\rangle. \tag{7.222b}$$

Using the expression (7.220b) of $U_j(-t)$, and integrating inside the commutator, we get

$$\mathcal{R}_{ij}(z) = -\frac{1}{\hbar}\int_0^\infty \mathrm{d}t' \langle [U_i(t'),\, (z - \mathcal{L})^{-1}U_j]\rangle. \tag{7.223}$$

Here, $R(z) = (z - \mathcal{L})^{-1}$ is called the resolvent of the evolution operator. According to the definition of the scalar product, we have

$$\mathcal{R}_{ij}(z) = [U_i, (z - \mathcal{L})^{-1}U_j] \tag{7.224a}$$

$$= (U_i, R(z)U_j) = \chi^0_{U_i^+, R(z)U_j}. \tag{7.224b}$$

The relaxation function is equal to the static generalised susceptibility of U_i and $R(z)U_j$.

Now we define a projector, P, on the n-dimensional Hilbert subspace, $\mathcal{H}_p = P\mathcal{H}$, according to

$$PU = \sum_i \sum_j U_i(\chi^{0-1})_{ij}(U_j, U) \tag{7.225}$$

$(\chi^{0-1})_{ij}$ is the (i, j) element for the inverse of the matrix χ^0 defined by (7.221b). If Q is the projector on the orthogonal complement, $\mathcal{H}_Q = Q\mathcal{H}$, of $\mathcal{H}_P$, we have the following properties:

$$P + Q = 1 \tag{7.226a}$$

$$P = P^+ = P^2 \tag{7.226b}$$

$$Q = Q^+ = Q^2 \tag{7.226c}$$

$$PQ = QP = 0. \tag{7.226d}$$

Using the trivial identity

$$z(z - \mathcal{L})^{-1} = 1 + \mathcal{L}(z - \mathcal{L})^{-1} \tag{7.227}$$

and the definition of the projectors, we obtain the set of coupled equations

$$\begin{aligned}(zP - P\mathcal{L}P)R(z)P - P\mathcal{L}QQR(z)P &= P \\ (zQ - Q\mathcal{L}Q)QR(z)P - Q\mathcal{L}PPR(z)P &= 0.\end{aligned} \tag{7.228a}$$

Combining the two equations, we find:

$$[zP - P\mathcal{L}P - P\mathcal{L}Q(z - Q\mathcal{L}Q)^{-1}Q\mathcal{L}P]PR(z)P = P. \tag{7.229}$$

Taking the i, j matrix element, we have

$$(U_i,[zP - P\mathcal{L}P - P\mathcal{L}Q(z - Q\mathcal{L}Q)^{-1}Q\mathcal{L}P]PR(z)PU_j) = (U_i, PU_j). \tag{7.230}$$

The different terms are easily evaluated. For the right-hand side, we get

$$\begin{aligned}(U_i, PU_j) &= (U_i, \sum_k \sum_l U_k(\chi^{0-1})_{kl}(U_1, U_j)) \\ &= \sum_k \sum_l \chi^0_{ik}\chi^{0-1}_{kl}\chi^0_{lj} = \chi^0_{ij}.\end{aligned} \tag{7.231}$$

Similarly,

$$(U_i,\ PR(z)PU_j) = \sum_k \sum_l (U_i,\ U_k \chi^{0-1}_{kl} (U_l,\ R(z)U_j))$$

$$= \sum_k \sum_l \chi^0_{ik} \chi^{0-1}_{kl} \mathcal{R}_{lj}(z) = \mathcal{R}_{ij}(z). \tag{7.232}$$

Finally, introducing a frequency matrix, $\boldsymbol{\Omega}$, with elements

$$\Omega_{ik} = \sum_l (U_i,\ \mathcal{L}U_l)\chi^{0-1}_{lk} = \sum_l (U_i,\ U_l)\chi^{0-1}_{lk} \tag{7.233}$$

and a memory matrix, $\mathbf{M(z)}$, defined by:

$$M_{ik}(z) = \sum_l (Q\mathcal{L}U_i,\ (z - Q\mathcal{L}Q)^{-1} Q\mathcal{L}U_l)\chi^{0-1}_{lk} \tag{7.234}$$

we are led to the final equation

$$\sum_k [z\delta_{ik} - \Omega_{ik} + M_{ik}(z)]\mathcal{R}_{kj}(z) = \chi^0_{ij} \tag{7.235}$$

or, in matrix form:

$$[z - \boldsymbol{\Omega} + \mathbf{M(z)}]\mathcal{R}(z) = \boldsymbol{\chi}^0. \tag{7.236}$$

Now we have to evaluate the memory matrix $\mathbf{M(z)}$. According to (7.234), it is a function analogous to $\mathcal{R}(z)$ but defined in the subspace $\mathcal{H}_0$. The time-evolution of the matrix elements $M_{ik}(z)$ is determined by the resolvent in $\mathcal{H}_Q$, $R_Q(z) = (z - Q\mathcal{L}Q)^{-1}$. Therefore, the same method can be applied again. Using the identity

$$z(z - Q\mathcal{L}Q)^{-1} = 1 + Q\mathcal{L}Q(z - Q\mathcal{L}Q)^{-1} \tag{7.237}$$

the terms $M_{ik}(z)$ can be represented like $\mathcal{R}_{ij}(z)$ by an expression analogous to (7.235). More precisely, we obtain

$$\sum_k [z^2\delta_{ik} + z\Omega^{(1)}_{ik} + \Omega^{(2)}_{ik}]M_{kj}(z) = z(Q\mathcal{L}U_i,\ Q\mathcal{L}U_j) + (Q\mathcal{L}^2U_i,\ Q\mathcal{L}U_j)$$
$$+ (Q\mathcal{L}^3U_i,\ (z - Q\mathcal{L}Q)^{-1} Q\mathcal{L}U_j) \tag{7.238a}$$

with

$$\Omega^{(n)} = \sum_l (U_i,\ \mathcal{L}^n U_l)\chi^{0-1}_{lk}. \tag{7.238b}$$

Continuing in this way, it is possible to obtain a representation of $\mathcal{R}_{ij}(z)$ in terms of a continued fraction expansion. Anyway we have to stop at any order. The simplest approximation for the memory matrix consists in replacing the third term on the right-hand side of (7.238a) by a complex number. For simple systems, this value can be found analytically. We shall not discuss this point further, but refer the reader to De Raedt and De Raedt (1977) for more information. In order to make

clearer this rather abstract development, we shall examine its application to a set of secular variables $\{U_i, \dot{U}_i\}$, $i = 1, 2, \ldots$, composed of the symmetry-adapted functions and of their time-derivatives. To simplify the calculations, we assume, as it often turns out in practice, that there is no coupling between functions with different index i, the static susceptibility matrix is diagonal and given by

$$\boldsymbol{\chi}^0 = \begin{pmatrix} \ddots & & & & \\ & (U_1, U_1) & \cdots & & 0 \\ & & (U_i, U_i) & & \\ & & & (\dot{U}_1, \dot{U}_1) & \cdots \\ & 0 & & & (\dot{U}_i, \dot{U}_i) \\ & & & & & \ddots \end{pmatrix} \tag{7.239}$$

The projector P on the space spanned by the secular variables is defined by

$$PU = \sum_i \left\{ \frac{(U_i, U)}{(U_i, U_i)} U_i + \frac{(\dot{U}_i, U)}{(\dot{U}_i, \dot{U}_i)} \right\} \dot{U}_i \tag{7.240}$$

The frequency matrix and the memory matrix are respectively:

$$\boldsymbol{\Omega} = \begin{pmatrix} 0 & (\dot{U}_i \dot{U}_i) \\ (\dot{U}_i U_i) & 0 \end{pmatrix} \tag{7.241}$$

$$\mathbf{M(z)} = \begin{vmatrix} 0 & 0 \\ 0 & m_{ii}(z) \end{vmatrix} \tag{7.242}$$

$$\text{where } m_{ii}(z) = -\frac{(Q\mathscr{L}^2 U_i, (z - Q\mathscr{L}Q)^{-1} Q\mathscr{L}^2 U_i)}{(\dot{U}_i, \dot{U}_i)} \tag{7.243a}$$

$$= -\frac{(Q\ddot{U}_i, (z - Q\mathscr{L}Q)^{-1} Q\ddot{U}_i)}{(\dot{U}_i, \dot{U}_i)}. \tag{7.243b}$$

Now the solution of (7.235) for $\mathscr{R}_{U_i U_i}(z)$ reads

$$\mathscr{R}_{U_i U_i}(z) = \frac{(U_i, U_i) z + m_{ii}(z)}{z^2 + z m_{ii}(z) - \dfrac{(\dot{U}_i, \dot{U}_i)}{(U_i, U_i)}}. \tag{7.244}$$

The memory matrix can be evaluated as discussed above. Defining the second moment by

$$\langle \omega_i^{2n} \rangle = \frac{1}{\langle U^i U^i \rangle} \left\langle \frac{\mathrm{d}^n U_i}{\mathrm{d}t^n} \frac{\mathrm{d}^n U_i}{\mathrm{d}t^n} \right\rangle \tag{7.245}$$

we obtain (de Raedt and de Raedt 1977, de Raedt and Michel 1979)

$$m_{ii}(z) = -\frac{1}{\langle \omega_i^2 \rangle} \frac{(\langle \omega_1^4 \rangle - \langle \omega_i^2 \rangle^2)}{z + \mathrm{i}(\langle \omega_i^4 \rangle / \langle \omega_i^2 \rangle)^{1/2}} \tag{7.246}$$

and finally, substituting this expression for $m_{ii}(z)$ into (7.244) and

calculating $\mathcal{R}''_{ii}(\omega)$ by means of (7.219), we get from (7.218)

$$C_{ii}(\omega) = \frac{\langle U_i U_i \rangle}{\pi} \frac{(\langle \omega_i^4 \rangle - \langle \omega_i^2 \rangle^2)(\langle \omega_i^4 \rangle / \langle \omega_i^2 \rangle)^{1/2}}{\omega^2(\omega^2 - \langle \omega_i^4 \rangle / \langle \omega_i^2 \rangle)^2 + (\omega^2 - \langle \omega_i^2 \rangle)^2 \langle \omega_i^4 \rangle / \langle \omega_i^2 \rangle}. \tag{7.247}$$

Thus, the correlation functions $C_{ii}(\omega)$ occurring in the expansion of the scattering law (7.214) have been expressed in terms of their moments $\langle \omega_i^2 \rangle$ and $\langle \omega_i^4 \rangle$. Before going further in the evaluation of (7.247), this relation was derived under a rather simple approximation for the memory function, keeping in its time-evolution equation terms up to second order. Going beyond this approximation involves higher-frequency moments. Full details can be found in original papers. According to the value of the various moments, an expression such as (7.247) can exhibit either a single or a two-peak structure. A two-peak structure corresponds to torsional oscillations while a central peak feature is related to reorientational relaxation. Moreover, since the moments are defined as thermal averages by means of (7.245), the aspect of the dynamic orientational correlation functions will depend on temperature, and it is possible to observe the transition from one regime to another.

As a concrete example, we consider a dumbbell molecule in an octahedral potential. This case has been treated by de Raedt and Michel (1979) and we shall report here the most remarkable results of their analysis. Because the orientation of the dumbbell in the octahedral field is fully specified by giving its polar and azimuthal angle θ and ϕ, the symmetry-adapted functions are the surface (cubic) harmonics with $\mathbb{O}_h$ symmetry. These are listed in table 7.1, up to $l = 4$ as a function of the spherical harmonics. For $l = 0$, we have one single function with A_{1g} symmetry, $K_{01} = Y_{00}$. Similarly, for $l = 1$, there are three functions of T_{1u} symmetry, and for the case $l = 2$, we have two functions belonging to the E_g representation and three functions belonging to the T_{2g} representation, etc. Starting from the Sears expansion of $\exp(i\boldsymbol{Q}\cdot\boldsymbol{R})$ into spherical harmonics (7.201), and using the definition of the surface harmonics (7.180) the intermediate scattering law $I(\boldsymbol{Q}, t)$ can be written

$$I(\boldsymbol{Q}, t) = 16\pi^2 \sum_l \sum_{l'} \sum_q i^{(l+l')}(-1)^{l'} j_l(QR) j_{l'}(QR) \times K_{lq}(\boldsymbol{\Omega}_Q) K_{l'q}(\boldsymbol{\Omega}_Q) \langle K_{lq}(t) K_{lq'}(0) \rangle \tag{7.248}$$

where (t) stands for $\theta(t)$, $\phi(t)$. In writing down this equation, it has been taken into account that the expectation value of the product of two symmetry-adapted functions belonging to different irreducible representations or to different columns of the same irreducible representation

vanishes (Wigner 1959). Therefore, only expectation values with the same indexes $q = q'$ are different from zero. Owing to the presence of the first-order Bessel functions, it is sufficient to consider terms up to $l + l' = 4$ in the expansion (7.248). Therefore the relevant terms are:

$$l = 0,\ l' = 0 \quad A_{1g}^{(0)}(t) = \langle K_{01}(t)K_{01}(0)\rangle = \frac{1}{4\pi} \tag{7.249a}$$

$$l = 1,\ l' = 1 \quad T_{1u}^{(1)}(t) = \langle K_{11}(t)K_{11}(0)\rangle = \langle K_{12}(t)K_{12}(0)\rangle = \langle K_{13}(t)K_{13}(0)\rangle \tag{7.249b}$$

$$l = 2,\ l' = 2 \quad E_g^{(2)}(t) = \langle K_{21}(t)K_{21}(0)\rangle = \langle K_{22}(t)K_{22}(0)\rangle \tag{7.249c}$$

$$l = 2 \quad l' = 2 \quad T_{2g}^{(2)}(t) = \langle K_{23}(t)K_{23}(0)\rangle = \langle K_{24}(t)K_{24}(0)\rangle = \langle K_{25}(t)K_{25}(0)\rangle \tag{7.249d}$$

$$l = 1 \quad l' = 3 \quad T_{1u}^{(1,3)}(t) = \langle K_{11}(t)K_{31}(0)\rangle = \ldots \tag{7.249e}$$

$$l = 0 \quad l' = 4 \quad A_{1g}^{(0,4)}(t) = \langle K_{01}(t)K_{41}(0)\rangle. \tag{7.249f}$$

With our restriction $l + l' < 4$, there is no term with symmetry T_{2u} or $A_{2u}(l = 3)$ or $T_{1g}(l = 4)$. The following terms with symmetry E_g (i.e. $E_g^{(2,4)} l = 2,\ l' = 4$) and T_{2g} (i.e. $T_{2g}^{(2,4)} l = 2,\ l' = 4$), would have to be considered only in the limit $l + l' < 6$, which is not necessary in the Q range usually accessible to experiments. Using the explicit expressions of the cubic harmonics given in table 7.1 and taking the Fourier transform of (7.248), the scattering law becomes:

$$\begin{aligned} S(\boldsymbol{Q}, \omega) = {} & [j_0^2(QR) + 8\pi^2 j_0(QR) j_4(QR) K_{41}(\boldsymbol{\Omega}_Q)\langle K_{41}(0)\rangle]\delta(\omega) \\ & + 12\pi^2 j_1^2(QR) T_{1u}^{(1)}(\omega) \\ & + 30\pi j_2^2(QR)(q_x^4 + q_y^4 + q_z^4 - \tfrac{1}{3}) E_g^{(2)}(\omega) \\ & + 30\pi j_2^2(QR)(1 - q_x^4 - q_y^4 - q_z^4) T_{2g}^{(2)}(\omega) \\ & + 20\pi j_1(QR) j_3(QR)\sqrt{21}(q_x^4 + q_y^4 + q_z^4 - \tfrac{3}{5}) T_{1u}^{(1,3)}(\omega) \end{aligned} \tag{7.250}$$

where $T_{1u}^{(1)}(\omega)$, $E_g^{(2)}(\omega)$, $T_{2g}^{(2)}(\omega)$ and $T_{1u}^{(1,3)}(\omega)$ are Fourier transforms of $T_{1u}^{(1)}(t)$, $E_{2g}^{(2)}(t)$, $T_{2g}^{(2)}(t)$ and $T_{1u}^{(1,3)}(t)$, respectively. q_x, q_y and q_z stand for vector components

$$q_x = \frac{Q_x}{Q},\ q_y = \frac{Q_y}{Q},\ q_z = \frac{Q_z}{Q}$$

of the scattering vector $\boldsymbol{Q}(Q_x, Q_y, Q_z)$. The first term on the right-hand side defines the EISF

$$A_0(\boldsymbol{Q}) = j_0^2(QR) + 8\pi^2 j_0(QR) j_4(QR) K_{41}(\boldsymbol{\Omega}_Q)\langle K_{41}(0)\rangle. \tag{7.251}$$

The evaluation of $\langle K_{41}(0)\rangle$ requires knowledge of the orientational probability at equilibrium, $P(\boldsymbol{\Omega})$. Conversely, starting from an expan-

sion of $P(\mathbf{\Omega})$ into cubic harmonics (belonging to the representation identity):

$$P(\mathbf{\Omega}) = \sum_{lq} a_{lq} K_{lq}(\mathbf{\Omega}) \tag{7.252}$$

a measurement of the variations of $A_0(\boldsymbol{Q})$ as a function of both the modulus and the direction of $\boldsymbol{Q}$ can, in principle lead to the determination of the first coefficients a_{lq} with low l values. Because $A_0(\boldsymbol{Q})$ involves a thermal average, the intensity of the purely elastic line will depend on temperature. The other terms in (7.250) constitute the quasielastic part of the spectrum, which can be evaluated according to (7.247). Before dealing with that aspect of the problem, it is worth noting that the weight of the various terms in (7.247) is essentially determined by the value of the Bessel functions $j_l(QR)$ and by the direction of $\boldsymbol{Q}$. Thus it is possible to make some selection among the different contributions: the $T_g^{(2)}$ contribution disappears if $\boldsymbol{Q}$ is chosen along any [100] direction, while the $E_g^{(2)}$ contribution vanishes for $\boldsymbol{Q}$ lying along [111] directions, and the $T_u^{(1,3)}$ contribution for $q_x^4 + q_y^4 + q_z^4 = 3/5$. Conversely, the $T_u^{(1)}$ contribution does not depend on the $\boldsymbol{Q}$-direction, but only on its modulus, via the Bessel function $j_1(QR)$ so that it essentially predominates at low Q values.

Evaluation of the various terms $T_u^{(1)}(\omega)$, etc, according to (7.247) involves thermal averages (the $2n$th moments) calculated with the equilibrium distribution function

$$g(\dot{\theta}, \dot{\phi}, \theta, \phi) = \frac{1}{Z} \exp(-H/k_B T) \tag{7.253a}$$

with

$$Z = \int \mathrm{d}\dot{\theta} \int \mathrm{d}\dot{\phi}\, \mathrm{d}\theta\, \mathrm{d}\phi \sin\theta\, g(p_\theta, p_\phi, \theta, \phi). \tag{7.253b}$$

Here H is the hamiltonian

$$H = \tfrac{1}{2} I(\dot{\theta}^2 + \sin^2\theta\, \dot{\phi}^2) + V(\theta, \phi) \tag{7.253c}$$

$V(\theta, \phi)$ is the potential acting on the molecule, which can be expanded in terms of the cubic surface harmonics belonging to the identical representation A_{1g}

$$V(\theta, \phi) = a_0 K_{01} + a_4 K_{41}(\theta, \phi) + a_6 K_{46}(\theta, \phi) + \ldots \tag{7.254}$$

Restricting ourselves again to $l = 4$, given the expressions of table 7.1 and dropping the constant terms which are irrelevant, de Raedt and Michel choose

$$V(\theta, \phi) = s(x^4 + y^4 + z^4) \tag{7.255}$$

with $x = \sin\theta\cos\phi$, $y = \sin\theta\sin\phi$, $z = \cos\theta$.

According to (7.253a), any change in the magnitude of the potential is

equivalent to a temperature change. Thus the sign of the potential, $s = \pm 1$, is the only relevant factor because it governs the directions of the maxima, minima and saddle points of $V(\theta, \phi)$ in space.

De Raedt and Michel have studied the behaviour of the various modes $T_{iu}^{(1)}(\omega)$, etc, as a function of the temperature. For $s = -1$ and at low temperatures, the $T_{2g}^{(2)}$ mode shows well-defined off-centre resonances (figure 7.16(a)), symmetric with respect to the origin and corresponding to oscillatory motion: the $T_{2g}^{(2)}$ mode has a librational character for $s = -1$. Conversely, for the same potential, the behaviour of the $E_g^{(2)}$ mode is quite different (figure 7.16(b)). At low temperature, the spectrum consists of a sharp central peak, whose width grows with increasing temperature. At high temperature, the $T_{2g}^{(2)}$ and $E_{2g}^{(2)}$ modes become very similar. Thus, the $E_{2g}^{(2)}$ mode appears to have a reorientational character at low temperature, the molecule being trapped in one of the potential minima with a very small probability of going over the potential barrier. At high temperature, the reorientations become faster and the spectrum broadens, reaching finally the hindered rotation regime if the temperature is higher than the potential height; differences between the $E_g^{(2)}$ and $T_{2g}^{(1)}$ modes disappear at high temperature.

The $T_{1u}^{(1)}$ mode is found to have the same behaviour as the $E_{2g}^{(2)}$ mode. Finally, when changing the sign of s, the characters of the $E_g^{(2)}$ and $T_{2g}^{(2)}$

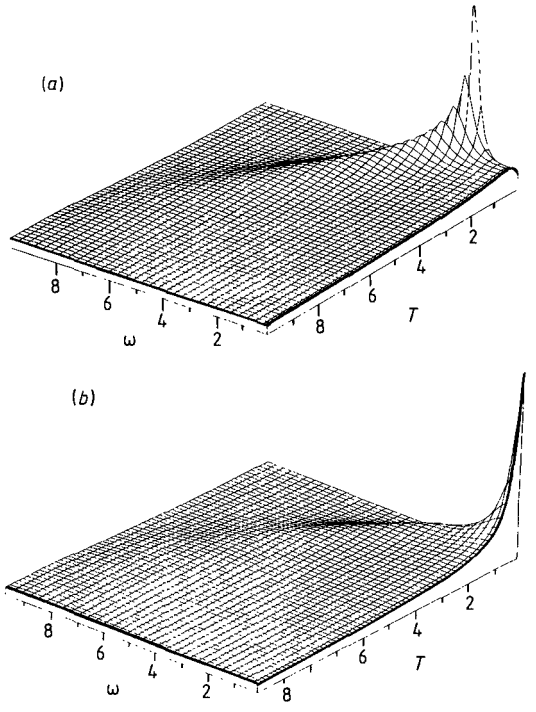

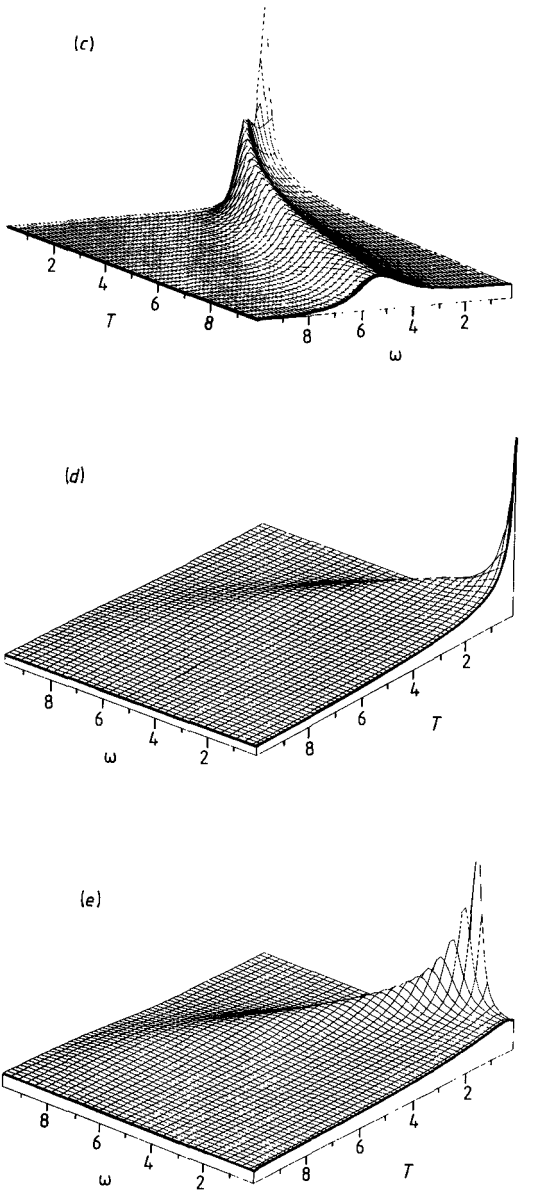

Figure 7.16 Variation of the various modes $T_{1u}^{(1)}(\omega)$, $T_{2g}^{(2)}(\omega)$, $E_2^{(2)}(\omega)$ as a function of the temperature, in the case of a dumbbell molecule reorienting in an octahedral field of negative or positive sign, $s = \pm 1$. (*a*), $T_{2g}^{(2)}(\omega)$ mode, $s = -1$; (*b*), $E_g^{(2)}(\omega)$ mode, $s = -1$; (*c*), $T_{1u}^{(1)}(\omega)$ mode, $s = \pm 1$; (*d*), $T_{2g}^{(2)}(\omega)$ mode, $s = +1$; (*e*), $E_g^{(2)}(\omega)$ mode, $s = +1$. Temperatures and energy transfers are expressed in degrees.

modes are inverted, corresponding to the exchange of the potential minima and maxima.

De Raedt and Michel made a comparison of their theoretical results with Raman experiments on CN impurities in KCl, KBr and NaCl (Callender and Pershan 1970). They found an overall agreement for the general form of the side-band data and their classification but also for the temperature behaviour of the librations and the change to the quasi-free-rotation regime.

7.9 Investigation of Orientational Disorder by Raman and Infrared Spectroscopies

The object of this section is to show how it is possible to obtain information on the orientational dynamics of molecules in a disordered phase, through infrared and Raman spectroscopy of their internal modes. We shall see that the integrated intensity of these modes can lead to the derivation of some independent coefficients of the orientation probability distribution $P(\boldsymbol{\Omega})$ while the study of the band profiles provides information about the time-scale of reorientation mechanisms. We shall not here go into all the details of the calculations. In particular, obtaining the information above relies on a certain number of approximations which will not be discussed here; we refer the reader to the original paper of Yvinec and Pick (1983) and to practical applications (Sauvajol 1983).

7.9.1 Theoretical aspects

The basic formula which relates the Raman scattered intensity $I(\omega)$ to the fluctuations of the macroscopic polarisability of the sample is

$$I(\omega) = I_0 \frac{k^4}{2\pi} \int_{-\infty}^{\infty} \langle (\boldsymbol{e}_0 \cdot \boldsymbol{\varepsilon}(0) \cdot \boldsymbol{e})(\boldsymbol{e}_0 \cdot \boldsymbol{\varepsilon}(t) \cdot \boldsymbol{e}) \rangle \exp(-i\omega t)\, dt \quad (7.256)$$

where, I_0 is the incident intensity, ω is the frequency shift, $\boldsymbol{e}_0$ and $\boldsymbol{e}$ are the polarisation vectors of the incident and scattered lights, respectively. k is the modulus of the scattered wavevector. $\boldsymbol{\varepsilon}(t)$ and $\boldsymbol{\varepsilon}(0)$ are the total polarisability tensor at time t and at time zero. The brackets denote an average over a thermal equilibrium distribution of the sample states.

The infrared energy absorbed per unit thickness of sample, $\mathcal{J}(\omega)$ follows an analogous relation. If $\mathcal{J}_0$ denotes the incident energy, we have:

$$\mathcal{J}(\omega) = \frac{2\pi \mathcal{J}_0}{3hcV} \omega \left\{ 1 - \exp\left(- \frac{\hbar\omega}{k_B T} \right) \right\} \times \int_{-\infty}^{\infty} \langle \boldsymbol{e}_0 \cdot \boldsymbol{\pi}(0) \rangle \langle \boldsymbol{e} \cdot \boldsymbol{\pi}(t) \rangle \exp(-i\omega t)\, dt \quad (7.257)$$

where $\boldsymbol{\pi}(t)$ and $\boldsymbol{\pi}(0)$ are the total dipole moment in the volume V of the sample, at time t and at time zero, respectively. The total polarisability tensor $\boldsymbol{\varepsilon}(t)$ and the dipole moment $\boldsymbol{\pi}(t)$ can be written as a sum of molecular contributions, $\boldsymbol{\varepsilon}^L(t)$ and $\boldsymbol{\pi}^L(t)$:

$$\boldsymbol{\varepsilon}(t) = \sum_L \boldsymbol{\varepsilon}^L(t) \tag{7.258a}$$

$$\boldsymbol{\pi}(t) = \sum_L \boldsymbol{\pi}^L(t). \tag{7.258b}$$

These time-dependent quantities depend on both the external dynamics of the molecules (translational and orientational) and on their internal vibrational modes. The former gives rise to the low-frequency part of the spectra, the latter, providing that modes are sufficiently decoupled from each other, leads to spectral lines, the intensity and lineshape of which is our subject of interest in this section. We assume that these internal lines are well separated from the low-frequency part of the spectrum and that no overlapping exists between lines arising from different internal modes. Under these conditions we can write the expansions

$$\boldsymbol{\varepsilon}(t) = \sum_L \sum_j \sum_n \frac{\partial \boldsymbol{\varepsilon}^L(t)}{\partial Q^L_{jn}} Q^L_{jn}(t) \tag{7.259a}$$

$$= \sum_L \sum_j \sum_n \boldsymbol{\varepsilon}^L_{jn}(t) Q^L_{jn}(t) \tag{7.259b}$$

and

$$\boldsymbol{\pi}(t) = \sum_L \sum_j \sum_n \frac{\partial \boldsymbol{\pi}^L(t)}{\partial Q^L_{jn}} Q^L_{jn}(t) \tag{7.260a}$$

$$= \sum_L \sum_j \sum_n \boldsymbol{\pi}^L_{jn}(t) Q^L_{jn}(t) \tag{7.260b}$$

where $Q^L_{jn}(t)$ is the nth component of the normal coordinate corresponding to the mode j of the molecule L. Here three main approximations have to be made:

(1) The Kastler Rousset hypothesis assumes that the individual Raman and infrared tensors $\boldsymbol{\varepsilon}^L$ and $\boldsymbol{\pi}^L$ have well-defined, time-independent components in the molecular axes, depending only on the considered vibration n. Therefore, in the crystal axes, the components of these tensors depend on time only via the molecular reorientational motion

$$\boldsymbol{\varepsilon}^L_{jn}(t) = \boldsymbol{\varepsilon}_{jn}(\boldsymbol{\Omega}_L(t)) = \mathbf{R}^+(\boldsymbol{\Omega}_L(t))\boldsymbol{\varepsilon}^0_{jn}\mathbf{R}(\boldsymbol{\Omega}_L(t)) \tag{7.261}$$

$$\boldsymbol{\pi}^L_{jn}(t) = \boldsymbol{\pi}_{jn}(\boldsymbol{\Omega}_L(t)) = \mathbf{R}(\boldsymbol{\Omega}_L(t))\boldsymbol{\pi}^0_{jn} \tag{7.262}$$

where $\boldsymbol{\varepsilon}^0_{jn}$ and $\boldsymbol{\pi}^0_{jn}$ are the Raman and infrared tensor of the molecule in its own axes, and $\mathbf{R}(\boldsymbol{\Omega})$ is the usual rotation matrix associated with the

set of three Euler angles $\mathbf{\Omega}$ which bring the crystal axes in coincidence with the molecular axes.

(2) The second hypothesis assumes that the rotational motions and the vibrational dynamics are statistically independent, so that the correlation function appearing in (7.256) and (7.257) can be written as a product of two correlation functions related respectively to the components of the Raman or infrared tensors (i.e the reorientational motion) and to the normal coordinates (i.e. the vibrational part).

(3) There is no coupling between the different internal modes of the same molecules nor between the internal modes of different molecules. Hence

$$\langle Q_{jn}^{L}(\mathbf{\Omega}(0)) Q_{jn'}^{L'}(\mathbf{\Omega}(t)) \rangle = \delta_{LL'} \delta_{nn'} \phi_j^{\text{vib}}(t) \tag{7.263}$$

The vibrational correlation function $\phi_j^{\text{vib}}(t)$ is simply

$$\phi_j^{\text{vib}}(t) = \exp(\mp\, \mathrm{i}\omega_j t) \exp(-\gamma_j t) n(\omega_j) \tag{7.264}$$

Here the term γ_j takes into account the finite time duration of the vibration. ω_j is the frequency of the mode j under interest. $n(\omega_j)$ is the Bose factor relative to this mode.

With these hypotheses, the Raman and infrared lineshapes related to a molecular internal mode become

$$I^j(\omega) = I_0 \frac{k^4}{2\pi} \int_{-\infty}^{\infty} \exp(-\mathrm{i}\omega t)\, \mathrm{d}t \sum_L \sum_{L'} \sum_n \sum_{n'} \langle Q_{jn}^{L}(0) Q_{jn'}^{L'}(t) \rangle \tag{7.265}$$
$$\times \langle (\boldsymbol{e}_0 \cdot \boldsymbol{\varepsilon}_{jn}(\mathbf{\Omega}_L(0)) \cdot \boldsymbol{e})(\boldsymbol{e}_0 \cdot \boldsymbol{\varepsilon}_{jn}(\mathbf{\Omega}_L(t) \cdot \boldsymbol{e}) \rangle$$

$$\mathcal{J}^j(\omega) = \frac{2\pi \mathcal{J}_0}{3hcV} \omega \left\{ 1 - \exp\left(- \frac{\hbar\omega}{k_B T} \right) \right\} \int_{-\infty}^{\infty} \exp(-\mathrm{i}\omega t)\, \mathrm{d}t \tag{7.266}$$
$$\times \sum_L \sum_{L'} \sum_n \sum_{n'} \langle Q_{jn}^{L}(0) Q_{jn'}^{L'}(t) \rangle \langle [\boldsymbol{e}_0 \cdot \boldsymbol{\pi}_{jn}(\mathbf{\Omega}_L(0))][\boldsymbol{e} \cdot \boldsymbol{\pi}_{jn'}(\mathbf{\Omega}_{L'}(t))] \rangle$$

Or, introducing cartesian components relative to crystal axes, to take into account the polarisation of incident and scattered lights and using (7.263) above

$$I^j(\omega) = k^4 I_0 \sum_\alpha \sum_\beta \sum_\gamma \sum_\delta e_{0\alpha} e_{0\beta} e_\gamma e_\delta I^j_{\alpha\beta,\gamma\delta}(\omega) \tag{7.267}$$

$$\mathcal{J}^j(\omega) = \frac{4\pi^2 \mathcal{J}_0}{3hcV} \sum_\alpha \sum_\beta \mathcal{J}^j_{\alpha\beta}(\omega) e_{0\alpha} e_{0\beta} \tag{7.268}$$

with the following expression of the Raman and infrared tensors

$$I^j_{\alpha\beta,\gamma\delta}(\omega) = \frac{1}{2\pi} \int_{-\infty}^{\infty} \exp(-\mathrm{i}\omega t)\, \mathrm{d}t \langle [\varepsilon_{jn}(\mathbf{\Omega}_L(0))]_{\alpha\beta} [\varepsilon_{jn}(\mathbf{\Omega}_L(t)]_{\gamma\delta} \rangle \otimes \phi_j^{\text{vib}}(\omega) \tag{7.269}$$

$$\mathcal{J}^{j}_{\alpha\beta}(\omega) = \frac{1}{2\pi}\int_{-\infty}^{\infty} \exp(-i\omega t)\, dt \langle [\pi_{jn}(\Omega_L(0))]_\alpha [\pi_{jn}(\Omega_L(t))]_\beta \rangle \otimes \phi_j^{vib}(\omega) \tag{7.270}$$

$\phi_j^{vib}(\omega)$ is the time-Fourier transform of $\phi_j^{vib}(t)$ and $\otimes$ denotes a convolution product.

Equations (7.269) and (7.270) indicate that we observe, centred around the vibration ω_j, a line, the intensity of which according to the different polarisations $(\alpha\beta, \gamma\delta)$, depends on the orientational probability distribution of the molecule and the width of which depends on the reorientational motions.

The integrated intensity of internal lines is a very useful quantity which provides information about the various molecular orientations and which enables the evaluation of a certain number of the coefficients of the expansion of the orientational probability, $P(\Omega)$.

$$S^{j}_{\alpha\beta,\gamma\delta} = \sum_n \int [\varepsilon_{jn}(\Omega)]_{\alpha\beta} [\varepsilon_{jn}(\Omega)]_{\gamma\delta} P(\Omega)\, d\Omega \tag{7.271}$$

It is convenient to make use of the formalism developed for the study of orientational disorder in liquids (Steel 1964) and for molecular impurities in a matrix (Callender and Pershan 1970). This formalism has also been used in the case of orientationally disordered phases (Pick and Yvinec 1980, Sauvajol *et al* 1982, Sauvajol 1983, Yvinec and Pick 1983). We shall define the irreducible components of the tensor with respect to the crystal and molecular symmetry group. Given a tensor defined for instance by its cartesian components $T_{\mu\nu}$ in the crystal axes $(\mu, \nu = x, y, z)$, it can be split into its spherical components T^l_m (Rose 1957), which, under the effect of a rotation of the axis system, transform according to the Wigner matrices of the same index D_l

$$\mathbf{R}^+(\Omega) T^l_{m'} \mathbf{R}(\Omega) = \sum_{m=-l}^{l} T^l_m D^l_{mm'}(\Omega). \tag{7.272}$$

For example, the irreducible spherical components of the Raman polarisability tensor, relative to the internal mode j of the isolated molecule, $(\varepsilon^0_{jn})^l_m$, are given in the general case by:

$$(\varepsilon^0_{jn})^0_0 = \frac{1}{\sqrt{4\pi}}[(\varepsilon^0_{jn})_{xx} + (\varepsilon^0_{jn})_{yy} + (\varepsilon^0_{jn})_{zz}] \tag{7.273a}$$

$$(\varepsilon^0_{jn})^2_0 = \sqrt{\left(\frac{5}{16\pi}\right)}\,[2(\varepsilon^0_{jn})_{zz} - (\varepsilon^0_{jn})_{xx} - (\varepsilon^0_{jn})_{yy}] \tag{7.273b}$$

$$(\varepsilon^0_{jn})^2_{\pm 1} = \sqrt{\left(\frac{15}{8\pi}\right)}[(\varepsilon^0_{jn})_{zx} \pm i(\varepsilon^0_{jn})_{zy}] \tag{7.273c}$$

$$(\varepsilon^0_{jn})^2_{\pm 2} = \sqrt{\left(\frac{15}{32\pi}\right)}[(\varepsilon^0_{jn})_{xx} - (\varepsilon^0_{jn})_{xy} \pm 2i(\varepsilon^0_{jn})_{xy}]. \tag{7.273d}$$

The six independent components of the tensor $\boldsymbol{\varepsilon}^0_{jn}$ can be obtained by inverting the relations (7.273) above:

$$\boldsymbol{\varepsilon}^0_{jn} = (\varepsilon^0_{jn})^0_0 \mathbf{d}^0_0 + \sum_{m=-2}^{2} (\varepsilon^0_{jn})^2_m \mathbf{d}^2_m \tag{7.274}$$

with (Callender and Pershan 1970)

$$\mathbf{d}^0_0 = \frac{2}{3}\sqrt{\pi}\begin{pmatrix} 1 & 0 & 0 \\ 0 & 1 & 0 \\ 0 & 0 & 1 \end{pmatrix} \quad \mathbf{d}^2_0 = \frac{2}{3}\sqrt{\frac{\pi}{5}}\begin{pmatrix} -1 & 0 & 0 \\ 0 & -1 & 0 \\ 0 & 0 & 2 \end{pmatrix}$$

$$\mathbf{d}^2_{\pm 1} = \left(\frac{2\pi}{5}\right)^{1/2}\begin{pmatrix} 0 & 0 & \mp 1 \\ 0 & 0 & \mathrm{i} \\ \mp 1 & \mathrm{i} & 0 \end{pmatrix} \quad \mathbf{d}^2_{\pm 2} = \left(\frac{2\pi}{15}\right)^{1/2}\begin{pmatrix} 1 & \mp\mathrm{i} & 0 \\ \mp\mathrm{i} & -1 & 0 \\ 0 & 0 & 0 \end{pmatrix}. \tag{7.275}$$

More generally, for a molecule in the orientation $\boldsymbol{\Omega}_L = \boldsymbol{\Omega}_L(r)$:

$$[\varepsilon_{jn}(\boldsymbol{\Omega}_L)]_{\alpha\beta} = \sum_l \sum_{m=-l}^{l} d^l_{\alpha\beta,m} [\varepsilon_{jn}(\boldsymbol{\Omega}_L)]^l_m \tag{7.276a}$$

$$[\pi_{jn}(\boldsymbol{\Omega}_L)]_{\alpha} = \sum_l \sum_{m=-l}^{l} d^l_{\alpha,m} [\pi_{jn}(\boldsymbol{\Omega}_L)]^l_m. \tag{7.276b}$$

From the spherical components $[\varepsilon_{jn}]^l_m$ and $[\pi]^l_m$ we can define, through unitary transformations new tensorial components $[\varepsilon_{jn}]^l_q$ and $[\pi]^l_q$ which transform according to the irreducible representations of the crystal group:

$$[\varepsilon_{jn}(\boldsymbol{\Omega}_L)]^l_q = \sum_{m=-l}^{l} S^l_{mq}(L) [\varepsilon_{jn}(\boldsymbol{\Omega}_L)]^l_m \tag{7.277a}$$

$$[\pi_{jn}(\boldsymbol{\Omega}_L)]^l_q = \sum_{m=-l}^{l} S^l_{mq}(L) [\pi_{jn}(\boldsymbol{\Omega}_L)]^l_m. \tag{7.277b}$$

The unitary matrices $S^l(L)$ have been already encountered in the definition of surface harmonics (7.180). The index q is a shorthand notation for a composite index

$$q = (\Gamma, \mu, \nu) \tag{7.278}$$

where Γ denotes an irreducible representation of the site symmetry-group, μ labels the different occurrences of that representation, and ν numbers the different components in the case of a degenerate representation.

We can write

$$[\varepsilon_{jn}(\boldsymbol{\Omega}_L)]_{\alpha\beta} = \sum_l \sum_q [\varepsilon_{jn}(\boldsymbol{\Omega}_L)]^l_q s^l_{\alpha\beta,q}(L) \tag{7.279a}$$

and

$$[\pi_{jn}(\mathbf{\Omega}_L)]_\alpha = \sum_l \sum_q [\pi_{jn}(\mathbf{\Omega}_L)]^l_q s^l_{\alpha,q}(L) \tag{7.279b}$$

with the definitions:

$$s^l_{\alpha\beta,q}(L) = \sum_{m=-l}^{l} d^l_{\alpha\beta,m} S^{l*}_{mq}(L) \tag{7.280a}$$

and

$$s^l_{\alpha,q}(L) = \sum_{m=-l}^{l} d^l_{\alpha,m} S^{l*}_{mq}(L). \tag{7.280b}$$

The expressions of the Raman and infrared tensors (7.269) and (7.270) become

$$I^j_{\alpha\beta,\gamma\delta}(\omega) = \sum_{l_1} \sum_{q_1} \sum_{l_2} \sum_{q_2} I^{jl_1l_2}_{q_1q_2}(\omega) s^{l_1}_{\alpha\beta,q_1}(L) s^{l_2}_{\gamma\delta,q_2}(L) \tag{7.281a}$$

$$\mathcal{J}^j_{\alpha\beta}(\omega) = \sum_{l_2} \sum_{q_1} \sum_{l_2} \sum_{q_2} \mathcal{J}^{jl_1l_2}_{q_1q_2}(\omega) s^{l_1}_{\alpha,q_1}(L) s^{l_2}_{\beta,q_2}(L) \tag{7.281b}$$

together with the definitions:

$$I^{jl_1l_2}_{q_1q_2}(\omega) = \frac{1}{2\pi} \int_{-\infty}^{\infty} \exp(-\mathrm{i}\omega t)\, \mathrm{d}t \langle [\varepsilon_{jn}(\mathbf{\Omega}_L(0))]^{l_1}_{q_1} [\varepsilon_{jn}(\mathbf{\Omega}_L(t))]^{l_2}_{q_2} \rangle \tag{7.282a}$$

$$\mathcal{J}^{jl_1l_2}_{q_1q_2}(\omega) = \frac{1}{2\pi} \int_{-\infty}^{\infty} \exp(-\mathrm{i}\omega t)\, \mathrm{d}t \langle [\pi_{jn}(\mathbf{\Omega}_L(0))]^{l_1}_{q_1} [\pi_{jn}(\mathbf{\Omega}_L(t))]^{l_2}_{q_2} \rangle. \tag{7.282b}$$

It is important to note that the averages in (7.282) concern symmetry-adapted components of individual Raman and infrared tensors in the crystal axes. These can be derived from the symmetry-adapted components in the molecular axes, as a function of the rotation $\mathbf{\Omega}_L(t)$ which characterise the orientation of the L molecule with respect to lattice axes. Again, the transition from one symmetry-group to the other will be provided by the rotator functions.

The calculation first goes through the spherical components in the crystal axes. Inverting (7.276),

$$[\varepsilon_{jn}(\mathbf{\Omega}_L)]^l_m = \sum_q S^{l*}_{mq}(L) [\varepsilon_{jn}(\mathbf{\Omega}_L)]^l_q \tag{7.283a}$$

$$[\pi_{jn}(\mathbf{\Omega}_L)]^l_m = \sum_q S^{l*}_{mq}(L) [\pi_{jn}(\mathbf{\Omega}_L)]^l_q. \tag{7.283b}$$

Then, from the definition of irreducible spherical components

$$[\varepsilon_{jn}(\mathbf{\Omega}_L)]^l_m = \sum_{m'} D^l_{m'm}(\mathbf{\Omega}_L^{-1})[\varepsilon^0_{jn}]^l_{m'}$$

$$= \sum_{m'} D^{l*}_{mm'}(\mathbf{\Omega}_L)[\varepsilon^0_{jn}]^l_{m'} \tag{7.284a}$$

$$[\pi_{jn}(\mathbf{\Omega}_L)]^l_m = \sum_{m'} D^l_{m'm}(\mathbf{\Omega}_L^{-1})[\pi^0_{jn}]^l_{m'}$$

$$= \sum_{m'} D^{l*}_{mm'}(\mathbf{\Omega}_L)[\pi^0_{jn}]^l_{m'}. \tag{7.284b}$$

Introducing the expression of the Wigner matrices, $D^l_{mm'}(\mathbf{\Omega})$, as a function of the rotator functions, $R^l_{qq'}(\mathbf{\Omega})$

$$D^l_{mm'}(\mathbf{\Omega}) = \sum_q \sum_{q'} S^l_{mq}(L) R^l_{qq'}(\mathbf{\Omega}) S^{l*}_{m'q'}(M) \tag{7.285}$$

we get finally:

$$[\varepsilon_{jn}(\mathbf{\Omega}_L)]^l_q = \sum_{q'} R^l_{qq'}(\mathbf{\Omega}_L)[\varepsilon^0_{jn}]^l_{q'} \tag{7.286a}$$

$$[\pi_{jn}(\mathbf{\Omega}_L)]^l_q = \sum_{q'} R^l_{qq'}(\mathbf{\Omega}_L)[\pi^0_{jn}]^l_{q'}. \tag{7.286b}$$

Here, $[\varepsilon^0_{jn}]^l_{q'}$ and $[\pi^0_{jn}]^l_{q'}$ are symmetry-adapted components for the molecule group. These are related to cartesian components $[\varepsilon^0_{jn}]_{\alpha\beta}$ of the Raman and infrared individual tensors in molecular frame through:

$$[\varepsilon^0_{jn}]_{\alpha\beta} = \sum_l \sum_{q'} [\varepsilon^0_{jn}]^l_{q'} s^l_{\alpha\beta,q'}(M) \tag{7.287a}$$

$$[\pi^0_{jn}]_{\alpha} = \sum_l \sum_{q'} [\pi^0_{jn}]^l_{q'} s^l_{\alpha,q'}(M) \tag{7.287b}$$

with the definitions, analogous to (7.280)

$$s^l_{\alpha\beta,q'}(M) = \sum_{m'} d^l_{\alpha\beta,m'} S^{l*}_{m'q'}(M) \tag{7.288a}$$

$$s^l_{\alpha,q'}(M) = \sum_{m'} d^l_{\alpha,m'} S^{l*}_{m'q'}(M). \tag{7.288b}$$

The $S^l(M)$ are the unitary matrices which define the surface harmonics for the molecule symmetry group (7.280).

Plugging (7.286) into (7.282), we obtain finally:

$$I^{jl_1l_2}_{q_1q_2}(\omega) = \frac{1}{2\pi}\int_{-\infty}^{\infty} \exp(-\,\mathrm{i}\omega t)\,\mathrm{d}t \sum_{q_1'} \sum_{q_2'} [\varepsilon^0_{jn}]^{l_1}_{q_1'} [\varepsilon^0_{jn}]^{l_2}_{q_2'}$$
$$\times \langle R^{l_1}_{q_1q_1'}(\mathbf{\Omega}_L(0)) R^{l_2}_{q_2q_2'}(\mathbf{\Omega}_L(t)) \rangle \otimes \phi^{\mathrm{vib}}_j(\omega) \tag{7.289a}$$

and

$$I^{j}_{\alpha\beta,\gamma\delta}(\omega) = \sum_{l_1}\sum_{q_1}\sum_{l_2}\sum_{q_2} I_{q_1q_2}^{jl_1l_2}\, s^{\,l_1}_{\alpha\beta,q_1}(L)\, s^{\,l_2}_{\gamma\delta,q_2}(L). \tag{7.289b}$$

Similarly,

$$\mathcal{J}^{jl_1l_2}_{q_1q_2}(\omega) = \frac{1}{2\pi}\int_{-\infty}^{\infty} \exp(-\,\mathrm{i}\omega t)\,\mathrm{d}t \sum_{q_1'}\sum_{q_2'} [\pi^0_{jn}]^{l_1}_{q_1'}\,[\pi^0_{jn}]^{l_2}_{q_2'} \times \langle R^{\,l_1}_{q_1q_1'}(\boldsymbol{\Omega}_L(0)) R^{\,l_2}_{q_2q_2'}(\boldsymbol{\Omega}_L(t))\rangle \otimes \phi^{\mathrm{vib}}_j(\omega) \tag{7.290a}$$

and

$$\mathcal{J}^{j}_{\alpha\beta}(\omega) = \sum_{l_1}\sum_{q_1}\sum_{l_2}\sum_{q_2} \mathcal{J}^{jl_1l_2}_{q_1q_2}(\omega)\, s^{\,l_1}_{\alpha,q_1}(L)\, s^{\,l_2}_{\beta,q_2}(L). \tag{7.290b}$$

The main advantage in writing the Raman and infrared tensors in the form of (7.289) and (7.290) is that the relevant symmetries for both site and molecule groups are clearly evidenced, for the polarisation conditions of the incident and scattered lights.

Equations (7.289) and (7.290) may appear as rather complicated expressions. However, we are concerned with dipole moments and polarisability tensors which are first rank tensors and second rank symmetric tensors, respectively. A first rank tensor projects only once on the components relative to $l = 1$, while a second rank symmetric tensor projects twice, on the components relative to $l = 0$ and $l = 2$. Thus the sums in (7.290b) restrict to $l_1 = l_2 = 1$ and the sums in (7.289b) to $l_1, l_2 = 0, 2$.

Equations (7.289) and (7.290) are analogous to (7.204). They show that the observed intensities result from the convolution of a vibrational scattering function $\phi^{\mathrm{vib}}_j(\omega)$ relative to the mode j with a rotational scattering function, $I^{jR}_{\alpha\beta,\gamma\delta}(\omega)$ and $\mathcal{J}^{jR}_{\alpha\beta}(\omega)$, according to

$$I^{j}_{\alpha\beta,\gamma\delta}(\omega) = I^{jR}_{\alpha\beta,\gamma\delta}(\omega) \otimes \phi^{\mathrm{vib}}_j(\omega) \tag{7.291a}$$

$$\mathcal{J}^{j}_{\alpha\beta}(\omega) = \mathcal{J}^{jR}_{\alpha\beta}(\omega) \otimes \phi^{\mathrm{vib}}_j(\omega). \tag{7.291b}$$

Both $I^{jR}_{\alpha\beta,\gamma\delta}(\omega)$ and $\mathcal{J}^{jR}_{\alpha\beta}(\omega)$ involve correlation functions of symmetry-adapted (rotator) functions

$$C^{\,l_1\;l_2}_{q_1q_1'q_2q_2'}(t) = \langle R^{\,l_1}_{q_1q_1'}(\boldsymbol{\Omega}(0)) R^{\,l_2}_{q_2q_2'}(\boldsymbol{\Omega}(t))\rangle. \tag{7.292}$$

Making explicit the infinite-time limit,

$$\tilde{C}^{\,l_1\;l_2}_{q_1q_1'\;q_2q_2'}(t) = C^{\,l_2\;l_2}_{q_1q_1'\;q_2q_2'}(t) - C^{l_1\;l_2}_{q_1q_1'\;q_2q_2'}(\infty) \tag{7.293}$$

in order to deal with correlation functions which tend to zero at infinite time, we get formally:

$$I^{jR}_{\alpha\beta,\gamma\delta}(\omega) = I^{j\,\mathrm{elas}}_{\alpha\beta,\gamma\delta}(\omega) + I^{j\,\mathrm{quasi}}_{\alpha\beta,\gamma\delta}(\omega) \tag{7.294a}$$

$$\mathcal{J}^{jR}_{\alpha\beta}(\omega) = \mathcal{J}^{j\,\mathrm{elas}}_{\alpha\beta}(\omega) + \mathcal{J}^{j\,\mathrm{quasi}}_{\alpha\beta}(\omega). \tag{7.294b}$$

As in the case of neutron scattering, the light intensity appears to be composed of a sharp delta component, superimposed on a wider contribution, whose width depends on the dynamics of the rotational motion. Thus, in principle, the same information can be obtained from neutron and light spectroscopy methods. However, in this latter case, some limitations are imposed.

(i) The number of correlation functions accessible is restricted to $l \leqslant 2$.

(ii) The components of the Raman polarisability tensor or of the dielectric tensor are not known.

However, some important features of the description of plastic phases can be analysed by this formalism. We shall report on recent Raman studies of cyanoadamantane (Sauvajol *et al* 1982) and bicyclo[2,2,2]octane (Sauvajol 1983) where conclusions of x-ray and neutron scattering could be confirmed.

7.9.2 Measurement of the orientational probability distribution $P(\mathbf{\Omega})$

The orientational probability function $P(\mathbf{\Omega})$ describes the probability, for a molecule to have the orientation $\mathbf{\Omega}$. It can be developed on the canonical basis of rotator functions $R^l_{qq'}(\mathbf{\Omega})$ adapted to the site and the molecule symmetry (see §7.7.4), according to (see (7.195))

$$P(\mathbf{\Omega}) = \sum_l \sum_q \sum_{q'} \frac{(2l+1)}{8\pi^2} A^l_{qq'} R^l_{qq'}(\mathbf{\Omega}). \tag{7.295}$$

This development allows only a reduced set of relevant and non-redundant coefficients. Yvinec and Pick (1980) have given the full prescription for their derivation. Our purpose in this part is to show how the measurement of the integrated intensity of Raman internal lines provides a numerical determination of some of them. So we shall consider whether it is strictly not true that the relevant coefficients $A^l_{qq'}$ in (7.295) are those for which the indices q and q' belong to the identity representation of respectively the site and the molecule group.

The integrated intensity of a Raman internal line

$$S^j_{\alpha\beta,\gamma\delta} = \int_{-\infty}^{\infty} I^j_{\alpha\beta,\gamma\delta}(\omega)\, \mathrm{d}\omega$$

$$= \sum_{l_1} \sum_{q_1} \sum_{l_2} \sum_{q_2} S^{jl_1l_2}_{q_1q_2} s^{l_1}_{\alpha\beta,q_1}(L) s^{l_2}_{\alpha\beta,q_2}(L) \tag{7.296a}$$

$$S^{jl_1l_2}_{q_1q_2} = \sum_{q_1'} \sum_{q_2'} [\varepsilon^0_{jn}]^{l_1}_{q_1'} [\varepsilon^0_{jn}]^{l_2}_{q_2'} \langle R^{l_1}_{q_1q_1'}(\mathbf{\Omega}_L(0)) R^{l_2}_{q_2q_2'}(\mathbf{\Omega}_L(0)) \rangle n(\omega_j) \tag{7.296b}$$

where $n(\omega_j)$ is the Bose factor for the mode j with mean frequency ω_j.

The width of the vibrational scattering function $\phi_j^{\text{vib}}(\omega)$ has been assumed to be negligible, so that

$$\phi_j^{\text{vib}}(\omega) = n(\omega_j)\delta(\omega). \tag{7.297}$$

The thermal averages in (7.296b) become

$$\begin{aligned}\langle R^{l_1}_{q_1q_1'}(\boldsymbol{\Omega}_L(0))R^{l_2}_{q_2q_2'}(\boldsymbol{\Omega}_L(0))\rangle &= \int_{-\infty}^{\infty} R^{l_1}_{q_1q'}(\boldsymbol{\Omega})R^{l_2}_{q_2q_2'}(\boldsymbol{\Omega})P(\boldsymbol{\Omega})\,\mathrm{d}\boldsymbol{\Omega} \\ &= \sum_{l_3}\sum_{q_3}\sum_{q_3'}\frac{(2l_3+1)}{8\pi^2}A^{l_3}_{q_3q_3'}\int R^{l_1}_{q_1q_1'}(\boldsymbol{\Omega})R^{l_2}_{q_2q_2'}(\boldsymbol{\Omega})R^{l_3}_{q_3q_3'}(\boldsymbol{\Omega})\,\mathrm{d}\boldsymbol{\Omega} \\ &= \sum_{l_3}\sum_{q_3}\sum_{q_3'}A^{l_3}_{q_3q_3'}C^{l_1l_2l_3}_{q_1q_2q_3}(L)C^{*\,l_1l_2l_3}_{q_1'q_2'q_3'}(L)\end{aligned} \tag{7.298}$$

where the coefficients $C^{l_1l_2l_3}_{q_1q_2q_3}(L)$ and $C^{l_1l_2l_3}_{q_1'q_2'q_3'}(M)$ have been already defined (equation (7.254)) in terms of Clebsch–Gordan coefficients. From the properties of the Clebsch–Gordan coefficients, the only non-vanishing terms in (7.298) are such that

$$|l_1 - l_2| \leqslant l_3 \leqslant l_1 + l_2.$$

Therefore, because the two indices l_1 and l_2 are restricted to the values 0 or 2, only coefficients $A^{l_3}_{q_3q_3'}$ with $l_3 \leqslant 4$ can be determined.

A major difficulty occurs because, in the general case, the constants $[\varepsilon^0_{jn}]^l_q$ characterising the Raman activity of the mode are not known. However, in many cases, it is possible to use intensity measurements with different polarisation to eliminate these constants.

The cyanoadamantane molecule ($C_{10}H_{15}CN$) exhibits a C_{3v} symmetry. The 75 internal modes of cyanoadamantane can be decomposed into 17 modes with symmetry A_1, 25 modes with symmetry E and 8 modes with symmetry A_2. The Raman polarisability tensor, relative to an A_1 mode is

$$\boldsymbol{\varepsilon}^0(A_1) = \begin{pmatrix} a & 0 & 0 \\ 0 & a & 0 \\ 0 & 0 & b \end{pmatrix}. \tag{7.299}$$

The expansion of $P(\boldsymbol{\Omega})$ into rotator functions reads:

$$P(\boldsymbol{\Omega}) = \frac{1}{8\pi^2}[1 + 9A_4^{11} + \ldots]. \tag{7.300}$$

The integrated intensities of lines of internal modes with A_1 symmetry have been reported in table 7.3 for two crystal orientations and different polarisation conditions. In both orientations the scattered light issuing from the crystal along the direction of a fourfold (y) axis is analysed. In the first one, the incident beam enters the sample along another fourfold (x) axis and in the second case it enters along a twofold [110] axis. The geometry is illustrated in figure 7.17. The two sums

$S_{VV} + S_{VH}$ and $S'_{VV} + S'_{VH}$ are equal to each other. This quantity is taken as invariant for the normalisation of the experiments. From the measurement of the experimental ratio

$$R_{exp} = \frac{S'_{VH}}{S_{VH}} \tag{7.301}$$

and from the theoretical calculation

$$\frac{S'_{VH}}{S_{VH}} = \frac{1 + \frac{16}{7}f'_4}{1 - \frac{16}{7}f'_4} \tag{7.302}$$

$$A_4^{11} = \tfrac{8}{9}\sqrt{\tfrac{12}{7}}f'_4 \tag{7.303}$$

the following value was obtained from analysis of two lines at 382.5 cm^{-1} and 900 cm^{-1}

$$\nu = 382.5\ cm^{-1} \qquad A_4^{11} = 0.56 \pm 0.02$$

$$\nu = 900.0\ cm^{-1} \qquad A_4^{11} = 0.57 \pm 0.01.$$

In both cases, these values are in full agreement with those obtained from x-ray crystallographic analysis: $A_4^{11} = 0.57 \pm 0.06$. A similar analysis was made in the case of bicyclo-octane, which is also in agreement with the structure analysis.

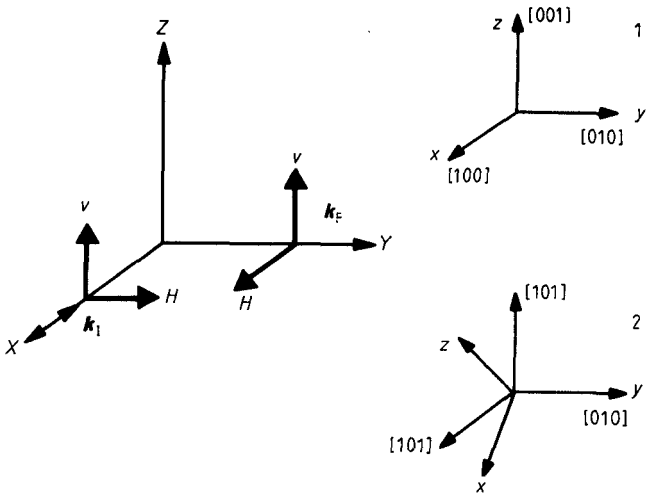

Figure 7.17 Experimental geometry corresponding to the different polarisation conditions of table 7.2.

Table 7.3 Integrated intensities for internal modes with A_1 symmetry in cyanoadamantane.

	Polarisation	
Orientation 1	$x(zz)y$	$S_{VV} = f^2 + \frac{4}{5}g^2(1 + \frac{16}{7}f_4')$
	$x(zx)y$	
	$x(yz)y$	$S_{VH} = \frac{3}{5}g^2(1 - \frac{32}{21}f_4')$
	$x(yx)y$	
Orientation 2	$(x - z)(x + z, x + z)y$	$S'_{VV} = f^2 + \frac{4}{5}g^2(1 - \frac{4}{7}f_4')$
	$(x - z)(x + z, x - z)y$	$S'_{VH} = \frac{3}{5}g^2(1 + \frac{16}{7}f_4')$
	$(x - z)(y, x + z)y$	
	$(x - z)(y, x - z)y$	$S'_{HH} = \frac{3}{5}g^2(1 - \frac{32}{21}f_4')$

$f = \frac{1}{3}(2a + b)$; $f_4' = \frac{9}{8}(\frac{7}{12})^{1/2}A_4^{11}$; $g = \frac{1}{3}(a - b)$

7.9.3 Analysis of internal-line broadening

As an example of an analysis of the broadening of Raman lines relative to internal modes in terms of the formalism described above, we report here the detailed study of bicyclo[2,2,2]octane (Sauvajol 1983). The molecule symmetry being D_{3h}, (see figure 6.27), three types of symmetry, A_1', E' and E'', are active in Raman spectroscopy. When analysing the Raman diffusion tensor in terms of correlation functions of rotator functions, it appears that the modes with symmetry A_1' involve rotator functions which take into account only the tumbling of the threefold molecule axis from one [111] lattice direction to another. Conversely, modes with E' and E'' symmetry also take into account the uniaxial rotation of the molecule about its C_3 axis. The shapes and the widths of different Raman lines were therefore analysed, in order to obtain the relaxation times relative to each motion and to compare them to the values given by the neutron scattering technique (Bée *et al* 1982). The different correlation functions

$$C^{l_1\ l_2}_{q_1q_1'q_2q_2'}(t) = \langle R^{l_1}_{q_1q_1'}(\mathbf{\Omega}(0))R^{l_2}_{q_2q_2'}(\mathbf{\Omega}(t))\rangle$$

were evaluated on the basis of a jump model in which the probability for a molecule to be in the orientation $\mathbf{\Omega}(t)$ at time t, if it was in $\mathbf{\Omega}(0)$ at time zero is expressed by

$$P(\mathbf{\Omega}(0), \mathbf{\Omega}(t)) = \frac{1}{N}\sum_a\sum_b \delta(\mathbf{\Omega}(0) - \mathbf{\Omega}_a)P(\Omega_a, \Omega_b; t)\delta(\mathbf{\Omega}(t) - \mathbf{\Omega}_b) \tag{7.304}$$

the sums over indexes a and b run over a set of N well-defined orientations $\mathbf{\Omega}_a$, $\mathbf{\Omega}_b \cdot P(\mathbf{\Omega}_a\mathbf{\Omega}_b; t)$ is the probability of a molecule being

in the orientation $\mathbf{\Omega}_a$ at time t if it was in $\mathbf{\Omega}_b$ at time zero. We have seen in chapter 6 that the set of probabilities $P(\mathbf{\Omega}_a, \mathbf{\Omega}; t)$ could be determined from the solution of a system of coupled master equations. It is easier to apply the formalism of Thibaudier and Volino (1975) to evaluate the correlation functions of the rotator functions. We obtain without difficulty:

$$C^{l_1\ l_2}_{q_1q_1'\ q_2q_2'}(t) = \sum_{\mu} \psi^{l_1\ l_2}_{\mu q_1q_1'\ q_2q_2'} \exp(-t/\tau_\mu) \tag{7.305a}$$

with:

$$\psi^{l_2\ l_2}_{\mu q_1q_1'q_2q_2'} = \frac{1}{N}\sum_{\alpha}\sum_{\nu}\sum_{\eta}\frac{\chi^{\mathrm{Ee}}_{\mu}\chi^{\nu\eta}_{\mu}}{g}\sum_{\mathrm{C}_\nu}\sum_{\mathrm{M}_\eta} R^{l_1}_{q_1q_1'}(\mathbf{\Omega}_a)R^{l_2}_{q_1q_2'}(\mathrm{C}_\nu\mathrm{M}_\eta\mathbf{\Omega}_a). \tag{7.305b}$$

The sum over μ runs over all the irreducible representations of the group product of the molecule and lattice groups. The dimension of this group is g. The lattice group is formed of the rotations C_ν, the molecule group of the rotations M_η. The identity operations are E and e, respectively and $\chi^{\nu\eta}_{\mu}$ are the character of the product of the two rotations $\mathrm{C}_\nu\mathrm{M}_\eta$ in the representation μ.

With the help of judicious symmetry considerations, Sauvajol evaluated the relevant $\psi^{l_1\ l_2}_{\mu q_1q_1'q_2q_2'}$ coefficients and, using several Raman lines, could obtain the two correlation times $\tau_{\mathrm{C}_4} \simeq 5.4 \times 10^{-12}$ s and $\tau_{\mathrm{M}_6} \simeq 3.0 \times 10^{-12}$ s for the reorientations about crystal and molecule axes, respectively. The corresponding relaxation times obtained from IQNS are $\tau_{\mathrm{C}_4} = 7.4 \times 10^{-12}$ s and $\tau_{M_6} = 1.8 \times 10^{-12}$ s at the same temperature $T = 295$ K.

In this section, we have somewhat emphasised the application of the rotator function formalism to Raman scattering. This formalism appears very fruitful in the sense that it allows us to obtain, via different techniques, data which are directly comparable to each other. Moreover it introduces symmetry considerations which often provide great simplification of the problem. Another conclusion is that Raman and neutron spectroscopies appear very complementary. This is a major feature which should be developed in the future.

Chapter 8 Single-Crystal and Partially Oriented Sample Studies

Although the incoherent scattering law does not involve any selection rule in the reciprocal space, it still depends on the scattering vector. One can take advantage of this geometrical experimental parameter in order to get more information on the problem under test. Powder samples average the relevant signal over all the Q-directions in space and leave only the dependence on the modulus for Q. This is already an enormous advantage of the neutron scattering technique over other spectroscopic methods. The primordial interest in EISF as a source of information about the geometry of motion has been heavily emphasised in chapters 6 and 7. Besides, when jump distances related to various independent motions largely differ from each other, analysis of spectra obtained at large Q or small Q values enables us to determine the relevant correlation times. In the next chapter, we shall illustrate how, for a particle diffusing inside a restricted volume, the variation as a function of Q of the h.w.h.m. of the broadened part of the quasielastic spectra yields the knowledge of the size of the cavity. Here, we are interested in the macroscopically anisotropic specimen and the use of the dependence of the scattering law on the orientation of the scattering vector with respect to precise directions within the material (crystallographic axes, direction of preferential alignment, etc). Reorientations of molecules or chemical groups lead to a scattering law where the Q-dependence (via the structure factors) is well separated from the $\hbar\omega$-dependence (via the lorentzian functions). Judicious orientations of

the sample with respect to the laboratory frame permit us to reduce and even to eliminate from the scattering law the contributions of some terms. Then, the characteristic times related to the others can be determined. On the other hand, scattering laws related to translational diffusion problems involve the Q-dependence directly in the lorentzian term. For partially oriented samples, the average over the Q-directions yields a deviation of the signal from a lorentzian shape.

8.1 Single-Crystal Studies

From a mathematical point of view, single-crystal specimens provide the purest example of neutron scattering from oriented samples. However, the numerous technical difficulties arising in this type of experiment have, until now, severely restricted the number of measurements effectively performed.

Apart from the difficulty of producing single-crystals of acceptable quality at the temperature required for the measurements, and thus assuming that the problem of eventual destructive phase-transitions has been solved, the major question arises from the size and the shape of the sample. Indeed, crystals are macroscopically bulk specimens, with a cross section roughly twice that of the same chemical compound in powder form. Hydrogen compounds generally require very small neutron paths in them ($\simeq 0.5$ mm) in order to keep a reasonable transmission and to neglect multiple scattering effects. The IQNS technique cannot deal with so small a specimen. To get a sufficiently scattered neutron flux, one has to use either rod-shaped samples with small diameter or plane slabs cut as thinly as possible. To a certain extent, the use of crystals formed by solid solutions in which deuterated molecules have been randomly substituted for hydrogenated ones imposes less severe conditions on the slab thickness or the rod diameter. However, this technique, providing that it is effectively possible and that it does not modify the physical properties of the specimen under test, is necessarily limited because the random substitution introduces in the measured intensity a non-negligible part of 'diffuse scattering'. That contribution, essentially elastic in nature, is more important at low Q values and originates from the coherent scattering from non-identical molecules randomly distributed.

We shall close these general considerations by pointing out that the different orientations of the scattering vector in a crystal study are obtained by rotating the sample with respect to the incident beam. Therefore, once a sample shape has been chosen in order to minimise the absorption and the multiple scattering effects for a given orientation, it is unlikely also to be optimised for another orientation, and it may be

necessary to use several samples individually adapted for each orientation.

We shall not further discuss the technical aspect of these experiments and refer the reader to original papers for more details. In this section, we shall focus our analysis essentially on the mathematical side of this matter, i.e. how the different terms in the scattering law can be revealed by judicious choices of the orientations of the crystal.

8.1.1 C_4 rotational jumps in plastic adamantane

Adamantane, $C_{10}H_{16}$, has already been presented in chapter 6, where it provided an illustration of the evaluation of the neutron scattering law with the help of group theory. Referring to information given in §6.9.6 for the mathematical details and the conclusions of the original IQNS studies on a powder sample, and also to the results of other techniques, we shall briefly remind the reader that, according to the occurrence of precise reorientations about crystal axes, i.e. according to the value of the related jump rates in front of the instrument resolution, three models are possible. These can be described as follows:

(i) model C: $\tau_{C_2}^{-1}$, $\tau_{C_3}^{-1}$ and $\tau_{C_4}^{-1}$ are all much smaller than the instrument resolution. The only relevant rotations are the 180° jumps about the three $\langle 100 \rangle$ axes.

(ii) model B: $\tau_{C_2}^{-1}$ and $\tau_{C_4}^{-1}$ both tend toward zero. Therefore the molecule performs 120° jumps about $\langle 111 \rangle$ lattice axes. The existence of 180° jumps about $\langle 100 \rangle$ axes is also allowed.

(iii) model A: there are either C_4 jumps about $\langle 100 \rangle$ lattice axes, or C_4' jumps about $\langle 110 \rangle$ directions, or both. Other reorientations (i.e. C_2 jumps or C_3 jumps) can also exist, but not necessarily.

The three models described above lead to different EISF as illustrated in figure 8.1, in the case of a polycrystalline sample. Clearly, model C differs strongly from the others. But the EISFS corresponding to the hypotheses A and B remain close to each other, even at large momentum transfer value. The reason is the rather small contribution of the irreducible representation Γ_2 with symmetry A_2, resulting from averaging the structure factor $a_2(\boldsymbol{Q})$ over all $\boldsymbol{Q}$-directions in space. The second feature is the presence of the four quasielastic contributions, whatever the value of the momentum transfer modulus. Their relative contributions vary only little, in the usual Q range ($Q \leqslant 2.0\,\text{Å}^{-1}$) accessible to time-of-flight (t.o.f) instruments, with an acceptable resolution. These are the main reasons why it was so difficult to distinguish between the different models with a polycrystalline sample. Backscattering high-resolution analyses (Lechner and Heidemann 1976) made it possible to decide between models A, B and C in favour of model A. But t.o.f.

measurements could not distinguish, among the various possibilities, the relevant reorientations on the 10^{-11} s time-scale.

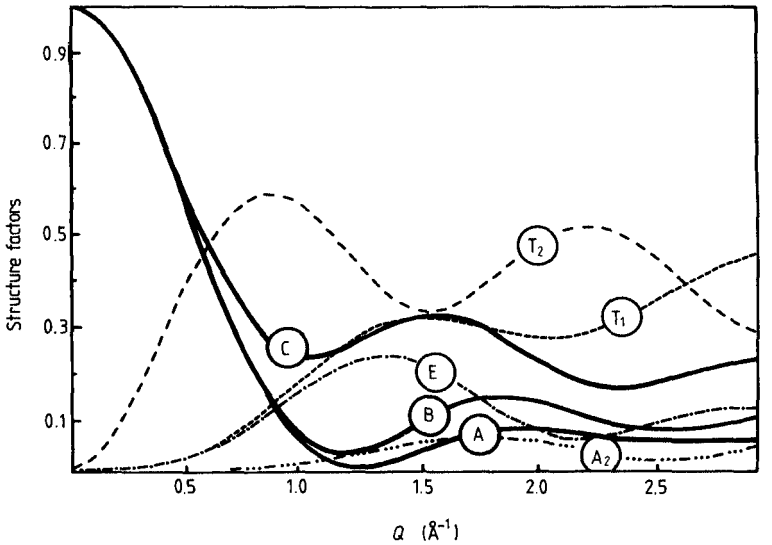

Figure 8.1 Elastic (EISF) and quasielastic structure factors for polycrystalline adamantane. The EISF curves are labelled A, B, C, according to the three relevant models. The structure factors $a_2(Q)$, $a_3(Q)$, $a_4(Q)$ and $a_5(Q)$ are related to the irreducible representations A_2, E, T_1 and T_2, respectively.

Conversely, when using a single-crystal specimen, the variations of the structure factors are enhanced, especially because of the presence in their expression of the scalar products of the scattering vector with the different jump vectors. Figure 8.2 illustrates these variations as a function of both the modulus of $\boldsymbol{Q}$ and of its direction with respect to lattice axes. The most striking feature is the absence of the contribution of certain irreducible representations in several directions. For instance, when Q lies along any $\langle 100 \rangle$ or $\langle 110 \rangle$ direction, the structure factor $a_2(\boldsymbol{Q})$ is strictly vanishing. So the EISFs related to models A and B are identical. Likewise, when $\boldsymbol{Q}$ is oriented along $\langle 111 \rangle$, it is seen from figure 8.2 that $a_3(\boldsymbol{Q})$ is equal to zero, leading to the same EISF for models B and C. Finally $a_4(\boldsymbol{Q})$ vanishes along the $\langle 100 \rangle$ direction.

Concerning the EISF, its value predicted by the model A in the range $Q < 2.0$ Å^{-1} is close to the value for a powder sample, whatever the $\boldsymbol{Q}$ direction. For model C, when $\boldsymbol{Q}$ is aligned along $\langle 110 \rangle$ lattice axes, the difference with respect to the powder case is weak, while it is appreciable along the $\langle 100 \rangle$ and $\langle 110 \rangle$ directions, in accordance with the

amplitude of $a_3(\boldsymbol{Q})$: large along $\langle 100 \rangle$ and vanishing along $\langle 111 \rangle$. It is noteworthy that along $\langle 111 \rangle$ the difference between the EISFs predicted by the models A and B is larger than in the powder case. Therefore, a single-crystal experiment should easily distinguish model C from the other two with $\boldsymbol{Q}$ along $\langle 100 \rangle$ and should decide between models A and B with an orientation of $\boldsymbol{Q}$ along $\langle 111 \rangle$.

Time-of-flight and backscattering machines have been described in chapter 3. Clearly, the geometry of these instruments does not enable us to obtain, in a single measurement, spectra corresponding to wavevector-transfer vectors lying along the same direction in reciprocal space: in figure 8.3 the momentum transfers (for elastic scattering, $\hbar\omega = 0$) associated with the various scattering angles cannot be collinear. That constitutes a serious difficulty in the study of single crystals by the usual IQNS techniques. In the case of the experiments with adamantane on which we are reporting, an exhaustive analysis of the possibilities for the shape of the crystal and for its orientation with respect to the incident beam (taking into account numerous factors such as transmission, multiple scattering, etc) led to the following solution.

The sample had the shape of a thin slab cut normal to the $\langle 1\bar{1}0 \rangle$ direction and thus coinciding with the plane $(\bar{1}10)$ containing the three directions $\langle 110 \rangle$, $\langle 111 \rangle$ and $\langle 001 \rangle$ (see figure 8.3). By rotating the sample about the normal to its plane, it was thus possible to bring successively each of these directions into the horizontal scattering plane, which was then identical with the (001), $(\bar{1}\bar{1}2)$ and (110) lattice planes, respectively. Following the earlier t.o.f. experiments (Bée *et al* 1980b), another series of measurements was carried out, using the backscattering technique (Bée *et al* 1988), at an incident wavelength $\lambda = 2.23$ Å. The angle between the incoming neutron beam and the sample plane was 120°, when $\boldsymbol{Q}$ was lying along the relevant crystal directions at a scattering angle $2\theta = 60°$, with a modulus $Q = 4.32$ Å^{-1}.

Figure 8.4. illustrates the variation of the EISF and of the quasielastic structure factors as a function of the scattering angle, for the three orientations of the single crystal. The particular value of the scattering angle $2\theta = 60°$ has been evidenced. With (001) as scattering plane, the quasielastic structure factor $a_2(\boldsymbol{Q})$ vanishes at all scattering angles. Moreover, it can also be neglected, in the Q range of analysis, when the scattering plane coincides with (110). Therefore, for these two orientations, the EISFs corresponding to models A and B are identical.
Conversely, in the third case with $(\bar{1}\bar{1}2)$ as scattering planes, the three EISFs are different and, above all, the difference between the models A and B is larger than in the powder case.

We have somewhat insisted on this example to illustrate the geometrical aspects of single-crystal studies. From a refinement to the experimental data of the correlation times given by (6.107), Bée *et al*

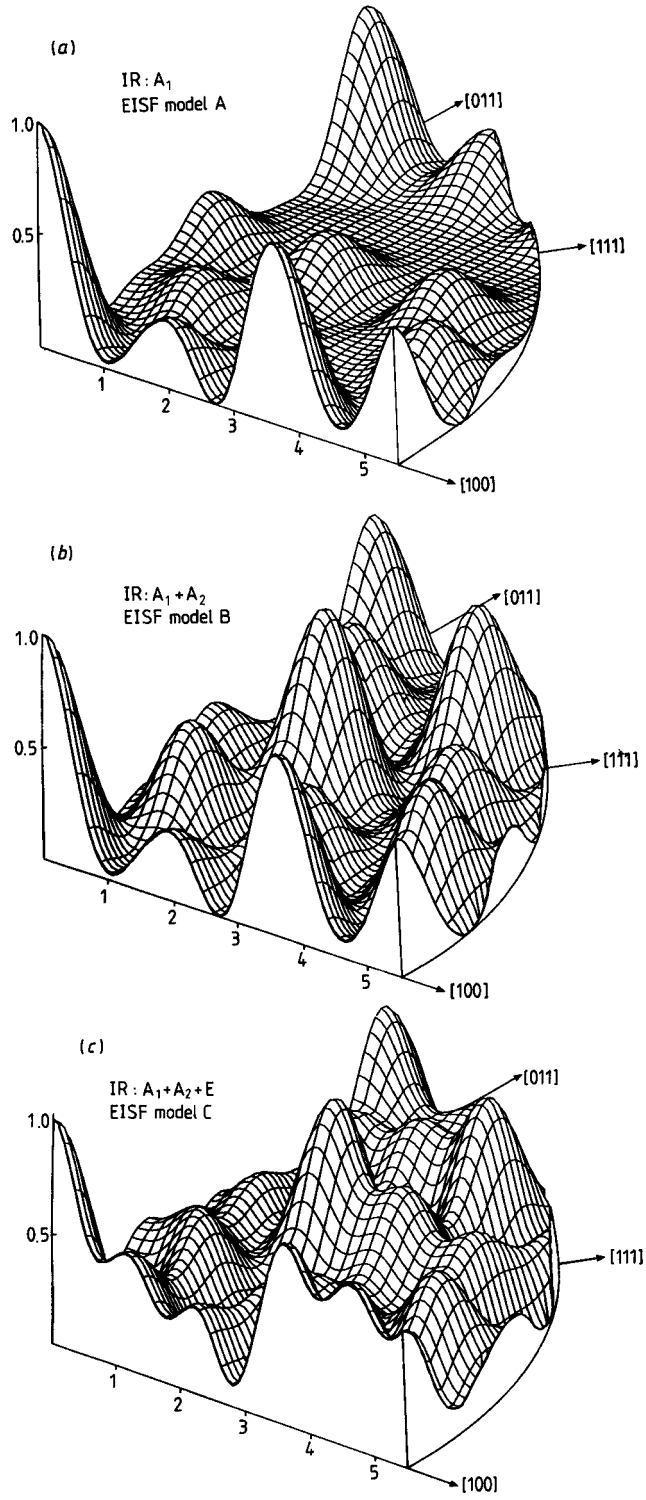
(a)
IR: A_1
EISF model A
1.0
0.5
[011]
[111]
[100]
1
2
3
4
5
(b)
IR: $A_1 + A_2$
EISF model B
1.0
0.5
[011]
[1$\bar{1}$1]
[100]
1
2
3
4
5
(c)
IR: $A_1 + A_2 + E$
EISF model C
1.0
0.5
[011]
[111]
[100]
1
2
3
4
5

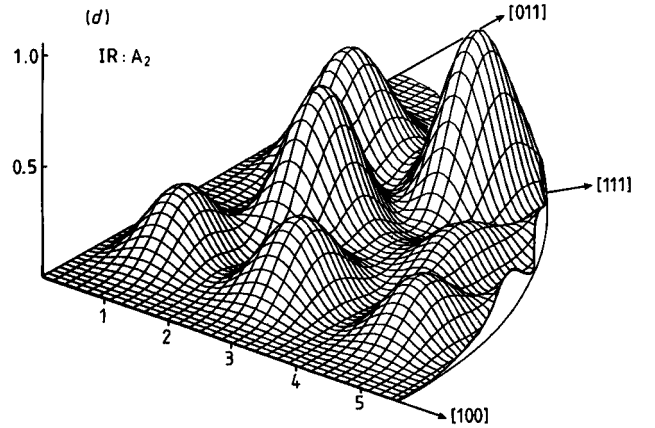
(d)
IR: A_2
1.0
0.5
[011]
[111]
[100]
1
2
3
4
5

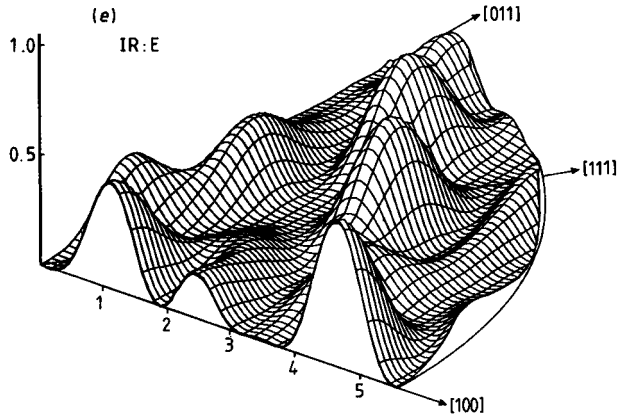
(e)
IR: E
1.0
0.5
[011]
[111]
[100]
1
2
3
4
5

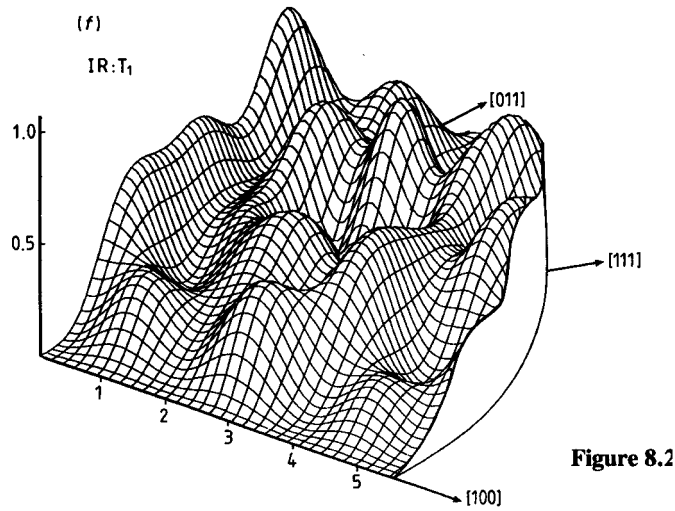
(f)
IR: T_1
1.0
0.5
[011]
[111]
[100]
1
2
3
4
5

Figure 8.2

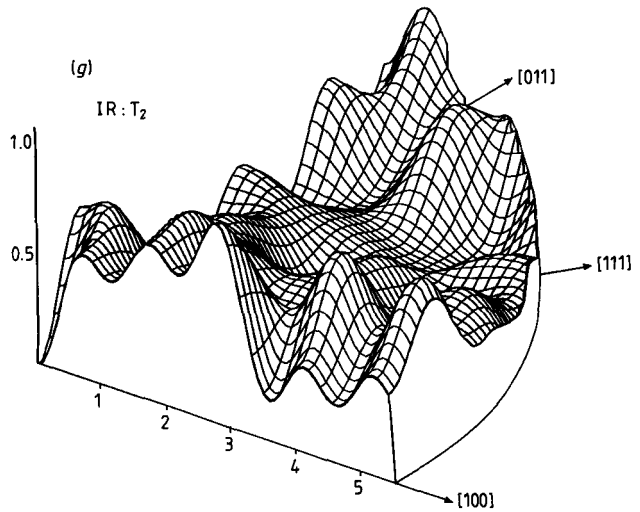

Figure 8.2 Variation of the elastic and quasielastic structure factors as a function of $\boldsymbol{Q}$ in the $[\bar{1}10]$ plane of the reciprocal lattice containing the three [001], [111] and [110] directions.

(1980c, 1988) could prove that, on the 10^{-11} s time-scale, the only existing cubic rotations are effectively 90° rotational jumps of the molecules about fourfold symmetry axes of the crystal lattice, with a correlation time and an activation energy given by

$$\tau_{C_4}^{-1} = 5.6 \times 10^{12} \exp(-1397/T)\ \mathrm{s}^{-1}.$$

8.1.2 Ammonium chloride NH_4Cl

The ammonium ion appears as a well-suited subject of study for a better understanding of the angle-dependent interactions of a polyatomic ion with other atoms or ions in the crystal. Its main interesting properties are the following:

(i) It is highly symmetric (T_d).

(ii) It has a small moment of inertia, I; its rotational constant $\hbar^2/2I$ is equal to $8.4K$.

(iii) It is encountered in a large variety of chemical compounds ($(NH_4)_2SnCl_6$, NH_4Br, NH_4Cl, etc) with different crystal structures. Therefore the influence of different symmetries and strengths of the orientational potential that it experiences can easily be investigated.

(iv) There are four hydrogen atoms in its structure which permit its study by the IQNS technique, with the possibility of total or partial deuteration.

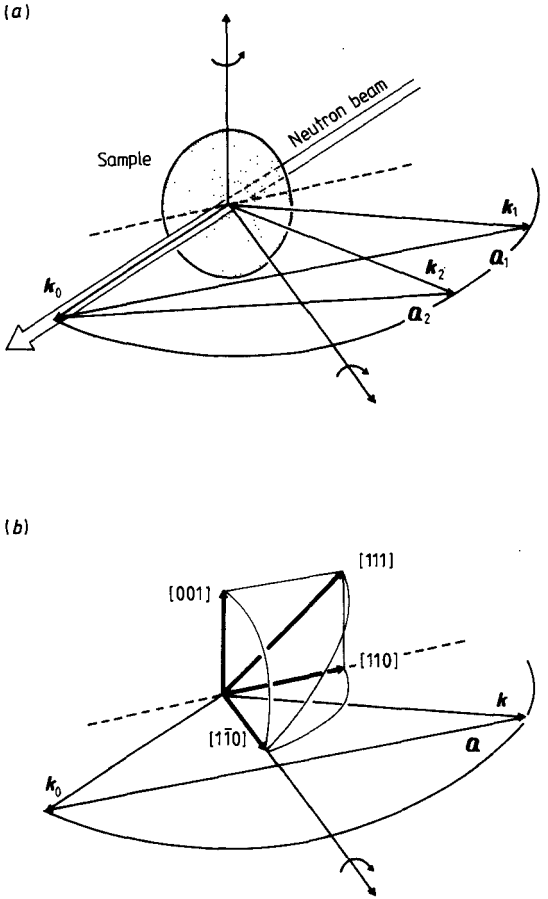

Figure 8.3 (*a*) Geometrical arrangement in a time-of-flight or back-scattering experiment. The extremity of the scattering vector (assumed for no energy transfer; $\hbar\omega = 0$) is over a circle passing by the origin of the reciprocal lattice. (*b*) Orientation of the single-crystal specimen.

Among the various ammonium compounds which have been investigated, ammonium chloride, NH_4Cl, is probably the best understood. A first-order phase transition has been evidenced at $T_c = 242$ K (Hovi *et al* 1973, Fredericks 1971, Mohler and Pitka 1974), with a pretransitional effect (Simon 1922, Schwartz 1971). Under high pressure this transition becomes second order (Mandena and Trappeniers 1974). X-ray diffraction measurements show that the average crystal structure is of the CsCl type (Simon and Von Simson 1926), with no change at the transition. It was established from neutron diffraction (Yelon *et al* 1974, Levy and Peterson 1951, 1952) that above T_c a disorder of the NH_4 ions exists

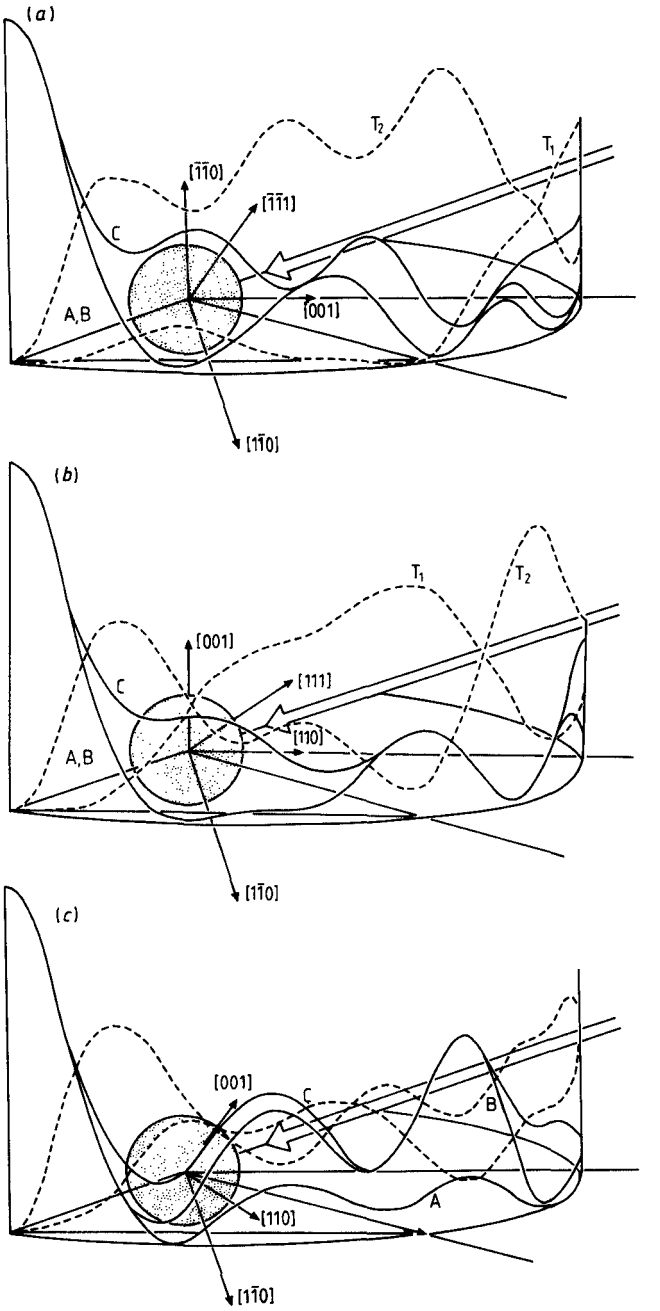

Figure 8.4 Variations of the structure factors versus the scattering angle 2θ, in the case of the backscattering experiment (Bée *et al* 1988). (*a*), (*b*) and (*c*) correspond to orientations of the slab bringing [001], [110] or [111] in the scattering plane, respectively. At the scattering angle $2\theta = 60°$, $\boldsymbol{Q}$ is exactly parallel to these directions.

over two orientations (see figure 8.5). Conversely, below T_c the order increases and a preferred orientation of the tetrahedra appears.

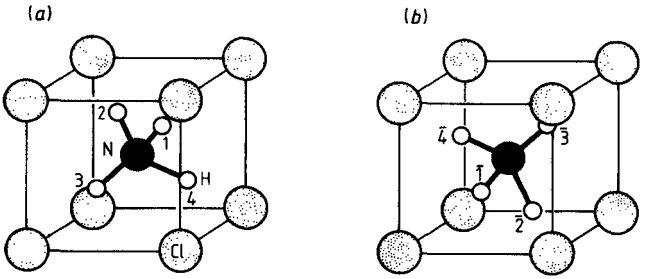

Figure 8.5 Two orientations of the NH_4^+ ion in NH_4Cl.

The dynamical character of the disorder is clearly shown by NMR (Mandena and Trappenier 1974). Rapid molecular motions are demonstrated to occur in both phases. The evolution of the characteristic time as a function of the temperature shows a clear discontinuity at the phase transition, from 2.1×10^{-10} s just below T_c to 8.3×10^{-11} s just above T_c. The activation energy is found to change from 220 meV to 192 meV in these phases, respectively. In order to define the type of orientational motion and specify the change at the phase transition, Töpler *et al* (1978) have performed a very careful incoherent quasielastic neutron scattering experiment. Using a single-crystal sample, they were able to distinguish between 90° jumps of the NH_4^+ ion around a fourfold symmetry axis of the lattice and 120° jumps about a threefold axis. We shall report on this experiment now.

For $T > T_c$ the two discernible orientations of the ammonium ion in the lattice can be considered as equiprobable. Moreover, collective aspects of the NH_4 rotations were not considered. More precisely, the fluctuating part of the orientational potential originating from the reorientation of the surrounding ions was neglected and threefold and fourfold jumps were considered to occur over *average* barriers. The neutron scattering function has been evaluated by Michel (1973), by directly solving the set of rate equations for the probabilities of the tetrahedron orientations. In fact, the relevant correlation times and structure factors can be more easily derived using the group-theory method developed by Thibaudier and Volino (1975), reported in chapter 6.

In table 8.1, we have listed the positions accessed by a hydrogen atom of the NH_4^+ ion, under the effects of all the rotations of the cubic symmetry group, starting from all possible locations. The characters for these rotations corresponding to the different irreducible representations

of the $\mathbb{O}$ group are given in table 6.7. The structure factors associated with these representations are easily evaluated from the general relation (6.102), namely:

$$A_1: A_0(\boldsymbol{Q}) = \tfrac{1}{24}\{1 + C_{110}(\boldsymbol{Q}) + C_{100}(\boldsymbol{Q}) + C_{111}(\boldsymbol{Q})\} \quad (8.1a)$$

$$A_2: A_1(\boldsymbol{Q}) = \tfrac{1}{24}\{3 + C_{110}(\boldsymbol{Q}) - C_{100}(\boldsymbol{Q}) - C_{111}(\boldsymbol{Q})\} \quad (8.1b)$$

$$E: A_2(\boldsymbol{Q}) = 0 \quad (8.1c)$$

$$T_1: A_3(\boldsymbol{Q}) = \tfrac{1}{24}\{3 - C_{110}(\boldsymbol{Q}) + C_{100}(\boldsymbol{Q}) - 3C_{111}(\boldsymbol{Q})\} \quad (8.1d)$$

$$T_2: A_4(\boldsymbol{Q}) = \tfrac{1}{24}\{3 - C_{110}(\boldsymbol{Q}) - C_{100}(\boldsymbol{Q}) + 3C_{111}(\boldsymbol{Q})\} \quad (8.1e)$$

where

$$C_{110}(\boldsymbol{Q}) = \cos(Q_x + Q_y)a + \cos(Q_x + Q_z)a + \cos(Q_y + Q_z)a + \cos(Q_x - Q_y)a + \cos(Q_x - Q_z)a + \cos(Q_y - Q_z)a \quad (8.2a)$$

$$C_{100}(\boldsymbol{Q}) = \cos Q_x a + \cos Q_y a + \cos Q_z a \quad (8.2b)$$

and

$$C_{111}(\boldsymbol{Q}) = \cos(Q_x + Q_y + Q_z)a + \cos(Q_x + Q_y - Q_z)a + \cos(Q_x - Q_y + Q_z)a + \cos(Q_x - Q_y - Q_z)a \quad (8.2c)$$

where $\boldsymbol{Q} = (Q_x, Q_y, Q_z)$ is the scattering vector with respect to lattice axes and a the length of the cube edge.

The structure factor related to the irreducible representation E is strictly vanishing for symmetry reasons. The correlation times can be evaluated from the relation (6.70). We obtain

$$A_1: \tau_0^{-1} = 0 \quad (8.3a)$$

$$A_2: \tau_1^{-1} = 2\tau_{C_4}^{-1} \quad (8.3b)$$

$$E: \tau_2^{-1} = \tau_{C_4}^{-1} + \tfrac{3}{2}\tau_{C_3}^{-1} \quad (8.3c)$$

$$T_1: \tau_3^{-1} = \tfrac{2}{3}\tau_{C_4}^{-1} + \tau_{C_3}^{-1} \quad (8.3d)$$

$$T_2: \tau_4^{-1} = \tfrac{4}{3}\tau_{C_4}^{-1} + \tau_{C_3}^{-1}. \quad (8.3e)$$

In the ordered phase, i.e. for $T < T_c$, it has to be taken into account that one orientation is preferable to the other. Therefore two probabilities for the 90° jumps have to be distinguished, namely jumps to an unfavourable orientation from a favourable one (rate $\tau_{C_4}^{-1}$) and conversely jump from an unfavourable to a favourable orientation (rate $\bar{\tau}_{C_4}^{-1}$). Denoting by n^+ and n^- the average populations for the favourable and the unfavourable orientation respectively, the detailed balance condition requires

Table 8.1 Positions accessed by a hydrogen atom of the ammonium ion under the effect of the rotations of the cubic group

Oper. $t = 0$	E	C_3 [111]	C_3^2 [111]	C_3 [$\bar{1}\bar{1}$1]	C_3^2 [$\bar{1}\bar{1}$1]	C_3 [1$\bar{1}\bar{1}$]	C_3^2 [1$\bar{1}\bar{1}$]	C_3 [$\bar{1}$1$\bar{1}$]	C_3^2 [$\bar{1}$1$\bar{1}$]	C_2 [100]	C_2 [010]	C_2 [001]
1	1	1	1	3	4	4	2	2	3	3	4	2
2	2	4	3	2	2	1	4	3	1	4	3	1
3	3	2	4	4	1	3	3	1	2	1	2	4
4	4	3	2	1	3	2	1	4	4	2	1	3
$\bar{1}$	$\bar{1}$	$\bar{1}$	$\bar{1}$	$\bar{3}$	$\bar{4}$	$\bar{4}$	$\bar{2}$	$\bar{2}$	$\bar{3}$	$\bar{3}$	$\bar{4}$	$\bar{2}$
$\bar{2}$	$\bar{2}$	$\bar{4}$	$\bar{3}$	$\bar{2}$	$\bar{2}$	$\bar{1}$	$\bar{4}$	$\bar{3}$	$\bar{1}$	$\bar{4}$	$\bar{3}$	$\bar{1}$
$\bar{3}$	$\bar{3}$	$\bar{2}$	$\bar{4}$	$\bar{4}$	$\bar{1}$	$\bar{3}$	$\bar{3}$	$\bar{1}$	$\bar{2}$	$\bar{1}$	$\bar{2}$	$\bar{4}$
$\bar{4}$	$\bar{4}$	$\bar{3}$	$\bar{2}$	$\bar{1}$	$\bar{3}$	$\bar{2}$	$\bar{1}$	$\bar{4}$	$\bar{4}$	$\bar{2}$	$\bar{1}$	$\bar{3}$

Oper. $t = 0$	C_4 [100]	C_4^3 [100]	C_4 [010]	C_4^3 [010]	C_4 [001]	C_4^3 [001]	C_2' [110]	C_2' [1$\bar{1}$0]	C_2' [010]	C_2' [10$\bar{1}$]	C_2' [011]	C_2' [01$\bar{1}$]
1	$\bar{2}$	$\bar{4}$	$\bar{3}$	$\bar{2}$	$\bar{4}$	$\bar{3}$	$\bar{2}$	$\bar{1}$	$\bar{4}$	$\bar{1}$	$\bar{3}$	$\bar{1}$
2	$\bar{3}$	$\bar{1}$	$\bar{1}$	$\bar{4}$	$\bar{3}$	$\bar{4}$	$\bar{1}$	$\bar{2}$	$\bar{2}$	$\bar{3}$	$\bar{2}$	$\bar{4}$
3	$\bar{4}$	$\bar{2}$	$\bar{4}$	$\bar{1}$	$\bar{1}$	$\bar{2}$	$\bar{3}$	$\bar{4}$	$\bar{1}$	$\bar{3}$	$\bar{3}$	$\bar{2}$
4	$\bar{1}$	$\bar{3}$	$\bar{2}$	$\bar{3}$	$\bar{2}$	$\bar{1}$	$\bar{4}$	$\bar{3}$	$\bar{4}$	$\bar{2}$	$\bar{1}$	$\bar{4}$
$\bar{1}$	2	4	3	2	4	3	2	1	4	1	3	1
$\bar{2}$	3	1	1	4	3	4	1	2	2	3	2	4
$\bar{3}$	4	2	4	1	1	2	3	4	1	3	3	2
$\bar{4}$	1	3	2	3	2	1	4	3	4	2	1	4

$$\frac{\tau_{C_4}}{\bar{\tau}_{C_4}} = \frac{n^+}{n^-} = \exp\left(\frac{\Delta E}{k_B T}\right) \tag{8.4}$$

where ΔE is the energy difference between the two orientations. Clearly, under a 120° rotation about any C_3 axis, the type of orientation under which the molecule is lying (i.e. favourable or unfavourable) is not modified. Töpler *et al* made the additional assumption that the residence time in the unfavourable orientation was short and neglected the threefold jumps in this orientation, introducing only τ_{C_3}.

Values obtained for τ_{C_3} and τ_{C_4} are illustrated in figure 8.6. The most striking feature is the stepwise change of τ_{C_4} by a factor of nearly 3 at T_c. This result is consistent with the fact that the 90° jumps about fourfold axes are responsible for the orientational disorder. Conversely, the change in τ_{C_3} is less than 10%. In the ordered phase, both residence times τ_{C_3} and τ_{C_4} are of the same order of magnitude. These values of τ_{C_3} and τ_{C_4} agree with those found by NMR. Töpler *et al* evaluated the activation energies related to these motions. For the fourfold jumps, the

energy was found equal to 18 kJ mol^{-1} just above T_c and 20.5 kJ mol^{-1} just below T_c. These values agree quite well with all NMR experimental results and also with those theoretically calculated by Venkataraman *et al* (1966) and by Hüller and Kane (1974), which developed a purely electrostatic potential in terms of symmetry-adapted cubic rotator functions $R^l_{mn}(\mathbf{\Omega})$ depending on the orientation $\mathbf{\Omega}$ of the NH_4 ion (see §7.7.3)

$$V(\mathbf{\Omega}) = A^4 R^4_{11}(\mathbf{\Omega}) + A^6 R^6_{11}(\mathbf{\Omega}) + A^3 R^3_{11}(\mathbf{\Omega}). \tag{8.5}$$

In this expression, the terms A^4 and A^6 result essentially from the interaction between the NH_4 and the Cl ions. The term A^3 takes into account the interaction between the NH_4 ions themselves. It depends on the rotational disorder and vanishes above T_c.

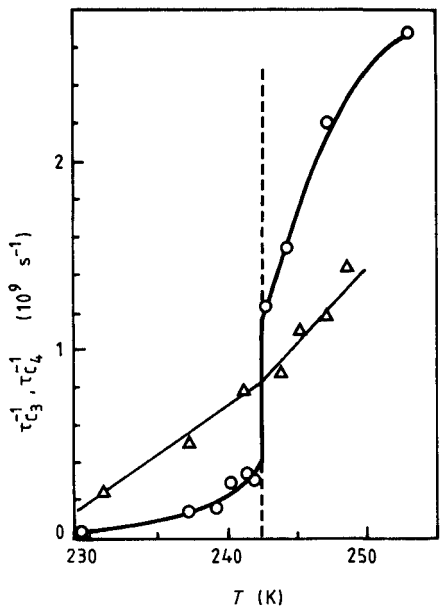

Figure 8.6 Correlation times for reorientations of NH_4^+ about threefold or fourfold lattice axes (Töpler *et al* 1978).

According to this expansion, a 120° rotation about a threefold axis crosses a maximum of $V(\mathbf{\Omega})$ with an energy $E_3 = 29$ kJ mol^{-1} and not a saddle point. Thus it is difficult to make a comparison with the experimental value $E_3 = 19$ kJ mol^{-1} for the threefold activation energy on both sides of the transition. The electrostatic potential predicts at $T = 250$ K a ratio $\tau_{C_3}/\tau_{C_4} = 60$, whereas experimentally it turned out

that the two residence times are very similar $\tau_{C_3}/\tau_{C_4} = 1.5$. Recently, Gerling and Hüller (1983) have performed a molecular-dynamic simulation study of this problem. They started from the idea that the path for a threefold jump does not necessarily lead across the maximum of the potential barrier and that the molecule might find a way to avoid the maximum, by rotating in a more complicated fashion. Computer simulations gave the expected solution in the occurrence of multiple jumps. Most of the 120° jumps around the threefold axis are in fact the result of two or more consecutive 90° jumps around the fourfold axes. The comparison with the experimental results yields a very good agreement.

It must be pointed out that the influence of multiple jumps on the experimental data had been suspected for a long time. Brot *et al* (1979) in their analysis of the data of quinuclidine introduced an 'anywell jump model' which, to some extent, takes into account multiple jumps. This effect could provide the solution to other cases where the interpretation of experimental data leads to puzzling discrepancies with theoretical considerations.

8.2 Two-Dimensional Compounds

Many compounds grow preferentially in a bidimensional space, giving rise to lamellar compounds represented, for instance, by graphite, clays, chalcogenides, β-alumina, etc. Microcrystallites are made of regular stacking of the layers perpendicular to one axis, with, conversely, a disorder within the plane normal to this axis. Depending on the size of the crystallite, one gets platelet powder of pseudo-crystals.

Atoms or molecules can be absorbed on these samples, as in the case of the physisorption of rare gases or alkanes on exfoliated graphite. They can also be inserted between the sheets, giving rise to a lot of intercalated compounds with particular chemical and physical properties. An extensive documentation of these properties can be found in the book edited by Whittingham (1982).

Under normal conditions, these intercalated species are rarely immobile but generally undergo some kind of motion, i.e. reorientational and/or long-range diffusive motions. The original character of these systems is the bidimensionality which appears in the formulation of the corresponding scattering law.

This scattering function corresponding to anisotropic self-diffusion has been derived first by Rosciszewski (1972) in the case of liquid crystals in nematic phases. Dianoux *et al* (1975) have treated the rotational case. These calculations have been adapted by other authors to the scattering from adsorbed or intercalated species.

The anisotropy in the scattering function induced by the

bidimensionality of the adsorbant can be checked by appropriate orientations of the specimen with respect to the incident neutron beam. Figure 8.7 illustrates a geometrical arrangement commonly used in these sorts of experiments. The flat-shaped specimen is a powder of platelets whose layers are parallel to its plane. Clearly, with an angle $\alpha = 45°$ between the incident neutron beam and the plane of the sample the momentum transfer vector $\boldsymbol{Q}$ corresponding to a scattering angle equal to 90° is normal to the layers. On the contrary, when $\alpha = 135°$, this scattering vector at $2\theta = 90°$ becomes parallel to the layers. Now, for molecule rotations having their axis perpendicular to the layers, the displacement of the scatterer, $\boldsymbol{R}$, occurs within the plane of the layers and the scalar product $\boldsymbol{Q}\cdot\boldsymbol{R}$ vanishes for $\alpha = 45°$, or is maximum for $\alpha = 135°$.

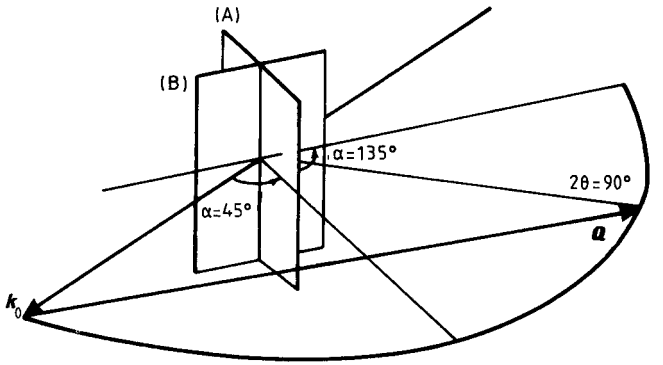

Figure 8.7 Geometrical arrangement commonly used to check orientational effects. In the out-of-plane configuration (*a*) the momentum transfer corresponding to a scattering angle equal to 90° is perpendicular to the specimen plane. Conversely, it is parallel to it with the in-plane configuration (*b*).

It must be pointed out that, when dealing with a powder of platelets, an average has to be taken over all the possible directions of $\boldsymbol{Q}$ with respect to the normal to the surface. Besides, even if the specimen is composed of an assembly of layers parallel to each other, this geometrical arrangement is never perfect and the resulting scattering is averaged by the distribution $g(\beta)$ of the angles of the normal to the layers with respect to their mean direction.

8.2.1 Anisotropic translational diffusion

Rosciszewski (1972) has considered the case of self-diffusion in anisotropic phases. Denoting by $G(\boldsymbol{r}, t)$ the probability for a scatterer to be at r

at time t, the relevant diffusive equation is obtained from a generalisation of the equation for an isotropic liquid, i.e.

$$D\nabla^2 G(\boldsymbol{r}, t) = -\frac{\partial}{\partial t} G(\boldsymbol{r}, t) \tag{8.6}$$

where ∇^2 is the laplacian operator and D the isotropic diffusion constant. Writing (8.6) in the equivalent form,

$$\nabla\cdot[D\nabla G(\boldsymbol{r}, t)] = -\frac{\partial}{\partial t} G(\boldsymbol{r}, t) \tag{8.7}$$

and using the well-known theorem about the divergence

$$\oint_S D\nabla G(\boldsymbol{r}, t)\,\mathrm{d}S = -\frac{\partial}{\partial t}\int_V G(\boldsymbol{r}, t)\,\mathrm{d}V \tag{8.8}$$

where the integral on the r.h.s. runs over any surface S around the volume V. $\boldsymbol{J}(\boldsymbol{r}, t) = D\nabla G(\boldsymbol{r}, t)$ is the current of $G(\boldsymbol{r}, t)$. In the case of an anisotropic medium, this current is no more directly proportional to $\nabla G(\boldsymbol{r}, t)$, but takes the form

$$\boldsymbol{J}(\boldsymbol{r}, t) = \mathbf{D}\cdot\nabla G(\boldsymbol{r}, t) \tag{8.9}$$

$\mathbf{D}$ is the diffusion tensor. Clearly, the symmetry properties of the medium require certain conditions to be fulfilled between the components of $\mathbf{D}$. Neverthelesss, denoting by D_{ij} the components of this tensor, the most general form of the equation for anisotropic translational diffusion is

$$\sum_{i=1}^{3}\sum_{j=1}^{3} D_{ij}\frac{\partial^2}{\partial x_i \partial x_j} G(\boldsymbol{r}, t) = -\frac{\partial}{\partial t} G(\boldsymbol{r}, t) \tag{8.10}$$

together with the initial condition

$$G(\boldsymbol{r}, 0) = \delta(\boldsymbol{r}). \tag{8.11}$$

The intermediate scattering function $I(\boldsymbol{Q}, t)$ is the space-Fourier transform of $G(\boldsymbol{r}, t)$

$$I(\boldsymbol{Q}, t) = \int G(\boldsymbol{r}, t)\exp(\mathrm{i}\boldsymbol{Q}\cdot\boldsymbol{r})\,\mathrm{d}\boldsymbol{r}. \tag{8.12}$$

It follows the following equation, easily derived from (8.10)

$$\frac{\partial}{\partial t} I(\boldsymbol{Q}, t) = \sum_{i=1}^{3}\sum_{j=1}^{3} D_{ij} Q_i Q_j. \tag{8.13}$$

The general solution of (8.13) is

$$I(\boldsymbol{Q}, t) = \exp\left(-\sum_{i=1}^{3}\sum_{j=1}^{3} D_{ij} Q_i Q_j |t|\right) \tag{8.14}$$

and the relevant scattering function, $S(\boldsymbol{Q}, \omega)$, obtained by time-Fourier transform of $I(\boldsymbol{Q}, t)$,

$$S(\boldsymbol{Q}, \omega) = \frac{1}{2\pi}\int I(\boldsymbol{Q},t)\exp(-i\omega t)\,dt \tag{8.15}$$

is

$$S(\boldsymbol{Q}, \omega) = \frac{1}{\pi}\frac{(\Sigma_{i=1}^{3}\Sigma_{j=1}^{3}D_{ij}Q_iQ_j)}{\omega^2 + (\Sigma_{i=1}^{3}\Sigma_{j=1}^{3}D_{ij}Q_iQ_j)}. \tag{8.16}$$

Dianoux *et al* (1975) have considered the anisotropic self-diffusion of liquid crystals in the nematic phases. If the nematic axis is taken as Oz axis, the diffusion tensor is diagonal

$$\mathbf{D} = \begin{vmatrix} D_\perp & 0 & 0 \\ 0 & D_\perp & 0 \\ 0 & 0 & D_\parallel \end{vmatrix} \tag{8.17}$$

where $D_\parallel$ and $D_\perp$ denote, respectively, the diffusion coefficient along and perpendicular to the nematic axis (director). Introducing the spherical coordinate system in Q space, the expression (8.16) of $S(\boldsymbol{Q}, \omega)$ becomes

$$S(\boldsymbol{Q}, \omega) = \frac{1}{\pi}\frac{(D_\parallel\cos^2\theta + D_\perp\sin^2\theta)Q^2}{\omega^2 + [D_\parallel\cos^2\theta + D_\perp\sin^2\theta]^2Q^4} \tag{8.18}$$

where θ is the angle between $\boldsymbol{Q}$ and the director. In absence of external constraints (e.g. electrical field or pressure) the liquid crystals are organised in small domains having their main axis randomly oriented in space. Therefore the experimentally observed scattering law is the average of $S(\boldsymbol{Q}, t)$ over all directions of $\boldsymbol{Q}$ with respect to the director

$$S(Q, \omega) = \frac{1}{2}\int_0^\pi S(\boldsymbol{Q}, \omega)\sin\theta\,d\theta. \tag{8.19}$$

In the case of anisotropic translation on a surface, the diffusion tensor $\mathbf{D}$ can still be put in the diagonal form (8.17). The normal to the surface is naturally chosen as the Oz axis and $D_\parallel$ and $D_\perp$ denote the diffusion coefficients parallel and perpendicular *to this normal*. $S(\boldsymbol{Q}, \omega)$ can still be written in the form (8.18). Integration according to (8.19) to take into account all possible directions of the surface with respect to the scattering vector yields (Dianoux *et al* 1975):

$$S(Q, \omega) = \frac{1}{\pi D_\perp Q^2}\left\{\frac{\lambda}{8\mu\delta}\ln\frac{\delta - \lambda + \mu}{\delta + \lambda + \mu} + \frac{[2\delta(\mu + 1)]^{1/2}}{4\mu\delta}\tan^{-1}\frac{[2\delta(\mu + 1)]^{1/2}}{\mu - \delta}\right\} \tag{8.20}$$

where δ is the anisotropy, defined by

$$\delta = \frac{D_\parallel - D_\perp}{D_\perp} \tag{8.21}$$

and where the following terms have been introduced:

$$\alpha = \frac{\omega}{D_\perp Q^2} \tag{8.22a}$$

$$\mu = \frac{\delta}{|\delta|}(1 + \alpha^2)^{1/2} \tag{8.22b}$$

$$\lambda = [2\delta(\mu - 1)]^{1/2}. \tag{8.22c}$$

When $D_\parallel$ is only weakly higher than $D_\perp$, one can show (Rosciszewski 1972) that the shape of the scattering function predicted by (8.20) is practically a lorentzian, with h.w.h.m.

$$\Delta\omega = \bar{D}Q^2 \tag{8.23a}$$

where

$$\bar{D} = D_\perp \frac{\sqrt{\delta}}{\tan^{-1}(\sqrt{\delta})}. \tag{8.23b}$$

Conversely, when $D_\parallel$ is much smaller than $D_\perp$, then $\delta \gtrsim -1$ and $S(Q, \omega)$ is no longer lorentzian in shape. In particular, for no energy transfer $\omega = 0$ (i.e. $\mu = 1$, $\lambda = 2(-\delta)^{1/2}$) one gets

$$S(Q, 0) = \frac{1}{\pi D_\perp Q^2} \frac{1}{2(-\delta)^{1/2}} \log \frac{1 + (-\delta)^{1/2}}{1 - (-\delta)^{1/2}} \tag{8.24}$$

which exhibits a logarithmic divergence at $\omega = 0$ if $D_\parallel \to 0 (\delta = -1)$, i.e. in the case of diffusion on a surface.

Nevertheless, it is worthwhile pointing out that the simple diffusion model is strictly valid only on the limit $Ql \to 0$, where l is a molecular dimension. Referring to chapter 5, it is known that for $Ql > 1$, the details of the motion on short distance becomes of importance. This is usually taken into account by using a description in terms of 'jump diffusion models', where the broadening of the spectra (h.w.h.m.) is

$$\Delta\omega_{3d} = \frac{1}{\tau}[1 - j_0(Ql)] \tag{8.25}$$

in the three-dimensional case. Here j_0 is a spherical Bessel function and τ the mean time between jumps. Clearly, in the limit $Ql \to 0$

$$\lim_{Ql \to 0} \Delta\omega_{3d} = \frac{1}{\tau} \frac{Q^2 l^2}{6} = D_{3d} Q^2 \tag{8.26}$$

where the three-dimensional diffusion constant D_{3d} is related to the jump length and to the mean time between jumps by

$$D_{3d} = \frac{l^2}{6\tau}. \tag{8.27}$$

Stockmeyer *et al* (1976) have shown that the scattering law for the

two-dimensional jump-diffusion model over a triangular array was a lorentzian function

$$S(Q, \omega) = \frac{1}{\pi} \frac{\Delta\omega_{2d}}{\omega^2 + (\Delta\omega_{2d})^2} \tag{8.28}$$

whose broadening (h.w.h.m.) is given by

$$\Delta\omega_{2d} = \frac{1}{\tau}[1 - J_0(Q_\perp l)] \tag{8.29}$$

j_0 being a cylindrical Bessel function and $Q_\perp = Q \sin\theta$ the component of the scattering vector in the plane of diffusion. θ is the angle of $\boldsymbol{Q}$ with respect to the normal to the surface. Consequently

$$\lim_{Ql \to 0} \Delta\omega_{2d} = \frac{1}{\tau} \frac{Q_\perp^2 l^2}{4} = D_{2d} Q^2 \tag{8.30}$$

where the two-dimensional diffusion constant D_{2d} is now expressed by

$$D_{2d} = \frac{l^2}{4\tau}. \tag{8.31}$$

Thus both the two- and three-dimensional cases exhibit the same behaviour of the quasielastic broadening at low Q values. The dimensionality of the particle diffusion is reflected only by the occurrence of either a spherical or a cylindrical Bessel function in the expression of the quasielastic broadening at larger Q values.

After averaging over all orientations of the surface relative to the neutron momentum transfer, the scattering law (8.28) exhibits a logarithmic singularity at $\omega = 0$, which in fact is revealed only if the spectrometer resolution is sufficiently high.

Renouprez *et al* (1977) have given an illustration of the particular shape at low Q of the two-dimensional scattering function by studying the surface diffusion of hydrogen on a nickel catalyst. The experiment was carried out on the backscattering spectrometer IN10 at the Institut Laue–Langevin. It was shown that if the quasielastic broadening is small, as compared with the instrument resolution, the experimental spectra can be approximated by a lorentzian shape, whose width is given by expression (8.30).

Figures 8.8(a) and 8.8(b) show the quality of this approximation. On figure 8.8(a) the experimental curve is fitted by a lorentzian convoluted with the resolution function. The surface diffusion constant D_{2d} was found equal to $3 \times 10^{-7}\,\mathrm{cm^2\,s^{-1}}$. Figure 8.8($b$) shows the quasielastic peak computed from the resolution function (curve A) convoluted with a lorentzian (curve B) or with the scattering law for a bidimensional diffusion (curve C). The difference between curves B and C, which are both computed with the same jump-length ($l = 2.5$ Å) and residence

time $\tau = 6 \times 10^{-8}$ s, is negligible compared to the statistical error of the data, given here as about 10%.

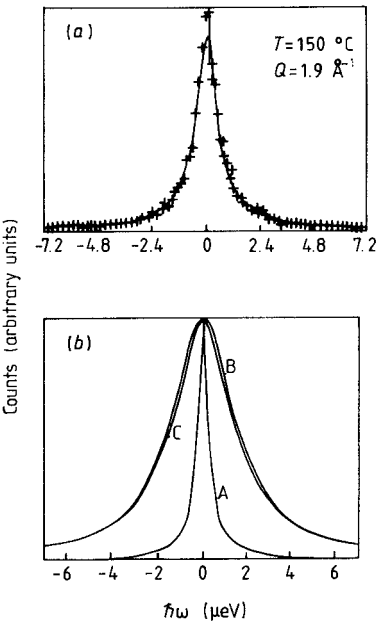

Figure 8.8 (*a*) Quasielastic neutron scattering from chemisorbed hydrogen on a nickel catalyst. The full curve corresponds to the refinement of the experimental data (crosses) with a lorentzian function folded with the instrument resolution function. (*b*) Quasielastic peak computed from the convolution of the instrument resolution function (curve A) with a lorentzian (curve B) or with the two-dimensional scattering law (curve C) (Renouprez *et al* 1977).

The jump-length of 2.5 Å corresponds to the nearest-neighbour distance on a Ni(111) surface and on a Ni(100) surface, i.e. the distance between the midpoints of the cube edges. This experiment of hydrogen diffusion on a Ni surface confirms that in most cases it is valid to neglect bidimensional character of the motion when studying diffusion on powder of platelets, particularly for small broadenings, for instance when the substrate itself gives an important purely elastic contribution to neutron scattering.

Anisotropy of bidimensional diffusion has been checked by Coulomb *et al* (1981) in mobility measurements of two kinds of two-dimensional

fluids given by methane adsorbed on graphite at different temperatures.

Monolayers physisorbed on well-defined cleavage faces of crystals are a good representation of a bidimensional physical situation despite the influence of the adsorption potential of the substrate. Coulomb *et al* (1981) studied the phase transitions between solid and isotropic liquid, over which there is some controversy. If 2D-melting is a first order transition one can expect, as in bulk matter, to observe two kinds of dense fluids. One, called 2D liquid, is stable between a 2D triple point and a 2D critical temperature and has a very narrow existence domain in density and does not cover the whole surface. At $T > T_c$ a 'supercritical fluid', highly compressible, appears, which covers the whole available surface of the solid. By performing careful analysis of the 2D fluids below and above the 2D critical temperature, the authors confirmed the first-order nature of the melting transition of a submonolayer of methane by measuring the mobility which must be very sensitive to the local density.

The substrate is a recompressed exfoliated graphite called papyex. Its important volumetric adsorption area ($20\ m^2\ cm^{-3}$) is mainly made of basal plane (0001) surfaces. Therefore it is suitable for studies on two-dimensional phases by neutron scattering. In order to measure the 2D translational mobility they put the sample in transmission geometry (figure 8.7(b)) get the in-plane diffusion measurements. Since the sample is a 'monocrystal' the translational scattering law can be written, according to (8.18)

$$S(\boldsymbol{Q}, \omega) = \frac{1}{\pi} \frac{D_\perp Q^2 \sin^2\theta}{(D_\perp Q^2 \sin^2\theta)^2 + \omega^2}$$

where it has been assumed that $D_\parallel = 0$. Actually this pseudo monocrystal of papyex has an orientational distribution $g(\beta)$ of the (0001) planes of graphite, with respect to its normal. This distribution was determined from diffraction experiments performed on the diffractometer D1B at the Institut Laue–Langevin. Rocking-curve measurements revealed a f.w.h.m. of $g(\beta)$ equal to nearly 30°. Consequently the influence of the disorder of the crystallite on the shape of the scattering law was taken into account by averaging

$$\bar{S}(\boldsymbol{Q}, \omega) = \int_0^{2\pi} \int_0^{\pi} S(\boldsymbol{Q}, \omega) g(\beta) \sin\theta \, d\theta \, d\eta \qquad (8.33)$$

where the meaning of the angles β, θ and η is indicated in figure 8.9. $g(\beta)$ was chosen in the form of a Poisson kernel (Ruland and Tompa 1968). The perturbation due to the distribution of orientations is shown in figure 8.10 where the scattering law evaluated from (8.33) and convoluted with the resolution function is compared with the corresponding ones for a random powder and for a 'turbostratic single crystal', i.e. a specimen composed of parallel graphite planes. The line is

lorentzian for a turbostratic single crystal, more peaked for a randomly oriented powder, and for papyex, the lineshape is intermediate between the two extreme situations.

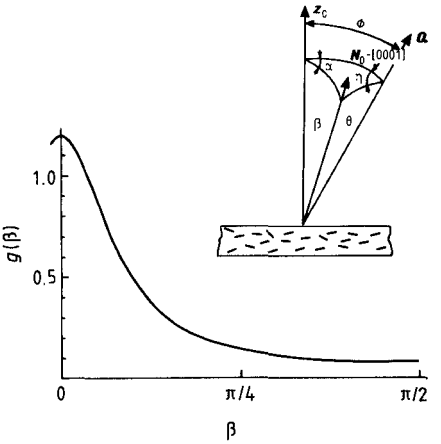

Figure 8.9 Orientational distribution $g(\beta)$ of the (0001) planes in the recompressed exfoliated papyex sample. The insert shows the notations for the various angles between the normal to the sheet (z_0), the normal to an individual (0001) plane (N_0) and the scattering vector (Coulomb *et al* 1981). (Reproduced by permission of *Journal de Physique*.)

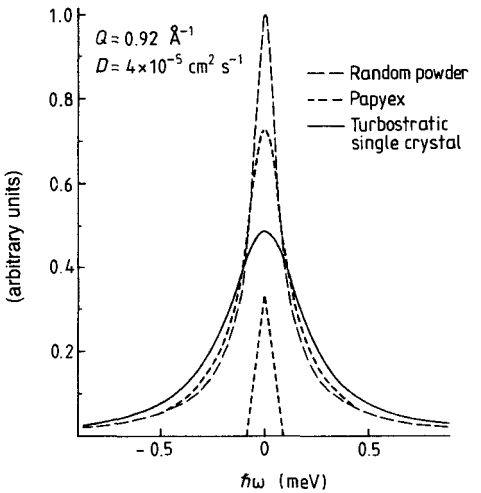

Figure 8.10 Scattering law evaluated from (8.33) (folded with the instrument resolution function, and with integrated intensity normalised to unity), for a turbostratic single crystal (all surfaces parallel), a random-oriented powder and papyex (Coulomb *et al* 1981). (Reproduced by permission of *Journal de Physique*.)

By comparing the width obtained by using equation (8.32) instead of equation (8.33) the authors noticed that the respective diffusion coefficients were in a constant ratio independent of Q.

Figures 8.11(a) and 8.11(b) represent two experiments performed on the same sample at $T = 91.5$ K, for a scattering vector modulus $Q = 1.3$ Å^{-1}. They were obtained in the in-plane and out-of-plane geometry, respectively. Clearly, the two spectra are very different. In the out-of-plane geometry, the spectrum is very intense and nearly purely elastic, indicating that the mobility perpendicular to the basal plane is very small. In fact, if the graphite crystallites in the sample were perfectly oriented, no broadening should be observed. The small wings in the spectra result from the contribution of the misoriented crystallites. Conversely, in the in-plane geometry, a broad peak is observed, indicating a strong mobility along the graphite basal planes.

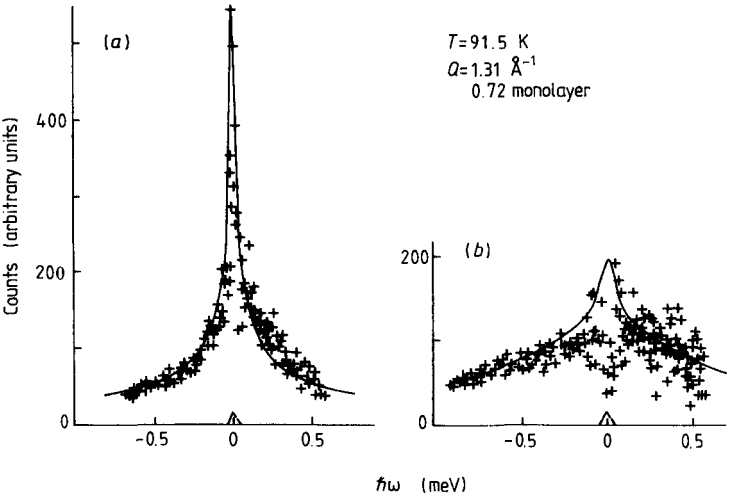

Figure 8.11 Experimental spectra in the in-plane ($Q_{\parallel} = 1.31$ Å^{-1}) and out-of-plane geometries ($Q_{\perp} = 1.31$ Å^{-1}). The full line is the refinement result (Coulomb *et al* 1981). (Reproduced by permission of *Journal de Physique*.)

These experiments permit us to distinguish two types of adsorbed fluids. Below T_c, a 2D self-bounded liquid, made of two-dimensional droplets coexists with a 2D gas separating the droplets. Because the density of the 2D gas is too small to permit an investigation from neutrons, these latter give information about the 2D liquid phase. It was checked that the mobility stays constant when coverage changes, with values of about $(4.2 \pm 0.5)\ 10^{-5}$ cm^2 s^{-1} and $(8.3 \pm 0.8)\ 10^{-5}$ cm^2 s^{-1} at

$T = 61.7$ K and 71.5 K, respectively. These values are quite typical for the mobility of a bulk liquid. Conversely, above T_c, a hypercritical fluid appears, which covers the whole graphite surface. Its density varies continuously with coverage and the diffusion coefficient is both temperature- and coverage-dependent. The same behaviour has been found more recently for the 2D liquid phase of ethane adsorbed on graphite (Coulomb *et al* 1985).

8.2.2 Anisotropic reorientational motion

Anisotropy of uniaxial rotational motions can also be illustrated for molecular species adsorbed onto surfaces or inside bidimensional compounds. An illustration is provided by Conard *et al* (1984) in the study of water dynamics in a planar hydrate Li^+3H_2O in the interlamellar space of hectorite, a swelling clay.

Swelling clays are lamellar silicates, where isomorphic substitutions in the network are balanced at the surface by exchangeable cations, responsible for the particular behaviour of clays with water. Cations and water form a coordination polyhedron in the interlamellar space of smectites (Ben Brahim *et al* 1984). In the case of lithium in hectorite, this polyhedron is a triangle. This system was investigated by Conard *et al* (1984), who first analysed the lower stable hydration state, corresponding to the flat hydrate Li^+3H_2O. It is worth reporting here on the main results they obtained, because these allow a model to be constructed which can be applied to other homoionic smectites.

^1H and ^7Li NMR data (Conard 1976) yield the following dynamical model involving two different time-scales. The lithium is in an axial symmetry site and the protons are involved in two rotational motions around two perpendicular axes (figure 8.12): a rotation of the entire hydrate around the *c*-axis of the clay platelet and a rotation of the water molecule around its own C_2 axis. Because the momenta of inertia involved in each of these motions are largely different, the relevant correlation times associated with each of them are assumed to differ noticeably, the whole-hydrate rotation being much slower than the water motion about its axis. The Li^+3H_2O hydrate is centred above the hexagonal hole of the sheet. Its rotation involves twelve possible sites for one proton on the structural oxygens, distributed over a circle with a 2.4 Å radius. Simultaneously, the water rotation occurs over six sites associated two by two on a circle with small radius (1.23 Å). This model was compared with the quasielastic spectra obtained on IN5, using two different incident neutron wavelengths (5 Å and 10 Å), i.e. two different instrument resolution functions (140 μeV and 17 μeV f.w.h.m., respectively).

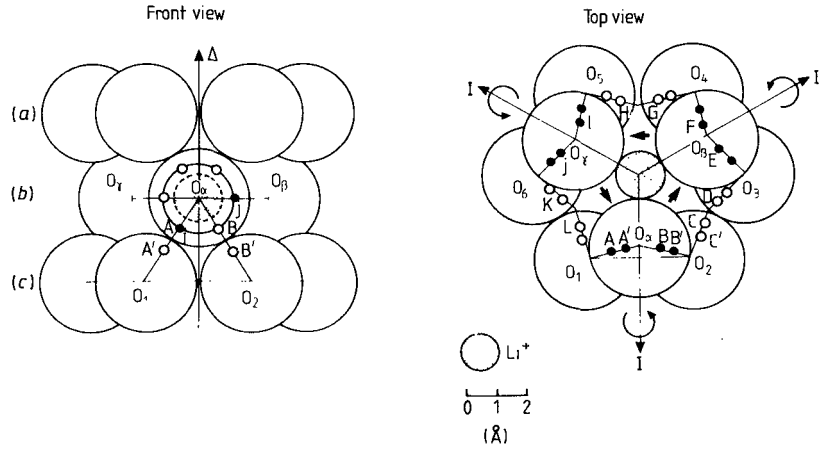

Figure 8.12 Proposed model for (Li^+3H_2O) hectorite (Conard *et al* 1984). (*a*) and (*c*) are the basal planes of the clay layers in which O_1, O_2, . . ., O_6 are the oxygen atoms. (*b*) is the planar hydrate with water oxygens O_α, O_β, O_γ. The water molecules are involved in two types of uniaxial rotations: (i), a rotation of the whole hydrate around the Δ axis over twelve sites on the lattice oxygen; (ii), a rotation of the water molecules about their own C_2 axis, over 6 sites. (Reproduced by permission of *Journal de Physique*.)

Neutron scattering from H_2O adsorbed on clays is largely dominated by the incoherent cross section of hydrogen. More precisely, the refined scattering function must take into account the complete proton content of the sample, i.e. the mobile protons of the lithium hydrate, but also the static protons of the structural hydroxyl groups. These latter give rise to a purely elastic contribution. When dealing with the mobile protons, so far as the two relevant motions in which they are implied can be considered as uncorrelated, the resulting scattering function is the convolution product of the individual scattering law related to each motion. Therefore, one obtains:

$$S(\boldsymbol{Q}, \omega) = \exp(-\langle u^2 \rangle Q^2)\{S^{R_1}(\boldsymbol{Q}, \omega) \otimes S^{R_2}(\boldsymbol{Q}, \omega)[1 - C\delta(\omega)] + C\delta(\omega)\} \tag{8.34}$$

where R_1 refers to the water molecule rotation and R_2 to the whole-hydrate rotation. C is the fraction of fixed protons with respect to the total amount of protons in the sample.

For both R_1 and R_2 rotations, the number of equilibrium positions is large enough (6 or 12) to allow a description in terms of a continuous rotation over a circle, at least in the Q range of experiment: $Q_{max}(\lambda = 5\ \text{Å}) = 2.10\ \text{Å}^{-1}$, $Q_{max}(\lambda = 10\ \text{Å}) = 1.05\ \text{Å}^{-1}$. The relevant radii being respectively $r_1 = 1.23$ Å and $r_2 = 2.49$ Å, the condition $Q_r \leqslant \pi$ is fulfilled in both cases. The scattering law is given by (6.26)

$$S^{R}(\boldsymbol{Q}, \omega) = J_0^2(Qr\sin\theta)\delta(\omega) + 2\sum_{m=1}^{\infty} J_m^2(Qr\sin\theta)\frac{1}{\pi}\frac{\tau_m}{1+\omega^2\tau_m^2} \tag{8.35}$$

where the correlation times τ_m are expressed by

$$\frac{1}{\tau_m} = m^2 D_r \tag{8.36}$$

in terms of the rotational diffusion constant. θ is the angle between the momentum transfer $\boldsymbol{Q}$ and the rotation axis.

The bidimensionality of the clay sample should be manifested by a difference in the shape of the spectra for two experiments carried out in the in-plane and in the out-of-plane geometry. More precisely, when considering the whole-hydrate rotation alone, there might be an absence of broadening in the spectra when $\boldsymbol{Q}$ is perpendicular to the rotation plane and, conversely, the presence of a marked broadening when $\boldsymbol{Q}$ is parallel to this plane. Such drastic behaviour should be observed with pseudomonocrystals, well ordered in the *c*-direction but disordered in the *a–b* plane. Actually, the films are not perfectly oriented: the *c*-axis of the individual platelets are tilted around the mean axis of the film. The orientation distribution, measured by EPR in Cu-hectorite reveals a h.w.h.m. equal to about 15°. Therefore it is possible to define an anisotropy factor by the ratio $A_{\parallel}/A_{\perp}$ of the quasielastic intensities of the spectra obtained respectively for $Q_{\parallel}$ and $Q_{\perp}$ (figure 8.13). Owing to the distribution of the orientations, this factor is not infinite.

Conard *et al* (1984) have evaluated this anisotropy factor, from the scattering law (8.35). Only the first term ($m = 1$) in the expansion of the quasielastic scattering, which gives the main contribution in the explored Q range, was considered.

$$A(\theta) = \int_0^{\pi}\int_0^{2\pi} J_1^2[Qr\sin(\boldsymbol{Q}\cdot\boldsymbol{c})]p(\beta)\sin\beta\,\mathrm{d}\beta\,\mathrm{d}\phi \tag{8.37}$$

where the scalar product $\boldsymbol{Q}\cdot\boldsymbol{c}$ depends on θ, the angle between $\boldsymbol{Q}$ and the normal to the specimen and on the spherical coordinates (β, ϕ) of the $\boldsymbol{c}$ unit vector. $p(\beta)$ is the axially symmetric distribution. It is normalised, i.e.

$$\int_0^{\pi} p(\beta)\sin\beta\,\mathrm{d}\beta = 1. \tag{8.38}$$

For the fast rotations of the water molecule around its own C_2-axis, the anisotropy factor is nearly equal to 1 ($A_{\parallel}/A_{\perp} \simeq 0.64$) when evaluated from a Maier–Saupe distribution

$$p(\beta) = \frac{1}{Z}\exp(\delta\cos^2\beta) \tag{8.39}$$

where Z is the normalisation coefficient and where δ determines the h.w.h.m. β_0 of the distribution. For the whole-hydrate rotation, the

anisotropy was found more pronounced: $A_{\parallel}/A_{\perp} = 8.2$ (respectively 2.9) with a h.w.h.m. $\beta_0 = 15°$ (respectively 19°). The value found experimentally was 2.9.

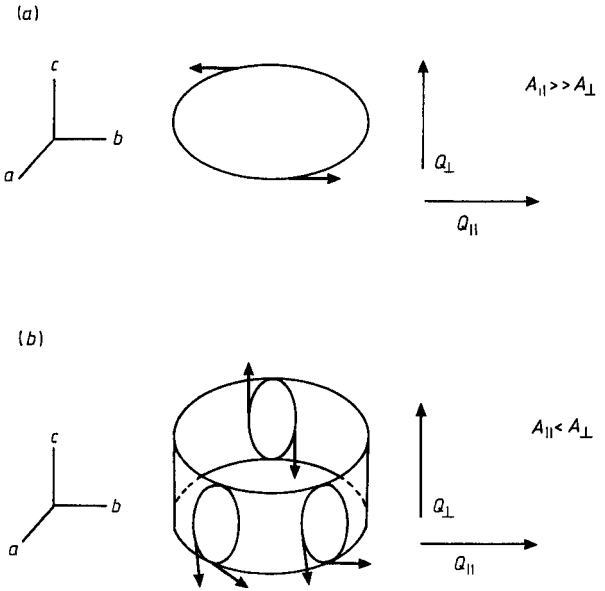

Figure 8.13 Estimation of the anisotropy factors: (*a*), slow rotation: (*b*), fast rotation.

Extension of this model to other clays can be envisaged. The anisotropy of the first water layer is also expected in the case of Ca-vermiculite where the hydration polyhedron is a cube. Two water molecules of opposite edges are in the hexagonal hole of the clay sheet (de la Calle *et al* 1977), and thus on the axis of rotation of the whole hydrate (Poinsignon *et al* 1986).

Chapter 9 Quasielastic Neutron Scattering for Continuous or Random Jump-Diffusion of Molecules in Bounded Media

There is a large variety of physical situations in which the problem of diffusion of small molecules or atoms in restricted geometries is encountered. Typical examples are lamellar systems such as certain liquid crystalline phases (Hayter *et al* 1974) or layered host graphite lattices, clay minerals (Hall *et al* 1977, Hall and Ross 1978), zeolites (Cohen de Lara and Kahn 1981), or ionic polymers (Volino *et al* 1982). This problem is closely related to the analysis of the diffusion in the presence of a potential that we presented in chapter 7. In that chapter we reported on the neutron incoherent scattering law for a rotational motion in an orientational potential. The problem of translational diffusion in a cosine potential in one dimension was also solved. In this chapter we shall present some formalisms which have been developed to calculate the incoherent scattering law in different cases of translational

diffusion. First we shall consider the situation where the translation is restricted between rigid impermeable boundaries and in addition we shall deal with an arbitrary potential of spherical symmetry.

9.1 One-Dimensional Diffusion Between Two Walls

The simplest case of diffusion within a restricted region is the problem of diffusion in one dimension between two rigid, impermeable boundaries separated by a distance L, i.e. at the respective abscissae $x = 0$ and $x = L$ (figure 9.1). The probability $G(x, x_0, t)$ for a particle to be at x at time t, given it was at $x = x_0$ at initial time, is given by the solution of the equation

$$\frac{\partial}{\partial t}G(x, x_0, t) = D_x \frac{\partial^2}{\partial x^2}G(x, x_0, t) \tag{9.1}$$

where D_x is the diffusion coefficient along x. Equation (9.1) is quite similar to the diffusion equation along an infinite line.

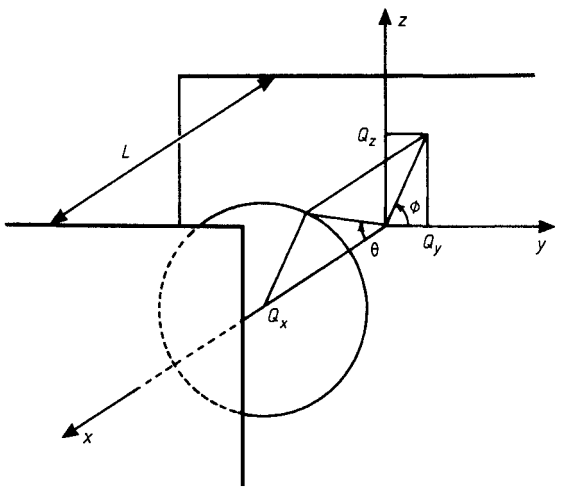

Figure 9.1 Set of coordinates for a particle diffusing along the x-axis, between two impermeable walls separated by a distance L.

The restricted nature of the motion appears with the boundary conditions which $G(x, x_0, t)$ must satisfy. These are

(i) $$G(x, x_0, t = 0) = \delta(x - x_0) \tag{9.2}$$

(ii) $$\left(\frac{\partial G}{\partial x}\right)_{x = 0, L} = 0$$

for all $t > 0$. In other words, because there is no net flow of particles across the potential barrier, a zero concentration gradient is implied immediately inside the boundary.

The solution of (9.1) is obtained in the form of a series expansion (Hall and Ross 1978)

$$G(x, x_0, t) = \frac{1}{L} + \frac{2}{L}\sum_{n=1}^{\infty} \cos\left(\frac{n\pi x}{L}\right)\cos\left(\frac{n\pi x_0}{L}\right)\exp\left(-\frac{n^2\pi^2 D_x t}{L^2}\right). \tag{9.3}$$

The (incoherent) self-correlation function $G_{\text{inc}}(x', t)$ (see equation (2.111)), i.e. the probability of finding a particle at time t at the position x', given that this same scatterer was at the origin at time $t = 0$ is readily obtained by introducing $x' = x - x_0$ in (9.3) and averaging over all possible initial x_0 positions, the limits being 0 and $L - x'$. One obtains

$$G_{\text{inc}}(x', t) = \frac{L - x'}{L^2} + \sum_{n=1}^{\infty}\left[\frac{L - x}{L^2}\cos\left(\frac{n\pi x'}{L}\right) - \frac{1}{nL\pi}\sin\left(\frac{n\pi x'}{L}\right)\right] \times \exp\left(-\frac{n^2\pi^2 D_x t}{L^2}\right). \tag{9.4}$$

A double Fourier transformation yields the scattering law:

$$S_{\text{inc}}(\boldsymbol{Q}, \omega) = \frac{1}{2\pi}\int_{-\infty}^{\infty} \mathrm{d}t \int_{-L}^{L} \mathrm{d}x' G_{\text{inc}}(x', t)\exp[\mathrm{i}(Q_x x' - \omega t)] \tag{9.5}$$

where Q_x is the component of the scattering vector $\boldsymbol{Q}$, along the x-direction. With the notations used throughout this book,

$$S_{\text{inc}}(\boldsymbol{Q}, \omega) = A_0(Q_x L)\delta(\omega) + \sum_{n=1}^{\infty} A_n(Q_x L)\mathcal{L}_n(\omega) \tag{9.6}$$

where the half-widths of the relevant lorentzian functions $\mathcal{L}_n(\omega)$ are given by

$$\tau_n^{-1} = \frac{n^2\pi^2 D_x}{L^2}. \tag{9.7}$$

The elastic and quasielastic structure factors are expressed, respectively by

$$A_0(Q_x L) = \frac{2[1 - \cos(Q_x L)]}{(Q_x L)^2} = j_0^2\left(Q_x \frac{L}{2}\right) \tag{9.8a}$$

$$A_n(Q_x L) = \frac{4(Q_x L)^2[1 - (-1)^n \cos(Q_x L)]}{[(Q_x L)^2 - (n\pi)^2]^2}. \tag{9.8b}$$

They satisfy the normalisation condition

$$\sum_{n=0}^{\infty} A_n(Q_x L) = 1 \tag{9.8c}$$

An important feature of the result of equation (9.6) above is the presence in the scattering function of a purely elastic term, in an analogous manner as for the rotational diffusion models. The origin arises from the spatial restriction of the scatterer displacements, as evidenced quite generally in §2.10. Clearly, from (9.8a) the EISF tends to 1 at low Q value and to zero for large momentum transfers ($Q_x L = \pi$).

Also, the structure factors defined by (9.8a) and (9.8b) exhibit a dependence on the orientation of the scattering vector $Q = (Q_x, Q_y, Q_z)$ with respect to the direction along which to diffusion occurs. Which $\boldsymbol{Q}$ is perpendicular to it, $Q_x = 0$ and

$$A_0(Q_x L) = 1$$
$$A_n(Q_x L) = 0 \qquad (n \neq 0).$$

Thus the scattering is purely elastic. Polycrystalline samples in which the scatterers diffuse along straight directions, like channels or fibres, require an average over all possible orientations of the crystallites with respect to the scattering vector. This yields an average of the expressions (9.8) over all $\boldsymbol{Q}$-directions. The main consequence is that the EISF curve as a function of Q does not decrease to a vanishing value, but only to a minimum value. Now let us consider a scatterer which, in addition to its diffusion along a segment in the x-direction, also undergoes any kind of other motion in the perpendicular y and z directions. The solution for the full three-dimensional case can be written as the product of the one-dimensional solutions related to each direction, providing that these motions can be considered as uncorrelated. For instance, let us assume that the displacements of the scatterers are restricted between two parallel planes perpendicular to the x-direction. The self-correlation functions $G_{\text{inc}}(y, t)$ and $G_{\text{inc}}(z, t)$ corresponding to unbounded diffusion in either the y- or z-directions are given by (see chapter 5)

$$G_{\text{inc}}(y, t) = \frac{1}{\sqrt{4\pi D_y t}} \exp\left(-\frac{y^2}{4} D_y t\right) \tag{9.9a}$$

$$G_{\text{inc}}(z, t) = \frac{1}{\sqrt{4\pi D_z t}} \exp\left(-\frac{z^2}{4} D_z t\right) \tag{9.9b}$$

and

$$G_{\text{inc}}(\boldsymbol{r}, t) = G_{\text{inc}}(x, t)\, G_{\text{inc}}(y, t)\, G_{\text{inc}}(z, t) \tag{9.10a}$$

$$= \frac{1}{4\pi\sqrt{D_y D_z}} G_{\text{inc}}(x, t) \exp\left[-(y^2 D_y^2 + z^2 D_z^2)\frac{t}{4}\right] \tag{9.10b}$$

where $G_{\text{inc}}(x, t)$ is given by (9.4).

The corresponding three-dimensional scattering law is

$$S(\boldsymbol{Q}, \omega) = \sum_{n=0}^{\infty} A_n(Q_x L)\mathcal{L}_n\left(D_y Q_y^2 + D_z Q_z^2 + \frac{n^2\pi^2 D_x^2}{L^2}\right). \quad (9.11)$$

Introducing polar coordinates (see figure 9.1)

$$Q_x = Q\cos\theta \quad (9.12a)$$

$$Q_y = Q\sin\theta\cos\phi \quad (9.12b)$$

$$Q_z = Q\sin\theta\sin\phi \quad (9.12c)$$

and assuming that the diffusion parallel to the plane is isotropic ($D_y = D_z = D_\parallel$, $D_x = D_\perp$), (9.11) can be compared with the scattering function for unbounded anisotropic diffusion (Dianoux *et al* 1975)

$$S(\boldsymbol{Q}, \omega) = \frac{1}{\pi}\frac{(D_\parallel \sin^2\theta + D_\perp \cos^2\theta)Q^2}{(D_\parallel \sin^2\theta + D_\perp \cos^2\theta)^2 Q^4 + \omega^2}. \quad (9.13)$$

Clearly, for small L, all the lorentzian functions, $\mathcal{L}_n$, except for $n = 0$ become very broad in energy, and contribute to the scattering law in the form of a flat background with vanishing amplitude as L approaches zero. Conversely the single remaining structure factor $A_0(Q_x L)$ tends towards unity. Therefore, the limiting form of (9.11) as $L \to 0$ is

$$S(\boldsymbol{Q}, \omega) = \frac{1}{\pi}\frac{D_\parallel \sin^2\theta\, Q^2}{D_\parallel^2 \sin^4\theta\, Q^4 + \omega^2} \quad (9.14)$$

which is the two-dimensional form of (9.13), where $D_\perp = 0$. On the other hand, in the limit as $L \to \infty$, assuming that $D_x = D_y = D_z = D$, it can be proved that (9.11) reduces to the usual expression for unbounded translational motion

$$S(\boldsymbol{Q}, \omega) = \frac{1}{\pi}\frac{DQ^2}{D^2Q^4 + \omega^2}. \quad (9.15)$$

It is worth comparing the variation as a function of the scattering vector of the broadening of the spectra predicted respectively by the unbounded and bounded continuous diffusion models. The former situation yields the well-known DQ^2 law (figure 9.2), while (9.6) consists of an elastic component superimposed on a series of lorentzians with widths $\Delta\omega_n = n^2\pi^2 D/L^2$ independent of Q but with relative weights periodic in Q, according to (9.8). The width of the resulting broadened component is determined by the relative magnitudes of the structure factors A_n, and varies versus Q as reported in figure 9.2. At low values of Q^2L^2, the half-width at half-minimum of the quasielastic part of the spectra is practically constant and tends asymptotically to $\pi^2 D/L^2$, i.e. to the h.w.h.m. of the $n = 1$ term. As Q^2L^2 increases, the h.w.h.m. increases also slightly, crosses the straight line relative to the DQ^2 law and then, changing its behaviour tends to the h.w.h.m. of Fick's law as $Q^2L^2 \to \infty$.

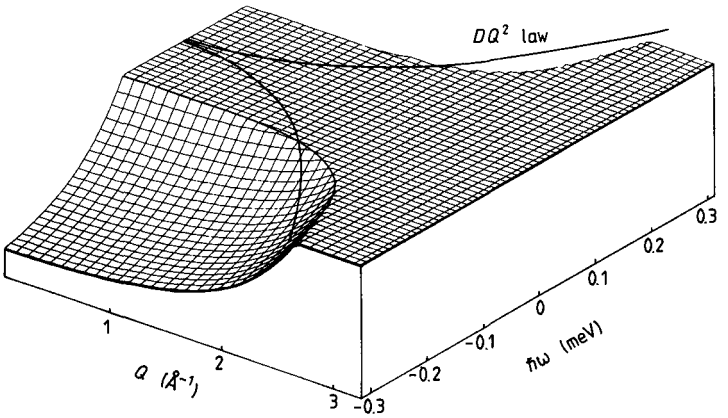

Figure 9.2 Three-dimensional schema representing in the (Q, ω) space the quasielastic part of the scattering law (9.6) for diffusive motion between two walls, limited at the half of its maximum amplitude (all the $\hbar\omega$ curves for the different Q-values have been normalised to 1) in order to show the Q-dependence of the h.w.h.m., as compared with the DQ^2 law.

The model reported above can be readily generalised to other geometries. For instance, if the scatterer can diffuse inside a rectangular capillary with impermeable boundaries such that $0 \leqslant x \leqslant L_x$ and $0 \leqslant y \leqslant L_y$, the relevant scattering function takes the form:

$$S(\boldsymbol{Q}, \omega) = \sum_{m=0}^{\infty} \sum_{n=0}^{\infty} A_m^x(Q_x L_x) A_n^y(Q_y L_y) \mathcal{L}_{mn}\left(D_z Q_z^2 + \frac{m^2\pi^2 D_x}{L_x^2} + \frac{n^2\pi D_y}{L_y^2}\right). \tag{9.16}$$

Similarly, in the case of a scatterer diffusing inside a rectangular box, we obtain:

$$S(\boldsymbol{Q}, \omega) = \sum_{m=0}^{\infty} \sum_{n=0}^{\infty} \sum_{p=0}^{\infty} A_m^x(Q_x L_x) A_n^y(Q_y L_y) A_p^z(Q_z L_z) \times \mathcal{L}_{mnp}\left(\frac{m^2\pi^2 D_x}{L_x^2} + \frac{n^2\pi^2 D_y}{L_y^2} + \frac{p^2\pi^2 D_z}{L_z^2}\right). \tag{9.17}$$

Equations (9.16) and (9.17) hold for a crystal sample and usually require a powder average. Above all, they are valid under the assumption that the motions along the different axes are uncorrelated. In the case of a spherical geometry, this hypothesis is no longer true, and the use of a set of polar coordinates is more convenient to derive the corresponding scattering law. The general formalism is presented in the next section

and then applied to the case of the diffusion inside a sphere of radius a having an impermeable surface.

9.2 Three-Dimensional Diffusion in a Potential of Spherical Symmetry

9.2.1 General case

We consider a particle undergoing a diffusive motion in a potential $V(r) = V(r, \theta, \phi)$. r stands for the vector defining the particle position. θ and ϕ denote the polar and azimuthal angles of r, respectively. The probability function $P(r, r_0; t)$ for the particle to be at r at the time t, given that it was at r_0 at time zero, is the solution of the Smoluchowski equation (see chapter 7):

$$\frac{1}{D}\frac{\partial}{\partial t}\mathcal{P}(r, r_0; t) = \nabla^2\mathcal{P}(r, r_0; t) + \frac{1}{k_B T}\nabla[(\nabla V(r))\mathcal{P}(r, r_0; t)] \quad (9.18)$$

D is the diffusion coefficient, k_B is the Boltzmann constant and T is the temperature. Introducing the expression of the laplacian in polar coordinates, i.e.:

$$\nabla^2 = \frac{1}{r^2}\frac{\partial}{\partial r}\left(r^2\frac{\partial}{\partial r}\right) + \frac{1}{r^2\sin\theta}\frac{\partial}{\partial\theta}\left(\sin\theta\frac{\partial}{\partial\theta}\right) + \frac{1}{r^2\sin^2\theta}\frac{\partial^2}{\partial\phi^2}. \quad (9.19)$$

Equation (9.18) can be put in the form

$$\begin{aligned}\frac{1}{D}\frac{\partial}{\partial t}\mathcal{P}(r, r_0; t) = {} & \frac{1}{r^2}\frac{\partial}{\partial r}\left(r^2\frac{\partial\mathcal{P}}{\partial r} + \frac{1}{k_B T}r^2\frac{\partial V}{\partial r}\mathcal{P}\right) \\ & + \frac{1}{r^2\sin\theta}\frac{\partial}{\partial\theta}\left(\sin\theta\frac{\partial\mathcal{P}}{\partial\theta} + \frac{1}{k_B T}\sin\theta\frac{\partial V}{\partial\theta}\mathcal{P}\right) \\ & + \frac{1}{r^2\sin^2\theta}\frac{\partial}{\partial\phi}\left(\frac{\partial\mathcal{P}}{\partial\phi} + \frac{1}{k_B T}\frac{\partial V}{\partial\phi}\mathcal{P}\right). \quad (9.20)\end{aligned}$$

Now, we introduce the operator $\hat{L}$ equivalent to the orbital angular momentum

$$\hat{L}_x = \sin\phi\frac{\partial}{\partial\theta} + \cot\theta\cos\phi\frac{\partial}{\partial\phi} \quad (9.21a)$$

$$\hat{L}_y = -\cos\phi\frac{\partial}{\partial\theta} + \cot\theta\sin\phi\frac{\partial}{\partial\phi} \quad (9.21b)$$

$$\hat{L}_z = -\frac{\partial}{\partial\phi} \quad (9.21c)$$

with

$$\hat{L}^2 = \hat{L}_x^2 + \hat{L}_y^2 + \hat{L}_z^2 = \frac{1}{\sin\theta}\frac{\partial}{\partial\theta}\left(\sin\theta\frac{\partial}{\partial\theta}\right) + \frac{1}{\sin^2\theta}\frac{\partial^2}{\partial\phi^2}. \quad (9.21d)$$

Under these conditions, we get easily

$$\frac{1}{D}\frac{\partial\mathcal{P}}{\partial t} = \frac{1}{r^2}\frac{\partial}{\partial r}\left(r^2\frac{\partial\mathcal{P}}{\partial r} + \frac{1}{k_B T}r^2\frac{\partial V}{\partial r}\mathcal{P}\right) - \frac{1}{k_B T}\hat{L}\cdot[(\hat{L}V)\mathcal{P}] - \hat{L}^2\mathcal{P}. \quad (9.22)$$

If the potential $V(r, \theta, \phi)$ is independent of the radius r, i.e. $V = V(\theta, \phi)$ (9.22) reduces to

$$\frac{1}{D}\frac{\partial\mathcal{P}}{\partial t} = -\frac{1}{k_B T}\hat{L}\cdot[(\hat{L}V(\theta, \phi))\mathcal{P}] - \hat{L}^2\mathcal{P} \quad (9.23)$$

which is nothing other than the equation (7.157) in the case of an isotropic diffusion tensor $\mathbf{D}^2 = D[I]$. However, (9.23) is somewhat different from (7.157) because here we are dealing with a point-like particle, designated by its polar coordinates (θ, ϕ) whilst (7.157) is expressed in terms of the Euler angles $\boldsymbol{\Omega}$ of a molecule experiencing a static orientational potential $V(\boldsymbol{\Omega})$. Nevertheless, the treatment of (9.23) is quite analogous to the derivation of §7.7, and even simpler. The probability $P = P(\theta, \phi)$ and the potential $V(\theta, \phi)$ are both expanded in terms of the surface harmonics (see 7.180)

$$L_{lp}(\theta, \phi) = \sum_{m=-l}^{l} S^l_{mp}(L)Y_{lm}(\theta,\phi) \quad (9.24)$$

adapted to the symmetry of the potential acting on the particle. Calculations closely follow the method indicated by Brondeau and Goulon (1975) for deriving the correlation functions of spherical harmonics.

In this section we are more concerned with the case of potentials of spherical symmetry

$$V(\boldsymbol{r}) = V(r) \quad (9.25)$$

so that (9.22) reduces to

$$\frac{1}{D}\frac{\partial\mathcal{P}}{\partial t} = \frac{1}{r^2}\frac{\partial}{\partial r}\left[r^2\frac{\partial\mathcal{P}}{\partial r} + \frac{1}{k_B T}r^2\frac{dV}{dr}\mathcal{P}\right] - \frac{\hat{L}^2}{r^2}\mathcal{P}. \quad (9.26)$$

The general solution of (9.26) has to be sought in the form

$$\mathcal{P}(\boldsymbol{r}, \boldsymbol{r}_0; t) = \sum_{l=0}^{\infty} A_l(r, r_0; t)\sum_{m=-l}^{l} Y_{lm}(\theta, \phi)Y^*_{lm}(\theta_0, \phi_0). \quad (9.27)$$

The spherical harmonics functions Y_{lm} are the eigenfunctions of the operator $\hat{L}^2$ corresponding to the square of the orbital momentum

$$\hat{L}^2 Y_{lm}(\theta, \phi) = l(l+1) Y_{lm}(\theta, \phi) \tag{9.28}$$

and we get an equation for the $A_l(r, r_0; t)$ coefficients

$$\frac{1}{D}\frac{\partial A_l}{\partial t} = \frac{1}{r^2}\frac{\partial}{\partial r}\left[r^2 \frac{\partial A_l}{\partial r} + \frac{1}{k_B T} r^2 \frac{dV}{dr} A_l\right] - \frac{l(l+1)}{r^2} A_l. \tag{9.29}$$

Substituting the effective radial potential (Volino and Dianoux 1980):

$$v_l(r) = \frac{1}{2k_B T}\left[\frac{d^2 V}{dr^2} + \frac{2}{r}\frac{dV}{dr} - \frac{1}{2k_B T}\left(\frac{dV}{dr}\right)^2\right] - \frac{l(l+1)}{r^2} \tag{9.30}$$

(9.29) yields the one-dimensional Schrödinger-like equation

$$\frac{1}{D}\frac{\partial a_l}{\partial t} = \frac{\partial^2 a_l}{\partial r^2} + v_l(r) a_l \tag{9.31}$$

in which the coefficients $a_l(r, r_0; t)$ are related to the coefficients $A_l(r, r_0; t)$ by

$$a_l(r, r_0; t) = r A_l(r, r_0; t) \exp\left\{\frac{V(r)}{2k_B T}\right\}. \tag{9.32}$$

The solution of (9.31) can be found in the form

$$a_l(r, r_0; t) = a_l^t(t) \cdot a_l^r(r, r_0) \tag{9.33}$$

where $a_l^t(t)$ and $a_l^r(r, r_0)$ are the solutions of the two differential equations

$$\begin{cases} \dfrac{d}{dt} a_l^t(t) + D\lambda_l^n a_l(t) = 0 & \text{(9.34a)} \\ \dfrac{d^2}{dr^2} a_l^r(r, r_0) + (v_l(r) + \lambda_l^n) a_l^r(r, r_0) = 0. & \text{(9.34b)} \end{cases}$$

Calling $\psi_l^n(r)$ the eigenfunction related to the $(n+1)$th eigenvalue λ_l^n of (9.34b) the general expression for the $A_l(r, r_0; t)$ is, for any arbitrary potential $V(r)$

$$A_l(r, r_0; t) = \sum_{n=0}^{\infty} \psi_l^n(r) \psi_l^{n*}(r_0) \exp[-D\lambda_l^n t] \times \frac{1}{r r_0} \exp\left[\frac{V(r_0) - V(r)}{2k_B T}\right]. \tag{9.35}$$

This expression satisfies the usual conditions required for $\mathcal{P}(r, r_0; t)$

(i) $\mathcal{P}(r, r_0; t)$ is normalised to unity

$$\begin{aligned} &\int \mathcal{P}(r, r_0; t)\, d^3 r \\ &\quad = \iiint \sum_{l=0}^{\infty} A_l(r, r_0; t) \sum_{m=-l}^{l} Y_{lm}(\theta, \phi) Y_{lm}^*(\theta_0, \phi_0) \times r^2 \sin\theta\, dr\, d\theta\, d\phi \\ &\quad = \int A_0(r, r_0; t) r^2\, dr = 1 \end{aligned} \tag{9.36}$$

(ii) At initial time $t = 0$

$$\mathcal{P}(\boldsymbol{r}, \boldsymbol{r}_0; 0) = \sum_{l=0}^{\infty}\sum_{n=0}^{\infty}\psi_l^n(r)\psi_l^{n*}(r_0) \times \sum_{m=-l}^{l} Y_{lm}(\theta, \phi)Y_{lm}^*(\theta_0, \phi_0)\frac{1}{rr_0}\exp\left[\frac{V(r_0) - V(r)}{2k_BT}\right]. \quad (9.37)$$

The $\psi_l^n(r)$ form a complete set of orthogonal functions; also, using the well-known properties of the spherical harmonics, we get

$$\mathcal{P}(\boldsymbol{r}, \boldsymbol{r}_0; 0) = \frac{1}{r^2}\delta(r - r_0)\delta(\theta - \theta_0)\delta(\phi - \phi_0) = \delta(\boldsymbol{r} - \boldsymbol{r}_0). \quad (9.38)$$

(iii) Finally, at infinite time $t \to \infty$, $\mathcal{P}(\boldsymbol{r}, \boldsymbol{r}_0; t)$ tends to the stationary distribution corresponding to the null eigenvalue $\lambda_0^0 \equiv 0$ related to $l = 0$.

According to (9.27)

$$\mathcal{P}(\boldsymbol{r}, \boldsymbol{r}_0; \infty) = A_0(r, r_0; \infty)Y_{00}(\theta, \phi)Y_{00}^*(\theta_0, \phi_0) = \frac{1}{4\pi}A_0(r, r_0; \infty) \quad (9.39)$$

And, from (9.29)

$$A_0(r, r_0; \infty) = |\psi_0^0|^2 = \frac{1}{Z}\exp\left[-\frac{V(r)}{k_BT}\right] \quad (9.40a)$$

with

$$Z = \int_0^{\infty}\exp\left[-\frac{V(r)}{k_BT}\right]r^2\,dr \quad (9.40b)$$

so that

$$\mathcal{P}(\boldsymbol{r}, \boldsymbol{r}_0; \infty) = p(r) = \frac{1}{4\pi Z}\exp\left\{-\frac{V(r)}{k_BT}\right\} \quad (9.41)$$

is independent of the initial conditions.

From the knowledge of $\mathcal{P}(\boldsymbol{r}, \boldsymbol{r}_0; t)$ and $p(\boldsymbol{r})$, the intermediate scattering function

$$I(\boldsymbol{Q}, t) = \int \exp[i\boldsymbol{Q}\cdot(\boldsymbol{r} - \boldsymbol{r}_0)]\mathcal{P}(\boldsymbol{r}, \boldsymbol{r}_0; t)p(\boldsymbol{r}_0)\,d\boldsymbol{r}\,d\boldsymbol{r}_0 \quad (9.42)$$

can be readily evaluated. Using (9.27), (9.33), (9.41) and introducing the expansion (7.200a) of the exponential term, we obtain

$$I(\boldsymbol{Q},t) = \sum_{l=0}^{\infty}(2l + 1)\sum_{n=0}^{\infty}A_n^l(Q)\exp[-D\lambda_l^n t] \quad (9.43)$$

where we have introduced the structure factors

$$A_n^l(Q) = \frac{1}{Z}\left|\int_0^{\infty}\psi_l^n(r)j_l(Qr)r\,dr\right|^2 \quad (9.44)$$

It is worth pointing out that the final expression (9.44) does not depend on the orientation of $\boldsymbol{Q}$, because of the spherical symmetry of the problem.

This formalism permits us to calculate the incoherent scattering law for a particle diffusing in any potential $V(r)$ of spherical symmetry. The method consists in finding the eigenvalues and the eigenfunctions of the equation (9.34) and then in calculating the structure factors $A_n^l(Q)$ according to (9.44). In practice, depending on the expression of $V(r)$, the eigenfunctions of (9.34) are not always easily found in an analytic form and a numerical treatment is often required.

9.2.2. Diffusion inside a sphere with impermeable boundaries

Let us consider the case of a particle moving in a spherically symmetric, infinitely deep potential well, that is the case where the potential energy can be written as

$$V(r) = 0 \qquad \text{for } 0 < r < R$$

and

$$V(r) = +\infty \qquad \text{for } r > R. \tag{9.45}$$

Under these conditions the effective potential $v_l(r)$ reduces to

$$v_l(r) = -\frac{l(l+1)}{r^2} \tag{9.46}$$

and (9.34b) becomes

$$\frac{\mathrm{d}^2}{\mathrm{d}r^2}a_l^r + \left(-\frac{l(l+1)}{r^2} + \lambda_l^n\right)a_l^r = 0. \tag{9.47}$$

Let us first consider the case $l = 0$ which is determined by the equation

$$\frac{\mathrm{d}^2}{\mathrm{d}r^2}a_l^r + \lambda_0^n a_l^r = 0. \tag{9.48}$$

The general solution of (9.48) can be written in the form

$$\psi_0^n(r) = c_1 \sin(r\sqrt{\lambda_0^n}) + c_2 \cos(r\sqrt{\lambda_0^n}). \tag{9.49}$$

The constants c_1 and c_2 are determined by the boundary conditions, which are that the flux is zero at $r = 0$ and R

$$\left[\frac{\partial \mathscr{P}(r, r_0; t)}{\partial r}\right]_{r=0,R} = 0. \tag{9.50}$$

Using (9.27) and (9.35), this condition is equivalent to

$$\frac{\mathrm{d}}{\mathrm{d}r}\left[\frac{1}{r}\psi_l^n(r)\right]_{r=0,R} = 0. \tag{9.51}$$

Introduction of (9.49) in (9.51) yields

$$\left\{c_1\left[-\frac{\sin(r\sqrt{\lambda_0^n})}{r^2}+\sqrt{\lambda_0^n}\frac{\cos(r\sqrt{\lambda_0^n})}{r}\right]+c_2\left[-\frac{\cos(r\sqrt{\lambda_0^n})}{r^2}-\sqrt{\lambda_0^n}\frac{\sin(r\sqrt{\lambda_0^n})}{r}\right]\right\}_{r=0,R}=0 \tag{9.52a}$$

or, introducing the spherical Bessel functions:

$$c_1 j_1(r\sqrt{\lambda_0^n})-c_2 j_{-2}(r\sqrt{\lambda_0^n})=0. \tag{9.52b}$$

The condition at $r=0$ implies that $c_2=0$. The condition at $r=R$ provides the equation which determines the eigenvalues λ_0^n

$$\frac{c_1}{R\sqrt{\lambda_0^n}}\left[\frac{\sin(R\sqrt{\lambda_0^n})}{R\sqrt{\lambda_0^n}}-\cos(R\sqrt{\lambda_0^n})\right]_{r=0,R}=0 \tag{9.53a}$$

or else,

$$c_1 j_1(R\sqrt{\lambda_0^n})=0. \tag{9.53b}$$

Thus the eigenvalues λ_0^n are determined by the zero of the spherical Bessel function $j_1(x_0^n)$, x_0^n

$$x_0^n=R\sqrt{\lambda_0^n}. \tag{9.54}$$

The constant c_1 is obtained from the normalisation condition of the eigenfunctions (9.49), i.e.

$$\int_0^R|\psi_0^n(r)|^2\,\mathrm{d}r=c_1^2\int_0^R\sin^2(r\sqrt{\lambda_0^n})\,\mathrm{d}r=1 \tag{9.55a}$$

$$=c_1^2\int_0^R\frac{1}{2}[1-\cos(2r\sqrt{\lambda_0^n})]\,\mathrm{d}r \tag{9.55b}$$

$$=c_1^2\frac{1}{2}\left[R-\frac{\sin(2R\sqrt{\lambda_0^n})}{2\sqrt{\lambda_0^n}}\right]. \tag{9.55c}$$

Or using the equation (9.53b) giving the eigenvalues:

$$c_1=\frac{1}{\sqrt{R}\sin(R\sqrt{\lambda_0^n})} \tag{9.56}$$

so that

$$\psi_0^n(r)=\sqrt{\left(\frac{2}{R}\right)}\frac{\sin(r\sqrt{\lambda_0^n})}{\sin(R\sqrt{\lambda_0^n})}. \tag{9.57}$$

In the particular case of the null eigenvalue λ_0^0, (9.48) becomes

$$\frac{\mathrm{d}^2a_0^r}{\mathrm{d}r^2}=0 \tag{9.58}$$

and thus

$$\psi_0^0(r) = c_1 r + c_2. \tag{9.59}$$

The limiting conditions applied to $\psi_0^0(r)$ enable us to determine the constant c_1 and c_2. Namely

$$\left[\frac{\mathrm{d}}{\mathrm{d}r}\left(\frac{1}{r}\psi_0^0(r)\right)\right]_{r=0,R} = \left[-\frac{c_2}{r^2}\right]_{r=0,R} \tag{9.60}$$

implies $c_2 = 0$, and from

$$\int_0^R c_1^2 r^2 \,\mathrm{d}r = c_1^2\left[\frac{r^3}{3}\right]_0^R = 1 \tag{9.61}$$

one gets

$$\psi_0^0(r) = \left(\frac{3}{R^3}\right)^{1/2} r. \tag{9.62}$$

Using this expression in (9.44), the EISF for the incoherent scattering law is easily obtained:

$$\begin{aligned} A_0^0(Q) &= \frac{1}{Z}\left|\int_R^0 \psi_0^0(r) j_0(Qr) r \,\mathrm{d}r\right|^2 \\ &= \frac{3}{R^3}\left|\int_0^R r\frac{\sin(Qr)}{Q}\,\mathrm{d}r\right|^2\left(\int_0^R r^2\,\mathrm{d}r\right)^{-1} \\ &= \left[\frac{3j_1(QR)}{QR}\right]^2. \end{aligned} \tag{9.63}$$

Let us now turn to the general case, including the case where $l \neq 0$. The general solution of the Schrödinger-like equation (9.47) is (Volino and Dianoux 1980)

$$\psi_l^n(r) = c_l^n r j_l(r\sqrt{\lambda_l^n}) + c_{-(l+1)}^n r j_{-(l+1)}(r\sqrt{\lambda_l^n}) \tag{9.64}$$

where $j_l(x)$ and $j_{-(l+1)}$ are spherical Bessel functions. The boundary condition that the flux is zero at $r = 0$ implies that

$$c_{-(l+1)}^n = 0 \tag{9.65}$$

while the condition at the surface of the sphere ($r = R$) gives the set of equations which determines the eigenvalues λ_l^n

$$l j_l(R\sqrt{\lambda_l^n}) - R\sqrt{\lambda_l^n} j_{l+1}(R\sqrt{\lambda_l^n}) = 0 \tag{9.66}$$

for $l > 0$ together with the relation (9.53b)

$$j_1(R\sqrt{\lambda_0^n}) = 0 \tag{9.67}$$

when $l = 0$. The normalisation condition yields

$$\psi_l^n(r) = \left[\frac{2}{R}\frac{R^2\lambda_l^n}{j_l^2(R\sqrt{\lambda_0^n})[R^2\lambda_l^n - l(l+1)]}\right]^{1/2} r j_l(r\sqrt{\lambda_l^n}). \quad (9.68)$$

Putting $l = 0$, $n \neq 0$ in this expression for $\psi_l^n(r)$ gives the relation (9.57). Using the properties of the j_l, the final expression for the structure factors $A_n^l(Q)$ can be evaluated

$$A_n^l(Q) = \frac{6R^2\lambda_l^n}{R^2\lambda_l^n - l(l+1)}\left[\frac{QRj_{l+1}(QR) - lj_l(QR)}{R^2[Q^2 - \lambda_l^n]}\right]^2 \quad (9.69a)$$

if $Q^2 \neq \lambda_l^n$, and, otherwise

$$A_n^l(Q) = \frac{3}{2}j_l^2(R\sqrt{\lambda_l^n})\frac{R^2\lambda_l^n - l(l+1)}{R^2\lambda_l^n}. \quad (9.70b)$$

Both expressions (9.69a) and (9.69b) above hold for $\{l, n\} \neq \{0, 0\}$. In that case, the EISF is given by (9.63). The final expression for the incoherent scattering law is

$$S(Q, \omega) = A_0^0(Q)\delta(\omega) + \sum_{\{l,n\}\neq\{0,0\}} (2l+1)A_n^l(Q)\mathcal{L}(\lambda_l^n D; \omega) \quad (9.71a)$$

where $\mathcal{L}(\lambda_l^n D; \omega)$ are lorentzian functions, with half-widths at half-maximum $\lambda_l^n D$,

$$\mathcal{L}(\lambda_l^n D; \omega) = \frac{1}{\pi}\frac{\lambda_l^n D}{(\lambda_l^n D)^2 + \omega^2}. \quad (9.71b)$$

Volino and Dianoux (1980) solved (9.47) numerically, calculating the 99 first eigenvalues λ_n^l. They evaluated the structure factors $A_n^l(Q)$. These are illustrated in figure 9.3 where they have been classified according to the values of the index n. Clearly as soon as $Qa \geq \pi$, the EISF $A_0^0(Q)$ becomes very small and a large number of terms have to be taken into account in the scattering law, to get a sufficient accuracy. The variation as a function of QR of the h.w.h.m. of the quasielastic component of the scattering law is shown in figure 9.4 where it is compared with the variation according to the usual DQ^2 law for an infinite medium. For $QR \to \infty$, the effects of the walls become unsignificant and the DQ^2 law is retrieved. Conversely, for $Qa \ll \pi$, the width is practically constant and equal to $\lambda_0^l D$, as for the rotational models.

9.2.3 Water mobility in a water-soaked Nafion® membrane

As a first example of diffusion of particles inside a restricted geometry, we shall report on a neutron quasielastic study of the mobility of water in water-soaked perfluorinated membranes. These are materials mainly used as separators in electrochemical applications. We shall be essentially concerned with Nafion® polymers where the backbone of the chains

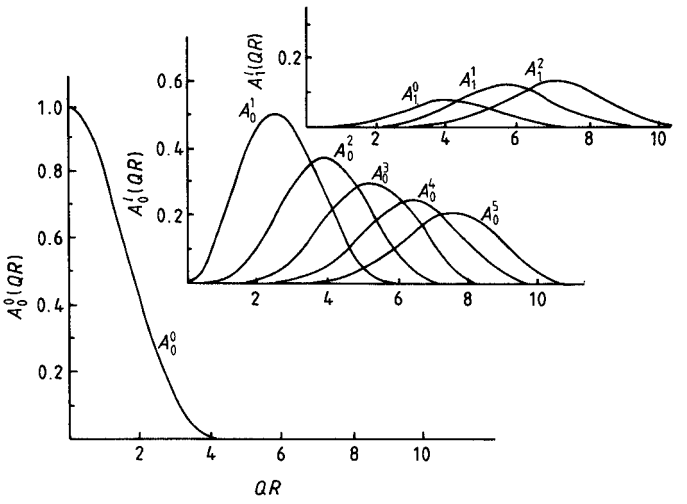

Figure 9.3 Elastic and quasielastic structure factors, evaluated from (9.8) as a function of Q.

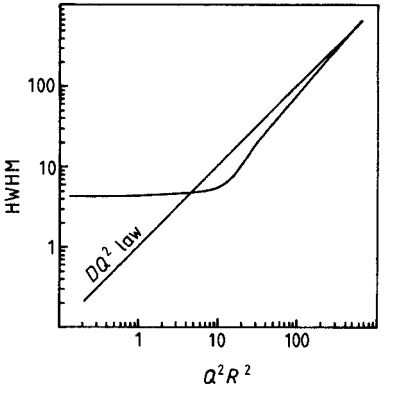

Figure 9.4 H.w.h.m. of the quasielastic component of the scattering law for a particle diffusing inside a sphere with radius R, evaluated as a function of QR. (Reproduced by permission of Taylor & Francis Ltd.)

consists of perfluoroethylene units with side groups

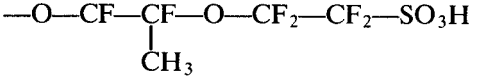

A large amount of work has been published on their commercial

applications but the relation between their macroscopic properties and microstructure is still not well established. Membranes made with Nafion® can absorb large quantities of water (typically 15 wt% in the study reported here), and their properties depend significantly on the amount of absorbed water. From results of small-angle x-ray scattering and dynamical mechanical experiments, the hypothesis of ion-clustering has been proposed by Yeo and Eisenberg (1977) and then confirmed from experimental and theoretical studies (Gierke 1977, Hopfinger *et al* 1977). The microstructure of the Nafion® water system is composed of three rather well-separated phases: a crystalline phase, an amorphous hydrophobic phase and an ionic hydrophilic phase. The microcrystallites act as physical crosslinks and limit the swelling of the ionic phase, which contains most of the water (Roche *et al* 1981, 1982). Diffraction experiments (Volino *et al* 1982) show a broad peak between 0.9 and 1.4 Å^{-1}, originating from the lateral packing of the perfluoroethylene chains. It can be separated into two components, attributed to the amorphous and crystalline parts of the membrane. Above all, the wet sample exhibits very intense small-angle scattering, meaning that the water is not uniformly distributed in the sample, but is located in clusters. Inside these clusters, NMR experiments suggest that the water molecules move with a correlation time of the order of 10^{-11} s at room temperature (Duplessix *et al* 1980). Most of the results obtained on these materials have been summarised in the book by Yeager and Eisenberg (1982). Recently, sorption–desorption phenomena during thermal cycling have been evidenced (Pineri *et al* 1985). We shall concentrate on the investigation with neutron scattering (Volino *et al* 1982, Dianoux *et al* 1982).

The experiments were carried out on the multi-chopper time-of-flight spectrometer IN5 at the Institut Laue–Langevin, with an energy resolution ranging from 9 to 18.5 μeV corresponding to a time-scale of 3.5×10^{-11} s to 7×10^{-11} s, and in a Q range 0.4–1.1 Å^{-1}, i.e. in a region where the (elastic) small-angle scattering was negligible and where the scattered intensity originates mainly from the water molecules.

Refinements of a single lorentzian line, convoluted with the instrument resolution function, show a systematical deviation of the shape of the quasielastic part of the experimental range; this deviation increases as a function of Q. In figure 9.5, the widths of the best-fit lorentzian curves have been reported. It is clear that the width is practically constant at low Q and then increases at larger values, in accordance with the model of diffusion in a sphere. This latter is illustrated (full line) using the average values $D = 1.8 \times 10^{-5}\ \text{cm}^2\,\text{s}^{-1}$ and $a = 4.25$ Å of the diffusion constant and of the sphere radius determined by refining each spectrum individually. The dashed line corresponds to the theore-

tical width predicted by the simple self-diffusion model with $D = 2.5 \times 10^{-5}\ \mathrm{cm^2\,s^{-1}}$ (bulk water).

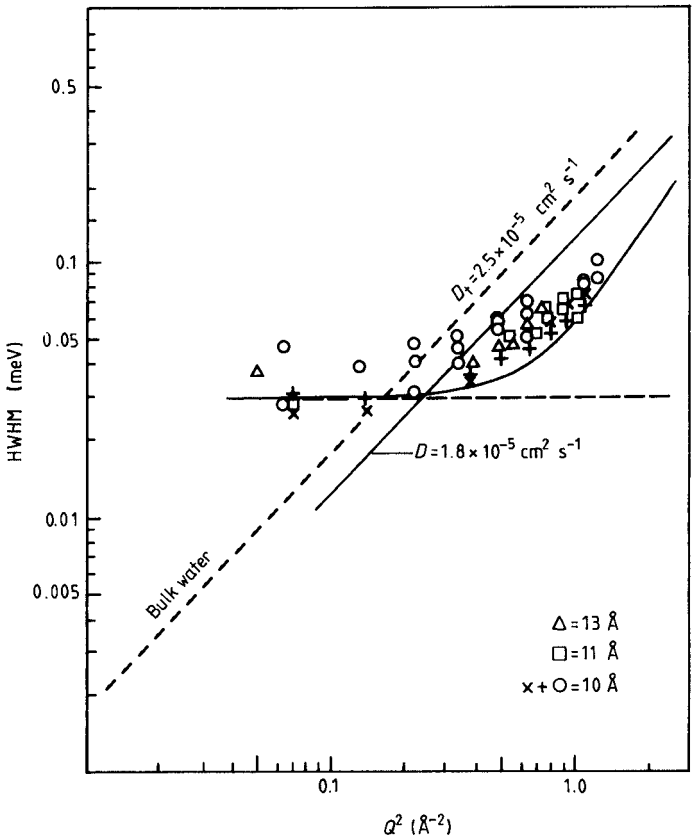

Figure 9.5 Widths of the quasielastic part of the neutron spectra obtained with Nafion® membranes (Volino *et al* 1982). (Reproduced by permission of Taylor & Francis Ltd.)

To describe correctly the central part of the spectra recorded at $Q \simeq 0.6$ Å, the long-range self-diffusion of the water molecules between the spheres has to be included in the model. The macroscopic self-diffusion coefficient was determined using an isotopic tracer added to the solution on one side of the membrane. The corresponding D_t value obtained at 298 K is $(1.6 \pm 0.1) \times 10^{-6}\ \mathrm{cm^2\,s^{-1}}$. An Arrhenius dependence on temperature is observed, with an activation energy of $\simeq 40.6 \pm 2.1\ \mathrm{kJ\,mol^{-1}}$. However, for $Q > 1\ \mathrm{Å^{-1}}$, a limitation of the model was found, coming probably from the assumption that the motion is diffusive. It is likely that in that range the finite jump distance between two successive positions of the proton should be taken into

account. We shall deal with this particular point later in this chapter.

9.3 Restricted Diffusion Inside a Volume with an Anisotropic Shape

Volino *et al* also invoked the possible reason that the small volumes were in fact not exactly spherical. So Dianoux *et al* (1982) also derived the neutron incoherent scattering law for molecules diffusing inside a cylinder with an impermeable surface. The calculations combine both the result of the one-dimensional diffusion over a segment of length L and the method described in §9.2.2 applied to the two-dimensional case of diffusion inside a circle.

The basic assumption is that the diffusive motions inside the cylinder along the axis and perpendicular to it are not coupled. Let us choose the cylinder axis as Oz axis (figure 9.6) and if θ denotes the polar angle of the neutron momentum transfer $\boldsymbol{Q}$ with respect to this axis, the scattering law can be written as the convolution product in ω

$$S(\boldsymbol{Q}, \omega) = S^{\parallel}(Q_z, \omega) \otimes S^{\perp}(Q_c, \omega) \tag{9.72}$$

of the incoherent scattering laws $S^{\parallel}$ and $S^{\perp}$ for diffusion parallel and perpendicular to Oz, respectively. $Q_z = Q\cos\theta$ and $Q_c = Q\sin\theta$ are the projections of $\boldsymbol{Q}$ along Oz and perpendicular to Oz (see figure 9.6). Using the expressions (9.6), (9.7) and (9.8), we can write

$$S^{\parallel}(Q\cos\theta, \omega) = A_0(Q_z)\delta(\omega) + \sum_{n=1}^{\infty} A_n(Q_z)\mathcal{L}_n(\omega) \tag{9.73a}$$

where $\mathcal{L}_n(\omega)$ are normalised lorentzian functions with half-widths

$$\tau_n^{-1} = \frac{n^2\pi^2}{L^2} D_z. \tag{9.73b}$$

The elastic structure factor $A_0(Q_z)$ and the quasielastic structure factors $A_n(Q_z)$ are expressed by

$$A_0(Q_z) = j_0^2\left(\frac{Q_z L}{2}\right) \tag{9.74a}$$

and

$$A_n(Q_z) = \frac{4(Q_z L)^2[1 - (-1)^n \cos(Q_z L)]}{[(Q_z L)^2 - (n\pi)^2]^2}. \tag{9.74b}$$

To derive the expressions $S^{\perp}(Q_c, \omega)$, we follow closely the successive steps of the preceding section. The relevant diffusion equation for the probability function is

$$\frac{1}{D_c}\frac{\partial}{\partial t}\mathcal{P}(\boldsymbol{r}, \boldsymbol{r}_0; t) = \nabla^2\mathcal{P}(\boldsymbol{r}, \boldsymbol{r}_0; t). \tag{9.75}$$

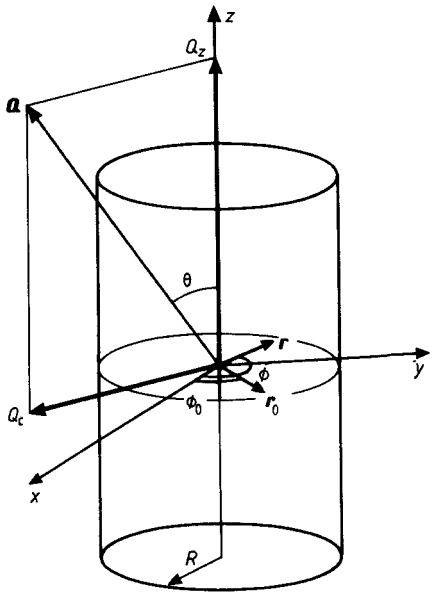

Figure 9.6 Set of coordinates for a particle diffusing inside a cylinder.

We look for a solution by expanding $\mathcal{P}(\boldsymbol{r}, \boldsymbol{r}_0; t)$ in terms of symmetry-adapted functions which, in the case of a cylindrical symmetry are simply periodic exponential functions $\exp[in(\phi - \phi_0)]$, ϕ and ϕ_0 being the angular coordinates of $\boldsymbol{r}$ and $\boldsymbol{r}_0$, respectively (see figure 9.6). Formally,

$$\mathcal{P}(\boldsymbol{r}, \boldsymbol{r}_0; t) = \frac{1}{\pi} \sum_{n=-\infty}^{\infty} A_n(r, r_0; t) \exp[in(\phi - \phi_0)]. \tag{9.76}$$

Using an expression of the laplacian operator in polar coordinates, the functions $A_n(r, r_0; t)$ verify the equation

$$\frac{1}{D_c} \frac{\partial A_n}{\partial t} = \frac{1}{r} \frac{\partial}{\partial r} \left(r \frac{\partial A_n}{\partial r} \right) - \frac{n^2}{r} A_n \tag{9.77}$$

and the usual condition of normalisation:

$$\int_0^R \mathcal{P}(\boldsymbol{r}, \boldsymbol{r}_0; t) \, \mathrm{d}\boldsymbol{r} = \int_0^R A_0(r, r_0; t) \, \mathrm{d}r = 1. \tag{9.78}$$

Similarly, at initial time $t = 0$, we have necessarily

$$\mathcal{P}(\boldsymbol{r}, \boldsymbol{r}_0; 0) = \delta(\boldsymbol{r} - \boldsymbol{r}_0) = \frac{1}{r} \delta(r - r_0) \delta(\phi - \phi_0) \tag{9.79}$$

which implies that

$$A_n(r, r_0; 0) = \frac{1}{r}\delta(r - r_0). \tag{9.80}$$

The limit at infinite time of the distribution $\mathcal{P}(r, r_0; t)$ is stationary

$$\mathcal{P}(r, r_0; \infty) = p(r) = \frac{1}{\pi R^2}. \tag{9.81}$$

The boundary conditions are that the flux is null at $r = 0$ and R.

$$\left[\frac{\partial}{\partial r}\mathcal{P}(r, r_0; t)\right]_{r=0,R} = 0. \tag{9.82}$$

We refer to the original work of Dianoux *et al* (1982) for more information about the calculations, which are similar to the method developed in the sphere case. The result is

$$S^{\perp}(Q_c, \omega) = \sum_{n=0}^{\infty}\sum_{m=0}^{\infty} B_m^0(Q_c)\mathcal{L}(x_m^n, \omega) \tag{9.83}$$

where $\mathcal{L}(x_m^n, \omega)$ are normalised lorentzian functions,

$$\mathcal{L}(x_m^n, \omega) = \frac{1}{\pi}\frac{(x_m^n)^2 D_c/R^2}{[(x_m^n)^2 D_c/R^2]^2 + \omega^2} \tag{9.84a}$$

if $x_m^n \neq 0$, and otherwise:

$$\mathcal{L}(0, \omega) = \delta(\omega). \tag{9.84b}$$

The term x_m^n is the $(m + 1)$th root of the equation for the cylindrical Bessel functions $J_n(x)$

$$\frac{\mathrm{d}}{\mathrm{d}x}[J_n(x)] = 0 \tag{9.85}$$

imposed by the boundary condition at $r = R$. These values are tabulated by Abramovitz and Stegun (1965). The structure factors $B_m^n(Q_c)$ are

$$B_m^n(Q_c) = \frac{4(x_m^n)^2}{(x_m^n)^2 - n^2}\left[\frac{Q_c J_{n+1}(Q_c R) - nJ_n(Q_c R)}{(Q_c R)^2 - (x_m^n)^2}\right]^2. \tag{9.86}$$

In particular, the EISF is given by

$$B_0^0(Q_c) = \left[\frac{2J_1(Q_c R)}{Q_c R}\right]^2. \tag{9.87}$$

Using the expressions (9.72), (9.83) and (9.6), the complete scattering function appears as the sum of the elastic term corresponding to the EISF

$$C_{00}^0(\boldsymbol{Q}) = A_0(Q_z)B_0^0(Q_c) = A_0(Q\cos\theta)B_0^0(Q\sin\theta) \tag{9.88}$$

and of lorentzian lines, associated to the structure factors

$$C_{lm}^n(\boldsymbol{Q}) = A_l(Q_z)B_m^n(Q_c) = A_l(Q\cos\theta)B_m^n(Q\sin\theta) \tag{9.89}$$

whose h.w.h.m. are

$$x_{lm}^{n} = \frac{l^2\pi^2}{L^2}D_z + \frac{(x_m^n)^2}{R^2}D_c. \tag{9.90}$$

It must be pointed out that the calculations above have been developed for a crystalline sample. When dealing with a powder specimen, the structure factors have to be averaged over all possible directions of $\boldsymbol{Q}$,

$$C_{lm}^{n}(Q) = \frac{1}{\pi}\int_0^{\pi} C_{lm}^{n}(\boldsymbol{Q}) \sin\theta \, d\theta. \tag{9.91}$$

Dianoux and Volino have evaluated the variation of the EISF and of the width of the quasielastic part, as a function of the ratio $\delta = L/2R$. Depending on the value of this parameter, the shape of the volume inside which the diffusion occurs will be more or less close to a sphere. Extreme situations are the rod-shape volume ($\delta \rightarrow \infty$) and the disc-shape volume ($\delta \rightarrow 0$). The analysis was carried out as a function of the value of the maximum distance between the centre of the cylinder and the surface $\rho = [R^2 + L^2/4]^{1/2}$. It turns out that, providing that the general shape does not deviate too much from a globular form, the results are similar to those for a sphere. Conversely, significant differences occur as soon as $\delta \gg 1$ or $\delta \ll 1$ (see figures 9.7 and 9.8). For both disc-shape and rod-shape volumes, the EISF decreases slowly and the h.w.h.m. remains nearly constant until large values of $Q\rho$. Actually, for the Nafion® membrane, Volino *et al* found that the anisotropy of the

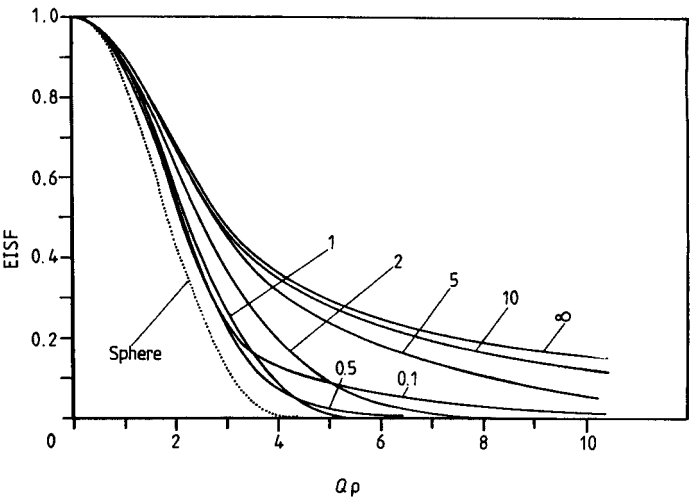

Figure 9.7 Model of a particle diffusing inside an impermeable cylinder of radius R and length L. Variation of the EISF as a function of $Q\rho$, $(\rho = (R^2 + L^2/4)^{1/2})$ for various values of $\delta = L/2R$. The case of an impermeable sphere of radius ρ is also reported (by courtesy of Dianoux *et al* 1982). (Reproduced by permission of Taylor & Francis Ltd.)

shape of the restricted volume was small. Moreover, from experiment they show that a stretching of the sample introduces no anisotropy in the neutron data, which was not found in the case of small-angle x-ray scattering experiments.

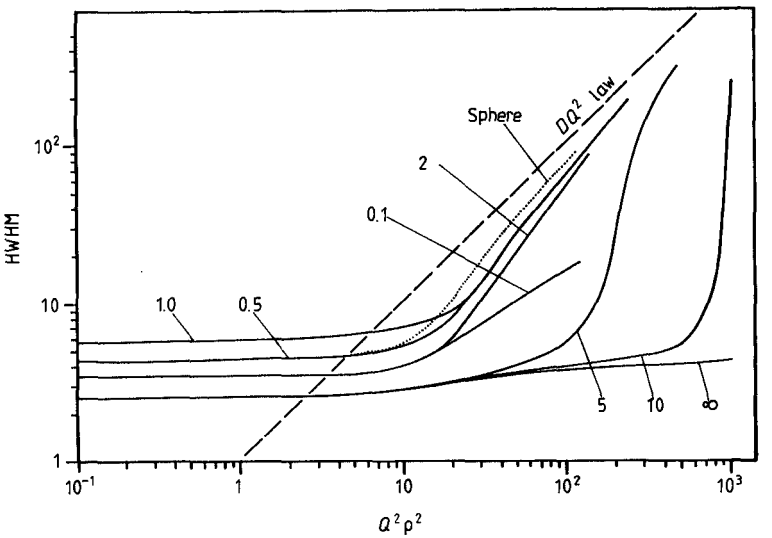

Figure 9.8 Model of a particle diffusing inside an impermeable cylinder of radius R and length L. Variation of the h.w.h.m. of the broadened component of the scattering law, as a function of $(Q\rho)^2$, $(\rho = R^2 + L^2/4)^{1/2}$ for various values of $\delta = L/2R$. The unit for the ordinate scale is D/ρ^2. The curve for an impermeable sphere of radius ρ and Fick's law are also plotted (by courtesy of Dianoux *et al* 1982). (Reproduced by permission of Taylor & Francis Ltd.)

9.4 Random Jump-Diffusion in Bounded Media

So far, the restricted diffusion models that we have presented have been based on the assumption of continuous diffusion in the allowed region. All of them predict a linear dependence of the broadening of the quasielastic part on Q^2, at sufficiently high values of Q. Indeed, for small distances in comparison with the dimensions of the allowed volume, the dimensions of the boundaries become insignificant and the form of the scattering law tends to the lorentzian shape for unbounded diffusion, with a h.w.h.m. of DQ^2.

However, considerable deviations from linearity at high Q are sometimes observed, as in the case of diffusion of water molecules in

montmorillonite clays (Hall *et al* 1978, Ross and Hall 1980): the broadening tends towards an asymptotic value independent of Q. Referring to chapter 4, where the problem of long-range diffusion is widely analysed, such a behaviour is more in accordance with a jump-diffusion rather than with a continuous diffusion model.

In this section we derive the form of the scattering law for particles undergoing a random-walk diffusion between two impermeable boundaries. This random-walk is assumed to be characterised by a gaussian distribution of jump-lengths. Following the original calculation of Hall and Ross (1981), we shall first derive the scattering function for an unrestricted random-walk diffusion, and then extend the method to the restricted case.

The basic statement considers the jump-diffusion as a markovian process, according to which successive jumps are uncorrelated but governed by a spatial probability distribution $\rho(r)$. In the absence of precise information about the microscopic dynamical behaviour of the particles, the choice of the distribution function is not unique. In their original work, Hall and Ross (1981) found it convenient to work with an isotropic distribution of jump-lengths.

$$\rho(r) = \frac{2r^2}{r_0^3\sqrt{2\pi}} \exp(-r^2/2r_0^2). \tag{9.92}$$

One verifies easily that this distribution is normalised:

$$\int_0^\infty \rho(r)\,\mathrm{d}r = 1 \tag{9.93}$$

and that it corresponds to a mean-square jump-length

$$\begin{aligned} \langle r^2 \rangle &= \int_0^\infty r^2 \rho(r)\,\mathrm{d}r \\ &= 3r_0^2. \end{aligned} \tag{9.94}$$

Therefore, the relevant distribution for a jump in any direction exhibits a simple gaussian form:

$$\rho(r) = \frac{1}{(r_0\sqrt{2\pi})^3} \exp\left(-\frac{r^2}{2r_0^2}\right). \tag{9.95}$$

The spatial distribution after two jumps is the self-convolution of $\rho(r)$

$$\rho_2(r) = \int \rho(r')\rho(r' - r)\,\mathrm{d}r. \tag{9.96}$$

Using (9.95), we easily find

$$\rho_2(r) = \frac{1}{(r_0\sqrt{4\pi})^3} \exp\left(-\frac{r^2}{4r_0^2}\right). \tag{9.97}$$

Similarly, the spatial distribution after n jumps

$$\rho_n(\boldsymbol{r}) = \int \mathrm{d}\boldsymbol{r}_1 \int \mathrm{d}\boldsymbol{r}_2 \ldots \int \mathrm{d}\boldsymbol{r}_{n-1} \rho(\boldsymbol{r}_1)\rho(\boldsymbol{r}_2) \ldots \rho(\boldsymbol{r}_{n-1} - \boldsymbol{r}) \quad (9.98)$$

is a gaussian distribution of mean square deviation nr_0^2

$$\rho_n(\boldsymbol{r}) = \frac{1}{(r_0\sqrt{2n\pi})^3} \exp\left(-\frac{r^2}{2nr_0^2}\right). \quad (9.99)$$

Simultaneously, the probability of a scatterer having made n jumps after a time t is a Poisson distribution

$$P(n; t) = \frac{1}{n!}\left(\frac{t}{\tau}\right)^n \exp\left(-\frac{t}{\tau}\right) \quad (9.100)$$

where τ is the mean between two successive jumps. Under the assumptions above, the probability of finding a scatterer at $\boldsymbol{r}$ at time t, is given by

$$G(\boldsymbol{r}, t) = \sum_{n=0}^{\infty} \rho_n(\boldsymbol{r}) P(n; t). \quad (9.101)$$

Actually, this relation is quite general and does not depend on the precise forms for $\rho_n(\boldsymbol{r})$ and $P(n; t)$. The intermediate scattering function is the Fourier transform of $G(\boldsymbol{r}, t)$

$$I(\boldsymbol{Q}, t) = \int G(\boldsymbol{r}, t) \exp[\mathrm{i}\boldsymbol{Q}\cdot\boldsymbol{r}]\, \mathrm{d}\boldsymbol{r}. \quad (9.102)$$

Using the expression of $P(n; t)$ (9.100) and taking into account the well-known property of the Fourier transform of a convolution product, we get

$$\begin{aligned} I(\boldsymbol{Q}, t) &= \sum_{n=0}^{\infty} \left[\int \rho(\boldsymbol{r}) \exp(\mathrm{i}\boldsymbol{Q}\cdot\boldsymbol{r})\, \mathrm{d}\boldsymbol{r}\right]^n \frac{1}{n!}\left(\frac{t}{\tau}\right)^n \exp\left(-\frac{t}{\tau}\right) \\ &= \exp\left\{-\left[1 - \int \rho(\boldsymbol{r}) \exp(\mathrm{i}\boldsymbol{Q}\cdot\boldsymbol{r})\, \mathrm{d}\boldsymbol{r}\right]\frac{t}{\tau}\right\} \\ &= \exp\left\{-\Delta(\boldsymbol{Q})\frac{t}{\tau}\right\} \end{aligned} \quad (9.103)$$

where we have introduced

$$\Delta(\boldsymbol{Q}) = 1 - \int \rho(\boldsymbol{r}) \exp(\mathrm{i}\boldsymbol{Q}\cdot\boldsymbol{r})\, \mathrm{d}\boldsymbol{r}. \quad (9.104)$$

The incoherent scattering function, i.e. the time-Fourier transform of $I(\boldsymbol{Q}, t)$ takes the form of a lorentzian function

$$S(\boldsymbol{Q}, \omega) = \frac{1}{\pi} \frac{\Delta(\boldsymbol{Q})\tau}{[\Delta(\boldsymbol{Q})]^2 + \omega^2\tau^2} \quad (9.105)$$

of half-width

$$\Delta\omega(\boldsymbol{Q}) = \frac{1}{\tau}\Delta(\boldsymbol{Q}). \quad (9.106)$$

Assuming the gaussian distribution $\rho(r)$ given by (9.95), it is easily found that the h.w.h.m. of the scattering function is given by

$$\Delta\omega(\boldsymbol{Q}) = \frac{1}{\tau}\left[1 - \exp\left(-\frac{Q^2 r_0^2}{2}\right)\right]. \tag{9.107}$$

Clearly, when $Qr_0 \to \infty$, $\Delta\omega(\boldsymbol{Q})$ tends to an asymptotic value equal to τ^{-1}, while for small Qr values

$$\lim_{Qr_0 \to 0} \Delta\omega(\boldsymbol{Q}) = \frac{Q^2 r_0^2}{2\tau} = DQ^2 \tag{9.108}$$

where the relationship

$$D = \frac{\langle r^2 \rangle}{6\tau} \tag{9.109}$$

between continuous diffusion and jump-diffusion, derived from equations (5.8) and (9.94), has been taken into account. The variation of the broadening evaluated from (9.107) as a function of Qr is illustrated in figure 9.9. The straight line corresponding to Fick's law has also been plotted. Clearly, the rapidity of the convergence of the broadening curve towards its asymptotic value at high Q strongly depends on the precise expression which is chosen for the distribution. Hall and Ross have made a comparison with the early model by Singwi and Sjölander reported in chapter 5, which is based on a succession of continuous diffusions and oscillatory motions of the particle. Referring to (5.97), the quasielastic broadening (h.w.h.m.) is

$$\Delta\omega(\boldsymbol{Q}) = \frac{1}{\tau_0}\left[1 - \frac{\exp(-2W)}{1 + DQ^2\tau_0}\right]. \tag{9.110}$$

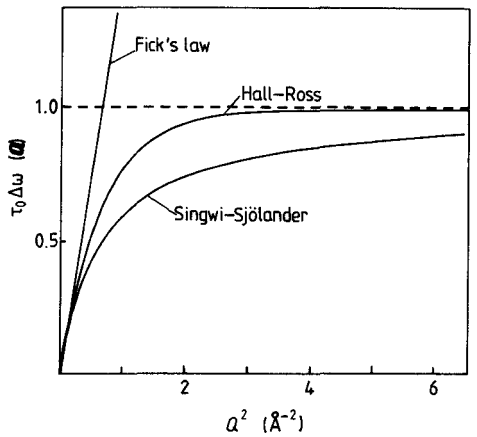

Figure 9.9 Comparison of the variation as a function of Q^2 of the quasielastic broadening for three different models.

Here τ_0 is the lifetime of the oscillatory motion between two diffusive steps. In the limiting case of a small Debye–Waller factor ($2W$),

$$\Delta\omega(\boldsymbol{Q}) = \frac{DQ^2}{1 + DQ^2\tau_0}. \tag{9.111}$$

This expression was found to converge more slowly than (9.107) to the asymptotic value $1/\tau_0$ at high Q. Actually, according to (9.104), an experimental determination of $\rho(r)$ could be obtained from a simple Fourier transform of $\Delta(\boldsymbol{Q})$ providing that $\Delta\omega(\boldsymbol{Q})$ could be measured over a sufficient $\boldsymbol{Q}$ range. To our knowledge, no attempt at such a direct determination has so far been made.

When dealing with the problem of jump-diffusion within a bounded medium, we must ensure that the concentration gradient immediately inside each boundary is nil. This condition is fulfilled under the assumption that any particle which encounters the boundary is simply reflected, and that the total jump-length is unchanged. This hypothesis is similar to the assumption of the velocity conservation in the continuous case. Let us consider a scatterer performing a jump-diffusion in one dimension between two impermeable walls separated by L. The probability distribution of being at x between 0 and L, after a single jump, given that the particle was located at x_0 at $t = 0$ can be expressed as

$$\rho_1(x, x_0) = \sum_{p=-\infty}^{\infty} \rho_{1p}(x, x_0) \tag{9.112}$$

where $\rho_{1p}(x, x_0)$ takes into account a single-jump process involving p reflections on the boundaries, such that the total travel is $x \pm x_0 + 2pL$. Using a gaussian form for $\rho_{1p}(x, x_0)$

$$\rho_1(x, x_0) = \frac{1}{r_0\sqrt{2\pi}} \sum_{p=-\infty}^{\infty} \{\exp[-(x - x_0 + 2pL)^2/2r_0^2] + \exp[-(x + x_0 + 2pL)^2/2r_0^2]\}. \tag{9.113}$$

The original calculations of Hall and Ross consist in an expansion of $\rho_1(x, x_0)$ into a Fourier series of cosine functions

$$\rho_1(x, x_0) = \frac{1}{L} + \frac{2}{L}\sum_{n=1}^{\infty} \cos\left(\frac{n\pi x}{L}\right)\cos\left(\frac{n\pi x_0}{L}\right)\exp\left[-\frac{n^2\pi^2 r_0^2}{2L^2}\right]. \tag{9.114}$$

Therefore, the spatial distribution after m jumps appears as an expansion into exponential terms with a mean-square jump-distance mr_0^2

$$\rho_m(x, x_0) = \frac{1}{L} + \frac{2}{L}\sum_{n=1}^{\infty} \cos\left(\frac{n\pi x}{L}\right)\cos\left(\frac{n\pi x_0}{L}\right)\exp\left[-\frac{mn^2\pi r_0^2}{2L^2}\right]. \tag{9.115}$$

According to (9.101)

$$G(x, x_0; t) = \sum_{m=1}^{\infty} \rho_m(x, x_0) P(m; t)$$
$$= \frac{1}{L} \sum_{n=-\infty}^{\infty} \cos\left(\frac{n\pi x}{L}\right) \cos\left(\frac{n\pi x_0}{L}\right) \exp\left\{-\frac{t}{\tau}\left(1 - \exp\left[-\frac{n^2\pi^2 r_0^2}{2L^2}\right]\right)\right\} \tag{9.116}$$

where a Poisson form (9.100) of $P(m; t)$ has been assumed.

If all the initial positions x_0 can be considered as equally probable (i.e. $p(x_0) = 1/L$), the intermediate scattering function

$$I(Q_x, t) = \int \mathrm{d}x_0 p(x_0) \int \mathrm{d}x G(x, x_0; t) \exp[\mathrm{i}Q_x(x - x_0)] \tag{9.117}$$

yields, after time-Fourier transform, the following scattering law

$$S(Q_x, \omega) = A_0(Q_x L)\delta(\omega) + \sum_{n=1}^{\infty} A_n(Q_x L)\mathcal{L}_n(\omega) \tag{9.118}$$

where the half-widths of the lorentzian functions $\mathcal{L}_n(\omega)$ are expressed by

$$\Delta\omega_n = \frac{1}{\tau}\left[1 - \exp\left(-\frac{n^2\pi^2 r_0^2}{2L^2}\right)\right] \tag{9.119}$$

while the structure factors $A_0(Q_x L)$ and $A_n(Q_x L)$ are exactly given by (9.8).

It is noteworthy that the jump-diffusion model and the continuous diffusion model differ from each other only in the expressions of the half-widths of the lorentzian functions of their respective scattering laws.

Figure 9.10 shows the comparison of the variation with Q^2L^2 of the broadening of the quasielastic part of the scattering functions related to the jump-diffusion or continuous diffusion models. Use has been made of the relation $D = r_0^2/2\tau$ and the ordinates are expressed in units of $r_0^2/2\tau L^2$ and D/L^2, respectively. Clearly, the h.w.h.m. for the random-jump restricted diffusion model exhibits the characters both of the jump models and of the 'diffusion within a restricted volume' model, tending to asymptotic values at low and high Q. At low Q, we are mainly concerned with the large distances, i.e. with the effects of the boundaries, which force the h.w.h.m. to deviate from the DQ^2 law and to tend to $\pi^2 r_0^2/2L^2\tau$. Conversely, at large Q, the nature of the motion over short distances predominates and, because the elementary displacements of the particle are not infinitely small, the h.w.h.m. of the quasielastic component tends to the asymptotic value $1/\tau$. This is illustrated in figure 9.11, where the quasielastic part of the scattering function is represented as a function of both the energy transfer and the scattering momentum transfer. Clearly, at low Q, a strong increase of the maximum appears, which is linked to the simultaneous decrease of the EISF. At intermediate Q values, the maximum rapidly decreases.

Indeed the maximum and the width of a normalised lorentzian function are strongly correlated and in this region, the quasielastic part broadens according to the DQ^2 law. Then, at larger Q values, the maximum remains nearly constant, corresponding to the asymptotic behaviour of the broadening.

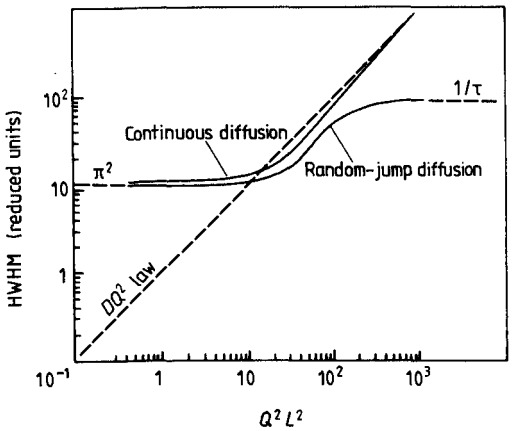

Figure 9.10 Comparison of the variation against Q^2 of the h.w.h.m. of the broadening for three models corresponding to the translation along one direction: the continuous diffusion and the random-jump diffusion along a straight line of length L and the usual Fick's law. (Reproduced by permission of Taylor & Francis Ltd.)

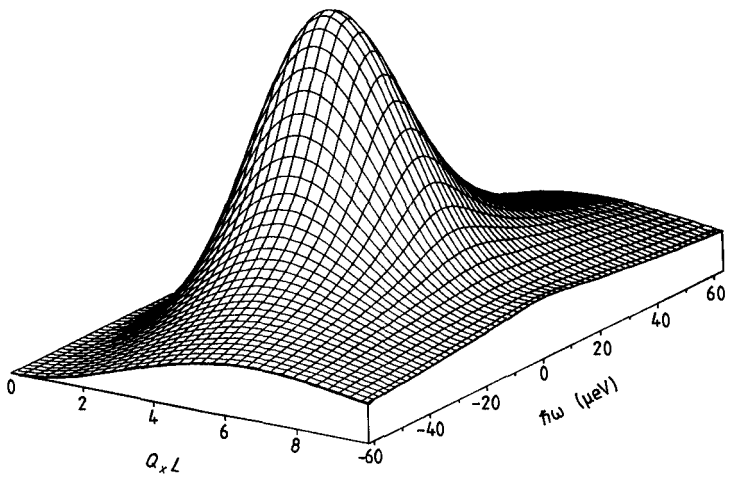

Figure 9.11 Three-dimensional representation in the (Q, ω) space of the quasielastic part of the scattering function corresponding to jump diffusion along a segment of length L.

As in the continuous case, the generalisation to three dimensions is straighforward. Assuming no correlations between the three directions, we get

$$S(\boldsymbol{Q}, \omega) = \sum_{mnp} A_m^x(Q_x L_x) A_n^y(Q_y L_y) A_p^z(Q_z L_z) \mathcal{L}_{mnp}(\omega) \quad (9.120)$$

where $\mathcal{L}_{mnp}(\omega)$ is a lorentzian function, the width of which is given by

$$\Delta\omega_{mnp} = \frac{1}{\tau}\left\{1 - \exp\left[-(m^2 + n^2 + p^2)\frac{\pi^2 r_0^2}{2L^2}\right]\right\}. \quad (9.121)$$

9.5 Adsorption of Molecules by Zeolites

To conclude this chapter, we shall report on recent results obtained in the study of zeolites. The interpretations of these experiments provide illustrations of the various models we have presented, insofar as the molecules trapped inside them can move more or less freely depending on their size and on the strength of their interaction with the zeolite surface.

Zeolites are porous aluminosilicate crystals which exhibit, in some structural types, nearly spherical cavities regularly distributed over the crystal lattice. These cavities are connected through channels, whose diameters depend on the nature of the zeolite. Because the size of their cavities and channels are of the order of molecular dimensions, these materials offer an interesting tool insofar as they can be used for molecular sieving and catalysis (Breck 1973, Barrer 1978). Zeolites reversibly adsorb and desorb molecules. The access of these molecules to the interior of a zeolite is essentially governed by the dimensions of its access pores, which make it possible to discriminate between molecules on the basis of their size and shape. Zeolites with a low Si:Al ratio interact strongly with polar molecules. They are hydrophilic and widely used as desiccants. Conversely, the siliceous zeolites are rather organophilic.

Zeolites are widely used in heterogeneous catalysis, and especially in catalytic cracking of the heavier components of crude oil into lighter, more volatile materials. The necessity of good stabilities in stream atmospheres has stimulated the synthesis of rare-earth-exchanged materials or ultrastable desalinated Y zeolites with very high activities.

9.5.1 Rotational and translational dynamics of ethylene adsorbed by sodium-13-X zeolite

Both infrared spectroscopy and microcalorimetry have provided information about the adsorption of ethylene on a series of ion-exchanged

synthetic zeolites. The nature of the adsorption of the ethylene molecule was found to be dependent on the nature of the exchangeable cations. Except in the case of Cd-X and Ag-X adsorbents, the ethylene is relatively weakly held. Moreover, measurements of the linewidths of the bands of the adsorbed molecules, associated with symmetry considerations, show that except for Ag-X, all of the adsorbed ethylene molecules are freely rotating (Carter *et al* 1966). The proposed model assumes that the planar molecules are adsorbed parallel to the cage wall, and interact via their π-electrons oriented towards the ions of the zeolite. Reorientations occur about the C_2-molecule axis perpendicular to the surface. Simultaneously the existence of these interactions yields a lowering of the translational diffusion.

More recently, the IQNS technique was used to characterise the dynamics of the ethylene molecule (Wright and Riekel 1978). The contributions to the scattering due to rotation and translation were investigated separately by time-of-flight and backscattering technique, respectively. The former series of data was analysed on the basis of the uniaxial rotation model involving 90° or 180° jumps. Experimental values of the EISF are reported in figure 9.12.

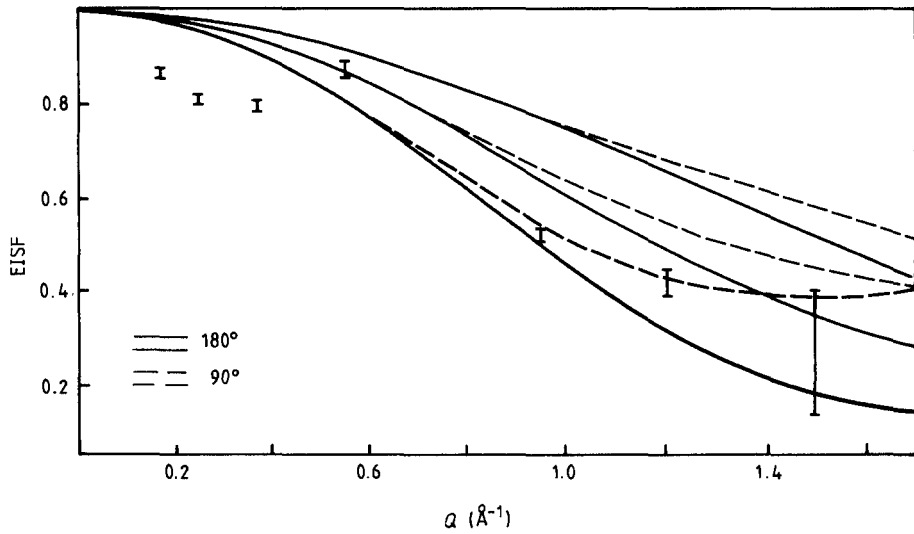

Figure 9.12 Experimental EISF values for ethylene molecules adsorbed in Na-X zeolite (Wright and Riekel 1978). These are compared with theoretical curves predicted by models based upon 180 or 90° rotations about an axis coinciding with the twofold molecule axis (bold curves) or perpendicular to it (thin curves). (Reproduced by permission of Taylor & Francis Ltd.)

Clearly, they are consistent with the theoretical curves predicted by the model in which rotations occur about the C_2 molecule axis. Conversely the models based on rotations about the two other principal axes can be ruled out. However, the distinction is not easy whether we are concerned with 90° or 120° jumps. Wright and Riekel gave preference to the twofold rotation model and deduced a mean residence time equal to $6 \pm 1.5 \times 10^{-12}$ s.

It must be mentioned that a non-negligible broadening of the elastic peak was visible, even with the time-of-flight spectrometer, originating from the long-range translational diffusion of the molecules. It was taken into account by a DQ^2 law, and refinements at low values of Q yielded a diffusion constant $D = 3.1 \pm 0.4 \times 10^{-6}\,\mathrm{cm^2\,s^{-1}}$. On the other hand, this broadening strongly deviates from the DQ^2 law and becomes nearly constant at high Q values, a behaviour which is typical of a jump mechanism. Backscattering experiments confirmed these values. Taking an approximate jump-distance of 5 Å (i.e. a molecule diameter), a value of $1.3 \pm 0.1 \times 10^{-10}$ s is obtained for the residence time between jumps for the translational diffusion, i.e. a value 20 times longer than between two rotational jumps.

9.5.2 Dynamics of benzene in Na-mordenite

Mordenites are zeolites with a high Si:Al ratio. They have numerous applications in catalysis owing to their structural and chemical properties. The crystal structure of Na-mordenite was determined by Meier (1961). The large pores consist of 12-membered rings which form the straight elliptical cylinders (7.0×5.8 Å). These main channels are connected together by smaller side channels composed of 8-membered rings. Schlenker *et al* (1979) have determined the composition as $Na_{7.3}K_{0.2}Ca_{0.03}Al_{8.3}Si_{39.9}O_{96}$. Mordenite has a marked shape selectivity for reactions such as benzene alkylation, because the free aperture of the largest pores is close to the critical dimension of the benzene molecule (only the large-pore variety adsorbs benzene). From quantum chemical and NMR investigations, it appears that the adsorption of benzene occurs as a result of the interaction between the π-electrons and the cations (Sauer and Deininger 1982). The Na cations are located at three different sites, denoted I′, IV and VI, with site occupancies equal to 3.1, 2.6 and 1.5, respectively. Site I′ is located at the centre of the distorted 8-membered ring, in the side channel; the other Na cations occupy positions in the main channel (site VI) and off-centre of the side-channel entrance (site IV). The only possible sites for benzene in Na-mordenite are sites IV and VI.

IQNS measurements were carried out for two values of benzene coverage, θ_1 and θ_2, corresponding to 0.85 and 1.4 benzene molecules adsorbed per tube of unit-cell length ($c = 7.52$ Å) (Jobic *et al* 1984). Experimental data consist of an almost purely elastic peak, slightly broadened, superimposed on a much wider quasielastic part. These two broadenings were attributed to long-range translational motion and localised rotational motion respectively, which, unlike what is found in the liquid state, are very different in magnitude. Thus the translational motion can be ignored in the analysis of the rotational profiles. The experimental EISF was found to be in agreement with a uniaxial rotation model involving 60° jumps of the molecule about its sixfold axis (see figure 9.13). At $T = 300$ K, the mean time between successive jumps was found to be equal to $\tau = 1.45 \times 10^{-12}$ s for θ_1 and $\tau = 2.05 \times 10^{-12}$ s for θ_2. An Arrhenius plot gave the same activation energy for θ_1 and θ_2: $E_A = 4.51$ kJ mol^{-1}.

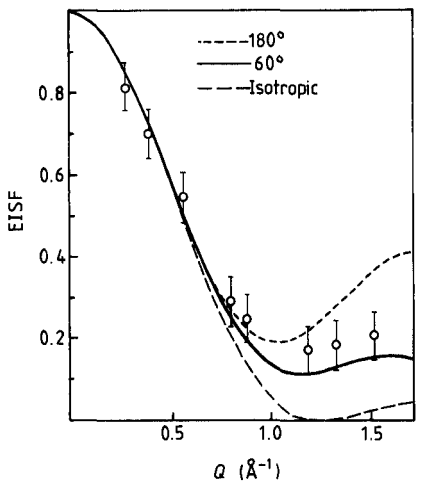

Figure 9.13 Experimental EISF values for benzene in Na mordenite (Jobic *et al* 1984), compared with various rotation models about the molecule six-fold axis.

It is interesting to compare these values of the mean residence time to those obtained in liquid benzene (Winfield and Ross 1972), where $\tau = 2.2 \times 10^{-12}$ s at $T = 300$ K or in the organometallic compound $(C_6H_6)Cr(CO)_3$ (Lucazeau 1983) in which case $\tau = 5.0 \times 10^{-11}$ s at $T = 300$ K. Clearly, it turns out that the rotational motions of benzene are very fast in zeolites, on the same scale as in the liquid. This confirms

the weak bonding of the benzene molecules to the sodium ions. From the analysis of the slight broadening of the elastic peak versus Q^2 a linear variation was observed and the slope gave the value $D_{\parallel} = 2 \times 10^{-6}\,\mathrm{cm^2\,s^{-1}}$ for the diffusion coefficient relative to the translation along the cylindrical pores. The corresponding activation energy was found to be very low ($0.85\,\mathrm{kJ\,mol^{-1}}$). Comparing this result with the diffusion coefficients obtained by pulsed field gradient NMR on a zeolitic system, it can be seen that in Na-X zeolite, Kärger and Ruthven (1981) have obtained at 300 K a diffusion coefficient of $0.2 \times 10^{-6}\,\mathrm{cm^2\,s^{-1}}$ for concentrations ranging from 1.1 to 2.5 molecules of benzene per cage. Using the same system, Zikanova *et al* (1980) have obtained at 360 K, in the case of low concentrations of benzene, a diffusion coefficient of $0.4 \times 10^{-6}\,\mathrm{cm^2\,s^{-1}}$. Moreover, for concentrations of more than half of the saturation capacity, a decrease of the self-diffusion was observed in the IQNS experiment where the broadening for the high coverage data (θ_2) was too small to be refined.

9.5.3 Methane in Na-A zeolite

Cohen de Lara and Kahn (1981) studied the dynamical behaviour of methane molecules adsorbed in Na-A-type zeolite, with chemical composition $Na_{12}(SiO_2AlO_2)_{12}$. The mean diameter of the cavities is 11.4 Å. They are connected through access pores of diameter 4.2 Å. Methane molecules, whose diameter is of the order of 4 Å can penetrate the cavities. In a previous experiment by Stockmeyer *et al* (1980), it was found that at room temperature the methane molecules move in the zeolite Na-A lattice almost freely. Conversely, at 25 K, the molecular centre of mass appears fixed to the cage wall and the rotational motion is hindered. This hindrance seems to be mainly due to the crystal field in the cavity (Cohen de Lara and Nguyen-Tan, 1976). Indeed the form of the quasielastic peak is almost unaffected by a variation of the methane density. This effect has also been studied on nitrous oxide (Cohen de Lara 1972, Cohen de Lara and Vincent 1976). Neutron diffraction experiments (Kahn *et al* 1982) show that the methane sites are probably in front of the Na(III) cations. Potential energy calculations for the couple CH_4–Na^+ lead to the conclusion that the most favourable orientation is such that the carbon–Na^+ axis is a C_{3v} axis with three hydrogens pointing to the cation and the least favourable is such that a single hydrogen is pointing to the Na^+ ion (Mouche *et al* 1984, Sauer *et al* 1980).

Among the four fundamental vibrations of the CH_4 molecule, in the gas phase, two are infrared active (ν_3 at $3020\,\mathrm{cm^{-1}}$ and ν_4 at $1306\,\mathrm{cm^{-1}}$). The two others (ν_1 at $2914\,\mathrm{cm^{-1}}$ and ν_2 at $1526\,\mathrm{cm^{-1}}$) are

only Raman active. In the adsorbed state, the dipolar moment induced by the field existing in the cavity allows the forbidden band ν_1 to appear, while ν_3 is split into two components (Cohen de Lara and Kahn 1984). Both lines are shifted towards lower frequencies as in the liquid and solid states. For ν_1, the frequency shift increases when the temperature decreases, owing to stronger interactions with the wall of the zeolite, and simultaneously its width is reduced. Under the assumption that this width is only dependent on the lifetime of the vibration, it is possible to deduce a residence time τ equal to 5×10^{-13} s at 273 K and 1.3×10^{-12} s at 210 K, i.e. corresponding to an activation energy of 6.28 kJ mol^{-1}.

Cohen de Lara and Kahn analysed their neutron scattering data with a rather simple model where the CH_4 molecules move more or less uniformly in the volume contained between two spheres of radii R_1 and R_2. They calculate the EISF by direct integration within the allowed volume, i.e.

$$A_0(Q) = \left| \frac{1}{Z} \int g(r) \exp(i\boldsymbol{Q}\cdot\boldsymbol{r})\, d\boldsymbol{r} \right|^2 \tag{9.122a}$$

with

$$Z = \int g(r)\, d\boldsymbol{r} \tag{9.122b}$$

$g(r)$ is the probability of finding the atom at a distance r from the centre of the spheres

$$g(r) = 1 \qquad R_1 < r < R_2 \tag{9.123a}$$

$$g(r) = 0 \qquad r \leqslant R_1 \text{ and } r \geqslant R_2 \tag{9.123b}$$

The final result is

$$A_0(Q) = \left\{ \frac{3R^2}{a^2 + 3R^2} \left[j_0(QR) j_0(Qa) + \frac{a}{R} \frac{\cos(Qr)}{Qr} j_1(Qa) \right] \right\}^2 \tag{9.124}$$

where we have introduced

$$R = \tfrac{1}{2}(R_2 + R_1) \tag{9.125a}$$

and

$$a = \tfrac{1}{2}(R_2 - R_1). \tag{9.125b}$$

It turns out that this expression can be obtained from the method developed in §9.2 which, in addition, provides an expression of the quasielastic part of the scattering law.

(a) Diffusion between two concentric impermeable spheres

The calculations follow exactly the lines of §9.9.2 except that the boundary conditions, equivalent to (9.51) are now:

$$\frac{\mathrm{d}}{\mathrm{d}r}\left[\frac{1}{r}\psi_l^n(r)\right]_{r=R_1,R_2} = 0 \tag{9.126}$$

where R_1 and R_2 ($R_2 > R_1$) are the radii of the spheres. Using the general solution (9.49) of (9.48) we get a system of linear equations analogous to (9.52)

$$-c_1 j_1(R_1\sqrt{\lambda_0^n}) + c_2 j_2(R_1\sqrt{\lambda_0^n}) = 0 \tag{9.127a}$$

$$-c_1 j_1(R_2\sqrt{\lambda_0^n}) + c_2 j_2(R_2\sqrt{\lambda_0^n}) = 0 \tag{9.127b}$$

Here $j_1(x)$ and $j_2(x)$ are spherical Bessel functions. The eigenvalues λ_0^n are determined from the condition

$$j_1(R_1\sqrt{\lambda_0^n})j_{-2}(R_2\sqrt{\lambda_0^n}) - j_1(R_2\sqrt{\lambda_0^n})j_{-2}(R_1\sqrt{\lambda_0^n}) = 0 \tag{9.128}$$

Introducing the roots of this equation into (9.127) the constant c_2 is related to c_1, via

$$c_2 = c_1 \frac{j_1(R_1\sqrt{\lambda_0^n})}{j_{-2}(R_1\sqrt{\lambda_0^n})} = \frac{-\sin(R_1\sqrt{\lambda_0^n}) + R_1\sqrt{\lambda_0^n}\cos(R_1\sqrt{\lambda_0^n})}{\sin(R_1\sqrt{\lambda_0^n}) + R_1\sqrt{\lambda_0^n}\cos(R_1\sqrt{\lambda_0^n})}$$

c_1 is itself obtained from the normalisation condition

$$\int_{R_1}^{R_2} |\psi_0^n(\mathrm{r})|^2\,\mathrm{d}r = 1 \tag{9.128a}$$

$$= c_1^2\left[\int_{R_1}^{R_2} \sin^2(r\sqrt{\lambda_0^n})\,\mathrm{d}r + \frac{j_1^2(R_1\sqrt{\lambda_0^n})}{j_{-2}^2(R_1\sqrt{\lambda_0^n})}\int_{R_1}^{R_2} \cos^2(r\sqrt{\lambda_0^n})\,\mathrm{d}r\right.$$

$$\left. + \frac{j_1(R_1\sqrt{\lambda_0^n})}{j_{-2}(R_1\sqrt{\lambda_0^n})}\int_{R_1}^{R_2} \sin(2r\sqrt{\lambda_0^n})\,\mathrm{d}r\right]. \tag{9.128b}$$

In the case of the vanishing eigenvalue λ_0^0, the limiting conditions applied to $\psi_0^0(r)$ given by (9.59) lead to

$$\frac{\mathrm{d}}{\mathrm{d}r}\left[\frac{1}{r}\psi_0^0(r)\right]_{r=R_1,R_2} = -\left[\frac{c_2}{r^2}\right]_{r=R_1,R_2} = 0. \tag{9.129}$$

Thus $c_2 = 0$ and from the normalisation condition

$$\int_{R_1}^{R_2} |\psi_0^0(r)|^2\,\mathrm{d}r = \int_{R_1}^{R_2} c_1^2 r^2\,\mathrm{d}r = 1 \tag{9.130}$$

we get

$$c_1 = \left(\frac{3}{R_2^3 - R_1^3}\right)^{1/2} \tag{9.131}$$

and

$$\psi_0^0(r) = \frac{r\sqrt{3}}{(R_2^3 - R_1^3)^{1/2}}. \tag{9.132}$$

It follows that the EISF for the incoherent scattering law takes the form

$$A_0^0(Q) = \frac{1}{Z}\left|\int_{R_1}^{R_2} \psi_0^0(r) j_0(Qr) r \, dr\right|^2 \tag{9.133}$$

$$= \frac{3\left|\int_{R_1}^{R_2} r \frac{\sin(Qr)}{Q} dr\right|^2}{(R_3^2 - R_1^3)\int_{R_1}^{R_2} r^2 \, dr} \tag{9.134}$$

$$A_0^0(Q) = \frac{3[R_2^2 j_1(QR_2) - R_1^2 j_1(QR_1)]^2}{Q^2(R_2^3 - R_1^3)^2}. \tag{9.135}$$

In the particular case $R_1 = 0$, the expression (9.63) of the EISF for a diffusive motion inside a sphere of radius R_2 is retrieved

$$\lim_{R_1 \to 0} A_0^0(Q) = \left[\frac{3j_1(QR_2)}{R_2}\right]^2. \tag{9.136}$$

Now, if we make the change of parameters defined by (9.125), it turns out that the expression (9.135) of the EISF is strictly identical to the expression (9.124) derived by Cohen de Lara and Kahn.

(b) Experimental results

The EISF of this model is illustrated in figure 9.14 as a function of both QR_2 and the ratio $\rho = R_1/R_2$. The limiting situation $\rho = 0$ corresponds to a diffusion inside a sphere of radius R_2 while $\rho \to 1$ describes the situation in which the motion is restricted to the immediate vicinity of the sphere of radius R_2. At room temperature the values $R_1 = 0$ Å and $R_2 = 10.4$ Å were found, indicating a diffusion inside the whole cavity. Conversely, for $T < 200$ K, $\rho = 1$ which means that the molecules remain close to the walls. Moreover experimental EISF values could be described only by introducing another parameter $\alpha = \tau_1/(\tau_0 + \tau_1)$, where τ_1 is the time the molecule is trapped in sites and τ_0 the time it moves along the walls. α was found equal to 0.35 at $T = 200$ K and 0.6 at $T = 150$ K.

From the width of the quasielastic broadening of their spectra, Cohen de Lara and Kahn deduced a characteristic time $\tau = 5.7 \times 10^{-13} \exp(700/T)$ s and an activation energy $E_a = 5.81$ kJ mol^{-1} in accordance with the result of the IR measurements. Finally, at low temperature, they observed a relatively well-defined peak at about 80 cm^{-1}, whose intensity grows as the temperature decreases and that they assign to the vibration of the whole molecule trapped in a potential well. Extensive calculations of the potential of a methane molecule in a Na-A cavity have been carried out by these authors (Mouche *et al* 1984). They are illustrated in figure 9.15. Given the formalism developed in the preceding sections it turns out that the CH_4–Na-A system is a very interesting case in the study of adsorbed phases and that its

analysis should be pursued further, requiring perhaps new neutron scattering measurements.

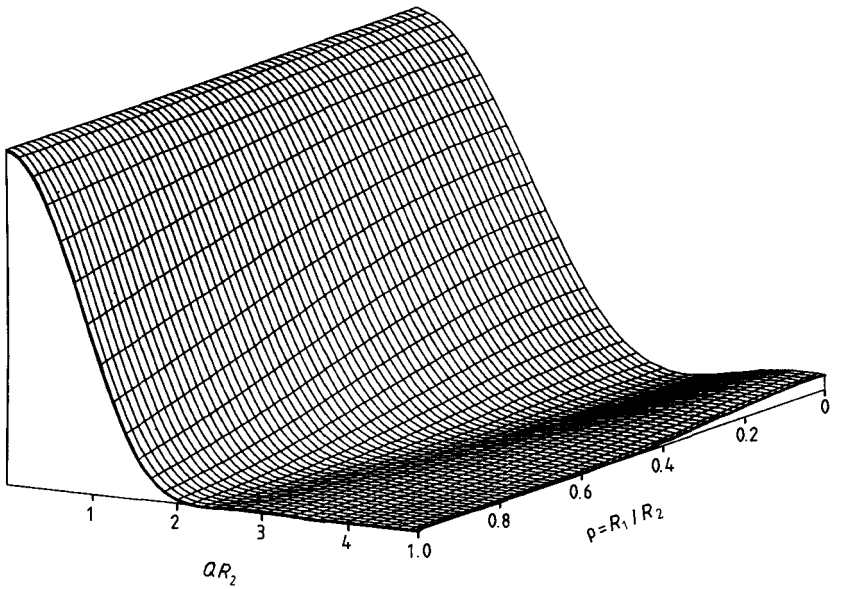

Figure 9.14 Three-dimensional representation of the variations of the EISF related to the model for a particle diffusion between two spheres of radii R_1 and R_2.

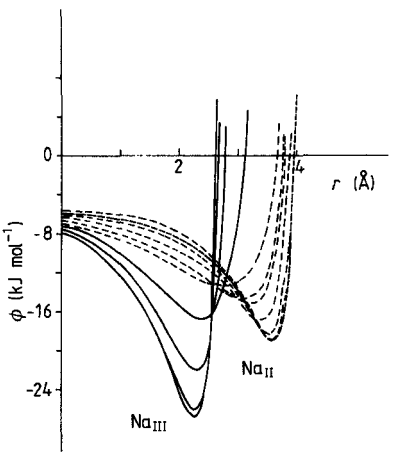

Figure 9.15 Potential curves for a methane molecule adsorbed in a Na-A cavity (after Mouche *et al* 1984). (Reproduced by permission of Taylor & Francis Ltd.)

9.5.4 Methanol adsorbed on H-ZSM-5 zeolite

Among other commercially important properties, ZSM-5 class zeolites are very effective for the conversion of methanol to hydrocarbons (Meisel *et al* 1976). The reaction mechanism is still a matter of discussion, but it is generally admitted that the active centres are the acid sites of Brönsted type (Chang and Silvestri 1977, Derouane *et al* 1978, Anderson *et al* 1979), with a possible contribution from the basic lattice sites in the initial step. The framework structure of the H-ZSM-5 zeolite (chemical formula: $Na_{0.1}H_3Al_{3.1}Si_{92.9}O_{192}$ has been determined by Kokotailo *et al* (1978). It contains two types of channels consisting of 10-membered oxygen rings. The straight elliptical channels (5.7–5.2 Å) are interconnected by near-circular channels (5.4 Å) in a zigzag fashion. The particular shape selectivity of H-ZSM-5 is related to the intermediate size of its channels. The adsorption of methanol in H-ZSM-5 has been extensively studied by numerous techniques including infrared spectroscopy, thermogravimetry, etc, and recently neutron scattering (Jobic *et al* 1986).

On the time-scale 10^{-11}–10^{-12} s, the data could be described by a model involving

(i) molecules fixed to the channel-walls with only a uniaxial rotation of their methyl groups, and

(ii) molecules diffusing within a restricted volume approximated by a sphere. The proportion of the mobile species was found to be temperature-dependent and the radius of the sphere inside it diffuses, i.e. 4.8 Å was found to be in good agreement with the dimensions of the channels.

At 300 K, eight molecules out of ten are fixed per unit-cell. This value is in agreement with thermogravimetric results indicating seven methanol molecules per unit cell at 307 K (Ison and Gorte 1984). In the case of adsorption of ammonia on this zeolite, nine molecules per unit cell were found adsorbed at 293 K. Considering the diffusion molecules in the 4.8 Å diameter sphere, a diffusion constant equal to $D = 2.8 \times 10^{-5}\ cm^2\,s^{-1}$ was deduced from refinement of the model developed in §9.2.1. Thus the methanol molecules diffuse locally as fast as in their liquid state ($D = 2.4 \times 10^{-5}\ cm^2\,s^{-1}$).

Backscattering measurements yielded the investigation of the translational motion along the channels. A plot of the broadening of the lineshape as a function of Q (figure 9.16) clearly exhibits a maximum at $Q = 0.9\ Å^{-1}$ characteristic of jump diffusion. An approximate jump-length of 5 Å and a mean residence time between jumps $\tau = 4.0 \times 10^{-9}$ s were evaluated.

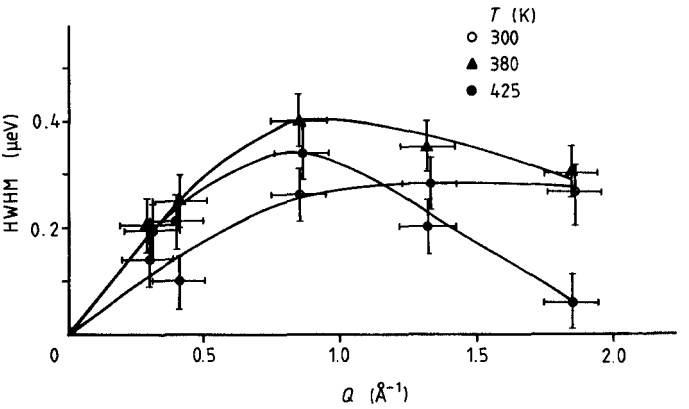

Figure 9.16 Quasielastic broadening related to the long-range translational diffusion of methanol in H-ZSM-5 zeolite (after Jobic *et al* 1986).

9.5.5 Water in zeolites. The evidence of several types of bonding

There have been a considerable number of studies of water adsorbed by zeolites, using a large variety of techniques such as NMR, infrared spectroscopy, calorimetry, dielectric relaxation, etc (Barrer 1978). An extensive review of all the results would be beyond the scope of this book. However, neutron scattering experiments have recently been carried out for a series of zeolites (Na-A, Na-X, Na-Y, Na-ZSM-5) with water adsorbed at different concentrations. These measurements have been interpreted in parallel with dielectric relaxation studies (Carru 1986). In particular, the analysis of the inelastic part of the neutron spectra leads to a better understanding of the behaviour of the water molecules inside the zeolite cavities.

Previous dielectric studies, essentially on A zeolites and faujasites, were a matter of discussion, concerning for instance the existence of one of several types of adsorbed water molecules (Morris 1969, Chapoton 1973, Schoonheydt 1975, Ducros 1960). Also, the occurrence of a phase transition of water below 273 K is another debating point (Schoonheydt 1975, Ducros 1960, Morris 1969). Carru observed a large variation of the critical frequency over several orders of magnitude as a function of the water concentration, showing that these molecules, and particularly the first adsorbed ones, strongly interact with the cations. Figure 9.17 can be separated into three regions, which were interpreted as follows. At low water concentration, the important increase of F_c is essentially due to the presence of water molecules of type A (figure 9.17), i.e.

bonded to the Na^+ cation by an ion–dipole interaction. In the intermediate region, the lower increase of F_c results from the existence of water molecules, linked to the zeolite wall by hydrogen bonds (type B) producing an electrostatic shielding. For very high water concentrations, the critical frequency remains constant, indicating the presence of water molecules of the type C, i.e. linked together by hydrogen bonds, without interaction with the cations. The concentrations related to apparition of the different types of water depends on the nature of the zeolite.

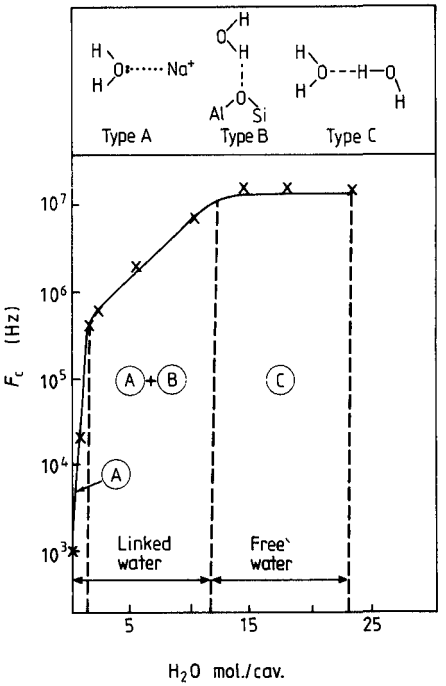

Figure 9.17 Variation of the critical frequency as a function of the concentration of water in the Na-A zeolite.

These conclusions were confirmed by inelastic neutron scattering experiments carried out between 80 K and 373 K. At low concentrations (typically less than eight molecules per cavity), a well-defined line can be observed, centred at about 4 meV (see figure 9.18). Its position and its shape do not change when the temperature is varied. Conversely, for intermediate and high concentrations of water, a wide band centred at about 7.5 meV appears. When the temperature is increased, this band is broadened and shifted towards the low frequencies. It is not noteworthy that the line at 4 meV has disappeared. By comparison with the lines

observed by infrared, Raman and neutron spectroscopy with liquid water or hexagonal ice, this band at 7.5 meV, together with another occuring at 65 meV can be attributed to intermolecular vibrations between water molecules linked by hydrogen bonds (type C). The line at 4 meV exists neither in the liquid state nor in the hexagonal ice. It is characteristic of molecules linked to the walls (type A or B).

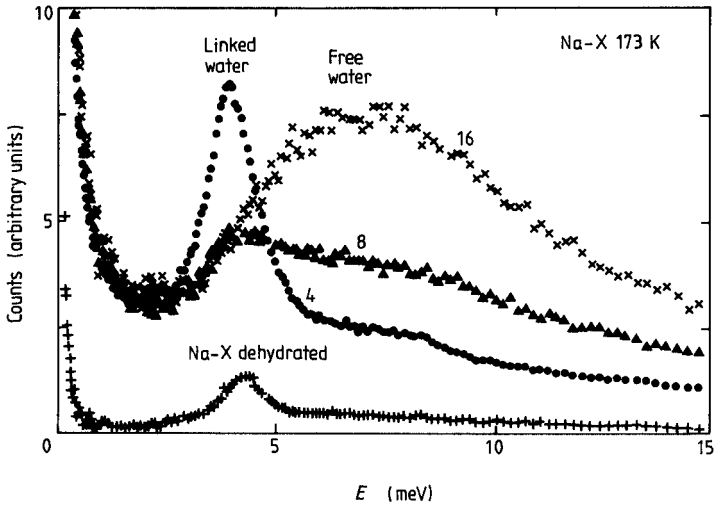

Figure 9.18 Inelastic neutron scattering from water in Na-X zeolite, at $T = 173$ K, for various concentrations (given in H_2O/c).

Now if we consider the problems of the localisation of these different types of water, and if we take into account recent results (Stanley *et al* 1984), according to which liquid water is constituted of groups of molecules linked together with a mean dimension of 8 Å, it is clear that the molecules of type C can be present only in the large cavities. Considering the molecules of type A and B, Carru (1986) showed that they were localised, not only in the sodalite blocks as indicated by NMR (Oehme *et al* 1984) but also in the large cavities. Indeed the line at 4 meV could be observed for concentrations up to nine molecules per cavity, whilst the maximum number of molecules inside a sodalite block is only four. It is interesting to point out that the absolute intensity of this line strongly increases up to four molecules per cage and then drastically decreases to eight molecules per cage. Simultaneously the band at 7.5 meV appears. This can be interpreted as follows: the cations inside the cavities tend to prevent the formation of water of type C as long as each of them is not interacting with 1 molecule. Afterwards, the

number of molecules having a single hydrogen bond (i.e.type A or B) decreases because of the appearance of links with additional molecules leading to a type-C behaviour.

Chapter 10 Dynamical Studies of Polymers and Biomolecules

So far, we have been concerned with rather simple systems: molecules of known geometries, reorienting amongst a set of well-defined preferential orientations, ions or atoms diffusing over a network of sites or inside cavities. Conversely, this chapter will deal with the use of neutron quasielastic and inelastic scattering to the investigation of more complicated systems: polymers and biological substances.

The engineering and technological uses of polymeric materials in plastic and rubbers are numerous, and deal essentially with the solid state. The earliest studies were concerned with polymers in dilute and concentrated solutions. The neutron scattering technique offers the possibility of studying both fully protonated and partially or fully deuterated polymer chains, and of comparing the properties of the latter with those of protonated chains which have already been investigated for many years.

The field of biomolecular neutron spectroscopy has been developing rather slowly because of the complexity of biological samples, the need to develop the quantitative analysis of neutron spectra, and the demands on instrument time. As a result of advances in instrumentation and rapidly expanding numerical simulation work, much progress is currently being made in this area.

10.1 Polymers in Solution and in Melts

So far, the number of publications concerned with neutron scattering experiments on polymeric systems has been very large. Many of them deal with small-angle neutron scattering (SANS) and thus are focused on the static aspect of the problem; but polymeric systems have also stimulated dynamical studies by application of quasielastic and inelastic scattering. It would be beyond the scope of this book to give here an extensive survey of all the neutron analyses of polymeric systems which have been performed in previous years. Readers are referred for details to some relevant articles and reviews (Higgins 1982, 1983). Here we just outline the general features of neutron scattering from polymers in dilute, semi-dilute and concentrated solutions or in melts. We also present the basic assumptions underlying the theoretical models commonly used in the interpretation of the data.

10.1.1 Quasielastic scattering from the motion of the main chain

The type of motion observed in a scattering experiment by polymers will be determined essentially by the Q range of investigation.

The centre-of-mass motion, i.e. the motion of the polymer chain as a whole, can be observed at very small Q values, $Q < 1/R_g$, where R_g is the molecular radius of gyration. The relevant intermediate function in this diffusion regime is simple:

$$I(Q, t) = \exp(-\Omega_m t) \tag{10.1}$$

with

$$\Omega_m = D_m Q^2 \tag{10.2}$$

D_m is the diffusion constant of the centre of mass. For larger values of Q, there exists another regime called the 'universal' regime because neither the molecular size nor the chemical structure of the polymer has any influence. This regime corresponds to $1/R_g < Q < 1/\sigma$, where σ is a length characteristic of the local structure of the chains and of the order of a few repeating monomer units. Descriptions of the motions in this regime are based essentially on two models. Rouse (1953) considered only the 'free draining limit', namely when the velocity of each subunit depends only on the forces applied to it. The treatment of Zimm (1956) is more realistic in the sense that the motion of the solvent is also taken into account. Because of the viscosity of the solvent, η_0, a displacement of a subunit induces a velocity field around it. These hydrodynamic effects lead to long-range interactions between distant subunits. For both the Rouse and the Zimm model, the scattering function has been derived (De Gennes 1967, Dubois-Violette and De Gennes 1967). The long chain is divided into N subunits, marked by the

points $r_0, r_1, \ldots, r_N$, with intervals $a_n = r_{n+1} - r_n$. The internal distances between subunits of the chain are assumed to obey classical random-walk statistics, and to be uncorrelated in the absence of external forces

$$\langle a_n(t) \cdot a_m(t) \rangle = \sigma^2 \delta_{nm} \tag{10.3}$$

σ^2 being the mean-square end-to-end dimension of one subunit. The equation of motion of a subunit takes the simple form (Richter *et al* 1984)

$$\frac{\mathrm{d}}{\mathrm{d}t} r_n = W\left[a_n - a_{n-1} + z \sum_{n \neq m} \frac{a_m - a_{m-1}}{\sqrt{|m-n|}}\right] \tag{10.4}$$

z is a geometrical factor defined from the ratio between the size, b, of a subunit and σ.

$$z = \sqrt{\left(\frac{6}{\pi}\right)} \frac{b}{\sigma} \tag{10.5}$$

W is the rate factor, related to the viscocity η_0 of the solvent via an Einstein–Stokes relation

$$W = \frac{k_B T}{2\pi \eta_0 b \sigma^2}. \tag{10.6}$$

The term proportional to z in (10.4) results from the hydrodynamic effects. Putting $z = 0$ yields the simple Rouse model. The eigenmodes of (10.4) are very simple, namely

$$r_n = \text{const.} \exp(ipn) \exp(-t/\tau_p) \tag{10.7}$$

with relaxation frequencies $1/\tau_p$ given by

$$(W\tau_p)^{-1} = 2(1 - \cos p) + 4z \sum_{s=1}^{\infty} \frac{\cos(ps)}{\sqrt{s}} (1 - \cos p). \tag{10.8}$$

The modes of main interest are the modes of low relaxation frequency ($p \ll 1$) for which (10.8) reduces to

$$(W\tau_p)^{-1} = p^2 + \sqrt{2\pi}\, z p^{3/2} \tag{10.9}$$

p appears as a coordinate conjugate to the index n labelling the subunits. The Rouse modes ($z = 0$) have a dispersion $\tau_p^{-1} \sim p^2$. But as soon as $z \neq 0$, the Zimm modes dominate and behave as $\tau_p^{-1} \sim p^{3/2}$.

Referring to original papers for their derivations (De Gennes 1967, Dubois-Violette and De Gennes 1967, Richter *et al* 1984) we summarise the respective scattering functions: in the Rouse limit, the coherent intermediate function is

$$I_{\mathrm{coh}}^{\mathrm{Rouse}}(Q, t) = 2\int_0^{\infty} \mathrm{d}s \exp\left\{-\frac{Q^2\sigma^2}{6}\left[s + \sqrt{\left(\frac{Wt}{\pi}\right)} g\left(\frac{s^2}{4W|t|}\right)\right]\right\} \tag{10.10}$$

the function $g(x)$ being defined according to

$$g(x) = \int_1^\infty \exp(-xu^2)(\mathrm{d}u/u^2). \tag{10.11}$$

Similarly, in the Zimm model one obtains

$$I_{\mathrm{coh}}^{\mathrm{Zimm}}(Q, t) = 2\int_0^\infty \mathrm{d}s \exp\left\{-\frac{Q^2\sigma^2}{6} s[1 + h(s|\tilde{W}t|^{-2/3})]\right\} \tag{10.12}$$

with the definition of the function $h(x)$

$$h(x) = \frac{4}{\pi}\int_0^\infty [1 - \exp(-u^3x^{-3/2})]\cos u^2\,(\mathrm{d}u/u^3) \tag{10.13}$$

and

$$\tilde{W} = \sqrt{2\pi}\, zW. \tag{10.14}$$

Dubois-Violette and De Gennes have evaluated the scattering function $S_{\mathrm{coh}}(Q, \omega)$ corresponding to both the Rouse and the Zimm models, by numerical Fourier transform of (10.10) and (10.12). Apart from constants of order unity the h.w.h.m. is

$$\omega_c(Q) = W(Q\sigma)^4 + \tilde{W}(Q\sigma)^3. \tag{10.15}$$

The main result is that in the Rouse model ($\tilde{W} = 0$) one has $\omega_c(Q) \sim Q^4$, whilst in the Zimm model ($\tilde{W} \neq 0$) one gets $\omega_c(Q) \sim Q^3$.

Quasielastic scattering both of light (photon correlation spectroscopy) and of neutrons have been applied to the observation of polymer motion in dilute solution. The former technique observes the intermediate scattering law in a range up to ca 2×10^{-3} Å^{-1}. The latter covers down to ca 10^{-1} Å^{-1}. So their wavevector ranges do not overlap. The Zimm model with hydrodynamic interactions through the solvent describes very well the changeover from centre of mass diffusion to internal motion observed by light-scattering (Adam and Delsanti 1977a, 1977b, Han and Akcasu 1981). High-resolution neutron scattering evidences an analogous changeover from local bond motion at high Q to Zimm behaviour at lower Q values (Nicholson *et al* 1981, Higgins *et al* 1983, Allegra *et al* 1986).

Recently, Richter *et al* (1984) investigated the single-chain dynamics of a linear polymer in solution over the full concentration range. They developed a phenomenological theory of single-chain dynamics in semi-dilute and dense polymer solutions. As a new concept, they introduced the idea of incomplete screening of the hydrodynamic interaction between chain segments. The relevant intermediate scattering function was explicitly evaluated. Approximate expressions were derived for the characteristic frequency which allowed the prediction of three dynamical regimes, namely the Zimm relaxation, the enhanced Rouse relaxation, and essentially a second Zimm regime due to incomplete screening. The experiments performed with polydimethylsiloxane (PDMS) in solution in C_6D_5Cl over the full concentration range showed that, for dilute

solutions, the segmental diffusion within polymers is well described by the Zimm model. For semi-dilute solutions, hydrodynamic screening was directly observed. The hydrodynamic screening length was evaluated and found to be close to the excluded volume screening length determined on the similar system PDMS/C_6D_6.

Motion in melts and networks is more complex. While light-scattering can no longer be used for the investigation of single-chain dynamics, neutron scattering offers the possibility of isotopically labelling molecules by H/D substitution to follow their individual motion in the bulk. The description currently most often used is the repeating-chain model of De Gennes (1971, 1980) extended by Doi and Edwards (1978) to elaborate a full theory of viscoelasticity. Because the polymer chains cannot pass through each other, the effects of the surrounding of one chain are to reduce its large-scale displacements to a worm-like motion inside a tube along the chain contour, with tube diameter d. Within the tube, the motions of the chain are assumed to be essentially free. The change in shape of the tube itself depends on the reorganisation of the mesh in which it is embedded, i.e. it depends on the entanglement effects. Typical values of tube diameters are 34 Å in the case of polyethylene and 83 Å for polystyrene (Graessley 1980). Neutron spectrometers at present available restrict the observation to local motion within the tube. Besides, chain–chain interactions such as entanglements contribute to the screening of the hydrodynamic interactions and the correlation function in the 'universal' regime is in the 'Rouse limit': the inverse characteristic time varies as Q^4 (Higgins *et al* 1977, Allen *et al* 1982, Higgins *et al* 1981, Richter *et al* 1981).

Another feature of the polymer melts is the introduction of a new length-scale: the distance between entanglements of the polymer chains. The effects of the entanglements intervene at $1/R_g < Q < 1/\sigma$. They modify the form of the scattering function by introducing a slowly decaying tail at long time-periods. Higgins and Roots (1985) recently observed the effects of molecular entanglements on the correlation functions, in the case of polytetrahydrofuran. The form of these correlation functions was found to agree with the theoretically predicted behaviour for entangled systems. An average value of ca 30 Å was extracted for the distance between entanglements.

10.1.2 Vibrations and Rotations of Polymer Side-groups

Torsional vibrations of side-groups of polymers, such as methyl or phenyl side-chains are often difficult to identify from conventional light-spectroscopy spectra. Conversely, their large amplitude makes them interesting candidates for neutron investigation, especially when a judicious selective deuteration permits confirmation of their assignment.

Methyl torsion is certainly the motion which has been the most extensively investigated, in a wide range of polymers: polyacetaldehyde (Longer and White 1969) polydimethylsiloxane (Henry and Safford 1969, Allen *et al* 1975, Amaral *et al* 1976), polymethylmethacrylate (Allen *et al* 1975), polypropylene (Yasukawa *et al* 1976), and polypropylene oxide (Allen *et al* 1972). Measurements on stretch-oriented polypropylene (Takeuchi *et al* 1982) evidence a large frequency dispersion for the CH_3-torsion mode around 230 cm^{-1} as a result of the coupling between chains by methyl groups on neighbouring molecules. Biopolymers also have stimulated neutron studies (reviewed by Middendorf 1984). Drexel and Peticolas (1975) in the case of poly-L-alanine in both its α-helical and β-sheet form, have shown conclusively that methyl torsion, not α-helical backbone vibration, was responsible for the strong band at 230 cm^{-1}.

Because the main chain motions broaden the quasielastic spectra, side-chain rotations are preferentially observed in samples at around or below their glass-transition temperatures. Such investigations were performed with polymethylmethacrylate (PMMA) which presents a high glass-transition temperature and thus offers a wide temperature range for studying the methyl rotation while the backbone motion is frozen out (Ma 1981). There are two methyl groups in the monomer unit. The barriers for the torsional frequencies are different enough to separate the two contributions to the quasielastic broadening. As a matter of fact, it was found that at room temperature, the α-methyl group is rotating at less than 10^9 Hz while the ester methyl moves much faster at less than 10^9 Hz while the ester methyl moves much faster at 10^{11} Hz.

Recently, Gabrys *et al* (1985) have carried out neutron experiments on the two stereospecific forms of PMMA, syndio (PMMAS) and isostatic (PMMAI), in a temperature range 35–391 K. They observed non-Arrhenius behaviour of the widths of quasielastic peaks and a difference in the value of the reorientational rates of PMMAS and PMMAI (Gabrys *et al* 1984). This effect was explained by inclusion of higher than V_3 terms in the Fourier series expansion of the potential function hindering the methyl group motion.

10.1.3 Phonon modes

Homopolymer macromolecules can crystallise, but it is almost impossible to obtain single crystals. Actually, most polymers are only semicrystalline with small crystallites embedded in an amorphous matrix. A molecule may exist in several crystallites as well as in the amorphous regions. In scattering experiments from semicrystalline polymers, most of the information concerning the polarisation directions of the modes is lost. Perdeuterated samples yield coherent scattering and sometimes allow dispersion curves to be obtained, as with polytetrafluoroethylene

(Twistleton and White 1972). Investigation of the polyethylene (Twistleton *et al* 1982) produced dispersion curves for both intermolecular and intramolecular modes. In the case of polyoxymethylene, the availability of single crystals allow the determination of most of the stiffness constants from an extensive analysis of the dispersion curves (Anderson *et al* 1982).

For hydrogenous polymers, only the weighted density of states can be observed, but, with stretch-oriented samples, some of the directional information is sometimes recovered, by orienting the Q vector either along the chain axis or perpendicular to it, in order to enhance longitudinal or transverse modes, respectively.

An inelastic neutron scattering analysis of *cis*-polyacetylene, *trans*-polyacetylene and iodine-doped *cis*-polyacetylene has recently been performed in the low-frequency region where in-plane skeletal vibrations, out-of-plane torsions and lattice vibrations are expected to appear. Torsional modes were assigned to a peak at 36 meV present in the three samples. They were suspected of also being responsible for another peak at 21 meV which does not appear in the pure *cis*-form (Tasumi *et al* 1985).

10.2 Biomolecular Applications of Quasielastic Neutron Scattering

The incoherent quasielastic neutron scattering technique has also been applied to the most challenging of all problems areas, that of the molecular organisation and function of biological systems. The first experiments of biological interest, on DNA fibres, were undertaken at Stockholm by Dahlborg and Rupprecht (1971) and were soon followed by a number of preliminary studies at Harwell on membranes and proteins: (Middendorf and Willis 1972; Middendorf and Stirling 1973; Wilkins *et al* 1974; Randall and Gilmour 1975). Actually, there was little progress until advanced spectrometers were gradually developed. It is only since around 1980 that biophysical and biochemical applications of quasielastic neutron scattering have been pursued more actively (Middendorf 1984, Middendorf and Randall 1985). Despite its exploratory flavour and the fact that much of the data interpretation is still at a semi-quantitative level, the field of biomolecular neutron spectroscopy is an exciting one because its development coincides with a period of tremendous growth in theoretical studies of molecular dynamics of proteins, nucleic acids, phospholipid and polysaccharide (Karplus and McCammon 1981, Levitt 1982, McCammon 1984).

10.2.1 Basic aspects

The macromolecules and molecular aggregates of living matter exhibit

an extraordinary structural and functional diversity. The most important biomolecules are linear heteropolymers twisted or folded into some unique three-dimensional shape. In their natural habitat these often coexist and interact with a variety of more flexible molecular aggregates or polymers built up from smaller entities such as lipids and saccharides. Diffraction techniques (using mainly x-rays, but also neutrons, electrons and photons) have been immensely successful in elucidating the atomic and molecular structure of hundreds of proteins and nucleic acids and of many phospholipid and polysaccharide assemblies. With the increasing application of sophisticated spectroscopic techniques in the life sciences (Sandorfy and Theophanides 1984), studies of the dynamical behaviour of biomolecules and the interrelation between structure, dynamics and function at the molecular level have become a central theme of molecular biology (Cooper 1981, Porter *et al* 1983).

Biomolecules work in an aqueous, essentially isothermal, environment. The water-content of all organisms is high, generally larger than 50%, and may reach 95% in some plants. Interactions with water are of fundamental importance, therefore, and are of interest at all levels of hydration (Franks and Mathias 1982, Finney and Poole 1984). A second basic aspect is that living systems are always in a state of quasi-equilibrium (Prigogine and Stengers 1984). Many classes of biomolecules are continuously being assembled and broken down in complex chains of biochemical reactions which are catalysed by a plethora of highly specific enzymes and associated cofactors. Although structurally well-defined during most of the time, they must be able to undergo small-scale or large-scale isomerisations and to associate or dissociate easily in response to the presence of other molecules, changes of ionic milieu, external stimuli, etc. Biomolecular systems therefore are usually metastable in a strict thermodynamic sense, and at the molecular level this is reflected in a rich spectrum of low-frequency fluctuations and collective processes. Interactions at and between active sites are of particular interest since their structural and dynamical properties govern a variety of molecular recognition, reaction and transduction processes. The way biological macromolecules have been adapted or tuned, through evolution, to exploit the coupling or competition between cooperative and dissipative modes of motion in such processes is a key problem (Careri *et al* 1979).

10.2.2 Time-scales and types of motion

Until the mid-1970s, as a consequence of the success of x-ray crystallography in determining precise three-dimensional structures, proteins and nucleic acids were generally regarded as static and rather rigid entities. Biomolecules were viewed as compact, quasicrystalline mole-

cules, the spectral properties of which were largely given by the well-known electronic and vibrational spectra in the 10^{15}–10^{13} s^{-1} range. It was difficult to reconcile this picture with the local and overall flexibility required for the functional interactions referred to above, with data on isotope exchange kinetics and with fundamental considerations based on the statistical mechanics of small systems (Cooper 1984). Most of these relate to motions with frequencies $\hbar\omega \leqslant k_B T$, i.e. $\hbar\omega \leqslant 27$ meV at physiological temperatures (310 K).

Recent work on the dynamics of biomolecules has been primarily concerned with detecting directly the cooperative motions of larger structural elements and building blocks as a function of specific interactions with other molecules and of solvent damping (Peticolas 1978). It is here, in the 10^{-12}–10^{-6} s range of time-scale (1 meV $\geqslant \hbar\omega \geqslant 10^{-6}$ meV), that neutron spectroscopy can provide the spatiotemporal information to advance our understanding of the relations between structure and function.

Because of the complexity of biological samples, it will be appropriate first to give a qualitative survey, focusing essentially on proteins and nucleic acids. The primary structure is a polypeptide chain (20 different amino acid residues) or a polynucleotide chain (four different nucleotide bases), respectively. The most conspicuous element of the secondary structure is helical (single, double or triple), but in the case of proteins there are other prominent structural motifs (β-sheets, loops, random coil regions). The complete 3D structure of one effectively indivisible unit is referred to as the tertiary structure (or conformation) of a biomolecule, and this may consist of spatially distinct, relatively compact domains. The quaternary structure, finally, is given by the non-covalent association of a few or many independent tertiary structure units (or subunits); these may or may not be identical. The most complex quaternary structure studied extensively by neutron diffraction is the ribosome from *Escherichia coli* which consists of 55 different protein subunits and 3 RNA molecules with a total molecular weight of about 3×10^6 (Moore *et al* 1986).

The low-frequency motions and diffusive processes observable by neutron scattering may be classified as follows.

(a) *Phonons and stochastic fluctuations.* Acoustical phonons with energies and well-defined dispersion properties have been observed in molecular crystals of biophysical interest (amino acids, pyrimidine, imidazole) (Powell and Martel 1980, 1982, Link 1985), and should be observable in fibrous paracrystals containing little water (polypeptides, DNA). Any biomolecular system approching 'natural' conditions will possess a strong continuous spectrum of quasistochastic fluctuations throughout the thermal and subthermal region. This may carry a few more or less broad, essentially non-dispersive bands in the range

0.1 meV $\leqslant \hbar\omega \leqslant$ 10 meV. These bands are variously referred to in the literature as 'phonon bands', 'soft modes', or 'breathing modes'.

(b) *Side group dynamics (Keniry et al 1983)* The side-groups along the main chain(s) of a biomolecule are to a lesser or greater degree involved in the dynamics of the structure as a whole. In nucleic acids the bases are essential coupling elements between the two helical strands, whereas in proteins there are great differences. Side-chains at the surface of proteins tend to be weakly coupled to the polypeptide backbone, and their low-frequency dynamics ($\hbar\omega < 1$ meV) is determined largely by solvent interactions. In the interior, amino acid side-chains are more of an integral part of the structure and their degrees of freedom are 'harder'. Here steric hindrances may be such that they are only able to perform rapid jumps between a small number of well-defined potential minima. Apart from amino acid side-chains, other covalently attached groups with distinct functional properties will often play an important role in the dynamics of surface and near-surface interactions.

(c) *Inter-domain and inter-subunit motions (Janin and Wodak 1983).* The tertiary and the quaternary structure of globular proteins give rise to low-frequency motions of massive parts of a molecule relative to each other. In general these will be highly damped, and the domains or subunits are likely to perform restricted Brownian motions around their equilibrium positions. The active sites of enzymes are usually located in clefts which separate two domains, and the inter-domain motions of functional interest are bending modes around the 'hinges' given by the polypeptide segments connecting the two domains.

(d) *Solvent interactions (Franks and Mathias 1982, Finney and Poole 1984).* Within a hydration shell of 5–10 Å thickness, the translational and rotational degrees of freedom of water molecules and small ligands are reduced by interactions with the macromolecular surface and its various features (ionic groups, polar and non-polar regions). Over larger-scale lengths, the integrated effects of these short-range interactions determine the translational and rotational diffusion of the macromolecules as a whole, and contribute also to its relative properties.

10.2.3 Survey of experimental work

Perhaps the most striking fact to emerge from a cursory inspection of the volume of published work in this area is that quasielastic neutron experiments, despite the limitations mentioned, have already been performed on an extremely wide range of samples, from proteins in solutions to membrane stacks, oriented DNA fibres, photosensitive preparations and whole cells. But in many cases it has not been possible to follow up initial results with sufficiently detailed experiments aimed at

a more comprehensive characterisation of the effects observed. Likewise, the level of data analysis is not yet comparable to that practised in other areas of applications. We have chosen three topics which we believe to be representative of current work: quasielastic neutron scattering from a lamellar system (lipid mobility in bilayer membranes), from oriented fibres (hydration of DNA), and from a globular protein (hydration and intramolecular dynamics of *in vivo* deuterated phycocyanin).

10.2.4 Membranes

All living cells, and most organelles within cells, are enclosed by a thin membrane (50–100 Å) which not only functions as a passive or active filter controlling the movements of ions and molecules across it, but is also the site of many biochemical recognition and transduction processes. Although any real plasma membrane is a complex 'fluid mosaic' assembly of lipids, proteins and saccharides, some structural and dynamical properties of the basic phospholipid bilayer matrix may be studied by means of model systems prepared from purified or synthetic lipids (Houslay and Stanley 1982).

Glycerophospholipids, like all amphipathic molecules, readily form bilayer structures which, depending on solvent-content and other conditions, aggregate to give a variety of phases. It is possible to produce plane lamellar stacks of hydrated bilayers resembling smectic liquid crystals, and preparations of this kind were used in the first neutron scattering studies on membranes. Dynamically, there are four relevant types of processes:

(i) Hydrocarbon chain motions (effect of temperature, degree of saturation, incorporation of smaller molecules such as cholesterol and anaesthetic agents).

(ii) Hindered rotations of headgroups (effect of ionic milieu and hydration level).

(iii) Diffusion of whole phospholipid molecules within or across a bilayer.

(iv) Low-frequency, long-wavelength excitations of a bilayer considered as a viscoelastic sheet (Sackman *et al* 1986).

At Harwell, quasielastic spectra were measured from D_2O-hydrated lamellar bilayers of dipalmitoyl-L-α-phosphotidylcholine (DPPC) without and with cholesterol (20–50% molar) between 20 °C and 51 °C (Middendorf and Willis 1972, Middendorf and Stirling 1973, Wilkins *et al* 1974). The high CH_2-content of lipids makes them almost ideal incoherent scatterers. For bilayer stacks under D_2O-hydrated conditions, any

quasielastic broadening is due to two possible effects: whole molecule motions relative to the bilayer matrix, and intramolecular motions. The broadenings observed were generally small compared to the resolution widths, but it was possible to show in carefully controlled on-beam difference experiments that for hydrated samples they increased systematically with cholesterol content and with temperature. The broadening measured for dry samples did not depend on temperature and may be used as the baseline value for the analysis of cholesterol and temperature-induced changes in membrane fluidity. Effective diffusion coefficients derived in this way range from 0.5 to $3 \times 10^{-7}\,\mathrm{cm^2\,s^{-1}}$ (Figure 10.1).

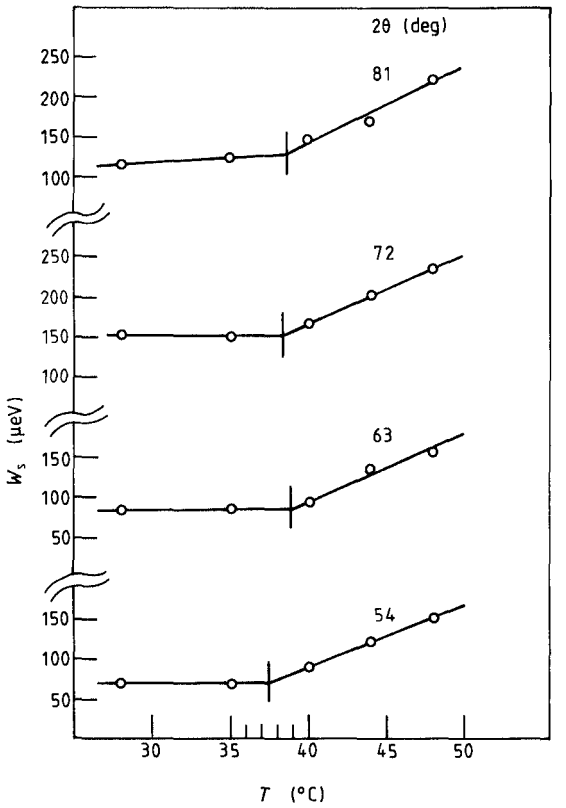

Figure 10.1 Temperature dependence of the quasielastic broadening (deconvoluted f.w.h.m.) for 100% D_2O-hydrated DPPC bilayer stacks, showing the gel-to-liquid-crystalline transition near 40 °C. Measured on the DIDO 6H spectrometer at AERE Harwell at Q-values between 1.2 and 1.7 Å (from unpublished work by H D Middendorf and G C Stirling)

Around 1976, further experiments (Wilkins *et al* 1976) on oriented membranes at higher resolution (IN10) confirmed and extended the early Harwell findings, but also highlighted the fact that neutron experiments persistently gave values for the phospholipid mobility exceeding those accepted in the biophysical literature, mainly based on NMR and other methods probing interaction distances of the order of micrometres. Actually data reported for biomolecular membranes are subject to considerable variability on account of different lipid species, preparation techniques and experimental conditions. Nevertheless, systematic discrepancies and the results of detailed experimental and theoretical work undertaken during the past few years on a wide range of related physicochemical problems now point to the conclusion that the interpretation of many older NMR measurements for heterogeneous systems of complex structure is in need of revision.

Tabony *et al* (Tabony and Korb 1985, Tabony and Perly 1986) have given a critical discussion of the different approaches to determining the rates of diffusion in liquid bilayers, and have studied quasielastic scattering from lamellar dispersions of both hydrogenous and fully chain-deuterated DPPC in D_2O (20% lipid content). The combined results of time-of-flight and backscattering experiments show clearly that the lateral diffusion of DPPC molecules in bilayer dispersions is characterised by coefficients $D_T > 10^{-7}\,cm^2\,s^{-1}$ which at 63 °C reach $4 \times 10^{-6}\,cm^2\,s^{-1}$ (Figure 10.2). The IN10 data allowed an activation energy of $4.4\,kcal\,mol^{-1}$ to be determined The possible rotational contributions to the broadening were scrutinised in this work and found to be negligible on the basis of lineshape analyses and the linearity of the broadening versus Q^2. Numerical simulations of the molecular dynamics of bilayers are becoming available (Van der Poeg and Berendsen 1983) but detailed comparisons with quasielastic neutron scattering data have not yet been made.

10.2.5 DNA

The celebrated x-ray studies which led to the discovery of the double helical structure of DNA were performed mostly on fibres drawn from viscous gels. They revealed three distinct hydration and salt-dependent conformations: a paracrystalline form designated as 'A' (relative humidity (RH) $\simeq$ 75%, Na salt, 11 base pairs per helix period), a semicrystalline 'B' form (RH > 90%, Na or Li base, 10 base pairs), and a more disordered 'C' form (RH $\simeq$ 50%, Li base, 9.3 base pairs). All are right-handed helices, and B-DNA is thought to be the biologically important form. It was found more recently, however, that there is also a rare left-handed form (Z-DNA). For a given preparation, water

uptake thus induces intrahelical and interhelical rearrangements resulting in more or less crystalline bonding patterns (Texter 1978).

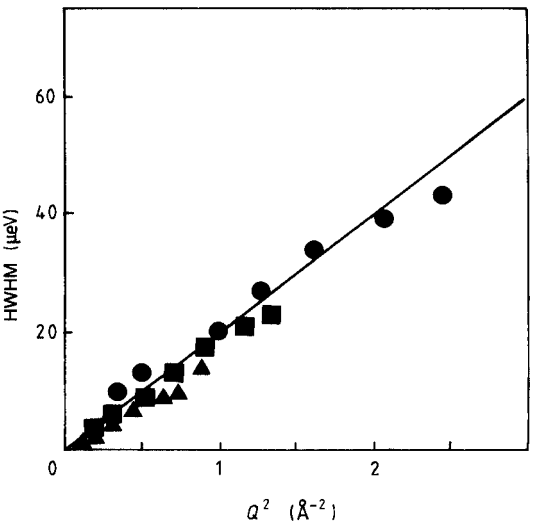

Figure 10.2 Variation of the quasielastic broadening (deconvoluted h.w.h.m. with Q^2 for chain-deuterated DPPC at 63 °C. Measured on the multichopper IN5 at Institut Laue–Langevin at incident wavelengths of 6 (●), 8 (■) and 10 (▲) Å (from J Tabony and B Perly 1986).

By analysing sets of neutron diffraction patterns and spectra taken in steps along a particular sorption isotherm, it is possible to investigate in some detail the structural and dynamical changes due to increasing or decreasing amounts of closely associated water. DNA is a highly charged polyion; equilibrating it with atmospheres of relative humidity between 5% and 98% gives specific hydrations from 1 to 25–30 H_2O or D_2O molecules per nucleotide, corresponding to $h \simeq 0.06$–1.5. Of these, 10 to 12 water molecules per nucleotide remain unfrozen at low temperatures and are regarded as 'bonded' to the double helix itself (figure 10.3). Additional water molecules hydrogen-bonded to the directly associated ones complete the primary hydration shell (Falk *et al* 1963). All quantitative neutron scattering studies of DNA have used well-oriented fibre samples of high molecular weight (10^5 bases) prepared by Rupprecht's wet-spinning technique. In the pioneering study already cited (Dahlborg and Rupprecht 1971), the hydration of calf-thymus Na-DNA fibres was investigated using a beryllium-filter spectrometer and a time-of-flight instrument. Wet-minus-dry structure factors $S_{coh}(\boldsymbol{Q})$ measured for $h = 0.15$ and 0.45 showed a pronounced, relative-

ly narrow peak at $Q = 1.85$ Å^{-1} when $\boldsymbol{Q}\cdot\boldsymbol{a} = 1$ ($\boldsymbol{a}$ being the unit vector along the helix axis). This suggests a certain degree of 'binding' and also some structuring of D_2O molecules along $\boldsymbol{a}$ because the corresponding peak is weak when $\boldsymbol{Q}\cdot\boldsymbol{a} = 0$. Anisotropic Debye–Waller factors determined for the two principal orientations differ by a factor of 2 to 3. The value is larger along the helix than across it, a result consistent with trans-groove water bridging. Small, orientation-independent quasielastic broadenings of the order of 10% of the resolution width were measured between $Q = 1$ and $Q = 2$Å^{-1}. The data only allowed a rough estimate to be made of the correlation time for hindered translational and rotational motions. Outside the quasielastic region, the low-frequency inelastic scattering revealed a distinct peak shifting from 30 to 60 cm^{-1} as a function of orientation. Certain conclusions of this study were corroborated in a later work (Dahlborg *et al* 1980), which focused on the coherent elastic scattering from D_2O-hydrated Na-DNA and Li-DNA, on the interpretation of wet-minus-dry difference patterns, and on the calculation of structure factors for the A, B and C forms.

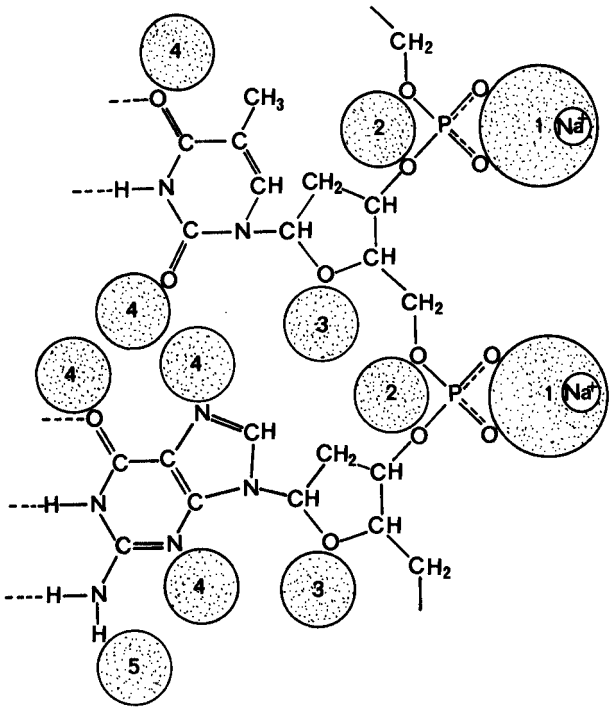

Figure 10.3 Segment of DNA strand with two bases (thymine and guanine), showing primary hydration sites as shaded circles (from Falk *et al* 1963).

Apart from some earlier test experiments (Lechner and Oberthür 1977), the only more detailed DNA study has been that of Schreiner and Pintar (1984, 1985). Time-of-flight spectra measured for wet-spun paracrystals of Na-DNA were analysed in conjunction with complementary NMR data. The quasielastic lineshapes obtained from one low (3.5 H_2O/nucleotide) and a few higher hydrations (9–13 H_2O/nucleotide, A-form of DNA), with $\boldsymbol{a}$ parallel as well as perpendicular to $\boldsymbol{Q}$, all consisted of essentially elastic peaks which for the runs at higher hydrations were superimposed on lorentzian-like broadened components. Up to $Q = 0.9$ Å^{-1} they reached almost twice the low-Q value. Both the half-width data and the EISF curves (figure 10.4) show clearly the activation of the rotational degrees of freedom of water protons as function of hydration, but there is no evidence of anisotropic motion relative to the fibre axis. Consistent with this and the negligible elastic peak broadening, it was possible to perform EISF analyses based on the Dianoux and Volino model of restricted diffusion within a sphere. At the higher hydrations investigated, where all water molecules are hydrogen-bonded directly to the DNA matrix, this gave radii of around 3 Å for the localised motions, in excellent agreement with the helix rise per base-pair in A-form DNA. The diffusion coefficients are only a little smaller than those for bulk water. These results show that for hydrations greater than about 8 H_2O/nucleotide the closely associated water is able to exchange between the hydrogen-bonding sites of each nucleotide, a conclusion that proved to be important for the modelling of NMR data.

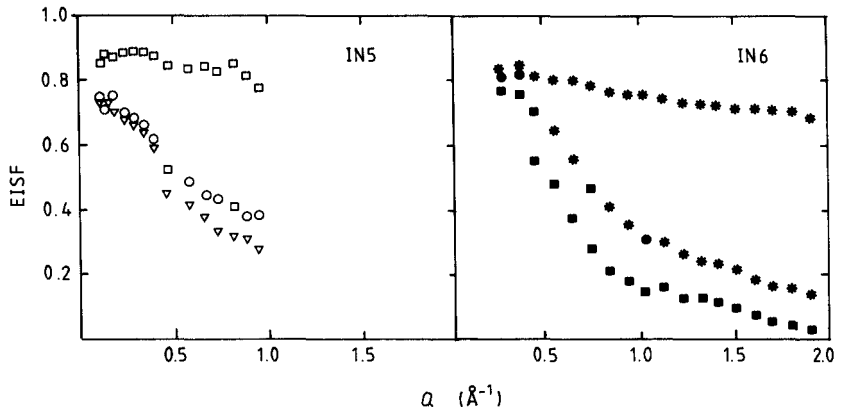

Figure 10.4 Q-dependence of the EISF for H_2O-hydrated DNA fibres, measured on IN5 and IN6 at Institut Laue–Langevin. The symbols indicate different orientations and hydrations ($\boldsymbol{Q} \perp \boldsymbol{a}$ and/or $\boldsymbol{Q} \parallel \boldsymbol{a}$, number of H_2O/nucleotide) as follows: □, (∥, 3.5); ○, (∥, 9); ▽, (⊥, 10); ⋆, (∥ or ⊥, 3.5); ●, (⊥, 11); ■, (⊥, 13) (from Schreiner 1985).

Fairly extensive computer simulations of structural and dynamical aspects of DNA hydration have been published (Clementi 1985), but there has been no effort so far to calculate the dynamical structure factors needed for comparing theoretical and experimental results.

10.2.6 Proteins

Protein molecules as a class are distinguished by a diversity of structural and functional properties not found in other biomolecules. Their dynamical behaviour is so complex that most of the quasielastic neutron scattering studies performed to date have been limited to sorption experiments. The hydration of fibrous proteins poses problems that are rather similar to those described above for DNA fibres. Some data on quasielastic scattering from H_2O-hydrated collagen fibres have been reported and discussed by Miller *et al* (1976, 1977) and by White (1977, 1981).

The only globular protein that has been studied over a wider spectral range is C-phycocyanin, a multimeric, crystallographically well-characterised chromoprotein isolated from blue-green algae grown in partially or fully deuterated cultures (Crespi and Katz 1972). Its quaternary structure is built up from $(\alpha\beta)$ heterodimers (MW $\simeq$ 30 000); the $(\alpha\beta)_6$ molecule is shaped like an oblate ellipsoid (diameter 110 Å, thickness 40 Å) with a central solvent channel of 10 Å radius and lateral clefts. There are three prolate ellipsoidal regions arranged symmetrically in 120° sectors around this channel, each corresponding to an $(\alpha\beta)_2$ unit. When the uptake of light water by gently dried samples of fully deuterated phycocyanin (d-PC) is monitored on a diffractometer (Rupley *et al* 1983), a broad peak develops at $Q = 2.5$ Å^{-1} and becomes more intense while shifting to $Q = 2$ Å^{-1} at RH $\geqslant$ 90%. Hydration thus induces the gradual build-up of order in the 3D arrangement of the subunits of d-PC and of whole molecules, characterised by correlation lengths between 100 and 300 Å. Because of the range of H/D contrast that can be realised with this protein at all stages in the sorption process, the activation of various intermolecular and intramolecular degrees of freedom (Rupley *et al* 1983) may be followed very effectively by neutron scattering.

Using the spin–echo technique to probe coherent small-angle scattering at very low energy transfers (0.01–0.1 meV), $I_{\mathrm{coh}}(Q, t)/I_{\mathrm{coh}}(Q, 0)$ was found essentially constant for dry D-exchanged powder samples of d-PC (Randall *et al* 1983, 1978, Middendorf and Randall 1980). The intermediate scattering function picks up a small time-dependent component when the protein is hydrated, and this appears to be due mainly to the activation of restricted brownian motions of the subunits of d-PC with effective diffusion coefficients of 1 to 2×10^{-6} cm^2 s^{-1}. Moving up in energy and using backscattering spectrometers to measure $S(Q, \omega)$

the wet-minus-dry difference broadenings observed within $0.15 \leq Q \leq 5.5$ Å^{-1} depend strongly on Q, H/D contrast and hydration level. With increasing D_2O hydration, up to equivalent monolayer coverage, the broadenings are very small. Since the scattering here is predominantly due to the bulk protein, it seems that its structure 'loosens up' slightly with the formation of a network of hydrogen bonds around polar surface groups and in the clefts and channels between subunits; but there is little one can say about the Q-dependence of this process. Upon hydration with H_2O, however, the incoherent scattering increases substantially and it becomes possible to observe wet-minus-dry difference broadenings which relate mainly to the functionally important outer shell of the protein, i.e. to the dynamics of the water of hydration and of the H_2O-hydrated side chains at or near the surface. Concomitant changes in the dynamics of the d-PC interior, although somewhat more 'visible' owing to partial H/D exchange, can be treated as correction terms. Difference experiments of this kind reveal that the time-scales for translational and rotational motions are well separated up to $h \simeq 0.5$, or values of water uptake equivalent to about 1.5 monolayers per ($\alpha\beta$) subunit. This is illustrated in figure 10.5 by lineshapes obtained on IN13 ($Q > 1.5$ Å^{-1}) for which EISF analyses have been performed; a full analysis is outstanding because data at lower Q are lacking. A more complete picture has emerged from detailed IN10 analyses on the broadening of the central peak which appears to be elastic at the resolution of IN13. The difference measurements at four hydration levels show that the broadening possesses an oscillatory structure with a first maximum between $Q = 0.4$ and $Q = 0.8$ Å^{-1} (figure 10.6). The position of this maximum shifts to higher Q with increasing hydration while the intensity increases and the following minimum between 0.7 and 1.1 Å^{-1} becomes progressively more shallow. A Chudley–Elliott jump-diffusion model was adopted as a working hypothesis to extract a characteristic length (water migration distance, d) and a characteristic time (residence time τ_0 at a hydration site) from the broadening data. The values obtained, $d = 6$ to 9 Å and $\tau_0 = 5$ to 30×10^{-9} s, agree well with average jump-distances derived from topological considerations in conjunction with measurements of hydration numbers.

The characteristic Y-shaped structure of the immunoglobulins gives rise to considerable intramolecular flexibility which is thought to be essential for antigen-recognition and interaction. Recently, a detailed spin–echo study of the low-frequency intramolecular modes in immunoglobulin G was performed (Alpert *et al* 1985). X-ray studies of crystalline immunoglobulin fragments (Deisenhofer *et al* 1976) and solution scattering data (Cser *et al* 1981a) provided information on the three-dimensional structure. The molecule consists of three relatively independent parts connected by loose sections of polypeptide chains.

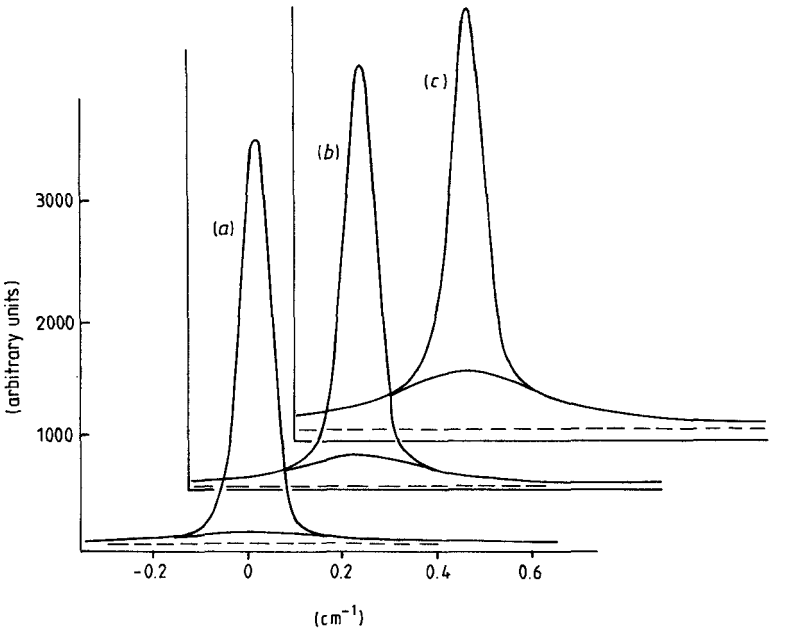

Figure 10.5 Quasielastic spectra at $Q = 1.5$ Å^{-1} showing activation of sidechain mobility (broad component) during H_2O hydration of biosynthetically deuterated phycocyanin: (*a*), 0.06; (*b*), 0.19; (*c*), 0.32 g/g water uptake. (From work at Institut Laue–Langevin by H D Middendorf, I Anderson and H L Crespi.)

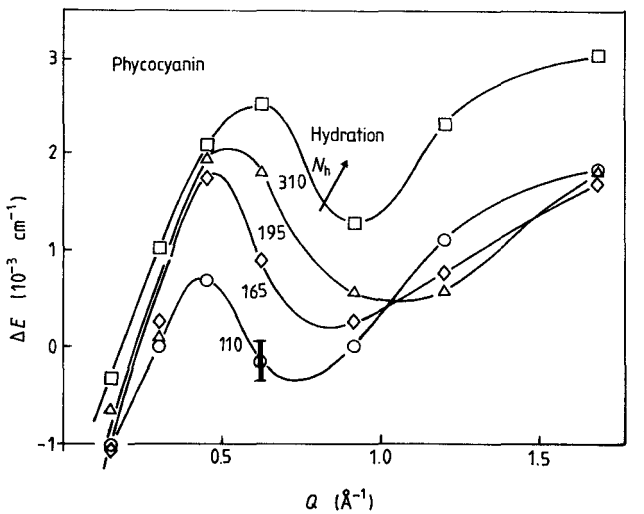

Figure 10.6 Hydration difference broadenings for powder samples of biosynthetically deuterated phycocyanin at four hydration levels corresponding to 110, 165, 195 and 310 $H_2O/(\alpha\beta)$ subunit (T + 24 °C) (from Middendorf and Randall 1980).

Low-angle scattering experiments (Cser *et al* 1981b) suggested that the molecule is flexible and that various modes of intramolecular motion occur, such as wagging and twisting of its individual parts. Numerous optical, NMR and ESR experiments have already been performed to characterise in detail these molecular motions and their relation to function (e.g. Hanson *et al* 1981). A recent neutron study using the spin-echo technique has provided valuable information (Alpert *et al* 1985).

Experimental data obtained from the neutron technique were analysed on the basis of two types of models. The first model assumed that the molecule was perfectly rigid, with a T-shaped form, and that its only motion, in addition to the translational diffusion was an isotropic diffusion about its centre of gravity. Conversely, in the second model, the molecule was considered as flexible and its arms were assumed to wobble around the hinge region. The intermediate scattering functions $I(Q, t)$ corresponding to these two models were derived, approximating the different parts of the molecule by prolate ellipsoids of revolution connected together at the end-points of their larger axes. The former model is described in §6.2 while the latter is close to the oscillation model described in §7.3. Both models could be fitted fairly well to the experimental points. However, the first model led to an unrealistically high value of the rotational diffusion constant. For the second model the independent arms of the molecule were found to wag within a cone of $\pm 50°$. Simultaneously the correlation time was found to be equal to 1.22×10^{-6} s, in good agreement with fluorescence measurements (1.05×10^{-6} s).

References

Abramovitz M and Stegun J A 1965 *Ha\ lbook of Mathematical Functions* (New York: Dover)

Achard J A, Dianoux A J, Lartigue C, Percheron-Guegan A and Tasset F 1982 *The Rare Earths in Modern Science and Technology* vol. 3 ed. G J McCarthy, J J Rhyne and H B Silver (New York: Plenum) p 481

Adam M and Delsanti M 1977a *J. Physique Lett.* **38** L271

Adam M and Delsanti M 1977b *Macromolecules* **10** 1229

Ageron P, Ewarld R, Harig H D and Verdier J 1971 *Energie Nucléaire* **13** 1

Akcasu A Z, Benmouna M and Han C C 1980 *Polymer* **21** 866

Albert S, Gutowsky H S and Ripmeester J A 1976 *J. Chem. Phys.* **64** 3277

Alfeld B, Richter D and Heidemann A 1984 *ILL Technical Report* 84LA25T

Allegra G, Higgins J S, Ganazzoli F, Lucchelli E and Bruckner S 1984 *Macromolecules* **17** 1253

Allen G, Brier P N and Higgins J S 1972 *Polymer* **13** 157

Allen G, Wright C J and Higgins J S 1975 *Polymer* **15** 319

Allen G, Higgins J S, Maconnachie A and Ghosh R E 1982 *J. Chem. Soc. Faraday Trans.* II **78** 2117

Alpert Y, Cser L, Farago B, Franek F, Mezei F and Ostanevich Y M 1985 *Biopolymers* **24** 1769

Amaral L W, Vinhas L A and Herdade S B 1976 *J. Pol. Sci. Pol. Phys.* **14** 1077

Amoureux J P and Bée M 1979 *Acta Cryst.* B **35** 2957–62

Amoureux J P and Bée M 1980a *Acta Cryst.* B **36** 2636–42

Amoureux J P and Bée M 1980b *J. Phys. C: Solid State Phys.* **13** 3577–83

Amoureux J P, Bée M and Damien J C 1980a *Acta Cryst.* B **36** 2633–6

Amoureux J P, Bée M and Virlet J 1980b *Mol. Phys.* **41** 313–24

Amoureux J P, Sauvajol J L and Bée M 1981a *Acta Cryst* A **37** 97–104

Amoureux J P, Castelain M, Bée M, Arnaud B and Shouteenten M L 1981b *Mol. Phys.* **42** 119-27

Amoureux J P, Bée M and Sauvajol J L 1982a *Acta Cryst* B **38** 1984–9

Amoureux J P, Bée M and Sauvajol J L 1982b *Mol. Phys.* **45** 709–19

Amoureux J P, Castelain M, Bée M, Arnaud B and Shouteenten M L 1982c *J. Phys* C: *Solid State Phys.* **15** 1319–27

Amoureux J P, Castelain M, Benadda M D, Bée M and Sauvajol J L 1983 *J. Physique* **44** 513–20
Amoureux J P, Castelain M, Bée M, Benadda M D and More M 1985 *Mol. Phys.* **55** 241–51
Amoureux J P, Noyel G, Foulon M, Bée M and Jorat L 1984 *Mol. Phys.* **52** 161–71
Anderson J R, Foger K, Mole T, Rajadhyasha R A and Sanders J V 1979 *J. Catal.* **58** 114
Anderson M R, Harryman M B M, Steinmann D K, White J W and Currat R 1982 *Polymer* **23** 569
Anderson I S, Heidemann A, Bonnet J E, Ross D K, Wilson S K P and McKergon M W 1984 *J. Less. Common Metals* **101** 405
Azokpota C, Calvarin G and Pommier C 1976 *J. Chem. Thermodyn.* **8** 283
Bacon G E 1975 *Neutron Diffraction* (Oxford: Clarendon)
Bacon G E 1977 *Neutron Scattering in Chemistry* (London: Butterworth)
Barar J F, Calvarin G, Weigel D, Chhor K and Pommier C 1980 *J. Chem. Phys.* **73** 438
Barnes J D 1973 *J. Chem. Phys.* **58** 5193–201
Barrer R M 1978 *Zeolites and Clay Minerals* (London: Academic)
Beaufils J P 1985 *Molecular Physics* **55** 433–43
Beckurts K H and Wirtz K 1964 *Neutron Physics* (Berlin: Springer)
Bée M 1982 *Mol. Phys.* **47** 83–96
Bée M and Amoureux J P 1982 *Mol. Phys.* **47** 533–50
Bée M and Amoureux J P 1983a *Mol. Phys.* **50** 585
Bée M and Amoureux J P 1983b *Mol. Phys.* **48** 63–79
Bée M, Amoureux J P and Dianoux A J 1980a *Mol. Phys.* **41** 325–39
Bée M, Amoureux J P and Lechner R E 1980b *Mol. Phys.* **39** 945–61
Bée M, Amoureux J P and Lechner R E 1980c *Mol. Phys.* **40** 617–41
Bée M, Sauvajol J L and Amoureux J P 1982 *J. Physique* **43** 1797–808
Bée M, Lechner R E , Amoureux J P and Fouret R 1983a *J. Phys. C: Solid State Phys.* **16** 4973–84
Bée M, Poinsignon C, Longueville W and Amoureux J P 1983b *J. Physique* **44** 215–30
Bée M, Dianoux A J and Volino F 1984 *Mol. Phys.* **51** 221
Bée M, Jobic H and Sourisseau C 1985a *J. Phys. C: Solid State Phys.* **18** 5771
Bée M, Sauvajol J L, Hedoux A and Amoureux J P 1985b *Mol. Phys.* **55** 637–52
Bée M, Jobic H and Caucheteux C 1986a *J. Chim. Phys.* **83** 10
Bée M, Lechner R E and Petry W 1988 *Mol. Phys.* (submitted to)
Bée M, Longueville W, Amoureux J P and Fouret R 1986b *J. Physique* **47** 305
Ben Brahim J, Besson G and Tchonbar C 1984 *J. Appl. Cryst.* **17** 179
Bernal J B and Fowler R H 1933 *J. Chem. Phys.* **1** 515
Bialek W and Goldstein R F 1985 *Biophys. J.* **48** 1027
Birr M, Heidemann A and Alefeld B 1971 *Nuclear Inst. Method* **95** 435
Bischoff F G 1970 *PhD Thesis* Rensselaer Polytechnic Institute.
Bischoff F G, Yeater M L and Moore W E 1972 *Nucl. Sci. Engng* **48** 266
Blanc Y 1983 *ILL Technical Report* 83BL21G
Bourtin H and Yip S 1968 *Molecular Spectroscopy with Neutrons* (Cambridge, Mass: MIT Press)

Bradley C J and Cracknell A P 1972 *The Mathematical Theory of Symmetry in Solids* (Oxford: Clarendon)
Breck D W 1973 *Zeolite Molecular Sieves* (New York: Wiley)
Briggs G A and Stirling W G 1976 *Neutron Diffraction Facilities at Western European Medium Flux Reactors* (Grenoble: Institut Laue–Langevin)
Brissaud-Lancin M, Meyer M and Philibert J 1982 *J. Phys. Chem. Solids* **43** 97 and 105
Brockhouse B N 1958 *Nuovo Cim. Suppl.* **9** 45
Brockhouse B N 1959 *Phys. Rev. Lett.* **2** 287
Brockhouse B N, Bergsma J, Dasannacharya B A and Pope N K 1963 *Proc. Int. Conf. Inelastic Scattering of Neutrons in Solids and Liquids* vol. 1 (IAEA: Vienna) p 189
Brondeau J and Goulon J 1975 *C. R. Hebd. Séanc. Acad. Sci. Paris* A **281** 715
Brot C 1969 *Chem. Phys. Lett* **3** 319
Brot C, Lassier-Govers B, Lechner R E and Volino F 1979 *J. Physique* **40** 563
Butler I S, Fitzpatrick P J, Gilson D and Gomez G 1983 *Com. J. Chem. (Canada)* **61** 737
Byung K O, Labes M M and Salomon R E 1976 *J. Chem. Phys.* **64** 3375
Cabib D and Benguigi L 1977 *J. Physique* **38** 419
Callender R and Pershan P S 1970 *Phys. Rev.* A **42** 672
Careri G, Fasella P and Gratton E 1979 *Ann. Rev. Biophys. Bioengineering* **8** 69
Carpentier J M, Lande G H and Windsor C G 1984 *Rev. Sci. Instr.* **7** 55
Carru J C 1986 *Thesis* Lille, France
Carter J L, Yates D J C, Lucchesi P J, Elliott J J and Kevor-Kian V 1966 *J. Phys. Chem* **70** 1126
Chadwick J 1932 *Nature* **129**; see also: (1932) *Proc. Roy. Soc. London, Ser. A* **136** 692
Chadwick A W and Forrest J W 1978 *J. Chem. Soc. Faraday Trans.* I **74** 2560–2
Chang C D and Silvestri A J 1977 *J. Catal.* **47** 249
Chang S S and Westrum E F 1960 *J. Phys. Chem.* **64** 1547
Chapoton A 1973 *Thesis* Lille, France
Chen S H, Teixeira J and Nicklow R 1982 *Phys. Rev.* A **26** 3477
Chhor K 1982 *Thesis* Paris XIII
Chhor K and Pommier C 1984 *Mol. Cryst. Liq. Cryst* **100** 193
Chhor K, Lucazeau G and Sourisseau C 1981 *J. Raman Spectrosc.* **11** 183
Chhor K, Sourisseau C and Lucazeau G 1982 *J. Mol. Struct.* **80** 485–8
Chhor K, Bocquet J F, Lucazeau G and Dianoux A J 1984 *Chem. Phys.* **91** 471
Chudley G T and Elliott R J 1961 *Proc. Phys. Soc.* **77** 353
Clark T, McKervey M A, Macckle H and Rooney J 1974 *J. Chem. Soc. Faraday Trans.* I **70** 1279
Clark T, Mc O.Knox T, Macckle H and McKervey M A 1977 *J. Chem. Soc. Faraday Trans* I **73** 1224
Clech G and Calvarin G 1981 *Mol. Cryst. Liq. Cryst.***75** 345
Clementi E 1985 *J. Phys. Chem.* **89** 4426
Clough S, Heidemann A and Paley M 1980 *J. Phys. C: Solid State Phys.* **13** 4009–15
Cocking S J and Egelstaff P A 1968 *J. Phys. C: Solid State Phys.* **1** 507
Cohen de Lara E 1972 *Mol. Phys.* **23** 555
Cohen de Lara E and Kahn R 1981 *J. Physique* **42** 1029–38

Cohen de Lara E and Kahn R 1984 *J. Physique Lett.* **45** L255
Cohen de Lara E and Nguyen-Tan T 1976 *J. Phys. Chem.* **80** 1917
Cohen de Lara E and Vincent J 1976 *J. Phys. Chem.* **80** 1922
Conard J 1976 *Mag. Res. in Coll. Interf. Sciences* (ACS Symp. Series T) pp 34–85
Conard J, Estrade-Szwarckopf H, Dianoux A J and Poinsignon C 1984 *J. Physique* **45** 1361
Cooper A 1981 *Sci. Prog. Oxf.* **66** 473
Cooper A 1984 *Prog. Biophys. Mol. Biol* **44** 181
Copley J R D 1974 *Comp. Phys. Commun.* **7** 289
Copley J R D 1975a *Comp. Phys. Commun.* **9** 59–63
Copley J R D 1975b *Comp. Phys. Commun* **9** 64–8
Copley J R D 1978 *ILL Report* 78CO163T
Copley J R D, Price D L and Rowe J M 1973 *Nucl. Instrum. Meth.* **107** 501; see erratum: ibidem (1974) **114** 411
Copley J R D and Rowe J M 1974a *Phys. Rev. Lett.* **32** 49
Copley J R D and Rowe J M 1974b *Phys. Rev.* A **9** 1656
Coulomb J P, Bienfait M and Thorel P 1981 *J. Physique* **42** 293
Coulomb J P, Bienfait M and Thorel P 1985 *Faraday Disc. Chem. Soc.* **80** 79
Crespi H L 1977 *Stable Isotopes in the Life Sciences* (Vienna: IAEA) p. 111
Crespi H L and Katz J J 1972 *Methods in Enzymology* **26C** 627
Cribier D and Jacrot B 1960 *J. Phys. Radium (France)* **21** 69
Cser L, Gladkikh I A, Franek F and Ostanevich Yu M 1981a *Colloid and Polymer Sci.* **256** 625
Cser L, Franek F, Gladkikh I A, Kunchenko A B and Ostanevich Yu M 1981b *Eur. J. Biochem.* **116** 109
Dahlborg U, Larsson K E and Pirkmajer E 1970 *Physica* **49** 1 (see erratum: Larsson 1970)
Dahlborg U and Rupprecht A 1971 *Biopolymers* **10** 849
Dahlborg U, Dimic V and Rupprecht A 1980 *Phys. Scripta* **22** 179
Dasannacharya B A and Rao K R 1965 *Phys. Rev.* **137** A417
Debye P 1929 *Polar Molecules* (New York: Dover)
De Gennes P G 1967 *Physics* **3** 37
De Gennes P G 1971 *J. Chem. Phys.* **55** 572
De Gennes P G 1980 *J. Physique* **42** 735
Deisenhofer J, Colman P M, Huber R, Haupt M and Schwick G 1976 *Hoppe-Seyler's Z. Biol. Chem.* **357** 435
De La Calle C, Pezerat H and Gasperin M 1977 *J. Physique Coll.* C7 **38** 128
Delise P, Allegra G A, Mognashi E R and Chierico A 1975 *J. Chem. Soc. Faraday Trans.* II 207
De Raedt H and De Raedt B 1977 *Phys. Rev.* B **15** 5379
De Raedt B and Michel K H 1979 *Phys. Rev.* B **19** 767
Deroche B, Charvolin J, Liebert L and Strzelecki L 1975 *J. Physique Coll.* **36** C1–21
Derouane E G, Nagy J B, Dejaifve P, Van Hooff J H C, Spekman B P, Vedrine J C and Naccache C 1978 *J. Catal.* **53** 40
Dianoux A J and Volino F 1977 *Mol. Phys.* **34** 1263
Dianoux A J, Volino F and Hervet H 1975 *Mol. Phys.* **30** 1181–94

Dianoux A J, Hervet H and Volino F 1977 *J. Phys. Paris* **38** 809
Dianoux A J, Pineri M and Volino F 1982 *Mol. Phys.* **46** 1129–37
Dickinson E 1985 *Chem. Soc. Rev.* **14** 421
Doi M and Edwards S F 1978 *J. Chem. Soc. Faraday Trans.* II **74** 1789; 1802; 1818
Dolling G 1974 *Dynamical Properties of Solids* vol 1, ed G K Horton and A A Maradudin (New York: North-Holland) ch 10, pp 541–629
Doucet J, Levelut A M and Lambert M 1974a *Phys. Rev. Lett* **32** 301
Doucet J, Levelut A M and Lambert M 1974b *J. Physique* **35** 773
Doucet J, Levelut A M, Lambert M, Liebert L and Strzelecki L 1975 *J. Physique Coll.* **36** C1–13
Drexel W and Peticolas W L 1975 *Biopolymers* **14** 715
Dubois-Violette E and De Gennes P G 1967 *Physics* **3** 181
Ducros P 1960 *Thesis* Paris
Duplessix R, Escoubes M, Rodmacq B, Volino F, Roche E, Eisenberg A and Pineri M 1980 *Water in Polymers* ed S P Rowland (Am. Chem. Soc. Symp. Ser 127).
Dvorjetski D, Volterra V and Wiener-Avnear E 1975 *Phys. Rev.* A **12** 681
Edmonds A R 1974 *Angular Momentum in Quantum Mechanics* (Princetown: Princetown University Press)
Edwards J W, Kington G L and Mason R 1959 *Trans. Faraday Soc.* **55** 660
Egelstaff P A 1954 *J. Nucl. Energy* **1** 57
Egelstaff P A 1956 *Proc. of 1st Int. Conf on the Peaceful Use of Atomic Energy* vol. IV (Vienna: IAEA) p 119
Egelstaff P A 1967 *An Introduction to the Liquid State* (London: Academic)
Egelstaff P A 1971 *Thermal Neutron Scattering* ed P A Egelstaff (New York: Academic)
Einstein A 1905 *Ann. Phys. Lpz.* **17** 549
Falk M, Hartman H A and Lord R C 1963 *J. Am. Chem. Soc.* **85** 387 and 391
Favro L D 1965 *Fluctuation Phenomena in Solids* ed. R E Burgess (New York: Academic)
Finney J L and Poole P L 1984 *Order out of Chaos* (London: Heinemann)
Finney J L, Goodfellow J M and Poole P L 1982 *Structural Molecular Biology—Methods and Applications* ed D B Davies, W Saenger and S S Danyluk (New York: Plenum) p 387
Folland R, Jackson D A and Rajacopal S 1975 *Mol. Phys.* **30** 1063
Folland R, Jackson R L and Strange J H 1973a *J. Phys. Chem. Solids* **34** 1713–26
Folland R, Ross S M and Strange J H 1973b *Mol. Phys.* **26** 27
Foulon M, Amoureux J P, Sauvajol J L, Lefebvre J and Descamps M 1983 *J. Phys. C: Solid State Phys.* **16** L265–9
Franks F and Mathias S 1982 *Biophysics of Water* (Chichester: Wiley)
Fredericks G E 1971 *Phys. Rev.* B **4** 911
Frenkel J 1935 *Acta Phys. Chim. URSS* **3** 23
Frost J C, Leadbetter A J and Richardson R M 1980a *Faraday Disc. Chem. Soc.* **69** 32–48
Frost J C, Leadbetter A J and Richardson R M 1980b *Phil. Trans. R. Soc. Lond.* B **290** 567–82

Frost J C, Leadbetter A J and Richardson R M 1982 *J. Chem. Soc. Faraday Trans.* II **78** 2139–54
Furic K 1984 *Chem. Phys. Lett.* **108** 518–21
Furry W H 1957 *Phys. Rev.* **107** 7
Gabrys B, Higgins J S, Ma K T and Roots J E 1984 *Macromolecules* **17** 560
Gabrys B, Higgins J S and Young D A 1985 *Polymer* **26** 355
Gardner A B, Howard J, Waddington T C, Richardson R M and Tomkinson J 1981 *Chem. Phys.* **57** 453
Gerling R W 1981 *Z. Phys.* B **45** 39
Gerling R W and Hüller A 1983 *J. Chem. Phys.* **78** 446–53
Gierke T D 1977 *Electrochemical Society Fall Meeting*, Atlanta, Georgia
Gissler W and Stumpf N 1973 *Physica* **65** 109
Glazer A N 1985 *Ann. Rev. Biophys. Biophys. Chem.* **14** 47
Gordon R C 1966 *J. Chem. Phys.* **44** 1830
Graessley W W 1980 *J. Polym. Sci. Phys. Ed.* **18** 27
Graf F, Meyer R, Ha T K and Ernst R R 1981 *J. Chem. Phys.* **75** 2914
Gray D A 1985 *Proc. Conf. Neutron Scattering in the Nineties* Jülich 14–18 January (Vienna: IAEA) p 261
Hall P L and Ross D K 1978 *Mol. Phys.* **36** 1549–54
Hall P L and Ross D K 1981 *Mol. Phys.* **42** 673
Hall P L, Ross D K, Tuck J J and Hayes M H B 1977 *Proc. IAEA Conf. Inelastic Neutron Scattering* vol. 1 (Vienna: IAEA) p 617
Hall P L, Ross D K, Tuck J J and Hayes M H B 1979 *Proc. of Int. Clay. Conf.* ed M M Mortland and V C Farmer (Amsterdam: Elsevier) p 121
Han C C and Akcasu A Z 1981 *Macromolecules* **14** 1080
Hanson D C, Yguerabide J and Shumaker V N 1981 *Biochemistry* **20** 6842
Harbrecht B 1981 *PhD Thesis* University of Aachen
Hasebe T, Nakamura N and Chihara H 1980 *J. Chem. Soc. Jpn.* **53** 1783
Hawthorne H M and Sherwood J N 1970 *Trans. Faraday Soc.* **66** 1783
Hayter J B, Hecht A M, White J W and Tiddy G J T 1974 *Faraday Disc. Chem. Soc.* **57** 130
Heidemann A and Magerl A 1983 *ILL Technical Report* 83HE02T
Henry A W and Safford G J 1969 *J. Polym. Sci.* A2 **7** 433
Hervet H, Volino F, Dianoux A J and Lechner R E 1974 *J. Physique Lett* **35** L151
Hervet H, Volino F, Dianoux A J and Lechner R E 1975 *Phys. Rev. Lett.* **34** 451
Hervet H, Dianoux A J, Lechner R E and Volino F 1976 *J. Physique* **37** 587
Higgins J S 1982 *Static and Dynamic Properties of the Polymeric Solid State* ed. J V Pethrick and R W Richards (Dordrecht: Reidel)
Higgins J S 1983 *Developments in Polymer Characterization* vol. 4 ed. J V Dawkins (Ann Arbor: Applied Science Publishers) p 131
Higgins J S and Roots J E 1985 *J. Chem. Soc. Faraday Trans.* II **81** 757
Higgins J S, Ghosh R E, Howells W S and Allen G 1977 *J. Chem. Soc. Faraday Trans.* II **73** 40
Higgins J S, Nicholson L K and Hayter J B 1981 *Polymer* **22** 163
Higgins J S, Ma K, Nicholson L K, Hayter J B, Semlyen A J and Dodgson K 1983 *Polymer* **24** 793

Hoch A, Funke K, Lechner R E and Ohachi T 1983 *Solid State Ionics* **9–10** 1353
Hoffmann H 1984 *ILL Technical Report* 84H0368
Hopfinger A J, Mauritz K A and Hora C J 1977 *Electrochemical Society Fall Meeting* Atlanta, Georgia
Hoser A, Joswig W, Prandl W and Vogt K 1985 (in preparation)
Hossain M A, Hursthouse M B and Malik M A 1979 *Acta Cryst.* B **35** 522
Houslay M D and Stanley K K 1982 *Dynamics of Biological Membranes* (Chichester: Wiley)
Hovi V, Mutikainen P and Pirinen J 1973 *Ann. Acad. Sci. Fennicae* A **6** 1
Hubbard P S 1958 *Phys. Rev.* **109** 1153
Hugues D J *et al* 1959 *Phys. Rev. Lett.* **3** 91
Hüller A 1977 *Phys. Rev.* B **16** 1844–57
Hüller A and Kane J W 1974 *J. Chem. Phys.* **61** 3599
Hüller A and Kroll D M 1975 *J. Chem. Phys.* **63** 4495
Hüller A and Press W 1979 *Acta Cryst.* A **35** 876
Hüller A and Press W 1981 *Phys. Rev.* B **24** 17–24
Ison A and Gorte R J 1984 *J. Catal.* **89** 150
Jackson R L and Strange J H 1971 *Mol. Phys.* **22** 313
Jacrot B 1970 *Instrumentation for Neutron Inelastic Scattering Research* IAEA Panel Proceedings Series
James H M and Keenan T A 1959 *J. Chem. Phys.* **31** 12
Janin J and Wodak S J 1983 *Prog. Biophys. Mol. Biol.* **42** 21
Jobic H, Bée M and Renouprez A 1984 *Surface Science* **140** 307
Jobic H, Renouprez A, Bée M and Poinsignon C 1986 *J. Phys. Chem.* **90** 1059
Johnson M W 1974 *UKAEA Harwell Report* AERE-R7682
Jurga S, Jurga K and Pajak Z 1981 *J. of Phys. C: Solid State Phys.* **14** 4433–46
Kahn R, Cohen de Lara E, Thorel P and Gignoux J L 1982 *Zeolites* **2** 260
Kara M and Kurki-Suonio K 1981 *Acta Cryst.* A **37** 201
Kärger J and Ruthven D M 1981 *J. Chem. Soc. Faraday Trans.* I **77** 1485
Karplus M and McCammon J A 1981 *CRC Crit. Rev. Biochem.* **9** 293
Kasper J S and Lonsdale K 1959 *International Tables for X-ray Crystallography* vol. II (Birmingham: Kynoch Press)
Keniry M A, Smith R L, Gutowsky H L and Oldfield E 1983 *Structure and Dynamics: Nucleic Acids and Proteins* ed. E Clementi and R H Sarma (New York: Adenine) p 435
Keyes P H and Daniels W B 1975 *J. Chem. Phys.* **62** 2000
Kokotailo G T, Lawton S L, Olson D H and Meier W M 1978 *Nature* **272** 437
Kondo S and Oda T, 1954 *Bull. Chem. Soc. Jpn.* **27** 567
Kostorz G 1978 *Neutron Scattering in Material Science* (New York: Academic)
Kroll D M and Michel K H 1977 *Phys. Rev.* B **15** 1136
Kruger G J, Spiesecke H and Van Steenwinkel R 1976 *J. Phys. Coll.* **37** C3–127
Kubo R 1966 *Rep. Prog. Phys.* **29** 255
Kurki-Suonio K 1967 *Ann. Acad. Sci. Fenn.* **A6** 263
Kurki-Suonio K 1968 *Acta Crystallogr.* **A24** 379
Kurki-Suonio K and Meisalo V 1967 *Ann. Acad. Sci. Fenn.* **A6** 241
Larsson K E 1970 *Phys. Rev.* A **2** 810 (see erratum: Dahlborg *et al* 1970)
Leadbetter A J and Lechner R E 1979 *The Plastically Crystalline State* ed J N

Sherwood (Chichester: Wiley)
Leadbetter A J and Turnbull A 1977 *J. Chem. Phys.* **73** 1788
Leadbetter A J, Richardson R M and Carlile C J 1976 *J. Physique Coll.* **37** C3–65
Leadbetter A J, Piper J, Richardson R M and Wrighton P G 1982 *J. Phys. C: Solid State Phys.* **15** 5921–36
Lechner R E 1976 *Proc. Conf. Neutron Scattering* Gatlinburg 1976 vol. 1 (Springfield, Virginia: Natl. Techn. Inform. Service US Dept. of Commerce) p 310
Lechner R E and Heidemann A 1976 *Commun. on Physics* **1** 213
Lechner R E and Oberthür R C 1977 *ILL Ann. Report* Annex p 376
Lechner R E, Volino F, Dianoux A J, Douchin F, Hervet H and Stirling G C 1973 *ILL Report* 73L8S
Lennard-Jones J and Pople J A 1951 *Proc. Roy. Soc.* A **205** 155
Levitt M 1982 *Ann. Rev. Biophys,. Bioengineering* **11** 251
Levy H A and Peterson S W 1951 *J. Chem. Phys.* **19** 1416
Levy H A and Peterson S W 1952 *Phys. Rev.* **86** 766
Link K H, Grimm H, Dorner B, Zimmermann H, Stiller H and Bleckmann P 1985 *J. Phys. Chem. Solids* **46** 135
Longer G F and White J W 1969 *Mol. Phys.* **17** 1
Longueville W, Bée M, Amoureux J P and Fouret R 1986 *J. Physique* **47** 291
Longueville W and Fontaine H 1976 *Mol. Cryst. Liq. Cryst.* **32** 73
Longueville W, Fontaine H, Baert F and Odou G 1978 *Acta Cryst.* A **34** S188
Longueville W, Fontaine H and Vergoten G 1982 *J. Raman Spectrosc.* **13** 273
Lovesey S W 1980 *Condensed Matter Physics; Dynamic Correlations* (Reading, Massachusetts: Benjamin/Cummings)
Lovesey S W 1984 *Theory of Neutron Scattering from Condensed Matter* (Oxford: Clarendon)
Lovesey S W and Stirling G C 1984 *Physica* **127B** 306
Lucazeau G 1983 *Solid State Ionics* **8** 1
Luz Z and Meiboom S 1973 *J. Chem. Phys.* **59** 275
Luz Z, Hew R C and Meiboom S 1974 *J. Chem. Phys.* **61** 1758
Ma K T 1981 *PhD Thesis* Imperial College, London
McCall D W and Douglass D C 1960 *J. Chem. Phys.* **33** 777
McCammon J A 1984 *Rep. Prog. Phys.* **47** 1
Maconnachie A and Richards R W 1978 *Polymer* **19** 739
Maier B 1983 *Neutron Facilities at the ILL High Flux Reactor* (Grenoble: Institut Laue–Langevin)
Maier-Leibnitz H and Springer T 1963 *J. Nucl. Energy* **17** 217
Mandena W and Trappeniers J 1974 *Physica* **76** 123; 73; 85; 102
Marsaguerra M and Pauli G 1959 *Nucl. Instr. Meth.* **4** 140
Marshall W and Lovesey S W 1971 *Theory of Thermal Neutron Scattering* (Oxford: Clarendon Press)
Meardon B H 1975 *ILL Report* 75M42
Meier W M 1961 *Z. Krist* **115** 439
Meier B H, Graf F and Ernst R R 1982 *J. Chem. Phys.* **76** 767
Meier B H, Meyer R, Ernst R R, Zolliker P, Furrer A and Hälg W 1983 *Chem. Phys. Lett.* **103** 169
Meier B H, Meyer R, Ernst R R, Stockli A, Furrer A, Hälg W and Anderson I

1984 *Chem. Phys. Lett.* **108** 522–3
Meirovitch E and Luz Z 1975 *Mol. Phys.* **30** 1589
Meisel S L, McCullough J P, Lechthaler C H and Weisz P B 1976 *Chem. Tech.* **6** 86
Meyer R J 1975 *Phys. Rev.* A **12** 1066
Meyer R J and McMillan W L 1974 *Phys. Rev.* A **9** 899
Mezei F (ed) 1980 *Proc. Workshop on Neutron Spin Echo* (Berlin: Springer)
Mezei F 1983 *Physica* **120B** 51
Michel K H 1973 *J. Chem. Phys.* **58** 1143–6
Michel K H and Kroll D M 1976 *J. Chem. Phys.* **64** 1300
Michel K H and Naudts J 1977 *J. Chem. Phys.* **67** 547
Michel K H and Naudts J 1978 *J. Chem. Phys.* **68** 216
Michel K H, Naudts J and De Raedt B 1978 *Phys. Rev.* B **18** 648
Middendorf H D 1984 *Ann. Rev. Biophys. Bioengineering* **13** 425
Middendorf H D and Willis B T M 1972 *Fourth International Liquid Crystal Conference* Kent, Ohio
Middendorf H D and Stirling G C 1973 *Molecular Dynamics of Cell Membranes* (report on membrane work at AERE Harwell, unpublished)
Middendorf H D and Randall J T 1980 *Phil. Trans. Roy. Soc. London* B **290** 639
Middendorf H D and Randall J T 1985 *Structure and Motion: Membranes, Nucleic Acids and Proteins* ed E Clementi, G Corongiu, M H Sarma and R H Sarma (New York: Adenine) p 219
Miller A, Jenkin G T, White J W and White S W 1976, 1977 *ILL Ann. Reports* Annex pp. 320, 373
Mohler E and Pitka R 1974 *Solid State Commun.* **14** 791
Moore P B, Capel M, Kjeldgaard M and Engelman D M 1986 *Structure, Function and Genetics of Ribosomes* ed. B Hardesty *et al* (New York: Springer)
Mori H 1965 *Prog. Theor. Phys.* **23** 423
Morris B 1969 *J. Phys. Chem. Solids* **30** 73
Mouche E, Cohen de Lara E and Kahn R 1984 *Mol. Phys.* **53** 749
Müller W and Hüller A 1982 *J. Phys. C: Solid State Phys.* **15** 7295–304
Nagaoka S, Terao T, Imashiro F, Saika A, Hirota N and Hayashi S 1981 *Chem. Phys. Lett.* **80** 580
Nagaoka S, Terao T, Imashiro F, Saika A, Hirota N and Hayashi S 1983 *J. Chem. Phys.* **79** 4694
Naudts J and Michel K H 1978 *Phys. Rev.* B **18** 667
Neusy E, Nose S and Klein M 1984 *Mol. Phys.* **52** 269–79
Nicholson L K, Higgings J S and Hayter J B 1981 *Macromolecules* **14** 836
Nimmo J K and Lucas B W 1976 *Acta Cryst.* B **32** 597–600
Nordio P L and Busolin P 1971 *J. Chem. Phys.* **55** 5485
Nordio P L, Rigatti G and Segre U 1972 *J. Chem. Phys.* **56** 2117
Nordman C E and Schmitkons D L 1965 *Acta. Cryst.* **18** 764
Oehme W, Michel D, Pfeifer H and Zhdanov S P 1984 *Zeolites* **4** 120
Ogasahara K, Sorai M and Suga H 1979 *Chem. Phys. Lett.* **68** 457
O'Reilly D E, Peterson E M, Scheie C E and Seyfarth E 1973 *J. Chem. Phys.* **59** 3576–84
Paalman H H and Pings C J 1962 *J. Appl. Phys.* **33** 2635

Peticolas W L 1978 *Methods Enzymol.* **61** 425
Pick R M and Yvinec M 1980 *J. Phys. Paris* **41** 1053
Pineri M, Volino F and Escoubes M 1985 *J. Polymer Sci.* **23** 2009
Poinsignon C, Estrade-Szwarckopf H, Conrad J and Dianoux A J 1986 *Proc. of Assoc. Int. pour l'Etude des Argiles (AIPEA)* ed F A Mumpton Denver, Colorado
Polnaszek C F and Freed J H 1975 *J. Chem. Phys.* **79** 2283
Polnaszek C F, Bruno G V and Freed J H 1973 *J. Chem. Phys.* **58** 3185
Poncet P F J 1976 *Thesis* University of Reading
Poncet P F J 1977a *ILL Internal Report* 77P015S
Poncet P F J 1977b *ILL Internal Report* 77P0139S
Poncet P F J 1978a *ILL Internal Report* 77P0199S
Poncet P F J 1978b *ILL Internal Report* 78P087S
Porter R, O'Connor M and Whelan J (eds) 1983 *Mobility and Function in Proteins and Nucleic Acids, CIBA Foundation Symp. 93* (London: CIBA)
Poulet H and Mathieu J P 1970 *Spectres de Vibration et de Symétrie des Cristaux* (Paris: Gordon & Breach)
Powell B M and Martel P 1980 *Biophys, J.* **34** 311
Powell B M and Martel P 1982 *Chem. Phys. Lett.* **67** 165
Prandl W 1981 *Acta Cryst.* A **37** 811
Press W 1973 *Acta Cryst.* A **29** 257
Press W 1981 *Single-particle Rotations in Molecular Crystals* (Berlin: Springer)
Press W and Hüller A 1973 *Acta Crystallogr.* A **29** 252
Prigogine I and Stengers I 1984 *Order out of Chaos* (London: Heinemann)
Press W, Grimm H and Hüller A 1979 *Acta Crystallogr.* A **35** 881
Pynn R 1984 *Rev. Sci. Instrum.* **55** 6
Pynn R and Fender B 1985 *Physics Today* **25** 80
Ramsay J D F, Poinsignon C and Bée M 1986 to be published
Randall J T and Gilmour S 1975 Work on C-phycocyanin at AERE Harwell (unpublished)
Randall J T, Middendorf H D, Crespi H L and Taylor A D 1978 *Nature* **276** 636
Randall J T, Middendorf H D, Hayter J B and Crespi H L 1983 unpublished
Reichl R E 1980 *A Modern Course in Statistical Physics* (New York: Edward Arnold)
Renouprez A, Fouilloux P, Stockmeyer R, Conrad H M and Goeltz G 1977 *Ber. Buns. Gesell. Phys. Chem.*
Resing H A 1969 *Mol. Crystals* **9** 101
Richardson R M and Taylor P 1984 *Mol. Phys.* **52** 525–40
Richter D, Baumgartner A, Binder K, Ewen B and Hayter J B 1981 *Phys. Rev. Lett.* **47** 109
Richter D, Binder K, Ewen B and Stühn B, 1984 *J. Phys. Chem.* **88** 6618
Rickaysen G 1980 *Green's Fuctions and Condensed Matter* (London: Academic)
Rigny P 1972 *Physica* **59** 707
Riste T 1970 *Nucl. Instrum. Meth.* **86** 1
Roche E J, Pineri M and Duplessix R 1982 *J. Polym. Sci. Polym. Phys. Ed.* **20** 107
Roche E J, Pineri M, Duplessix R and Levelut A M 1981 *J. Polym. Sci. Polym. Phys. Ed.* **19** 1

Rosciszewski I 1972 *Acta Phys. Polonica* A **41** 549
Rose M E 1957 *Elementary Theory of Angular Momentum* (New York: John Wiley)
Rouse P E 1953 *J. Chem. Phys.* **21** 1272
Rowe J W, Sköld K, Flotow H E and Rush J J 1971 *J. Phys. Chem. Solids* **32** 41
Ruland W and Tompa H 1968 *Acta Crystallogr.* A **24** 93
Rupley J A, Gratton E and Careri G 1983 *Trends Biochem. Sci.* **8** 18
Sack R A 1956 *Physica* **22** 917
Sackmann E, Duwe H P, Zeman K and Zilker H 1986 *Structure and Dynamics of Nucleic Acids, Proteins and Membranes* ed E Clementi and S Chin (New York: Plenum) p 25
Sandorfy C and Theophanides T (ed) 1984 *Spectroscopy of Biological Molecules* (Dordrecht: Reidel)
Sauer J and Deininger D 1982 *Zeolites* **2** 144
Sauer J, Hopza P and Zahradnik R 1980 *J. Phys. Chem.* **84** 3318
Sauvajol J L 1983 *Thesis* (University of Lille)
Sauvajol J L and Amoureux J P 1981 *J. Phys. C: Solid State Phys.* **14** 1537–44
Sauvajol J L, Bée M and Amoureux J P 1982 *Mol. Phys.* **46** 811
Scherm R, Carlile C, Dianoux A J, Suck J and White J 1976 *ILL Report* 76S23S
Schlaak M, Lassegues J C, Heidemann A and Lechner R E 1977 *Mol. Phys.* **33** 111–23
Schlenker J L, Pluth J J and Smith J V 1979 *Mater. Res. Bull.* **14** 751
Schmatz W, Springer T, Schelten J and Ibel K 1987 *J. Appl. Crystallogr.* **7** 96
Schoonheydt R A, de Wilde W and Velghe 1976 *J. Phys. Chem.* **80** 511
Schreiner L J 1985 *Thesis* University of Waterloo, Ontario, Canada
Schreiner L J and Pintar M M 1984 *J. Physique* **45** C7, 241
Schwartz P 1971 *Phys. Rev.* B **4** 920
Sears V F 1966 *Can. J. Phys.* **44** 1999
Sears V F 1967 *Can. J. Phys.* **45** 234
Sears V F 1975 *Adv. Phys.* **24** 1
Seiler P and Dunitz J D 1979 *Acta Crystallogr.* B **35** 1068
Seymour R S and Pryor A W 1970 *Acta Crystallogr.* B **26** 1487
Shimizu M 1962 *J. Chem. Phys.* **37** 765
Simon F 1922 *Ann. Phys.* **68** 241
Simon F and von Simson U 1926 *Naturwissenschaften* **14** 880
Singwi K S and Sjolander A 1960 *Phys. Rev.* **119** 863
Sköld K 1967 *Phys. Rev. Lett.* **19** 1023
Sköld K, Rowe J M, Ostrowski G and Randolf P D 1972 *Phys. Rev.* A **6** 1107
Smith G W 1978 *Comments Solid State Phys.* **9** 21–35
Smith G W 1979 *Phase Transitions* **1** 107
Smith J, Cusack S, Pezzeca U, Brooks B and Karplus M 1986 *J. Chem. Phys.* (in press)
Sourisseau C, Bée M, Jobic H and Dworkin A 1985 *J. Raman Spectrosc.* **16** 44–56
Sourisseau C, Lucazeau G, Dianoux A J and Poinsignon C 1983 *Mol. Phys.* **48** 367–77

Springer T 1972 *Quasielastic Neutron Scattering for the Investigation of Diffusive Motions in Solids and Liquids, Springer Tracts in Modern Physics* (Berlin: Springer)
Squires G L 1978 *Introduction to the Theory of Thermal Neutron Scattering* (Cambridge: Cambridge University Press)
Stahn M, Lechner R E, Dachs H and Jacobs H E 1983 *J. Phys. C: Solid State Phys.* **16** 5073–82
Stanley H E, Blumberg R L, Geiger A, Mausbach P and Texeira J 1984 *J. Physique* **9** C7 3
Steele W A 1964 *Adv. Chem. Phys.* **34** 1
Stockmeyer R 1969 *Discuss. Faraday Soc.* **48** 156
Stockmeyer R and Stiller H 1968 *Phys. Stat. Solidi* **27** 269
Stockmeyer R, Stortnik H J and Conrad H M 1976 *Proc. Conf. on Neutron Scattering, Gatlinburg, Tennessee* **1** p 303
Stockmeyer R, Stortnik H J and Monkenbusch M 1980 *J. Mol. Struct.* **60** 415
Tabony J and Korb J P 1985 *Mol. Phys.* **56** 1281
Tabony J and Perly B 1986 submitted
Takeuchi I, Higgins J S, Hill A, Macconachie A, Allen G and Stirling G C 1982 *Polymers* **23** 499
Takusagawa F and Koetzle T F 1979 *Acta Crystallogr.* B **35** 1074
Tasumi M, Harada I, Takeuchi H, Shirakawa H, Suzuki S, Maconnachie A and Dianoux A J 1985 *Synth. Met.* **10** 293
Texeira J, Bellissent-Funel M C, Chen S H and Dianoux A J 1982 *J. Physique Coll.* **45** C7, 65
Texeira J, Bellissent-Funel M C, Chen S H and Dianoux A J 1985 *Phys. Rev.* A **31** 1913
Texter J 1978 *Prog. Biophys. Mol. Biol.* **33** 83
Thibaudier C and Volino F 1973 *Mol. Phys.* **26** 5 1281
Thibaudier C and Volino F 1975 *Mol. Phys.* **30** 1159
Timmermans J 1938 *J. Chem. Phys.* **35** 331
Timmermans J 1961 *J. Phys. Chem. Solids* **18** 1
Topler J, Richter D R and Springer T 1978 *J. Chem. Phys.* **69** 3170
Twistleton J F and White J W 1971 *Pure Appl. Chem.* **26** 545
Twistleton J F, White J W and Reynold P A 1982 *Polymer* **23** 578
Urban S, Mayer J and Belushkin A I 1983 *Acta Phys. Polonica* A **64** 161–5
van der Ploeg P and Berensen H J C 1983 *Mol. Phys.* **49** 233
Venkataraman G, Usha Deniz K, Jyengar P K, Roy A P and Vijayaraghavan P R 1966 *J. Phys. Chem. Solids* **27** 1103
Vineyard G H 1953 *Phys. Rev.* **91** 239
Vineyard G H 1954 *Phys. Rev.* **96** 93
Vineyard G H 1958 *Phys. Rev.* **110** 999
Vineyard G H and Falicon L M 1984 *Rev. Sci. Instrum.* **55** 4
Virlet J, Quiroga L, Boucher B, Amoureux J P and Castelain M 1983 *Mol. Phys.* **48** 1289–303
Vogt K and Prandl W 1983 *J. Phys. C: Solid State Phys.* **16** 4753
Volino F 1978 Spectroscopic methods for the study of local dynamics in polyatomic fluids, in *Microscopic Structure and Dynamics of Liquids* ed J Dupuy and A J Dianoux (New York: Plenum)

Volino F and Dianoux A J 1978a *Ann. Phys.* **3** 151
Volino F and Dianoux A J 1978b *Mol. Phys.* **26** 389
Volino F and Dianoux A J 1980 *Mol. Phys.* **41** 271
Volino F, Dianoux A J and Heidemann A 1979 *J. Physique Lett.* **40** L583
Volino F, Dianoux A J and Hervet H 1976a *J. Physique Coll.* **37** C3, 55
Volino F, Dianoux A J and Hervet H 1976b *Solid State Commun.* **18** 453
Volino F, Dianoux A J, Hervet H and Lechner R E 1975 *J. Physique Coll.* **36** C1, 84
Volino F, Pineri M, Dianoux A J and de Geyer A 1982 *J. Polym. Sci. Polym. Phys. Ed.* **20** 481–96
White J W 1981 in *Water at Interfaces* ILL Report 81T055S, Grenoble
White J W and Windsor C G 1984 *Rep. Prog. Phys.* **47** 707
White S W 1977 *Thesis* University of Oxford, UK
Whittingham M S and Jacobson A J 1982 *Intercalation Chemistry* (New York: Academic)
Wilkins M H F, Middendorf H D, Stirling G C, Dianoux A J and Riekel C 1976 *ILL Ann. Rep. Annex* Grenoble
Wilkins M H F, Willis B T M, Middendorf H D and Blaurock A E 1974 *UK Neutron Beam Res. Comm., Ann. Rep.* p35
Windsor C G 1981 *Pulsed Neutron Scattering* (London: Taylor and Francis)
Winfield D J and Ross D K 1972 *Mol. Phys.* **24** 753
Wright C J and Riekel C 1978 *Mol. Phys.* **36** 695
Yasukawa T, Kimura M, Watanabe N and Yamada Y 1971 *J. Chem. Phys.* **55** 983
Yeager H L and Eisenberg A (ed) 1982 Perfluorinated ionomer membranes *Am. Chem. Soc. Symp. Ser.* **180** (Washington, DC: Americal Chemical Society)
Yelon W B, Cox D E, Kortman P J and Daniels W B 1974 *Phys. Rev.* B **9** 4843
Yeo S C and Heisenberg A 1977 *J. Appl. Polym. Sci.* **21** 875
Yvinec M and Pick R M 1980 *J. Physique* **41** 1045
Yvinec M and Pick R M 1983 *J. Physique* **44** 169
Zikanova A, Kocinik M, Bezus A, Vlcek A A, Bulow M, Shirmer W, Kärger J, Pfeifer H and Zhdanov S P 1980 in *The Properties and Applications of Zeolites* (London: Chemical Society) p 58
Zimm B H 1956 *J. Chem. Phys.* **24** 269

Index